CHEMOSTRATIGRAPHY OF JURASSIC–CRETACEOUS ITALIAN CARBONATE PLATFORMS

A dissertation submitted to the

University of Oxford

for the degree of

Doctor of Philiosophy

Richard Gareth Woodfine

St Edmund Hall

Department of Earth Sciences

Michaelmas Term, 2002

Table of contents

List of Figures

List of Tables

List of Plates

CHEMOSTRATIGRAPHY OF JURASSIC–CRETACEOUS ITALIAN CARBONATE PLATFORMS

A dissertation submitted to the **University of Oxford**
for the degree of **Doctor of Philiosophy**

Richard Gareth Woodfine
St Edmund Hall
Department of Earth Sciences

Michaelmas Term, 2002

Abstract

Samples of shallow-water carbonates were collected from Jurassic and Cretaceous Italian carbonate platforms and subjected to petrographic, diagenetic and chemostratigraphic analyses ($^{87}Sr/^{86}Sr$, $\delta^{13}C_{carb}$, $\delta^{13}C_{org}$, $\delta^{18}O$). In general, the new chemostratigraphic data generated reflect trends established by previous work, some of which has been carried out on biostratigraphically calibrated reference sections.

Consequently, chemostratigraphic correlations ($^{87}Sr/^{86}Sr$, $\delta^{13}C_{carb}$) of isotope profiles taken from platform carbonates with well-dated reference sections have allowed the application of high-resolution dating frameworks to the biostratigraphically poorly constrained carbonate platforms.

The increased resolution in dating of the Italian carbonate platforms has, furthermore allowed a detailed investigation into the facies response of these carbonate platforms to major geological events. In particular, platform responses to oceanic anoxic events and other periods of major perturbation in the global carbon cycle are analysed (early Toarcian, Aalenian–Bajocian, Oxfordian–Tithonian, Valanginian–Hauterivian, Aptian–Albian, Cenomanian–Turonian, Coniacian–Santonian).

Lower Jurassic levels of the Trento Platform record platform devastation in the early Toarcian synchronous with a major negative $\delta^{13}C_{carb}$ excursion, followed by platform recovery synchronous with a pronounced $\delta^{13}C_{carb}$ positive excursion and return to background values. The Campania–Lucania Platform shows negligible response to the oceanographic events of the early Toarcian even though the characteristic carbon-isotope profile is readily identifiable. The Trento Platform drowned at approximately the Aalenian–Bajocian Stage boundary, synchronously with a reproducible negative followed by positive $\delta^{13}C_{carb}$ excursion, whereas the Campania–Lucania Platform underwent a facies transition from oolite to cyclically bedded micrite. The Friuli Platform showed negligible depositional response to the carbon-cycle perturbations of the Kimmeridgian–Tithonian, Valanginian–Hauterivian, Aptian–Albian and Cenomanian–Santonian (as registered in the $\delta^{13}C_{carb}$ record). The Campania–Lucania Platform registered flooding and increased levels of organic-matter preservation coincident with pronounced positive $\delta^{13}C_{carb}$ excursions at Cenomanian–Turonian and Coniacian–Santonian levels.

Observations on the responses of carbonate platforms to oceanographic conditions during periods of global carbon burial lead to the conclusion that temperature excess is a hitherto neglected control on global carbonate accumulation rates.

Extended Abstract

Shallow-water platform carbonates from the Jurassic and Cretaceous of Italy (Trento, Friuli and Campania–Lucania Platforms) were analysed lithologically in the field. Bulk-rock samples were collected at relatively high-frequency intervals throughout the sections studied, and were subjected to petrographic analysis to determine microfacies changes and to assess the extent of diagenetic modification.

Biostratigraphic analyses by previous workers were used where possible to constrain the relative ages of the sections studied (generally derived from long-ranged benthic foraminifera and algae). In general, this biostratigraphic constraint reaches a maximum of stage resolution.

Chemostratigraphic frameworks of each of the three platforms were constructed by analysing the platform-carbonate samples that were collected for the following proxies: $^{87}Sr/^{86}Sr$, $\delta^{13}C_{carb}$, $\delta^{13}C_{org}$, and $\delta^{18}O$. The latter of these was used in conjunction with petrographic analyses to determine the extent of post-depositional diagenesis. $\delta^{13}C_{org}$ data were obtained where wt% TOC levels were high enough to justify analysis, and were used with the aim of verifying trends observed in $\delta^{13}C_{carb}$ data. The relatively broad trends of the platform-carbonate $^{87}Sr/^{86}Sr$ profiles were used in conjunction with the available benthic biostratigraphy to correlate at relatively low resolution with reference sections that are biostratigraphically constrained. This procedure allowed further relatively high-resolution correlation of $\delta^{13}C_{carb}$ profiles. These chemostratigraphic correlations facilitated a higher level of dating constraint to be applied to a number of levels in the platform carbonates (up to ammonite-subzone resolution).

Chemostratigraphic profiles obtained from samples collected from Lower Jurassic levels of the Trento Platform, which has undergone negligible diagenetic modification over the critical Pliensbachian–Aalenian interval, provide locally and globally reproducible isotopic features. In particular, the distinctive early Toarcian (*falciferum* Zone) negative followed by positive $\delta^{13}C$ excursions (a -2 ‰ shift and maximum value of +4.1 ‰ respectively) have been identified in marine (carbonate and organic matter) and terrestrial (organic matter) facies from sections with a global distribution. By detailed correlation of the platform carbonates with biostratigraphically

constrained sections through an epicontinental basin in northern Europe, it has been possible to refine dating of the Trento Platform during the Toarcian Stage up to ammonite-subzone resolution. This accuracy of dating of the carbonate platform has allowed an investigation into the response of the Trento Platform to the early Toarcian Oceanic Anoxic Event (*c.* 183 Ma). The synchroneity between maximum platform devastation, registered in the sedimentary record by a sharp transition to shaly facies, and a 2 ‰ negative $\delta^{13}C_{carb}$ excursion (in the late *semicelatum–falciferum* Subzones) is interpreted to represent a major platform crisis related to elevated sea-surface temperatures derived from methane-hydrate dissociation and subsequent oxidation to CO_2. It is also suggested that elevated marine nutrient levels encouraged the proliferation of filter feeders (particularly siliceous sponges, registered by the presence of spiculitic cherts) at the expense of carbonate producers immediately before and after the period of maximum devastation.

The Campania–Lucania Platform also records the early Toarcian negative followed by positive $\delta^{13}C_{carb}$ excursions (-2.5 ‰ shift and a maximum value of +4.5 ‰ respectively), allowing high-resolution chemostratigraphic correlation to biostratigraphically calibrated reference sections. However, in contrast to the Trento Platform, the sedimentary record does not register significant devastation of carbonate producers but rather a transition from cyclically bedded micritic limestones to oolite. The oolite continued to be deposited from latest Pliensbachian throughout the Toarcian and Aalenian with little interruption. It is therefore suggested that the Campania–Lucania Platform was in a temperature/nutrient 'shadow' during this period, and as a result isolated from the forcing mechanisms that caused the widespread demise of other carbonate platforms at this time.

The Trento Platform drowned at approximately the Aalenian–Bajocian Stage boundary (dated by ammonite biostratigraphy; 174 Ma), and in contrast to the early Toarcian, demise was prolonged, as registered in the sedimentary record by condensed intervals with ferromanganiferous hardgrounds throughout much of the Aalenian. The facies change from shallow-water oolite to the pelagic facies: "Rosso Ammonitico" is also transitional in nature as shown by the presence of ammonites and pink staining below the drowning unconformity and localised ooids and stromatolites above the contact. Therefore, drowning is suggested to have

been a relatively slow process that occurred at relatively shallow depths. Drowning is also coincident with reproducible prolonged negative followed by positive $\delta^{13}C_{carb}$ excursions, as previously identified from Tethyan basins, Scottish belemnites and English terrestrial organic matter. Mechanisms responsible for this carbon-cycle perturbation relate to the release of large volumes of CO_2 from volcanic outgassing (acting over a relatively long period of time). It is therefore believed that drowning of the Trento Platform is related to greenhouse conditions at this time: relatively shallow-water drowning due to eutrophication of surface waters, and/or elevated temperatures.

The Campania–Lucania Platform records an extremely pronounced (4 ‰) negative $\delta^{13}C_{carb}$ excursion at the Aalenian–Bajocian Stage boundary but, in contrast to the Trento Platform, does not drown. However, the platform does record a facies change from massive oolite to cyclically bedded micritic limestone that is peritidal in nature (indicative of relative sea-level fall). It therefore appears that the Campania–Lucania Platform was shielded from the degradative mechanisms that were affecting platform growth on the Trento Platform at this time.

The Friuli Platform registers distinctive $^{87}Sr/^{86}Sr$ and $\delta^{13}C_{carb}$ trends correlatable with reproducible isotope signals determined from globally distributed reference sections. In particular, chemostratigraphic correlation of $\delta^{13}C_{carb}$ signals during the Kimmeridgian–Tithonian, Valanginian–Hauterivian, Aptian–Albian and Cenomanian–Santonian with reference sections that have been biostratigraphically calibrated has improved the dating constraint of the carbonate platform up to ammonite/nannofossil/planktonic foraminiferal-zone resolution. However, platform growth appears to have been relatively unaffected by any of these carbon-cycle perturbations, although the introduction of non-reproducible/non-correlatable $\delta^{13}C_{carb}$ signals between the early Aptian and Cenomanian Stages signify that either the carbonate platform had restricted connection to open-ocean during that interval or that there has been post-depositional modification of the primary isotope signal. It is therefore suggested that the Friuli Platform was sheltered from the major oceanographic and/or atmospheric events of the Late Jurassic–Tertiary period.

Previous biostratigraphic analysis suggests that the Raia del Pedale section through the Campania–Lucania Platform records facies that ranges from Cenomanian–Santonian in age. Chemostratigraphic correlation of $^{87}Sr/^{86}Sr$ and $\delta^{13}C_{carb}$ with reference sections that have been biostratigraphically calibrated verifies this evidence, because isotope profiles of the carbonate platform register a distinctive shift to less radiogenic $^{87}Sr/^{86}Sr$ values coincident with a pronounced positive $\delta^{13}C_{carb}$ excursion (maximum value of +4.9 ‰) at the Cenomanian–Turonian Stage boundary. Furthermore, during the Coniacian–Santonian, $\delta^{13}C_{carb}$ values rise into another less pronounced but broad positive $\delta^{13}C_{carb}$ excursion. Coincident with these positive $\delta^{13}C_{carb}$ excursions at the Cenomanian–Turonian and Coniacian–Santonian levels is lithological evidence for platform flooding (presence of planktonic foraminifera) and elevated levels of preserved organic matter, which makes the facies similar in character to the previously described Sveti Duh Formation of the Dinaric Platform of Croatia. That the Campania–Lucania and Dinaric Platforms record the presence of potentially nutrient-rich/de-oxygenated waters without any noticeable effect on platform growth indicates that these platforms were not in a nutrient 'shadow', and yet suffered little adverse affect. Because many other carbonate platforms are recorded as having drowned at this time, it is conceivable that the relative 'success' of the Campania–Lucania and Dinaric Platforms is attributable to being shielded from the adverse effects of another known factor responsible for global devastation of carbonate producers: sea-surface temperature rise.

In summary: the historically accepted hypothesis regarding the effects of elevated marine nutrient levels on the growth of Jurassic–Cretaceous Italian carbonate platforms is investigated. Further discussion analyzes the possible influence of episodic elevated sea-surface temperatures on ancient carbonate-platform systems, and comparisons are made to modern Global Coral Bleaching Events, which are related to El Niño Southern Oscillations.

Acknowledgements

For academic support beyond the call of duty, I would like to thank my supervisor, Hugh Jenkyns. Additional aid and discussion were offered over the three years of study by Massimo Sarti, Steve Hesselbo, Stuart Robinson, Darren Gröcke, Carolyn Williams, Helen Morgans-Bell, and Sarah-Jane Schmidt. For funding of all work undertaken over the three-year course of this D.Phil., I am thankful for the NERC Grant GT04/1999/ES/0209, and Enterprise Oil Italiana Grant MDG98.

For invaluable assistance in the field, I am indebted primarily to Francesco Baroncini, and also in no small amount to John Hillier, Janine Machin and the Bonetti family.

Labwork, all of which was carried out in the Age and Isotope Lab, University of Oxford, could not have been carried out without the support of John Arden, Steve Wyatt, Julie Cartlidge, Richard Corfield, Owen Green, Roy Goodwin, Jeremy Hyde, Phil Jackson, Steve Baker and Richard McAvoy.

Finally, I would not have been able to complete this thesis without all those friends and family that have helped me to preserve a modicum of perspective during the last three years. In particular, special thanks are extended to Spike, Ivan, Stu, Geoff, José, Harilaos, Jim TB, Sam and Tom, and many other friends in Vincent's and Teddy Hall that have excelled in distracting me from my work. For her patience, friendship and love through all things, I thank Janine. And for inconquerable support, love and understanding over 24 years I must thank my parents, two brothers and grandparents. This thesis is dedicated to them.

Chapter 1: Introduction

Chapter 1: Introduction

1.1 Aims

The first aim of this project is to create chemostratigraphic frameworks (using strontium-, carbon- and oxygen-isotopes) for selected sections of Mesozoic, shallow-water carbonate-platform rock successions in Italy. To then correlate these new chemostratigraphic profiles against the relevant deeper-water facies reference curves obtained by previous workers (from biostatigraphically calibrated sections) refines the dating of shallow-water carbonates (up to ammonite sub-zones). These carbonates have otherwise proved notoriously difficult to date and correlate precisely because the contained long-lived, benthonic foraminifera and algae have long ranges and are environmentally sensitive (e.g. Chiocchini *et al.*, 1994). ***Chapters 2, 3, and 4*** are dedicated to describing the facies and isotope profiles of the sections studied from the Trento, Friuli, and Southern Apennine platforms respectively.

With chemostratigraphic profiles in place, the second aim of this project was to relate the detailed facies analyses of the sections to perturbations in the global carbon-, oxygen-, and strontium-cycles, which are registered by marked shifts in values within the isotopic profiles that were produced. After regional and global correlations of the isotope profiles were made (in ***Chapter 5***), observations of these platform-isotope relationships were recorded in ***Chapter 6***. Facies analyses of the sections have purposely focused on intervals when phenomena known as Oceanic Anoxic Events (OAE's), first described by Schlanger and Jenkyns (1976), are known to have occurred. The particular responses of the shallow-water carbonate platforms subjected to these major perturbations in the global carbon cycle are described in ***6.2***.

1.2 Evolution of the Tethyan carbonate platforms

The Triassic evolution of Tethyan carbonate platforms can be very broadly dealt with at this early stage, because the regional Tethyan setting was generally very uniform until the latest Triassic–Early Jurassic when environmental stresses acted with varying local affect on the often

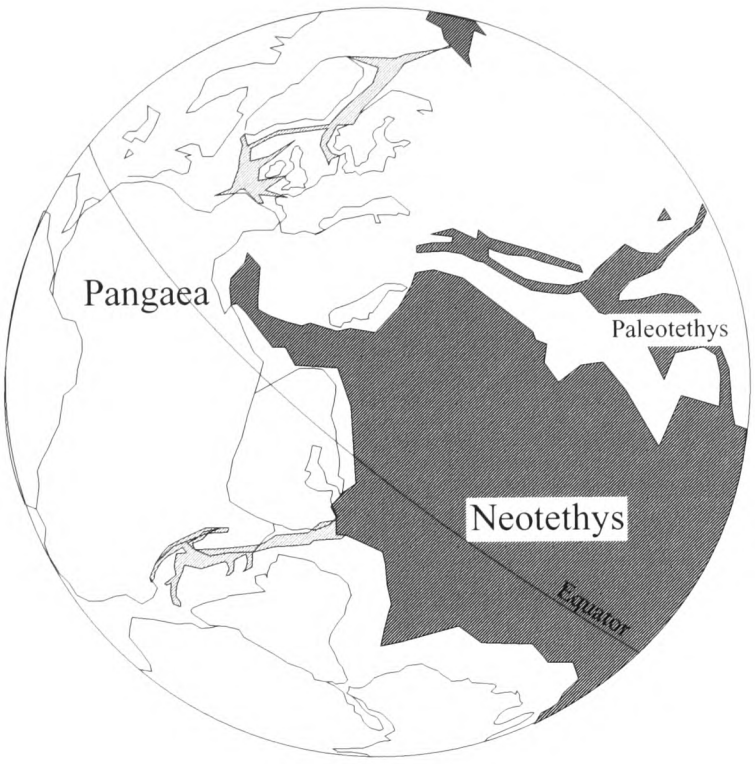

Early Norian

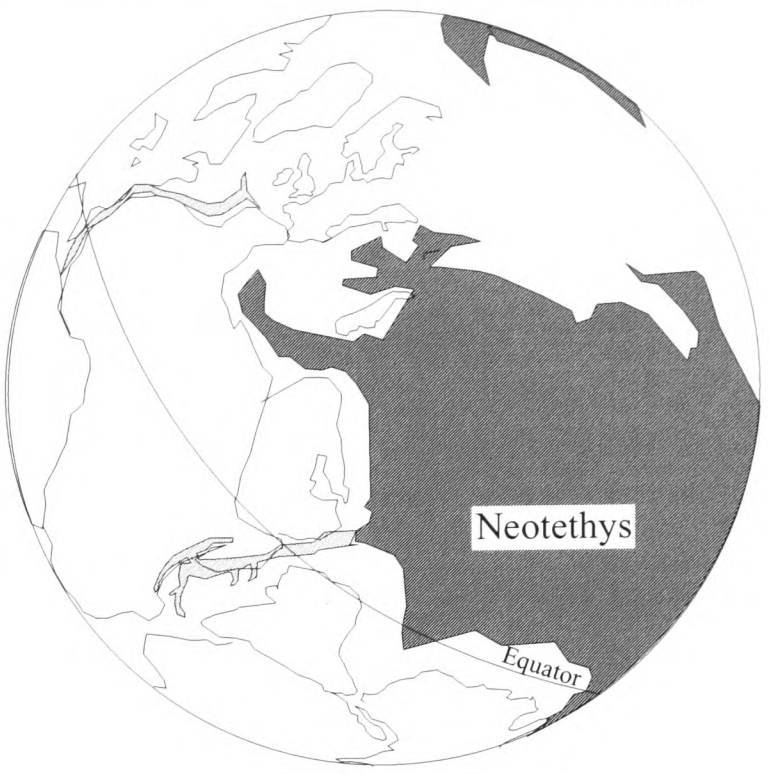

Sinemurian

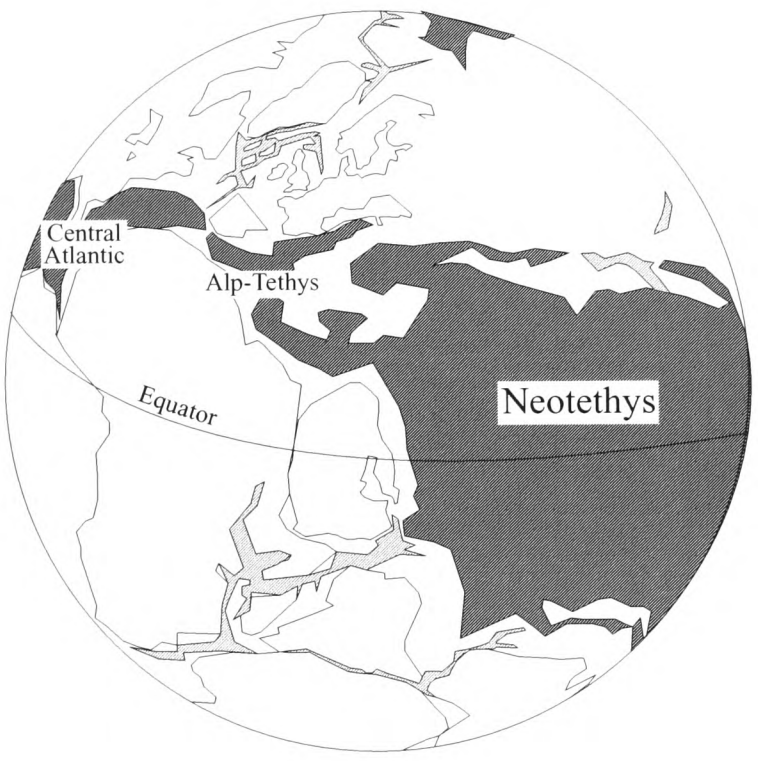

Oxfordian

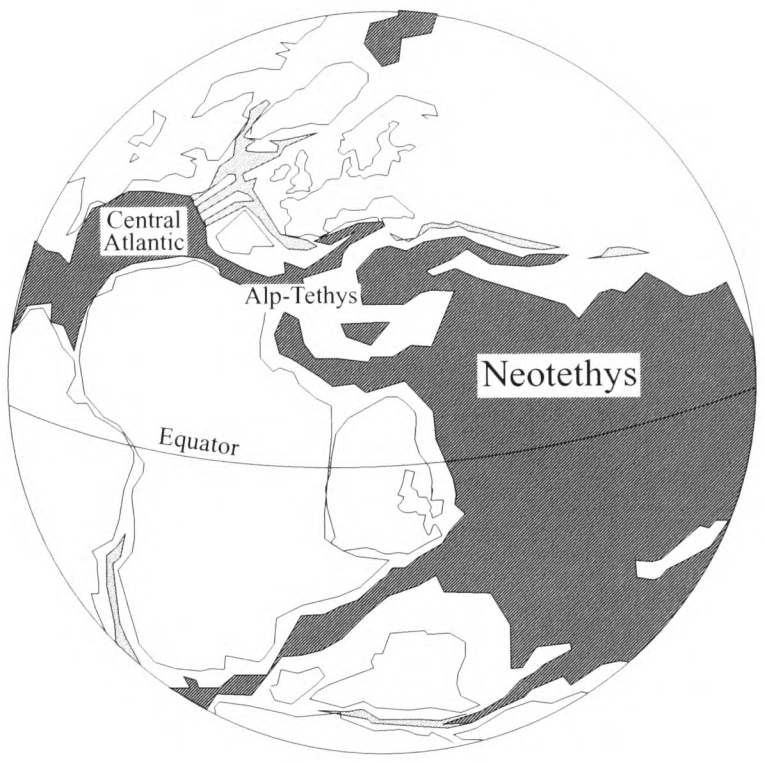

Aptian

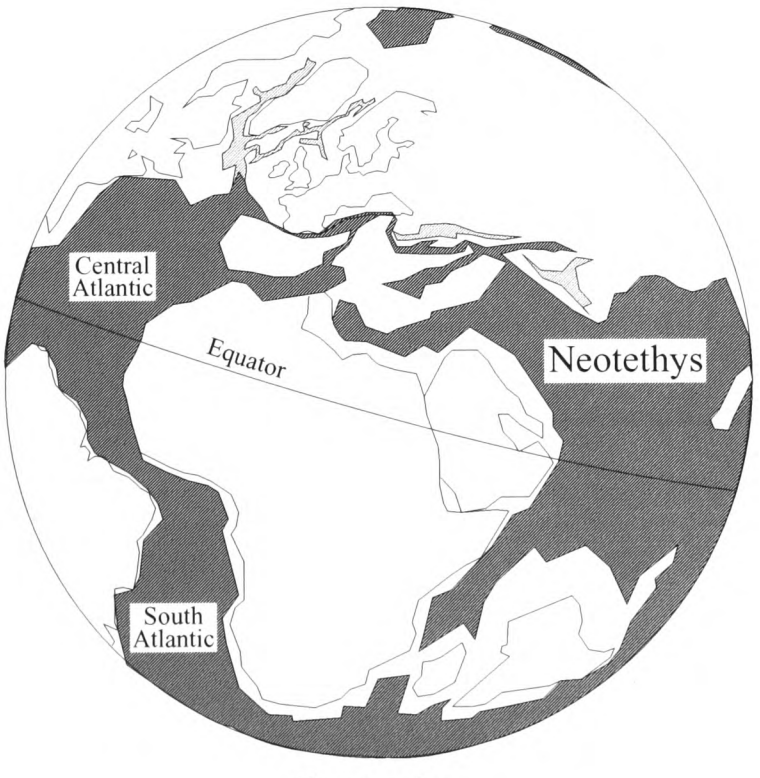

Santonian

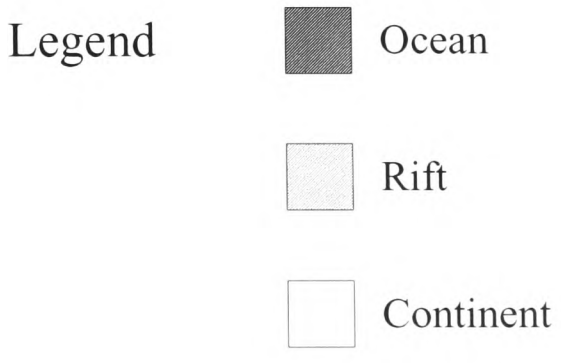

Figure 1.i. Triassic to Late Cretaceous evolution of Tethys and the continental break-up of Pangaea. Simplified after Stampfli and Borel (2002).

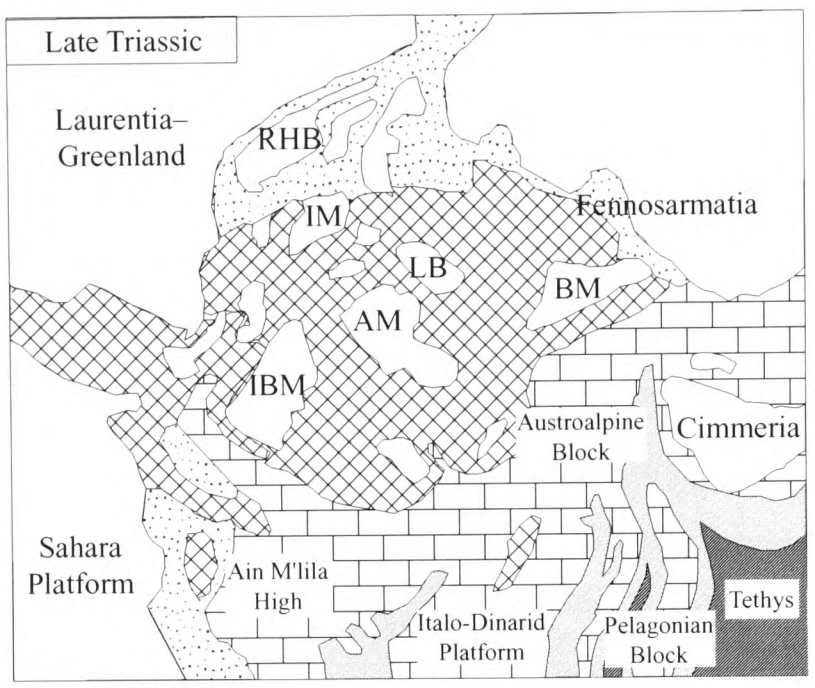

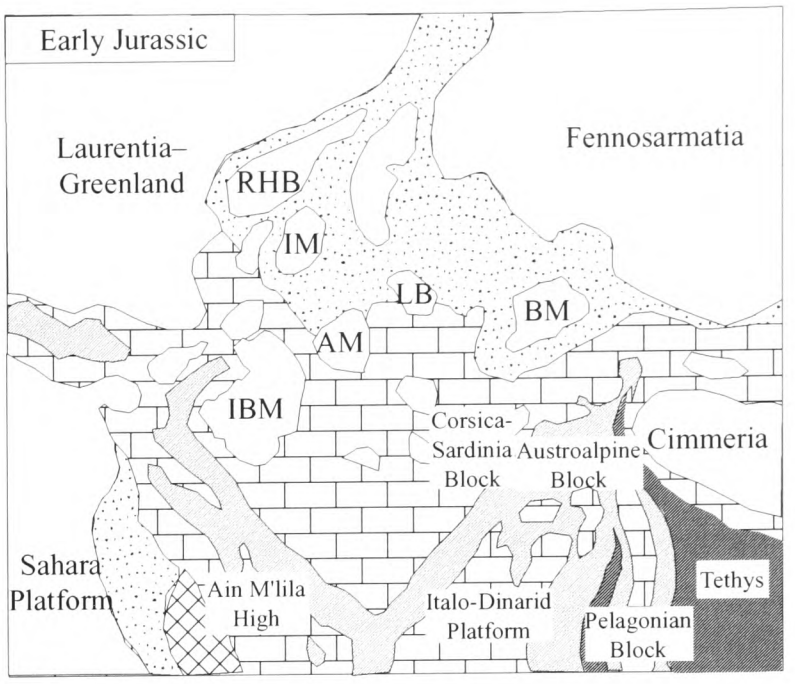

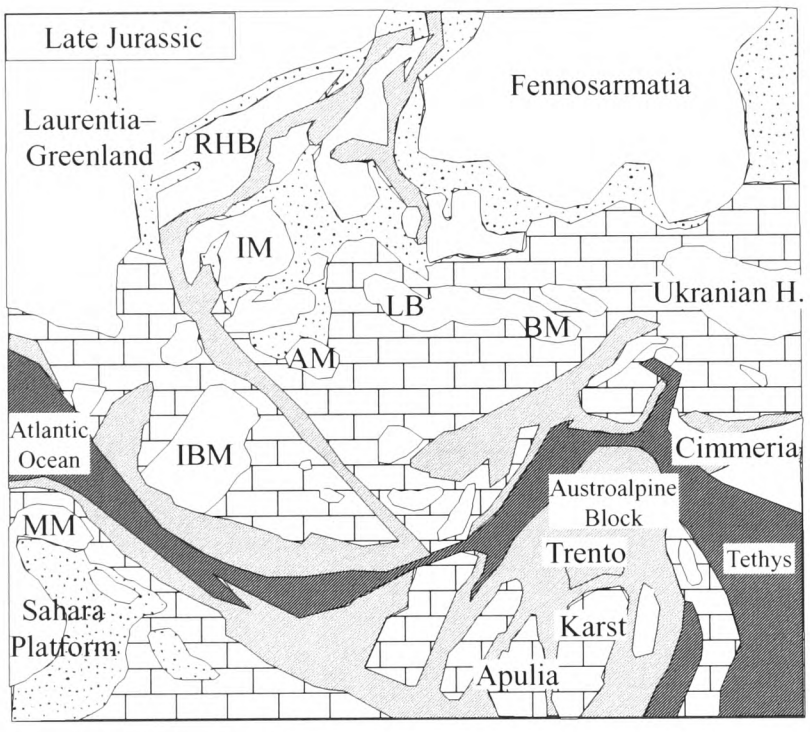

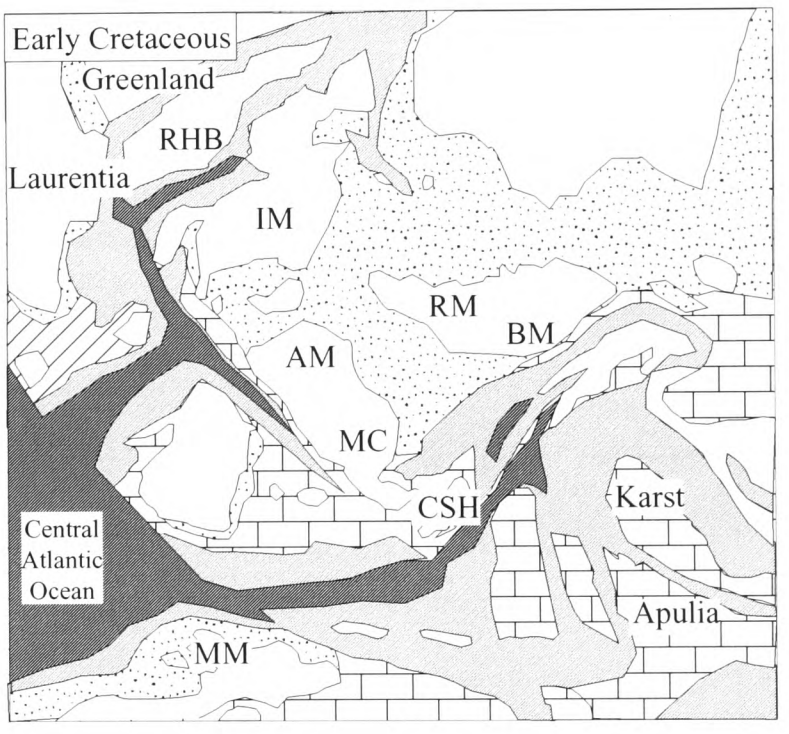

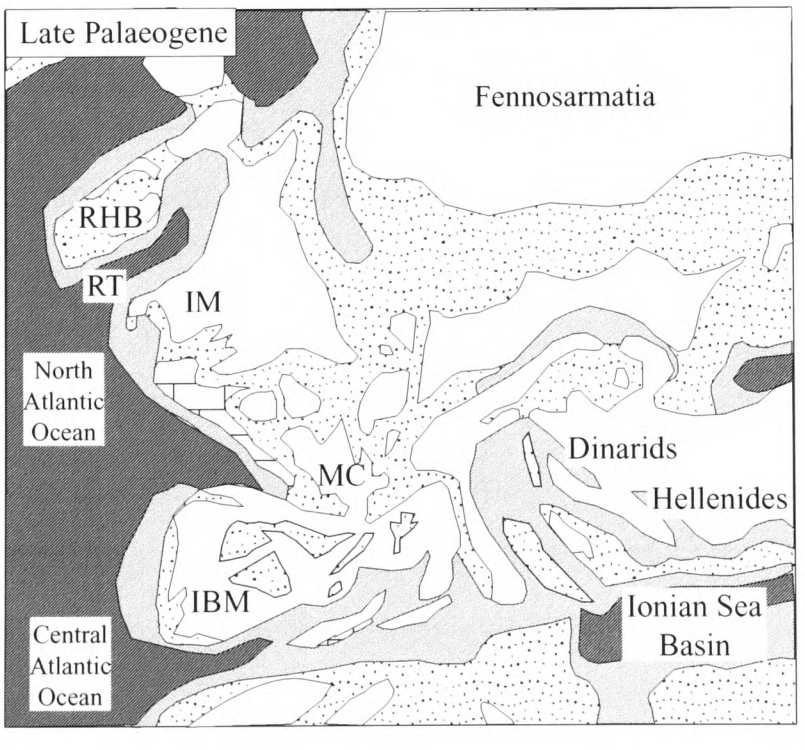

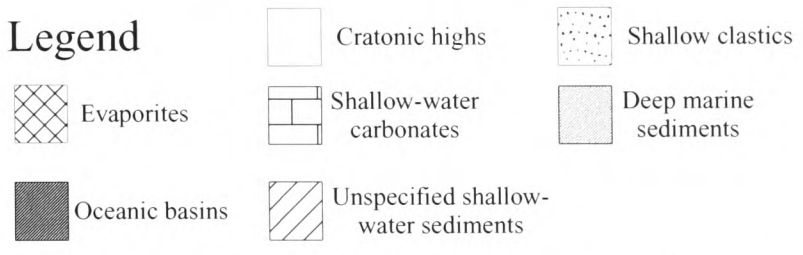

Figure 1.ii. Triassic to Tertiary evolution of southwestern Tethys. AM = Armorican Massif; BM = Bohemian Massif; CSH = Corsica–Sardinia High; IBM = Iberian Meseta; IM = Irish Massif; LB = London–Brabant Massif; MC = Massif Central High; MM = Morocco Meseta; RHB = Rockall–Hatton Bank; RM = Rhenish Massif; RT = Rockall Trough. Early Cretaceous includes Apulia–Africa land-link (Bosellini, 2002) Modified after Dercourt *et al.* (1986) and Ziegler (1988, 1990).

Jadoul *et al.*, 1992; Iannace and Frisia, 1994; Balog, 1995; Balog *et al.*, 1999). In this case it has generally been accepted that stable and long-lived semi-arid conditions acting on a wide pericontinental platform from the Late Carnian and through the entire Norian, with possible elevated sea-water Mg/Ca ratios (due to relatively low hydrothermal activity, and thus a restricted Mg-sink), fresh-water input and restricted ocean circulation, led to the dolomite precipitation stability required for such vast thicknesses of carbonate with this mineralogy to accumulate (Figure 1.iii; Stefani and Burchell, 1989; Iannace and Frisia, 1994).

However, the Rhaetian represents a transitional stage in the prevailing conditions before the Early Jurassic, which was a time when fragmented platforms accumulated thick calcitic carbonate sequences separated by deeper water basins (Gaetani, 1975; Winterer and Bosellini, 1981; Iannace and Frisia, 1994). D'Argenio (1974) was the first to hypothesise a causal link between climatic change (from arid to wet/humid) and the demise of dolomite formation in Tethys during the Rhaetian. Perhaps of even greater significance (and potentially a cause for climate change) is the sudden increase in tectonic activity (Upper Norian – Rhaetian) related to the initiation of rifting prior to the break-up of Pangea (Figure 1.ii; e.g. Bernoulli and Laubscher, 1972; Dewey *et al.*, 1973; Winterer and Bosellini, 1981; Iannace and Frisia, 1994), and the recently highlighted latest Triassic formation (200 Ma) of the Central Atlantic Magmatic Province (C.A.M.P.; McHone, 1996; Marzoli *et al.*, 1999; Pàlfy *et al.*, 2000a; Hesselbo *et al.*, 2002). The end-Triassic mass-extinction has also been related to this increase in volcanic activity and an observed major perturbation in the global carbon-cycle (as registered by the presence of major anomalies in the shallow-marine and atmospheric stable carbon-isotope records across the Triassic–Jurassic boundary (Pàlfy *et al.*, 2001; Ward *et al.*, 2001; Hesselbo *et al.*, 2002)). The same boundary has also been assigned as marking a worldwide transgression (Hallam and El Shaarawy, 1982; Hallam, 1997); the time at which the Arctic Ocean forged a link with Tethys significantly altering Tethyan oceanic circulation (through the Rockall–Faeroe Trough; Wicher, 1938; Ziegler, 1988; Cuif and Gautret, 1991; Iannace and Frisia, 1994); and a transition from aragonite seas to calcite seas: extremely significant if the dolomite of the Dolomia Principale is thought to form after the early replacement of less stable aragonite (Sandberg, 1983). All of the above factors present a significant overhaul of the relatively long-lived stable conditions of the pre-Rhaetian. Tectonic, palaeoenvironmental and

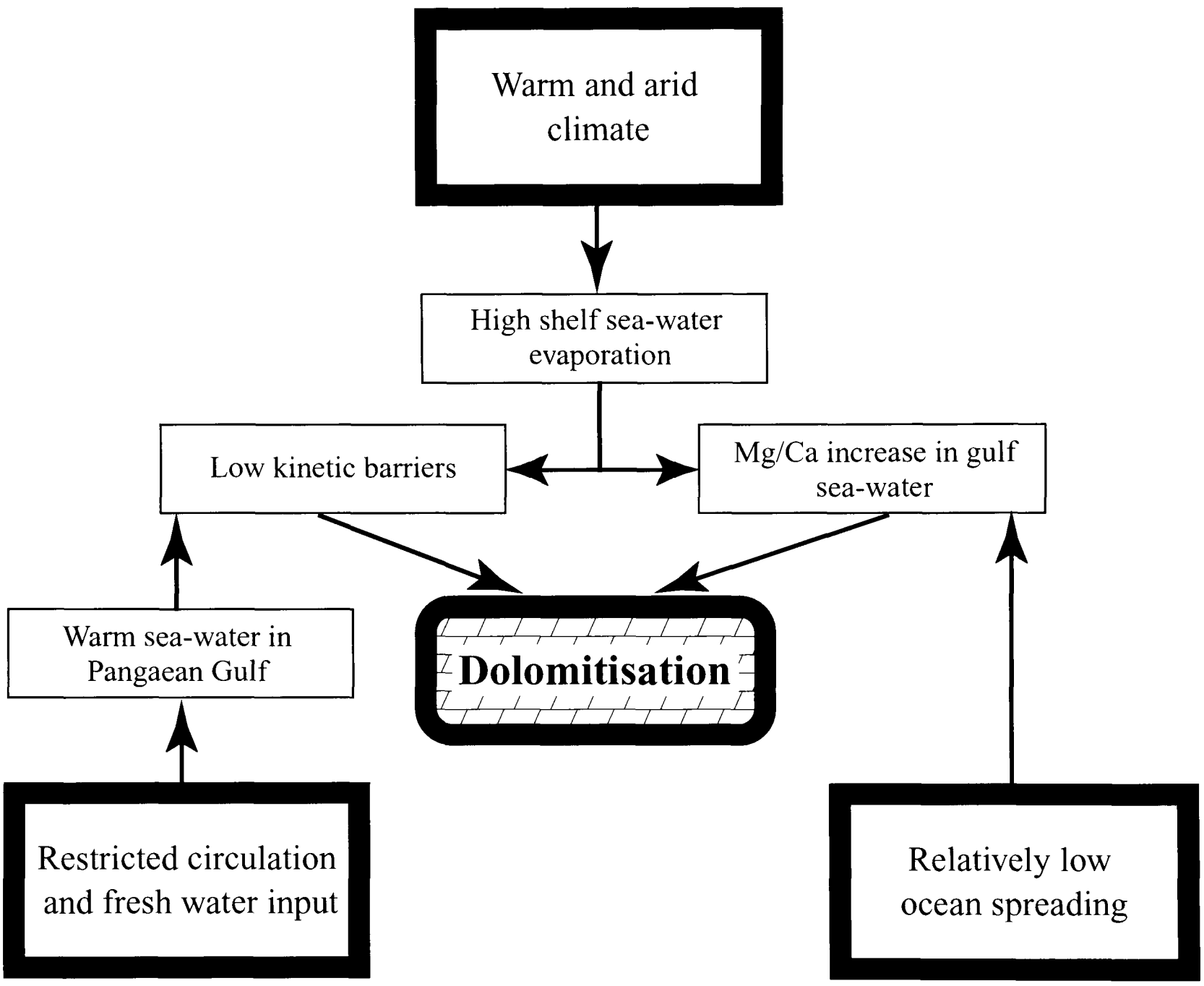

Figure 1.iii. Dolomitisation model for the vast Tethyan continental shelf build-up of platform carbonate during the Triassic. After Iannace and Frisia, 1994.

palaeoclimatic disturbances continued throughout the Early Jurassic, resulting in a very different and relatively complex Tethyan geological setting with acute differences in localised platform evolution, contrasting with the regional uniformity evident in the Alpine–Mediterranean Triassic.

Extensive Early Jurassic rifting related to the opening of the Central Atlantic Ocean resulted in the regional flooding of the Triassic shelf margins (from western Tethys to the Middle East, Oman, Somalia and Madasgascar; Bosellini, 1989; Stampfli and Borel, 2002). The extensional tectonic regime also led to the break-up of the uniform Triassic shelf platforms, and block-faulting (listric) and differential subsidence led to the prevalence of a half-graben tectonic setting as carbonate-calcitic platform-capped subsiding blocks failed to keep up with relative sea-level rise (Figures 1.i, 1.ii and 1.iv; Bernoulli and Jenkyns, 1974; Winterer and Bosellini, 1981). Bernoulli and Jenkyns (1974), and references therein (and later Davey, 1994), detail the drowning of Tethyan carbonate platforms in Lombardy (Italy), the Eastern Alps (Austria and Germany), the Bakony Mountains (Hungary) and the High-Tatric Zone (Poland and the former Czechoslovakia) at the Triassic–Jurassic boundary (Figure 1.v). The majority of the remaining Alpine–Mediterranean carbonate platforms that drowned in the Jurassic, did so at the Pliensbachian–Toarcian boundary, including the Subbetic (Spain), Northern Rif (Morocco), High Atlas (Morocco), Tunisian, western Sicily (Italy), Marche–Umbria–Toscana (Italy), Trento (Italy; 'partial drowning'), and Ionian Zone (Greece) platforms (Figure 1.v). When ecological conditions are favourable, shallow-water carbonate platforms can produce more than enough carbonate to keep up with rates of long-term, tectonically or eustatically forced sea-level changes (Schlager, 1981). Therefore, it is widely accepted that platform drowning occurs at times when ecological conditions are unfavourable and sea-level changes are very rapid (e.g. Schlager, 1981; Grigg, 1982; Hallock and Schlager, 1986; Bosellini, 1989; Föllmi *et al.*, 1994; Weissert *et al.*, 1998; Wilson *et al.*, 1998). Presumably one or both of these mechanisms applied for much of Tethys at the Triassic–Jurassic and Pliensbachian–Toarcian boundaries.

There are isolated examples of Tethyan carbonate platforms that escaped Late Triassic – Early Jurassic drowning (largely in the peri-Adriatic region; Bernoulli and Jenkyns, 1974). Notable examples include the Trento Platform (Italy), which survived until the

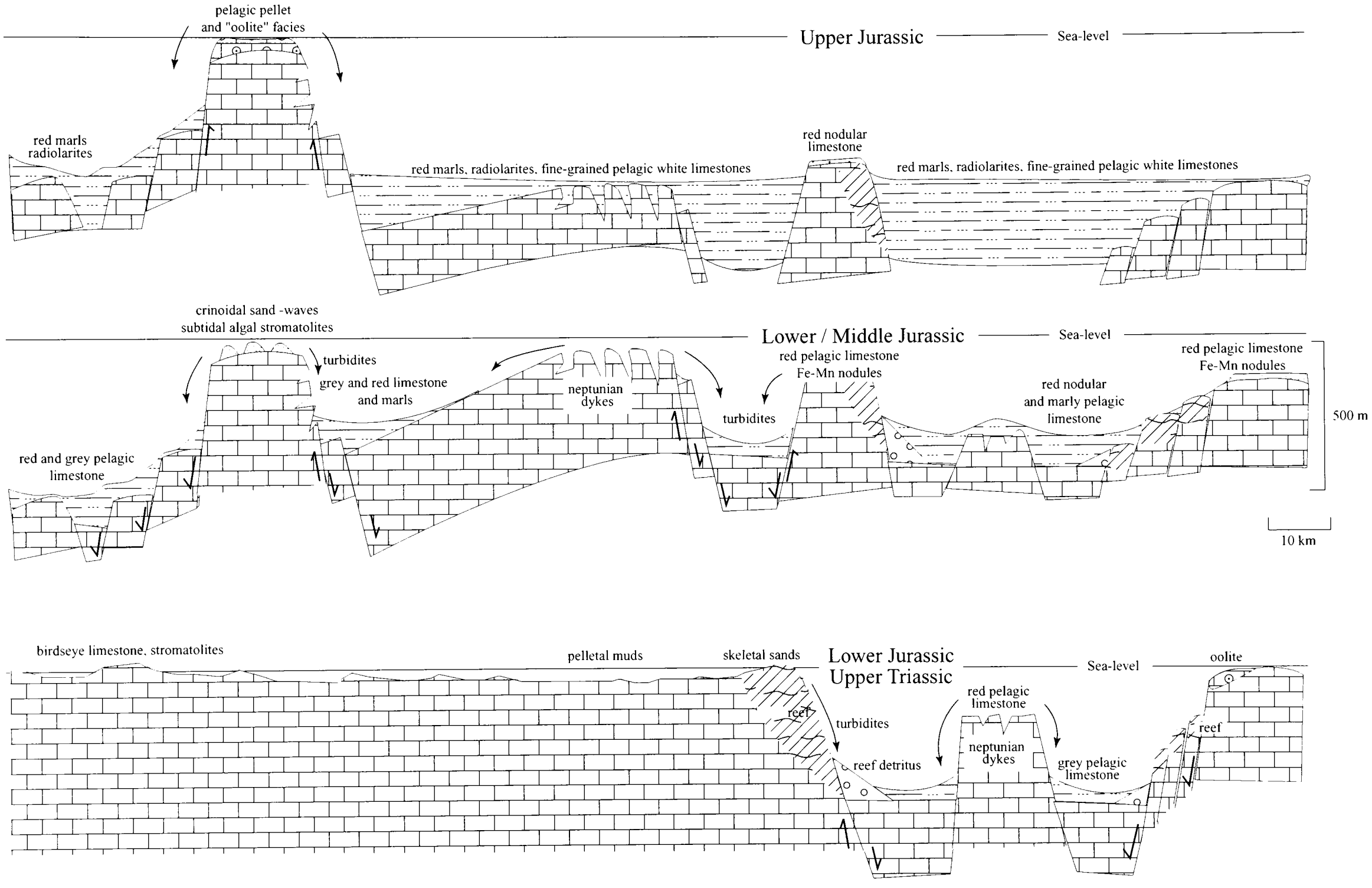

Figure 1.iv. Typical Jurassic evolution of southern Tethys margin carbonate platforms. Platforms in other areas continued to flourish in the Jurassic. Modified after Bernoulli and Jenkyns, 1974.

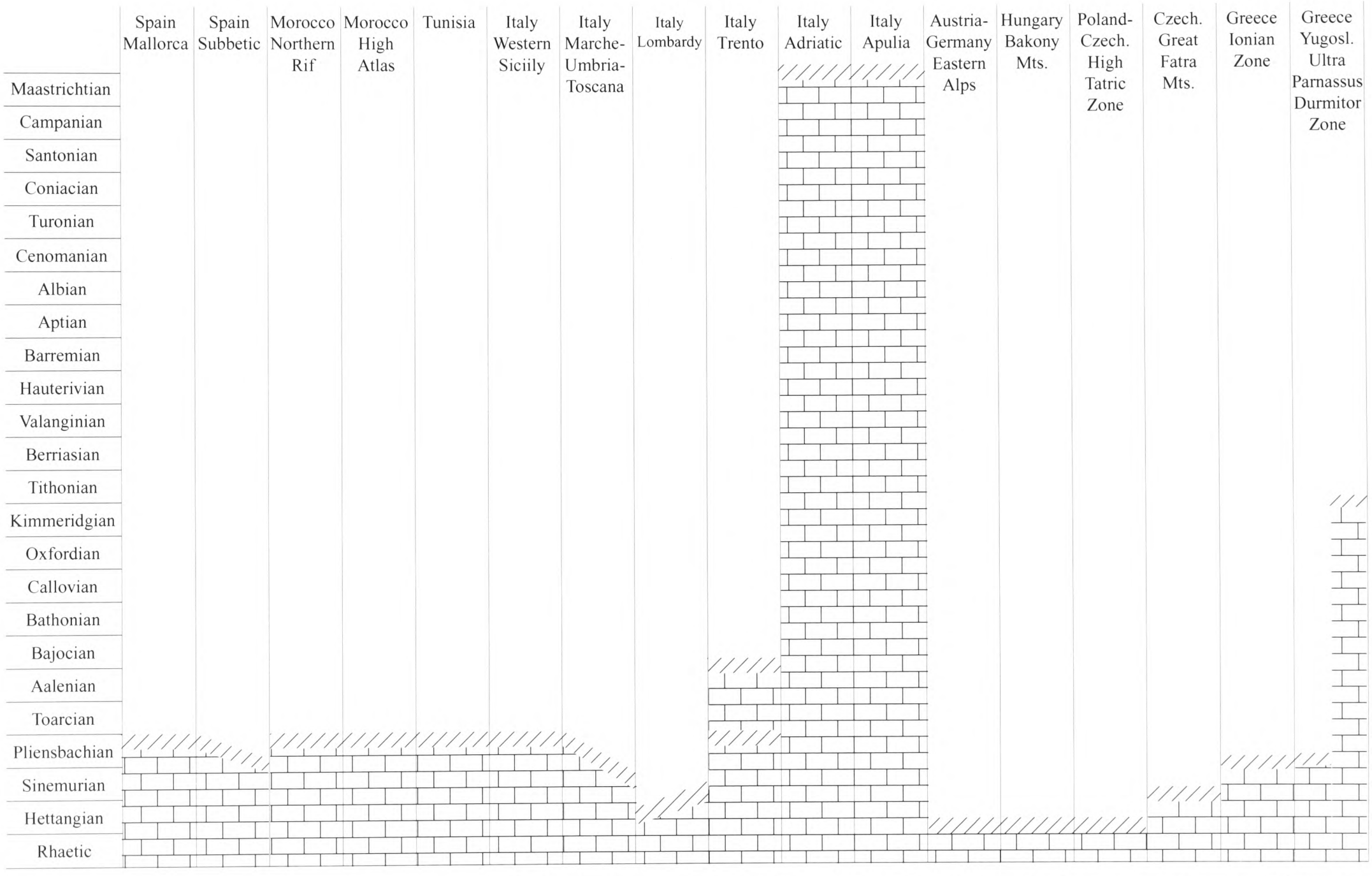

Figure 1.v. The drowning events that disrupted Tethyan carbonate platforms in the Mesozoic. In particular, the Triassic–Jurassic, Pliensbachian–Toarcian and Late Cretaceous–Early Tertiary boundaries were periods that resulted in widespread platform demise. Note the Trento Platform survived drowning at the Pliensbachian–Toarcian boundary, but fianlly succumbed in the Late Aalenian (Sturani, 1964). Modified after Bernoulli and Jenkyns, 1974, and Davey, 1994.

Aalenian–Bajocian boundary; the Urgonian Provence platform which withstood final drowning until the early Aptian; and the peri-Adriatic and Friuli carbonate platforms which persisted until the Tertiary (Figure 1.ii; Aubouin, 1963; Sturani, 1964; Cuvillier *et al.*, 1968; D'Argenio *et al.*, 1971; Bernoulli and Jenkyns, 1974; Gaetani, 1975; Winterer and Bosellini, 1981; Jenkyns, 1991; Davey, 1994). Jurassic and Cretaceous carbonate platform drowning (particularly in the Pliensbachian–Toarcian, Aalenian–Bajocian, Kimmeridgian–Tithonian, Valanginian–Hauterivian, early Aptian, and Cenomanian–Turonian) typically occurred at times associated with some or all of the following globally extensive characteristics: elevated organic-carbon burial (associated with high marine productivity), relatively high rates of oceanic spreading, high levels of volcanic activity, high pCO_2, elevated palaeotemperature, high eustatic sea-level, elevated sea-water nutrient levels, suspected methane dissociation events, and relatively high rates of continental weathering and run-off (e.g. Schlanger and Jenkyns, 1976; Scholle and Arthur, 1980; Arthur *et al.*, 1985; Jenkyns, 1985; Schlanger *et al.*, 1987; Arthur *et al.*, 1988; Jenkyns, 1988, 1991; Lini *et al.*, 1992; Gale *et al.*, 1993; Erba, 1994; Föllmi *et al.*, 1994; Jenkyns *et al.*, 1994; Jenkyns, 1996; Weissert and Mohr, 1996; Jenkyns and Clayton, 1997; Menegatti *et al.*, 1998; Weissert *et al.*, 1998; Bartolini *et al.*, 1999; Bartolini and Cecca, 1999; Larson and Erba, 1999; Hesselbo *et al.*, 2000; Jenkyns *et al.*, 2001; Wissler, 2001).

The Paleogene witnessed the ultimate demise of all of the remaining carbonate platforms of the Alpine–Mediterranean region, which had persisted for up to ~150 My (Figure 1.ii; e.g. Aubouin, 1963; Bosellini, 1989; Davey, 1994). Final drowning of the carbonate platforms occurred as a consequence of the Alpine Orogeny, and indeed Alpine influx of sediment was responsible for much of the damage. Bosellini (1989) describes "...[that] platforms were first subaerially exposed, then buried under huge thicknesses of turbidites and finally caught up in the overthrust pile". Tertiary tectonics and the closure of Tethys (as Africa collided with Europe) resulted in the emplacement of thick sequences of Mesozoic shallow-water limestones on the continents, where today's Alpine–Mediterranean outcrop and exposure allow for detailed analysis and diagnosis of platform origin, evolution and death.

1.2.1 The geological evolution of the Adriatic plate

The Trento, Friuli and Southern Apennine (Campania–Lucania specifically) Platforms described in this study are all located in the peri-Adriatic region of southern Europe (Figure 1.vi). The regional geological setting of these platforms is therefore best described in terms of the geological evolution of the Adriatic Plate (Adria) of which they are all part. The "Adria Problem" has been discussed in great detail in the past, predominantly (and controversially) concerning its evolution as either part of the African Plate ("African–Adriatic Promontory") or as an independent tectonic unit (e.g. Argand, 1924; Dercourt, 1972; Dewey *et al.*, 1973; Channell, 1976; Celet, 1977; Laubscher and Bernoulli, 1977; Channell *et al.*, 1979; Manatschal and Bernoulli, 1999; Bernoulli, 2001; Wortmann *et al.*, 2001; Bosellini, *In Press*).

Triassic continental rifting delineated the future Adria which, during the Mesozoic, was situated on the southern margin of the Tethys Ocean in proximity to the African continent to the south (Channell *et al.*, 1979). The relationship between Adria and Africa has been hotly debated over the last eighty years (Figure 1.vii) and the crux of the discussion has rested on the apparently incompatible Mediterranean stratigraphic and palaeomagnetic/seismic records. Recently, Bernoulli (2001) has described convincing evidence from the stratigraphic record that Adria was separated from the North African margin by a deep oceanic basin (Ionian Basin). Relics of a possible Permian–Triassic (Freund *et al.*, 1975; Hsü, 1977) to Cretaceous (Dercourt *et al.*, 1986) seaway are found in central Sicily, the Lagonegro Basin (between Southern Apennine and Apulia Platforms) and the Pindos Basin (Greece; Figure 1.vi), but their relationship to each other is unknown because of disturbance from subsequent compressional tectonics and thrusting in the region. However, interpretation of palaeomagnetic data by Channell *et al.* (1979), results in the description of Adria as a promontory of Africa that has moved in coordination with the African plate since the early Mesozoic. Further seismic data also indicated that thick Mesozoic sedimentary sequences correlated between Adria and Africa are continuous beneath the eastern Mediterranean. More recently, plate-kinematic modelling by Wortmann *et al.* (2001) suggests that independent relative movements of Africa and Adria are not necessary to satisfy both the palaeomagnetic and stratigraphic records. Bosellini (*In Press*)

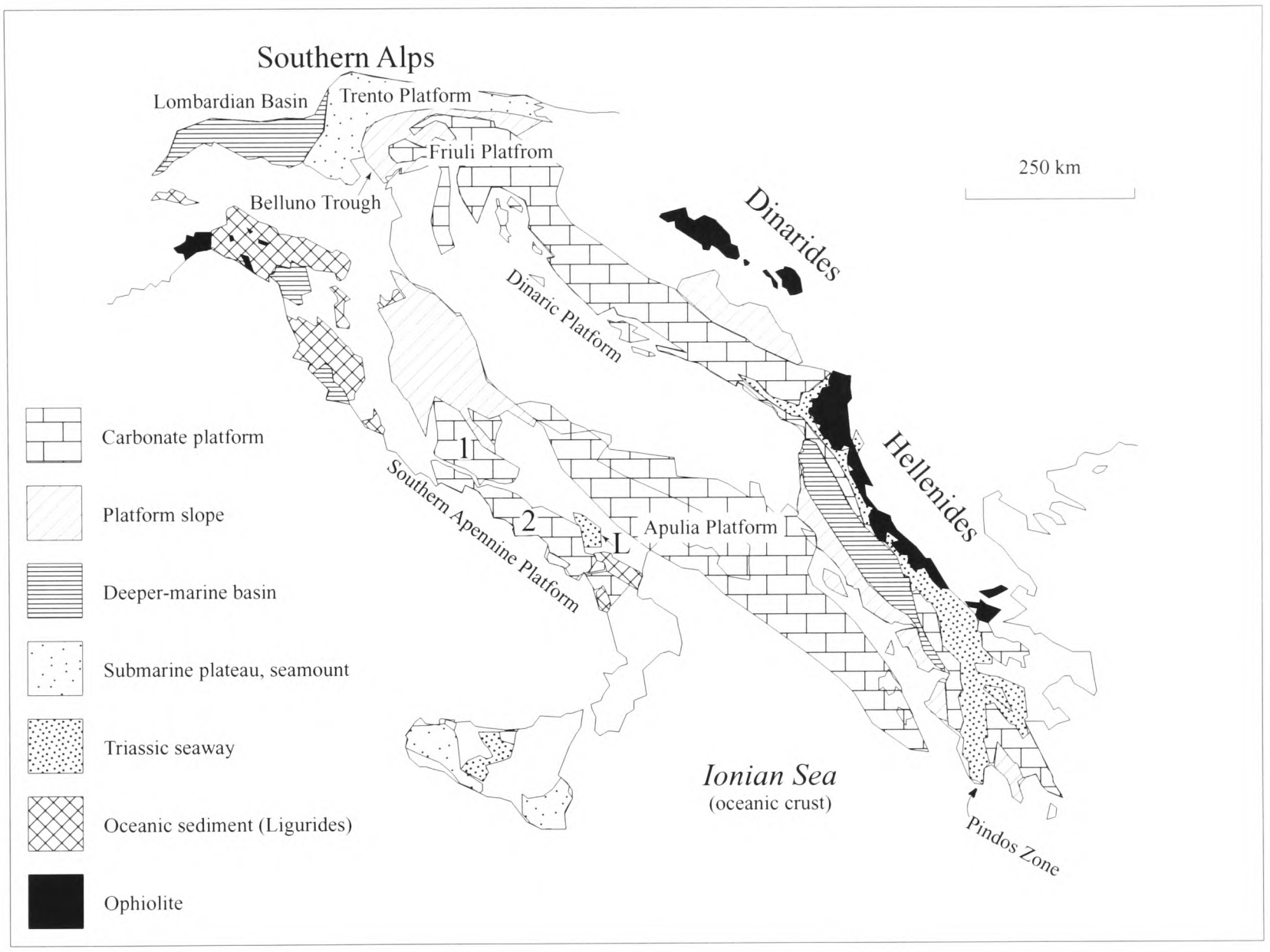

Figure 1.vi. The tectonic units of the peri-Adriatic region and their Late Jurassic depositional settings. 1 = Abbruzzi–Campania Platform; 2 = Campania–Lucania Platform; L = Lagonegro Basin. Modified after Bernoulli (2001).

A

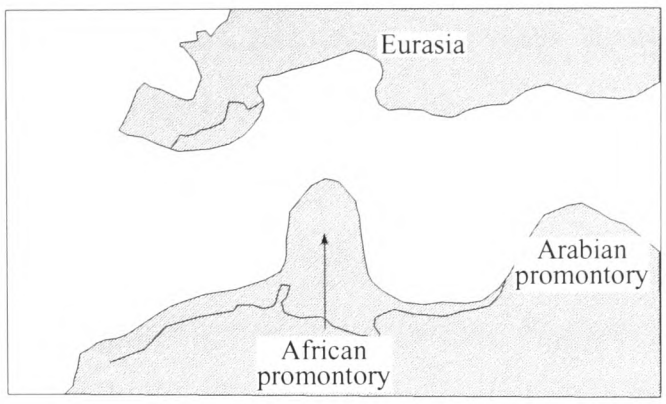

B

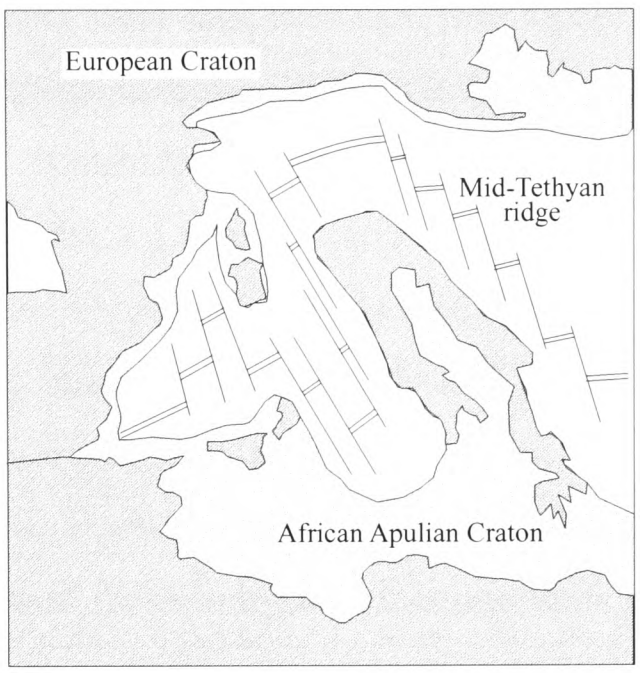

C

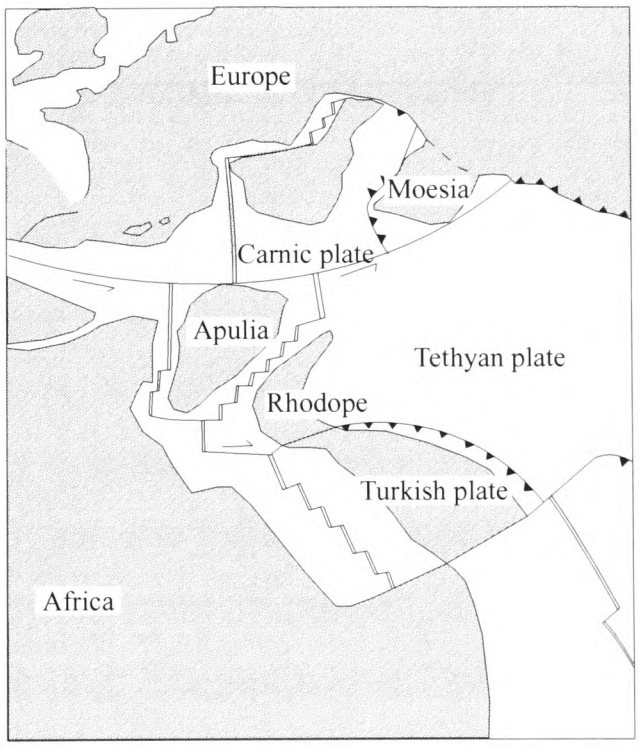

Figure 1.vii. A selection of structural-evolutionary models of the Tethys region focussing on the specific palaeogeographical dynamics of the peri-Adriatic area. Modified after Channell *et al.* (1979). **A** Argand (1924) suggested that Adria acted as a promontory of Africa and that on collision with Europe formed the Alpine foldbelt (Late Jurassic palaeogeography shown). **B** Dercourt (1972) extended the Argand (1924) perspective when he suggested that Adria moved as part of the African plate. **C** A very different viewpoint is that put forward on the basis of tectonics by Dewey *et al.* (1973): the Adriatic region was divided into two distinct plates (Carnic and Rhodope), which were both separated from Africa by oceanic crust since the Triassic.

has also suggested that the discovery of Cretaceous dinosaur footprints on the Apulia platform necessitate a land link from Adria to Africa at this time.

The Adria Problem remains unresolved but of more consequence to this study is the Adriatic intra-plate tectonic configuration and evolution. Figure 1.vi illustrates a general Late Jurassic geological setting for the tectonic units that together comprise the Adriatic Plate. The north Adria (now Southern Alps), west–east transition from open-marine basin (Lombardian) to offshore plateau (Trento Platform in Early–Mid Jurassic) to narrow dividing basin (Belluno Trough) and finally to 'true' continental platform (Friuli–Dinaric Platform) is apparent. The separation of the internal Campania–Lucania Platform (i.e. open-marine Tethys Ocean to the West) from the more external Abruzzi–Campania and Apulia Platforms by the Molise and Lagonegro Basins (remnants now found to north and south of the Southern Apennines respectively) can also be observed. This study focuses on sections located on the western (internal) margins of the Trento, Friuli and the Southern Apennine Platforms, and more detailed specific evolutionary histories of these individual tectonic units are outlined in ***Chapters 2, 3*** and ***4*** respectively.

1.3 Background strontium-isotope stratigraphy

Since Wickman (1948) predicted that sea-water strontium-isotopes (Sr-isotopes) increased linearly with time due to the decay of ^{87}Rb on the continents, the application of Sr-isotopes for age determination of carbonates has been utilised (albeit with a modified perspective from Wickman's original hypothesis). Burke *et al.* (1982) produced the first extensive and coherent Phanerozoic sea-water Sr-isotope curve (Cambrian–Holocene and taken from marine carbonates, phosphates and evaporites), and this has been built up in increasing resolution and precision since (e.g. Koepnick *et al.*, 1990; Jones *et al.*, 1994a; Jones *et al.*, 1994b; Veizer *et al.*, 2000; Gröcke, 2001; Jones and Jenkyns, 2001).

Modern Sr-isotope stratigraphy is based on three founding assumptions (Burke *et al.*, 1982; Palmer and Elderfield, 1985):

i) The Sr-isotope ratio of the oceans is homogenous at any one time as a result of the long residence time of strontium (2-4 Ma; Hodell *et al.*, 1989; Hodell *et al.*, 1990) and the relatively rapid mixing time of the oceans (~1-2 ka; Broecker and Peng, 1982)

ii) Sr-isotope ratios of the oceans have varied systematically with time through the Phanerozoic

iii) Carbonates precipitate strontium from sea-water in their lattice in the same isotopic ratio as that of the sea-water from which it is derived (i.e. there is no fractionation)

The two primary sources of strontium to the oceans are from:

i) fluvial inputs of continental, radiogenic strontium ($^{87}Sr/^{86}Sr \approx 0.7119$; Palmer and Edmond, 1989) derived from the decay of ^{87}Rb

ii) non-radiogenic strontium ($^{87}Sr/^{86}Sr \approx 0.7035$; Palmer and Elderfield, 1985) supplied to the ocean reservoir from the depleted upper mantle along ocean-ridges by hydrothermal processes and the submarine and continental weathering of basalts.

Buffering the oceanic balance of these two "end-member" contributions is the release into the system of strontium from dissolution or recrystallisation of ancient carbonates ($^{87}Sr/^{86}Sr \approx$ 0.707-0.709; Elderfield and Gieskes, 1982).

The primary Sr-isotope ratios of pristine Phanerozoic carbonates and present-day ocean-waters ($^{87}Sr/^{86}Sr \approx 0.7092$) are a result of the changing balance of these inputs with the progression of time. A simplified summary of the theory behind strontium-isotope stratigraphy is presented in Figure 1.viii.

1.3.1 Diagenetic considerations

Jones (1992) summarises the affect of carbonate diagenesis on strontium-isotope ratios as tending to increase from primary values due mainly to interactions with waters that have: 1) leached strontium with "continental" isotope-ratios from terrestrial rocks (Kastner *et al.*, 1990);

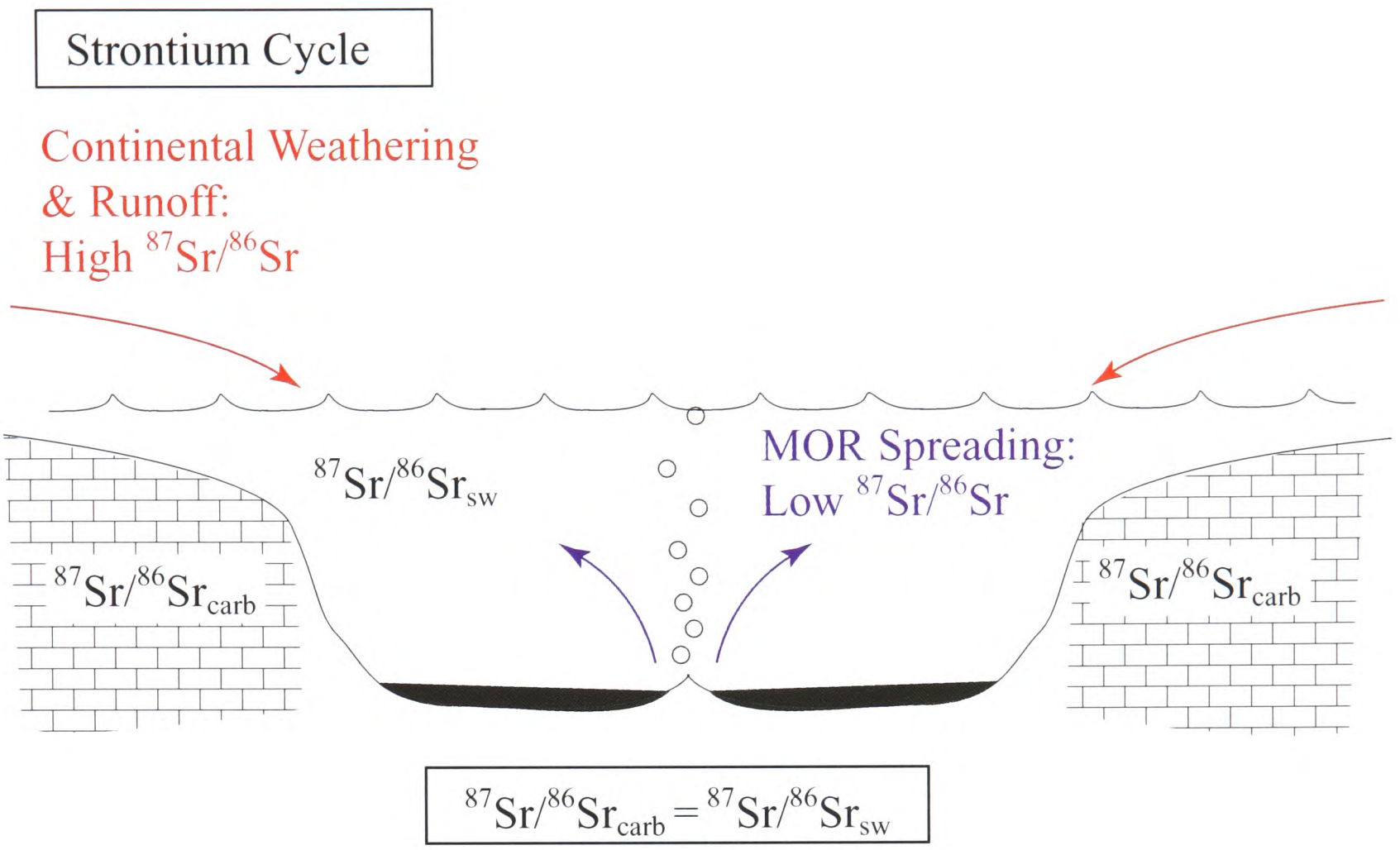

Figure 1.viii Simplified summary of the theory pertaining to the two end-member global strontium system.

2) interacted with the breakdown products of constituent minerals (this may release relatively radiogenic or non-radiogenic strontium, depending on the mineral source; Emery *et al.*, 1987); 3) originated from the compaction of sediments at depth (Richter and DePaolo, 1987, 1988). To adjust for the problem of diagenetically increased Sr-isotope ratios, Burke *et al.* (1982) constructed their 'best-estimate' curve along the lower limits of their data-set.

Sr-isotope analysis on diagenetically screened low-magnesium calcite of belemnite rostra and thick-shelled oysters was carried out by Jones *et al.* (1994a,b). Screening involved the rejection of those samples with Fe > 150 ppm *and/or* Mn > 50 ppm, because relatively high concentrations of these elements probably signify interactions with pore-fluids that have a diagenetic source (i.e. meteoric waters). The authors demonstrate that those samples found in mudrocks with relatively high iron and manganese concentrations are more likely to have Sr-isotope values that deviate from primary signals. Those samples found in sandstones and oolites were also observed to have relatively higher concentrations of iron and manganese: a reflection of their increased permeability due to the coarser grain-size (Jones, 1992). However, there is no standard threshold concentration of iron or manganese that can be used for diagenetic screening (Veizer, 1983), and various authors have used varying cut-off values for sample rejection (e.g. Anderson *et al.*, 1994; Jones *et al.*, 1994a; Jones *et al.*, 1994b; Ditchfield, 1997). McArthur *et al.* (2000a) and Jones *et al.* (1994a,b) found that their belemnite samples had iron and manganese concentrations suggestive of alteration, but through other criteria indicating the presence of pristine calcite they speculated that the iron and manganese concentrations do not give a true view of alteration, but may represent trace disseminated pyrite / iron oxide, or that any alteration was not so pervasive as to affect the Sr-isotope ratios.

1.3.2 The Jurassic–Cretaceous strontium-isotope curve

Figure 1.ix illustrates the most comprehensive high-resolution Jurassic and Cretaceous Sr-isotope dataset to date (Jones and Jenkyns, 2001). At low resolution, the relatively low Sr-isotope values of the Jurassic are interpreted to be the result of a period when oceanic spreading had more relative influence on sea-water Sr-isotope levels, and the later rise in values through the Cretaceous and Tertiary are associated with increasing influence of continental weathering

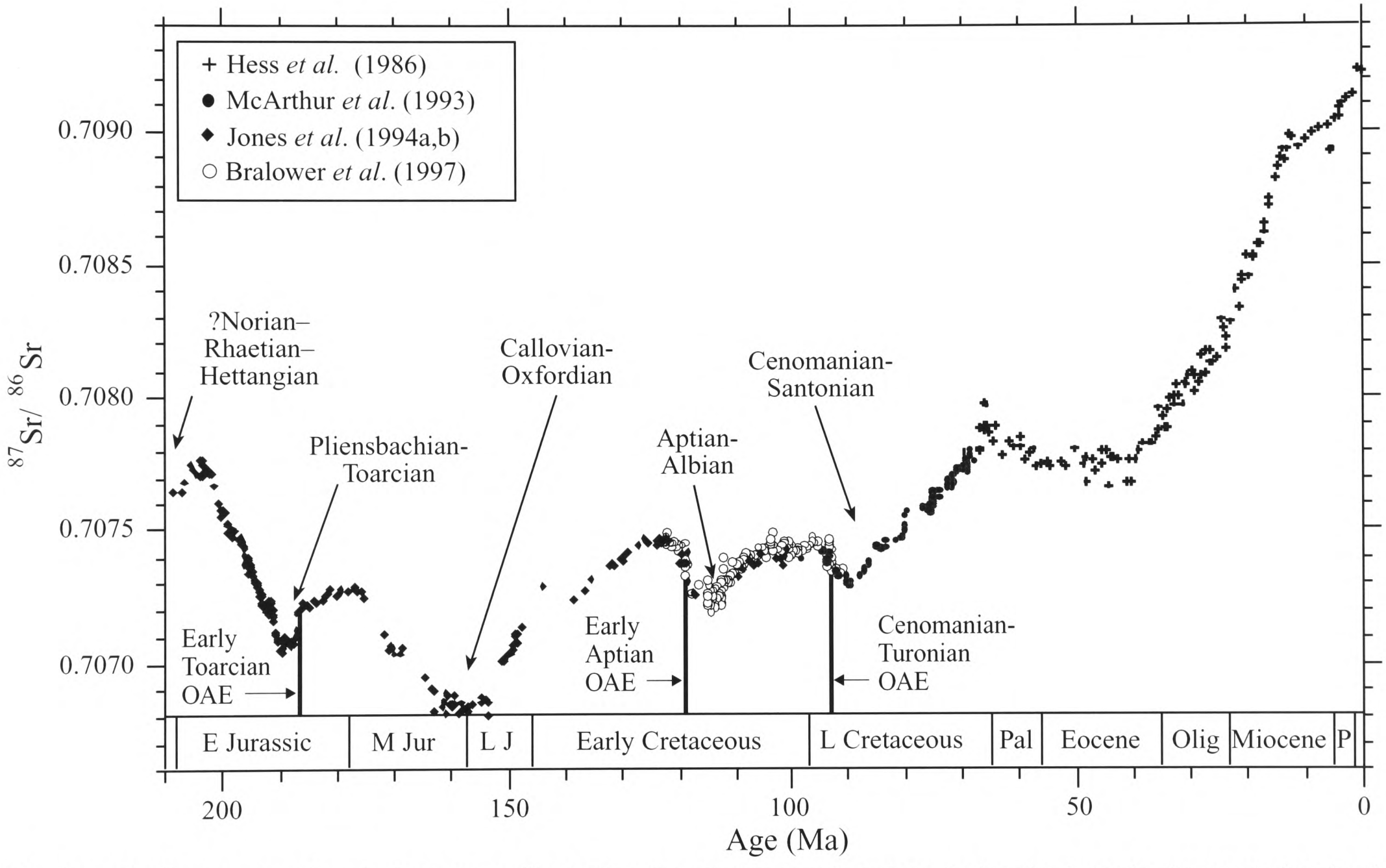

Figure 1.ix. Jurassic–Recent strontium-isotope curve illustrating the relative low in values during the Jurassic, interpreted to be the result of increased hydrothermal activity during the break-up of Pangea. The "saw-tooth" increase throughout the Cretaceous is interpreted as the result of relatively short periods of either high oceanic spreading or continental flood-basalt emplacement punctuating a general increasing trend in isotope values. The relatively rapid Tertiary rise in values is believed to reflect the increasing influence of continental weathering and run-off derived strontium on the system, related to the Himalayan orogeny. Modified after Jones and Jenkyns (2001).

and run-off on the world ocean. At higher resolution, the curve illustrates the distinctive "saw-tooth" pattern associated with the Sr-isotope curve (especially Cretaceous–Recent). This appearance is interpreted as the result of relatively short periods of either high oceanic spreading rates or continental flood-basalt emplacement (in the Late Triassic, Pliensbachian–Toarcian, Callovian–Oxfordian, Aptian–Albian, and Cenomanian–Santonian) punctuating a general increasing trend in isotope values (Jones and Jenkyns, 2001). After detailed analysis and modelling of the association between three major OAE's (early Toarcian, early Aptian, and Cenomanian–Turonian) and Sr-isotope minima, Jones and Jenkyns (2001) conclude that increased hydrothermal activity caused: 1) the strontium-isotope minima; 2) a rise in CO_2 flux into the ocean–atmosphere, in turn inducing global warming and an increased hydrological cycle leading to increased weathering and an enhanced flux of nutrients to biologically productive surface waters; 3) preconditioning of the global oceans to the major OAE's, but the actual trigger (sea-level rise) was a relatively independent mechanism. In summary, causal links between the carbon and strontium cycles were identified, and relevant mechanisms and associated processes discussed.

Correlating globally distinctive and potentially intrinsically linked excursions in the carbon- and strontium-isotope curves of biostratigraphically calibrated reference sections to the carbonate-platform isotope profiles of this study allows a notional temporal framework to be applied to the platforms. In addition, the effects of particular mechanisms, processes and events (reflected in isotope records by excursions) on those shallow-water carbonates studied can subsequently be assessed.

1.4 Background carbon-isotope stratigraphy

Scholle and Arthur (1980) were the first to realise the importance of carbon-isotope geochemistry as a potential global correlative tool for pelagic stratigraphic successions. Most studies since then have been based on pelagic carbonates (e.g. Schlanger *et al.*, 1987; Weissert and Lini, 1991; Lini *et al.*, 1992; Gale *et al.*, 1993; Marconi *et al.*, 1994; Erbacher and Thurow, 1997; Menegatti *et al.*, 1998; Weissert *et al.*, 1998; Voigt, 2000), and an extensive dataset of high-resolution reference curves has been collated.

The Jurassic and Cretaceous carbon-isotope curves show globally distinctive excursions to heavier or lighter carbon-isotopes values ($\delta^{13}C$) at particular intervals of time, termed oceanic anoxic events (OAE's; Schlanger and Jenkyns, 1976). The most significant of these excursions (see Figure 1.x) are known to occur in the early Toarcian (Early Jurassic; e.g. Jenkyns and Clayton, 1986; Jenkyns, 1988; Jimenez *et al.*, 1996; Jenkyns and Clayton, 1997; Duarte, 1998; Gröcke *et al.*, 1999; Hesselbo *et al.*, 2000; Rosales *et al.*, 2001), early Aptian (Early Cretaceous; e.g. Weissert and Channell, 1989; Weissert and Lini, 1991; Jenkyns, 1995a; Ferreri, 1997; Menegatti *et al.*, 1998; Bralower *et al.*, 1999; Erba *et al.*, 1999; Gröcke *et al.*, 1999; Jenkyns and Wilson, 1999; Luciani *et al.*, 2001) and over the Cenomanian–Turonian boundary (Mid-Cretaceous; e.g. Pratt and Threlkeld, 1984; Hilbrecht and Hoefs, 1986; Schlanger *et al.*, 1987; Jarvis *et al.*, 1988; Kuhnt *et al.*, 1990; Gale *et al.*, 1993; Curiale, 1994; Jenkyns *et al.*, 1994; Lamolda *et al.*, 1994; Paul *et al.*, 1994; Jenkyns, 1995a; Accarie *et al.*, 1996; Hasegawa, 1997; Stoll and Schrag, 2000; Voigt, 2000). The excursions at these times (found in marine carbonate, marine organic matter, and terrestrial organic matter) have been successfully correlated between globally distributed and facies-independent sections. In pelagic sections, the intervals in which the excursions occur are also characterised by the presence of various other phenomena, including elevated organic-carbon levels (black-shale deposits; e.g. Schlanger and Jenkyns, 1976; Jenkyns and Clayton, 1986), facies changes suggestive of eustatic sea-level rises in the Jurassic (e.g. Hallam, 1981, 1992, 1997; Hesselbo and Jenkyns, 1998; Hallam, 2001) and Cretaceous (e.g. Haq *et al.*, 1988), palaeotemperature maxima (Buchardt, 1978; Arthur *et al.*, 1985; Kemper, 1987; Jenkyns *et al.*, 1994; Podlaha *et al.*, 1998; Clarke and Jenkyns, 1999; Jenkyns and Wilson, 1999), "nannoconid-crises" (Erba, 1994; Bralower *et al.*, 1998), and carbonate platform drowning (Föllmi *et al.*, 1994; Drzewiecki and Simo, 1997; Weissert *et al.*, 1998; Graziano, 1999; van de Schootbrugge *et al.*, 2000; Wortmann and Weissert, 2000). A simplified illustration detailing some of the processes of the carbon-cycle operating over the duration of an O.A.E. is presented in Figure 1.xi (modified after Jenkyns, 1999).

Other Jurassic and Cretaceous intervals where less significant carbon-isotope excursions (in terms of geographical distribution and their affect on the sedimentary record) are evident, include the mid-Oxfordian (Late Jurassic; Jenkyns, 1996; Weissert and Mohr, 1996; Padden *et*

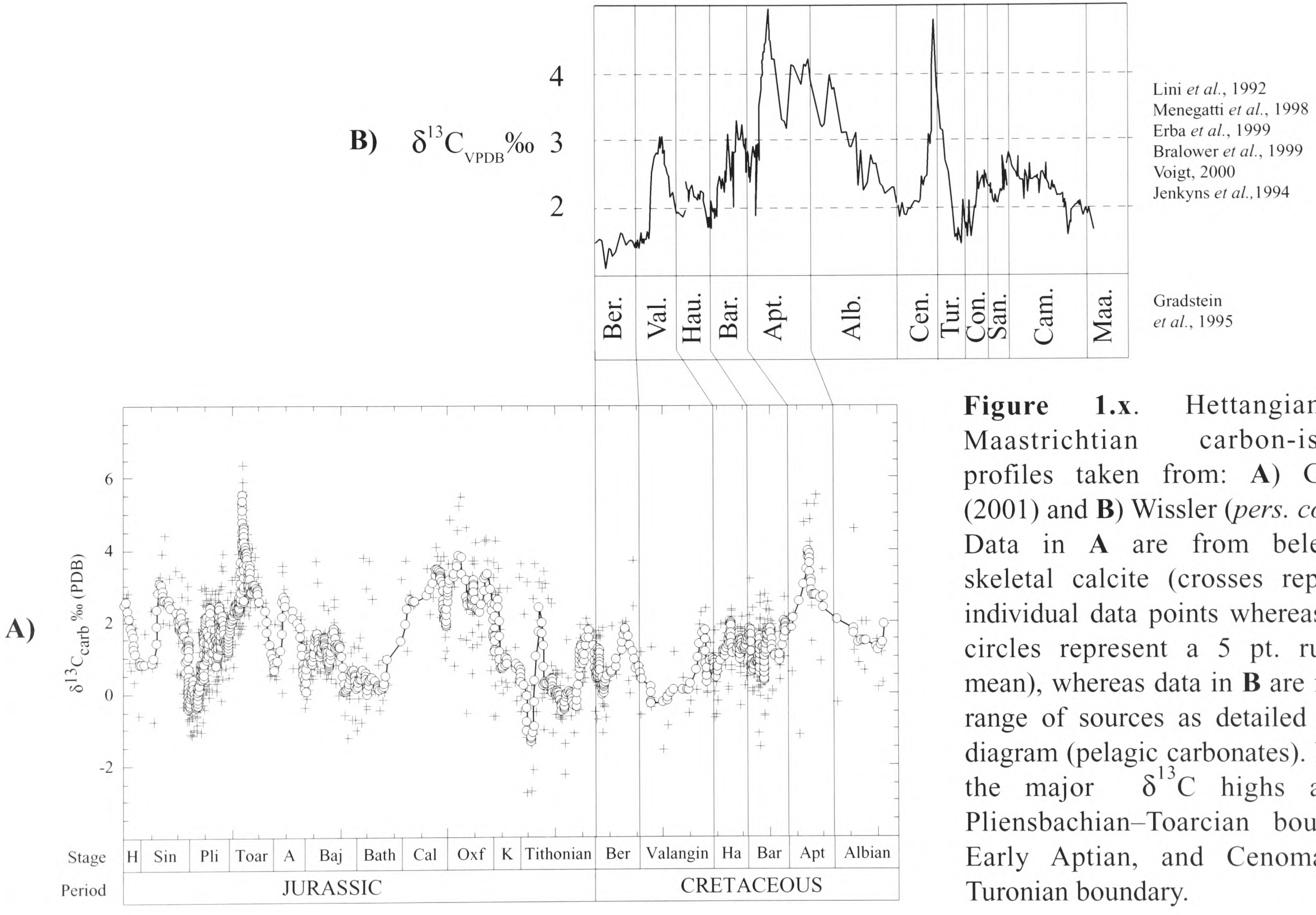

Figure 1.x. Hettangian to Maastrichtian carbon-isotope profiles taken from: **A**) Gröcke (2001) and **B**) Wissler (*pers. comm.*). Data in **A** are from belemnite skeletal calcite (crosses represent individual data points whereas open circles represent a 5 pt. running mean), whereas data in **B** are from a range of sources as detailed in the diagram (pelagic carbonates). Notice the major $\delta^{13}C$ highs at the Pliensbachian–Toarcian boundary, Early Aptian, and Cenomanian–Turonian boundary.

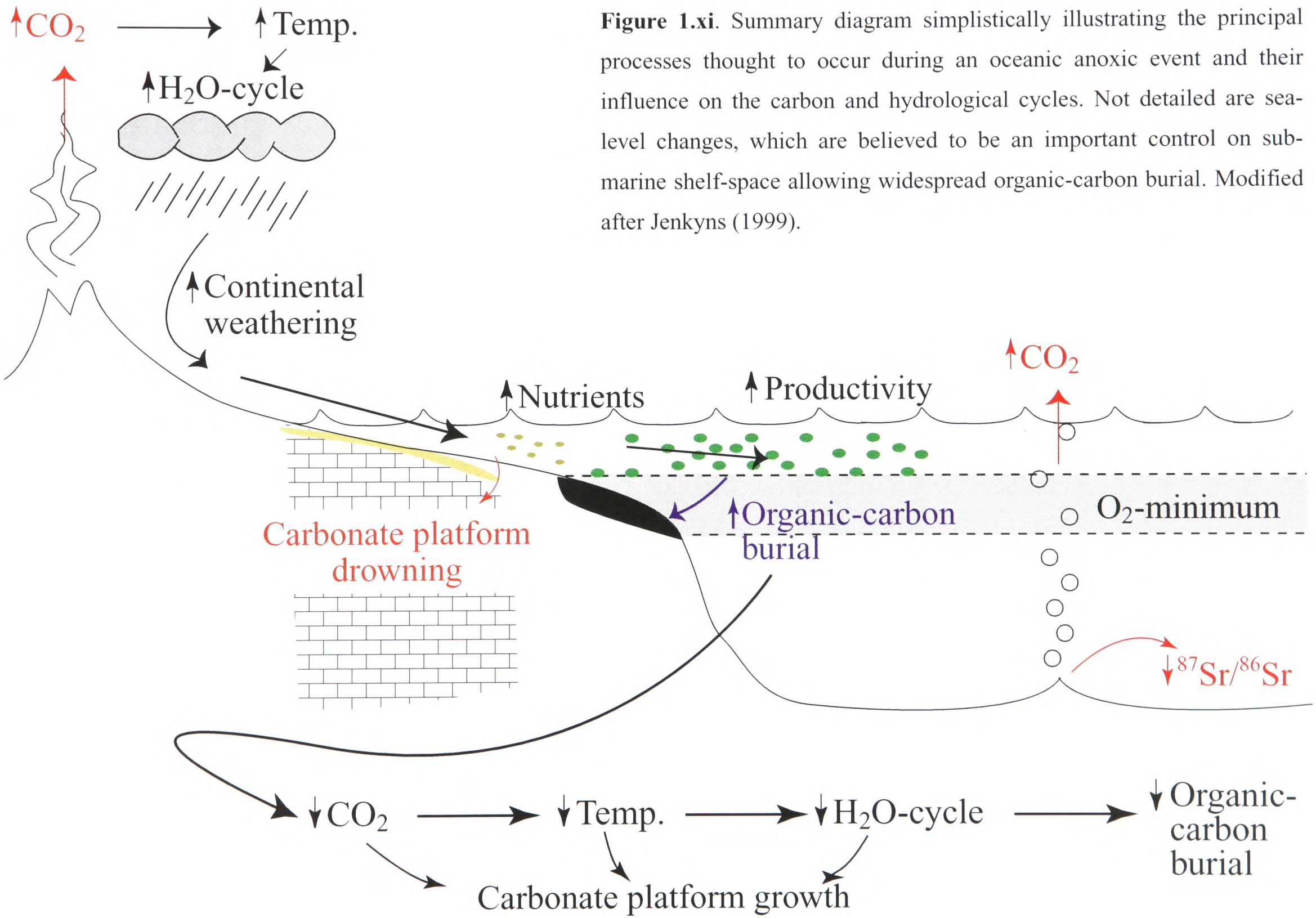

Figure 1.xi. Summary diagram simplistically illustrating the principal processes thought to occur during an oceanic anoxic event and their influence on the carbon and hydrological cycles. Not detailed are sea-level changes, which are believed to be an important control on sub-marine shelf-space allowing widespread organic-carbon burial. Modified after Jenkyns (1999).

al., 2001; Wierzbowski, 2002), late Kimmeridgian (Late Jurassic; Weissert and Mohr, 1996; Morgans-Bell *et al.*, 2001), Valanginian–Hauterivian (Early Cretaceous; Cotillon and Rio, 1984; Patton *et al.*, 1984; Lini *et al.*, 1992; Channell *et al.*, 1993; Graziano, 1999; van de Schootbrugge *et al.*, 2000; Wortmann and Weissert, 2000), Albian (Mid-Cretaceous; e.g Grötsch, 1998; Bralower *et al.*, 1999; Stoll and Schrag, 2000), and Santonian–Coniacian (Late Cretaceous; e.g. Jenkyns *et al.*, 1994; Crespo de Cabrera *et al.*, 1999; Stoll and Schrag, 2000). Although often more difficult to detect, these smaller scale/less widespread excursions can nevertheless provide useful anchor points when correlating between sections using carbon-isotopes.

1.4.1 The carbon-cycle and its influence on the carbon-isotope record

"The main [carbon-] cycle is from carbon dioxide to living matter and back to carbon dioxide. Some of the carbon, however, is removed by a slow epicycle that stores huge inventories in sedimentary rocks" (Bolin, 1970).

Bolin (1970) reviewed the carbon-cycle detailing rapid processes such as respiration and photosynthesis and longer-term processes such as carbonate sediment formation and the deposition of organic matter (Figure 1.xii). More recently, the carbon-cycle has been split into two cycles to reflect (and separate) the processes acting over the short- and long-term (Figure 1.xiii; Berner, 1999). Berner's long-term cycle involves the relatively slow (millions of years) cycling of carbon between rocks and the "surficial system" (ocean, atmosphere, biota and soils), whereas the short-term cycle only models the relatively rapid (e.g. residence time of carbon in the ocean reservoir ~100 ky) exchange of carbon exclusively within the surficial system. The carbon-bearing rocks involved in the long-term cycle are carbonates and organic-rich sediments, which act as sinks for carbon during deposition, but can release their carbon back into the surficial system over the long-term by volcanic, metamorphic (through subduction and/or burial of sediments) and diagenetic degassing (Figure 1.xiii A). Photosynthesis, respiration, organic-matter decay, river transport, soil degassing and ocean–atmosphere gas exchange are the relatively rapid processes responsible for carbon-cycling between the ocean, atmosphere, biota and soil reservoirs of the short-term surficial system (Figure 1.xiii B). Methane release from

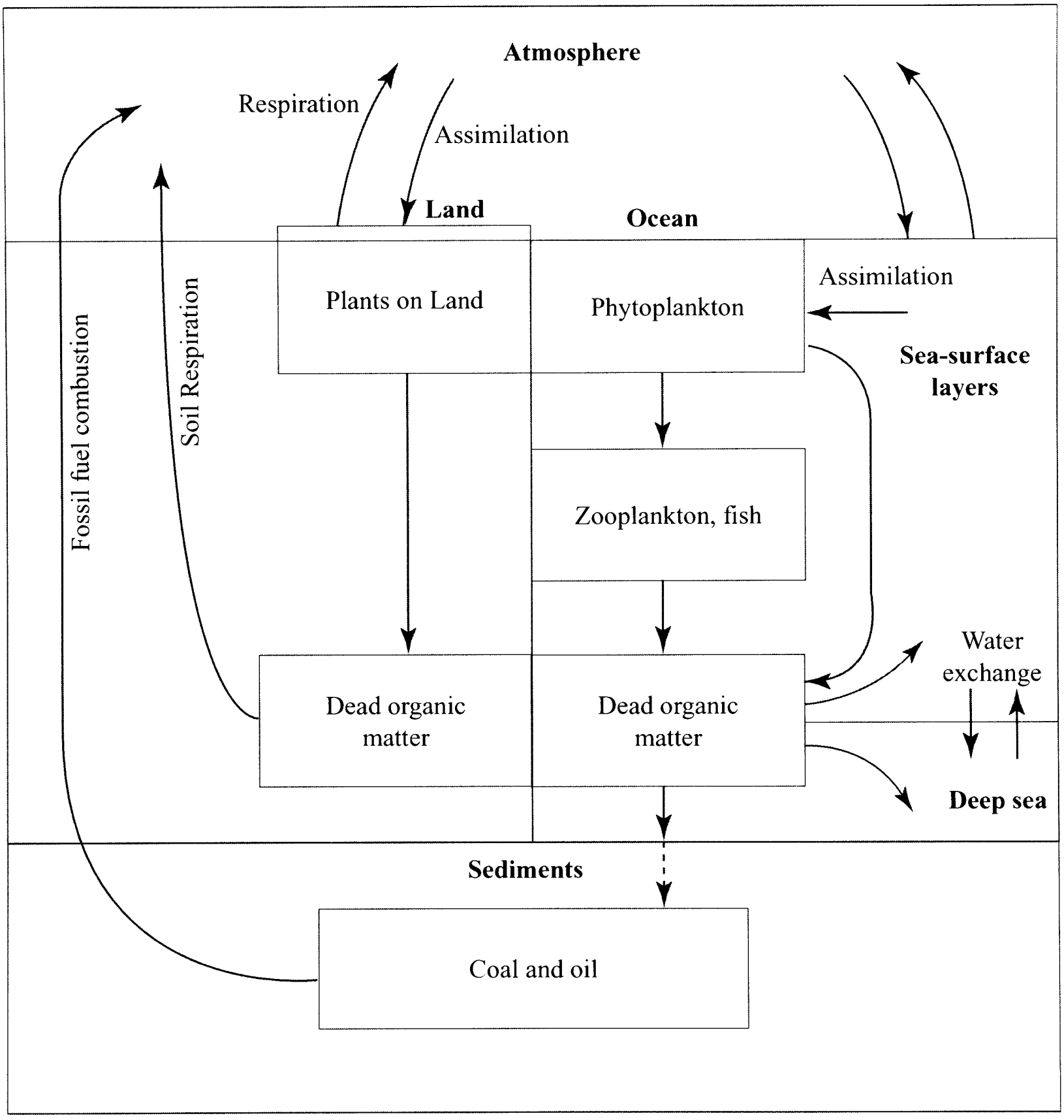

Figure 1.xii. The biospheric carbon-cycle, modified after Bolin (1970).

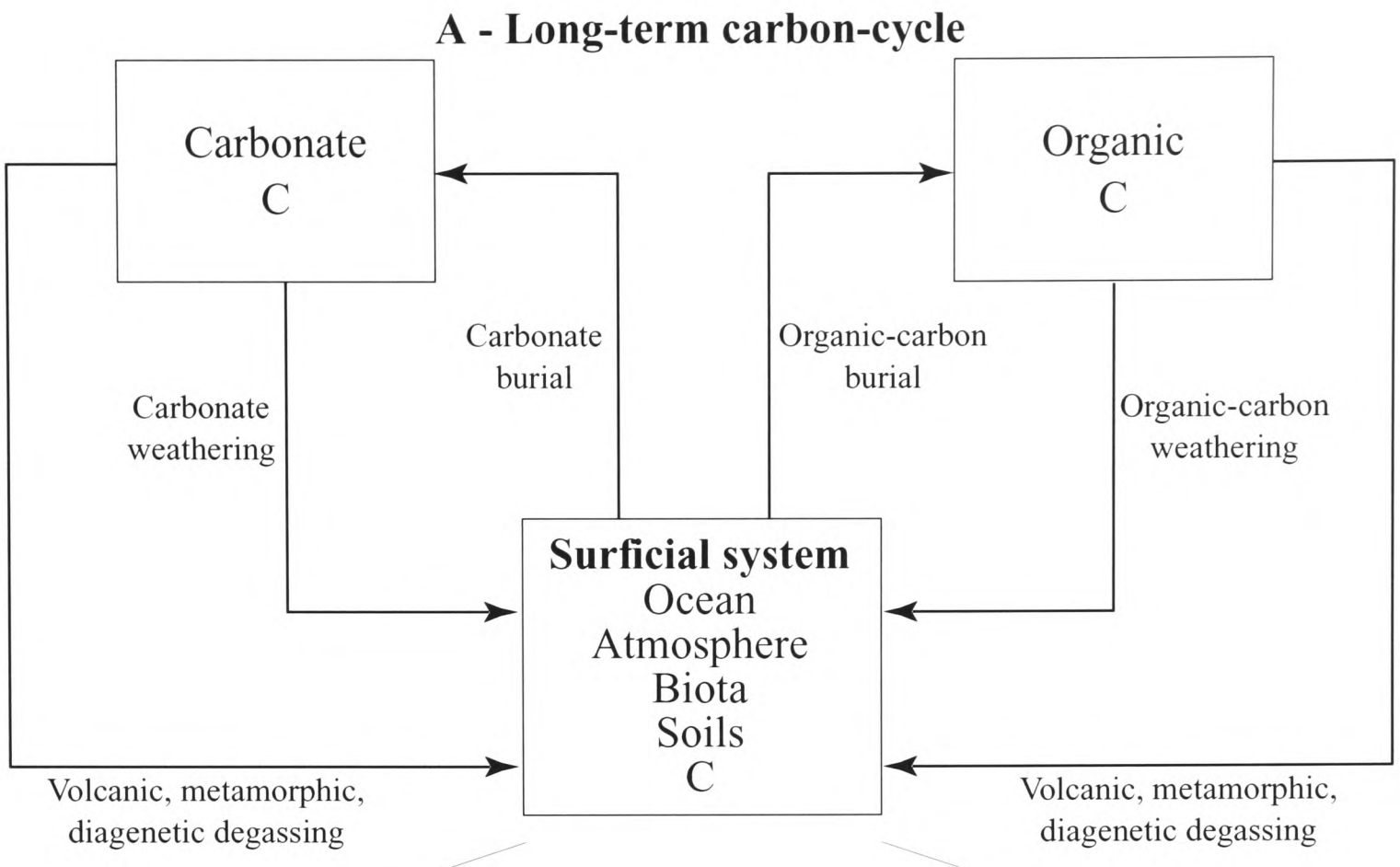

Figure 1.xiii. The reservoirs and exchange processes of the long- (**A**) and short-term (**B**) carbon-cycles. The short-term cycle is represented by the "Surficial system" in **A**. Anthropogenic influences are not expressed, but deforestation is equivalent to accelerating terrestrial respiration and fossil fuel burning is an acceleration of sedimentary organic-matter weathering. Modified after Berner (1999).

clathrate (methane hydrate) dissociation is not detailed, but could be included within degassing of sediments ultimately resulting in CO_2 formation by atmospheric oxidation (Berner, 1999).

Carbon-isotope excursion events are interpreted as the isotopic reflection of perturbations in the global carbon cycle, which cause partitioning of the global carbon pool into oxidised and reduced reservoirs (e.g. Scholle and Arthur, 1980; Arthur *et al.*, 1985; Weissert and Channell, 1989; Weissert *et al.*, 1998; Jenkyns *et al.*, 2002a). Jenkyns *et al.* (2002) summarises this process well: at any one time, the $\delta^{13}C$ of the ocean–atmosphere is governed by the balance of relative net rates of formation and burial of carbonate, bicarbonate and carbon dioxide (oxidised reservoir) compared to marine and terrestrial organic carbon (reduced reservoir). Organic fractionation of carbon leaves biomass relatively depleted in ^{13}C, and therefore isotopically light (typically $\delta^{13}C$ ~ -20 to -30‰). Elevated rates of deposition of organic-carbon therefore take ^{12}C-enriched matter out of the carbon cycle, resulting in an ocean–atmosphere $\delta^{13}C$ record (registered in marine and terrestrial carbonates and organic matter) with relatively elevated values (e.g. Mesozoic typically: $\delta^{13}C_{carb}$ ~ +4 to +5‰; $\delta^{13}C_{org}$ ~ -25 to -24‰; Figure 1.xiv). Equally, a significant flux of reduced carbon into the ocean—atmosphere reservoir will lead to a decrease in global $\delta^{13}C$ values (Figure 1.xiv). Mechanisms (much debated recently) that possibly contribute to negative carbon-isotope excursions (particularly those associated with the early Toarcian and early Aptian OAE's) include: 1) diagenetic modification (Jenkyns and Clayton, 1986; Jenkyns and Clayton, 1997); 2) deep-water anoxia followed by oceanic turnover forcing ^{12}C-enriched water from the deep ocean to surface waters with further impact on the atmosphere (Küspert, 1982; Hollander *et al.*, 1991; Sælen *et al.*, 1996); 3) a global decline in productivity/preservation of organic matter (Kump and Arthur, 1999); 4) an influx of volcanically outgassed CO_2 (Larson and Erba, 1999; Hesselbo *et al.*, 2000; Pàlfy and Smith, 2000); and 5) a rapid injection of isotopically-light CH_4 ($\delta^{13}C$ ~ -60‰) into the ocean–atmosphere (Dickens *et al.*, 1995; Jahren and Arens, 1998; Jenkyns and Wilson, 1999; Hesselbo *et al.*, 2000; Padden *et al.*, 2001). A simplified summary of some of these processes and the theory behind their expression in the carbon-isotope curve of the ocean–atmosphere system is illustrated in Figure 1.xiv, and the resulting actual isotope curve for the Jurassic and Cretaceous has the characteristics that are illustrated in Figure 1.x (Gröcke, 2001; Wissler, *pers. comm.*).

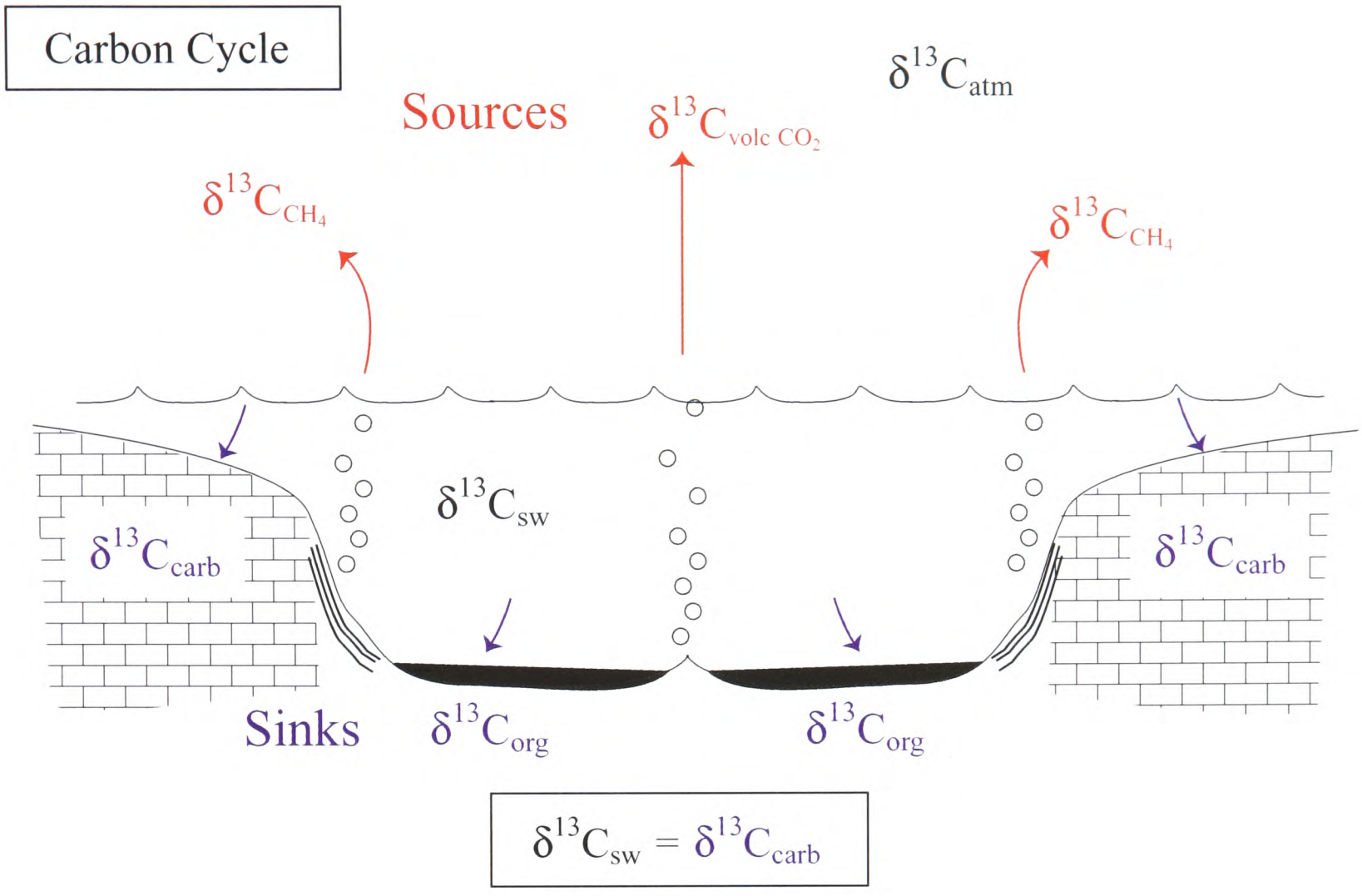

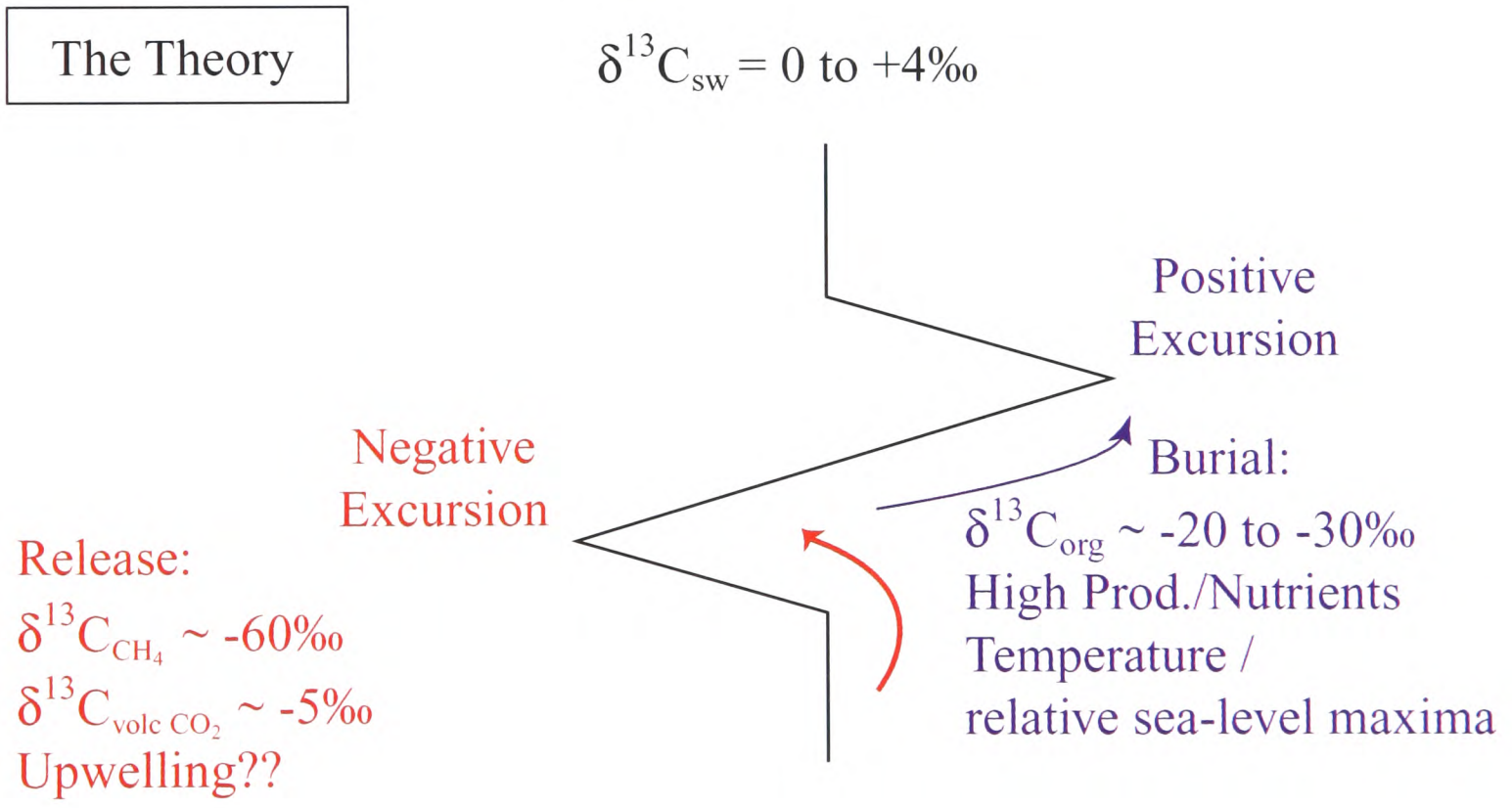

Figure 1.xiv. Simplified summary of the principal carbon-cycle sources and sinks affecting the carbon-isotope curve

As discussed in ***1.4***, the association of elevated organic matter burial and globally elevated $\delta^{13}C$ values that is characteristic of OAE's leads to intervals in the sedimentary record with distinctive features, interpreted as being the result of many different, but contemporaneous processes. To identify globally correlatable carbon-isotope excursions in shallow-water platform-carbonates allows further analysis and qualification of many of these processes from a very different perspective than has been possible in the past.

1.4.2 Chemostratigraphy of shallow-water platform carbonates

Shallow-water platform carbonates generally lack fossils of biostratigraphic worth and the carbon-isotope data they furnish from bulk rock analyses has been interpreted to be too laterally variable *and/or* are too influenced by diagenetic alteration by meteoric waters for detailed chemostratigraphic correlation (Allan and Matthews, 1982; Brasier and Green, 1993; Patterson snd Walter, 1994). However, it has recently become apparent that used alongside existing long-lived benthic foraminiferal biostratigraphy, carbon-isotope stratigraphy of shallow-water carbonates can allow correlations of well-known isotope excursions present in the stratigraphic record (Jenkyns, 1995a; Jenkyns, 1995b; Vahrenkamp, 1996; Ferreri, 1997; Grötsch, 1998; Wilson *et al.*, 1998; Davey and Jenkyns, 1999; Jenkyns and Wilson, 1999; Masse *et al.*, 1999; Wissler *et al.*, 1999; Wissler, 2001). When used in conjunction with the more diagenitically robust strontium-isotope stratigraphy, the three datasets together can offer even more conclusive evidence that correlations are well-founded (Jenkyns and Wilson, 1999; McArthur *et al.*, 2000a).

1.4.3 Diagenetic considerations

As discussed at length by Jenkyns and Wilson (1999) and references therein, shallow-water carbonates are particularly susceptible to meteoric-water diagenesis because they accumulate close to sea-level, small changes in which can lead to periodic emergence. This "Caribbean-style" diagenesis plays a particularly important role in an 'ice-house' world because rapid sea-level change is common and results in emergence, karstification and calcrete

formation (Gross, 1964). Typically, horizons such as this would have scattered and low carbon- and oxygen-isotope values, and when plotted against each other on a crossplot would exhibit a clear mixing-line trend (Allan and Matthews, 1982; Grötsch, 1998). However, it should be noted that, to date, the Jurassic and Cretaceous have widely been interpreted as a 'greenhouse' world without the presence of significant ice-caps (e.g. Crowell, 1982; Schlanger, 1986; Frakes *et al.*, 1992; Hallam, 1992). Eustatic sea-level change in a 'greenhouse' world has been proposed to be much slower than that resulting from glaciation–deglaciation (e.g. Schlager, 1981; Dewey and Pitman, 1998), and so it follows that intensive meteoric-water diagenesis should be less likely (Jenkyns and Wilson, 1999).

If primary carbonate replacement occurs at an early stage of burial, isotopic deviation is not always a result. Extensive research into the mimetic and finely crystalline dolomites of the Tethyan Upper Triassic (Norian) and dolomitisation of Early Jurassic peritidal platform carbonates of Gibraltar reveal that little modification of primary signals has occurred due to the almost contemporaneous replacement of less stable carbonate (?aragonite; Sandberg, 1983; Iannace and Frisia, 1994; Balog, 1995; Balog *et al.*, 1999; Qing *et al.*, 2001). However, many Rhaetian dolomites of Tethyan carbonate platforms have been designated as diagenetic due to their particularly negative oxygen-isotope values, and the textural truncation (by coarsely crystalline dolomite) of carbonate fabrics resulting from relatively 'late' dolomitisation (Iannace and Frisia, 1994).

Other possible causes for deviation of isotopic values from primary signals include the effect of skeletal grains that may exhibit non-equilibrium isotopic fractionation, the presence of void-filling secondary calcite (for example in inter/supratidal facies such as birdseye limestones; e.g. Grötsch, 1998; Davey and Jenkyns, 1999), or diagenetic alteration of originally aragonitic material (Davey and Jenkyns, 1999). It has also been observed on modern carbonate platforms that water-masses may become restricted by closure of connections to the open ocean (low-energy lagoonal facies in the ancient stratigraphic record), and be susceptible to a general depletion in ^{13}C because of the local 'containment' effect of, for example, organic matter oxidation (Brasier and Green, 1993; Patterson and Walter, 1994; Davey and Jenkyns, 1999). Such a mechanism was invoked for the whole dataset ~1 ‰ negative offset of globally

reproducible Barremian–Albian isotope trends found in the Gavrovo Platform, western Greece (Grötsch, 1998)

In this study, extensive visual and petrographic microscope inspections, and carbon- and oxygen-isotope cross-plots were undertaken to determine the extent of diagenetic modification of the bulk-carbonates analysed and therefore take account of their effects on the isotope profiles produced. Those altered samples that passed these tests may further be identified as the result of diagenetic alteration because they exhibit anomalous isotope values (abrupt shifts in carbon- *and/or* oxygen-isotope values to more negative figures, particularly if only one datum point, may signify local diagenetic overprinting; Davey and Jenkyns, 1999). In addition, it is also important to note that oxygen isotopes are generally the most sensitive of the proxies used in this study for diagenetic alteration, because of the abundance in circulating pore fluids of "alien" (meteoric-water) oxygen ions available for replacement of primary carbonate oxygen ions. Therefore, filtering of data dependent on oxygen-isotope values can be a useful technique for clarifying datasets, and is amongst those screening methods described above that have been used in this study. However, the extent of diagenesis on each platform section is individually assessed in detail in the following chapters.

Chapter 2: Trento Platform

Chapter 2: Trento Platform, Southern Alps, Italy

2.1 Geological setting and stratigraphy

The early Jurassic Southern Alps of northern Italy (Figure 2.i; Gaetani, 1975; Winterer and Bosellini, 1981; Smith *et al.*, 1994) have been interpreted as a passive south Tethyan continental margin subjected to major extensional movements over a long period of post-Variscan time (Sarti *et al.*, 1992). Although episodes of extension have been documented for the Late Permian and Middle Triassic, the most important extensional phase began in the latest Triassic – Early Jurassic, breaking up the previous Upper Triassic shallow-water carbonate (dolomitic) platform into an east-west-trending half-graben topography of basins and platforms/plateaux (Bernoulli and Jenkyns, 1974; Winterer and Bosellini, 1981; Bosellini, 1989). The eastward succession of platform drownings across the Southern Alps led Bosellini (1973) to infer that the extension was rift-related and the result of the creation of the Ligurian Ocean to the west (Aubouin, 1963; Gaetani, 1975; Winterer and Bosellini, 1981; Sarti *et al.*, 1992). Each half-graben has a west-tilted floor and is bounded on the west by an east-dipping listric master fault (Winterer and Bosellini, 1981). Half-grabens are each divided by antithetic faults creating a western deep-water basinal zone with relatively thick sediments, and a more shallow eastern plateau zone with thinner sediments (Sarti *et al.*, 1992). Aubouin (1964) described the alternating structural units from west to east as the Lombardian Basin, the Trento Ridge (now referred to as the Trento Plateau or Platform; Gaetani, 1975), the Belluno Basin, the Friuli Ridge (now referred to as the Friuli Shelf or Platform; Gaetani, 1975), and the Julian Basin. In terms of their half-graben structures, these structural units have since been roughly paired-up into the following, from west to east: 1) Monte Nudo–Arbostura (within the Lombardian Basin); 2) Monte Generoso–Albenza (within the Lombardian Basin); 3) West Sebino–Botticino (within the Lombardian Basin); 4) East Sebino–Trento; and 5) Belluno–Friuli zone (Sarti *et al.*, 1992 and references therein). Figure 2.ii illustrates the breaking up of this shallow-water shelf using palinspatic cross-sections of the region for the Hettangian and Early–Middle Jurassic (modified after Winterer and Bosellini, 1981 and Sarti *et al.*, 1992).

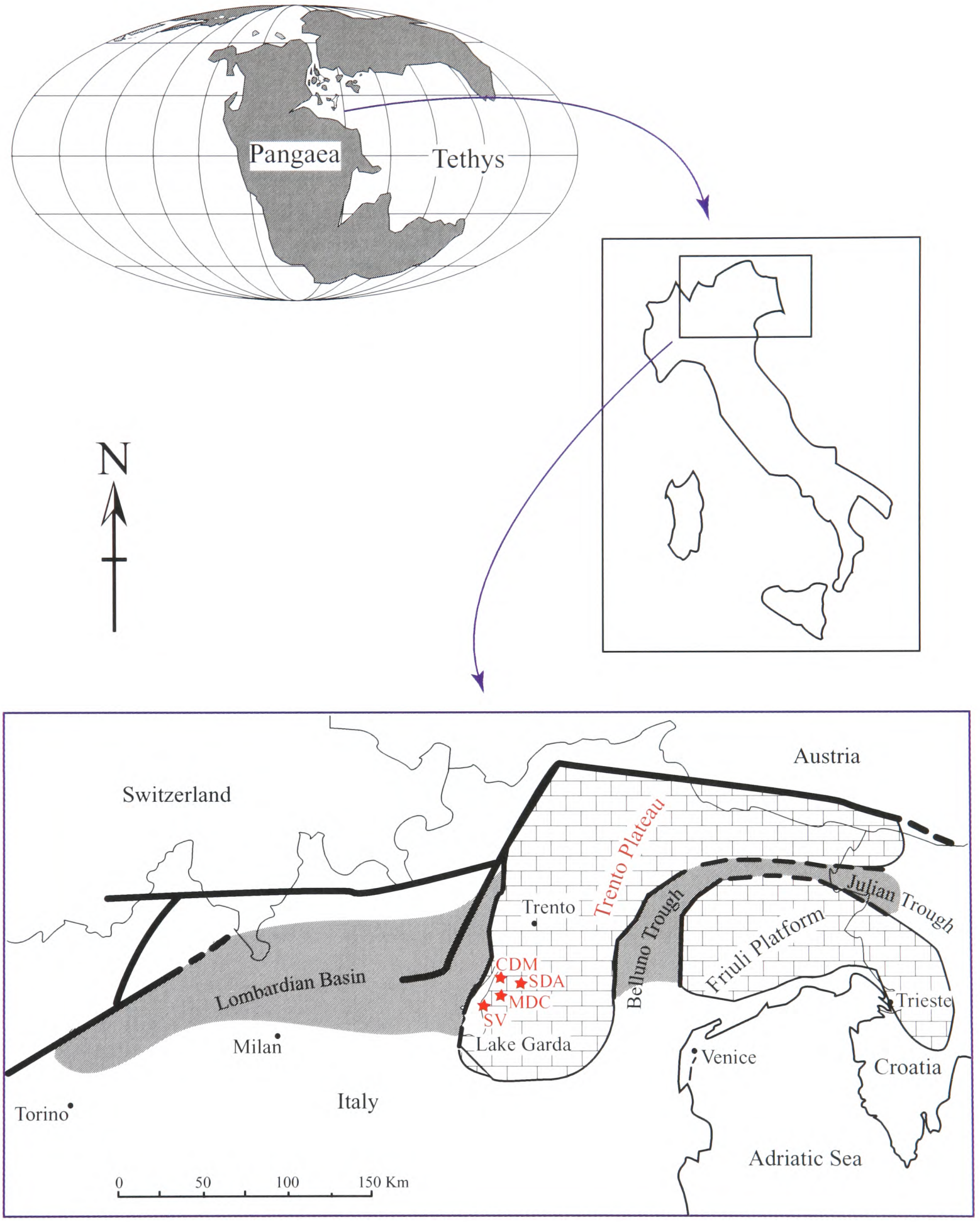

Figure 2.i. Paleogeographic reconstruction showing the northwest Tethyan location of the Southern Alps in the Toarcian (after Smith *et al.*, 1994), and its location in northern Italy today (after Gaetani, 1975). Highlighted in grey and brickwork are the major basins and platforms of the Southern Alps, respectively. The Friuli Platform forms the northwest margin of the Friuli Shelf, which extends into the Dinaric Shelf to the southeast. CDM = Colma di Malcesine; SDA = Sega di Ala; MDC = Madonna della Corona; SV = San Vigilio.

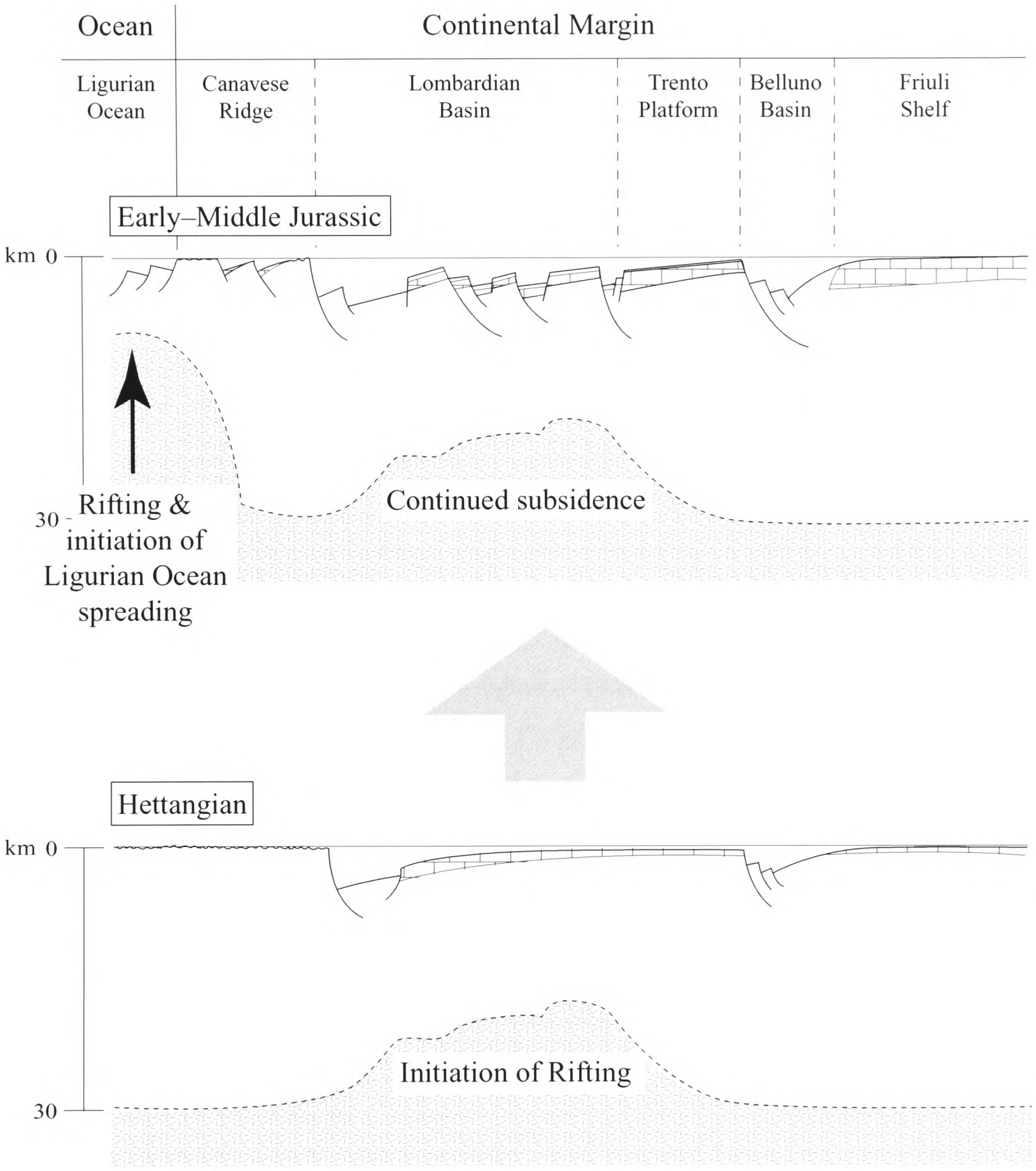

Figure 2.ii. Palinspastic reconstruction of the Southern Alps, northern Italy, for the Hettangian and Early–Middle Jurassic, simplistically showing the main structural units (modified after Winterer and Bosellini, 1981 and Sarti *et al.*, 1992). Vertical exaggeration is approximately 5x.

The sections described in ***Chapter 2*** of this manuscript are specifically located on the Trento Plateau. The Norian–Rhaetian (Late Triassic) depositional environment on the Trento Plateau was represented by shallow, flat and extended platforms with predominantly cyclic sub–intertidal and supratidal carbonate (dolomitic) deposition (Bosellini, 1967). However, during the Early Jurassic, the Trento Platform is generally interpreted to have been an offshore Bahamian-type platform bordered to the west and east by the pelagic Lombardian Basin (East Sebino Trough) and Belluno Trough respectively, the latter separating the Trento Platform from the continental shelf to the east (Friuli / Dinaric Platform; Figures 2.i and 2.ii; Aubouin, 1963; Gaetani, 1975; Winterer and Bosellini, 1981). Evidence from Po Plain drilling southwest of Venice reveals evidence that the Belluno Trough closed to the south, and as a result has been likened to the modern "Tongue of the Ocean" in the Bahamas (AGIP, 1959; Winterer and Bosellini, 1981). The isolation of the Trento Platform from the continental shelf, and its more westerly position (i.e. proximity to the centre of spreading / extension) forced a different history of sedimentation from that of the neighbouring Friuli Shelf, and subsequent events proved that ultimately the Trento Platform carbonates were more susceptible to drowning than the nearby shelf carbonates. Although drowning of the Trento Platform was heterochronous (the north and south of the platform were separated by a sysnsedimentary fault; Gaetani, 1975), in the south the western margin of the platform (in the region of Lake Garda, today) underwent definitive drowning in the late Aalenian and a pelagic plateau formed that was covered with slowly deposited red nodular limestones: the Rosso Ammonitico (Figure 2.iii; Sturani, 1964; Winterer and Bosellini, 1981; Zempolich, 1993).

The stratigraphic succession of the Trento Plateau is illustrated in Figure 2.iii, and documents deposition of sediments from the Late Triassic to the early Bajocian. Figure 2.iv illustrates the "sequential architecture" of these facies over the Trento Platform/Lombardian Basin margin (modified after Picotti and Cobianchi, 1996). The Triassic "Dolomia Principale" (or "Hauptdolomit") is generally regarded as the plateau 'basement' because the Norian (Late Triassic) is reported to have been a period of relative tectonic calm and little differential subsidence, allowing thick (1000 m) shallow-water and peritidal carbonates (dolomitic) of almost uniform thickness to develop across the entire Southern Alpine region (see ***1.2*** for a

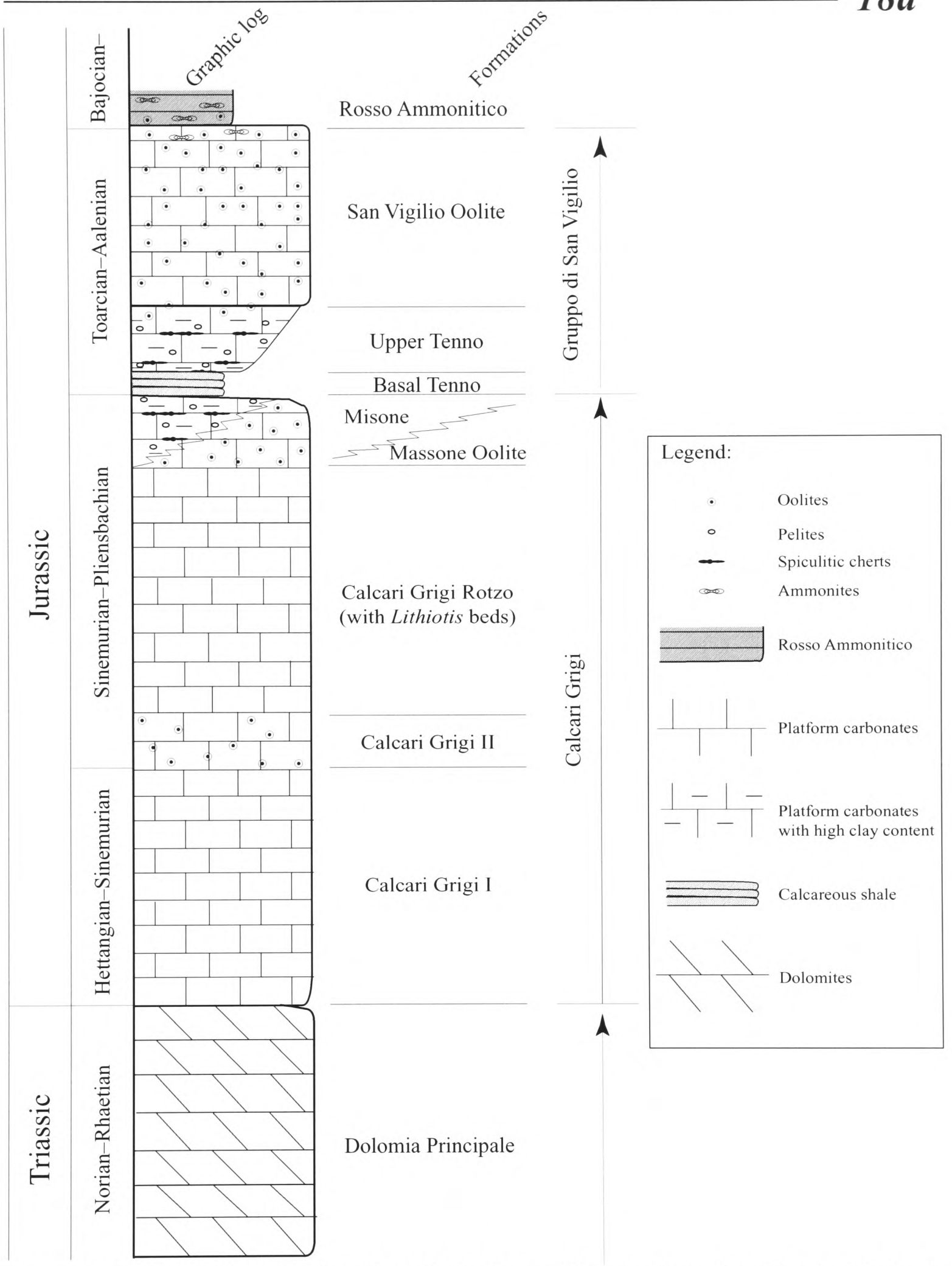

Figure 2.iii. Generalised stratigraphy of the Trento Plateau from the Triassic "Dolomia Principale" (or "Hauptdolomit"), to the definitive drowning of the platform in the late Aalenian, after which deposition of the pelagic Rosso Ammonitico continued on the sinking oceanic plateau (Sturani, 1964; Barbujani *et al.*, 1986; Picotti and Cobianchi, 1996). Biostratigraphic age after Bosellini and Broglio Loriga (1971), Geyer *et al.* (1986), Picotti and Cobianchi (1996), Cobianchi and Picotti (2001)..

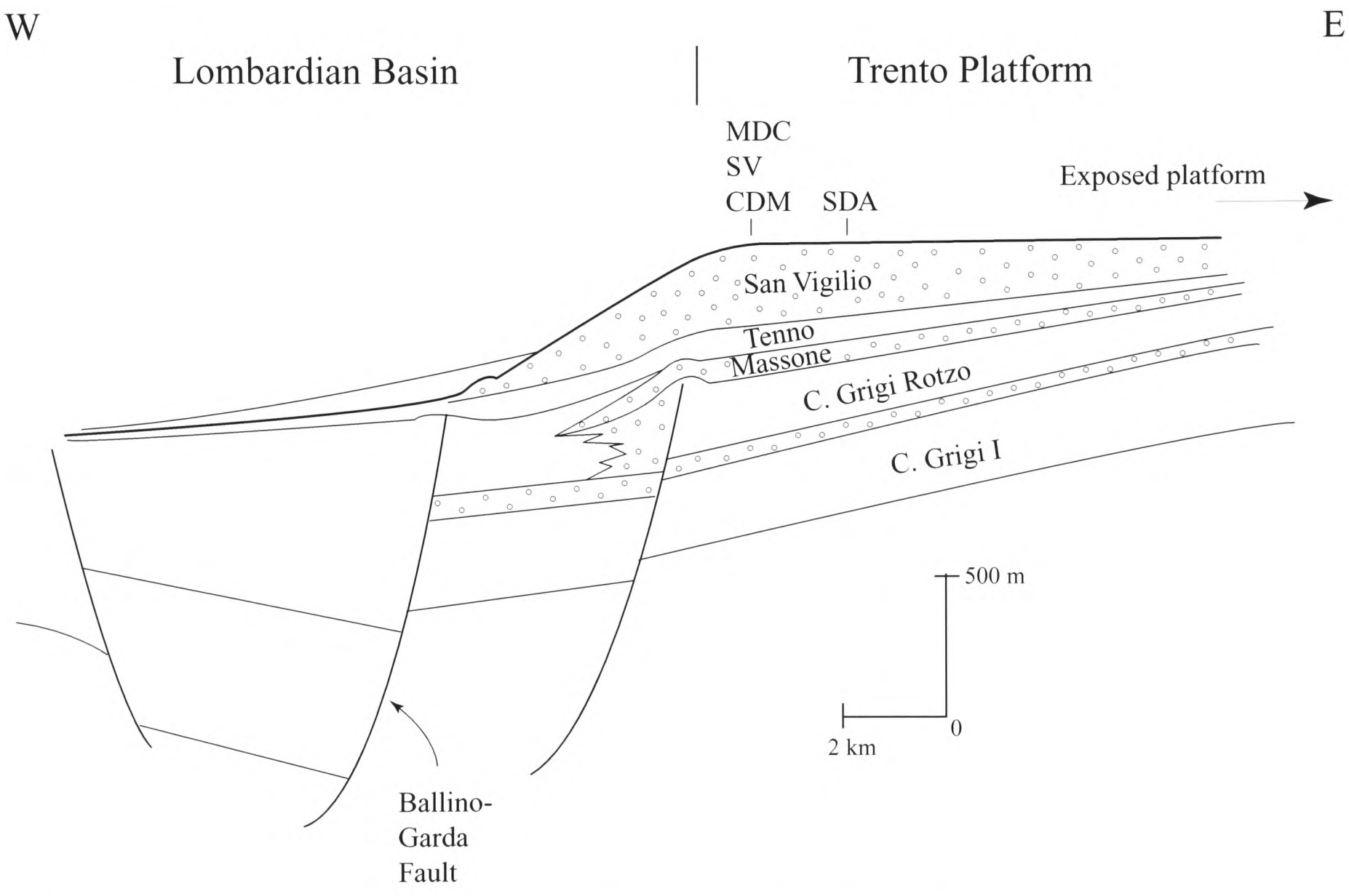

Figure 2.iv. Cross-section through the eastern Lombardian Basin and western margin of the Trento Platform detailing the facies succesion exposed at the four Trento Platform sections studies; MDC = Madonna della Corona; SV = San Vigilio; CDM = Colma di Malcesine; SDA = Sega d'Ala. Modified after Picotti and Cobianchi (1996).

more detailed discussion of regional Triassic sedimentary history; Winterer and Bosellini, 1981).

Bosellini (1967) deals more specifically with the Trento Plateau when he describes the 'ideal cyclothem' of the Dolomia Principale being composed of:

1) a basal unit of intraformational breccia, locally mixed with red / green argillaceous carbonate material
2) a lower intertidal (or transgressive) unit mainly consisting of biogenic dolomites and associated with evidence of subaerial desiccation (birseyes, sheetcracks)
3) a subtidal unit of massive crystalline dolomite with associated molluscan macrofauna
4) an upper intertidal (or regressive) unit similar, but thinner than (2)

The causes of this cyclicity have been reduced to three major controls: climatic (oscillations of sea-level), tectonic (spasmodic accelerations in subsidence); and sedimentary (sedimentation rate greater than subsidence rate; Bosellini, 1967; Bosellini and Hardie, 1985; Hardie *et al.*, 1986). The later work of Bosellini (1985), further splits the Dolomia Principale into two: the lower 500–600 m being represented by metre-scale peritidal cycles (Inferior Dolomia Principale), and an upper 200–300 m of more massive (3–5 m) subtidal and saccharoidal dolostone separated by diagenetic caps (Superior Dolomia Principale). While it is possible to explain the peritidal cyclicity of the Inferior Dolomia Principale with an autocyclic mechanism, it has been suggested that Milankovitch-style eustasy and local accelerations in subsidence were responsible for the relative sea-level drops (occurring every 1–100 ka) that were required to cause repeated subaerial exposure of the subtidal elements of this Superior Dolomia Principale (Bosellini and Hardie, 1985; Hardie *et al.*, 1986). As discussed in ***1.2***, Iannace and Frisia (1994) suggest that the two distinct depositional and dolomitisation styles of the Inferior (complete dolomitisation by fine, fabric-preserving dolomite) and Superior (incomplete dolomitisation by late, fabric-destructive, sucrosic dolomite) Dolomia Principale represent a change from the relative tectonic / climatic / palaeogeographic calm of the Norian into a Rhaetian stage of transition (which lead into the Early Jurassic and a time of global change: the consequence of the break-up of Pangaea).

On the Trento Plateau, the dolomites of the latest Triassic are overlain by the Hettangian–Sinemurian Calcari Grigi formation (Calcari Grigi I, 150–350 m thick), which was deposited during prevailing peritidal conditions (Bosellini and Broglio Loriga, 1971; Castellarin, 1972; Bosellini and Hardie, 1985; Stefani and Burchell, 1989). Although there is little evidence for Hettangian sediments, the Sinemurian is registered by the presence of benthic foraminifera, and the tidal-flat facies is interpreted to have gradually evolved into a barrier-island complex, expressed by the presence of 20–100 m thick transgressive oolite sand bars (Calcari Grigi II, Figure 2.iii; Gaetani, 1975; Picotti and Cobianchi, 1996). In the Sinemurian–Pliensbachian, slack-water lagoonal conditions developed behind the oolite barrier, registered in the stratigraphic record by the 150–300 m thick Calcari Grigi Rotzo member (Picotti and Cobianchi, 1996). At the height of maturity the lagoon began to infill: mud islands developed (colonised by tropical plants), and tidally aligned bivalve banks (similar to modern oyster banks) were recorded by the so-called "*Lithiotis*" limestone (Bosellini, 1972; Gaetani, 1975). Capping the Calcari Grigi Rotzo formation is the 60–100-m-thick Pliensbachian Massone Oolite (Barbujani *et al.*, 1986; Krautter, 1987), the marginal oolite sand barrier behind which lagoonal conditions could prevail. However, local development of a contemporaneous siliceous (cherty) lime wackestone can also be observed at this interval (specifically at the Madonna della Corona, and Sega d'Ala sections), and this has been named the Misone Formation (Beccarelli-Bauck, 1988; Picotti and Cobianchi, 1996).

A regional unconformity lies between carbonate-platform sediments that are Pliensbachian in age (i.e. Massone Oolite / Misone Formation) and the overlying early Toarcian (Tethyan *tenuicostatum* Zone; Geyer *et al.*, 1986; Picotti and Cobianchi, 1996) Basal Tenno Formation (also the base of the "Gruppo di San Vigilio"; Barbujani *et al.*, 1986). The Basal Tenno is a nodular, peloidal marl with abundant sponge-derived spicules and locally abundant radiolaria (Barbujani *et al.*, 1986). However, radiolaria were not identified in the petrographic analyses of this study (transverse sections of sponge spicules in thin section could possibly have been mistaken by Barbujani *et al.* (1986) for radiolaria). The Basal Tenno Formation has been interpreted as a rapid transgressive flooding horizon, opening the platform to the open ocean resulting in the deposition of these relatively deep-water calcareous marls (Castellarin, 1972;

Barbujani *et al.*, 1986; Beccarelli-Bauck, 1988). Conformably overlying the Basal Tenno formation is the 20–70-m-thick Upper Tenno Formation, which is a shallowing-upward unit of rhythmically bedded limestones with marl interbeds (Barbujani *et al.*, 1986; Bosellini, 1989). Spiculitic cherts, radiolaria (not found by this study), crinoid fragments, superficial ooids and peloids are locally abundant in this calcarenite (Barbujani *et al.*, 1986), but moving upsection these facies pass through a gradual transitional zone back into a (up to 200-m thick) facies dominated by oolite (San Vigilio Oolite; Castellarin, 1972; Barbujani *et al.*, 1986). The San Vigilio Oolite contains abundant ooids of primary radial calcite with micritic borings, as well as crinoid fragments and echinoid spines (Barbujani *et al.*, 1986), and is interpreted by (Gaetani, 1975) as a wide peripheral barrier-island complex, with a local presence of coral patch reefs, and colonised by a rich fauna of crinoids, sponges, rhynchonellid brachiopods, other bivalves, gastropods and echinoids (Jenkyns, 1972). Below the unconformable contact with the overlying Rosso Ammonitico, the San Vigilio Oolite becomes condensed, is pink in colour, and is punctuated by ferro-manganiferous hardgrounds (Jenkyns, 1972). Neptunian dykes and sills of laminated red micrite and sparry-calcite filled cavities are found generally following bedding planes and/or concave shear surfaces (Winterer *et al.*, 1991). Sedimentation on the Trento Platform is believed to have ceased in the early Aalenian (*scissum* Zone), and ammonites found in the hardground itself have been dated as late Aalenian (Sturani, 1964, 1971).

The unconformity at the base of the Rosso Ammonitico represents a hiatus of ~5 Ma (Winterer *et al.*, 1991), and ammonites found immediately above the contact were dated by Sturani (1964) as lower Bajocian. The Basal unit of the Rosso Ammonitico is a red pelagic limestone, the lower parts of which consisist of bivalve-rich (*Bositra buchii / Posidonia Alpina*), crinoidal and pelletal packstone, with iron-coated pellets of micrite and oolite fragments (Winterer *et al.*, 1991). Synsedimentary and post-diagenetic solutions are invoked to explain the nodular texture, reduced thickness and condensation of the Rosso Ammonitico, and stromatolitic dome structures found near the base have led to the conclusion that if the stromatolites were built by light-dependent cynaobacteria deposition at this time, the sea floor was in the photic zone but below wave base (Jenkyns, 1974; Clari and Martire, 1996). The initiation in deposition of the Rosso Ammonitico is therefore interpreted as another flooding horizon, which this time marks the definitive drowning of the Trento Platform, after which

subsidence and pelagic carbonate sedimentation continued on what had become a pelagic plateau (Trento Plateau; Gaetani, 1975; Winterer and Bosellini, 1981; Barbujani *et al.*, 1986; Picotti and Cobianchi, 1996).

2.1.1 Madonna della Corona

The Madonna della Corona (MDC) section through the Trento Plateau can be reached (from above) from the town of Spiazzi, on the eastern flank of Monte Baldo to the east of Lake Garda (Figures 2.i and 2.v). This section through the Trento Plateau is very important as it has relatively continuous exposure through well over 700 m of strata by virtue of the 'pilgrims' path' cut into the cliff leading to the Madonna della Corona sanctuary (see Plates A4.2.i and A4.2.ii). It is therefore by far the most complete Early Jurassic platform succession that can be studied in this region. A stratigraphic log produced by this study detailing those Lower Jurassic platform facies that outcrop at the Madonna della Corona is presented in Figure 2.vi. Sampling frequency for chemostratigraphic analysis was initially every 2 m, but re-sampling increased this to every 0.5 m of vertical thickness over critical intervals. A detailed petrographic analysis was performed on the upper 320 m of section.

At approximately –700 m, the very sporadic outcrops at the base of the Madonna della Corona section are of pelletal platform carbonates, locally rich in oncolites, and pass upsection into oolitic facies with rounded skeletal debris at –680 m. At –660 m this has become a typical "clean-washed" oolite shoal, although it should be noted that exposure and the outcrop itself is still poor at this level. Sparse oncolites are again present at –600 m, making this lower oolite body approximately 60-m thick in the Madonna della Corona section. The re-appearance of oncolites at –600 m signifies another facies change, and these are shortly followed upsection by bivalve and/or brachiopod shell fragments, and the facies becomes increasingly more massive and pelletal, before gastropods, oncolites, articulated and fragmented bivalve and/or brachiopods are found between –400 to –500 m. At –400 m ooids become the dominant constituent once more, and by –370 m the outcrop is massive 'clean-washed' oolite and this continues upsection to –320 m. The predominantly biomicritic sediments bound by oolites

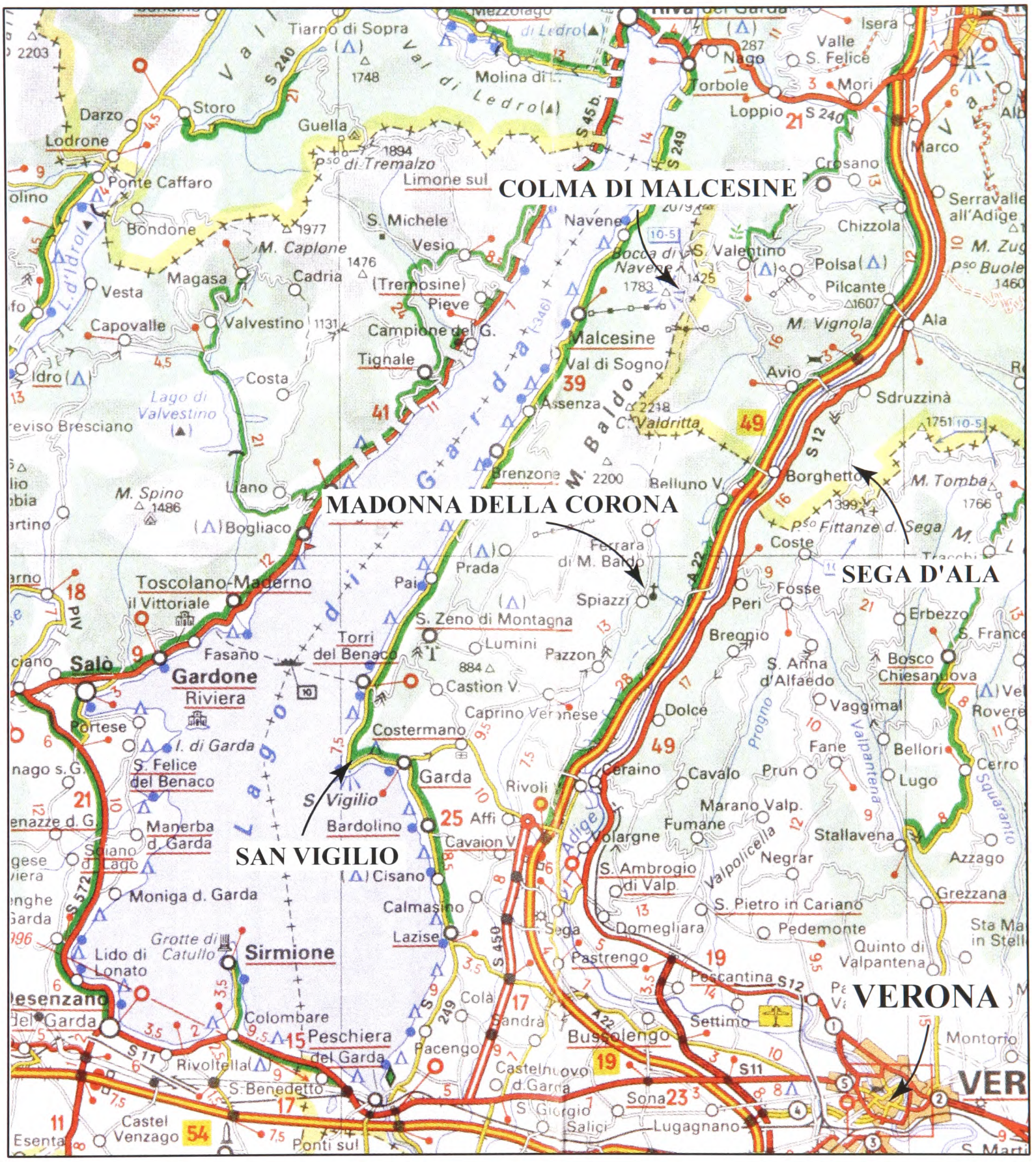

Figure 2.v. Locality map of the four sections studied on the Trento Platform, which are today in the vicinity of Verona and Lake Garda, northern Italy.

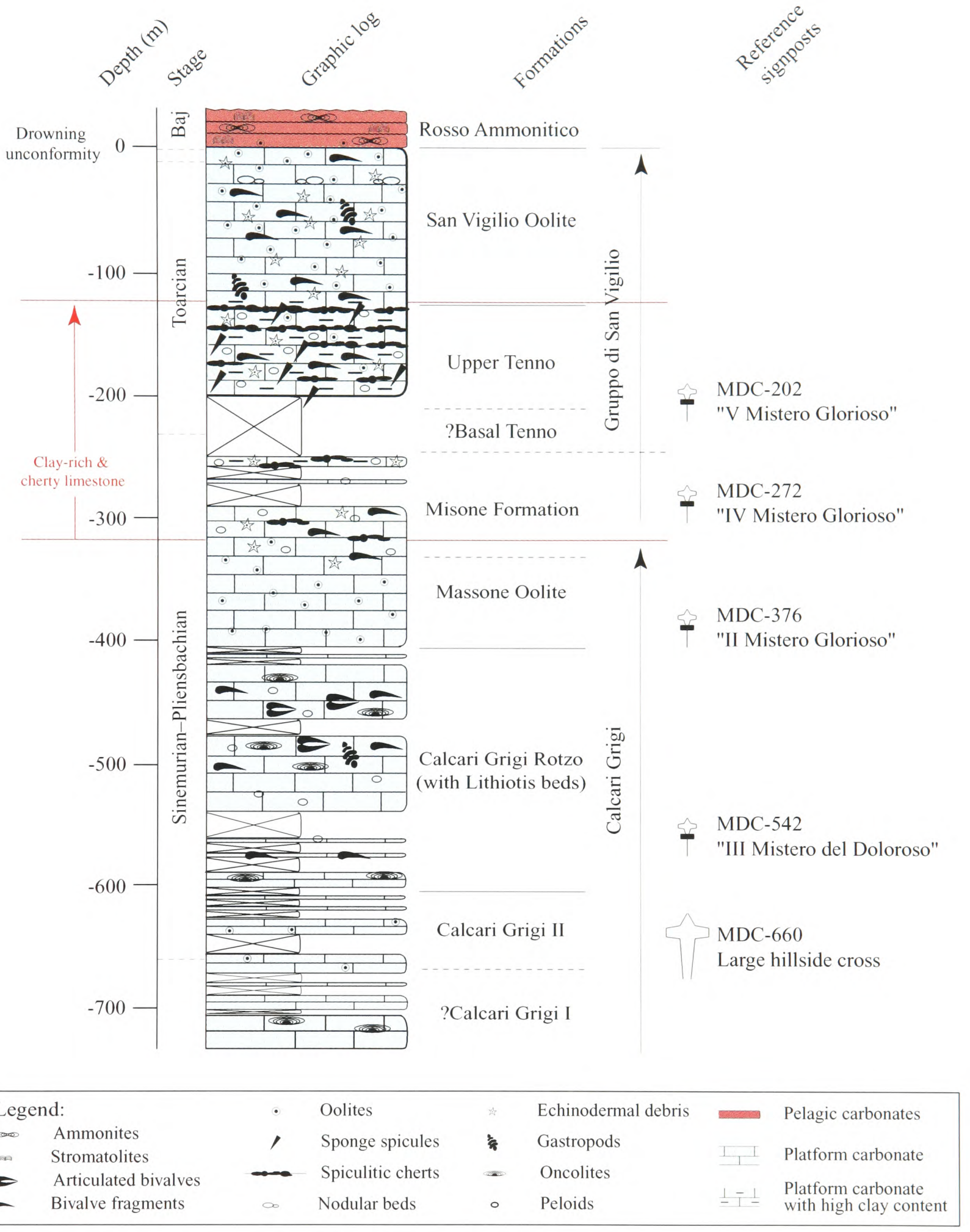

Figure 2.vi. Stratigraphic log detailing the platform-carbonate succession of the Madonna della Corona section through the Trento Plateau. Local formation names have been applied where possible, and reference signposts found on the "pilgrims' path", along which the section was sampled, are marked.

above and below are therefore approximately 200 m thick at the Madonna della Corona, and the overlying oolite is of the order of 80 m in thickness.

From just below the top of this overlying oolite body, the facies analysis undertaken becomes more detailed as it includes extensive thin-section analyses, and as a consequence the log description becomes more detailed.

At –320 m, there is a facies change to a more pelletal limestone including in its matrix echinodermal debris, bivalve fragments and minor silica. However, between –298 and –300 m there is what appears in outcrop to be a fault, resulting in a non-quantifiable displacement. There does not appear to be a major facies change across the fault, so in terms of section measurement its presence has been ignored. However, at –298 m sparse chert nodules are introduced for the first time, and whether this is a function of some fault displacement incurring lost sedimentary section is unknown. Following the possible fault, there is a gap in exposure between –272 and –292 m, and again between –258 and –270m. It also remains uncertain whether the outcrop between –272 and –270 is a slipped block or not. The following exposure between –248 and –258 m is of yellow clay-rich limestone with visible chert nodules and crinoid fragments (Plates A3.2.xiv and A3.2.xv).

Above the subsequent 50-m-thick exposure gap, upsection from –202 m, the carbonate platform is composed of rhythmically bedded pelletal limestone units (~20 cm) with thin marly interbeds (<0.5 cm; Plates A3.2.x to A3.2.xiii). Upsection, over the next 50 m, nodular and ribbon-like spiculitic cherts are abundant, generally found lying along bedding planes, and bivalve fragments and echinoderm debris become increasingly dominant sedimentary constituents (Plates A3.2.vii to A3.2.ix). From approximately –160 m, ooids are gradually re-introduced into the depositional system, and by –130 m (the highest identified chert; Plate A3.2.v and A3.2.vi), the facies transition back to 'clean-washed' oolite is virtually complete. Bivalve, gastropod, and echinoderm debris (generally crinoidal and also echinoid spines) remain important sedimentary constituents in the now massive oolite, which continues to the top of the section (0 m; Plates A3.2.i to A3.2.iv). However, over the topmost 10–15 m it is noticeable that the succession appears to become increasingly thin-bedded, pink and there are

ferromanganese hardgrounds present. However, no ammonites were seen at the top of the section in this study (though outcrop is poor and too inaccessible for detailed observations), although they have been identified at the quasi-equivalent interval in the San Vigilio section by previous authors (***2.1.2;*** Sturani, 1964; Winterer *et al.*, 1991).

It is clear that the Madonna della Corona stratigraphic section correlates well with previous descriptions of the Trento Plateau stratigraphy, which have already been discussed in detail in ***2.1*** (Figure 2.iii). However, to summarise, in this study the base of the Madonna della Corona section did not reach the Dolomia Principale 'basement' facies, but with the presence of oolites above the lowermost reach of the section, it is believed that the section begins in the Calcari Grigi I member (Hettangian–Sinemurian; see ***2.1***), although only the top 50–60 m of it were identified. The presence of 60 m of overlying oolites closely follows the Trento Plateau stratigraphic description of Bosellini and Broglio Loriga (1971) and Picotti and Cobianchi (1996), who termed this unit the Calcari Grigi II member (Sinemurian). The overlying 200 m Calcari Grigi Rotzo member of oncolites, bivalves, brachiopods and gastropods have been interpreted as a Sinemurian facies indicative of low-energy lagoonal environments found behind a marginal oolite-sand bar that was progressively infilled, before another oolite-sand barrier-island complex developed above. This facies is represented in the Madonna della Corona section by an 80-m-thick Pliensbachian Massone Oolite Formation (Bosellini and Broglio Loriga, 1971; Gaetani, 1975; Krautter, 1987; Picotti and Cobianchi, 1996).

The change in facies from oolite to yellow clay-rich pelletal limestone with abundant chert signifies the local presence of the Misone Formation (Beccarelli-Bauck, 1988; Picotti and Cobianchi, 1996). There is approximately 10 m of this facies exposed continuously before the exposure gap at –298 m, but similar sporadic deposits can be followed up to –250 m, signifying a 60-m-thick development of the Misone Formation. This exceeds the 10-m thickness assigned by Becarelli-Bauck (1988), although the interval previously described may be equivalent to the 10 m of continuous Misone Formation outcrop found directly overlying the Massone Oolite in this study. If this is true, it would be likely that Becarelli-Bauck (1988) did not take into account the sporadic outcrops between –250 and –298 m for fear that they were not *in situ*. Also, measurement of exposure gaps here may be inaccurate and complicating the story is the

presence of faults and apparently slipped blocks with recognised, but non-quantifiable, displacement.

On comparison with the Colma di Malcesine (CDM) section (see ***2.2.3***), it can be calculated by extrapolation that there should be approximately 110 m of combined Tenno Formations at the Madonna della Corona section, taking into account differences in sedimentation rate between the two localities (Barbujani *et al.*, 1986). If this calculation is correct, the top of the Misone Formation (or at least distinctive Pliensbachian platform facies) should be found at approximately –240 m (i.e. in the 50-m-thick exposure gap). Measuring the Upper Tenno Formation thickness from above, 70 m of continually exposed outcrop is present before the exposure gap at –200 m is reached. It is therefore credible that, at the Madonna della Corona, the 40 m of combined Tenno Formations missing from the calculated 110 m are hidden in the exposure gap between –200 and –250 m.

Previous interpretation of the Toarcian Upper Tenno Formation describes a platform that struggled to keep up with sea-level rise as a consequence of changes in atmospheric and/or oceanographic conditions (nutrient level and pCO_2 increases have been invoked; Cobianchi and Picotti, 2001). However, the platform was temporarily "rejuvenated", and this is reflected by the facies transition into the overlying San Vigilio Oolite (Barbujani *et al.*, 1986; Beccarelli-Bauck, 1988). In the Madonna della Corona section, the Toarcian and Aalenian San Vigilio Oolite (Sturani, 1964), which has been interpreted by Gaetani (1975) as a wide peripheral barrier-island complex, is recorded as being 130-m thick, before it is cut-off by a sharp unconformity and capped by pelagic Rosso Ammonitico.

2.1.2 San Vigilio

The lakeside road and quarry sections found at the Capo di San Vigilio (see Figures 2.i and 2.v) were first described and, more significantly, dated in detail by Sturani (1964). The exposed outcrop is sparse, with large gaps between, making measurements and clarity of location in the vertical stratigraphic column difficult to achieve. However, it proves to be one of the key sections in the region because of the well-dated ammonites that are found at the

platform top, and in the Rosso Ammonitico above, providing an all-important biostratigraphic 'anchor-point' for the drowning of the western margin of the southern Trento Platform. The section analysed by this study is illustrated in Figure 2.vii, and described in detail below. The sampling frequency for chemostratigraphic analyses was at 0.5 m intervals throughout, while the petrographic study concentrated primarily on the cherts found in the section.

The base of the San Vigilio (SV) section, found at the foot of one of the abandoned quarry sites (PV – quarry; Figure 2.vii) is characterised by the presence of cross-bedded 'clean-washed' oolite with abundant echinodermal debris (including echinoid spines and crinoid ossicles). This oolite body extends from –196 m to at least –142 m (though this also covers two exposure gaps amounting to 20 m thickness in total), but the –146 to –142 m interval is also characterised by the presence of cherts (this interval is found protruding from the road surface, and so it is not certain that the outcrop is *in situ*, although the dip appears consistent with outcrops above and below). After a 12-m exposure gap, there has been a facies change: upsection from –134 m to –122 m the outcrop is rhythmically bedded peloidal limestone with clay interbeds and abundant spiculitic cherts (Plates A3.2.xvi to A3.2.xviii). At –122 m, however, there is a transition to more oolitic limestone, still with abundant cherts. The cherts occur mainly as nodules or lenses, as they can extend in size up to 20 x 150 cm (horizontal extension along bedding planes).

An exposure gap of 40 m is then measured, before reaching the next outcrop found at the foot of a more recent quarry site (SVQ, Figure 2.vi) further to the northeast along the lakeside road. At –68 m, and for at least 15 m below (although in inaccessible outcrop), red/brown spiculitic chert nodules are abundant, which appear to extend for up to 50 cm along and across bedding planes (Plates A3.2.xix and A3.2.xx). The limestone, locally cross-bedded, in which the cherts can be found is oolitic with echinodermal fragments. Evidence of cherts cannot be found above –68 m, but the oolite body contines upsection to –41 m at the San Vigilio Viewpoint location (SVV, found on the cliff-top above SVQ; Figure 2.vii), where abundant echinodermal debris can still be discerned, and beyond the next 300-m thick exposure gap to the San Vigilio road section (SV; Figure 2.vi) further northeast along the road. Here, between –11 and –6 m, bivalve and brachiopod shell fragments are visible in the oolite, and at

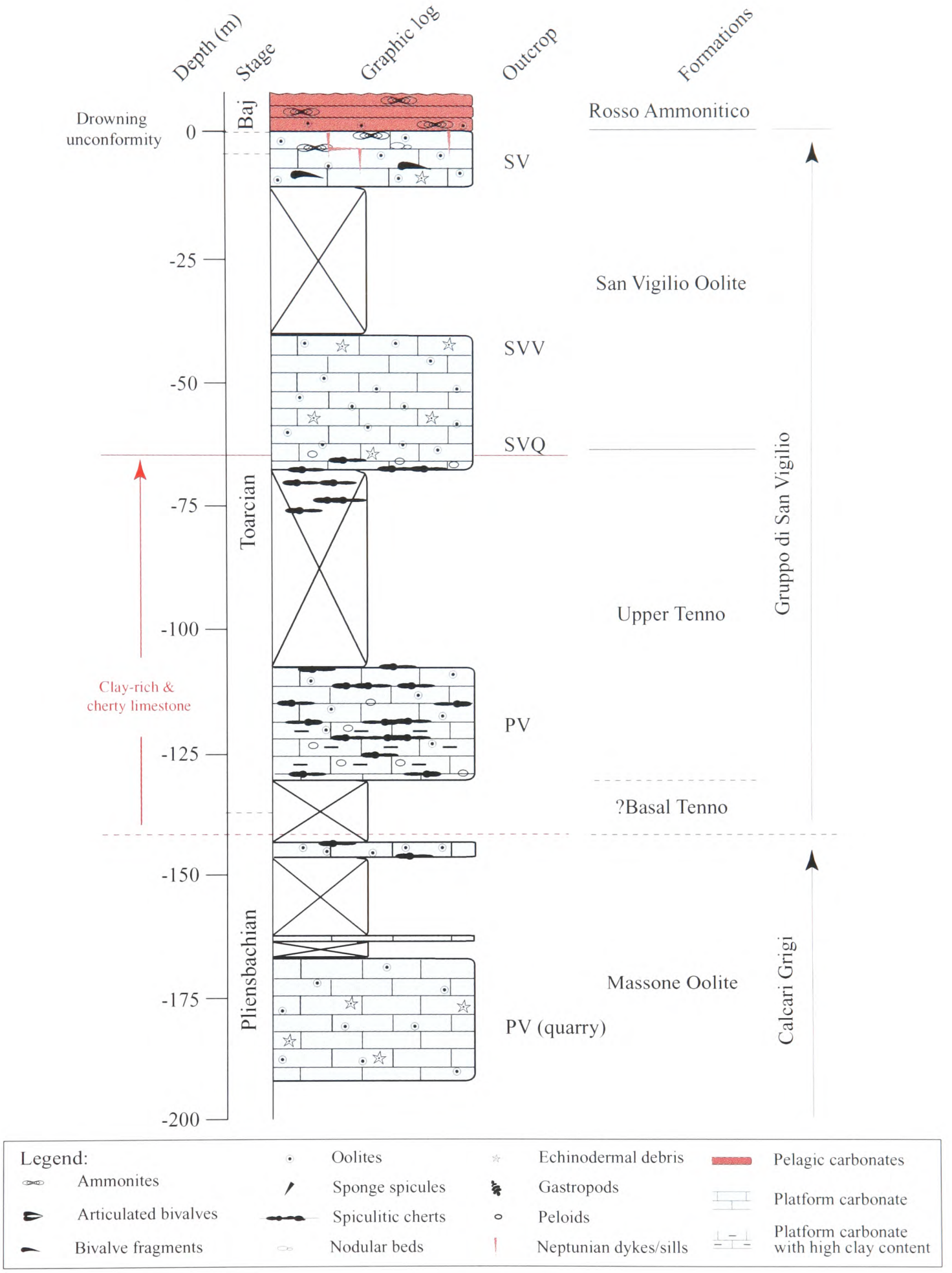

Figure 2.vii. Stratigraphic log depicting the facies identified at the San Vigilio section in the area of Capo di San Vigilio. Outcrops listed are those individual localities of exposed rock with substantial exposure gaps between. Some error may be incorporated into the measurement of the strata missing from the vertical section. At -75 m cherts are visible in an inaccessible cliff-face. SV = San Vigilio; SVV = San Vigilio Viewpoint; SVQ = San Vigilio Quarry; PV = Private Villa (abondoned quarry at base).

–4 m, red micritic pervasive sills and dykes are apparent. Hardgrounds with ferromanganiferous crusts are introduced, the oolite becomes pink in colour at –1.5 m and the first ammonites can also be identified at this level. At 0 m the sharp facies transition into pink micritic facies with abundant ammonites, intraclasts and ooid fragments is clearly recognisable making this exposure the best record of this change out of all the sections studied in this region (see Plate A4.2.iii).

The San Vigilio section, although the most marginal of the sections studied, records the facies changes we are accustomed to seeing in this area of the Trento Plateau (e.g. Sturani, 1964; Gaetani, 1975; Barbujani *et al.*, 1986; Picotti and Cobianchi, 1996; Cobianchi and Picotti, 2001). The 54-m-thick basal oolite body is interpreted as being the top of the Pliensbachian Massone Oolite (Bosellini and Broglio Loriga, 1971; Krautter, 1987) but, as with the Madonna della Corona section, the lower Toarcian Basal Tenno Formation (Geyer *et al.*, 1986; Picotti and Cobianchi, 1996) appears to be missing, and, following an exposure gap above the Massone Oolite, the facies change is straight into the rhythmically bedded cherty limestone of the Upper Tenno Formation. 13 m of this formation are exposed here, before the cherty base of the Toarcian and Aalenian San Vigilio Oolite is reached (Sturani, 1964). Noticeably, this is a very gradual transition in terms of the prevalence of the spiculitic cherts: they continue for an estimated 40–50 m (provided the exposure gap has been measured correctly). The San Vigilio Oolite has been measured at approximately 60-m thick, and characteristically has abundant echinodermal remains. Its upper exposed 10 m appear condensed, with numerous hard-grounds, neptunian dykes and ammonites, before the final drowning unconformity, which separates the platform facies from pelagic Rosso Ammonitico (Winterer *et al.*, 1991). This final 10 m of the San Vigilio Oolite has been dated using ammonite biostratigraphy as early Aalenian, and the unconformity itself contains late Aalenian ammonites, before early Bajocian fauna appear at the base of the Rosso Ammontico (Sturani, 1964).

2.1.3 Colma di Malcesine

Approximately 13 km north of Spiazzi, along the crest of the Monte Baldo is the Colma di Malcesine (CDM) section, on the summit of the slopes above the (Garda) lakeside town of

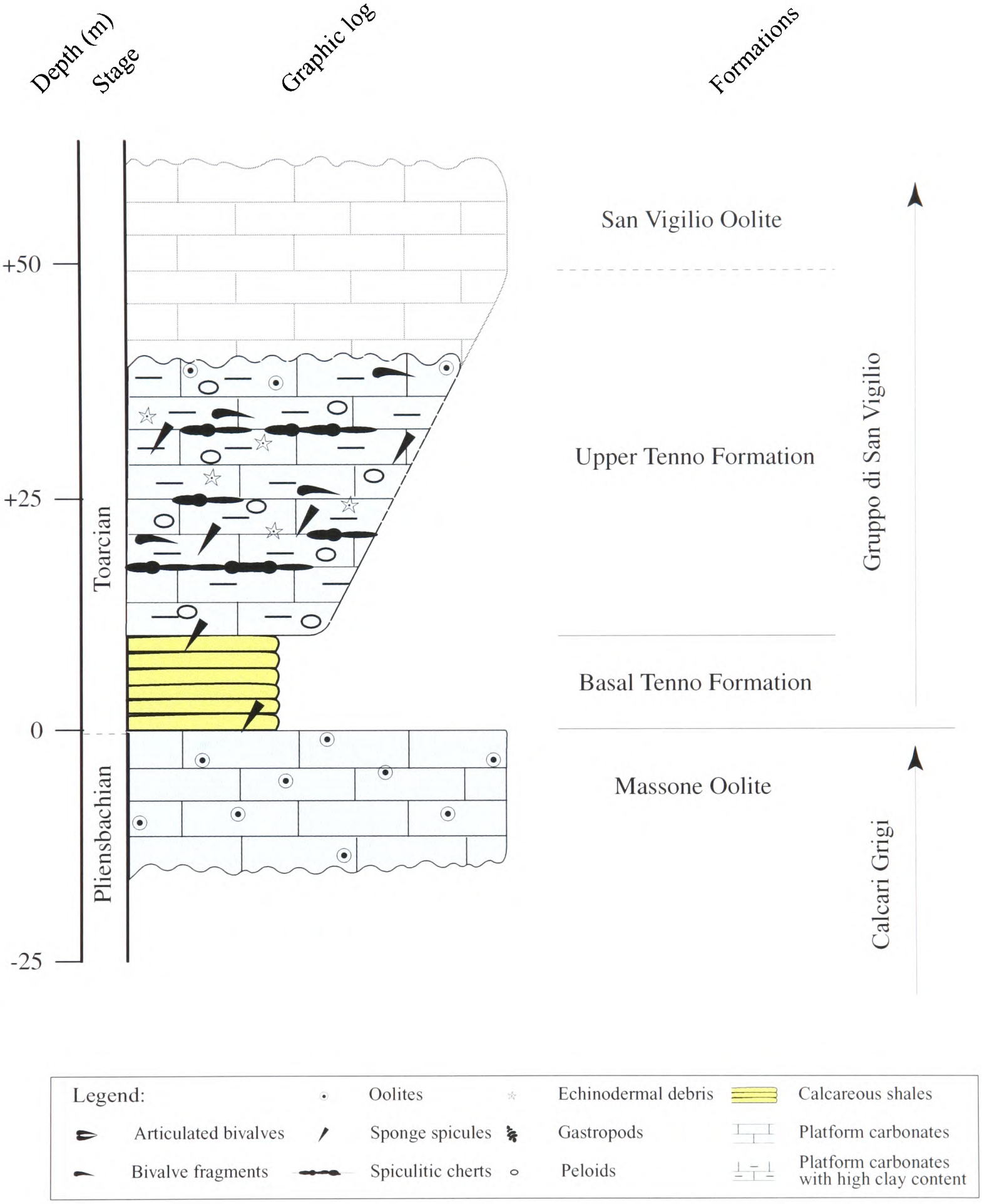

Figure 2.viii. Stratigraphic log of the Colma di Malcesine (CDM) section with formation names applied where appropriate. Although much of the succession is not accessible, the small amount that it documents a very important series of facies changes through the Trento Platform, which are not well-exposed elsewhere in the region.

Malcesine to the west (Figures 2.i and 2.v). A stratigraphic column illustrating the sedimentary succession at the Colma di Malcesine section is presented in Figure 2.viii. Sampling frequency for chemostratigraphic analyses was at 0.5 m intervals, while a petrographic study was carried out over the entire section.

The 13 m of basal unit to the section can only be studied at a point found by following the path along which the exposures are reached (right branch at the top of the car park) for approximately 0.5 km until it begins to descend the mountain toward the villages and town of Malcesine below. On the final spur before the path makes this descent, the desired outcrop can be located down a precipitous grassy slope that leads onto cliffs above the valley below. The 13 m of outcrop exposed here are characterised by being massive 'clean-washed' oolite (Plates A3.2.xxi and A3.2.xxii). Although lower parts of the section remain inaccessible, from what can be seen with the eye, there is no visible facies change down-section for many metres and the underlying cliffs appear to represent a thick (at least 30 m) and massive oolite body. The top surface of the oolite unit is sharp and marks a transition into calcareous shales lying above. These overlying marls are most easily studied at a point where the path crosses a tight gully only a couple of hundred metres from the car park. At the base, the marls have a nodular appearance, are grey, although weather to yellow–brown (see Plate A4.2.iv), and are devoid of fossil remains other than sparse sponge spicules that are apparent in thin-section (Plate A3.2.xxiii). They are moderately friable but become increasingly well cemented (thin sporadic cemented layers) over the following 9 m upsection, by which point the transition into rhythmically bedded peloidal limestone units with marly interbeds is complete (Plate A3.2.xxiv). The limestone beds are approximately 10–12 cm thick at this low level, with 1 cm marl interbeds (see Plate A4.2.v). Partially silicified echinodermal debris can be observed at +18.5 and +19.5 m in thin-section (Plates A3.2.xxv to A3.2.xxx) The first bivalve fragments visible in outcrop are found at +20 m, and the first ribbon-bedded spiculitic cherts are found at +21.2 m (Plates A3.2.xxxi to A3.2.xxxiii), along a marl interbed and there are more nodules (5 x 15 cm) at +29.5 m. Rhythmically bedded limestones are present up to +34 m, above which no more outcrop is accessible, although using the eye to extrapolate it is estimated that at approximately +55 m the facies undergoes a transition back into massive limestone.

Importantly, the Colma di Malcesine section has outcrop exposure through the problematic interval found between -200 and –300 m in the Madonna della Corona section (see ***2.1.1***). The basal oolite body, of which only 13 m is accessible at the Colma di Malcesine section, is interpreted here and by Barbujani *et al.* (1986) to be the Pliensbachian Massone Oolite (n.b. the clear absence of the Misone Formation above). The sharp facies transition into calcareous shale at its top is therefore interpreted to mark the early Toarcian (*tenuicostatum* Zone) initiation in deposition of the Basal Tenno Formation (which is absent from the Madonna della Corona section), and so this transition also represents the previously described flooding horizon (Barbujani *et al.*, 1986; Geyer *et al.*, 1986; Beccarelli-Bauck, 1988; Picotti and Cobianchi, 1996; Cobianchi and Picotti, 2001). After 9 m, this marl has undergone a gradual transition into the Upper Tenno Formation, which itself then continues upsection for 25 m in accessible outcrop, but for an estimated 45 m in total (visible but inaccessible). At approximately +55 m there is another apparent facies transition into massive limestone, which is interpreted here as the San Vigilio Oolite, an assumption confirmed by (Barbujani *et al.*, 1986).

2.1.4 Sega d'Ala

In the upper reaches of the Sega d'Ala section (SDA), under the trees found toward the top of the road, an approximately 50-m, near-continuous exposure through oolite, shale, rhythmically bedded limestones and overlying skeletal limestone can be encountered (Plate A4.2.viii). This section proves an important addition to that found at Colma di Malcesine, as it covers similar facies transitions within the upper few hundred metres of the Trento Platform. A graphic illustration of this succession is presented in Figure 2.ix, and is discussed further below. Sampling density for the chemostratigraphic analysis was at every metre between –10 and 0 m, every 20 cm between 0 and +5 m, every 50 cm between +5 and +31 m, and every metre between +31 and +44 m. Detailed petrographic analyses were not carried out, because the facies are assumed to correlate with those seen elsewhere (in particular, the Madonna della Corona and the Colma di Malcesine; see ***2.1.1*** and ***2.1.3***).

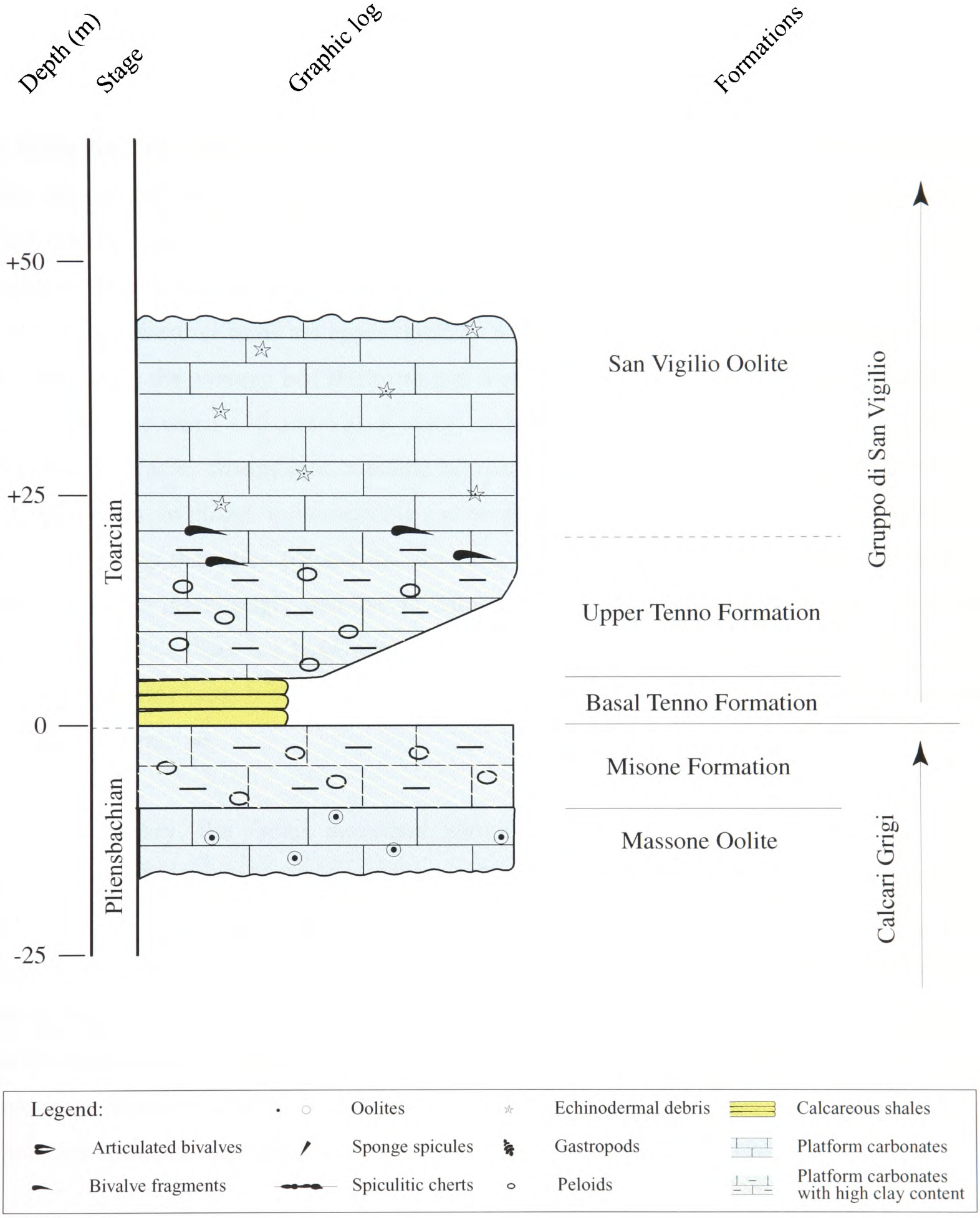

Figure 2.ix. Stratigraphic log detailing the platform succession found in the upper reaches of the Sega d'Ala section, above, below and including the Tenno formations (SDA).

From –15 to -8 m 'clean-washed' and massive oolite is present. Although normal faulting disrupts the bedding to a minor extent in the outcrop between –7 and –6 m it remains obvious that a facies transition occurs just above –8 m, and cyclically bedded micritic limestone is introduced (Plate A4.2.vii). The limestone units are on average between 15 and 20-cm thick, and continue upsection to 0 m. At 0 m there is another marked facies transition to calcareous shale (Plate A4.2.vi). Characterised by high clay content (relative to carbonate) and a distinctive nodular texture, the shaly interval extends for 5 m before a gradual transition into rhythmically bedded micritic limestones is achieved. These cyclically bedded units are very similar in character to those below the shale, and appear devoid of noticeable chert nodules. Between +10 and +13 m the limestone units are approximately 5–10 cm thick with irregular contact between them. By +17 m, the average bed thickness has increased to 10–20 cm and the clay content is relatively low. Between +18 and +21 m shelly remnants of bivalved organisms are apparent, and by +22 m a facies change into crinoidal biosparite has occurred, which continues until the top of the section. In places, cross-bedding can be distinguished, the result of current action on the skeletal grains that once formed the sea-floor (Plate A4.2.viii), but generally the actual bedding becomes increasingly massive in nature upsection: thicknesses of up to 1 m were observed. At +44 m, there is a large exposure gap with only patchy outcrops above, and so the studied section ends here. It should be noted that the patchy outcrops that can be found above are oolitic in nature.

In summary, the facies described above have been interpreted to represent the succession from Massone Oolite through to an 8-m-thick presence of the Misone Formation, found below the overlying 22 m combined Tenno Formations, which are topped by the San Vigilio Oolite. The continuous exposure offered by the Sega d'Ala through this succession of Trento Platform facies renders this section unique. The Madonna della Corona is incomplete in terms of exposure and, although the Colma di Malcesine is continuous in outcrop, the Misone Formation is absent (probably due to pinching out as opposed to a hiatus; see **2.2.3** and **2.4**), and does not extend as high upsection as the San Vigilio Oolite.

2.2 Chemostratigraphic results

Chemostratigraphic data for all of the above mentioned sections on the Trento Plateau are presented. Intra-platform correlations of these isotope profiles are carried out in ***2.5***, and ***Chapters 5 and 6*** discuss the application of these profiles to chemostratigraphic dating, and the relationships of the profiles to the facies from which they are obtained. For complete data tables see ***Appendix Data Tables 2.i–2.iv***.

2.2.1 Strontium-isotope results

Because strontium-isotope trends are relatively broad (see ***1.3***) most emphasis for a complete and detailed strontium-isotope profile (that is also very time-consuming to produce) is based on bulk carbonate samples of the thick and relatively continuous Madonna della Corona section. Sections that are relatively incomplete and/or cover short time durations are less useful for strontium-isotope analysis since long-term trends are difficult to recognise as important curve inflections occur over relatively thick intervals of outcrop. However, analyses of relatively sporadically distributed San Vigilio samples are considered.

Figure 2.x illustrates the data produced from 730 m of platform section collected at 2 m intervals from the Madonna della Corona locality. Values range from 0.707100 to 0.707523 and, apart from sporadic anomalous data points, the curve exhibits only limited scatter between –730 to –700 m, -500 to –400 m, and –50 to 0 m. At low-resolution, the broad-scale trend of a fall in values from ~0.7075 to 0.70715 between –730 and –200 m is discernible, and following this there is a rise back up to ~0.70732, which is found just below the drowning unconformity (0 m). Throughout the length of the profile there are also smaller scale fluctuations, namely two trough-like features, found between –550 m and –400 m, and also between –100 and –20 m, which give the curve a distinctive saw-tooth appearance, as discussed in ***1.3.2***. A third possible 'trough' in values may occur at ~ -575 m, but the lack of data at this interval makes it difficult to ascertain for certain.

A strontium-isotope profile of the 200-m-thick San Vigilio section is illustrated in Figure 2.xi. The lack of continuous exposure here proves problematic, as few distinctive trends can be ascertained from the curve. Values range from 0.70714 to ~0.70746 (although both of these values appear anomalous), and most uncertainty regarding real values due to scatter is between –105 and –130 m. Data points from the outcrop at the base of the section (in the abandoned quarry below the "Private Villa") cluster around 0.70728, and above the 50-m exposure gap (in what has been interpreted as Upper Tenno Formation), data are highly scattered about 0.7073. However, a possible primary signal can be identified amongst this scatter, which exhibits a rise in values from 0.70724–0.70731. Strontium-isotope data produced from samples between 40 and 70 m illustrate a rising trend from 0.70731–0.70736, before scattering to less radiogenic values toward the top of the outcrop. Above the next 30-m exposure gap, in the final 10 m of platform before the drowning unconformity is reached, values are not scattered and lie about an approximate value of 0.70733.

2.2.2 Carbon-isotope results

Less time-consuming carbon-isotope analyses (c.f. strontium-isotope analysis) were carried out on all four Trento Platform sections, and the most continuous and extensive profile obtained from these was that of the Madonna della Corona section, and this is displayed in Figure 2.xii. The visible broad-scale trend is that of a rise in $\delta^{13}C_{carb}$ values from +1.5 ‰ at the base of the section to >+4 ‰ at –178 m. Above this point values decrease until the drowning unconformity, where they are +2 ‰. Imprinted on this broad-scale trend are smaller-scale positive and negative shifts in values, not all of which necessarily represent changes in the primary isotope signal, but may be the result of post-depositional diagenesis. In the following description (and others in this study to follow), however, anomalous results and scatter have been ignored, and comments on trends refer to what appear to be primary signals (or at least coherent trends). From –730 m to –680 m $\delta^{13}C_{carb}$ values increase from +1.25 ‰ to +2 ‰, before a stepped decrease occurs to +0.5 ‰ at –625 m (disregarding the anomalous –632 m value of –0.87 ‰). Values soon recover, and return to +2.5 ‰ at –575 m before another marked decrease to a value of +1.4 ‰ found at –540 m. Above this interval, $\delta^{13}C_{carb}$ values rise for 60 m until they reach +3 ‰ at –480 m, after which point the primary signal appears to become

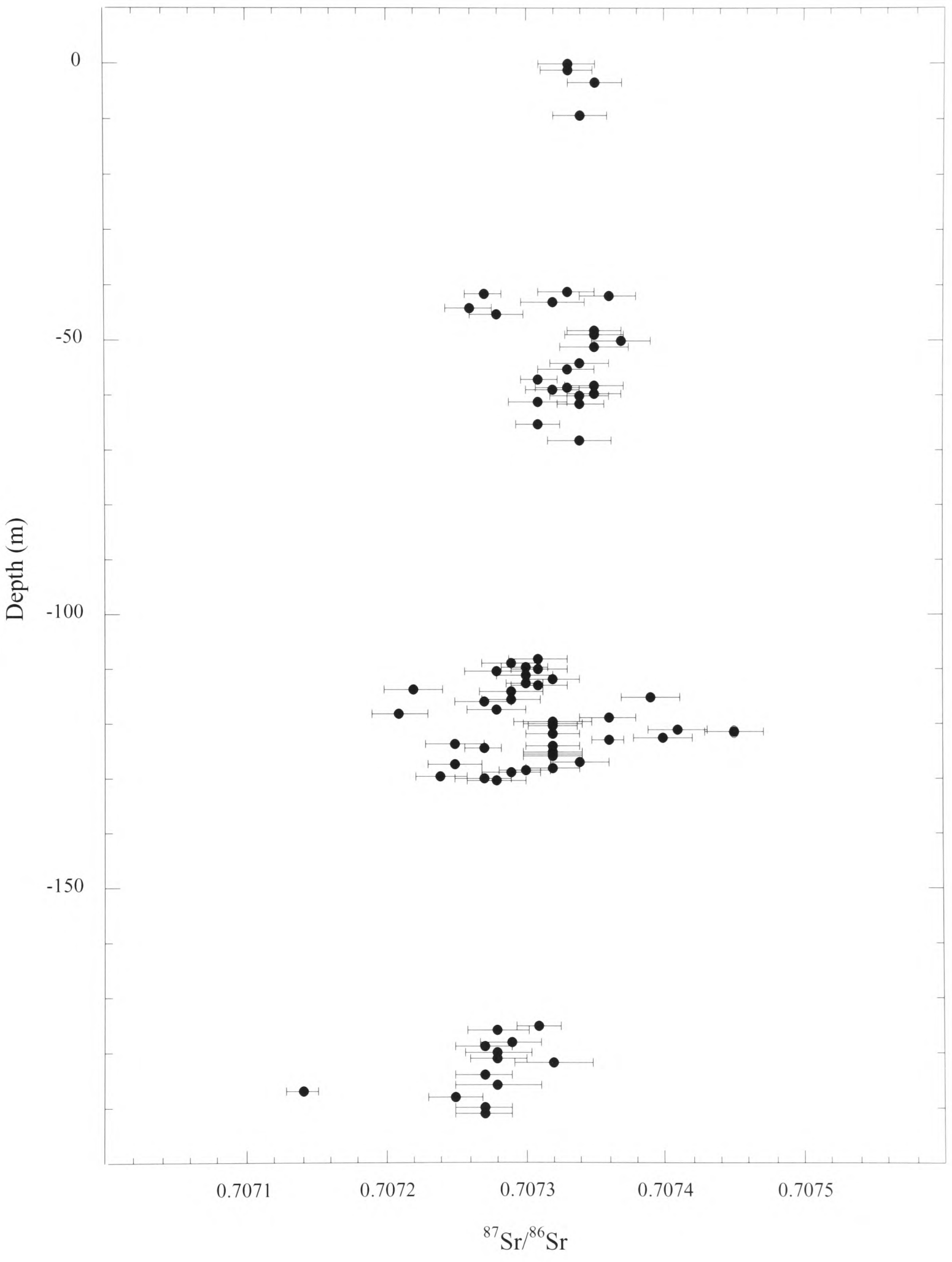

Figure 2.xi. Strontium-isotope profile of the 200-m-thick San Vigilio section. Although long-term trends are difficult to discern due to discontinuous outcrop exposure, possibilities of small-scale patterns can be ascertained. Data were normalised to a NIST SRM 987 value of 0.710250, the running average of standards being 0.710248, and $2\sigma = 0.000026$.

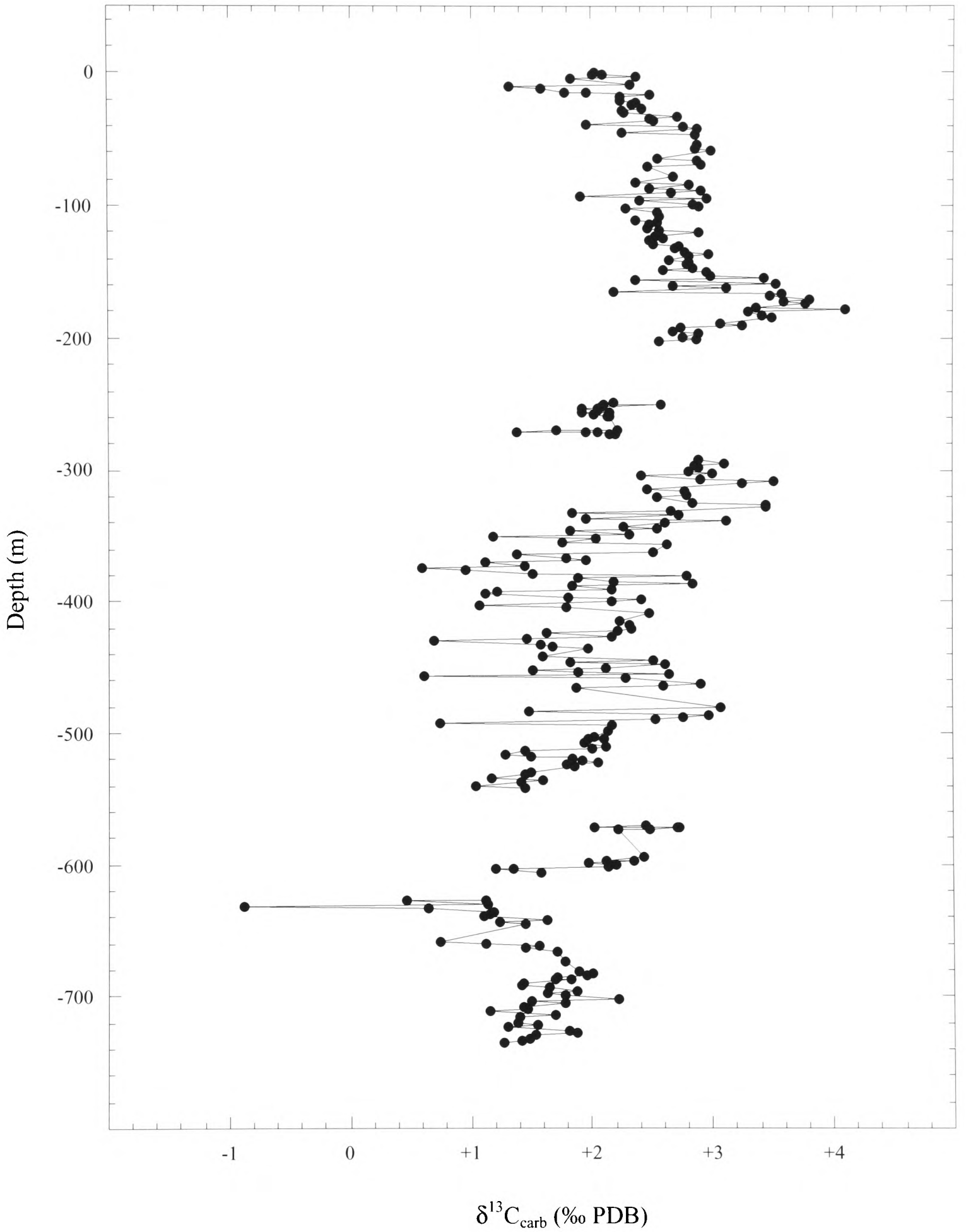

Figure 2.xii. Carbon-isotope profile of the 730-m-thick Madonna della Corona section. Distinctive excursions are recognisable and, although data produced from those bulk carbonate samples between -250 m and -550 m appear relatively scattered, a coherent signal can still be identified.

modified resulting in scatter of data making interpretation of the curve more difficult. However, what are believed to be primary isotope data show a further decrease in values to +1.6 ‰, found at –420 m, before another gradual rise to +3 ‰ occurs by –300 m. Here the profile becomes disjointed due to a lack of outcrop exposure (see ***2.1.1***), but from the carbonates that are available for sampling over a 20 m interval above and below –260 m, $\delta^{13}C_{carb}$ values recorded are ~+2 ‰. However, there appears to be a relatively rapid negative shift from +2.2 ‰ to + 1.5 ‰ and back again at -270 m, but as described in ***2.1.1***, these samples appear to be taken from a slipped block, and so are potentially unreliable. From the first data point after the next exposure gap (–202 m) until –178 m, values increase from +2.5 ‰ to +4.1 ‰, before decreasing to +2.5 ‰ by –130 m. Values remain relatively constant for 30 m, before beginning a gradual rise to +2.9 ‰, achieved at –70 m, and a subsequent gradual decrease to +2.2 ‰ by –18 m. Between –16 and –14.7 m, the gradual decrease steepens markedly into a negative $\delta^{13}C_{carb}$ excursion, which reaches +1.3 ‰ by –10 m. This is a drop in values of ~1 ‰ over 5 m of section. Values quickly recover to +2.3 ‰, and the final data points before the drowning unconformity record values of +2.1 ‰.

The carbon-isotope curve for the 200-m-thick San Vigilio section is illustrated in Figure 2.xiii and, although outcrop is patchy, there is little apparent scatter and distinctive trends are more easily recognisable than in the strontium-isotope curve because of the shorter residence time of carbon in the oceanic reservoir (i.e. the curve responds to its forcing mechanisms much more rapidly; Figure 2.x). Values obtained for carbonate samples between –196 and –161 m are relatively stable at approximately +2.5 ‰, before they show the initiation of a slight decrease in values which leads into a 15-m exposure gap, above which values reach a low of +1.3 ‰ at -145 m before a rapid rise of ~1‰ over a 2 m interval of rock (it is not certain that this horizon is an *in situ* outcrop exposure). Following this, there is a rapid decrease in $\delta^{13}C_{carb}$ values to +2 ‰, before another 13-m exposure gap, immediately above which values are similar until a further decrease to a minimum value of +1.1 ‰ is recorded at –124 m (data over the interval –127 to –121 m represents an isotopic minimum but is relatively scattered). From –121 to –112 m, $\delta^{13}C_{carb}$ values increase from +1.7 ‰ to +2.3 ‰, and above this there is some stability in values for the following 5 m before the next 40-m exposure gap. From –68 to –45 m, $\delta^{13}C_{carb}$ values gradually increase from +2.3 to a maximum of +2.8 ‰, before decreasing back to +2.4 ‰ in the

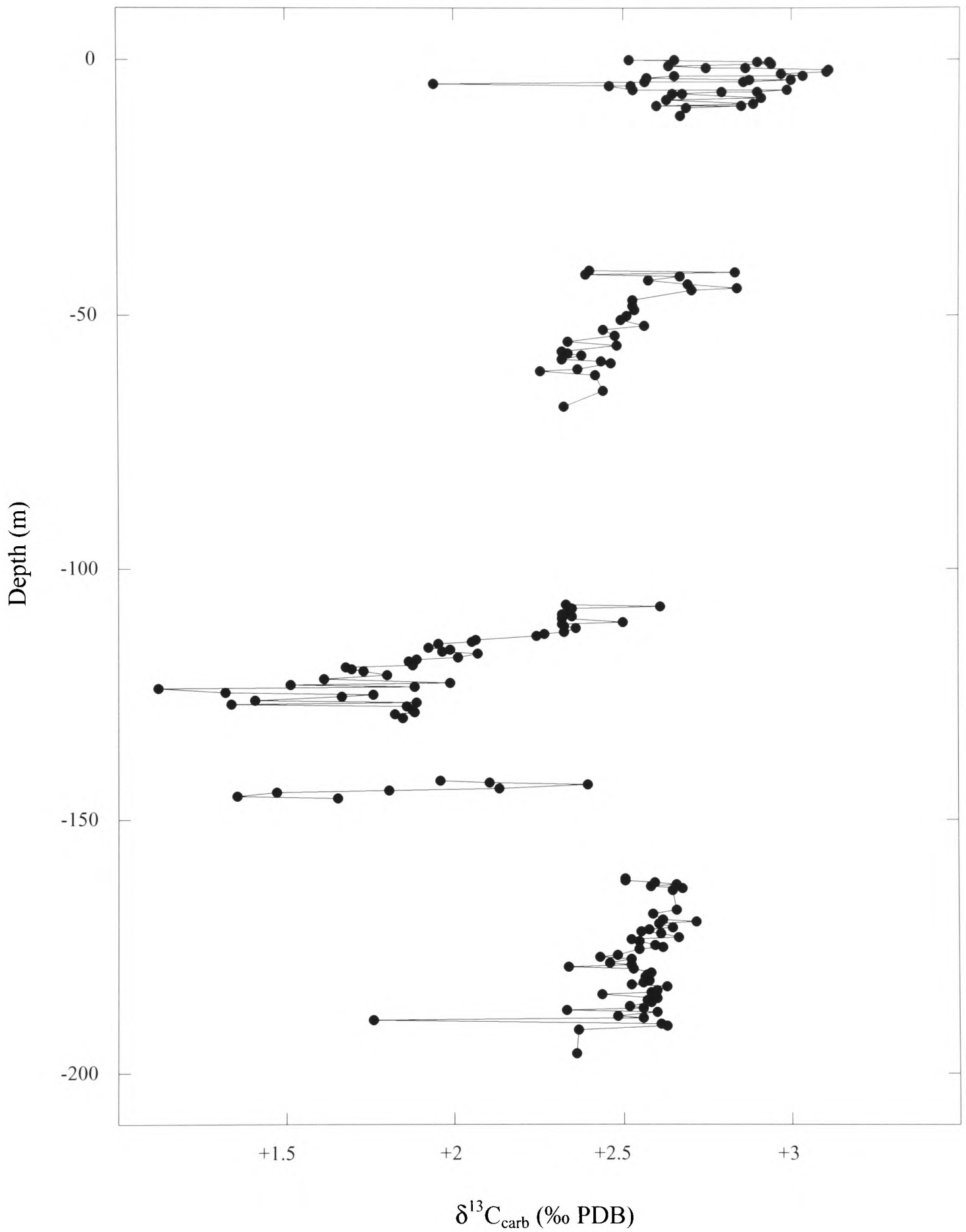

Figure 2.xiii. Carbon-isotope profile of the 200-m-thick San Vigilio section. Although exposed outcrop through the section is few and far between, the relatively rapid responses of the carbon-isotope curve to its forcing mechanisms (c.f. strontium-isotope curve) allows diagnostic features to be more easily distinguished.

4 m before the next exposure gap. Between –11 and 0 m values are relatively scattered about an approximate average of +2.75 ‰.

The carbon-isotope profile of the 47-m-thick Colma di Malcesine section is presented in Figure 2.xiv. Although not a thick section, exposure is relatively continuous and the isotope data obtained show remarkably little scatter. The lower 13 m of oolite outcrop reveal very stable $\delta^{13}C_{carb}$ values of +2.25 ‰ before a sharp decrease in values of 1.25 ‰ between 0 and +4 m (although this is preceded by an initial decrease between –1 and 0 m). After this minimum of +0.96 ‰, values begin to steadily climb and finally reach +3 ‰ at +34 m, the last accessible outcrop.

Figure 2.xv illustrates the carbon-isotope curve obtained from the 59-m-thick Sega d'Ala section. From –15 to –5 m $\delta^{13}C_{carb}$ values steadily increase from +2.2 to >+2.5 ‰, but between –5 and –4 m there is a marked jump in values from 2.5 to 3.3 ‰. This is shortly followed by a steep decrease in values between –4 and +0.4 m, by which point the $\delta^{13}C_{carb}$ value is +1.3 ‰. From a value of +1.9 ‰ at +0.6 m, there is a gradual increase in values to 3.7 ‰ at +33 m. Over the next 9 m, values level-off (with some minor scatter), and it is possible that values are just beginning to drop again before the section ends at +44 m.

2.2.3 Oxygen-isotope results

Analysis for carbon-isotopes also resulted in the production of oxygen-isotope data for all four sections of the Trento Plateau. Figure 2.xvi illustrates the oxygen-isotope profile of the 730-m-thick Madonna Della Corona section, and although many of the data points from the lower 500 m appear scattered, long-term coherent trends are visible, and scatter is evidently reduced in the upper 200 m of the platform. The broad trend of the curve registers a decrease in $\delta^{18}O$ values from approximately –2 ‰ at –730 m to –3.75 ‰ at –630 m, and this is followed by a sharp increase in values back to –2 ‰ over the following 30 m of outcrop. Isotope ratios remain scattered about this value until –575 m when, following an exposure gap, values have been reduced to –3.5 ‰ at –540 m. A subsequent maximum in values of –2 ‰ at –500 m leads into another minimum of –3.75 ‰ at –380 m, which is shortly followed by a final rise to –2.2

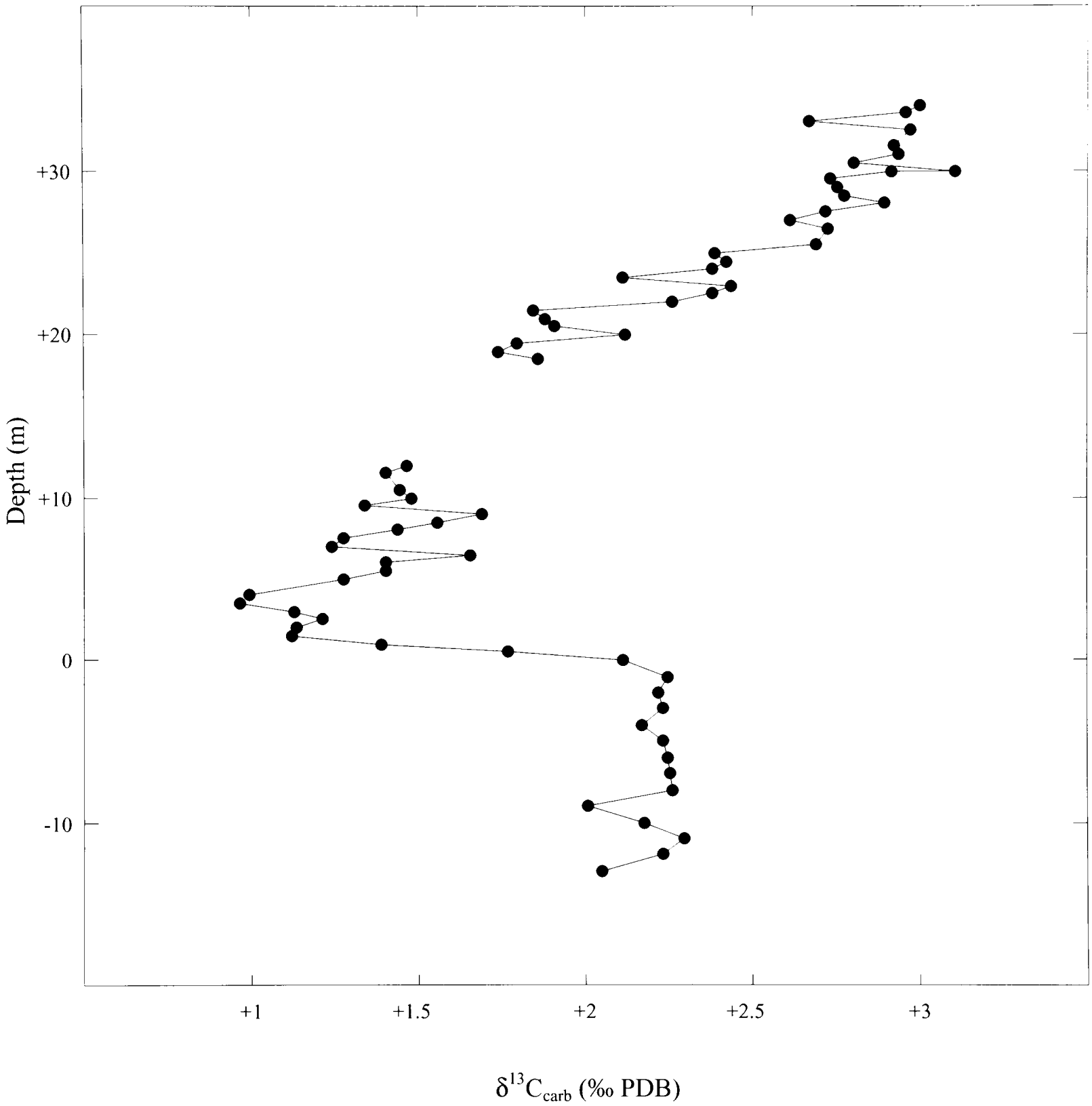

Figure 2.xiv. Carbon-isotope profile of the 47-m-thick Colma di Malcesine section, showing the sharp 1.25 ‰ negative isotope excursion between 0 and +4 m, followed by the subsequent recovery in values to +3 ‰ over the next 30 m.

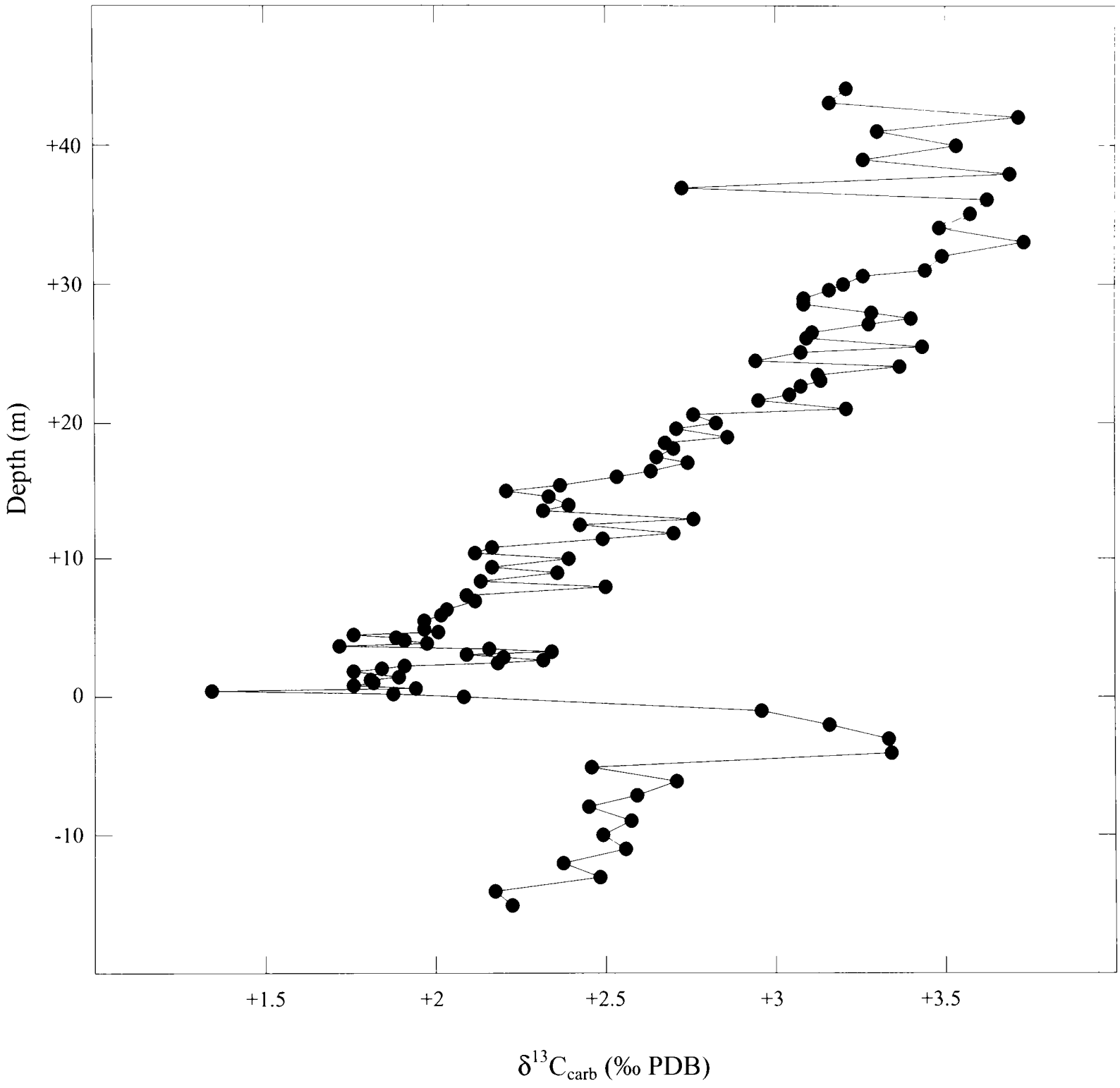

Figure 2.xv. Carbon-isotope profile of the 59-m-thick Sega d'Ala section, clearly illustrating a rapid increase in values of ~0.9 ‰ between -5 and -4 m, before a rapid decrease in values of 2 ‰ between -3 and +0.4 m. This negative isotope excursion is followed by a gradual increase in values of 2.4 ‰ over the subsequent 44 m of section.

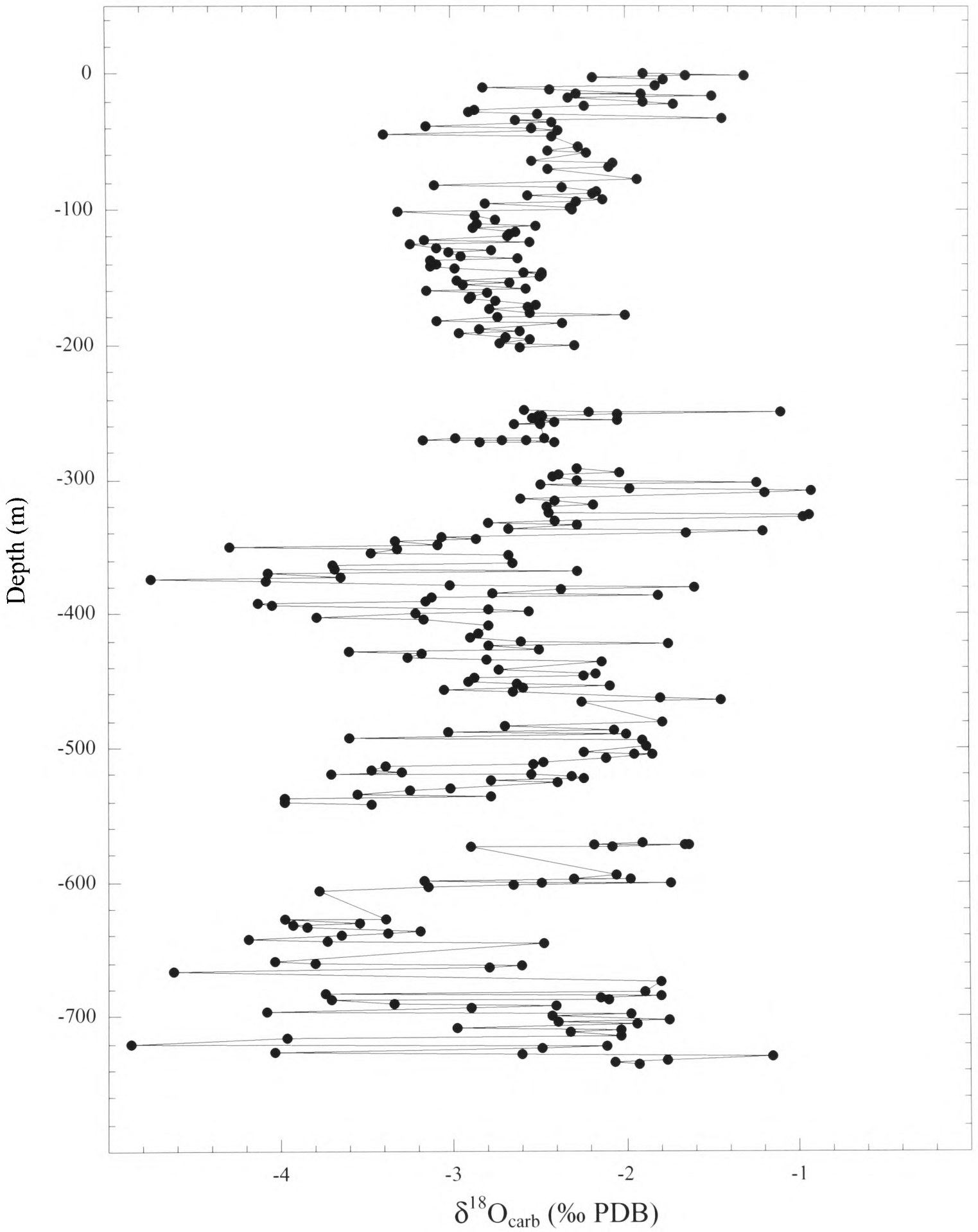

Figure 2.xvi. Oxygen-isotope profile of the 730-m-thick Madonna della Corona section. The isotope values appear to be scattered over much of the depth profile, although a faint coherent signal may still be discerned throughout. Note there is less scatter in the top 200 m of section.

‰ before the first of the two major exposure gaps between –200 and –300 m. Above the exposure gap, data are less scattered and the coherent oxygen-isotope signal is more obvious to recognise. Between –200 and –100 m there is a steady but slight decrease in $\delta^{18}O$values from approximately –2.6 ‰ to –2.8 ‰, before a relatively rapid increase to –2.2 ‰ found at –80 m. Another decrease to –2.5 ‰ at –40 m follows, preceding a final increase to –1.8 ‰ found at the drowning unconformity.

The San Vigilio oxygen-isotope profile is illustrated in Figure 2.xvii. The basal 35 m of section record data with relatively little scatter and with fairly constant values about –1.6 ‰, but above the first exposure gap (which is found between –160 and –145 m), the data become increasingly scattered and the primary signal appears to be masked, possibly due to the effects of post-depositional alteration of the oxygen-isotope ratios (see ***2.3***). However, there does seem to be a general decrease in values to approximately –3 ‰ possibly at –125 m (though data here are scattered) but certainly by –120 m, which is followed by a return to background values of –1.8 ‰ by –115 m. The next exposure, found between –70 and –40 m, registers less scattered and slightly decreasing $\delta^{18}O$ values between –70 and –50 m, from –1.5 to –1.9 ‰, before a relatively sharp rise in values to –1 ‰ occurs by –40 m. The final 11 m of outcrop below the drowning unconformity record a scattered increase in isotope values from –2.75 ‰ (though these values may be the result of scatter) to an approximate average of –0.75 ‰.

The oxygen-isotope profile of the 47-m-thick Colma di Malcesine section is illustrated in Figure 2.xviii, and despite displaying apparent data scatter at the scale used here a broad trend can still be recognised. There is a decrease in $\delta^{18}O$ values from –2.75 ‰ to –3.15 ‰ between –2 and 12 m. Above the following 7 m exposure gap, isotope values remain relatively constant (disregarding scatter) about a value of –2.75 ‰ until the top of the section.

Figure 2.xix illustrates the oxygen-isotope curve obtained from the Sega d'Ala section. Values fluctuate within a similar range to those obtained from the Colma di Malcesine section, and similarly, although they appear scattered at this scale, there is an apparent gradual increasing trend from –2.6 to –2 ‰ from the base of the section to the top.

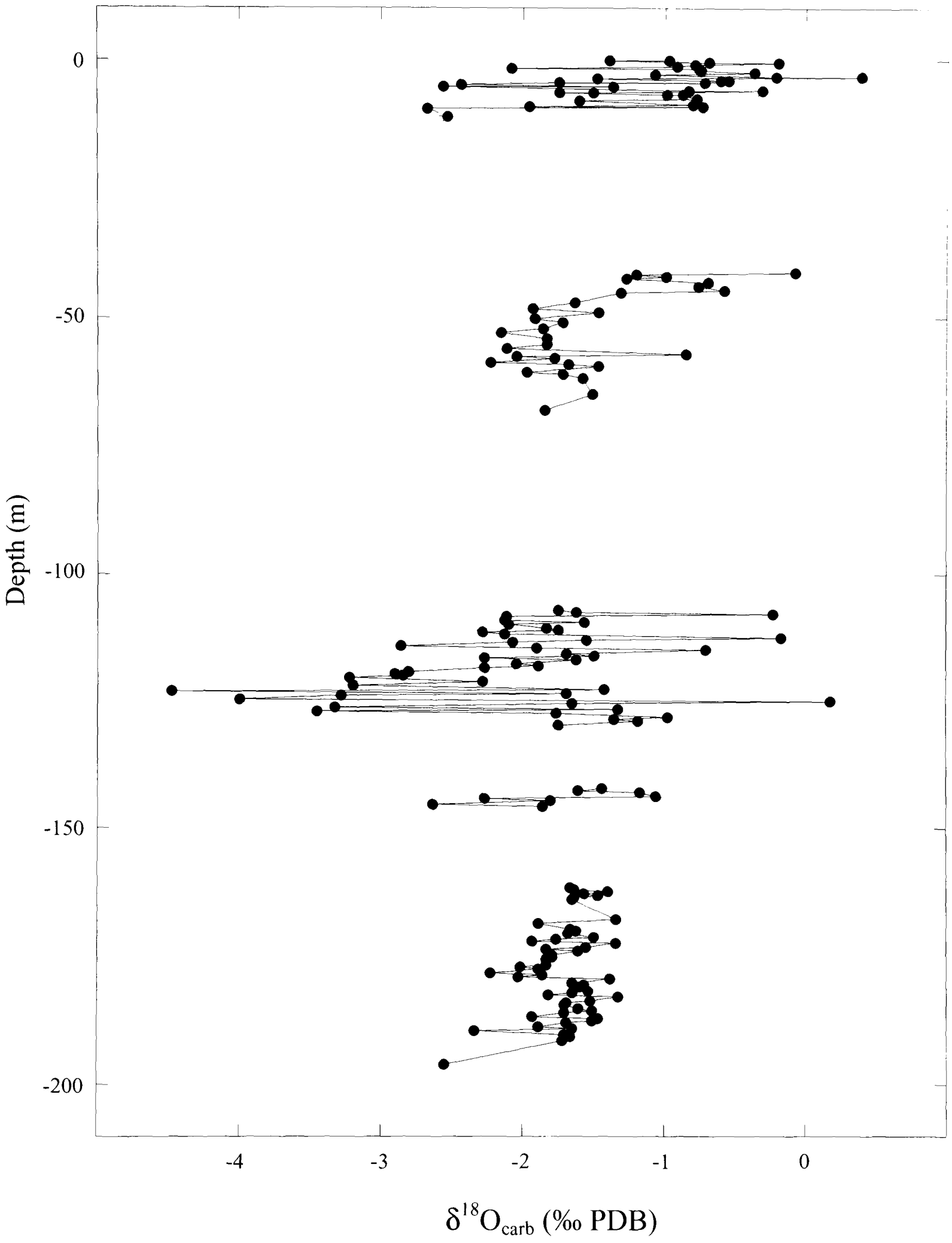

Figure 2.xvii. Oxygen-isotope profile of the 200-m-thick San Vigilio section. Data are relatively scattered between -100 and -150 m, and a marked increase to more positive isotope values is seen between -60 and -40 m.

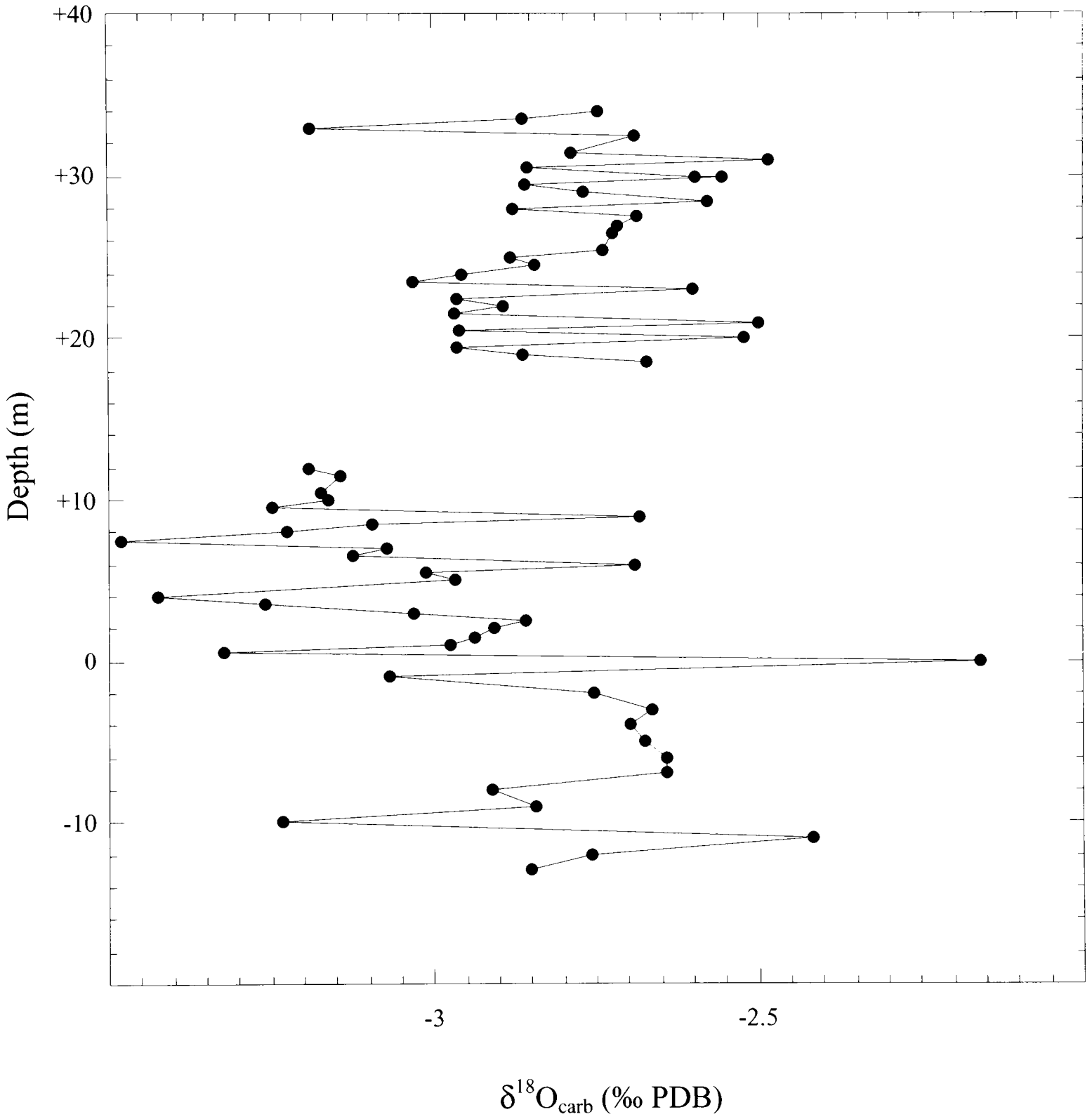

Figure 2.xviii. Oxygen-isotope profile of the 47-m-thick Colma di Malcesine section. Isotope values decrease into a minimum between -2 m and +12 m but, after an exposure gap, have returned to background values and remain so for the rest of the section. Data are relatively scattered, but a coherent trend can be discerned.

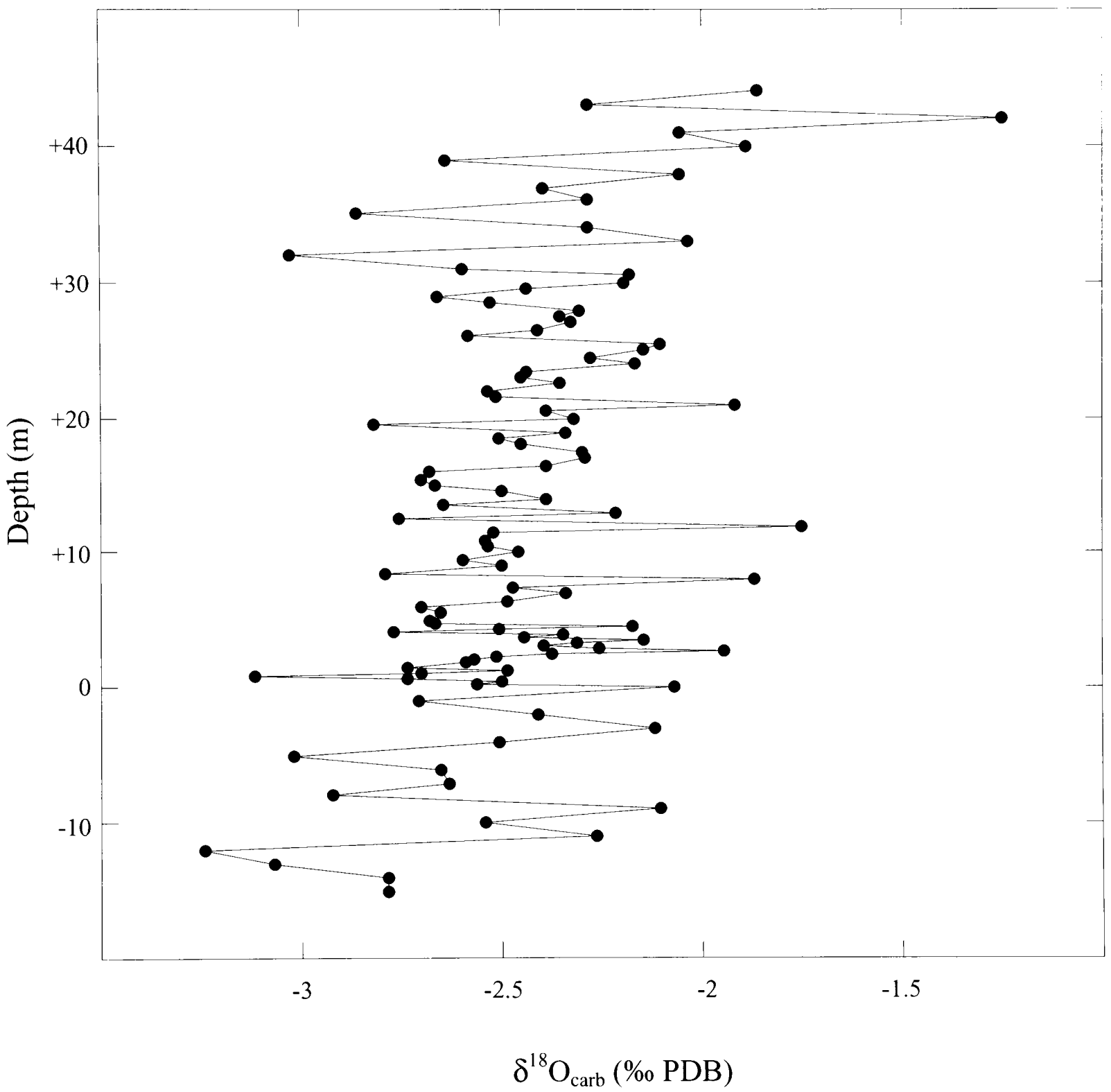

Figure 2.xix. Oxygen-isotope profile of the Sega d'Ala section. Isotope values show a scattered and gradual increase from an approximate average value of -2.75 to -2 ‰

2.2.4 Organic-carbon analyses

Organic-carbon analyses were carried out on the Tenno Formation (found at the Colma di Malcesine and San Vigilio sections) only, as these calcareous shales are the darkest-coloured facies encountered in the Trento Platform, and prior knowledge that this lower Toarcian shale-rich horizon had been approximately correlated with the organic-rich black shale facies found in the surrounding basins (and others globally) justifies the hypothesis that this interval is a likely candidate for elevated organic-carbon levels (***Chapter 5***; Jenkyns and Clayton, 1986; Jenkyns, 1988; Picotti and Cobianchi, 1996; Jenkyns and Clayton, 1997; Cobianchi and Picotti, 2001; Jenkyns *et al.*, 2001).

The wt% TOC data obtained from the calcareous shales found at the San Vigilio and Colma di Malcesine sections is presented in ***Appendix Data Tables 2.ii and 2.iii***, but it should be noted that only minimal traces of organic matter were recorded, and not enough for a thorough $\delta^{13}C$ organic-carbon investigation to be carried out. However, the drop from 99.7 % to 73.7 % carbonate at the Colma di Malcesine reflects the oolite–shale transition (the remainder being made up of clay), followed by a gradual increase back to higher carbonate percentages witnessed through the Upper Tenno Formation. The only significant levels of organic-matter discovered in these sections are found exclusively in the Basal Tenno Formation, and these reach a maximum concentration of approximately 0.3 % at the lowermost shale level. The $\delta^{13}C_{org}$ values obtained were assessed to be of low precision and significance because this analytical process is known to suffer when such low levels of organic carbon are present.

2.3 Diagenetic considerations

Firstly, the potential of post-depositional influences on the primary strontium-isotope signals of the Madonna della Corona (MDC) and San Vigilio (SV) carbonate successions are assessed (Figures 2.x and 2.xi respectively). In general, the strontium-isotope profile of the Madonna della Corona section appears coherent except for scatter found at the very base of the section (there is also some slight scatter between –400 and –500 m). The obvious 'fliers' at –294, -326, –572 and –572.5 m can also be disregarded as they lie significantly off the main

trend (see ***1.3.1***). The small amount of scatter mentioned above could be the result of either residual clays, whose relatively radiogenic strontium-isotope values have been leached into solution during preparation of the samples for analysis, or diagenetic modification of the primary signal (?possibly related to the proximal 'basal' dolomites of the Dolomia Principale). In order to minimise the effect of this visible distortion on the profile's trends, an approximate line of best fit is drawn along the minimum values of the curve illustrated in the summary of isotope profiles in Figure 2.xxvii (following the procedure of Burke *et al.* 1982). Of less significance (especially when correlating trends), is the generally more radiogenic values obtained from the Madonna della Corona section when compared to reference curves (e.g. Jones and Jenkyns, 2001). There is an elevation in values of approximately 0.00005 throughout the section. This is presumably due to a fairly constant background presence of residual clays that are leached in the bulk-rock carbonate analyses of this study, compared to the relatively 'clean' skeletal calcite of belemnites from which the reference curves are obtained. Clay-rich intervals such as the Tenno Formation may be expected to have even more elevated values.

The San Vigilio strontium-isotope profile is less straightforward to interpret. There is a large amount of scatter over the interval between –105 to –130 m, and this is most probably due to the relatively high percentage of residual clay in the bulk-rock samples (e.g. Burke *et al.*, 1982). The scatter is towards more radiogenic values and when taken into account that this interval represents the lower Toarcian clay-rich Tenno Formation (see ***2.4, Chapter 5*** and Geyer *et al.*, 1986; Picotti and Cobianchi, 1996), artificial $^{87}Sr/^{86}Sr$ ratios at this interval can be expected. The range of values obtained is also consistent with those obtained from Madonna della Corona samples and there is an apparent rising trend visible between –50 and –60 m, which may correlate to that of the Madonna della Corona section between –100 and –200 m. However, as the data are so patchy, and strontium-isotope trends are so broad, very little can be gained from this profile so it is not used further in any correlations of the Trento Platform sections.

After visual and petrographic microscope inspections, the data of those samples believed free of significant secondary calcite are presented in Figures 2.xx – 2.xxiii as $\delta^{13}C$ / $\delta^{18}O$ 'crossplots'. In theory, those data that follow a co-varying trend on one of these plots are falling

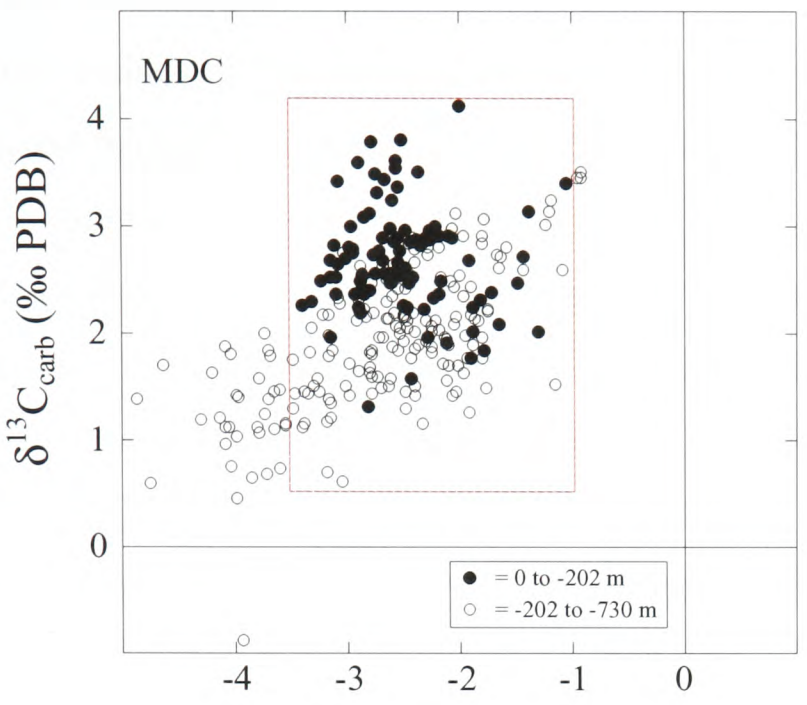

Figure 2.xix

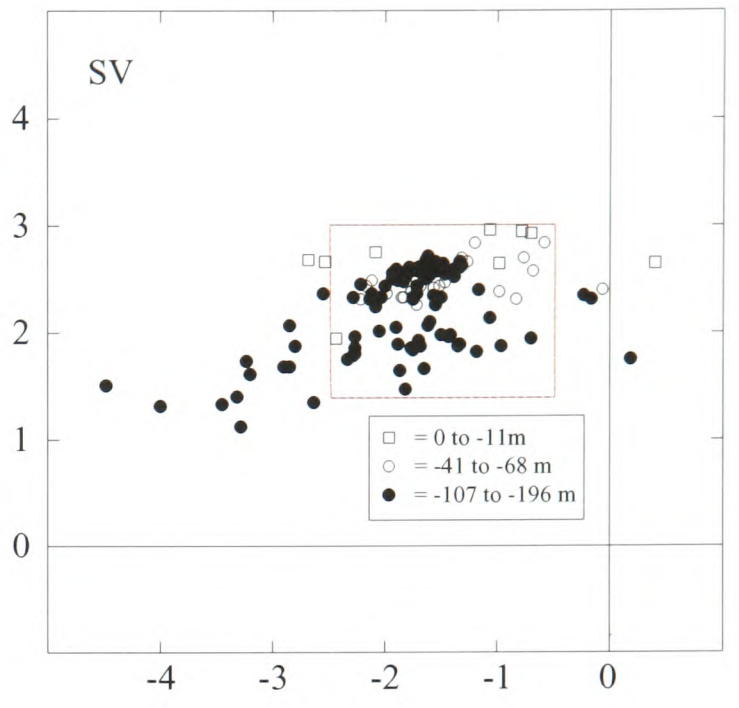

Figure 2.xx

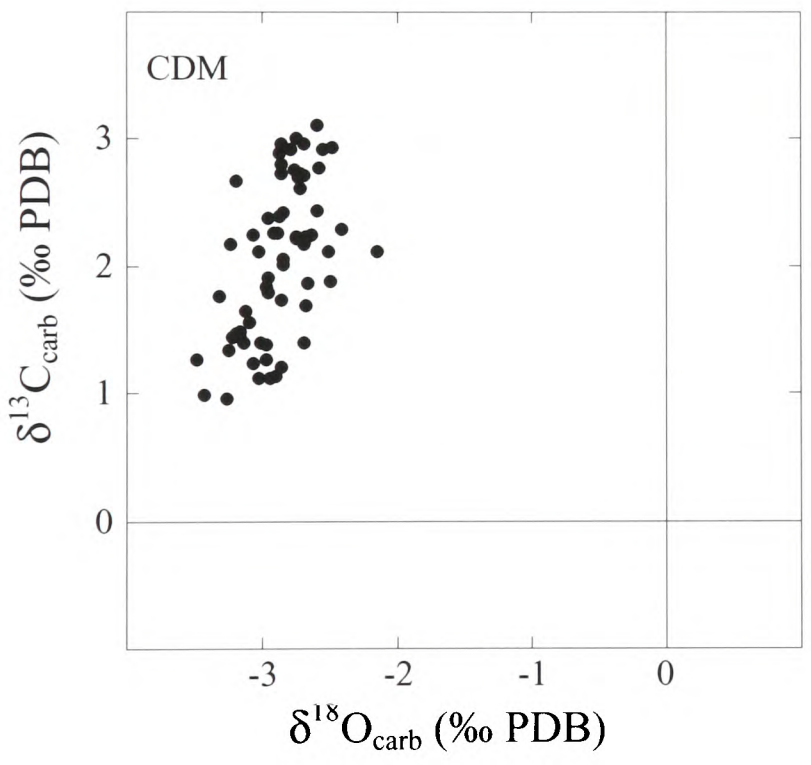

Figure 2.xxi

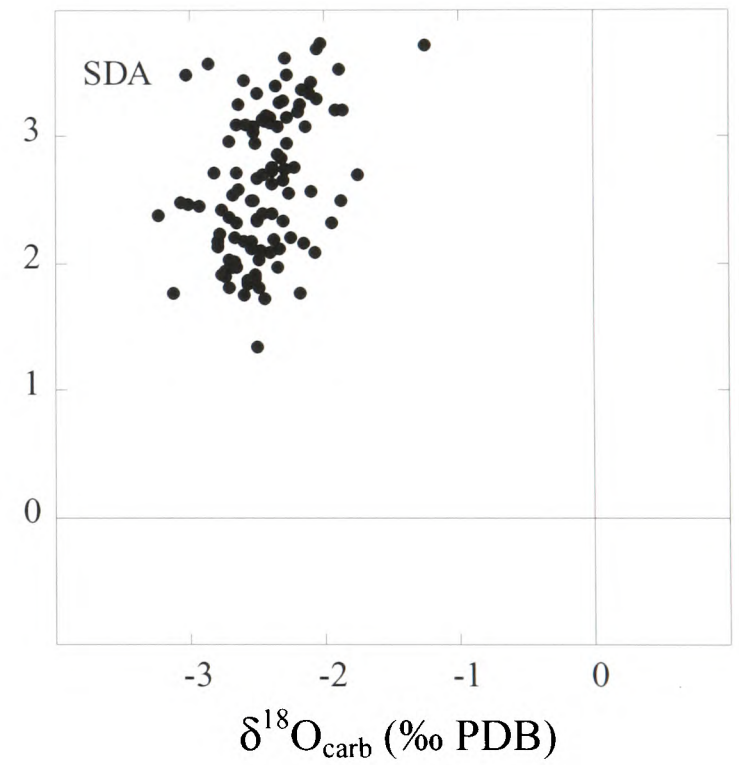

Figure 2.xxii

Figures 2.xx-2.xxiii. Carbon- and oxygen-isotope cross-plots of the data obtained from the four sections studied through the Trento Platform (Madonna della Corona, San Vigilio, Colma di Malcesine and the Sega d'Ala). For MDC and SV, data grouped as filled/unfilled circles/squares are separated in the vertical profile of each respective section by significant exposure gaps. Data lying outside of the red rectangles in Figures 2.xix and 2.xx were excluded in the carbon-isotope profiles illustrated in Figures 2.xxiii and 2.xxiv.

on a 'mixing-line' as the result of significant diagenetic overprinting that affected both carbon- and oxygen-isotope values (the 'mixing-line' represents the distribution of altered sample carbon- and oxygen-isotope values between end-member primary ratios and the more negative isotope values of the circulating fluid). In Figure 2.xx, it is visually apparent that those data grouped between the interval 0 to –202 m in the Madonna della Corona section (filled circles) are randomly clustered, but those found in the section below –202 m are stretched so as to fall on a possible 'mixing line'. This supports evidence of diagenetic affects seen in the carbon- and oxygen-isotope curves (Figures 2.xii and 2.xvi) that show data below this point are generally more scattered than those in the uppermost 200 m of section. It should therefore be considered in the interpretation of these data that although the upper 200 m of Madonna della Corona section may have survived post-depositional alteration with the primary isotope signals intact, isotope signals from below this point should be interpreted with caution. However, as expressed in ***2.2.2*** and ***2.2.3***, where a primary signal is still apparent regardless of data scatter, broad-scale global isotope trends may still be preserved.

Carbon-isotope data from the San Vigilio vary less (range = <2 ‰) relative to that of the oxygen-isotope data (range = <5 ‰), and a possible "mixing-line" trend is particularly apparent in those data from between –107 to –196 m in the section (filled circles; Figure 2.xxi). Through comparison with the oxygen-isotope profile of the San Vigilio section (Figure 2.xvii), it is obvious that those data with most negative values occur where there is most scatter, between –107 and –130 m. This is the interval where carbon-isotope ratios also show a coherent negative excursion (Figure 2.xiii), and so are interpreted to show a real trend with minor scatter. In which case, there is a possibility that oxygen isotopes (which are most susceptible to overprinting) have been altered due to the nature of the relatively weathering-prone facies from which they are obtained, but the carbon-isotope data appear less altered and, as the apparent trend is similar to that of other sections (over the same interval), it is interpreted as real.

The cross-plot of data from the Colma di Malcesine section (Figure 2.xxii) shows less variation of oxygen-isotope ratios (range = <1.5 ‰) relative to carbon-isotopes (range = <2.25 ‰). In this case, although a linear trend is apparent, it is not of simple co-variance and therefore the cross-plot shows little evidence of significant overprinting that has affected both signals.

This supports the visual appearance of the individual isotope curves when plotted against stratigraphic depth, as neither show high amounts of obvious data scatter (Figures 2.xiv and 2.xviii).

Figure 2.xxiii illustrates the carbon- and oxygen-isotope cross-plot of the Sega d'Ala section. The ranges of the data are very similar to that observed for the Colma di Malcesine and so have been treated in the same way. There is little discernible diagenetic modification of the isotope signals, no obvious 'mixing line' linearity to the cross-plot, and neither are there data lying away from the main cluster. This assertion is backed up by the coherent nature of the carbon-isotope curve (Figure 2.xv).

Oxygen-isotope ratios are the proxy most susceptible to alteration used in this study (usually resulting in a decrease in values), as discussed in ***1.4.3***, and so filtering the $\delta^{13}C$ dataset depending on sample oxygen-isotope values was aimed to exclude those points that mostly lie outside of the clustered cross-plot data and on the 'mixing-lines'. The data lying outside of the red rectangles marked on the two isotope cross-plot figures: 2.xx and 2.xxi, signify those points excluded from the carbon-isotope profiles presented in Figures 2.xxiv and 2.xxv (strontium-isotope ratios are more robust to fluid-derived diagenesis and as a result the Madonna della Corona profile is little scattered, so requires no screening; McArthur *et al.*, 2000b). Although varying extremes of screening can be performed on the oxygen-isotope data, those described here are purely subjective and qualitative, are unique to each section, and try to delimit 'affected' samples whilst maximising the number of data-points illustrated. As a result, those data with the higher probability of having been altered from their primary values do not feature in the resulting profiles. An inherent limitation and risk of this type of indiscriminate screening is that real signals may be excluded and altered data may not, but for this particular quantitative assessment, reliance is placed on the probability that the effects of major distorting influences on the data will be minimised.

Figure 2.xxiv displays the affect of carrying out the oxygen-isotope screening technique on the data from the Madonna della Corona section. Samples with $\delta^{18}O$ values falling outside of the range –3.5 to –1 ‰ were excluded from the dataset whose carbon-isotope ratios are plotted

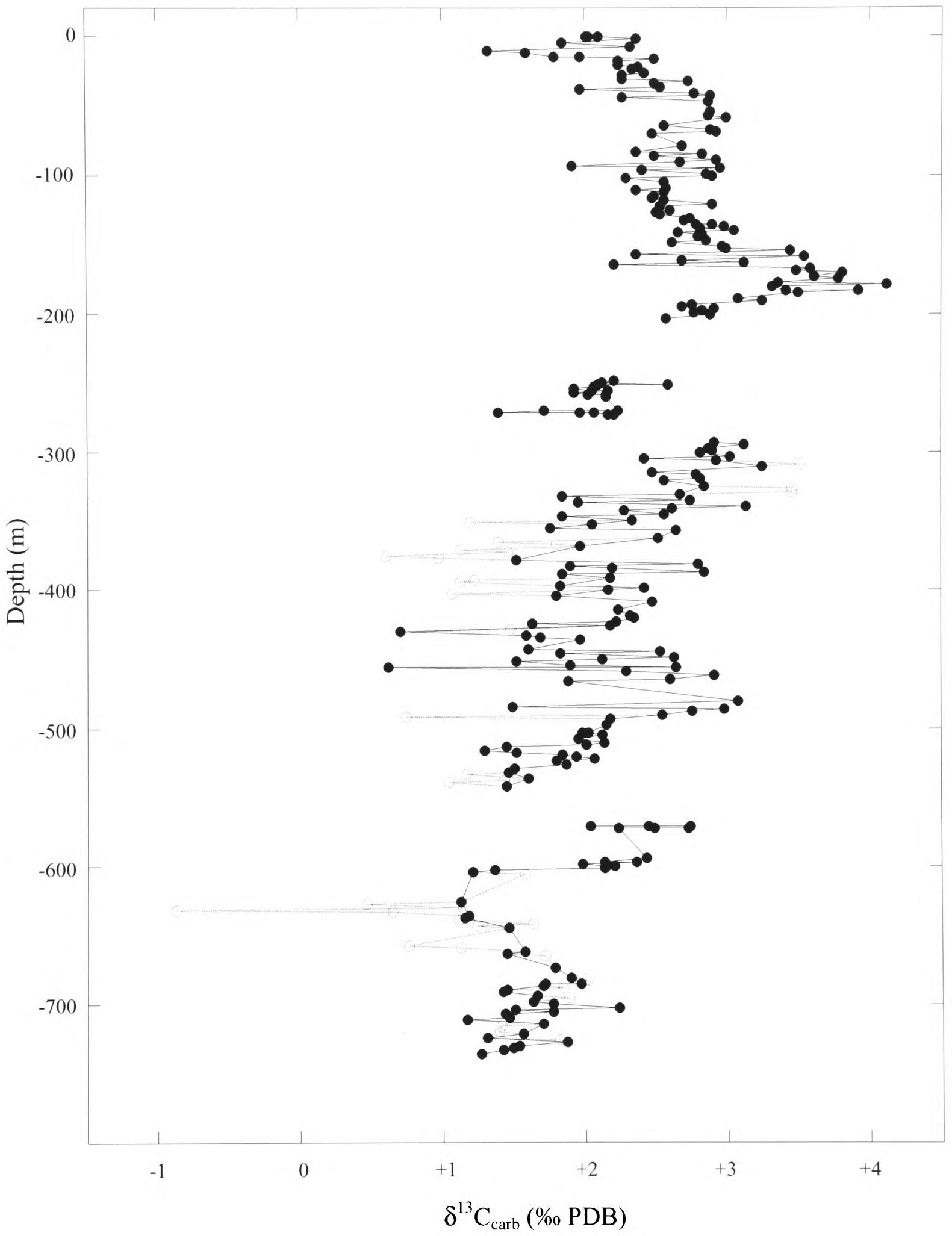

Figure 2.xxiv. Filtered carbon-isotope profile of the 730-m-thick Madonna della Corona section. The diagenetic screening process removed samples with oxygen-isotope values outside of the range: $-3.5 < \delta^{18}O < -1$. The grey unfilled circle data-points in the background are the original unscreened dataset.

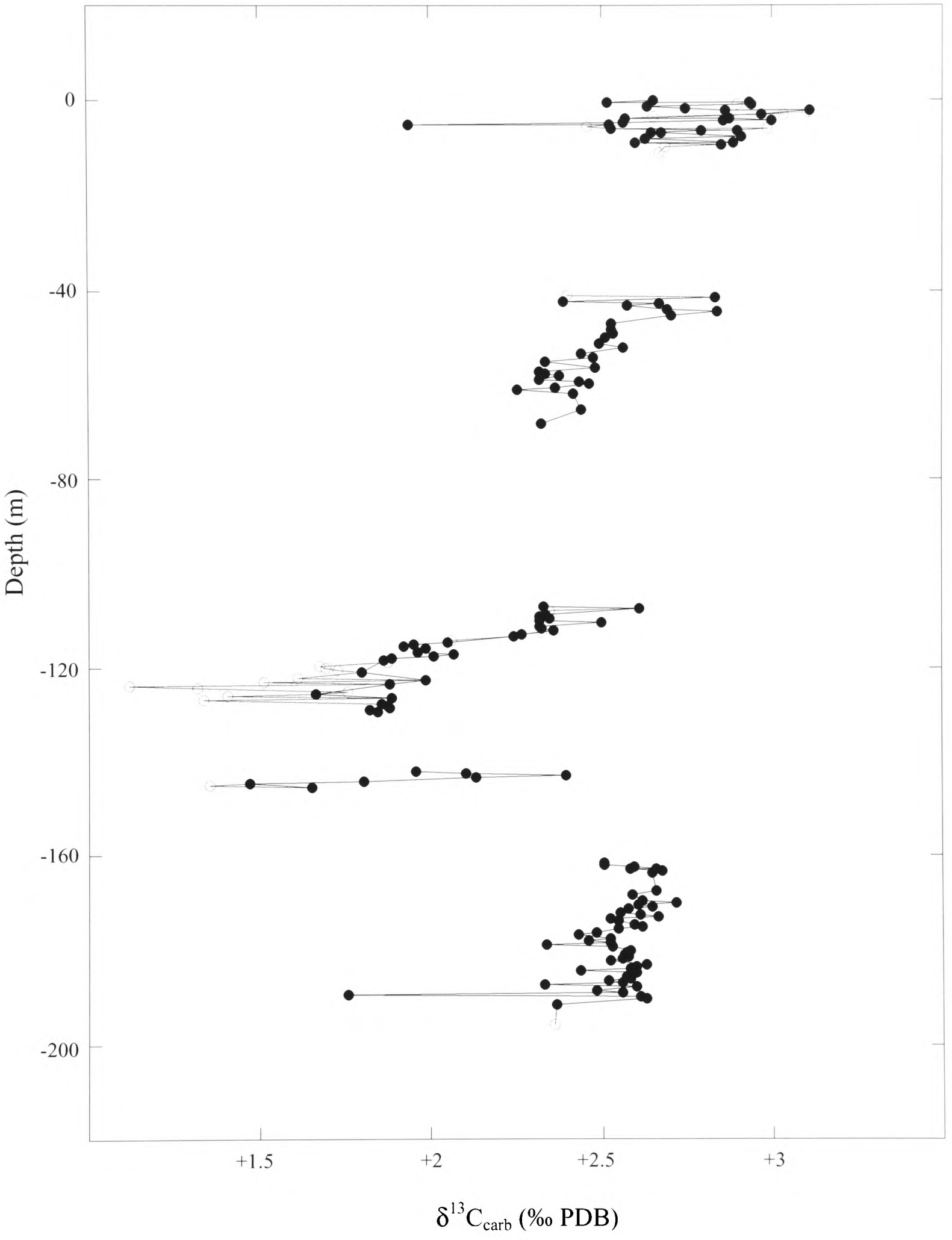

Figure 2.xxv. Filtered carbon-isotope profile of the 200-m-thick San Vigilio section. Diagenetic screening removed samples with oxygen-isotope values outside of the range: $-2.5 < \delta^{18}O < -0.5$. The grey unfilled circle data-points in the background are the original unscreened dataset.

as filled circles. The original data are plotted as unfilled circles in the background allowing for a useful comparison to ascertain the characteristics of the carbon-isotope values of the samples that were excluded as a result of their oxygen-isotope value. This comparison is itself a good test of whether the likely diagenetic candidates have been removed or not. Of primary significance is that no samples found above 300 m have been excluded, which suggests these data are not strongly affected by diagenetic overprinting in terms of affecting oxygen-isotope ratios. There still appear to be anomalous results in this portion of the section, which could still be the result of minor diagenetic alteration, or alternatively could be related to the abundance of skeletal debris on the bulk-carbonate ratios in this part of the section (***1.4.3***).

The majority of the data removed from the lower 450 m of the Madonna della Corona section appear to be anomalous (characterised by abrupt changes in carbon-isotope ratios to values off the main trend). However, not all of the scattered data are excluded, but by increasing the 'severity' of screening introduces the danger of losing 'real' data-points. Scattered data that remain (mainly found between –400 and –500 m) are therefore believed to result from the same mechanisms outlined above: the presence of abundant skeletal debris. In this case, suppliers of debris to these lower Calcari Grigi Rotzo facies are bivalves, brachiopods and gastropods (*Lithiotis* limestone).

In summary, where bioclastic debris is at a minimum in the Trento facies, the carbon-isotope curve appears much improved by the screening technique employed without removal of unaltered data. This is intuitive, as filtering of data with respect to oxygen-isotopes will remove unwanted samples affected by meteoric-water, but not samples affected by skeletal debris content. To remove the latter in this quantitative fashion would require filtering with respect to carbon-isotope ratios, which increases the risk of excluding primary data.

In order to achieve a similar result, the San Vigilio dataset was also subjected to the analytical process described above (data from the Colma di Malcesine and Sega d'Ala sections do not show enough oxygen- (and carbon-) isotope variation to warrant such an analysis), although the $\delta^{18}O$ value limits were adjusted to exclude data falling outside of the range –0.5 to –2.5 ‰ (Figure 2.xxii). The resulting screened carbon-isotope data are illustrated in Figure

2.xxv, once again with the original unscreened data displayed as grey unfilled circles in the background. Data were principally removed from between –130 and –120 m, which is where the San Vigilio data are most scattered. The facies developed at this interval is the Upper Tenno rhythmically bedded pelletal limestones with abundant spiculitic cherts, and a likely reason why meteoric-water diagenesis should particularly have an effect here is the clay-rich beds are more susceptible to weathering than are the massive carbonate intervals. This assumption is supported in outcrop, as the Tenno Formations are always heavily eroded back (and commonly vegetated), whereas the oolites above and below stand proud. It is unlikely that meteoric-water diagenesis could be the result of exposure during deposition, because the Tenno Formations are generally believed to be a relatively deeper-water facies deposited during a major transgressive episode (e.g. Barbujani *et al.*, 1986; Picotti and Cobianchi, 1996; Cobianchi and Picotti, 2001). The majority of other data excluded is from –45 to –40 m and over the final 10 m of platform carbonates below the drowning unconformity. Although the facies over this interval is San Vigilio Oolite (with abundant skeletal debris), the amount of carbon-isotope scatter is low, which indicates that the skeletal debris has a muted affect on analyses. However, potentially anomalous results from the final 10 m of section have not been screened and, as discussed above, this may be a consequence of abundant echinodermal, bivalve and/or brachiopod, and ammonite debris: each organism potentially having a varying degree of 'vital effect' on the isotope ratios of carbonate precipitated.

In summary: primary carbon- and oxygen-isotope profiles obtained from the Trento Platform appear to be distorted predominantly by either meteoric-water diagenisis and/or the variable abundance of skeletal debris. The first of these effects can be partially identified and eliminated using oxygen-isotope data and the latter is suggested by observation of bioclastic debris in the facies studied.

2.4 Intra-platform chemostratigraphic correlations

The chemostratigraphic profiles that have resulted from all of the above analyses facilitate multi-framework correlations (bio-, litho- and chemostratigraphic) of localised Trento Platform sections (using predominantly carbon-isotope profiles in this case). These local

correlations allow a full chemostratigraphic framework of the Trento Platform (or at least its western margin) to be constructed.

To aid the chemostratigraphic correlation, previously published works on Trento Platform biostratigraphy (particularly Sturani, 1964; Bosellini and Broglio Loriga, 1971; Geyer *et al.*, 1986; Picotti and Cobianchi, 1996) and lithostratigraphy (particularly Bosellini, 1967; Bosellini and Broglio Loriga, 1971; Castellarin, 1972; Bosellini and Hardie, 1985; Barbujani *et al.*, 1986) were utilised. Ultimately very few conflicts resulted between the three stratigraphic correlation tools.

Figure 2.xxvi illustrates the intra-platform carbon-isotope correlations made between the Madonna della Corona (MDC), San Vigilio (SV), Colma di Malcesine (CDM) and Sega d'Ala (SDA) sections expressed against the same metric scale on the vertical axis (the correlations are also based on lithostratigraphy; oxygen-isotope profiles are not utilised for correlations as the data from these shallow-water carbonates are so scattered and variable). An immediate tie-point between the Madonna della Corona and San Vigilio sections is the drowning unconformity found at the top of the platform facies, which is overlain by very distinctive Rosso Ammonitico (assuming that drowning was quasi-synchronous between the two proximal sections). Also, all four sections contain either one or both parts of the Tenno Formations (Basal and/or Upper), and the chemostratigraphic study focuses on this interval in particular because of the distinctive isotope signature it provides. This distinctive Trento Platform clay-rich interval of thin-bedded limestones with cherts is therefore relatively easy to correlate between sections lithostratigraphically. The Misone Formation, which is a very similar facies to the Upper Tenno Formation (but lies beneath the Basal Tenno Formation) is, however, not always present (e.g. Colma di Malcesine section). The carbon-isotope curve of the Madonna della Corona section illustrates a distinct positive maximum in the Upper Tenno Formation (directly above patchy more negative values). The carbon-isotope curve of the San Vigilio section is very incomplete, but shows a steeply rising carbon-isotope trend in what is Upper Tenno-like facies. The relatively complete $\delta^{13}C$ profile of the Colma di Malcesine section illustrates a sharp negative excursion at the Massone Oolite and the Basal Tenno Formation transition before rising to more positive values through the Upper Tenno Formation. The Sega d'Ala section differs from the

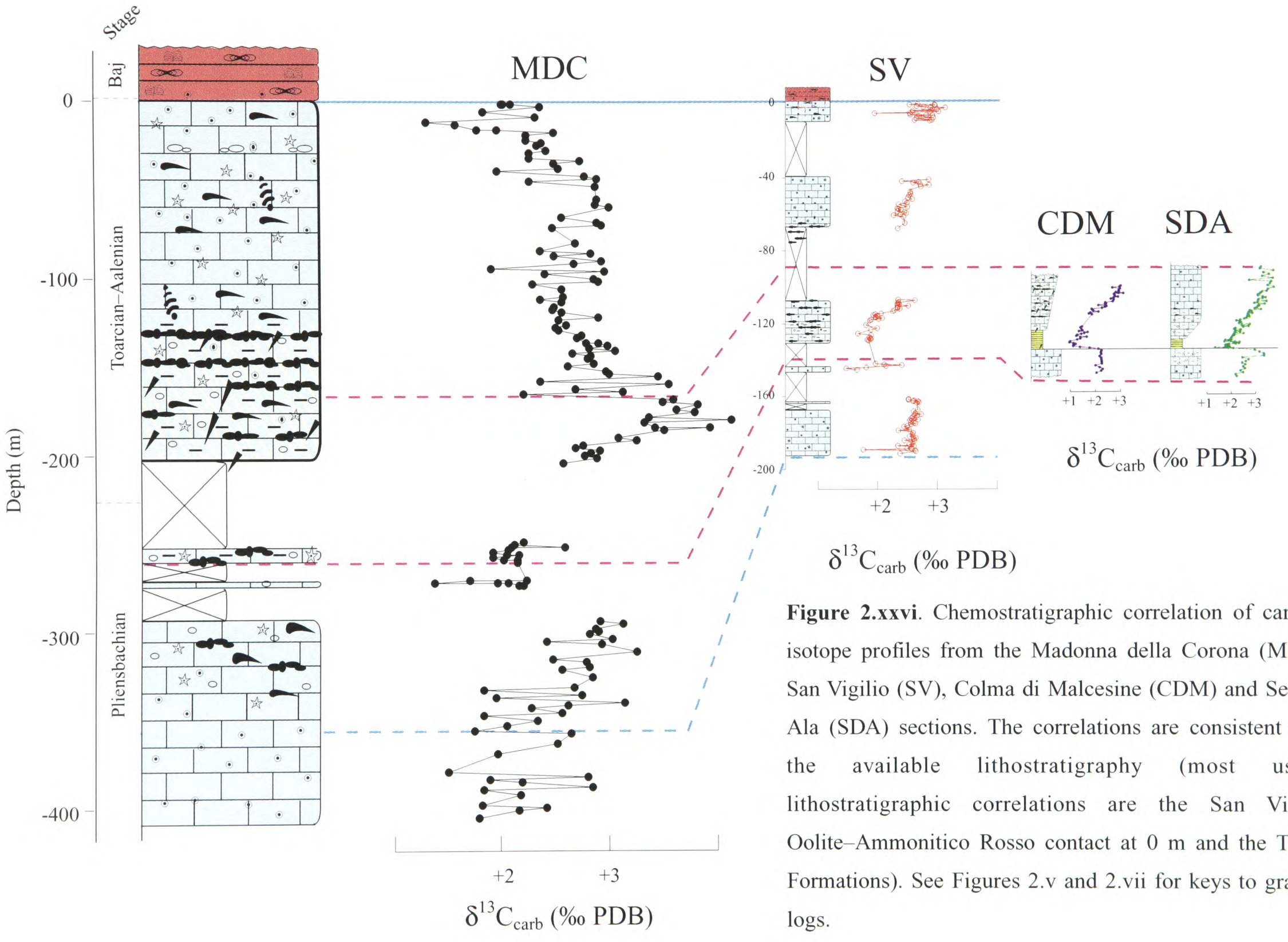

Figure 2.xxvi. Chemostratigraphic correlation of carbon-isotope profiles from the Madonna della Corona (MDC), San Vigilio (SV), Colma di Malcesine (CDM) and Sega d' Ala (SDA) sections. The correlations are consistent with the available lithostratigraphy (most useful lithostratigraphic correlations are the San Vigilio Oolite–Ammonitico Rosso contact at 0 m and the Tenno Formations). See Figures 2.v and 2.vii for keys to graphic logs.

Colma di Malcesine in that it includes the Misone Formation above the Massone Oolite, and at the top of this facies there is a rise in $\delta^{13}C$ values before the sharp negative excursion into the Basal Tenno Formation. Values then proceed to rise into a positive excursion through the Upper Tenno Formation (and into the San Vigilio Oolite at the top of the section).

The correlation between the pronounced negative followed by rising positive excursions in the Colma di Malcesine and Sega d'Ala sections is relatively straightforward (although there is the possibility of a hiatus at the Colma di Malcesine explaining the missing Misone Formation, and therefore also the rising $\delta^{13}C$ values prior to the pronounced negative excursion). The Upper Tenno Formation rising carbon-isotope values are also apparent in all four sections and can be relatively easily correlated, although what appears to be a carbon-isotope value minimum at the San Vigilio (at the base of the rising trend) is obtained from Upper Tenno-like facies and not Basal Tenno facies. Presumably the shaley Basal Tenno is covered by vegetation/regolith at the San Vigilio and Madonna della Corona sections and so the negative excursions are missing and should be found where there are now exposure gaps, between –130 and –142 m and –202 and -248 m respectively. It should be noted that the relatively rapid negative shifts in $\delta^{13}C$ values at –270 and –145 m in the Madonna della Corona and San Vigilio sections respectively, are possibly primary, but they are too low stratigraphically to represent the negative excursions observed in the Colma di Malcesine and Sega d'Ala sections. The excursions can therefore be loosely correlated, but the nature of the outcrop in both sections at this level (possibly not *in situ*; ***2.1.1*** and ***2.1.2***), means there is some uncertainty regarding their significance.

The oolite at the base of the San Vigilio section can also be correlated with the Massone Oolite at the Madonna della Corona, Colma di Malcesine and Sega d'Ala sections (at approximately –350 m, 0 to –12 m, and –8 to –15 m respectively). Not only do the facies correlate, but also $\delta^{13}C$ values are all at approximately +2.5 ‰, and below an interval of rising values.

The intra-platform correlations described above allow interpretation on the relative sedimentation rates at each respective locality on the western margin of the Trento Platform (as

Barbujani (1986) has also done). For example, the 200 m of section at the San Vigilio is equivalent to 350–375 m of carbonate succession at the Madonna della Corona. Also, the 44-m-thick carbonate succession at the Sega d'Ala (which had a similar sedimentation rate to the Colma di Malcesine) is equivalent to approximately (as exposure gaps) 50 and 90–100 m at the San Vigilio and Madonna della Corona sections respectively. In other words, the sedimentation rate at the Madonna della Corona locality on the Trento Platform was approximately 1.8–1.9 times that of the respective rates at the San Vigilio, Colma di Malcesine and Sega d'Ala sections (comparable to the relative rates suggested by Barbujani, 1986).

Finally, the above correlations allow a composite carbon-isotope profile of this portion of the Trento Platform to be constructed, and this is illustrated in full in Figure 2.xxvii. On this diagram, the vertical axis represents the stratigraphic depth of the Madonna della Corona section, to which all other sections have been fitted. This composite carbon-isotope profile is further illustrated against a composite graphic log of the platform and the strontium-isotope profile of the Madonna della Corona section in Figure 2.xxviii.

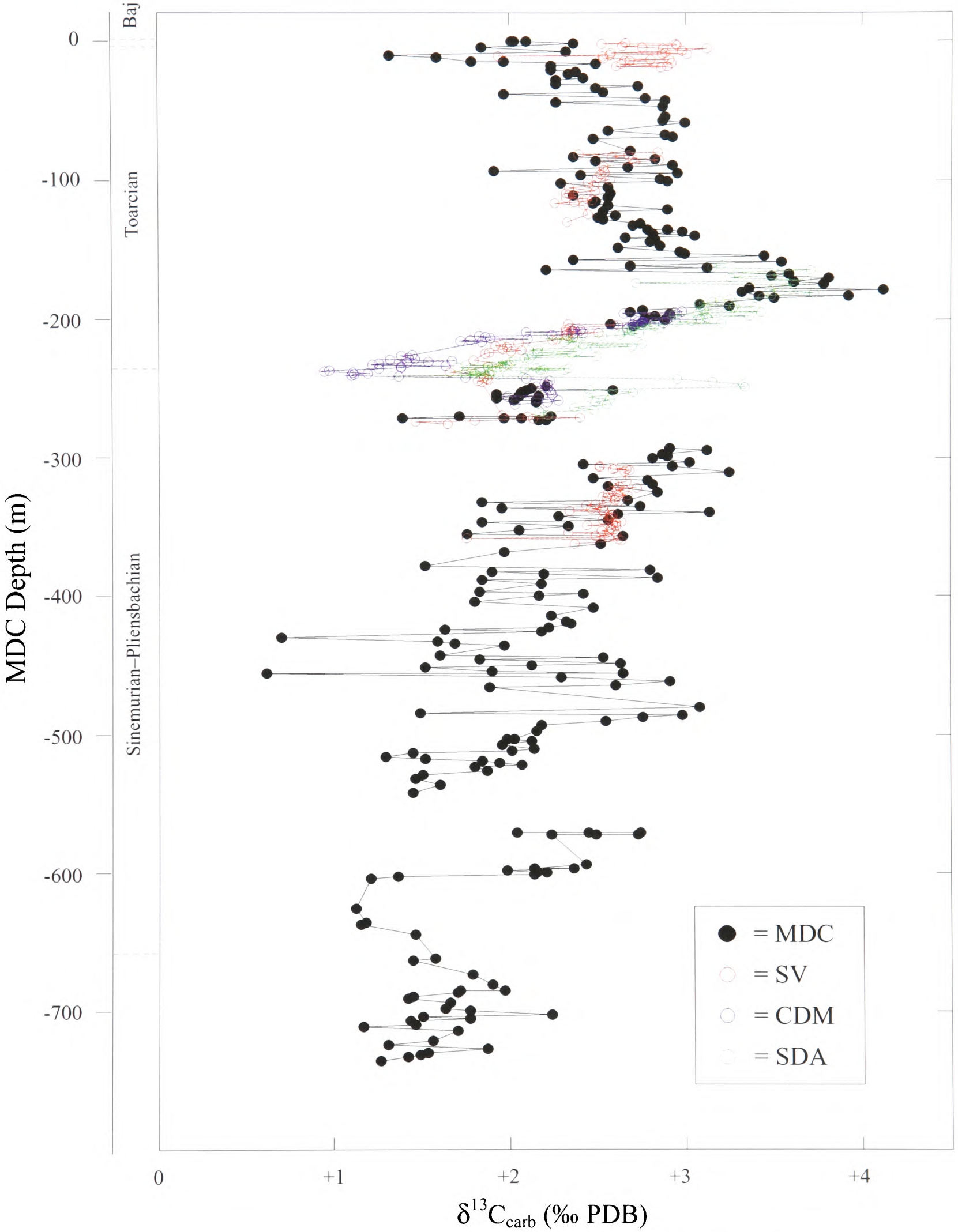

Figure 2.xxvii. Composite carbon-isotope profile of the Trento Platform, Southern Alps, Italy. All data are illustrated against stratigraphic depth of the Madonna della Corona section. For true individual section depths, see Figures 2.xxvii and 2.xxviii. MDC = Madonna della Corona; SV = San Vigilio; CDM = Colma di Malcesine; SDA = Sega d'Ala.

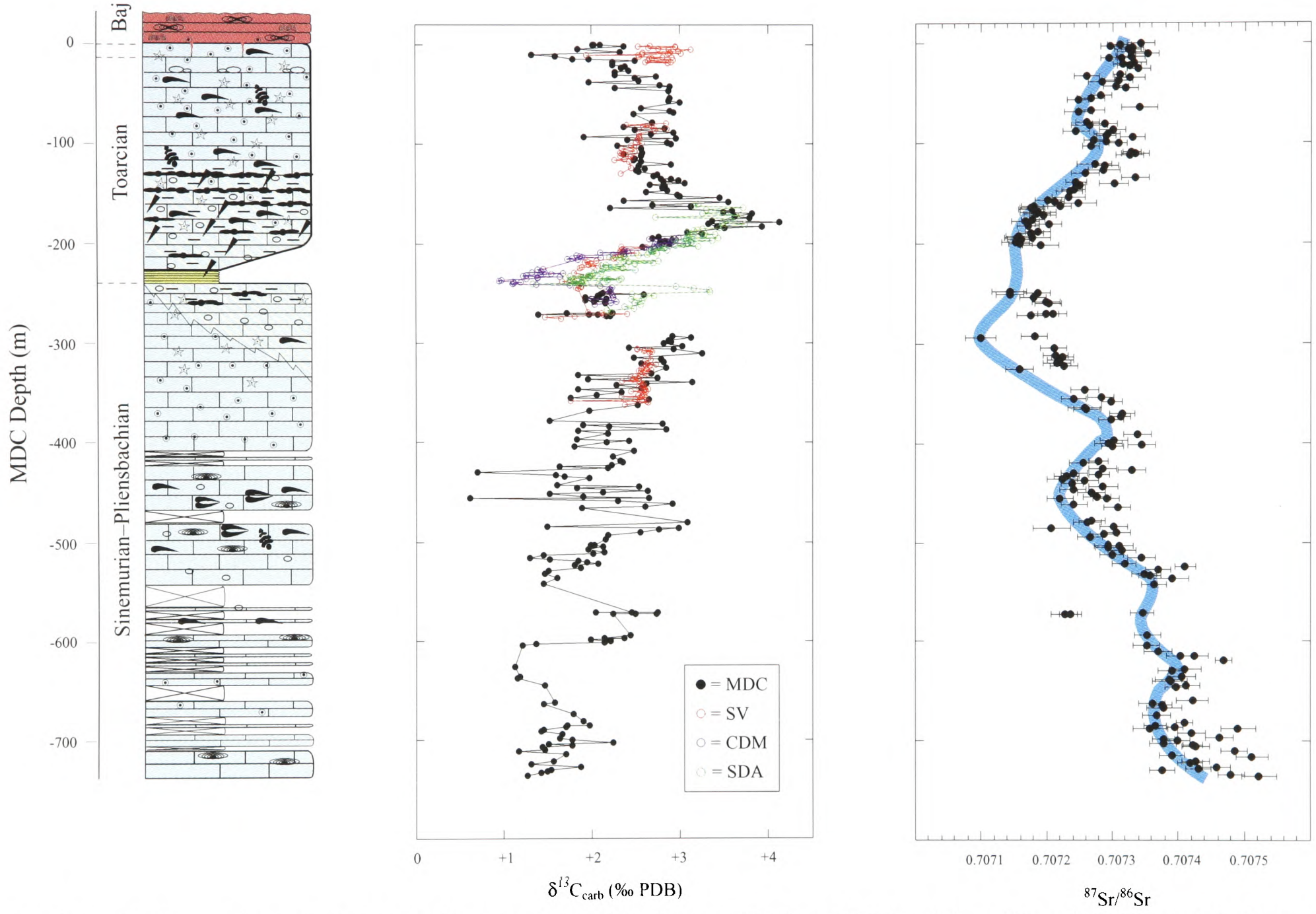

Figure 2.xxviii. Composite graphic log, carbon-, and strontium-isotope (Sr from MDC only) profiles of the Trento Platform. All data are illustrated against stratigraphic depth of the Madonna della Corona section. The blue line on the strontium profile is an approximate best fit (after Burke *et al.*, 1982). MDC = Madonna della Corona; SV = San Vigilio; CDM = Colma di Malcesine; SDA = Sega di Ala.

Chapter 3: Friuli Platform

Chapter 3: Friuli Platform, Southern Alps, Italy

3.1 Geological setting and stratigraphy

The geological and structural setting of the Friuli Carbonate Platform (Southern Alps, northern Italy; Figure 2.i) during the Mesozoic follows the extensional dynamic regime already discussed regarding the Trento Platform lying to the west (see ***2.1***). The platform was originally termed the Friuli Ridge by Aubouin (1963) in his description of the Southern Alps as an east–west trending succession of alternating structural-palaeogeographic zones. Later work interpreted the Southern Alps as a continental margin that underwent significant extension as the Ligurian Ocean was created to the west, resulting in a "shallow-water shelf that was gradually broken, submerged and conquered by the pelagic realm" (Bernoulli, 1972; Bernoulli and Laubscher, 1972; Bosellini, 1973; Gaetani, 1975; Bernoulli *et al.*, 1979; Winterer and Bosellini, 1981). The Friuli Platform, being the most easterly 'high' in the Southern Alpine zone, was least affected by the west–east drowning succession that took place between the end Triassic to the Bajocian (the Trento Platform being the last to succumb) and, as a result, thick shallow-water carbonate deposits extend from Triassic through to the Upper Cretaceous (Aubouin, 1963; Cuvillier *et al.*, 1968; Winterer and Bosellini, 1981). The Friuli Platform has also been interpreted as the most westerly promontory of the carbonate continental margin that extended as continuous area into the Dinaric Platform further to the east and south (Figures 1.vi and 2.ii; Gaetani, 1975). To the west, this carbonate platform was separated from the Trento Platform (from Sinemurian time onwards) by the deeper-water Belluno Trough, which extended round to the northeast into the Julian Trough rather like the modern, Bahamian "Tongue of the Ocean" (see ***2.1***; AGIP, 1959; Bosellini *et al.*, 1981; Winterer and Bosellini, 1981).

Previous workers have described the stratigraphy of the Friuli Platform from outcrop exposures and wells that range from the Early Jurassic through to early Tertiary age (Aubouin, 1963; Cousin, 1963; Cuvillier *et al.*, 1968; Gaetani, 1975; Cousin and Fourcade, 1982; Sartorio, 1986; Ghetti, 1987; Sartorio, 1987; Ghetti and Brigatti, 1991). Figure 3.i illustrates the typical facies associations described in the literature and appropriate formation names have been

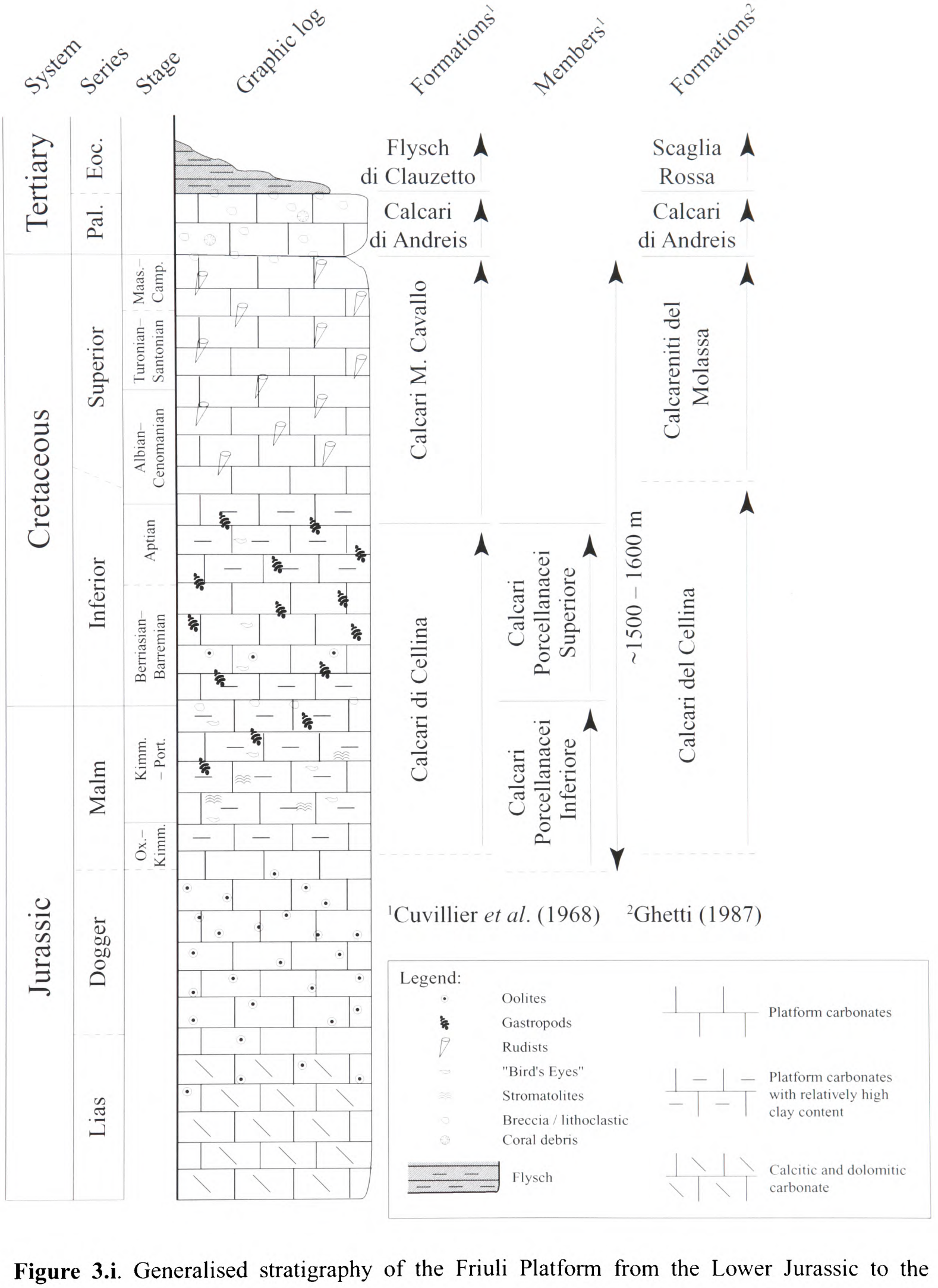

Figure 3.i. Generalised stratigraphy of the Friuli Platform from the Lower Jurassic to the Eocene. Modified after Aubouin (1963), Cuvillier *et al.* (1968), and Ghetti (1987). Ox. = Oxfordian; Kimm. = Kimmeridgian; Port. = Portlandian; Maas. = Maastrichtian; Camp. = Campanian; Pal. = Paleocene; Eoc. = Eocene.

assigned (modified after Aubouin, 1963; Cuvillier *et al.*, 1968; Ghetti, 1987). Gaetani (1975) described lagoon, rim and outer-slope carbonate-platform deposits that are recognisable throughout the Jurassic. The rim facies changed from oolitic sands in the Early Jurassic (some slightly dolomitised), through an oolitic Middle Jurassic, to very thick, more biogenically derived carbonates (algae/corals) by the Late Jurassic (Cousin, 1964; Gaetani, 1975). Drilling on the Friuli Plain discovered dolomites and cherty dolomites in the Lower Jurassic, with oolitic (or slightly dolomitised limestone) facies through the Middle and Upper Jurassic (Gaetani, 1975).

One of the best documented stratigraphic successions of the Friuli Platform, is that found along the disused road between the towns of Molassa and Maniago, which follows the Val Cellina river and gorge (see Figure 3.ii; Cuvillier *et al.*, 1968; Ghetti, 1987; Ghetti and Brigatti, 1991). These shallow-water platform carbonates were deposited in a restricted to very restricted lagoon on the north-western margin of the Friuli Platform (Ghetti and Brigatti, 1991). More specifically, Cuvillier *et al.* (1968) describes the 'Calcari Porcellanacei Inferiore' member (350 m thick) of the Calcari di Cellina formation (Oxfordian–Portlandian) as an intertidal platform facies deposited at a depth of 10–15 m and characterised by a prevalence of bioclasts (algal) with associated sporadic lagoonal horizons (Figure 3.i). The Berriasian–Aptian Calcari Porcellanacei Superiore member (550-m thick) represents a more restricted intertidal marine environment at less depth (1–5 m). Apparently these Lower Cretaceous sediments were subject to periodic atmospheric exposure, which is registered in the sedimentary record by the presence of birdseye structures, mud-crack traces and green clay levels intercalated with the carbonate proper. The latter of these was assigned the product of decalcifiфcation resulting from emersion (Ferasin, 1958), and this interpretation is supported by later work hypothesising that the "illite and chlorite (in the clay intervals) were generated by the conversion of smectite from Cretaceous soils at surface temperature and pressure in a transitional continental–marine area" (Ghetti and Brigatti, 1991). Ghetti (1987) does not subdivide the Calcari del Cellina formation into the two Calcari Porcellanacei members in the same way as do Cuvillier *et al.* (1968), but instead into five units, A – E.

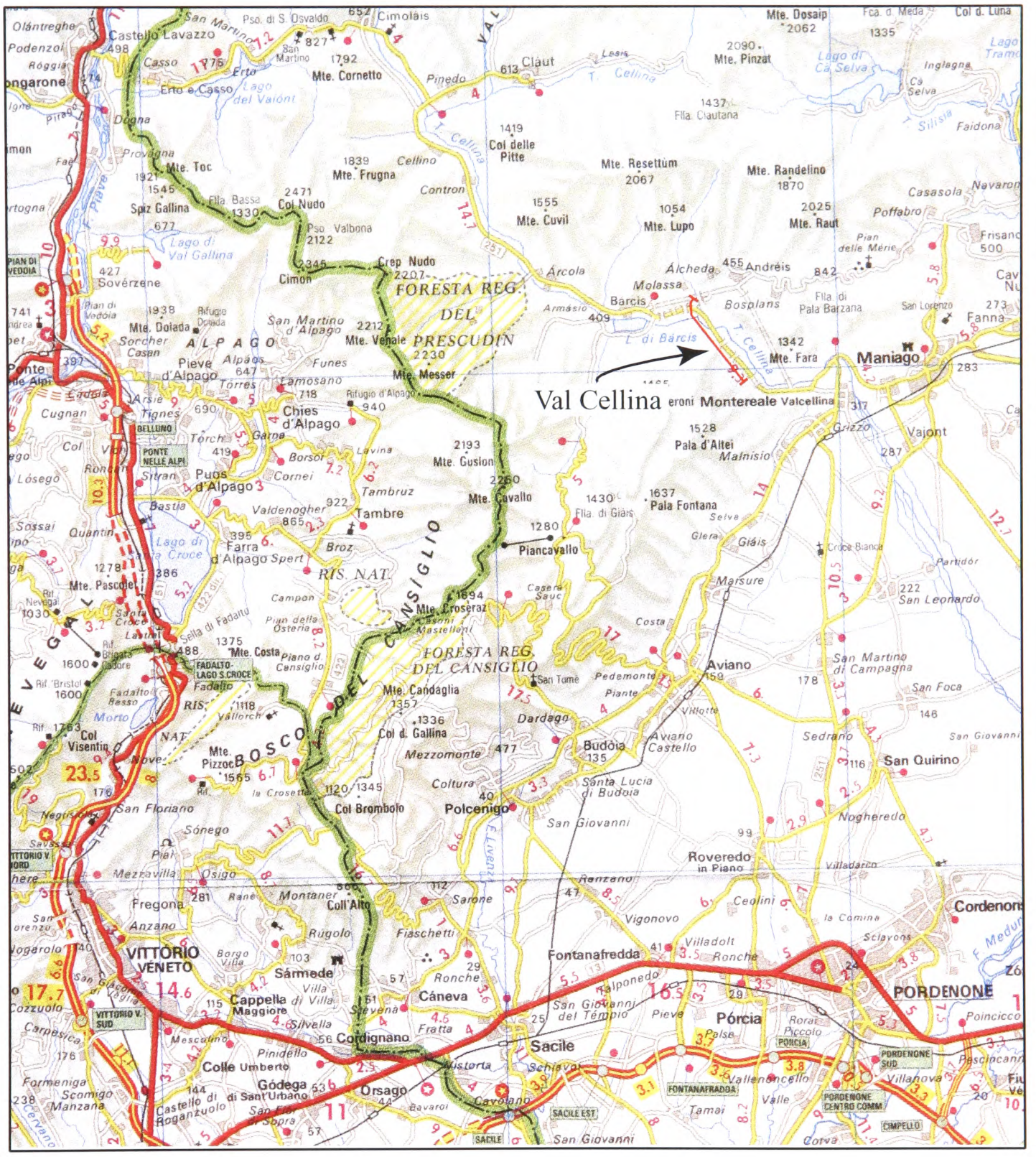

Figure 3.ii. Location map of the Val Cellina section, located between the towns of Montereale Val Cellina and Barcis, north of the city of Pordenone. The road along which the section is found is locked and disused.

Unit A is 289-m thick, and consists of subtidal micrites interbedded with inter–supratidal intervals. Associated with these facies at lower levels are benthonic foraminifera, dasycladacean algae (indicative of normal-salinity marine conditions with a muddy/sandy substrate in 3–5 m water depth; Ghetti, 1987), bivalves and echinoid spines, whereas towards the top of the unit, bioclasts (dasycladacean algae, gastropods, ostracods, foraminifera, bivalves, echinoderms and bryozoa), intraclasts, oncolites and peloids are found. Unit B is 147-m thick and is subdivided into two parts: a lower 100 m interval of cyclic shallowing-up sub–supratidal facies and a 50-m-thick upper part of carbonate sands and micrites with bioclasts (dasycladacean algae, gastropods, bivalves and echinoderms) and intraclasts. Unit C is 512-m thick and consists of laminated micrite with stromatolites and birdseyes, and is also punctuated by palaeosols registered by the presence of intervals with calcareous pebbles within sterile green clays (the result of subaerial dissolution). The entire unit also lacks biostatigraphic constraint. Unit D is a 95-m-thick member characterised by metre-scale peritidal cyclicity consisting of large organogenic debris (e.g. rudist fragments) held within a bioclastic (algae, benthonic foraminifera, bryozoa and bivalves) and small intraclastic matrix. Unit E is 91-m thick with a 25-m-thick lower interval of peritidal cycles with the following characteristics:

1) a basal layer of green marl
2) a 20-cm-thick layer weakly of laminated micrite
3) a 1–1.5-m-thick bioclastic (algae, benthic and planktonic foraminifera (indicators of communication between platform and the open ocean), rudist and coral fragments) body
4) a 20-cm-thick layer similar to (2)
5) green marl to close the cycle

The upper half of Unit E is dominated by subtidal micrite, which is at first represented by metre-scale beds without green marl interbeds, and later becomes increasingly thin-bedded with green marl permeating the limestone to produce a nodular appearance.

The Albian–latest Cretaceous witnessed the development of a reef barrier to the east, while the Val Cellina lagoon became more open-marine resulting in the deposition of the

Calcari di Monte Cavallo formation (550-m thick): the product of reef-facies sedimentation and talus originating from reef disaggregation (predominantly rudist debris forming biostromes and more rarely bioherms; Ferasin, 1958; Cuvillier *et al.*, 1968; Ghetti, 1987). Ghetti (1987) once again subdivides the Calcareniti del Molassa (almost equivalent to the Calcari di Monte Cavallo of Cuvillier *et al.* (1968), except at the base), but this time into two units, F and G. Unit F is 195 m thick and consists of alternating white limestone with large amounts of macrofossil fragments (gastropods and rudists) and conglomeratic levels or laminated micrite. The conglomeratic clasts comprise white pebbles 2–3 cm in size derived from reworked shell fragments in a bioclastic matrix. The laminated micrites are peloidal or bioclastic with local concentrations of fossil fragments. Unit G is 218 m thick and consists of alternations of the following lithofacies:

1) massive, white, micrite or sand with large bioclasts (locally rudists are found in place), algae, benthic *and planktonic* foraminifera, echinoid spines and rudist fragments
2) saccharoidal limestone whose bioclastic content is almost wholly made up of rudist fragments
3) micrite with centimetre-scale argillaceous joints, birdseyes and bioclasts (algae, ostracods, benthic and planktonic foraminifera and rudist fragments), similar to the Calcari del Cellina

The planktonic foraminifera observed by Ghetti (1987) and in this study occur between +1150 and +1420 m (dated by biostratigraphy as approximately mid-Cenomanian–uppermost Cretaceous). Planktonic elements have also been recorded amongst grains of shallow-water affinity on the neighbouring Dinaric Platform during the Cenomanian–Turonian, and this phenomenon was ascribed the result of widespread transgression and platform flooding in the Adriatic (Gusic and Jelanska, 1993; Davey and Jenkyns, 1999). Scholle and Kling (1972) describe partially analogous environments from the modern world, in which the authors discovered coccoliths deposited in the lagoonal waters of Honduras.

The above carbonate-platform depositional setting (that had continued for over 160 My) ceased at the end of the Maastrichtian with a period of emersion followed by further marine

sedimentation, which resumed in the Palaeocene. This is registered in the stratigraphic record by the presence of the Calcari di Andreis formation (<100 m of coralline and algal 'biolithite'/breccia), but Eocene flysch sedimentation (i.e. the 50-m-thick Flysch di Clauzetto Formation) signalled the termination of carbonate deposition in the region (Cuvillier *et al.*, 1968).

In terms of the previous biostratigraphic analyses performed on the Val Cellina, relatively long-lived indicators such as algae and benthic foraminifera have been used in an attempt to constrain the time dimension over the section (Cuvillier *et al.*, 1968; Ghetti, 1987). Figure 3.i illustrates the biostratigraphic resolution attained at the Val Cellina prior to the chemostratigraphic correlations that were made in this study. The available biostratigraphy clearly shows that problems were particularly encountered between the Berriasian and Aptian. Otherwise, in general, biostratigraphy provides a dating resolution that only reaches an average of one or two stages in constraint.

3.1.1 Val Cellina

As discussed in ***3.1***, the Val Cellina (VC) section can be reached along the disused road between the towns of Molassa and Maniago, roughly situated between the cities of Belluno and Udine, north of Pordenone, northeast Italy (Figure 3.ii). Starting at the eastern end of the road (now locked with gates - the key can be obtained from the municipal offices of Montereale), the section follows the river and gorge of the Val Cellina. The section discussed in this study begins at the first tunnel reached along the road (after a section charcterised by quasi-horizontal bedding), adjacent to the dam works on the river. With relatively continuous exposure from this point for 1435 m of vertical thickness, the section is an important record of the carbonate platform history of this area throughout the Late Jurassic and Cretaceous. The succession encountered is illustrated as a graphic log in Figure 3.iii. Sampling frequency for the chemostratigraphic analysis was initially every 5 m, but increased after re-visits up to every 0.5 m over critical intervals. Detailed petrographic analyses were carried out (in conjunction with Roberta Bruni, University of Ancona) over the 1435-m-thick section, and Bruni also carried out detailed biostratigraphic analyses over the entire section (these results are incorporated into this

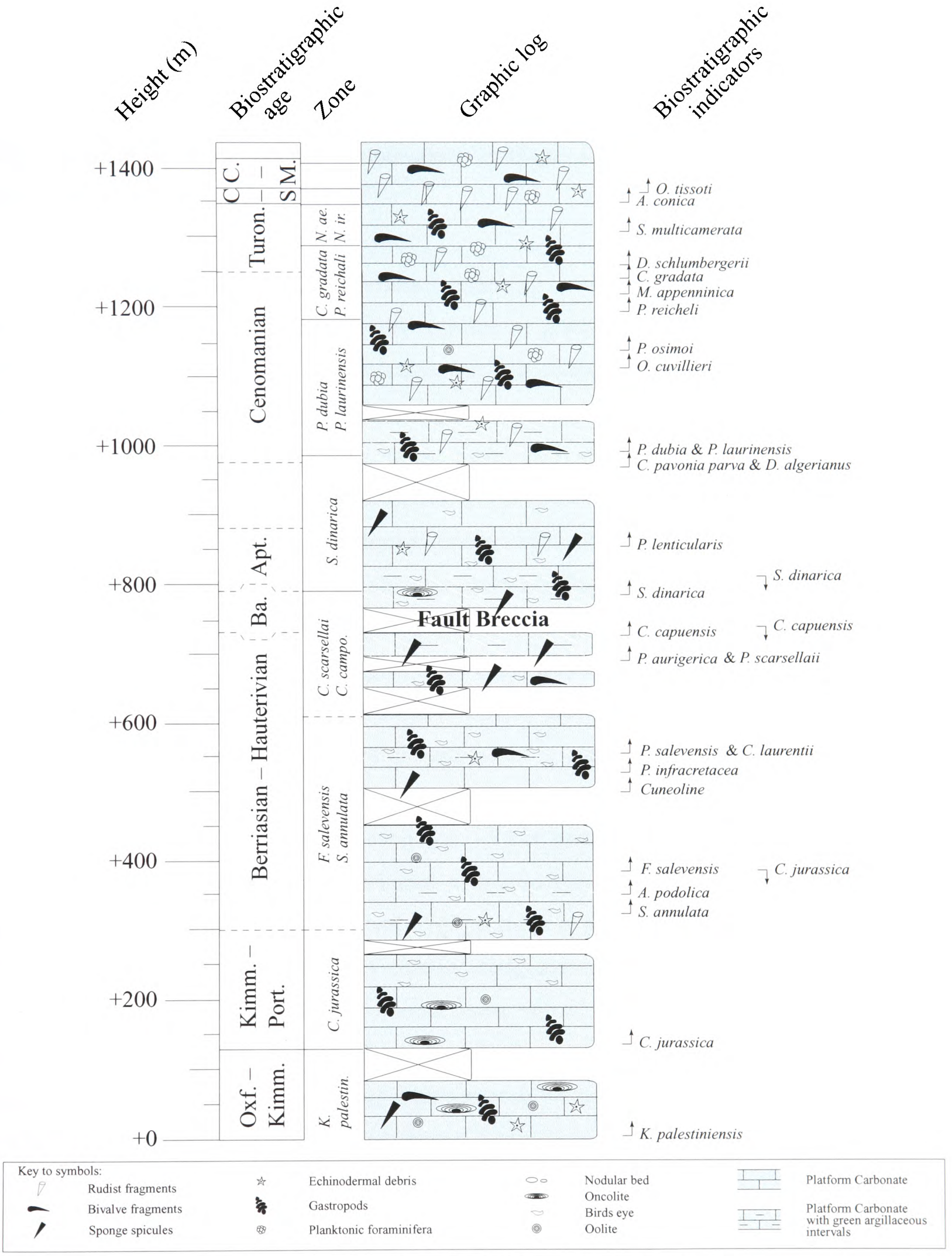

Figure 3.iii. Stratigraphic log detailing the 1435-m-thick Friuli Platform succession found along the Val Cellina (VC) disused road, near Maniago, Friuli, northern Italy. Biostratigraphy after Bruni (*unpubl.*), zones after Chiocchini *et al.* (1994); Oxf. = Oxfordian; Kimm. = Kimmeridgian; Port. = Portlandian; Ba. = Barremian; Apt. = Aptian; Turon. = Turonian; C – S = Coniacian – Santonian; C – M = Campanian – Maastrichtian.

thesis to give the broader picture of the results obtained). Petromicrographic plates are not cited directly from the text (for reasons of practicality with a section that is so thick), but the main lithotypes are illustrated in the "Atlas of photomicrographs" (***Appendix 3***) between Plates A3.3.i and A3.3.xii. Further to this, a selection of the primary biostratigraphic indicators is illustrated (taken from thin-sections obtained by this study) in Plates A3.3.xiii to A3.3.xix, and these are cited in the text below.

The lower levels of the Val Cellina section (up to +75 m) are characterised by being massive (beds ~2 m thick) and generally micritic or grain supported (peloids, oncoids and scattered ooids) with bioclasts of dasycladacean and codiacian algae, benthic foraminifera, gastropods, bivalves, ostracods and rare sponge spicules and echinoid spines. After a 60-m gap without exposure there is little change in the facies until +215 m, when birdseyes, traces of desiccation cracks and laminated mudstones are also recorded (arranged in Lofer Cycles; Fischer, 1964). Both of the above sedimentation patterns continue to be reflected in the rock record until +349.8, where there is a 2 cm mint-green argillaceous layer with limestone nodules within, and at +357 m a 20-cm-thick layer of grey, red and green marl (the latter being topmost; Plate A4.3.i). Also, at +547 m, a 3-cm green clay interval is observed, shortly followed by a 50-cm-thick clay-rich layer that is eroded back in outcrop leaving an argillaceous residue on the ledge below (Plate A4.3.ii). Stromatolitic lamination is apparent at +555 m, and birdseyes, bioclastic and peloidal sedimentation then continues without clay intervals until +700 m. Between +700 and +720 m there are seven thin (~5 cm) green argillaceous intervals, while the carbonate lithology around them is peloidal with associated bioclasts (benthic foraminifera, ostracods and algae). Between +720 and +760 m there is a zone of megabraccia, with large blocks randomly orientated amongst smaller conglomeratic rubble (Plate A4.3.iii). The megabreccia is bound on both sides by normal faults, one of which is clearly illustrated in Plate A4.3.iv. Between +760 and +810 m, the platform limestone is predominatly mixed mudstone/packstone (peloidal/bioclatic) with common birdseyes and is locally laminated (i.e. similar Lofer–type cyclicity as described above). A typical cycle is represented from base to top by:

1) a thin (5 cm) green argillaceous layer lying on an irregular bedding surface with green stylolites penetrating down through it
2) 'clean', birdseye limestone (locally laminated), commonly sterile and 10's of centimetres thick
3) relatively thick layer of mudstone/packstone with abundant bioclasts (benthic foraminifera, algae, gastropods, bivalves, ostracods)

Bedding becomes thinner upsection (from 1–2 m between +760 to +790 m, to 0.5–1 m thick above +790 m), and green argillaceous layers more common (Plates A4.3.v and A4.3.vi). This is clearly illustrated in the graphic log of Figure 3.iv, which represents in detail the section observed between +760 and +810 m.

From +823 m to +980 m, there is little change in the sedimentation style, except that there is an absence of the green argillaceous layers and birdseye limestones. However, between +980 and +1030 m, the green marl intervals are re-introduced once more and, at outcrop, the lithofacies are remarkably similar to those encountered between +760 and +810 m.

Between +1030 and +1075 m there is an exposure gap (what is exposed appears to be large-scale slip blocks), and outcrop resumes beyond the E.N.E.L. hydroelectric power station and dam, over the bridge and on the other side of the river/gorge (this part of the section is now closed off and can no longer be accessed without the collection of necessary keys from the E.N.E.L. offices in Pordenone). The lithofacies here (and continuing above to the top of the section) is markedly different to that developed below: floatstones and rudstones occur, predominantly composed of large rudist fragments that are virtually ubiquitous but occurring in varying quantities. Benthonic and planktonic foraminifera, algae, gastropods, bivalves and echinoid spines continue to be present as bioclastic debris virtually throughout the remaining section. Between +1325 m and the top of the section (+1435 m) rudist fragments dominate the sediment (locally reaching up to 100 % composition).

It is apparent that the log generated in this study correlates well with those published previously (Cuvillier *et al.*, 1968; Ghetti, 1987; Ghetti and Brigatti, 1991). The lower 1030 m of

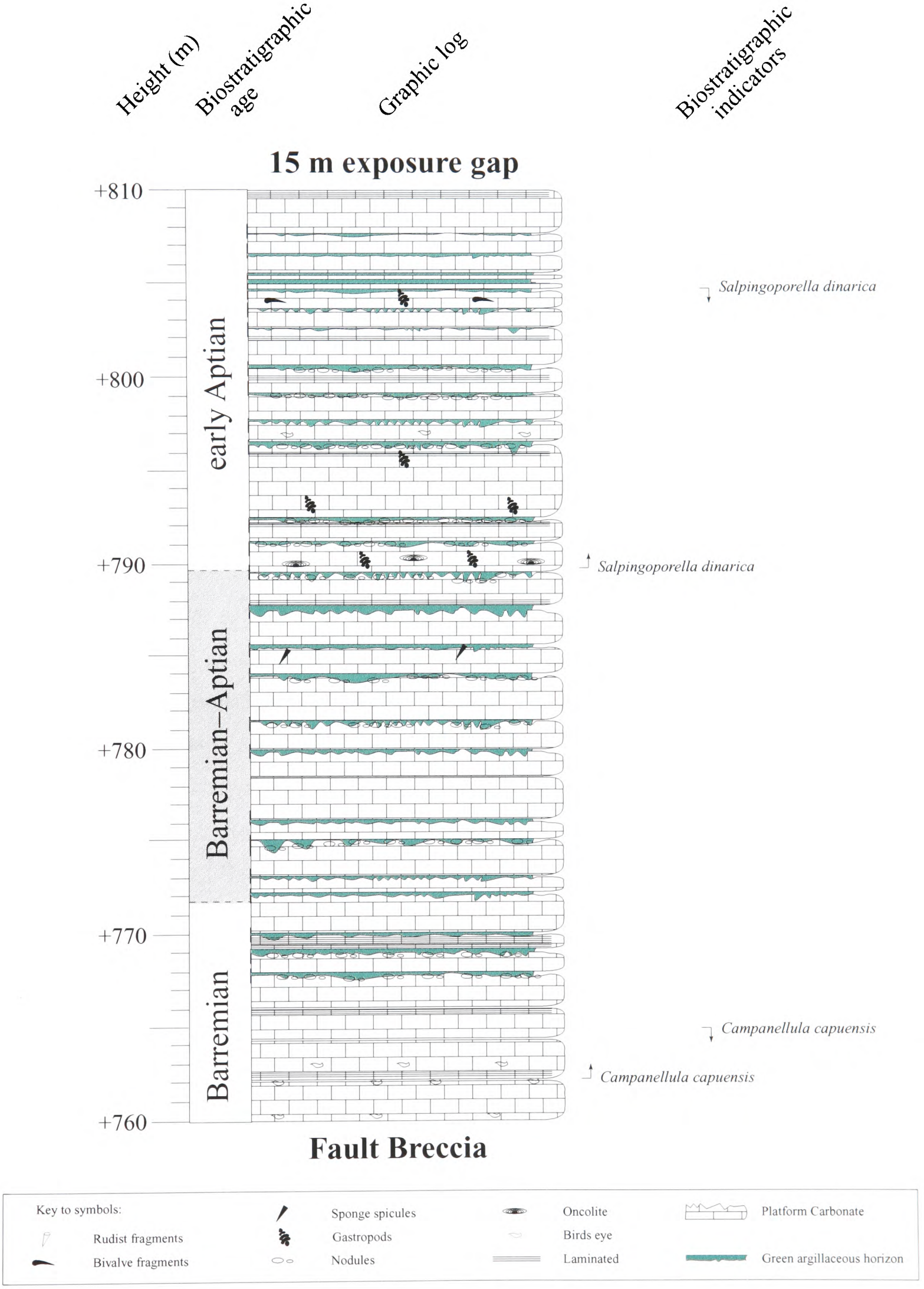

Figure 3.iv. Detailed stratigraphic log of the +760 to +810 m interval of platform carbonate cropping out in the Val Cellina section.

this section correlate with the Calcari di/del Cellina discussed by the earlier workers, and lithostratigraphic correlation with the individual units, A–E of Ghetti (1987) and the green argillaceous intervals of Ghetti (1991) can also be accomplished. The biostratigraphic constraints achieved by both studies are also useful for correlation despite the low level of resolution, and the Tethyan inner-shelf platform biostratigraphic indicators of Chiocchini *et al.* (1994) were utilised by Bruni (*unpubl.*) to aid the biostratigraphic process. To summarise, Unit A of Ghetti (1987), which was interpreted to be a sub–supratidal facies, correlates well with the lower 225 m of the section in this study, and furthermore the presence of *Kurnubia palestiniensis* was recorded at the base of this studied section and that of Cuvillier *et al.* (1968). *Clypeina jurassica* (Plate A3.3.xiii) was observed at the top of Unit A and throughout most of Unit B by Ghetti (1987) and between 90 and 410 m by Cuvillier *et al.* (1968). The same dasycladacean algae were also observed between +125 and +300 m in this study. Over this interval both Ghetti (1987) and this study register the introduction of birdseye limestones and local argillaceous layers (e.g. +300 and +347 m of this study). These clay-rich horizons are interpreted to be associated with peritidal cyclicity. Unit C of Ghetti (1987) and the *Salpingoporella annulata* sub-zone of Cuvillier *et al.* (1968) correlate well with the interval between +300 and +760 m observed by this study, characterised by the presence of birdseyes, laminated micrites and common argillaceous intervals. This stretch of the section has to date been the most difficult to constrain biostratigraphically. Ghetti (1987) uses *Orbitolina gr. texana* and *Paleorbitolina precursor* to define the Aptian (Unit D), whereas Cuvillier *et al.* (1968) use *Salpingoporella dinarica* (Plate A3.3.xiv). In this study, the presence of *Campanellula capuensis* (Plate A3.3.xv) is taken to register the Barremian Stage between +760 and +765 m, and the introduction of *Salpingoporella dinarica* announces the uppermost Barremian–lower Aptian at +787 m. Lithostratigraphically, Ghetti (1987 and 1991) describes Unit D and the lower levels of Unit E as being characterised by metre-scale peritidal cycles with the common presence of thin, green argillaceous intervals, which are also recognised between +760 and +810 m in this study. *Cuneolina pavonia parva* (Plate A3.3.xvi) was used to mark the initiation in deposition of the biohermal/biostromal Calcari di Monte Cavallo (Calcareniti del Molassa equivalent) by Cuvillier *et al.* (1968), above which the virtually ubiquitous presence of rudist fragments has been recorded by all previous workers and in this study (+975 m and above). Biostratigraphic constraint is once again poor, and the best resolution for the following

275 m suggests that this interval was deposited during the Albian–Cenomanian. The upper Cenomanian/lower Turonian is registered in this study and by Ghetti (1987) by the presence of *Pseudolituenella reicheli, Chrysalidina gradata* (Plate A3.3.xvii) and *Dicyclina schlumbergerii*, and the upper Turonian by the presence of *Nezzazatinella cf. Aegyptiaca* and *Nummuloculina cf. Irregularis* only in this study. The Coniacian–Santonian is registered by the presence of *Accordiella conica* (Plate A3.3.xviii) and *Rotorbinella scarsellai* in this study, and the Campanian–Maastrichtian by *Discorbidae, Miliolids* and *Orbitoides tissoti* (Plate A3.3.xix).

3.2 Chemostratigraphic results

Chemostratigraphic data for the 1435-m-thick Val Cellina section are presented below with biostratigraphic age assignments given in brackets, and the implications of global correlations and the assessment of observed relationships between the various isotope profiles and the facies associations are discussed in ***Chapters 5 and 6***. Data tables are included in ***Appendix Data Table 3.1***.

3.2.1 Strontium-isotope results

The complete strontium-isotope profile of the 1435-m-thick Val Cellina section is illustrated in Figure 3.v. Isotope values range from 0.7069 to 0.70781 and broadly exhibit a rising trend throughout the section. More specifically, the base of the section (0 to +150 m; Oxfordian–Kimmeridgian) shows a relative trough in values before a sustained increase in values between +150 and +810 m (Kimmeridgian–Aptian) resulting in isotope ratios as high as 0.70755. Between +810 and +885 m (Aptian) strontium-isotope values decrease relatively abruptly to 0.70729, but after a gap of 80 m values have returned to 0.70746, and remain fluctuating about this figure until +1370 m (Cenomanian–late Turonian). After this point, a rapid increase occurs resulting in an isotope value of 0.70781 at +1435 m (Conianian–Tertiary). There are a limited number of data points that lie off the main trend, but as the main trend is relatively easy to distinguish as the broad-scale changes in the curve are coherent, the 'fliers' can be identified with relative ease. However, it should be noted that there is increased scatter between +1100 and +1350 m

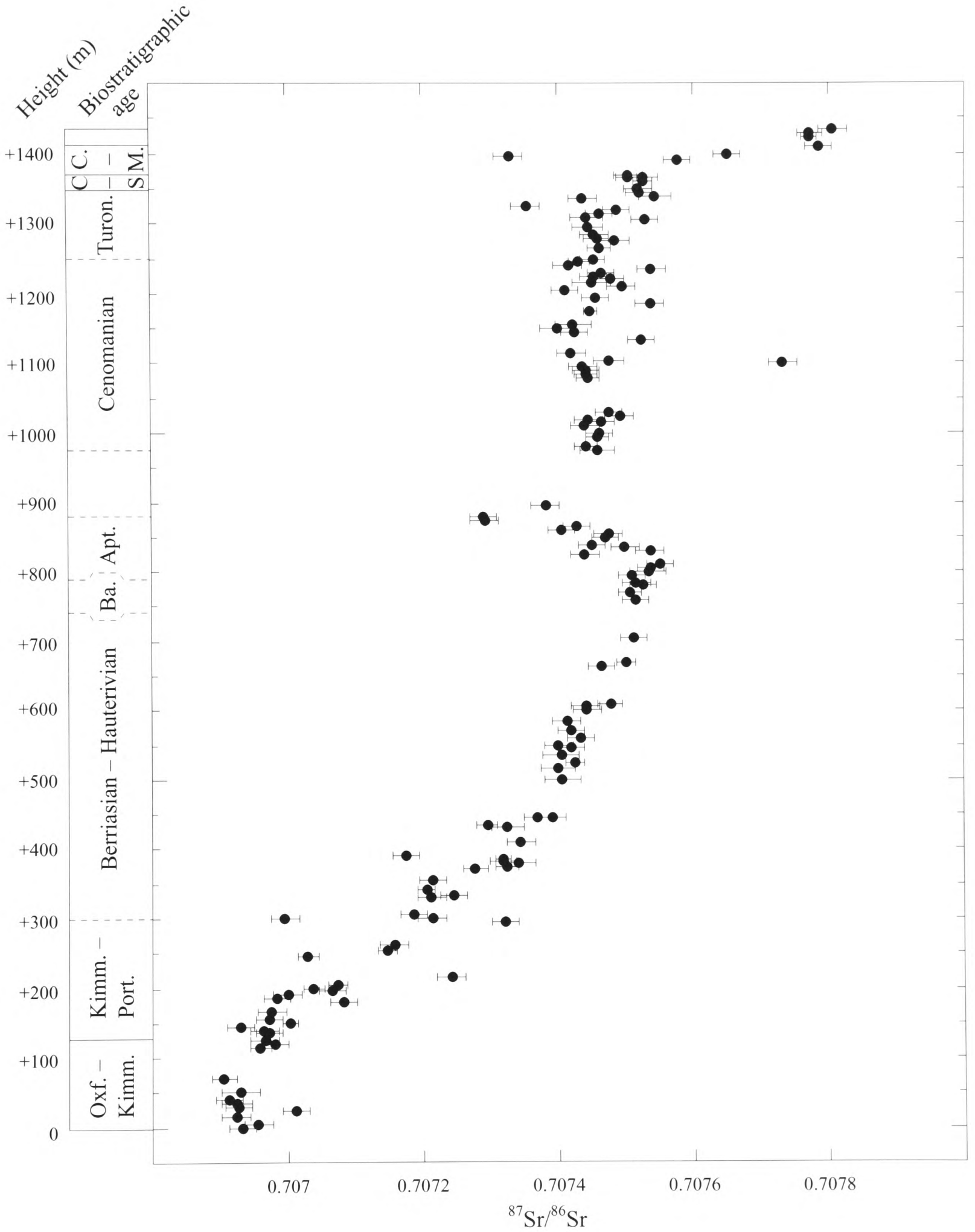

Figure 3.v. Strontium-isotope profile of the 1435-m-thick Val Cellina section with results normalised to a NIST SRM 987 value of 0.710250. n = 140, the running average of standards was 0.710248, and 2σ = 0.000026. Biostratigraphic age after Bruni (*unpubl.*). Oxf. = Oxfordian; Kimm. = Kimmeridgian; Port. = Portlandian; Ba. = Barremian; Apt. = Aptian; Turon. = Turonian; C – S = Coniacian – Santonian; C – M = Campanian – Maastrichtian.

3.2.2 Carbon-isotope results

Beacause the carbon-isotope curve exhibits higher frequency changes in values, the Val Cellina section has been segmented to illustrate the carbon- (and oxygen-; ***3.2.3***) isotope profiles more clearly (for complete carbon- and oxygen-isotope profiles of the entire Val Cellina section see Figure 3.x). The $\delta^{13}C_{carb}$ profile of the lower 500 m of the Val Cellina section is illustrated in Figure 3.vi. Isotope values range from –1.1 to +3.5 ‰, and begin with a ~0.7 ‰ negative shift to values of +2.5 ‰ (although only from one data-point) produced at +15 to +25 m (Oxfordian–Kimmeridgian). After a 25-m gap values have increased to +3.3 ‰ and reach +3.5 ‰ at +65 m. Above +115 m (after a 35-m gap) isotope values show a slight decreasing trend from +3.2 to +2.9 ‰ by +155 m, which is shortly followed by an increase to +3.2 ‰ over the next 10 m (Kimmeridgian?). From this point to +230 m, $\delta^{13}C_{carb}$ values decrease to a value of +0.9 ‰ (Kimmeridgian–Portlandian/Tithonian). After a 55-m exposure gap, values remain at +1.1 ‰, but undergo a relatively rapid increase to +2.1 ‰ at +315 m, which is followed by a rapid decrease to –1.1 ‰ at +352 m (Berriasian). By +370 m, values have climbed to ~0.5 ‰ and increase gradually thenceforth, attaining a value of +1.3 ‰ by +405 m. Above this point, values fall back to an average value of approximately +0.5 ‰, and fluctuate about this value until +500 m (Berriasian–Valanginian?).

From this average carbon-isotope value of +0.5 ‰, values go on to increase to +2.5 ‰ by +555 m (+545 m produces a single negative value of –0.5 ‰), as illustrated in Figure 3.vii (Berriasian–Hauterivian). There is then a subsequent decrease in values to +0.8 ‰ by +575 m, after which values remain relatively constant until +610 m. After a 35-m gap, values are similar at 0.5 ‰, but drop rapidly above +650 m to –1 ‰ by +653 m. This is followed by a more gradual rise to +0.8 ‰ by +668 m. After a 20-m gap, values between +695 and +720 m are relatively scattered (ranging from -0.7 to +0.9 ‰).

Above the fault-bounded megabreccia (> +760 m; Figure 3.viii), carbon-isotope values are less scattered and remain at approximately –0.5 ‰ until +766 m (Barremian). At +767 m there is a drop to –1.4 ‰ before a rise +0.5 ‰ by +770 m (Barremian). Values subsequently follow a stable and gradual negative trajectory reaching –3.7 ‰ at +790 m (Aptian). Above this

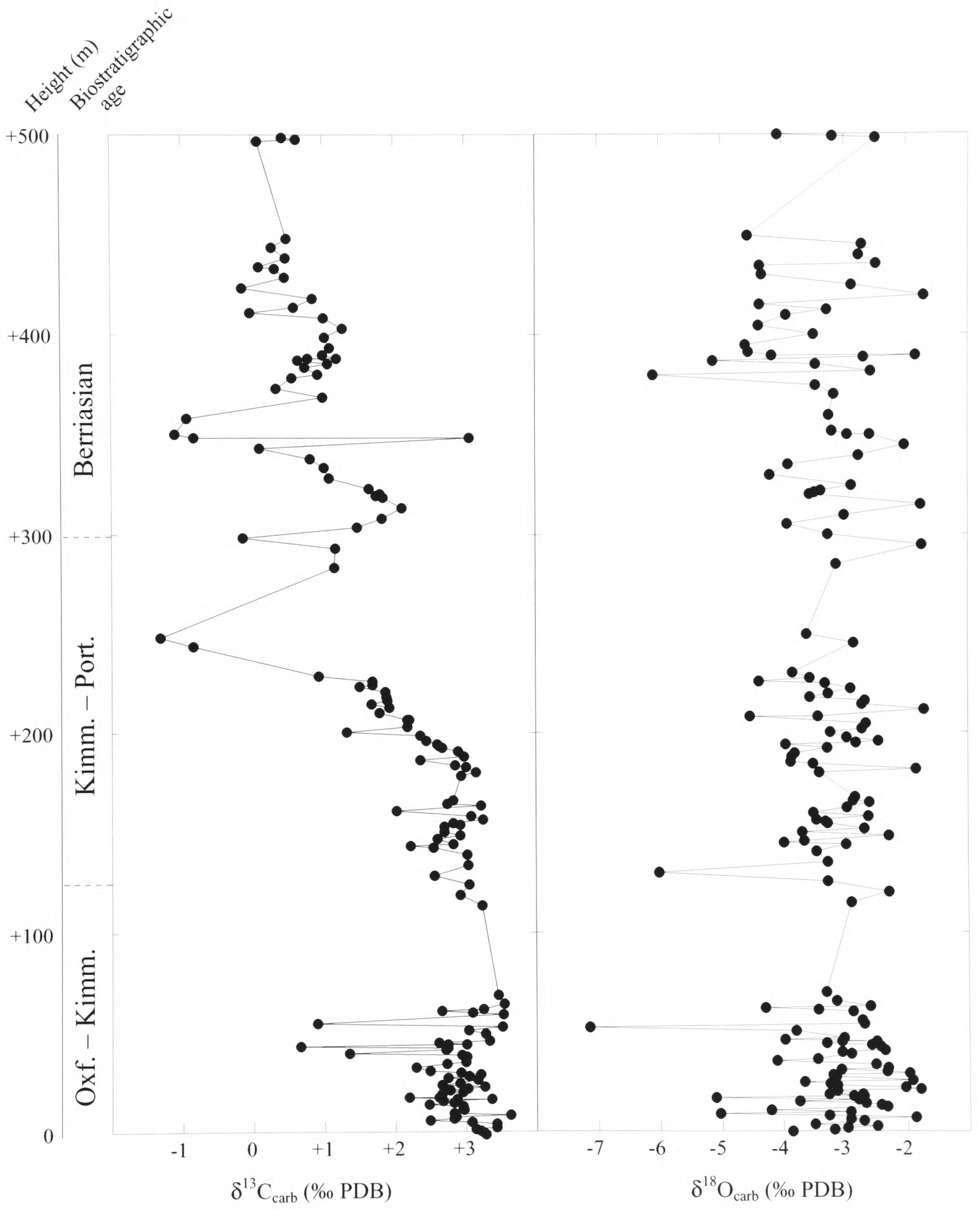

Figure 3.vi. Carbon- and oxygen-isotope profiles of the lower 500 m of the Val Cellina platform-carbonate section. Biostratigraphic constraint is included (after Bruni, *unpubl.*).

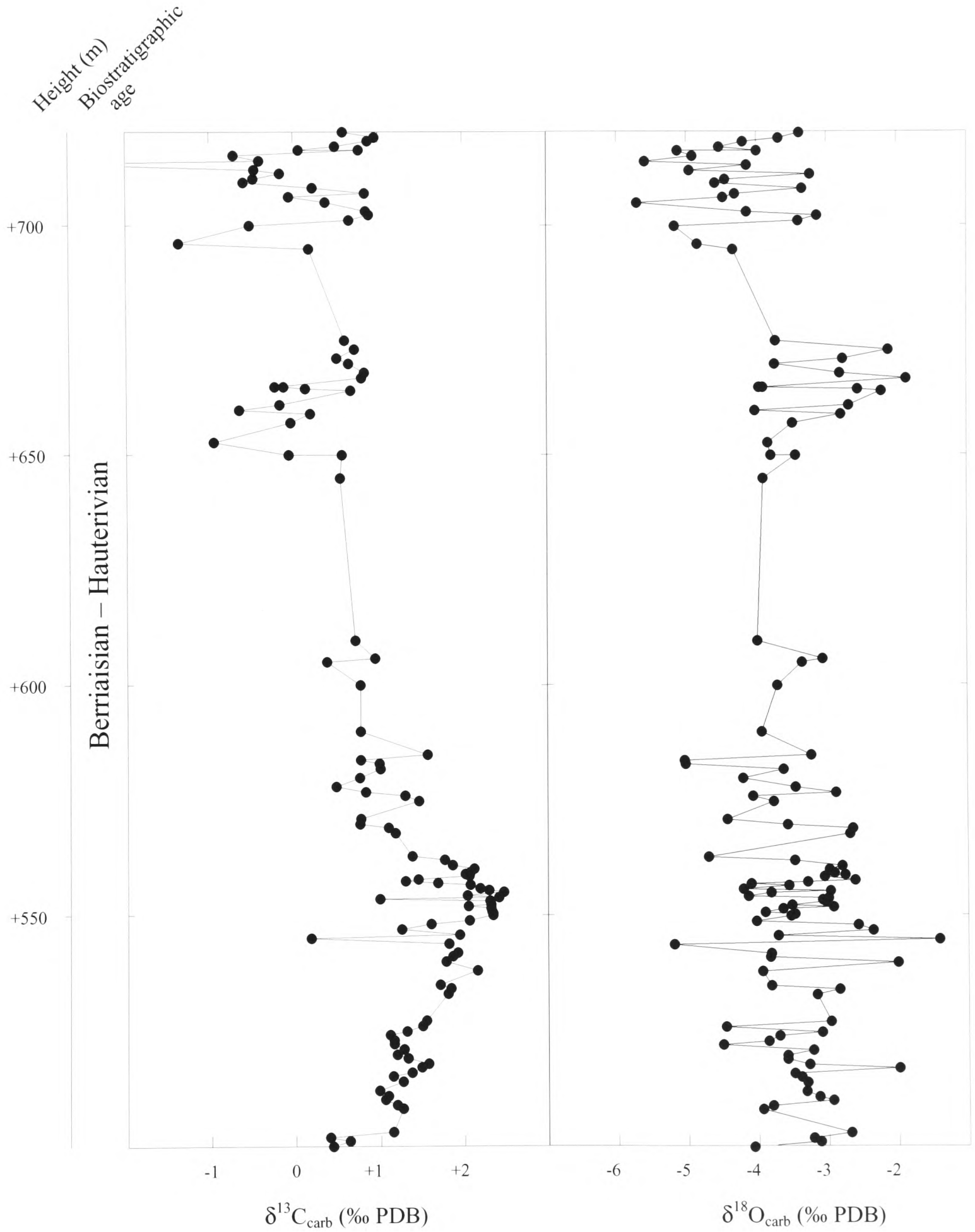

Figure 3.vii. Carbon- and oxygen-isotope profiles for the +500 to +720 m interval of the Val Cellina platform-carbonate section. Biostratigraphic constraint is included (after Bruni, *unpubl.*).

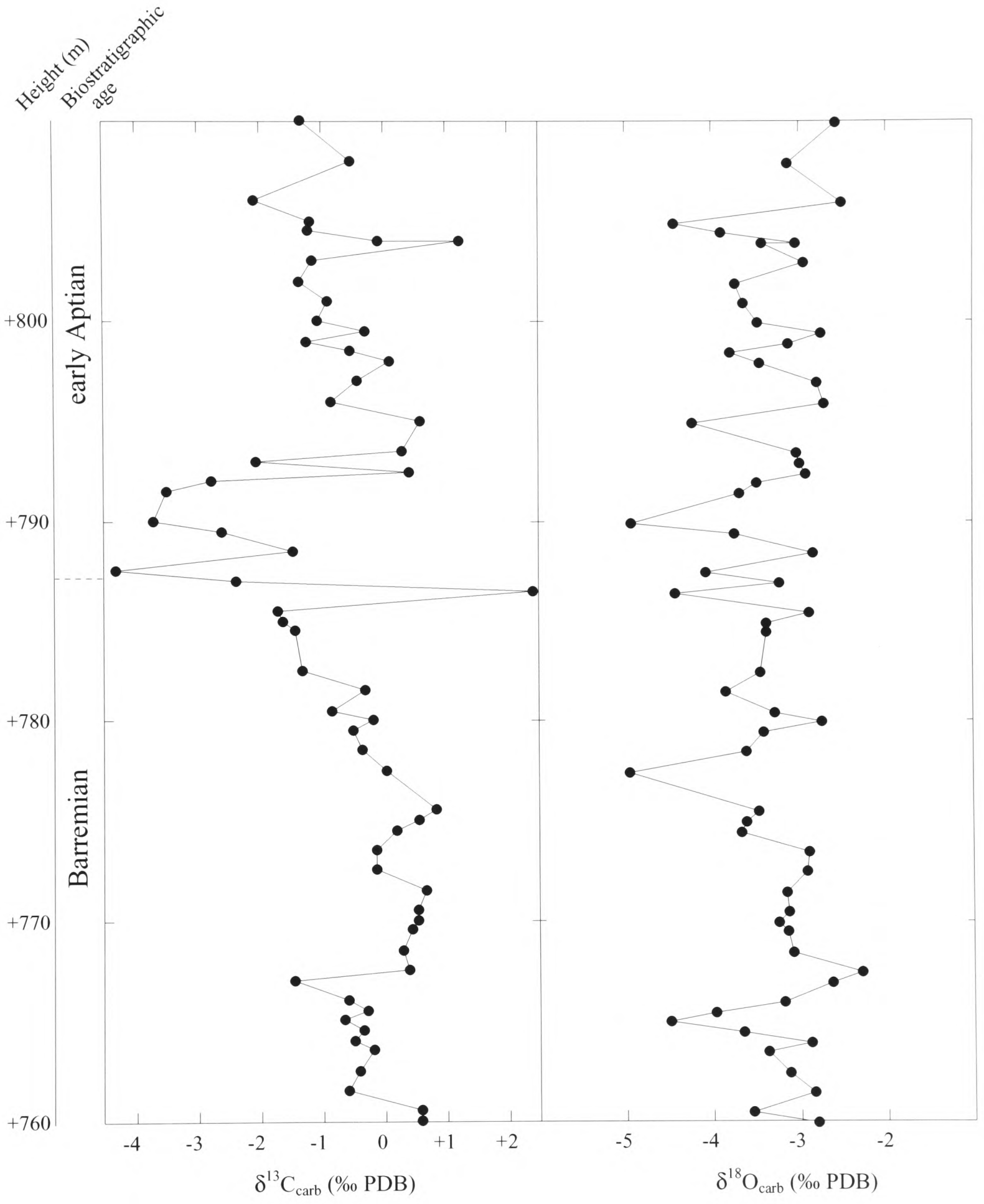

Figure 3.viii. Carbon- and oxygen-isotope profiles for the +760 to 810 m interval of the Val Cellina platform-carbonate section. Biostratigraphic constraint is included (after Bruni, *unpubl.*).

point, values rise in an equally coherent fashion to +0.6 ‰ by +795 m before continuing a general decrease to –1.3 ‰ by +810 m, with some associated scatter (it should also be noted that values rise briefly to +1.2 ‰ at +804 m).

Figure 3.ix illustrates the remaining 410 m of carbon-isotope profile for the Val Cellina section. $\delta^{13}C_{carb}$ values gradually increase from 0 to 2.5 ‰ between +826 and +872 m (Aptian). From this point to +975 m (including a 55-m gap) values fluctuate only slightly about an average of approximately +1 to +1.3 ‰. Between +975 and +995 m (Aptian–Cenomanian), however, there is a sharp fall in isotope values to –0.8 ‰, and values remain low but gradually increase to +0.1 ‰ by +1029 m. After a 46-m gap, values have risen to +1.7 ‰ and continue to increase until +1100 m where a value of +2.4 ‰ is attained (mid-Cenomanian). Following this point, isotope values decrease gradually to +0.7 ‰ by +1155 m (upper Cenomanian), before rising to +1.9 ‰ by +1210 m (Cenomanian–Turonian). At this point, there is another sharp decrease in values to approximately 0 ‰ (at +1230 m), followed by a relatively rapid (and slightly scattered) increase to +3.3 ‰ by +1290 (Cenomanian–Turonian). Above, a rapid decrease to –1.7‰ by +1330 m is recorded which is shortly followed by a sharp rise back to +2.5 ‰ by +1345 m (Turonian). After a drop to +1.6 ‰ registered at +1355 m (Coniacian–Santonian = +1357 to +1373 m), $\delta^{13}C_{carb}$ values climb gradually to +2 ‰ by +1395 m (Campanian–Maastrictian = +1373 to +1409 m), and subsequently drop to 0 ‰ at +1400 m, only to increase back to +2.4 ‰ by +1435 m (Cenozoic = +1409 m and above).

3.2.3 Oxygen-isotope results

The oxygen-isotope profiles for the Val Cellina section are illustrated adjacent to the carbon-isotope profiles discussed above, in Figures 3.vi to 3.ix. For a complete oxygen-isotope record of the entire Val Cellina section see Figure 3.x.

The $\delta^{18}O_{carb}$ curve of the lower 500 m of section is illustrated in Figure 3.vi, and first impressions suggest there are few recognisable trends to be observed over this segment of the section. The range of values is –6 to –1.7 ‰, although the majority of values recorded fall between –4.5 and –2.5 ‰. Distinguishing between real trends and those produced as a result of

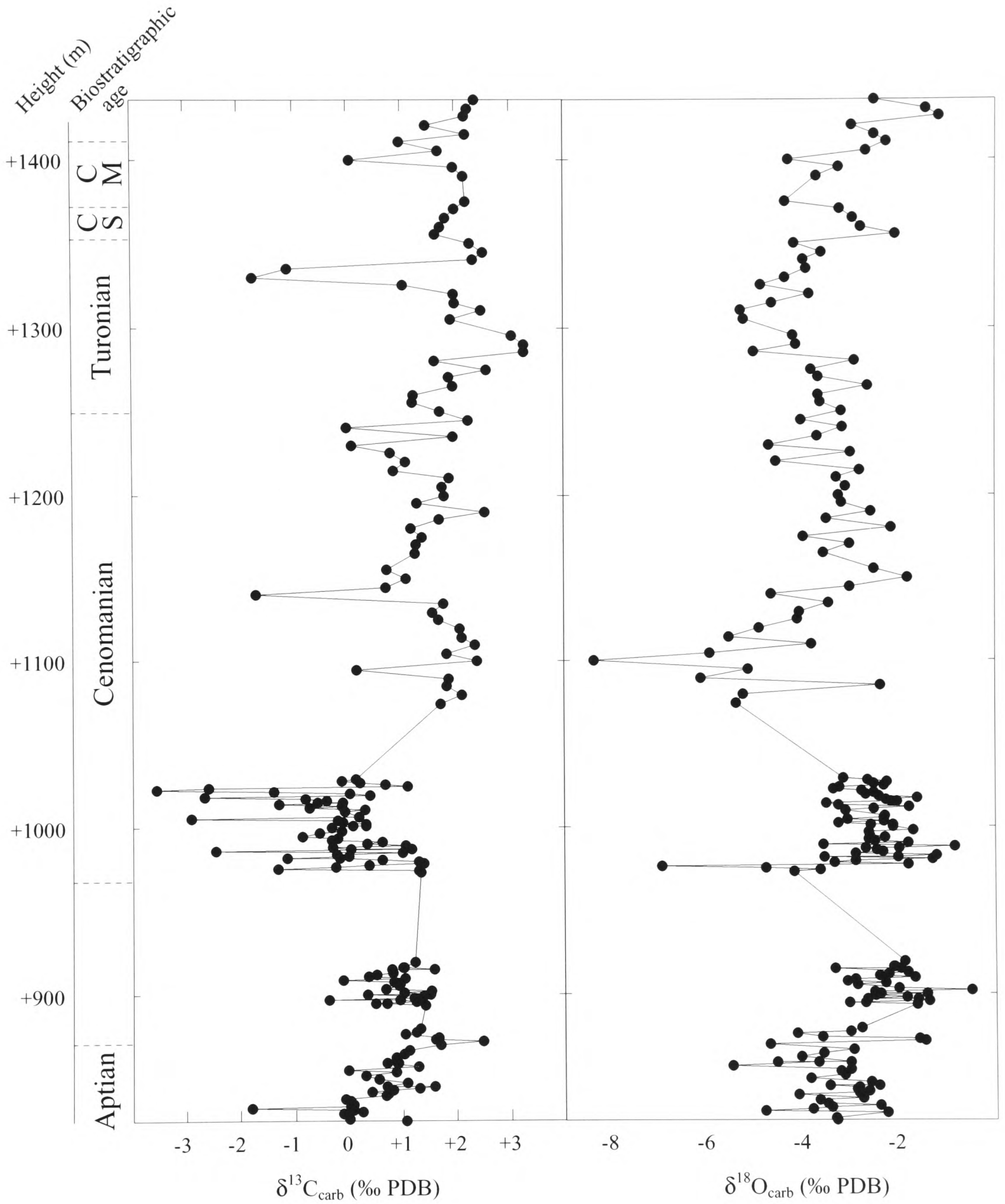

Figure 3.ix. Carbon- and oxygen-isotope profiles for the +825 to 1435 m interval of the Val Cellina platform-carbonate section. Biostratigraphic constraint is included (after Bruni, *unpubl.*). C S = Coniacian–Santonian; C M = Campanian–Maastrichtian.

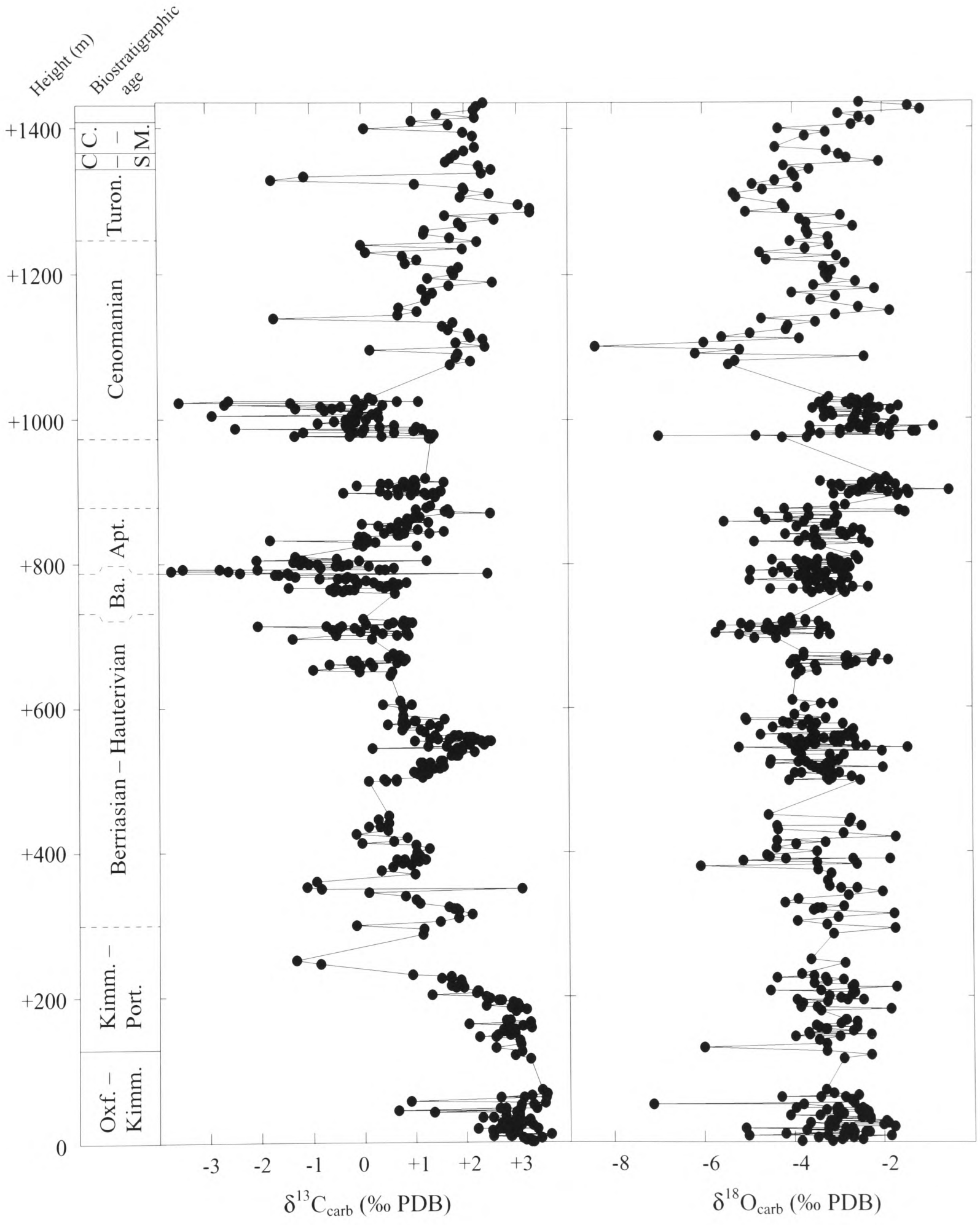

Figure 3.x. Carbon- and oxygen-isotope profiles of the 1435-m-thick Val Cellina section. Biostratigraphic age is after Bruni (*unpubl.*) Oxf. = Oxfordian; Kimm. = Kimmeridgian; Port. = Portlandian; Ba. = Barremian; Apt. = Aptian; Turon. = Turonian; C – S = Coniacian – Santonian; C – M = Campanian – Maastrichtian.

bias (derived from scatter) is difficult, especially at high resolution, but the broad trend is of relatively constant values throughout as there is little deviation from the fluctuation of values about an approximate value of –3.5 ‰. Scatter does appear to have a more significant influence on the data above +300 m (Berriasian–Valanginian?).

Figure 3.vii illustrates the oxygen-isotope curve derived from those samples collected between +500 and +720 m (Berriasian–Hauterivian). The range of values is –5.7 to –1.9 ‰, although the majority of values fall between –4 to –2 ‰, fluctuating above and below -3 ‰. Indeed, this appears the case from +500 to +675 (although there appears to be scatter between +650 and +675 m). Between +695 and +720 m there is a coherent decrease to more negative values recorded (Hauterivian?), reaching -5.7 ‰ at +705 m, followed by a gradual rise back up to –3.4 ‰ by +720 ‰.

Between +760 and +810 m values range from –4.9 to –2.5 ‰, and remain relatively constant throughout this segment of section (Figure 3.viii), if single datum 'fliers' are discounted. There is little coherence to trends below +795 m (Barremian–earliest Aptian), but at this point there is a gradual decrease in values from –2.7 to –3.7 ‰ by +802 m, before a jump up in values to –2.9 ‰ followed by a further decrease to –4.4 ‰ by +805 m (uppermost Barremian–lowest Aptian). A subsequent increase leads values back to –2.6 ‰ by +810 m.

Figure 3.ix illustrates the oxygen-isotope profile of +825 to +1435 m of the Val Cellina section. Data range from –8.3 to –1.1 ‰, and broad-scale trends appear more easily distinguishable over this segment of the section than below. Between +825 and +900 m there is a decrease to relatively depleted isotopic values (Aptian), reaching –4.7‰ at +870 m (although these data suffer from scatter, the trend appears real). After a gap of 54 m, $\delta^{18}O_{carb}$ values between +974 and +1029 m are scattered above and below an approximate average value of –2.5 ‰ before another 46-m gap is reached (lower Cenomanian). Between this point and +1150 m there is a marked 'low' in values where, at the minimum, data cluster about an average value of approximately –5.5 ‰ (the +1100 m datum registers at –8.4 ‰; mid-Cenomanian). After the minimum, values increase in a coherent fashion back to –1.8 ‰ by +1150 m. Between +1150

and +1310 m (Cenomanian–Turonian), values decrease gradually to –5.3 ‰ (with some scatter), before increasing gradually to –1.2 ‰ by +1425 m (Turonian–Cenozoic).

3.3 Diagenetic considerations

Petrographic analysis of the Val Cellina carbonate samples (performed in conjunction with colleagues at the University of Ancona) highlighted a minor portion of samples that may have been affected by diagenisis, and therefore have potentially suffered from significant isotopic overprinting. The following criteria were used to identify samples that may have suffered some modification in this way:

1) the presence of dolomite (note: in a predominantly calcitic succession)
2) the presence of other significant secondary cements
3) the presence of stylolites
4) the presence of texturally pervasive re-crystallisation.

Samples excluded due to observation of the above features were:

1) +190, +265, +300, +305, +310, +535, +705, +1080, +1105, +1130, +1340
2) +210, +230, +525, +1175
3) +215, +225, +290, +500, +795, +900, +995, +1240
4) +410

The carbon- and oxygen-isotope profiles that result after exclusion of the above data points are illustrated in Figures 3.xi (for a screened strontium-isotope profile, see the summary illustration of Figure 3.xiii).

To assess further the diagenetic impact on the Val Cellina carbonates, a carbon- and oxygen-isotope crossplot of those data remaining, after the petrographic screening outlined above, is illustrated in Figure 3.xii. The varying segments of section discussed in ***3.2.2*** and ***3.2.3*** (0 to +500 m, +500 to +720 m, +760 to +810 m, and +825 to +1435 m) are distinguished by different symbols to aid analysis. In general, no obvious linear mixing line is apparent for either

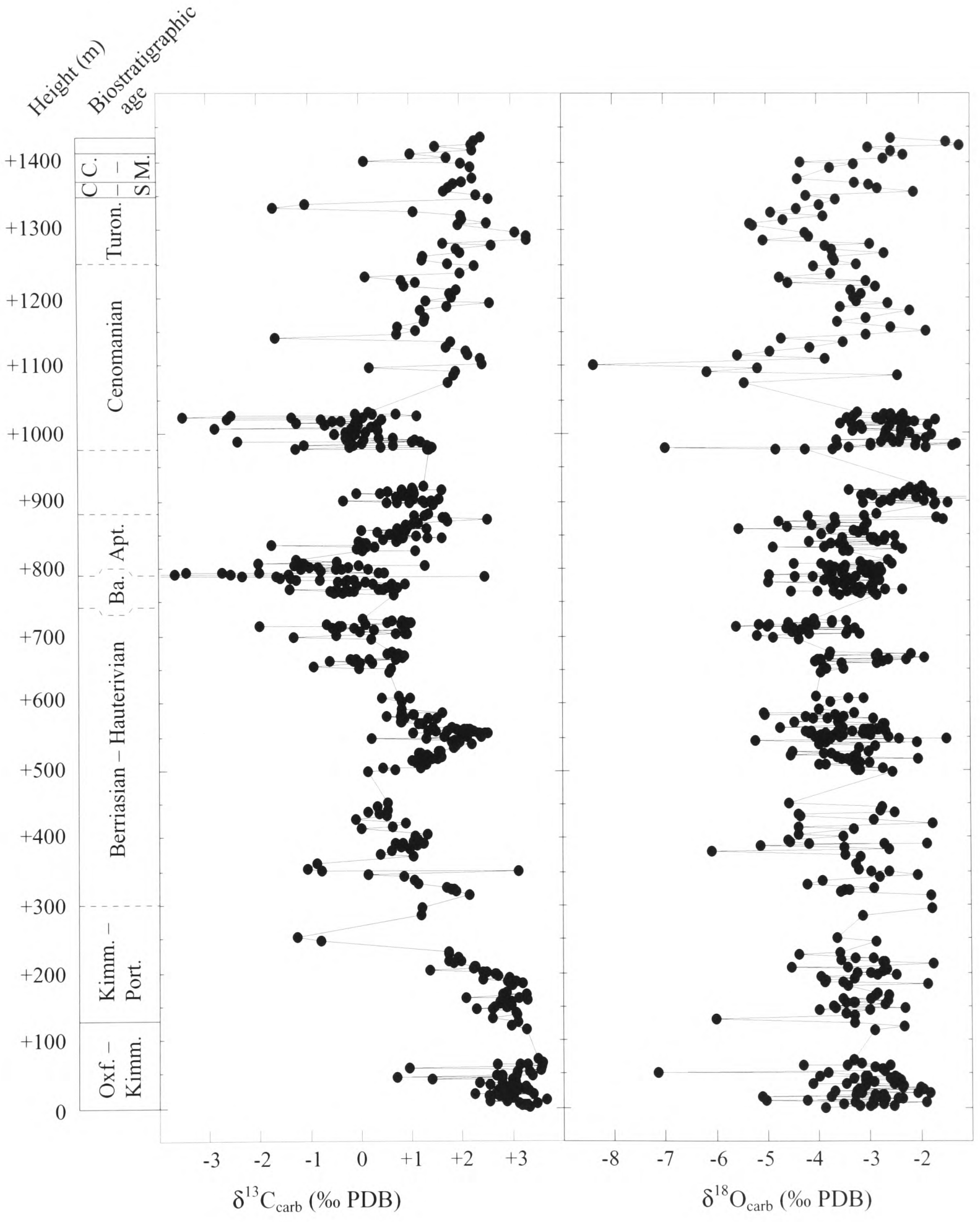

Figure 3.xi. Petrographically screened carbon- and oxygen-isotope profiles of the 1435-m-thick Val Cellina section. Biostratigraphic age is after Bruni (*unpubl.*). Oxf. = Oxfordian; Kimm. = Kimmeridgian; Port. = Portlandian; Ba. = Barremian; Apt. = Aptian; Turon. = Turonian; C – S = Coniacian – Santonian; C – M = Campanian – Maastrichtian.

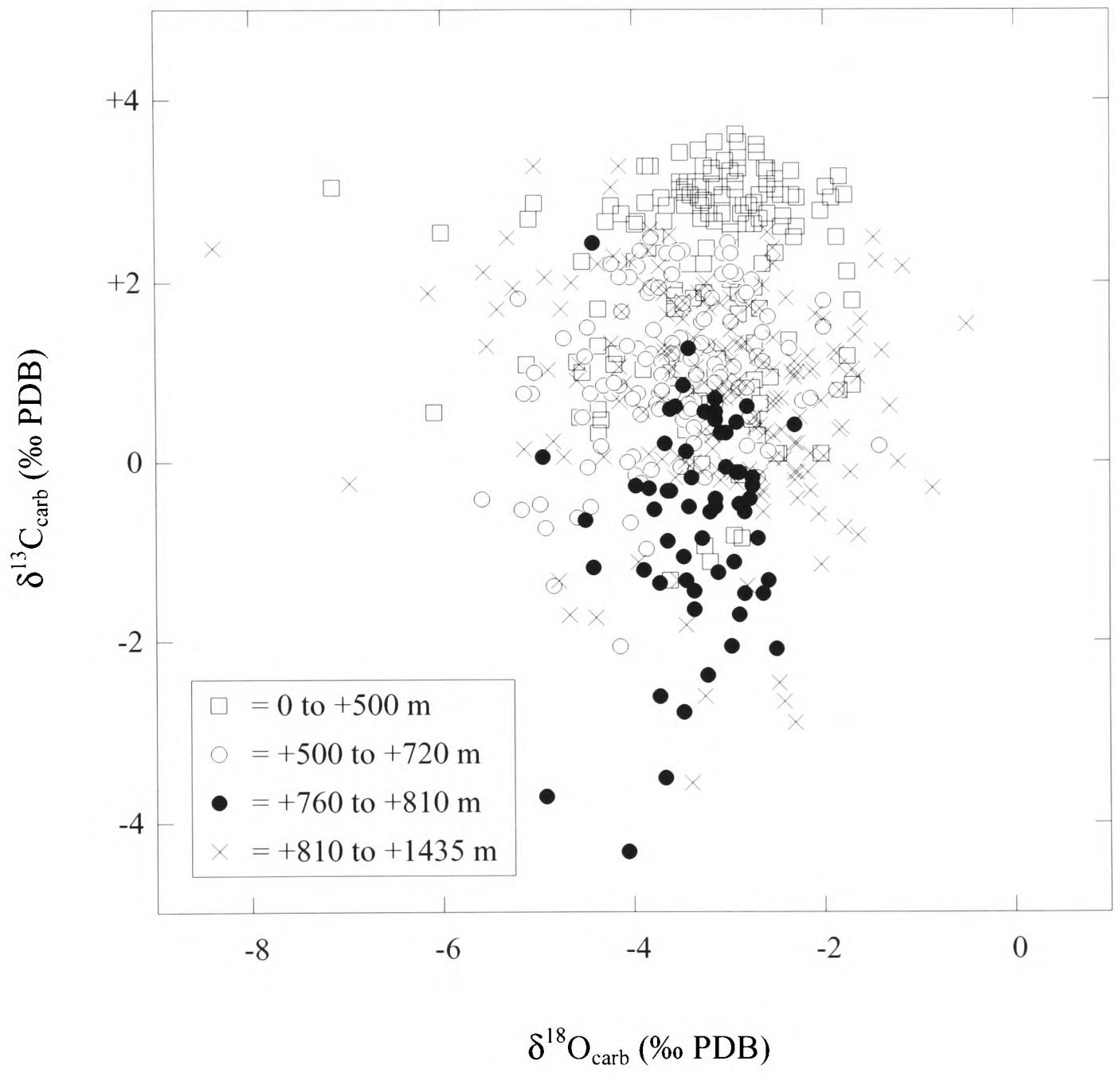

Figure 3.xii. Carbon- and oxygen-isotope cross-plot for the petrographically screened 1435-m-thick Val Cellina section.

the whole dataset or any of the segments when considered alone. There are relatively extreme (i.e. more negative) carbon- and oxygen-isotope values, but without any one sample having extremely negative carbon- *and* oxygen-isotope values, there is limited rationale for excluding any of the data by analysis of this cross-plot. Because oxygen-isotope values are more easily influenced by diagenesis (see ***1.4.3*** and ***2.3***), those samples with very low oxygen-isotope values could theoretically be removed in an attempt to screen for modification, but as the majority of the samples that would be excluded occur in the +825 to +1435 m segment of section, which also shows the most coherent trends of the oxygen-isotope curve, this procedure has not been performed.

It should also be noted that both the carbon- and oxygen-isotope curves display more negative values over their entirety (particularly above +760 m) than would be expected from, for example, a pelagic reference section. Grötsch (1998) and Jenkyns and Wilson (1999) discuss carbon- and oxygen-isotopes recorded in shallow-water limestones and suggest general dampening of isotopic signals can take place with global trends still being preserved. Therefore, removing data purely on the basis that they are more negative than expected cannot be justified and is avoided, unless further evidence of modification is discerned (e.g. restricted lagoonal environments may lead to the registration of non-open-marine isotope signals).

To summarise, the carbon- and strontium-isotope profiles (i.e. the most useful chemostratigraphic correlating tools) of the Val Cellina section are both illustrated against the complete graphic log and biostratigraphy (of Bruni, *unpubl.*) in Figure 3.xiii. The blue line on the carbon-isotope profile is a five-point moving average, whereas that on the strontium-isotope profile is an approximate best fit along minimum values on the main trend (following the rationale of Burke *et al.*, 1982).

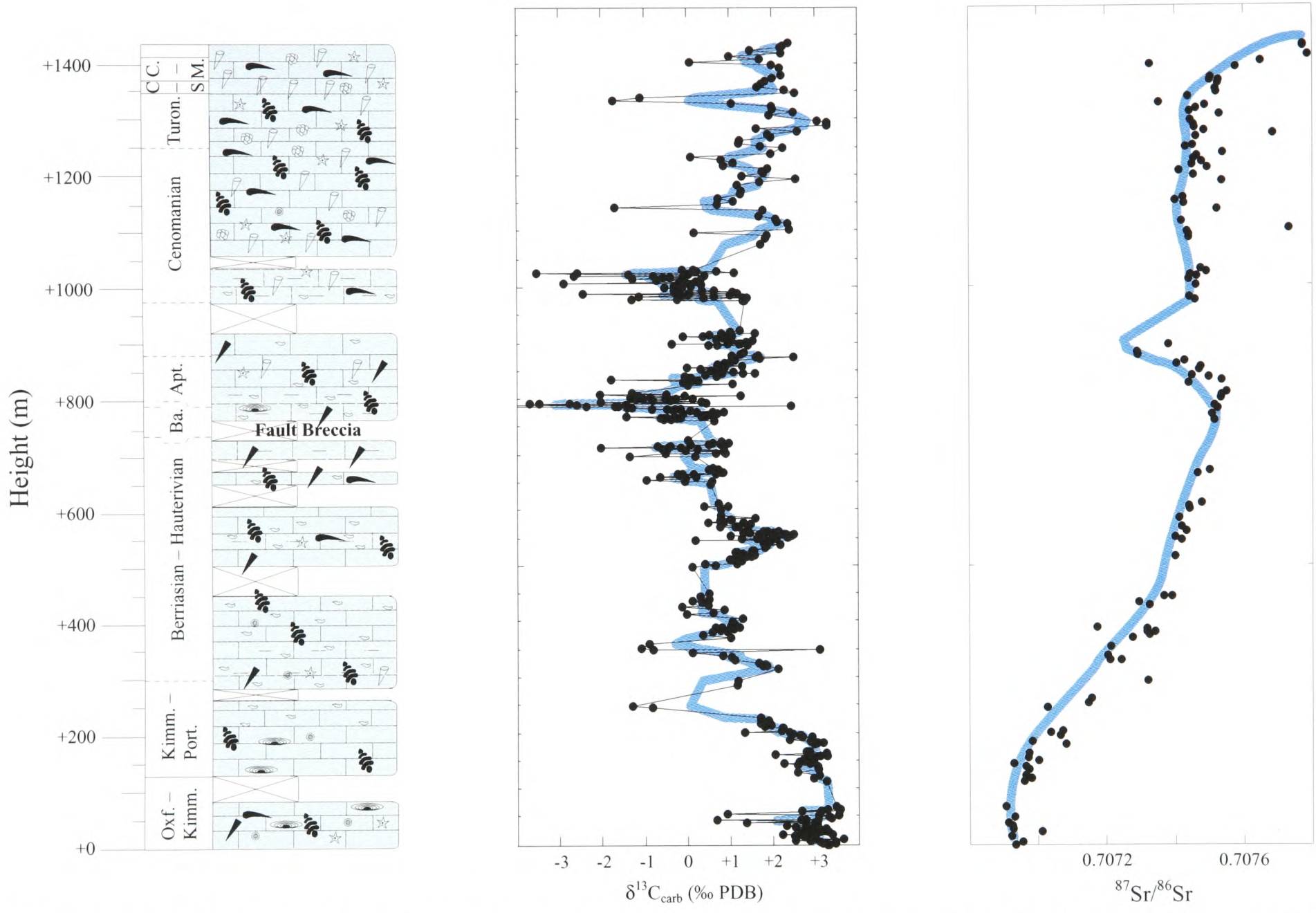

Figure 3.xiii. Biostratigraphic age, graphic log, carbon-, and strontium-isotope profiles of the Friuli Platform (Late Jurassic–Tertiary). The blue line on the carbon-isotope profile is a five-point moving average, whereas that on the strontium-isotope profile is a best fit through the least radiogenic values (after Burke *et al.,* 1982). Oxf. = Oxfordian; Kimm. = Kimmeridgian, Port. = Portlandian; Ba. = Barremian; Apt. = Aptian; Turon. = Turonian; C.–S. = Coniacian–Santonian; C.–M. = Campanian–Maastrichtian.

Chapter 4: Campania–Lucania Platform

Chapter 4: Campania–Lucania Platform, Southern Limestone Apennines, Italy

4.1 Geological setting and stratigraphy

The Southern Apennine Platform is described as being composed of two platforms that were separated since the Triassic by the Lagonegro Basin (remnants now found in the southern Southern Apennine region; Wood, 1981): the internal Campania–Lucania Platform (sometimes referred to as Latium–Campania–Lucania Platform) and the more external Abruzzi–Campania Platform. D'Argenio *et al.* (1975a) describe the Campania–Lucania Platform as a Bahamian type epioceanic carbonate platform throughout the Jurassic and Cretaceous (c.f. Trento Platform). The Molise Basin developed during the intense rifting characteristic of the Tethyan Jurassic (remnants now found in the northern Southern Apennine region) and eventually completely separated the Abruzzi–Campania Platform from the Apulia Platform to the east (Figures 1.vi and 4.i; e.g. D'Argenio *et al.*, 1975a; Catalano *et al.*, 1976; Channell *et al.*, 1979; Ziegler, 1988; D'Argenio *et al.*, *In Press*). This elongate belt of carbonate platforms separated by relatively deeper-water basins is a characteristic not only observed in different segments of the peri-Adriatic belt (although not always physically continuous along strike; Channell *et al.*, 1979), but has also been recognised in Bahamian facies of the same age (D'Argenio *et al.*, 1975a). As a result, the belt of basins and platforms has been suggested to have stretched thousands of kilometres along the southern Tethyan margin, linked by the present day northwest Africa, where Mesozoic platform carbonates are known to crop out. The Adriatic Plate has since been rotated and compressed by Alpine tectonics, whereas the Bahamas were pulled away from Europe by oceanic spreading in the Atlantic (D'Argenio *et al.*, 1975a).

Figure 4.ii illustrates a generalised stratigraphic evolution of the Campania–Lucania Carbonate Platform through the Mesozoic. The Upper Triassic algal and megalodont-bearing carbonates cyclically interbedded with stromatolitic dolomites have been described as representative of an intra-continental carbonate platform with widespread supralittoral facies, as found over much of the peri–Adriatic (Channell *et al.*, 1979). Carannante *et al.* (1978) describe the alternating subtidal (lagoonal) and intertidal (Loferitic) facies as typical of cyclothem

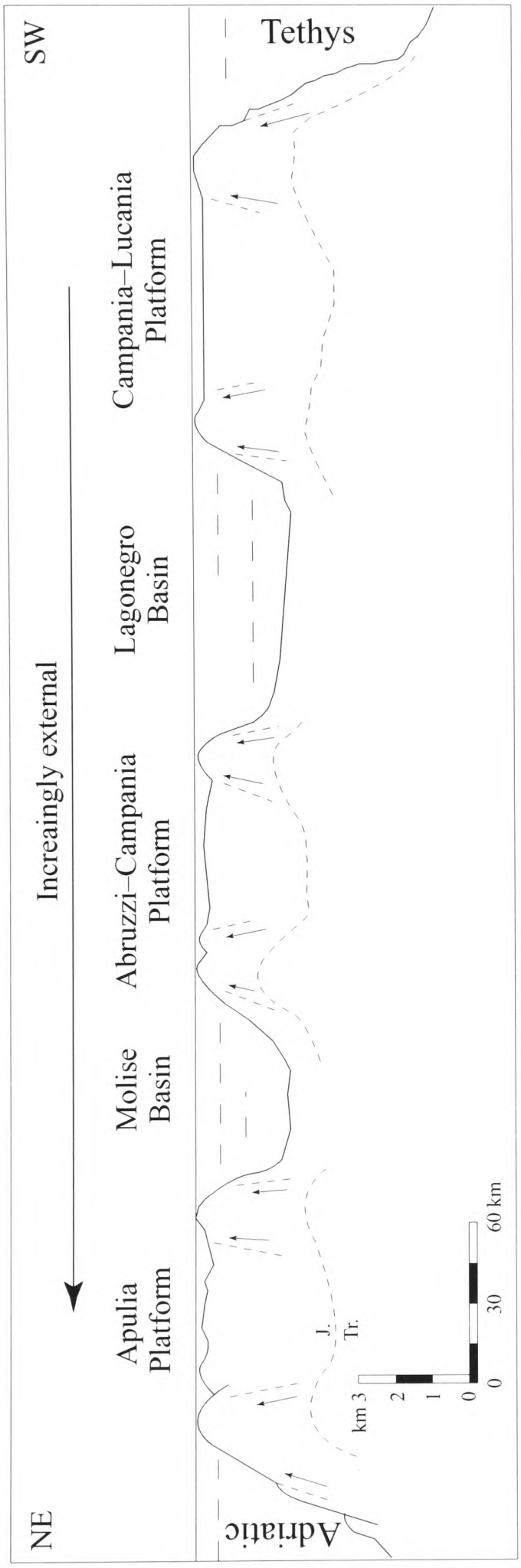

Figure 4.i. Schematic palaeogeographic section illustrating the suggested relationships between the carbonate platforms and basins of the Southern Apennines at the Jurassic–Cretaceous boundary. Tr. = Triassic; J = Jurassic. Modified after D'Argenio *et al.* (1975) and Catalano *et al.* (1976).

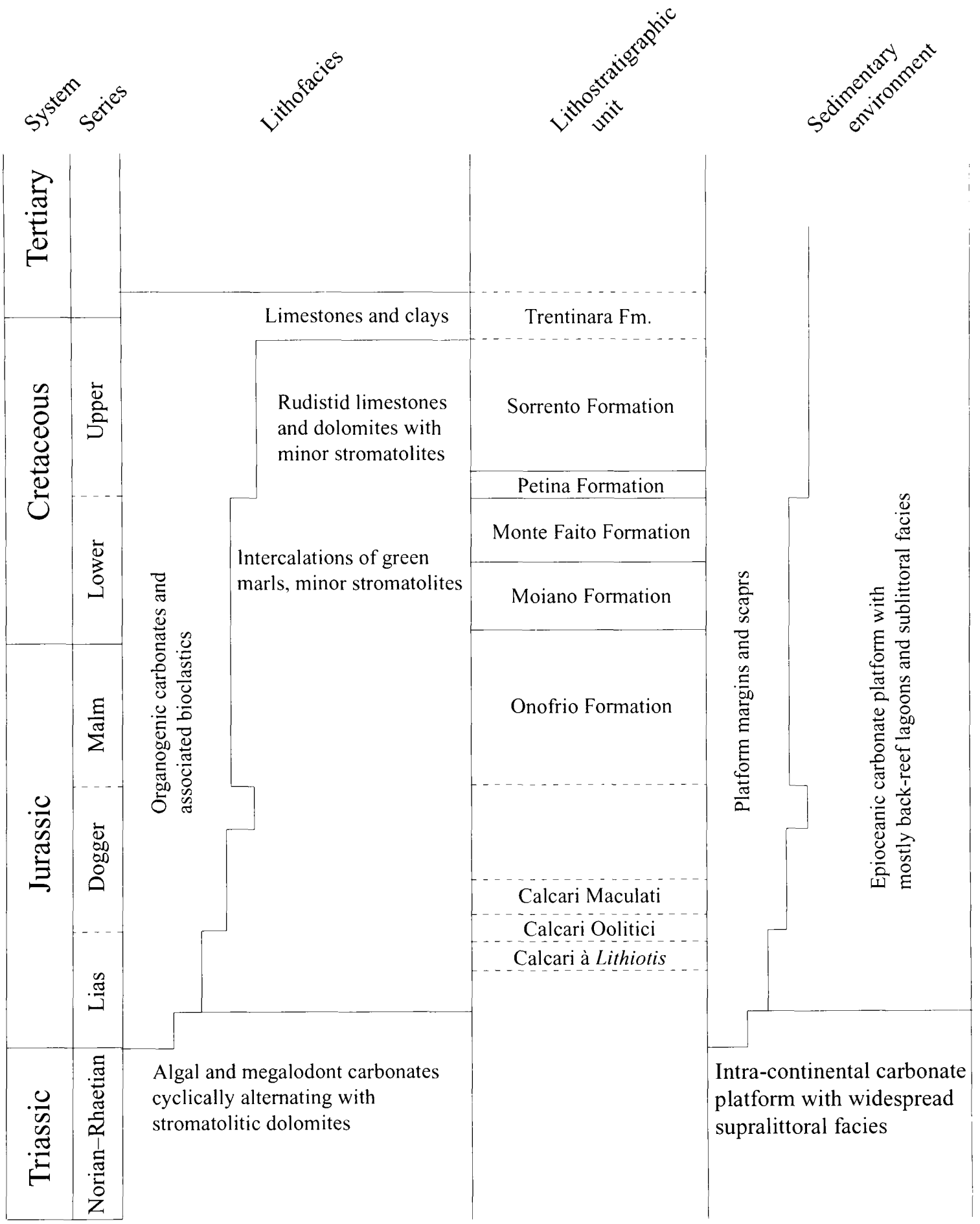

Figure 4.ii. Generalised lithostratigraphy of the Campania–Lucania Platform, Southern Apennines, from the Triassic–Tertiary. Formation names of lithostratigrpahic units are indicated as are the interpreted sedimentary environments believed necessary for the observed lithofacies. Modified after Channel *et al.* (1979), Robson (1989) and Violante (2000).

deposition (Fischer, 1964), and suggests that sub-aerial exposure was responsible for karstic-cavity development and dissolution of originally aragonitic bioclastic material (e.g. corals). The diagenetic fabrics were also believed to have derived from a tectonically controlled emplacement of the sediment pile in the phreatic zone prior to Early Jurassic deposition.

The onset of the Jurassic and the increased influence of Tethyan ocean spreading saw the break up of an extensive peri-Adriatic carbonate platform and the development of platform–basin alternations. The Campania–Lucania Platform made the transition to an epioceanic carbonate platform with calcitic and organogenic carbonate deposition (algae, benthic foraminifera, gastropods, brachiopods, echinoids, sponges and solitary corals) following a transition from aragonite–calcite deposition at the Triassic–Jurassic boundary (Sandberg, 1983; Stanley and Hardie, 1998). These facies and faunal assemblages have been interpreted as representing subtidal back-reef lagoon sedimentation (Channell *et al.*, 1979; Violante, 2000). As in the Southern Alps, there is a distinctive *Lithiotis*-rich interval (Calcari à *Lithiotis*) believed to be Late Liassic in age (*Palaeodasycladus mediterraneous* Zone) based on the available biostratigraphy (Bosellini and Broglio Loriga, 1971; Channell *et al.*, 1979; Violante, 2000). Overlying the *Lithiotis* beds, Violante (2000) documents deposition of the Calcari Oolitici and the Calcari Maculati Formations (up to lower Bajocian in age – *Selliporella donzellii* Zone). These formations are interpreted as reflecting restricted–open-lagoonal environments with no evidence of peritidal influences. Violante (2000) also describes condensed intervals (with boring-riddled bed surfaces and goethitic-crusts) at the boundaries between these three Lias–Dogger formations, although they are not believed to be due to exposure but to flooding of the platform. Upper Jurassic (and later, Lower Cretaceous) deposits represent restricted-shelf settings resulting in the accumulation of subtidal lagoonal facies with associated ooid and/or gastropod sand shoals (Onofrio formation; Robson, 1989).

The Early Cretaceous witnessed the continuation of epioceanic carbonate-platform growth in an intertidal and supratidal flat depositional setting resulting in the Moiano Formation (Berriasian–Barremian; Robson, 1989). Channell *et al.* (1979) describes Lower Cretaceous carbonates that are intercalated with green marls and are associated with stromatolites (c.f. Friuli platform). The Monte Faito Formation (Barremian–Albian) represents a return to subtidal

lagoon environments (with storm influence toward its top; Robson, 1989). The Petina Formation reflects the progradation of intertidal flats over the platform (with associated evaporites; Robson, 1989) in the Cenomanian. Emergence of mid-Cretaceous carbonates (upper Albian–mid-Cenomanian) resulted in localised bauxite interval formation (D'Argenio, 1969), whereas the Upper Cretaceous witnessed the development of rudistid limestones (with associated dolomites and stromatolites) that formed behind coral rudist reefs fringing the western margin of the platform (Sorrento Formation). Robson (1989) suggests that these 'flooded' Upper Cretaceous shallow-water carbonates replaced the restricted carbonates of the Lower Cretaceous as a result of a major tectono-eustatic rise in sea level.

Cessation of shallow-water carbonate sedimentation finally occurred at approximately the Cretaceous–Tertiary boundary and, as with all the remaining Tethyan carbonate platforms at this time, the Campania–Lucania Platform eventually succumbed to Alpine-orogen-derived flysch deposition (Bosellini, 1989). Between Late Triassic and Late Cretaceous times the sedimentation rate of the carbonate platforms decreased progressively from more than 100 m/m.y. to less than 10 m/m.y (Channell *et al.*, 1979).

4.1.1 Monte Sorgenza

Monte Sorgenza is located in the Aurunci Mountains immediately northeast of Formia in central Italy (Figures 4.iii and 4.iv). During the Mesozoic, Monte Sorgenza was on the western (internal) margin of the Campania–Lucania platform on the Apulian plate (Figure 1.vii). The section studied is reached by taking the Via Appia to Pinistro, before heading to Castellonorato (the view of the mountain on the approach to Castellonorato is shown in Plates A4.4.i and A4.4.ii). After exiting from Castellonorato, a sign-posted right turn for "Casa Annunciazata" leads through a crossroads before reaching a T-junction. After turning right at the T-junction the section is found above the green hut located at the end of the road. From sampling point MS (Monte Sorgenza) 0 at the base of the section, a 350-m-vertical thickness of platform carbonate was sampled initially at 1 m intervals. After a re-visit, the resolution of sampling was further increased to every 0.5 m over critical intervals. The stratigraphic succession encountered is illustrated in Figure 4.v by a graphic log. It should be noted that the section continues for a

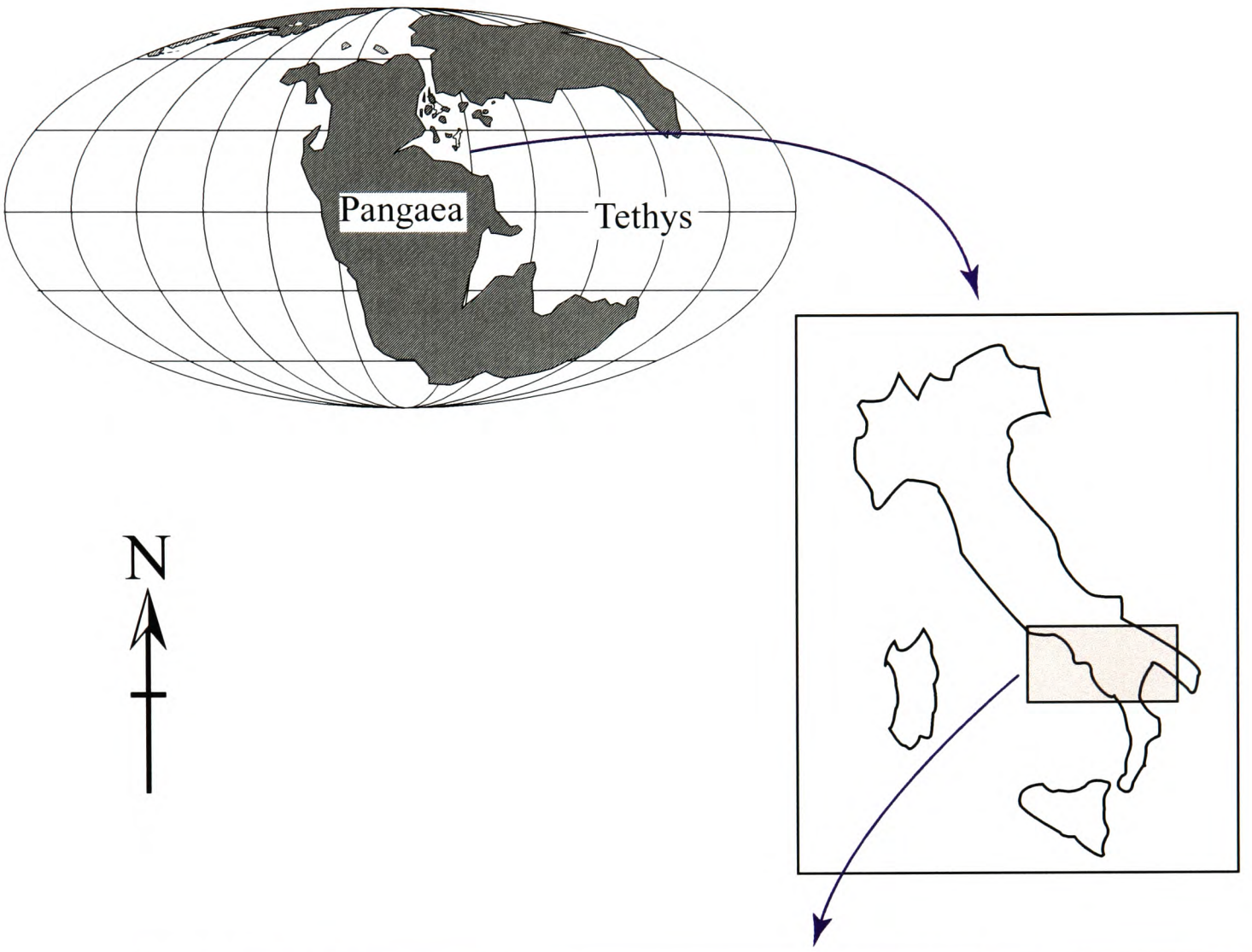

Figure 4.iii. Palaeogeographic reconstruction showing the northwest Tethyan location of the Campania–Lucania Platform of the Southern Apennines in the Toarcian (after Smith *et al.*, 1994), and its location in southern Italy today (after Catalano *et al.*, 1976; and D'Argenio *et al.*, *in press*). MS = Monte Sorgenza; RDP = Raia del Pedale.

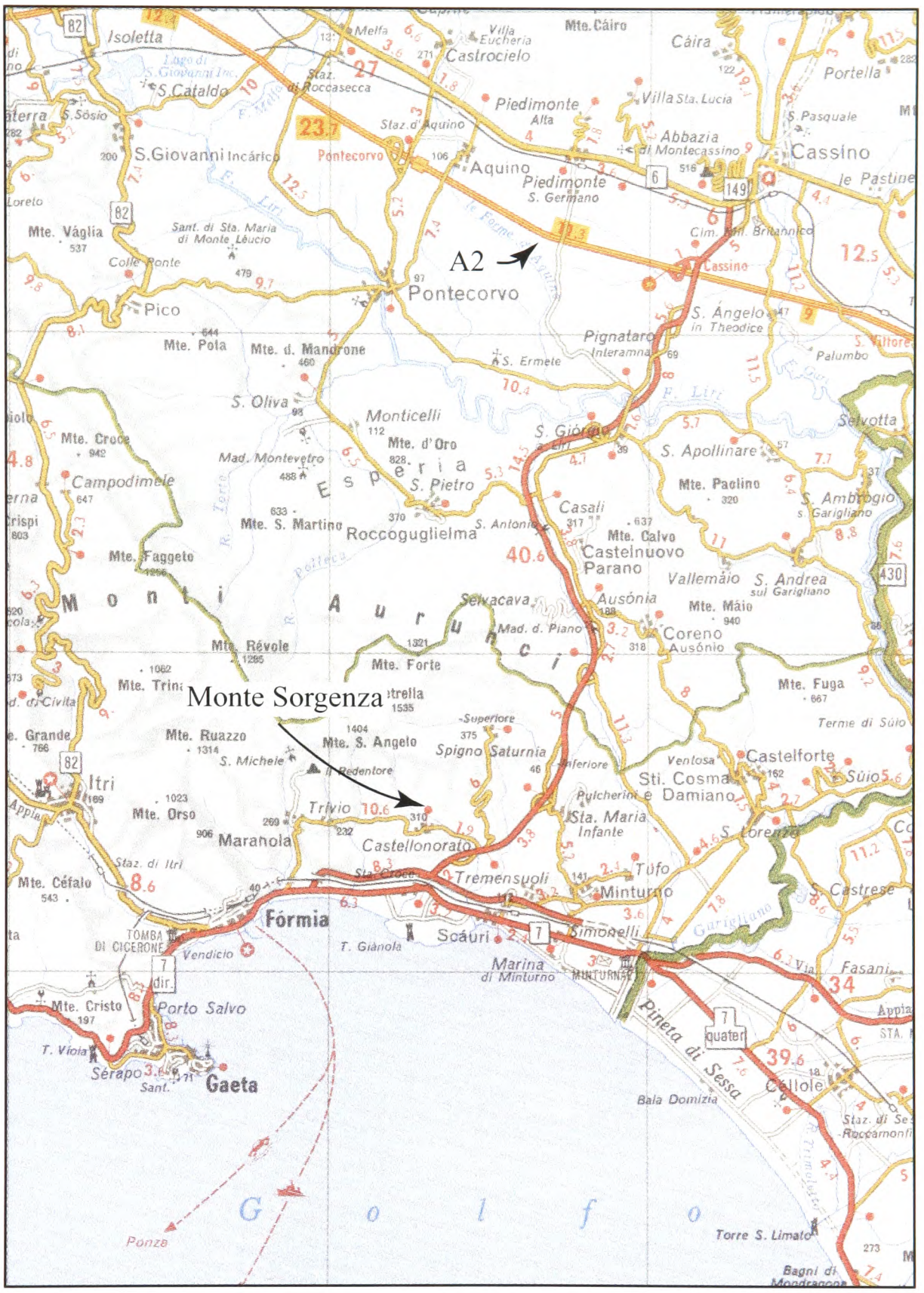

Figure 4.iv. Location map of the Monte Sorgenza section. The section is reached from the south, from the nearest town of Castellonorato.

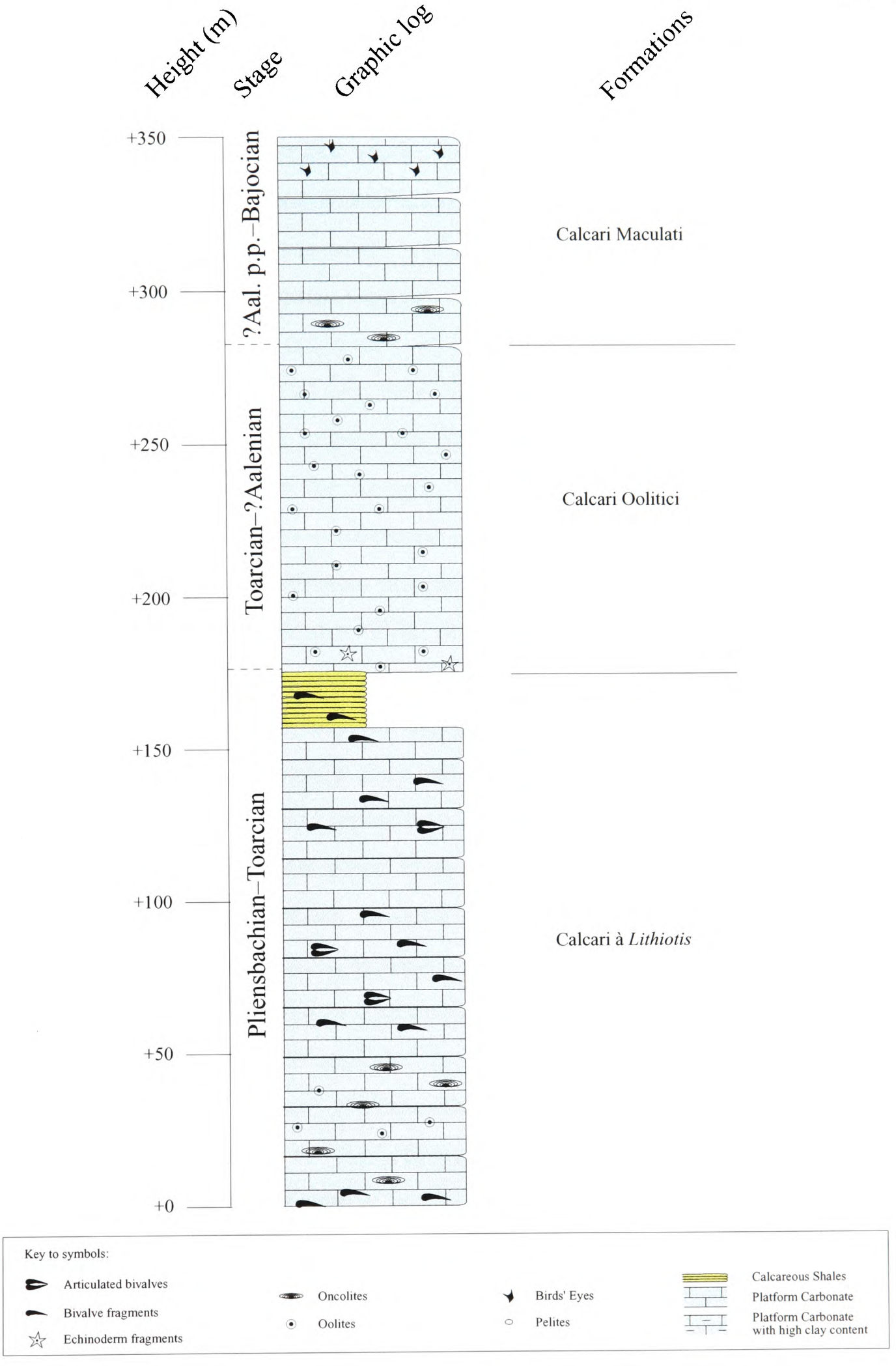

Figure 4.v. Stratigraphic log detailing the 350-m-thick platform-carbonate succession of the Monte Sorgenza (MS) section of the Campania–Lucania Platform, Aurunci Mountains, Southern Apennines, central Italy. Formation names are indicated (after Violante, 2000). Biostratigraphic ages are based on lithostratigraphic correlation (Damiani *et al.*, 1991a,b; Violante, 2000).

further ~400 m, but it was not within the scope of this project to study this further section due to time constraints.

Although a detailed petrographic study was not carried out over the entire Monte Sorgenza section, the more significant facies transitions are petrographically described, and a more general outcrop description was made whilst sampling. The lower 50 m of exposed section were characterised by fine-grained micritic matrix-supported wackestone (with metre-scale bedding), containing bivalve fragments, oncoids, rare ooids and dasycladacean algae (*Paleodasycladus mediterraneous*; Violante, pers. comm.). Between +50 and +158 m the fine-grained wackestone continued, rich in bivalves and particularly *Lithiotis* shells, commonly found in clusters and articulated in the upright "life position" (Plate A4.4.iii). A gradual thinning of limestone beds leads into a laminated clay-rich horizon found between +158 and +175.8 m (Plate A4.4.iv). This fossiliferous–biomicritic interval contains benthic foraminifera, algae and assorted shell fragments (Plates A3.4.i to A3.4.iii). No macrofossils were visible in outcrop. Over the last ~5 m the limestone beds gradually begin to thicken (~0.5 m; Plate A4.4.v), before the sharp contact with the overlying massive oolite body at +175.8 m. The basal few metres of the oolite package contain abundant re-crystallised shell fragments (under the microscope, dolomite can be identified replacing oosparite at +183.5 m, but this is related to fluid interaction on an unavoidable fault plane; Plate A3.4.iv), but for the following 100 m (until +281.6 m) it is otherwise monotonous massive cross-bedded oosparite (ooids are often "floating" and micritised, peloids can commonly be identified in the calcite cement, and echinoderm fragments can be identified as ooid nuclei; Plates A3.4.v and A3.4.vi). The samples collected between +184 and +197 m appeared to be taken from a fault plane, with clearly observable post-depositional influences of fluid-interactions and mechanical disturbance. The fault was not crossed so there should be little affect on the stratigraphic level sampled; however, the possibility of diagenetic modification has to be considered over this 13-m interval. Otherwise, the oolite body continues until +280 m, where it gradually becomes increasingly thin bedded (~20 cm) and pinkish in colour. Under the petrographic microscope, minor pressure solution is evident, identified by concavo-convex boundaries between ooids, and occasional sylolites.

At +281.6 m (last oosparite with "floating", micritised ooids and occasional stylolite) there is a facies transition from oolite to thin-bedded micritic wackestone with oncolites but devoid of obvious macrofossils. The transition from massive oolite to thin-bedded wackestone (pelmicritic with benthic foraminifera, assorted shell fragments, algae and ostracods - occasional birdseyes could be observed with the microscope for those samples collected from above +293 m; Plates A3.4.vii to A3.4.ix) marks a pronounced step in the morphological relief of the Monte Sorgenza, and this is clearly illustrated in Plate A4.4.vi. The thin-bedded nature of the wackestone at +285 m is further illustrated in Plate A4.4.vii. By +295 m, bed thicknesses increased to between 0.3–1 m, and were between 0.5 and 1 m by +326 m. Above +337.3 m, abundant birdseyes were visible in the same fine-grained limestone in outcrop (Plate A4.4.viii), and this same characteristic lithology continued until the top of the measured section (+350 m).

The lithologies described above are believed to support earlier descriptions of the Monte Sorgenza section (Violante, 2000). In summary, the interval found between 0 and +175.8 m represents the Calcari à *Lithiotis*; the massive oolite body between +175.8 and +281.6 m represents the Calcari Oolitici; and those intervals above +281.6 m represent the Calcari Maculati. However, there is a discrepancy between the apparent lack in evidence of peritidal environments in the Calcari Maculati description of Violante (2000) with the interpretation of birdseye limestones observed above +293 m in this study.

4.1.2 La Raia del Pedale

The Raia del Pedale section is located south of Salerno and can be reached by leaving the A3 autustrada at Buonabitacolo and following the road for Sanza. The section itself is found along the road between Sanza and Rofrano (Figure 4.vi and Plate A4.4.ix). The measured section is 318 m (c.f. 312 m, Robson, 1989) and initial sampling frequency was at 1 m intervals for the lower 100 m, every 2 m for the upper 220 m, and every 0.25 m between +16 and +27 m (across a shale-horizon). A subsequent re-visit increased sampling resolution to every 0.25 m between +27 and +86 m, and every 1 m for the upper 220 m of section.

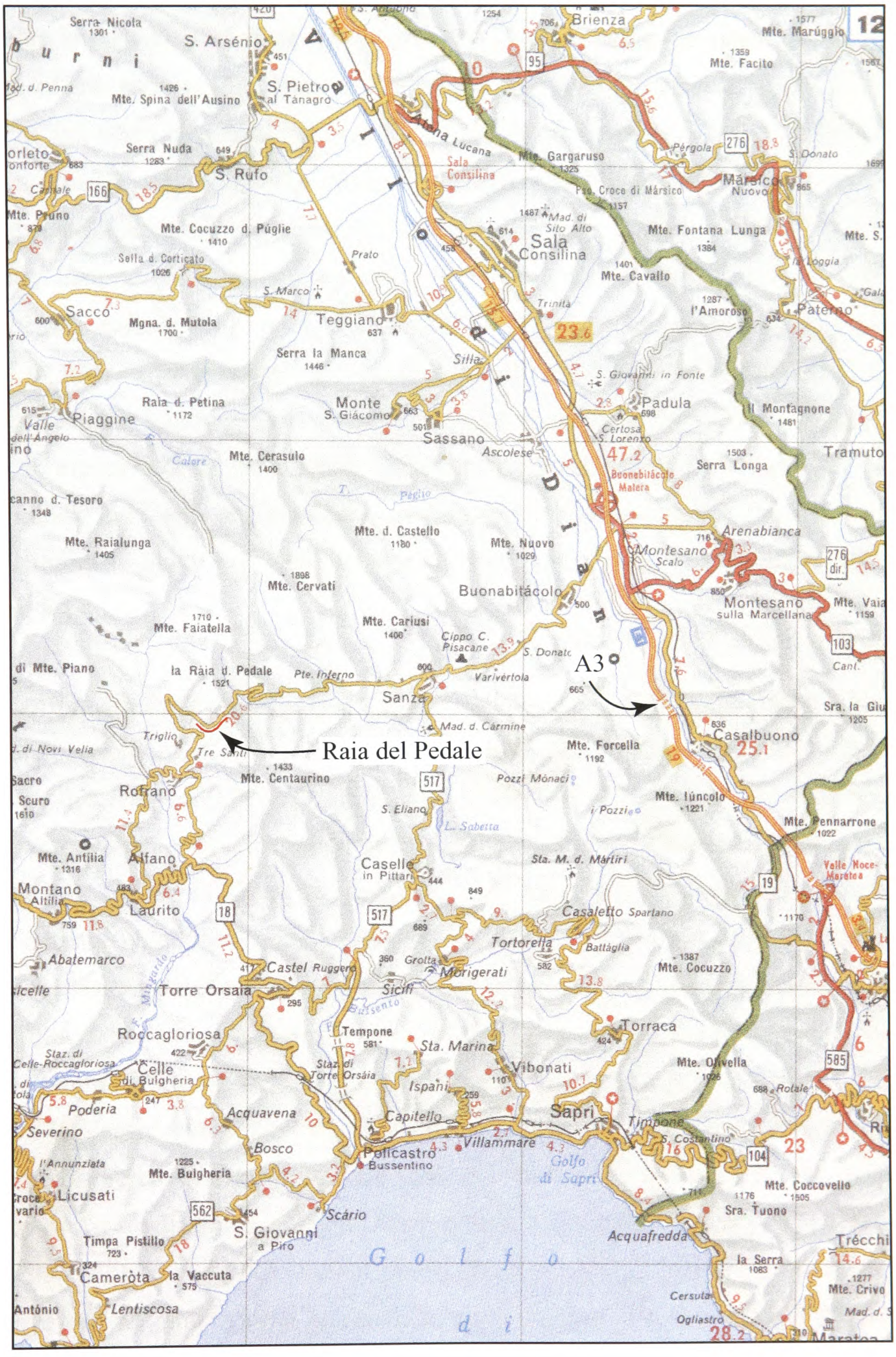

Figure 4.vi. Location map of the Raia del Pedale section, located beyond the town of Sanza, off the A3 Autostrada at the Buonabitacolo exit.

A graphic log of the sedimentary succession encountered at the Raia del Pedale is given in Figure 4.vii. Detail in the log (resulting from outcop observation and petrographic study) is focussed on the lower 100 m of section, but further occasional petrographic analyses add detail over the rest of the section. The Robson (1989) log was also available for any additional information as and when required. The first 4 m of section alternate between fossiliferous and pelmicrite on a metre scale, although this does not affect bedding, which is massive. Thin-sections and hand specimens are cut by fine veins of sparry calcite and fossil content is predominantly benthic foraminifera. At +4 m there is a distinct introduction of dolomite rhombs, generally found along veins, and between +5 and +10 m there is a fine-grained replacement of micrite by dolomite (Plates A3.4.x and A3.4.xi). Fossiliferous micrite with dolomite replacement grading from the presence of rhombs to pervasive and complete replacement continues to occur up to +18 m. Bedding throughout this interval is generally of the order of 1 m thick, but there are laminated horizons within some of the beds. Between +18 and +24 m the outcrop is finely laminated and shaly in appearance with an apparent high-clay content (Plate A4.4.x).

The petrographic microscope shows that the shales are benthic-foraminiferal biomicrite with occasional stylolites and spar-filled voids, and it is noticeable that evidence of dolomite wanes through this interval (Plate A3.4.xii). By +25 m bedding has increased to an average thickness of between 0.5–1 m and is fossiliferous micrite made up of benthic foraminifera and peloids (Plate A4.4.x). The overlying 30 m shows little change, except that the outcrop becomes increasingly massive with little evident bedding between +27 and +48 m. Generally, the rock is fossiliferous micrite/biomicrite composed of benthic foraminifera, rudist fragments and other unidentified bioclastic debris. Between +48 and +58 m the outcrop becomes relatively thin bedded (10–50-cm-thick), dark and fine-grained micrite (Plate A4.4.xi). At certain horizons the dark micrite is laminated and 'clinky' when hammered (e.g. RDP+51.65; Plate A4.4.xii). Under the petrographic microscope, however, the rock is still fossiliferous micrite or pelmicrite dominated by rudist fragments and benthic foraminifera, and much of the apparent lamination turns out to be stylolitic traces/dissolution seams (Plate A3.4.xiii). The same characteristics continue above +58 m, although the limestone is more massive in outcrop until +69 m when bedding thickness decreases once more to an approximate average of 20 cm. At +71 m there is

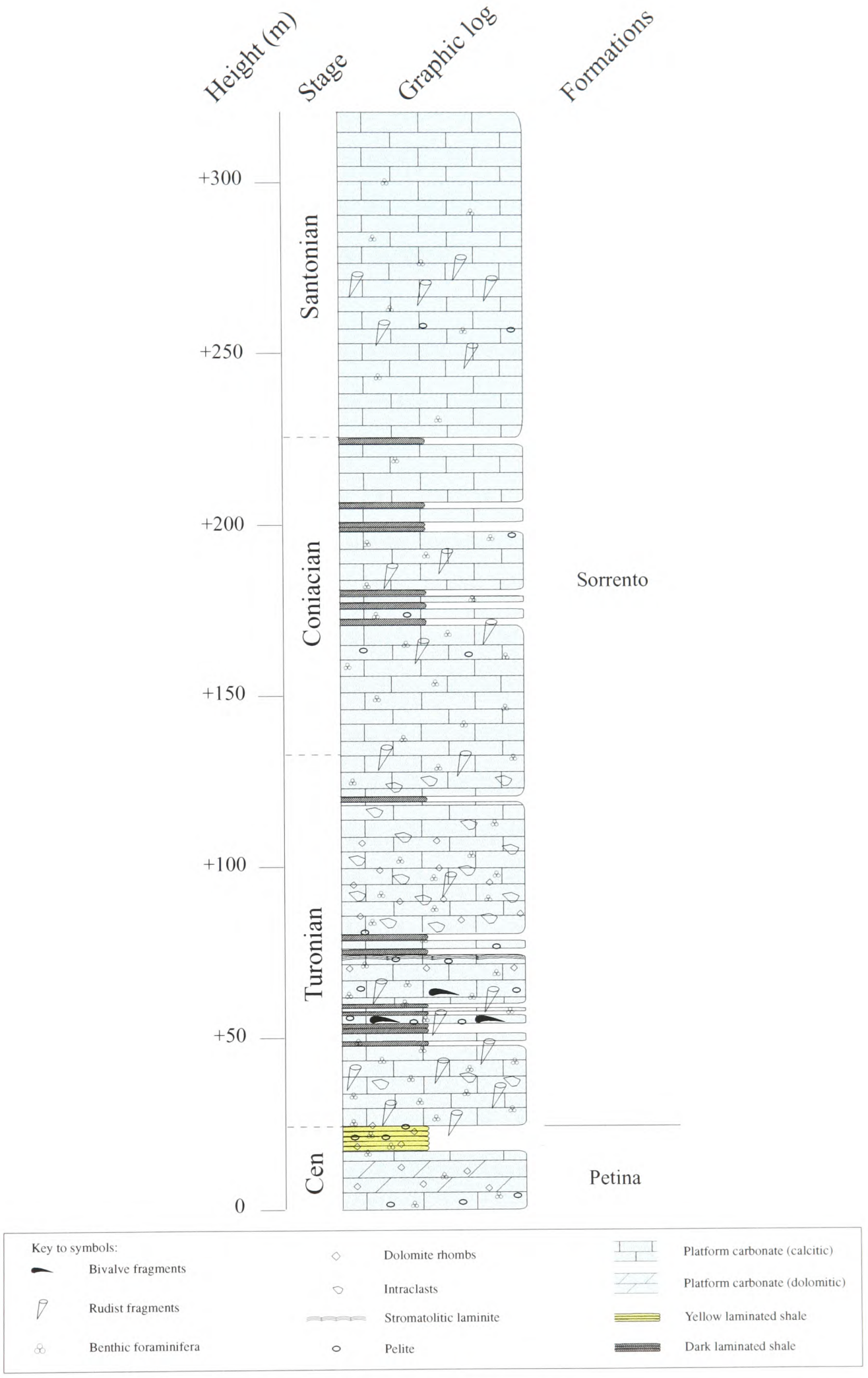

Figure 4.vii. Stratigraphic log detailing the 318-m-thick platform-carbonate succession of the Raia del Pedale (RDP) section of the Campania–Lucania Platform. Formation names are indicated, as are the biostratgraphic stage boundaries (after Robson, 1989). Cen = Cenomanian.

further evidence of dolomite rhombs. Just above this level, between +74 and +80 m the outcrop becomes increasingly reminiscent of that between +48 and +58 m: dark, fossiliferous micrite (with peloids) that is laminated and 'clinky'. Between +81 and +84 m the limestone is intramicritic (with similar bioclastic debris; Plates A3.4.xiv and A3.4.xv) and at +84 m dolomite rhombs are present once more. Above, the outcrop becomes increasingly massive and reverts to fosiliferous micrite/biomicrite (predominantly benthic foraminifera) and dolomite rhombs are once more observed at +91.75, +96, +98 and +108 m.

However, between +94 and +125 m the most striking feature of the rock at outcrop is the intraclastic nature of the sediment (Plate A4.4.xiii). Although intraclastic, the clasts and matrix still typically range from fossiliferous micrite to micrite. In thin-section, it is possible to recognise rare planktonic foraminifera over this interval (Plates A3.4.xiv to A3.4.xvi). Between +120 and +130 m the outcrop becomes thinner-bedded (typically ranging between 20 and 50 cm) but is still dark intramicrite with fossil fragments. Between +132 and +170 m rudist shell fragments are visible in outcrop, bed thickness is typically 50 cm and lithology is generally dark fossiliferous micrite/biomicrite (locally peloids) with fossil fragments predominantly composed of benthic foraminifera and rudist shell fragments (commonly found in locally concentrated horizons; Plate A4.4.xiv). Between +170 and +230 m there is a continuation in the presence of relatively monotonous dark fossiliferous micrite/biomicrite (with rudists and benthic foraminifera) with bed thicknesses generally ranging between 30–50 cm. Superimposed on this depositional style are discrete (10-cm-thick), dark, stylolitic/dissolution seamed, 'clinky' horizons found between +170 and +180 m, +198, +210 m and +224.5 m. Dark fossiliferous micrite continues as the dominant lithology for the remainder of the exposed section at the Raia del Pedale, and bed thickness remains at <50 cm (with an apparent cyclical nature) until the final 40 m of section, where it increase to an average of 1-m-thick (a range of 0.5–1.5-m-thick). Also of note is another concentration of rudist fragments between +256 and +275 m.

To summarise: the logged Raia del Pedale section of this study is strikingly similar to that described by Robson (1989), who marked the boundary between the Cenomanian–Turonian Stages (and also the Petina and Sorrento Formations) at the top of the last shaly layer at the base of the section (+24.8 m in both measured sections). Robson (1989) interprets the Petina

Formation, represented by dolomitised fossiliferous (and pel-) micrites (ranging from laminated to 1-m-thick bedding), as the deposits of a prograding intertidal flat. The Sorrento Formation, represented by rudistid biomicrites, is interpreted by Robson (1989), however, as reflecting back-reef lagoonal sedimentation and generally more open-marine conditions.

4.2 Chemostratigraphic results

The chemostratigraphic profiles of the Monte Sorgenza and Raia del Pedale sections are illustrated and described in the sections that follow. Discussion of these profiles can be found in ***Chapters 5 and 6.*** Data tables are included in ***Appendix Data Tables 4.i and 4.ii*** for the Monte Sorgenza and Raia del Pedale sections respectively.

4.2.1 Strontium-isotope results

Figure 4.viii illustrates the strontium-isotope profile of the Monte Sorgenza (MS) section. $^{87}Sr/^{86}Sr$ ratios of bulk carbonate range from 0.70714 to 0.70736 over the 256 m of analysed section. Between 0 and +132 m there is clearly a relatively large amount of scatter, but by tracing the minimum value trend (after a method first described by Burke *et al.*, 1982), it is possible to discern the primary signal: a relatively less radiogenic trough in values. After the increasingly radiogenic values at the top of the trough (0.70728 at +132 m), there is a second, more pronounced less radiogenic trough where values fall to 0.70714 by +160 m and have risen back up to >0.70730 by +200 m. Isotope values subsequently become less radiogenic and reach 0.7072 by +256 m.

Figure 4.ix illustrates the strontium-isotope profile of the Raia del Pedale (RDP) section. Isotope values range from 0.707304 to 0.707653 (probably not a primary value as too high for the Santonian) and, in general, a steeply decreasing trend to less radiogenic values (from approximately 0.707500 to 0.707350) can be observed between +20 and +150 m, before a return to more radiogenic values is observed between +150 and +300 m (from 0.707350 to 0.707500).

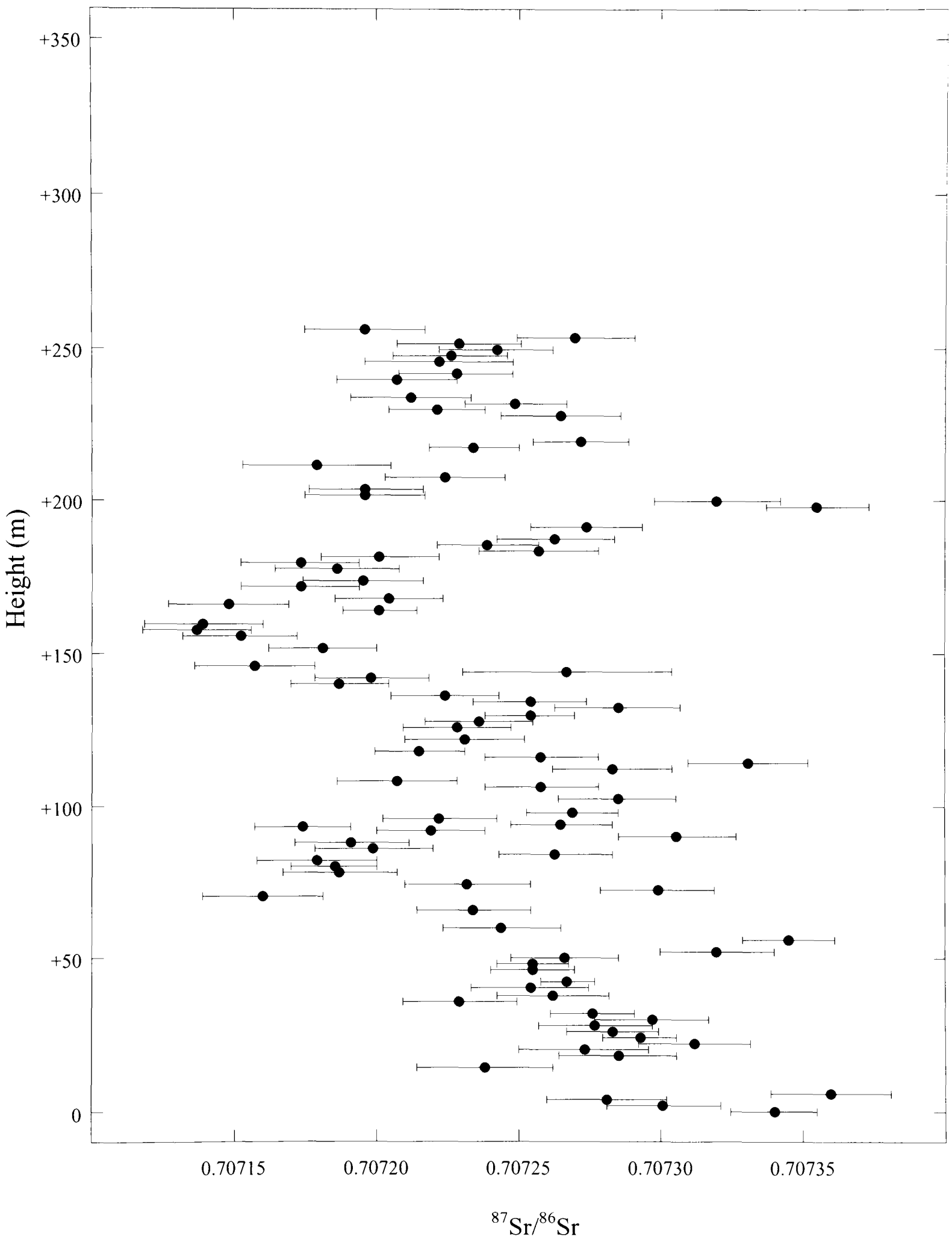

Figure 4.viii. Strontium-isotope profile of the Monte Sorgenza section, Aurunci Mountains, Southern Apennines. n = 93, and data were normalised to a NIST SRM 987 value of 0.710250, the running average of standards being 0.710248, and 2σ = 0.000026.

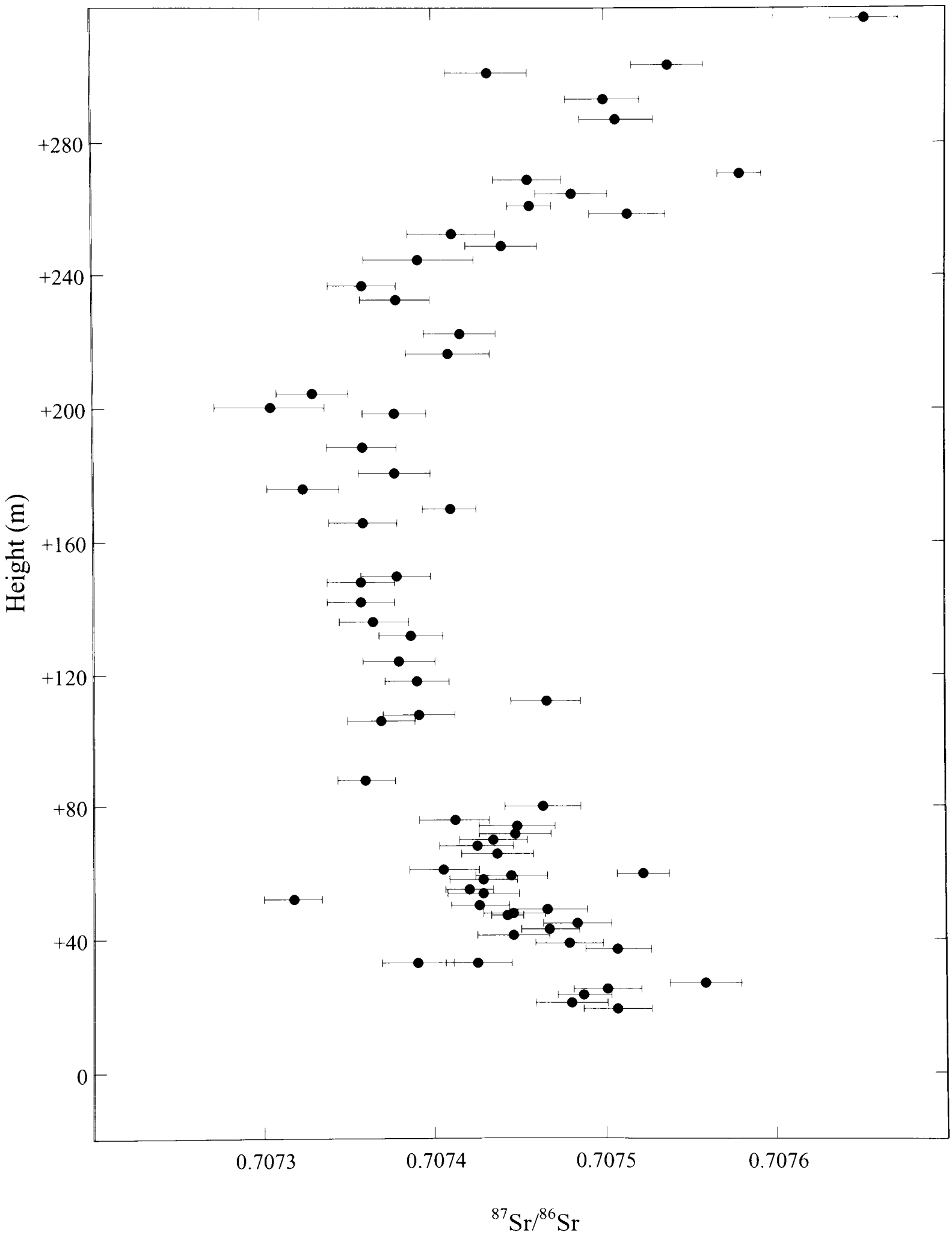

Figure 4.ix. Strontium-isotope profile of the 320-m-thick Raia del Pedale section. n = 66, and data were normalised to a NIST SRM 987 value of 0.710250, the running average of standards being 0.710248, and 2σ = 0.000026.

4.2.2 Carbon-isotope results

The carbon-isotope profile of the 350-m-thick Monte Sorgenza section is illustrated in Figure 4.x. $\delta^{13}C_{carb}$ values range from –3.6 to +4.5 ‰ and, although there is some scatter (mostly between +95 and +156 m, and +175 and +220 m), the majority of the trends are relatively coherent and easy to distinguish. On a broad scale, the two most prominent features of the curve are found between +150 and +225 m and +270 and +300 m: the first being a broad maximum in $\delta^{13}C_{carb}$ values with a negative "bite-out" between +170 and +190 m; the latter being a pronounced and coherent 5 ‰ negative isotope excursion. However, analysing the curve at higher resolution, between 0 and +80 m values rise from +1.7 to +3.1 ‰, before a relatively rapid decrease to +1.4 ‰ by +95 m (discounting the possible 'flier' at +96 m). $\delta^{13}C_{carb}$ values subsequently increase to +2.7 ‰ by +114 m before beginning a gradual decrease to approximately +1 ‰ (uncertainty due to scatter) by +155 m. At this point there is a relatively sharp increase to +2.2 ‰, which is followed by a further relatively scatter-free increase in carbon-isotope values to +3.6 ‰ by +172.5 m. Above this interval, values undergo a scattered decrease in values that is terminated at +192 m by a sharp coherent increase in $\delta^{13}C_{carb}$, which reaches a maximum value of +4.5 ‰ at +201.5 m. Data show some scatter through this maximum in carbon-isotope values, but it is still possible to determine the subsequent decrease in values that gradually takes place over the following 70 m, reaching +2.3 ‰ at +271.5 m. Above this point there is a pronounced, coherent decrease in carbon-isotope values reaching –3.1 ‰ at its minimum (+281.6 m), immediately followed by a sharp, coherent increase to approximately +2 ‰ (uncertainty due to slight scatter after negative excursion). Between +300 and +350 m there is a broad relatively negative trough in isotope values reaching +0.6 ‰ at +324 m, before rising back to +2.1 ‰ by +350 m.

The carbon-isotope profile of the Raia del Pedale section (RDP) is generally coherent over the lower 70 m of section, but scattered over the following 250 m (Figure 4.xi). The curve displays a very distinctive primary trend, which can be followed even through the scattered intervals. Values range between –3.6 to +4.9 ‰. The lower 20 m of section are relatively scattered but indicate the initiation of a rising trend from an approximate average value of –1.5 ‰ that goes on to rise to +4.9 ‰ by +53.75 m. This period of relative enrichment in the heavy

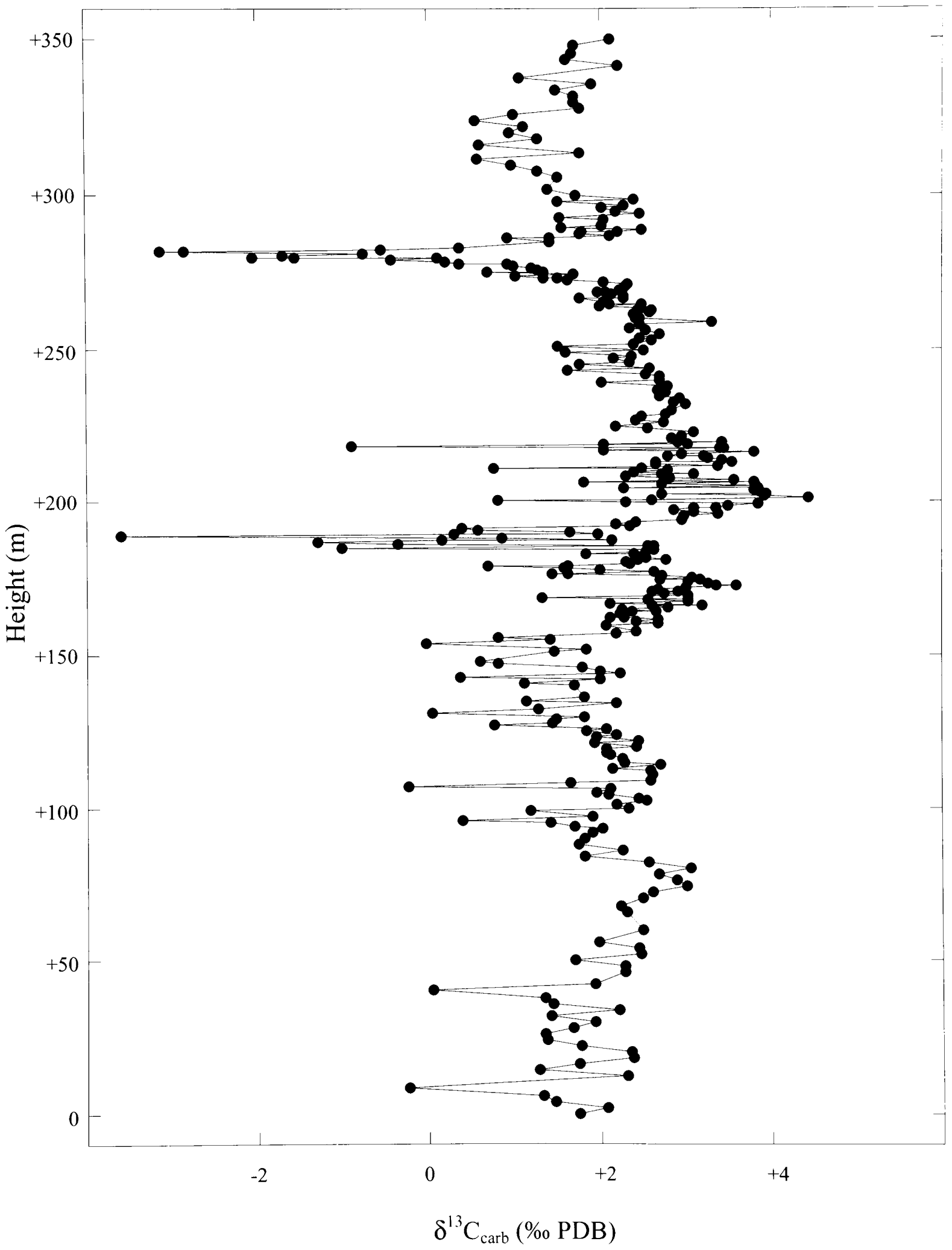

Figure 4.x. Carbon-isotope profile of the 350-m-thick Monte Sorgenza section. Distinctive excursions are recognisable, and although data produced from those bulk-carbonate samples between +175 m and +200 m appear relatively scattered, a coherent signal can still be identified.

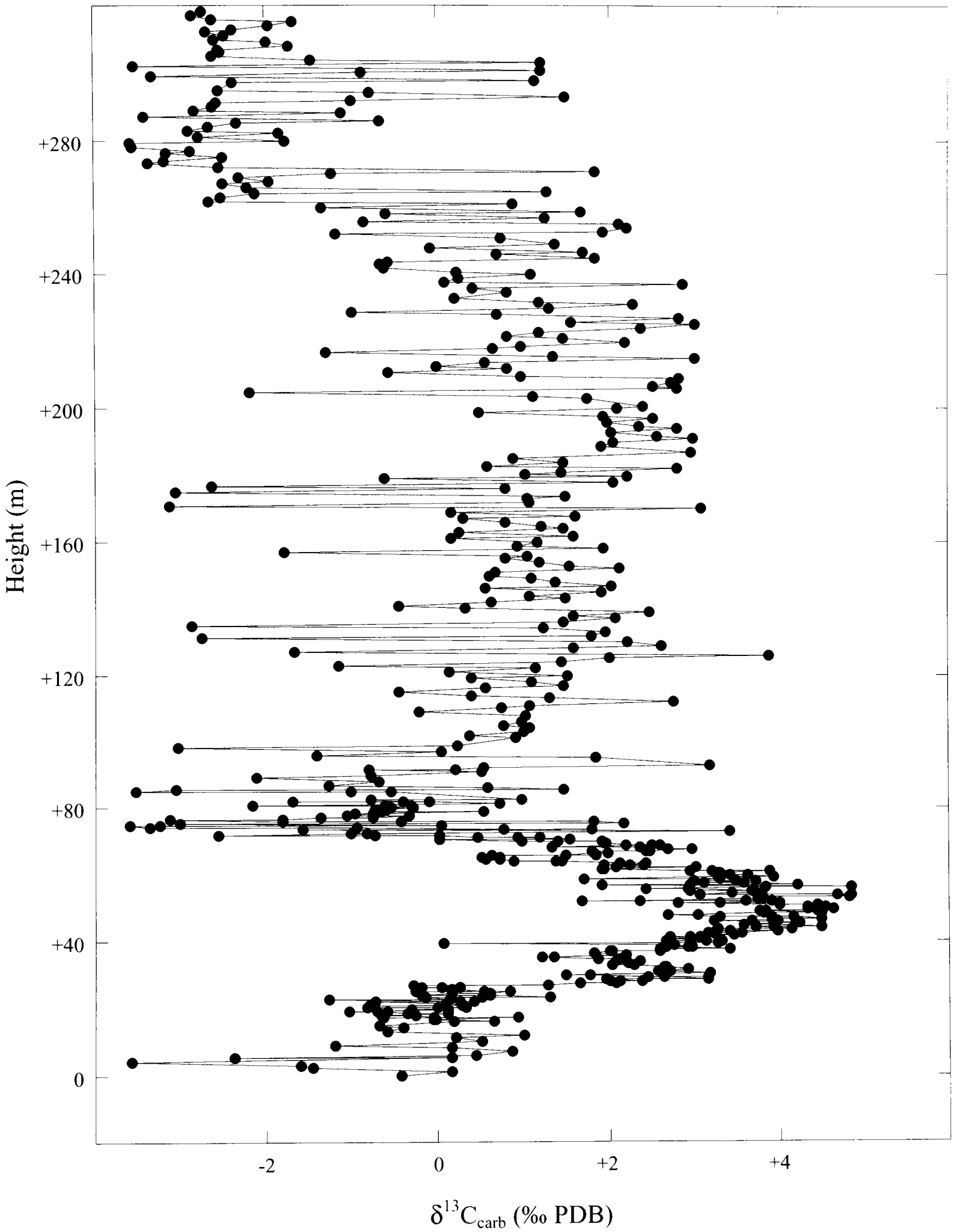

Figure 4.xi. Carbon-isotope profile of the Raia del Pedale section, Campania–Lucania Platform. A pronounced positive excursion is identifiable between +30 and +80 m, which is followed by a broad, scattered, relatively positive two-peaked 'hump' between +80 and +280 m.

isotope occurs relatively rapidly and results in the presence of a coherent and pronounced 'three-pronged' profile maximum between 0 and +80 m (there is a virtually symmetrical depletion after +53.75 m). Values become noticeably more scattered above +70 m, but from a value of approximately –1 ‰ at +75 m, there follows an increase in $\delta^{13}C$ values to an average of +2 ‰ by +135 m, which is in turn followed by a gradual depletion in carbon-isotope values, reaching +1 ‰ by +180 m. A relatively rapid enrichment in ^{13}C leads to average values of approximately +2.3 ‰ by +190 m, and this is followed by a subsequent gradual and prolonged relative depletion in $\delta^{13}C$ ratios, which reach –3 ‰ by +280 m. Subsequently, there is an irregular rise to -2 ‰, with a subsequent fall in isotope values over the final 40 m of section.

4.2.3 Oxygen-isotope results

Figure 4.xii illustrates the oxygen-isotope profile of the 350-m-thick Monte Sorgenza section. Data range from –8.6 (a probable 'aberrant' value recording post-depositional processes) to +0.7 ‰ and obvious scatter occurs predominantly between +160 and +270 m. A primary signal is discernible throughout the entire section, and indeed for the majority of the section the isotope profile is relatively coherent. At a broad scale, $\delta^{18}O$ values increase gradually from 0 to +175 m before a gradual decrease to +265 m. At this point there is a pronounced negative excursion, followed by a very sharp re-adjustment back to more positive values at +282 m. The curve remains relatively stable for the remainder of the section. In more detail, $\delta^{18}O$ values increase from approximately –2.5 to approximately –1 ‰ (there is a degree of uncertainty due to scatter) by +175 m with possible 'fliers' (especially +99 m). Although data from the overlying 50 m are relatively highly scattered, it is still possible to observe a relatively negative trough in isotope values reaching approximately –2.2 ‰ just above +200 m, before rising back to –1.8 ‰ at +230 m. Subsequently there is a gradual decrease in values to –2.4 by +261.5 m, followed by a relatively pronounced decrease in values to –4.2 ‰ by +280 m. By +283 m, $\delta^{18}O$ values have recovered to an average value of approximately –1.5 ‰ (uncertainty due to scatter), and from here they proceed to decrease gradually to –1.8 ‰ by +324 m before rising to –1.3 by +350 m.

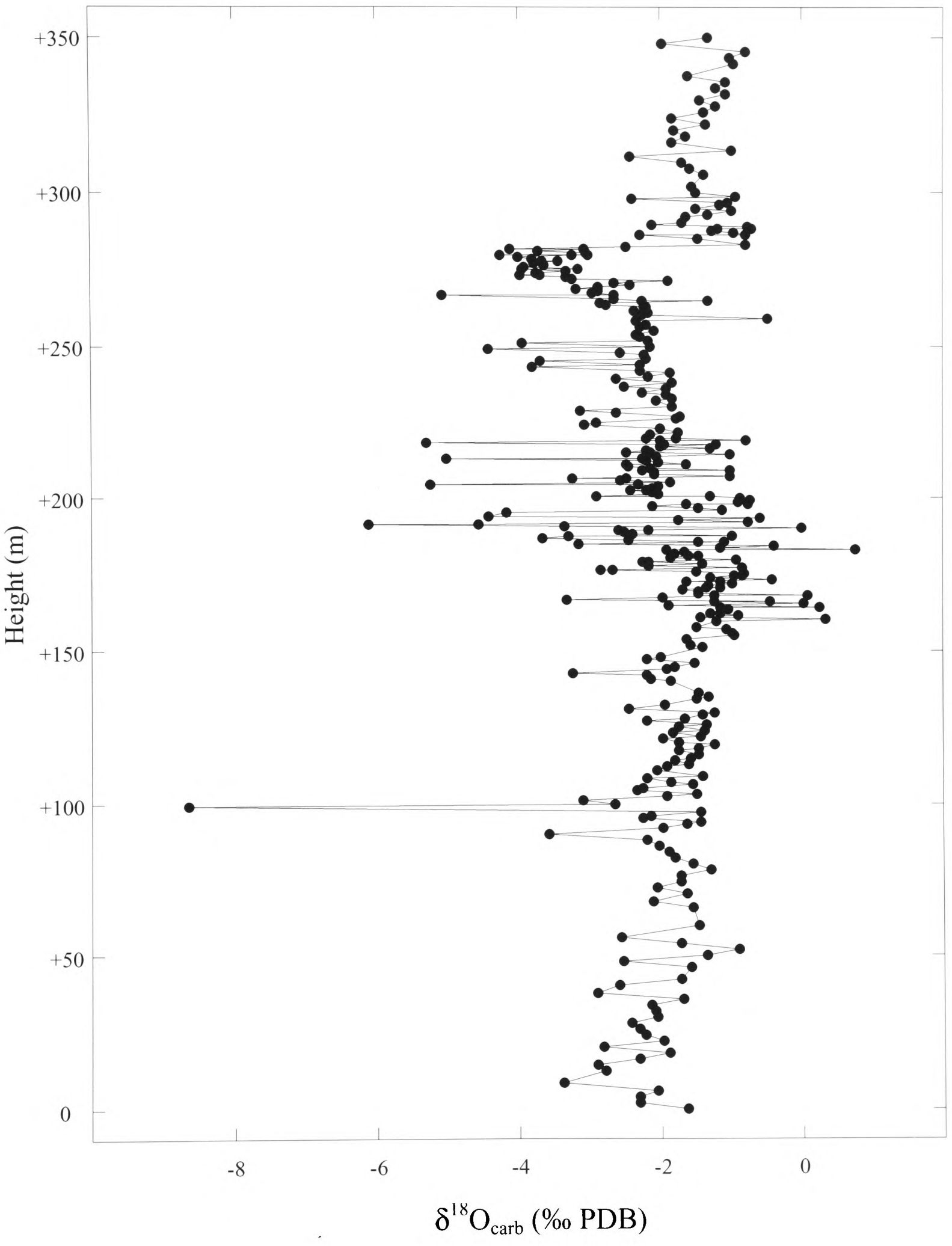

Figure 4.xii. Oxygen-isotope profile of the 350-m-thick Monte Sorgenza section. The isotope values appear to be relatively coherent over much of the depth profile, which allows a coherent signal to be discerned throughout.

Oxygen-isotope values obtained from the Raia del Pedale section range from –8.1 to +2.6 ‰, but generally fall in the range –5 to –2 ‰ (Figure 4.xiii). Over the lower 18 m of the section $\delta^{18}O$ values jump from an initial value of approximately –3 ‰ (0 to +4 m) to an average of approximately +1 ‰ (scattered) over the following 14 m of section. Above +18 m, values immediately stabilise, and continue in a coherent fashion to display a falling trend from –3 to –4.5 ‰ by +42 m. Subsequently, values proceed to increase gradually back to approximately –3 ‰ by +80 m, where high amounts of scatter distort the isotope signal until +110 m. Between +110 and +320 m, $\delta^{18}O$ values remain marginally scattered about a virtually constant average value of approximately –3.5 ‰, although there are occasional 'fliers' that disrupt the main trend.

4.2.4 Organic-carbon isotope analyses

A 'pilot' organic-carbon isotope study was performed on a selection of samples from the Raia del Pedale section that were believed to contain adequate amounts of organic matter for isotopic analyses by virtue of their dark brown–black colour in hand specimen. Only five samples of a selected twelve likely candidates provided enough organic matter to test, but the results indicate that organic carbon-isotope trends are similar to those of carbonate carbon-isotope trends (particularly those values from +55, +66 and +142 m; Figure 4.xiv). This work could be developed in more depth in the future.

4.3 Diagenetic considerations

Because highly detailed petrographic analyses were not carried out over the entire Monte Sorgenza section, exclusion of data due to petrographic features indicating diagenetic modification has not been possible (except for the sample from +183.5 m, which had been re-crystallised by dolomite; ***4.1.1***). However, Violante (2000) suggests that there is no sedimentary evidence signifying exposure or interactions with meteoric waters (excepting the fault-plane sampling described above between +184 and +197 m), although petrographic and outcrop analyses discerned birdseye limestones above +293 m in this study.

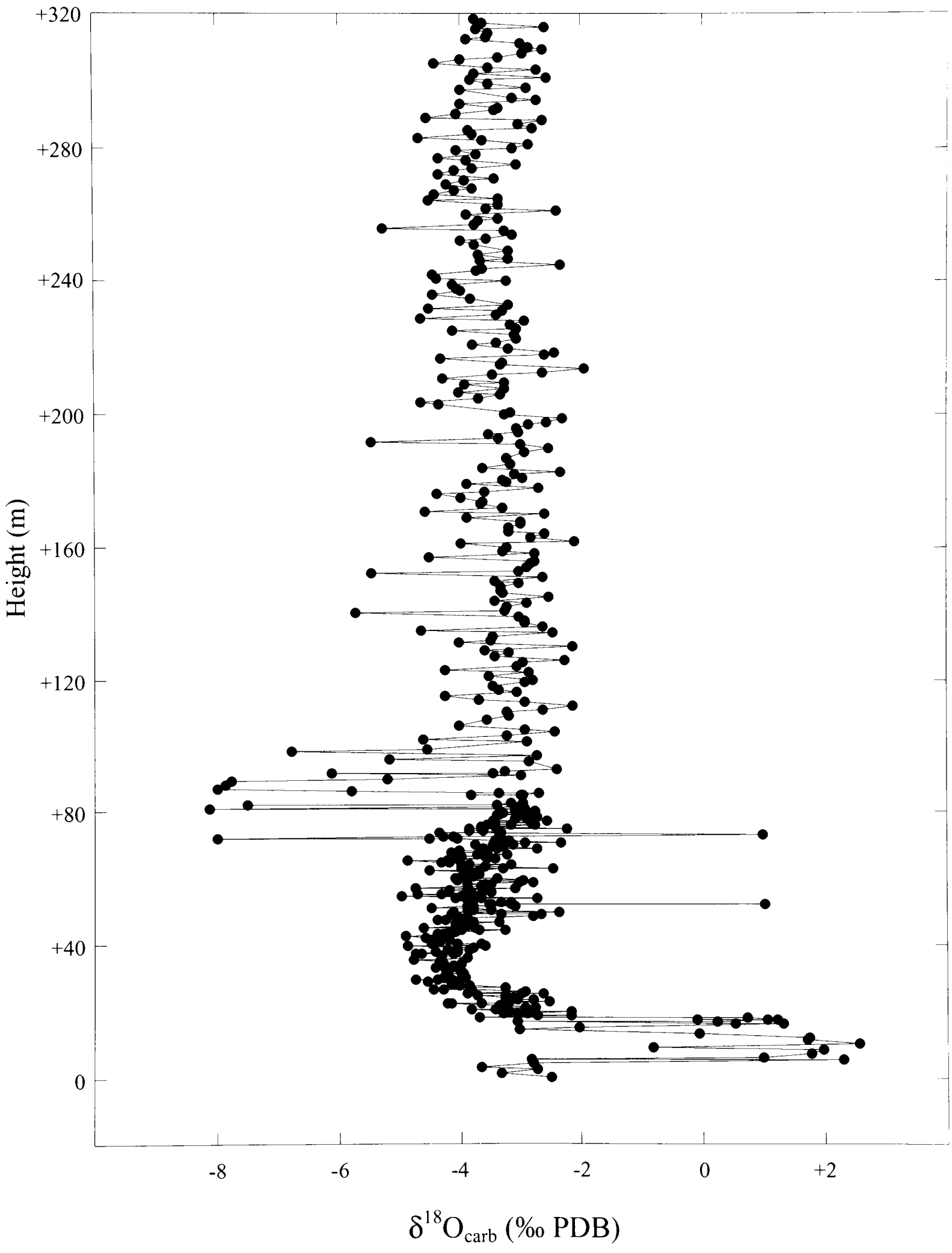

Figure 4.xiii. Oxygen-isotope profile of the Raia del Pedale section. In general the isotope values appear relatively stable throughout the entire section, except between +5 and +15 m, and +80 and +110 m. Otherwise, only the occasional 'flier' deviates from a coherent trend.

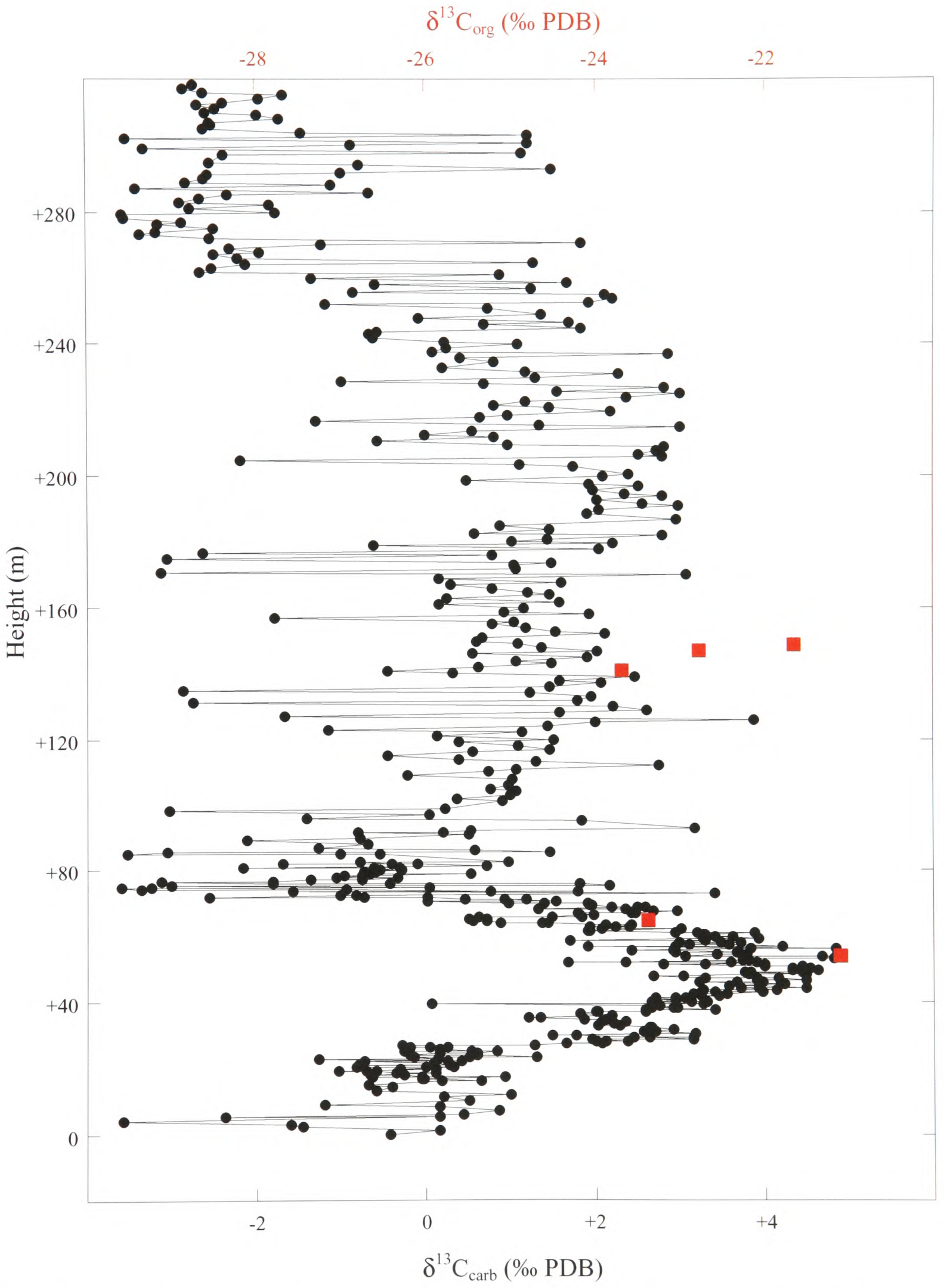

Figure 4.xiv. A comparison between the carbonate (black) and organic (red) carbon-isotope profiles of the Raia del Pedale section, Campania–Lucania Platform. Only five of a selected twelve samples had enough organic matter to test for $\delta^{13}C_{org}$.

Petrographic analyses of thin sections from the Raia del Pedale section have identified intervals affected by significant recrystallisation (namely by dolomite). As a result, the following samples are excluded from further consideration: +4 to +18 m, +71, +84, +91.75, +96, +98, and +108 m.

The strontium-isotope profile of the Monte Sorgenza section (Figure 4.xv) shows a relatively high amount of scatter (c.f. Trento Platform; ***2.2.1***). This scatter could either be due to post-depositional diagenetic influences or because the bulk-rock analytical process did not adequately remove detrital clays, whose strontium-isotope signals have been leached into solution and have modified the 'true' carbonate signal. The strontium-isotope signal is generally regarded as relatively robust to diagenesis (c.f. carbon- and oxygen-isotope ratios; Jones *et al.*, 1994a; Jones *et al.*, 1994b; McArthur *et al.*, 2000a), and, because primary signals tend to be modified to more radiogenic values, lines of best fit are drawn along the less radiogenic limits of the profile (Figure 4.xv; Burke *et al.*, 1982). In the case of Monte Sorgenza, the carbon- and oxygen-isotope signals do not seem to be significantly modified throughout the section by diagenesis (see below), leading to the conclusion that leaching of strontium from detrital clays in the bulk rock is the most significant cause of increased radiogenic ratios being acquired. However, the major trends of the primary signal still appear to be present (and they can be correlated with other strontium-isotope curves of this time period; ***Chapter 5***), and these trends are outlined by the approximate line of best fit in Figure 4.xv.

The strontium-isotope profile taken from samples from the Raia del Pedale section through the Campania–Lucania Platform (Figure 4.ix) is relatively coherent. Generally a broad relatively less radiogenic trough in isotope values occurs between 0 and +320 m.. Figure 4.xvi illustrates the strontium-isotope profile of the Raia del Pedale section with a line of best fit drawn along the minimum range of values (a procedure first adopted by Burke *et al.*, 1982).

As both sets of carbon- and oxygen-isotope curves display scatter and occasional extreme 'fliers', the additional data-screening method of filtering the original datasets in terms of oxygen-isotope values (as oxygen-isotopes are most susceptible to diagenetic modification from meteoric waters; see ***2.3***) has been applied. Figure 4.xvii (A) and (B) illustrate the carbon-

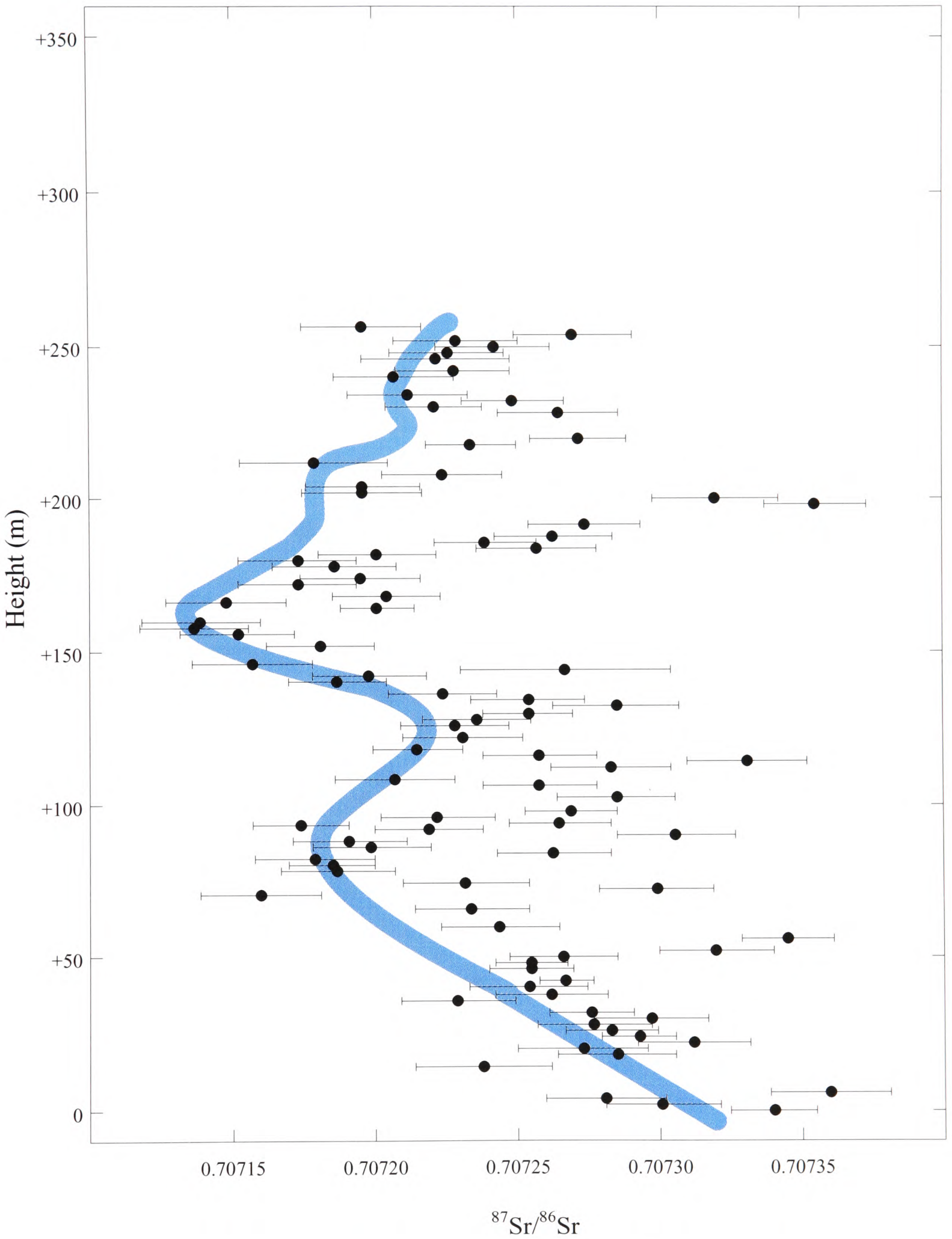

Figure 4.xv. Strontium-isotope profile of the of the Monte Sorgenza section with a line a best fit drawn approximately along the least radiogenic margin of data (method after Burke *et al.*, 1982). Data were normalised to a NIST SRM 987 value of 0.710250, the running average of standards being 0.710248, and $2\sigma = 0.000026$.

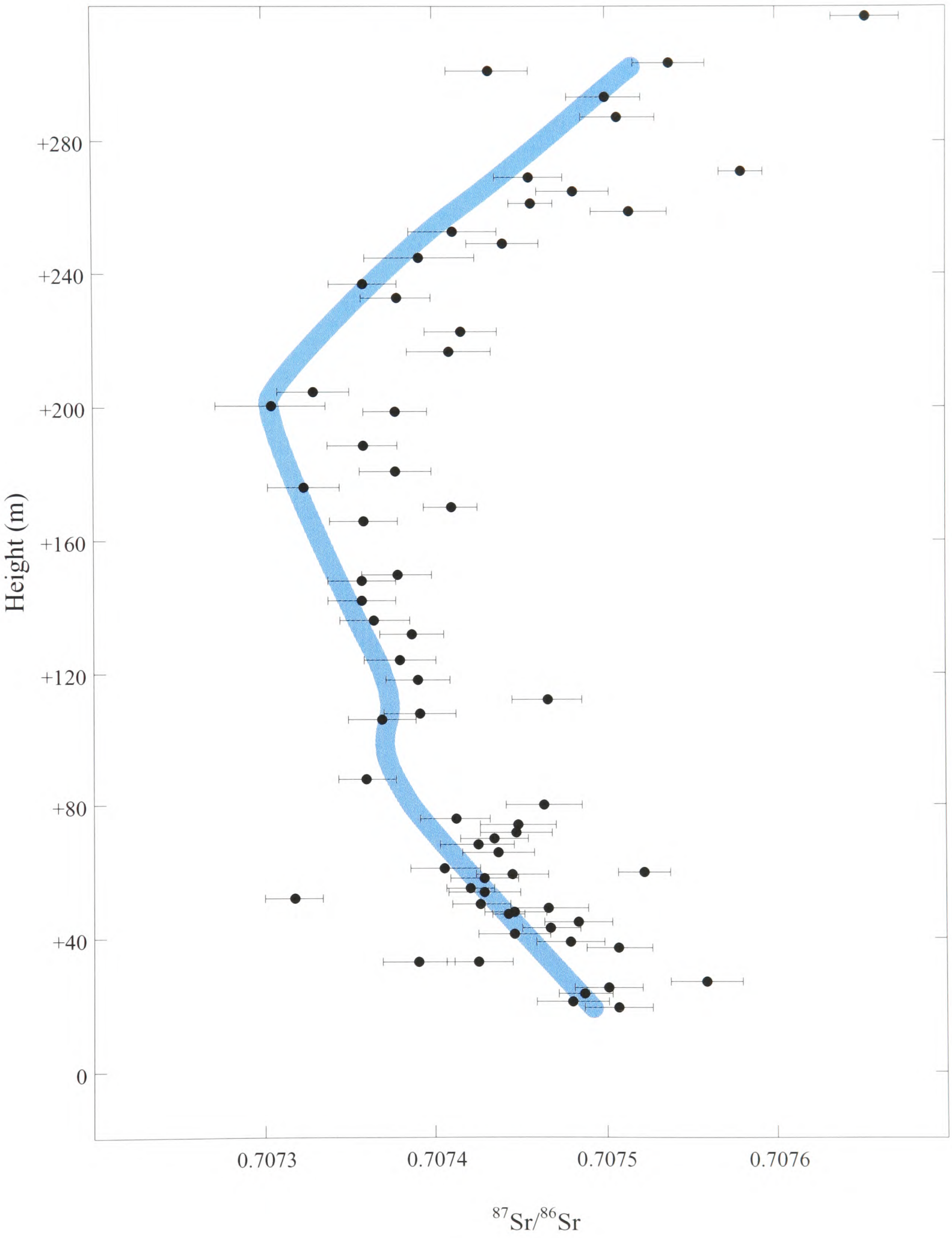

Figure 4.xvi. Strontium-isotope profile of the 320-m-thick Raia del Pedale section. The blue line is a line of best fit drawn along the least radiogenic values (method after Burke *et al.*, 1982).

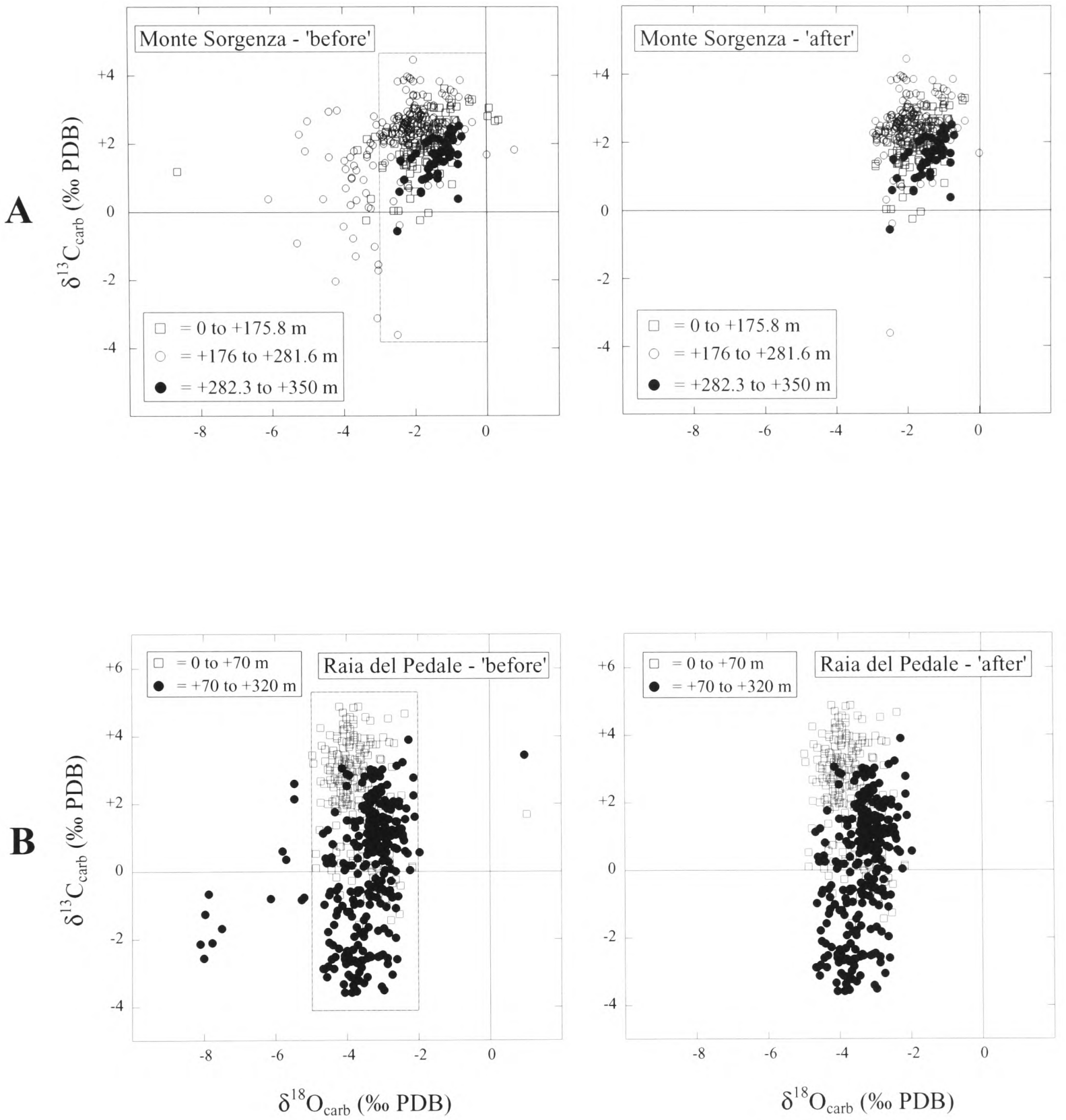

Figure 4.xvii. Carbon- and oxygen-isotope cross-plots for the Monte Sorgenza (**A**) and Raia del Pedale (**B**) sections. Red boxes mark the $\delta^{18}O$ filtering selections applied. 'Before' = unfiltered cross-plot, and 'after' = after data removal. For Monte Sorgenza: unfilled squares = Calcari à *Lithiotis*; unfilled circles = Calcari Oolitici; filled circles = Calcari Maculati.

and oxygen-isotope cross-plots of the original Monte Sorgenza and Raia del Pedale data respectively. Also illustrated are the Monte Sorgenza and Raia del Pedale cross-plots after the exclusion of data whose oxygen-isotope values lie outside the following respective ranges: $-3 < \delta^{18}O < 0$ ‰ and $-5 < \delta^{18}O < -2$ ‰.

The data in Figure 4.xvii (A) are grouped to illustrate the isotope values of the three different formations found in the section: the biomicritic Calcari à *Lithiotis* (unfilled squares), the Calcari Oolitici (unfilled circles) and the micritic Calcari Maculati (filled circles). The data in Figure 4.xvii (B) are grouped to illustrate the isotope values of the lower 70 (unfilled squares) and upper 250 m of the Raia del Pedale section.

It is obvious from Figure 4.xvii (A) that the Calcari Oolitici Formation is primarily responsible for much of the scatter in the Monte Sorgenza carbon-and oxygen-isotope profiles (as illustrated by the unfilled circles being 'pulled away' from the central cluster), and to a lesser extent the Calcari à *Lithiotis* shows variance out of the main cluster. Considering that the Calcari Maculati Formation shows signs of being deposited in the intertidal zone (birdseye limestones above +293 m), there is remarkably little isotopic scatter, suggesting that no significant diagenetic overprinting from exposure/meteoric-water influence has occurred. The majority of the data from all three formations cluster in the oxygen-isotope range $-3 < \delta^{18}O < 0$ ‰ (red box, Figure 4.xvii (A)).

Figure 4.xvii (B) illustrates that the clear majority of the Raia del Pedale data lie within an oxygen-isotope range of $-5 < \delta^{18}O < -2$ ‰. The data outside of this range are mostly from the upper 250 m of section (more negative). These data are excluded from the "after" cross-plot in Figure 4.xvii (B).

Monte Sorgenza samples with oxygen-isotope values that fall within the $-3 < \delta^{18}O < 0$ ‰ range are illustrated as a filtered carbon-isotope profile in Figure 4.xviii (filled circles). Those data that were excluded because their oxygen-isotope values fell outside of the filtering range are illustrated on the same figure as grey unfilled circles (i.e. the original dataset). It is noticeable in Figure 4.xviii that few data are excluded below +175 m. The majority of excluded

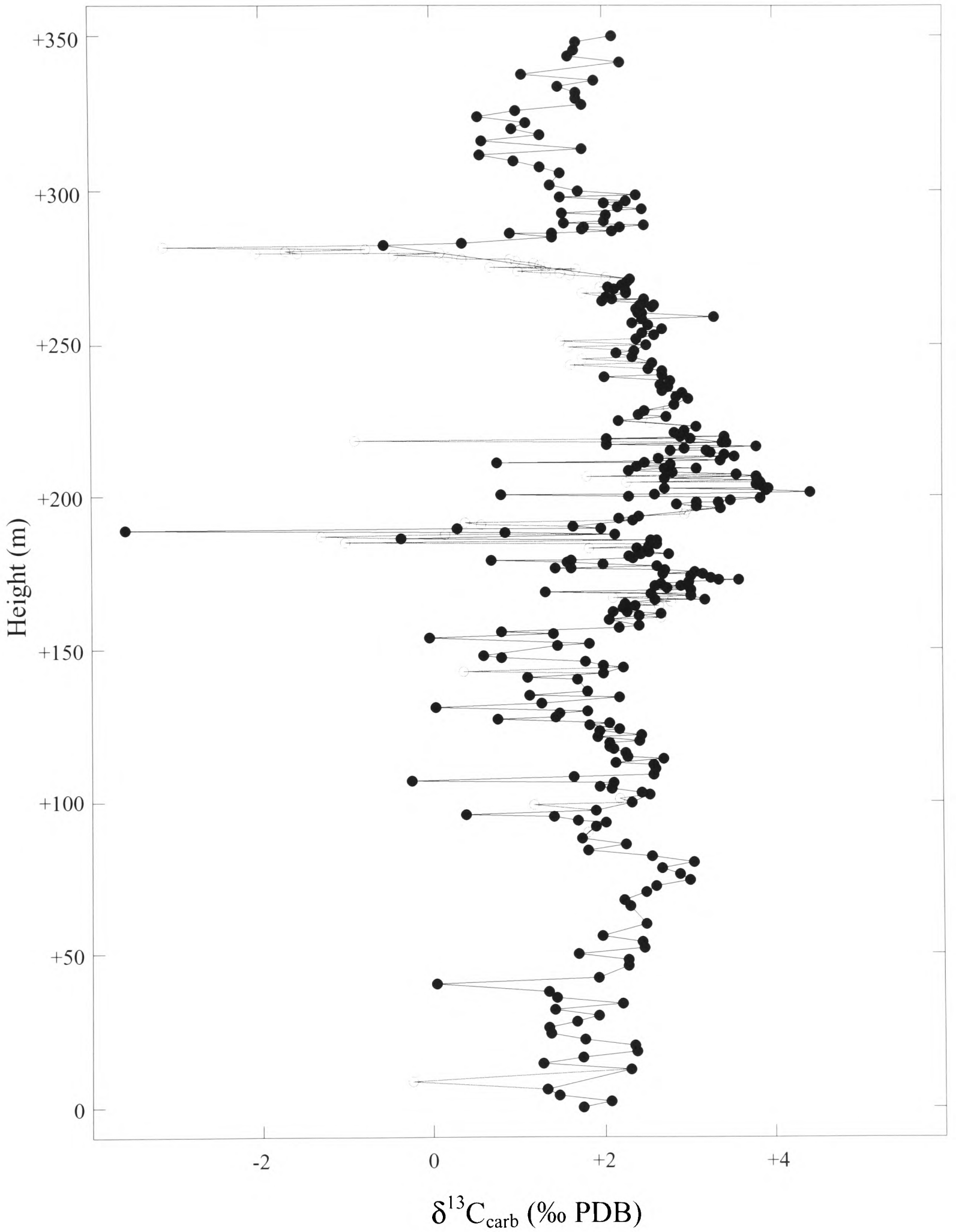

Figure 4.xviii. Filtered carbon-isotope profile of the 350-m-thick Monte Sorgenza section. Black filled circles represent those data that are not screened out due to their oxygen-isotope values (i.e. they fall within the range $-3 < \delta^{18}O < 0$), and the grey unfilled circles represent those original data that are excluded.

data points not only lie within the Calcari Oolitici (+175.8 to +281.6 m) but predominantly in the lower and upper 20 m of this formation. The upper portion of the lower 20 m of the Calcari Oolitici corresponds to the fault plane described above, which shows evidence of fluid interaction at outcrop and local dolomitic re-crystallisation in thin-section. The final 20 m of the Calcari Oolitici corresponds to the increasingly condensed/pinkish oolite below the contact with the Calcari Maculati. A diagenetic explanation for relatively low oxygen-isotope values in this interval could be due to a period of platform exposure (related to the increasingly condensed nature of the oolite) before conditions were right for deposition of the Calcari Maculati. However, there is no indication of exposure in the section (Violante, 2000), and it should be noted that this indiscriminate screening technique could equally be excluding 'real' data. The coherent fall and subsequent return to more positive values at the top of the Calcari Oolitici and base of the Calcari Maculati may prove significant in determining whether this negative carbon-isotope excursion is real, particularly as exposure/diagenetic modification of the oolite below should not affect the isotope ratios registered by the overlying facies. Due to the uncertainty in the origin of these Calcari Oolitici carbon-isotope trends, the data are re-included (Figure 4.xix) and a five-point moving average is added (in blue) to help delineate the primary trend.

Where data remain scattered and screening appears to have had little effect, alternatives to meteoric-water diagenesis are necessary to explain deviations from a primary oceanic isotope signal. In the Calcari à *Lithiotis*, the high quantity of skeletal fragments derived from bivalves (*Lithiotis*), gastropods, brachiopods, echinoids, sponges, and solitary corals may cause scatter unrelated to meteoric water (as described in ***1.4.3*** and ***2.3***). Scatter not removed from the oolite (especially between +200 and +225 m) may be related to the high porosity/permeability (due to large grain size) relative to micrite-based carbonates (Jones, 1992), although of course, it would be expected that any meteoric influence would result in low oxygen-isotope values.

The above diagenetic screening procedure aims to maintain the balance that most (but not necessarily all) modified signals are excluded on justifiable grounds, and that no real data are.

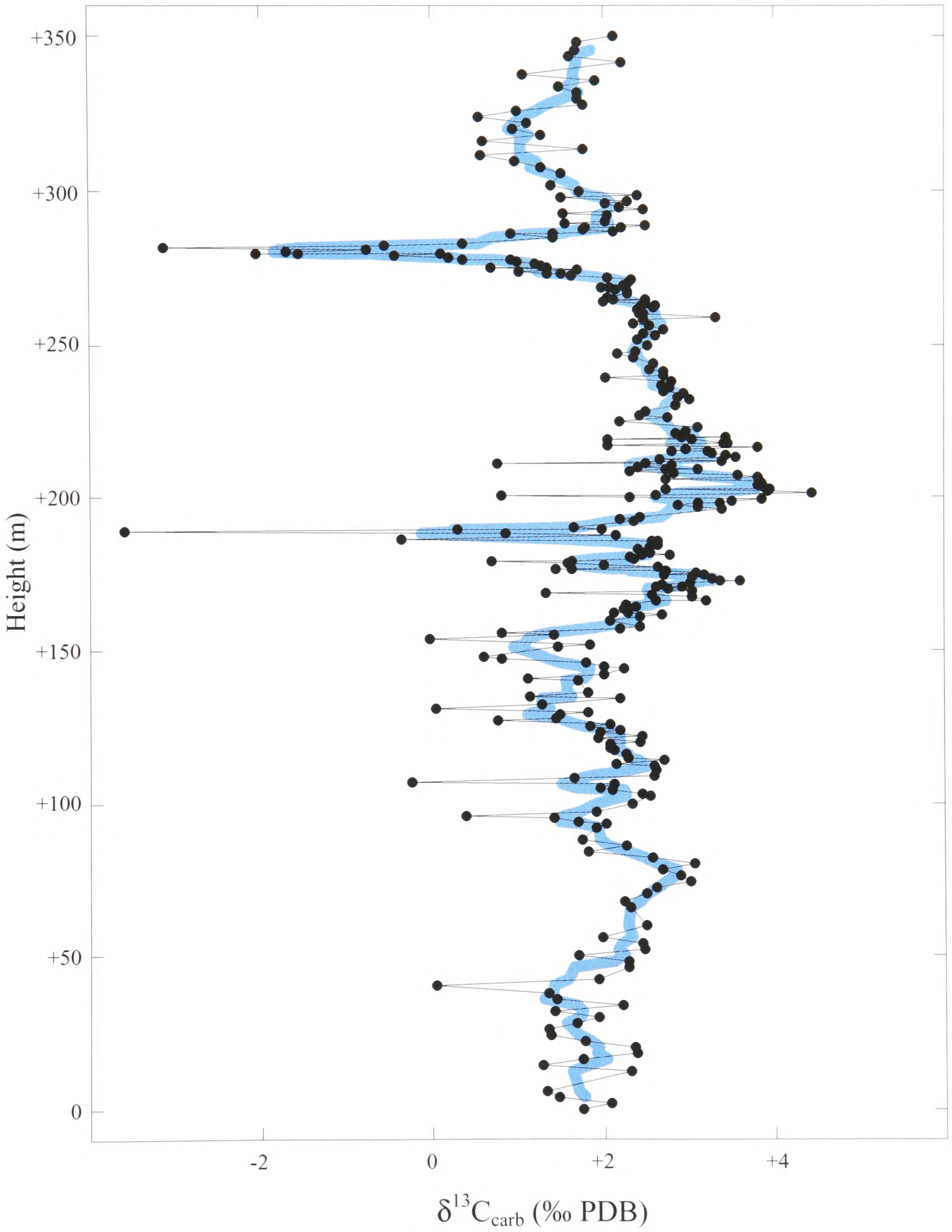

Figure 4.xix. Filtered carbon-isotope profile of the 350-m-thick Monte Sorgenza section (for -3 < $\delta^{18}O$ < 0) with the upper Calcari Oolitici coherent negative excursion re-included (see text). In blue is the five-point moving average.

Figure 4.xx illustrates the petrographically and oxygen-isotope-screened carbon-isotope profile of the Raia del Pedale section. The figure shows that further to the dolomitised samples that have been removed (see above), oxygen-isotope filtering of those data outside of the range $-5 < \delta^{18}O < -2$ removes a minor selection of the scatter from between +70 and +100 m. Presumably these samples were influenced by meteoric waters after deposition, which resulted in very negative secondary isotope signals being registered. The remaining high degree of scatter predominantly found between +70 and +320 m is possibly due to the effect of intraclastic breccias and bioclastic debris (rudist fragments – though not likely because rudist debris is present in the lower 70 m of the section) on the bulk carbonate-isotope signal. Alternatively, further non-identifiable modification of the primary signal over the upper 250 m of section is possible. The most likely cause of alteration, other than those already discussed, is the effect of further dolomite which has not been identified: Robson (1989) alludes to the presence of dolomite in the Sorrento Formation (***4.1***).

Generally, in the case of the Raia del Pedale section, petrographic screening of samples observed to contain dolomite was successful in removing scatter from the carbon- and oxygen-isotope profiles, but screening by virtue of oxygen-isotope values only had a very limited success in removing 'problematic' data. Without further screening tools to remove data resulting from other causes of primary isotope-signal modification, no further screening can take place with out the risk of excluding 'real' data.

Figures 4.xxi and 4.xxii summarise the Campania–Lucania Platform isotope profiles that are useful chemostratigraphic correlation tools. Figure 4.xxi illustrates the Monte Sorgenza carbon- and strontium-isotope profiles plotted alongside the full section graphic log. The blue line on the carbon-isotope profile is a five-point moving average of the data, and that on the strontium-isotope profile is a best-fit line that follows the least radiogenic values (a procedure adopted by Burke *et al.*, 1982). Likewise, Figure 4.xxii summarises the graphic log, carbon-, and strontium-isotope profiles of the Raia del Pedale section.

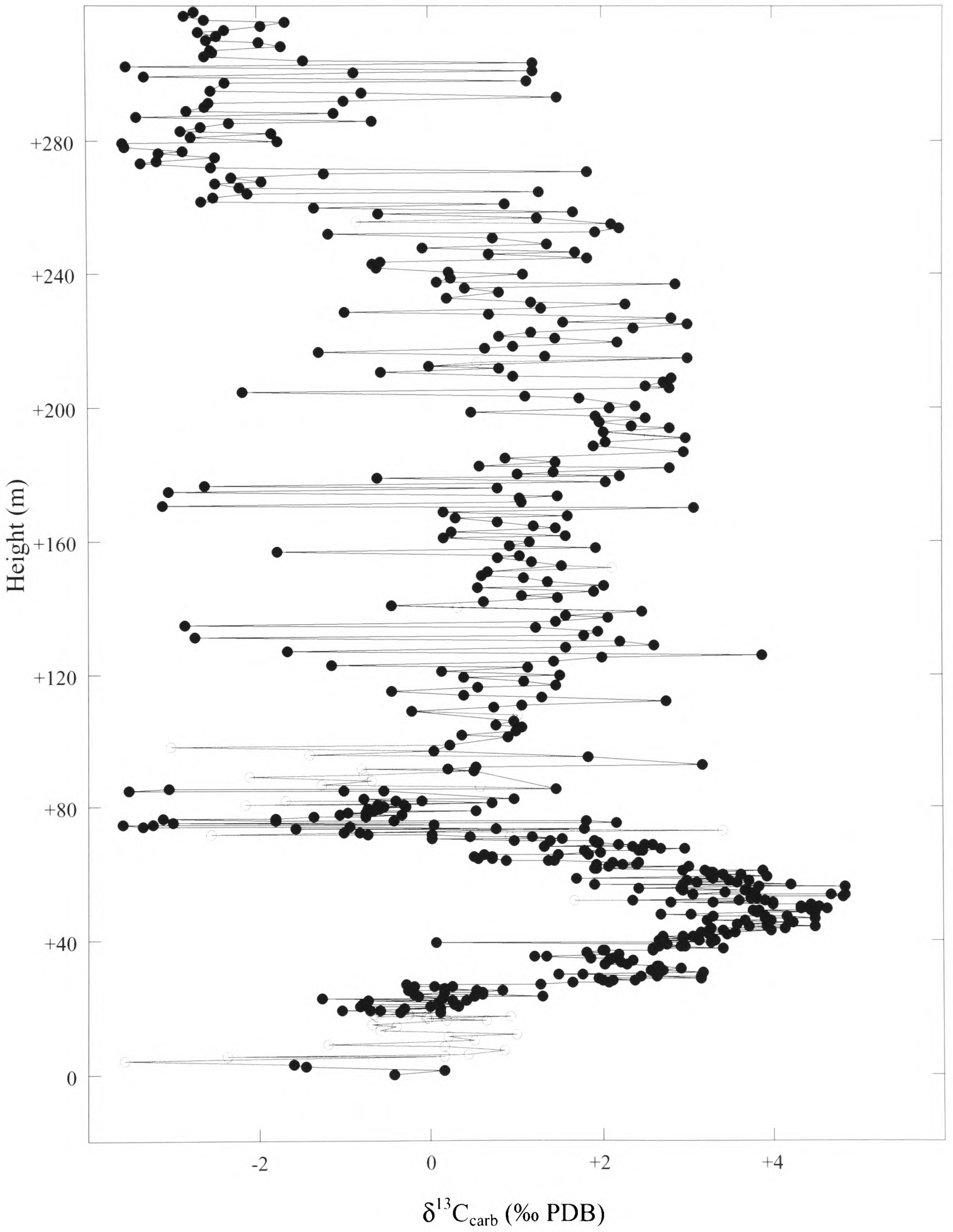

Figure 4.xx. Petrographically and oxygen-isotope screened carbon-isotope profile of the Raia del Pedale section, Campania–Lucania Platform. Grey unfilled circles represent original data that were excluded in the screening process.

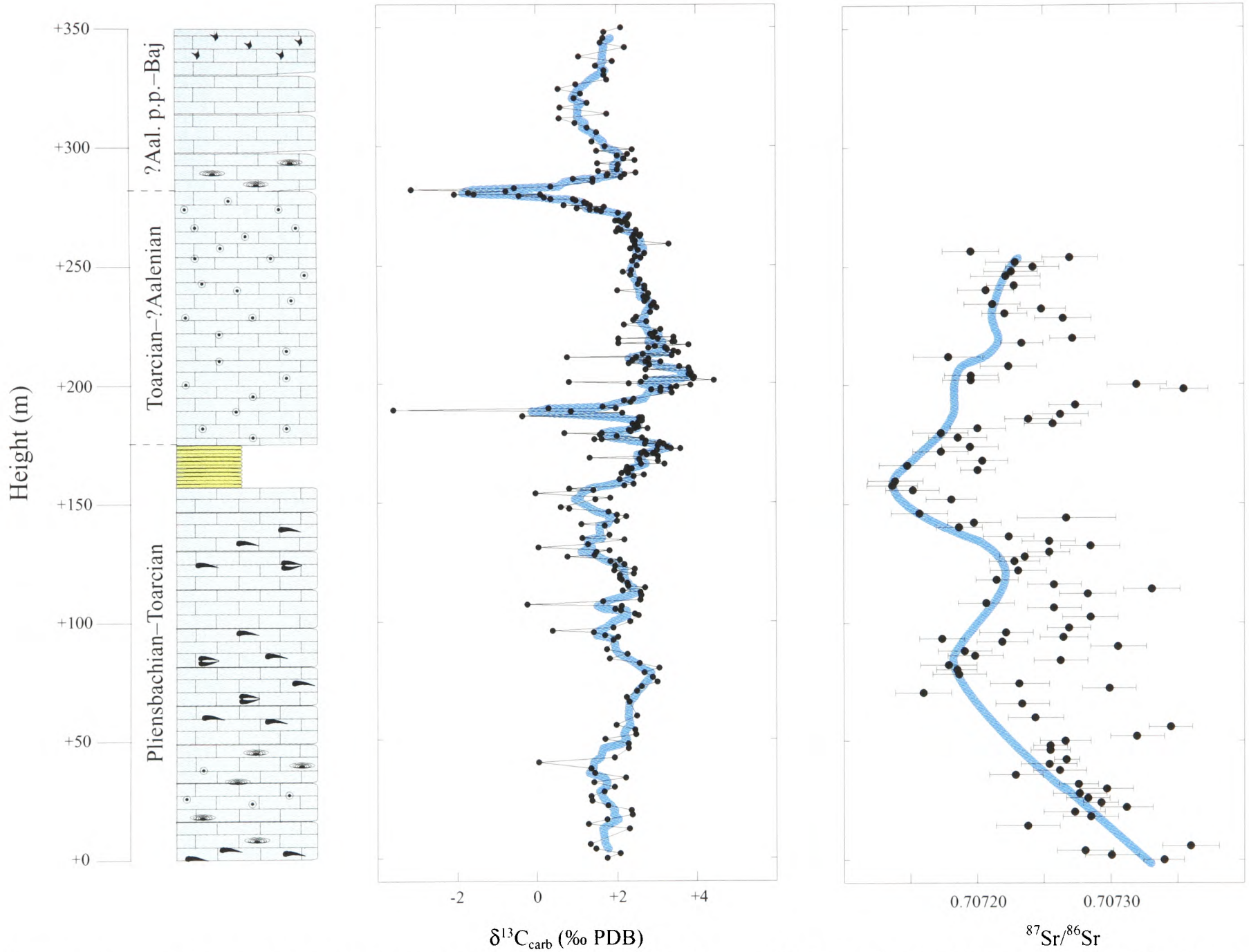

Figure 4.xxi. Graphic log, carbon-, and strontium-isotope profiles of the Campania–Lucania Platform (Jurassic). For key to graphic log, see Figure 4.v. Blue lines are: on the carbon-isotope profile a five-point moving average, and on the strontium-isotope profile an approximate best-fit line drawn along the least radiogenic margin of the data (procedure after Burke *et al.*, 1982) .

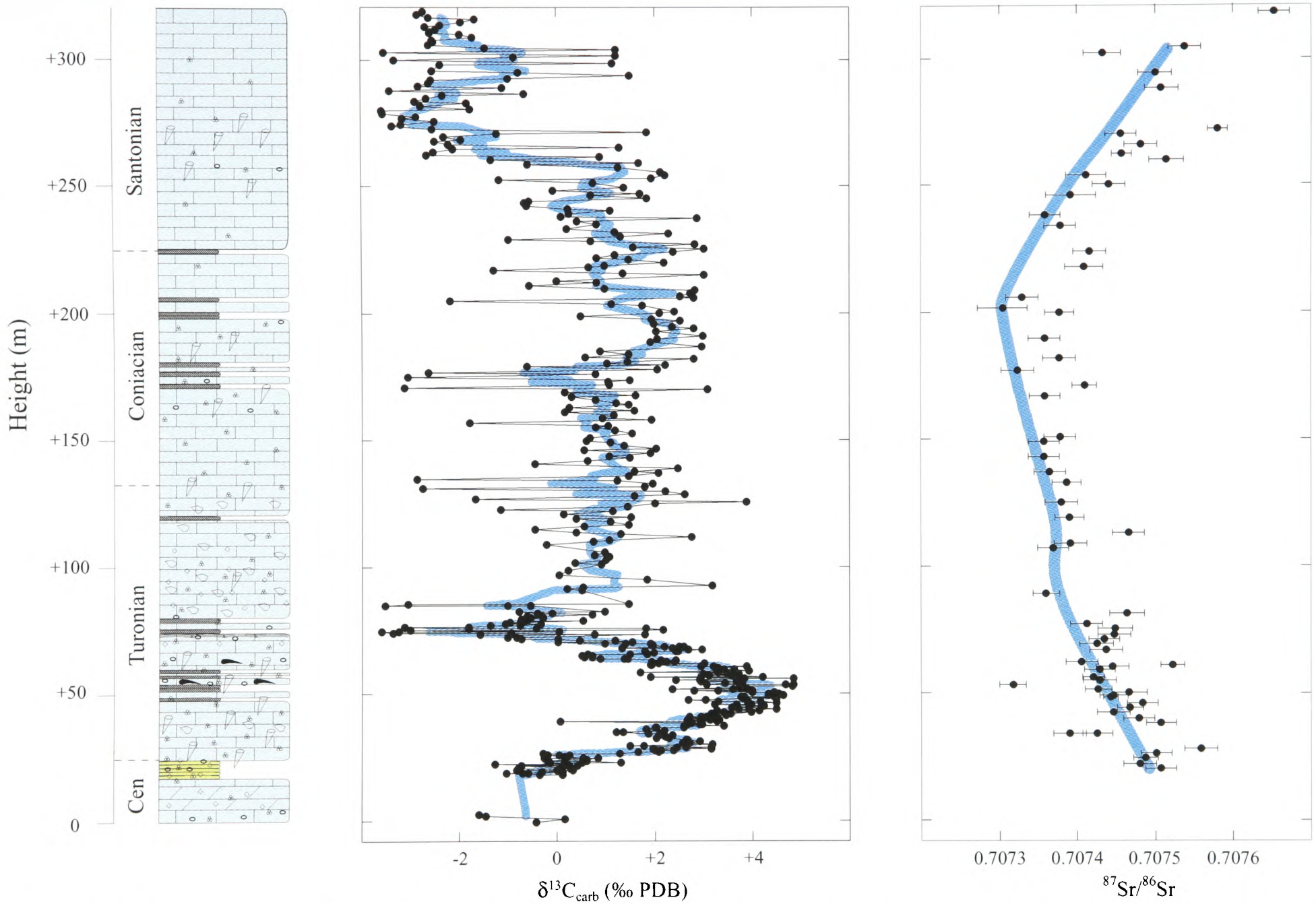

Figure 4.xxii. Graphic log, carbon-, and strontium-isotope profiles of the Campania–Lucania Platform (Upper Cretaceous). For key to graphic log, see Figure 4.vii. Blue lines are: on the carbon-isotope profile a five-point moving average, and on the strontium-isotope profile an approximate best-fit line (procedure after Burke *et al.*, 1982) .

Chapter5: Chemostratigraphic correlations

Chapter 5:Regional and global chemostratigraphic correlation of Italian shallow-water platform carbonates

Using diagrams similar to those illustrated in Figures 2.xxix, 3.xiii, 4.xxiv and 4.xxv, carbon- and strontium-isotope profiles have been used as correlation tools to allow a comparison of platform facies with: 1) other platforms within the Adria region (***5.1***); and 2) globally distributed and biostratigraphically calibrated pelagic, epicontinental and continental (terrestrial) sections (***5.2***). Oxygen-isotope profiles are not used by this study as a correlation tool because the data from platform carbonates are too scattered, most probably because of post-depositional modification (e.g. Allan and Matthews, 1982; Jenkyns, 1995b; Grötsch, 1998). However, the interpretation of oxygen-isotopes from shallow-water carbonates (and belemnites) is discussed in more detail in ***6.1***.

5.1 Regional (inter-platform) correlations

5.1.1 Trento / Campania–Lucania

Figure 5.i illustrates a visual correlation of the trends observed in carbon- and strontium-isotope profiles of the Lower Jurassic of the Trento and Campania–Lucania Platforms. The most obvious 'tie-points' between the two successions are the relatively negative troughs in carbon-isotope values coincident with a relatively radiogenic crest in strontium-isotope values (-480 to –290 m and +75 to +175 m on the Trento and Campania–Lucania Platforms respectively), and the negative–positive carbon-isotope excursions coincident with increasingly radiogenic strontium-isotopes (-250 to –180 m and +190 to +205 m on the Trento and Campania–Lucania Platforms respectively). A further possible tie can be made from the drowning unconformity of the Trento Platform to the facies transition interval from Calcari Oolitici–Calcari Maculati on the Campania–Lucania Platform (although this process is made more difficult by the drowning of the Trento Platform, and stratigraphically condensed pelagic facies). This latter correlation is not as straightforward as the previous two, and so requires more justification:

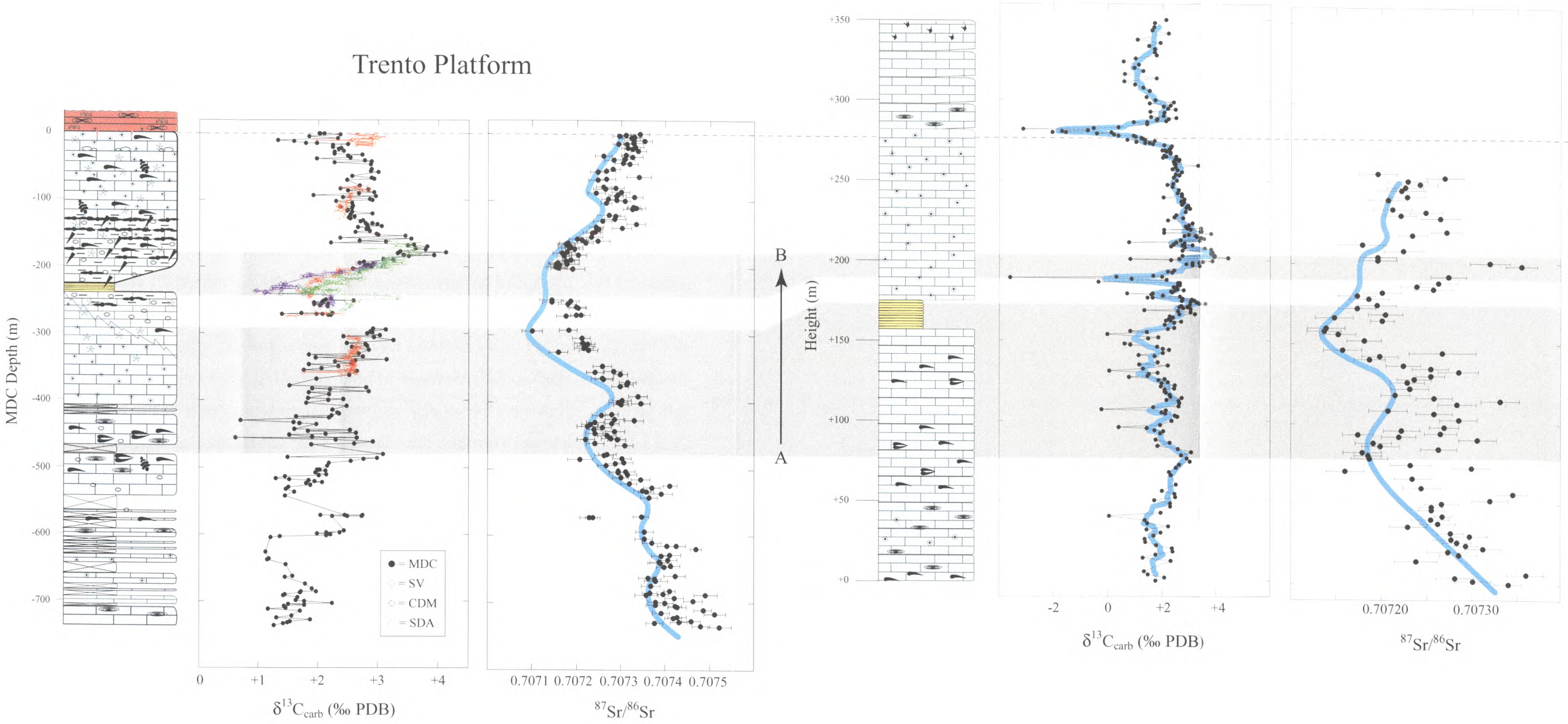

Figure 5.i. Chemostratigraphic (carbon- and strontium-isotope) correlation between the Early Jurassic, shallow-water Trento and Campania—Lucania Carbonate Platforms. The two profiles cover very similar periods of time, although the Monte Sorgenza section (Campania—Lucania Platform) continued carbonate deposition through (and beyond) the period of drowning suffered by the Trento Platform. A—B is equivalent to 300 m and 130 m vertical thickness for the Trento and Campania—Lucania Platforms respectively. The Early Jurassic sedimentation rate on the Trento platform was therefore approximately 2.3 times that on the Campania—Lucania Platform. For keys to graphic logs, see Figures 2.v and 4.v. Blue lines on the strontium-isotope profiles represent approximate lines of best fit drawn along minimum values (a technique first described by Burke *et al.,* 1982), and that on the carbon-isotope profile is a five-point moving average. MDC = Madonna della Corona; SV = San Vigilio; CDM = Colma di Malcesine; SDA = Sega d'Ala.

i. Both $\delta^{13}C$ profiles show decreasing values (although the Toarcian–Aalenian Stage boundary – also characterised by a negative excursion (see below) - is only 3 m below the drowning surface) leading into the respective facies transitions (San Vigilio Oolite–Rosso Ammonitico and Calcari Oolitici–Calcari Maculati)

ii. The strontium-isotope profiles support the correlation, in that the tie is immediately above a relative crest–trough transition

iii. The Calcari Maculati is lower Bajocian ("just below the first appearance of *Selliporella mediterraneous* Zone"; Violante, 2000), as is the base of the Rosso Ammonitico on the western margin of the Trento Platform (Sturani, 1964)

Following the correlation of distinctive chemostratigraphic tie-points between the Trento and Campania–Lucania Platforms, a comparison of time-equivalent facies can also be made. Violante (2000) suggests that the Campania–Lucania Calcari à *Lithiotis* is comparable to the Trento Calcari Grigi (especially the Rotzo member with *Lithiotis* beds; Figure 2.iii), and the biostratigraphy supports this claim (*Paleodasycladus mediterraneous* Zone; Bosellini and Broglio Loriga, 1971). The chemostratigraphic profiles also prove very useful in tying the Calcari Grigi, Rotzo Member with the Calcari à *Lithiotis*: the relatively low values in the $\delta^{13}C$ curves between –480 and –375 m (Trento) and +75 to +155 m (Campania–Lucania) with a coincident sequence of minimum followed by maximum (and on into a further minimum higher upsection) in the strontium-isotope curve are convincing evidence that these two intervals are correlatable. It must also be noted that the Massone Oolite, which overlies the Calcari Grigi, Rotzo Member on the Trento Platform, had begun to be deposited before cessation in the deposition of the Calcari à *Lithiotis* on the Campania–Lucania Platform (possibly due to local differences in subsidence; ***5.3***). As discussed in ***Chapters 2 and 4***, both the Calacari à *Lithiotis* and the Calcari Grigi, Rotzo Memberhave been interpreted as facies that reflect quiet subtidal back-reef (lagoonal) depositional environments with local development of oyster-like mounds of *Lithiotis* and other lagoonal organisms (e.g. Bosellini and Broglio Loriga, 1971; Gaetani, 1975; Picotti and Cobianchi, 1996; Violante, 2000). Therefore, it would appear that these conditions prevailed on both the Trento and Campania–Lucania Platforms during the Sinemurian–Pliensbachian interval.

Between the –375 and –300 m levels on the Trento and +155 to +175 m levels on the Campania–Lucania Platform, carbon-isotope values become relatively higher and strontium-isotopes become less radiogenic towards a minimum. It is therefore suggested that these two sections on each platform were deposited synchronously. In terms of the facies that are observed at this point: on the Treno Platform (at the Madonna della Corona section) there is a transition in deposition from oolite (Massone Oolite) to thin-bedded clay-rich pelletal limestone with abundant spiculitic cherts (Misone Formation); on the Campania–Lucania Platform there is a synchronous transition in deposition to thin-bedded (and laminated), clay-rich micritic shales. Because both platforms move towards the deposition of less carbonate-rich facies at this interval, it is plausible that these phenomena may be causally related (see ***6.2.1***).

Between the –300 and –250 m level on the Trento Platform and the +175 and +185 m level on the Campania–Lucania Platform there are significant decreases in carbon-isotope values, before a short-lived plateau (immediately before the next pronounced negative isotope excursion) accompanied by a shift to more radiogenic strontium-isotope values. On the Trento Platform, this interval is represented in the rock record by continued deposition of the Misone Formation (Massone Oolite at the Colma di Malcesine; Massone Oolite–Misone Formation transition at the Sega d'Ala). On the Campania–Lucania Platform, the initiation of this decrease in carbon-isotope values is synchronous with a facies transition from the shales and thin-bedded micritic limestones of the Calcari à *Lithiotis* to the massive oolite package of the overlying Calcari Oolitici.

The major negative carbon-isotope excurion at the –240 m level on the Trento Platform is synchronous with a pronounced facies change from thin-bedded limestones of the Misone Formation (Massone Oolite at the Colma di Malcesine) to the calcareous shales of the Basal Tenno Formation. The Basal Tenno Formation gradually undergoes a transition into thin-bedded pelletal limestones with cherts of the Upper Tenno Formation (very similar to the Misone Formation), as the carbon-isotope curve synchronously returns to more positive values and extends into a positive excursion in its own right. Throughout the negative and subsequent positive carbon-isotope excursions, the strontium-isotope profile displays increasingly radiogenic values as it rises out of the minimum. However, on the Campania–Lucania Platform,

the interval of rock that illustrates consecutive negative and positive carbon-isotope excursions with rising strontium-isotope values is a continuation of the relatively monotonous Calcari Oolitici. It therefore appears that whatever dynamics were affecting the isotope profiles they had little effect on the depositional environment of the platform.

As carbon-isotope values return to background values on the Trento Platform (approximately –130 m), the strontium-isotope profile flattens and there is a change in facies from thin-bedded Upper Tenno carbonates to echinoderm-rich San Vigilio Oolite. The mechanisms that result in the same isotope changes on the Campania–Lucania Platform once again failed to affect the depositional mode, and massive oolite continued to accumulate.

The final 50 m of platform-carbonate accumulation on the Trento Platform reveals a carbon-isotope profile that displays a gradual decrease in values, whereas strontium-isotope values become increasingly radiogenic. At 0 m, the platform evidently drowned. If the above-mentioned characteristics of the Trento Platform are correlated with the +275 to +290 m interval of the Campania–Lucania Platform, a similar negative carbon-isotope excursion is apparent (and very pronounced) and complete in that a coherent return to background values occurs before the profile extends for the remainder of the section. Coincident with this negative isotope excursion is a marked facies change from Calcari Oolitici to Calcari Maculati (oolite to cyclically bedded oncolitic biopelmicrites with benthic foraminifera, algae and ostracods). The isotope values of the negative excursion decrease at the top of the oolite before coherently increasing in the base of the Calcari Maculati. It is therefore conceivable that the facies change from San Vigilio Oolite–Rosso Ammonitico and Calcari Oolitici–Calcari Maculati on the respective Trento and Campania–Lucania Platforms are causally related (note: the Trento Platform Toarcian–Aalenian Stage boundary, as dated by Sturani, 1964, is only 3 m below the drowning surface – i.e. this interval is highly condensed).

To summarise: it appears that the top of the Calcari Grigi Formation (Rotzo and Massone Oolite Members) on the Trento Platform is time-equivalent to the Calcari à *Lithiotis* on the Campania–Lucania Platform (Figure 5.ii). The shaly facies of the Misone Formation (Trento) appear equivalent to the shaly top of the Calcari à *Lithiotis*, and the San Vigilio Group

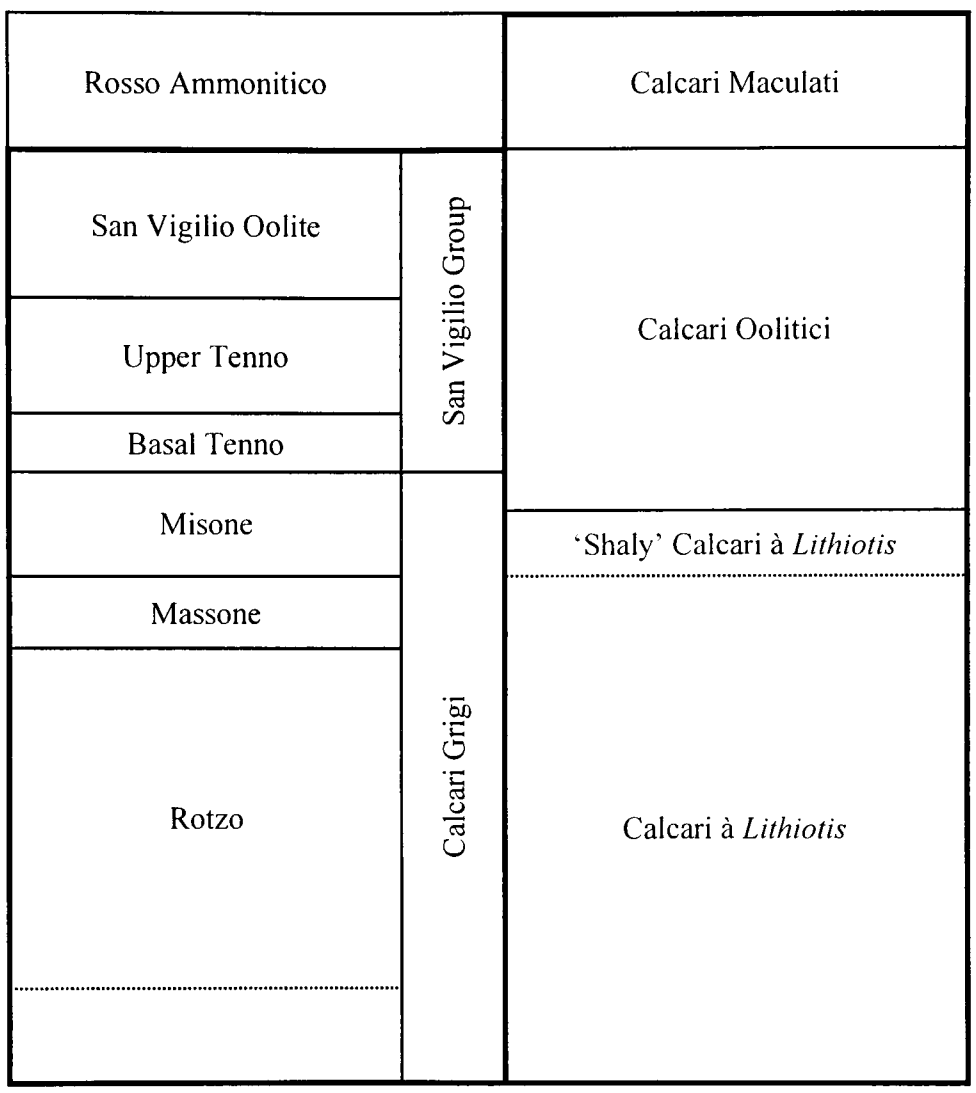

Figure 5.ii. Interpreted facies equivalence between the Trento and Campania–Lucania Platforms based on litho-, bio- and chemostratigraphy.

(Basal Tenno, Upper Tenno and San Vigilio Oolite; Barbujani *et al.*, 1986) are roughly equivalent to the Calcari Oolitici on the Campania–Lucania Platform (although deposition of the Calcari Oolitici marginally preceded that of the Basal Tenno Formation: *spinatum* compared to *falciferum* Zones; also see Figures 6.i and 6.ii). The Rosso Ammonitico and Calcari Maculati are also time-equivalent, although the latter records continued shallow-water carbonate-platform sedimentation as opposed to a deeper-water pelagic facies that characterised the post-drowning phase of the Trento Platform (Trento Plateau). Also of potential significance is the comparison of sedimentation rates (strictly accumulation rates with no corrections for compaction) between the Trento and Campania–Lucania Platforms, which is now possible as a result of the chemostratigraphic correlations. The shaded-area correlations in Figure 5.i amount to approximately a 300-m interval on the Trento Platform, but only 125 m on the Campania–Lucania Platform. Also assuming that the carbon-isotope profiles of the two platforms parallel each other until the Trento Platform drowning, 730 m of section on the Trento Platform are equivalent to 280 m on the Campania–Lucania Platform (Figure 5.v). The accumulation rate on the Trento Platform was therefore almost 2.5 times that on the Campania–Lucania Platform during the Early Jurassic (for further details on accumulation rates, see ***5.3***).

5.1.2 Friuli / Campania–Lucania

Figure 5.iii illustrates the chemostratigraphic correlations of the Friuli and Campania–Lucania Platforms, which are supported by the available biostratigraphy (Robson, 1989; Bruni, 2003). The Friuli section (Val Cellina) covers much more geological time than the Campania–Lucania Platform section (Raia del Pedale), and displays very distinctive carbon- and strontium-isotope profiles throughout. However, the specific interval correlated is that which is believed to range in age, determined by biostratigraphy, from late Cenomanian–Santonian. In this interval of time, the section through the Campania–Lucania Platform displays a very pronounced positive carbon-isotope excursion between 0 and +80 m (maximum), immediately followed by a broader positive excursion with two maxima, between +80 and +280 m. Although studied in less resolution (the top of the section was inaccessible after the initial 'pilot' sampling), the Friuli Platform illustrates two similar carbon-isotope

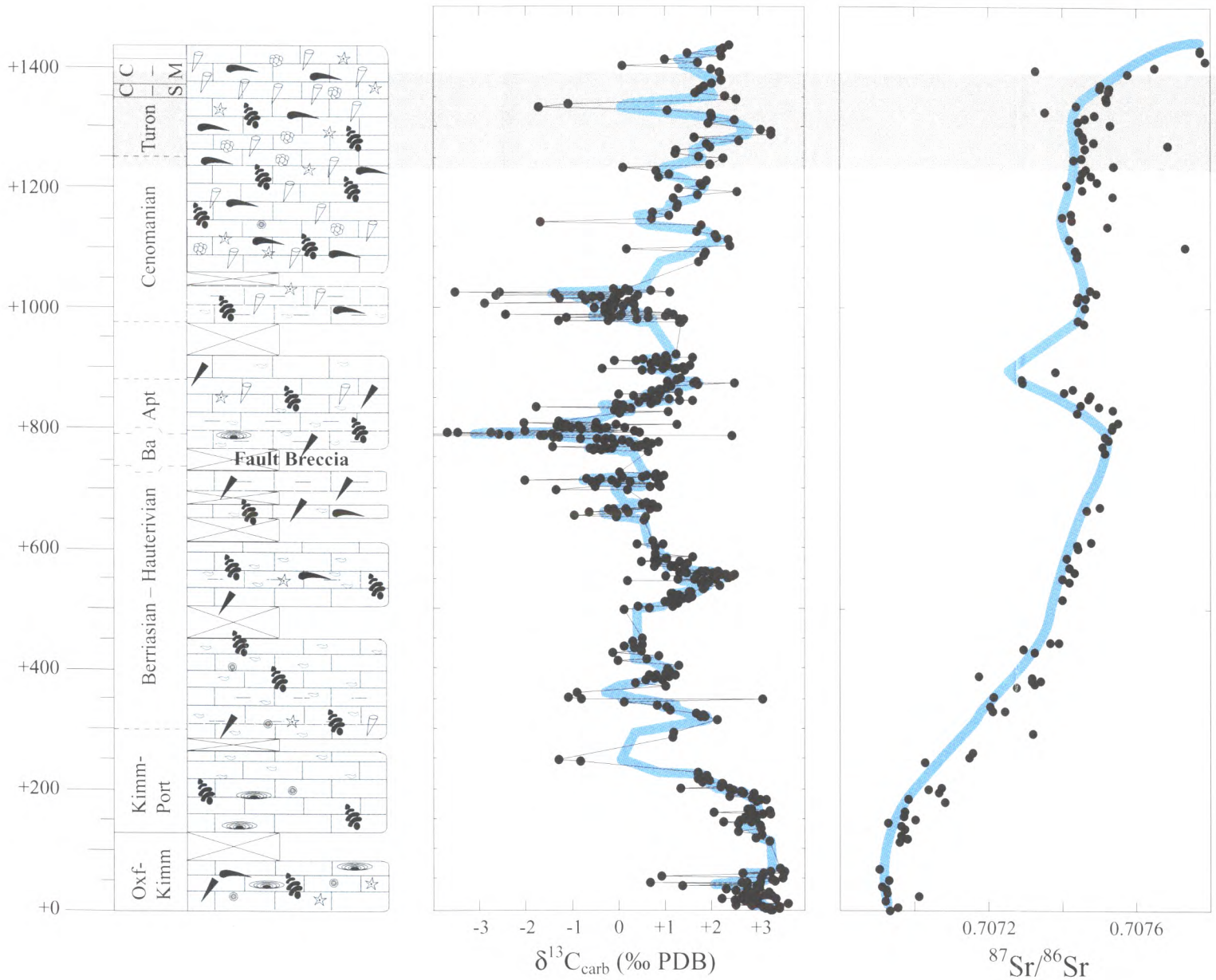

Figure 5.iii. Carbon- and strontium-isotope correlation between Cretaceous carbonates of the Friuli and Campania-Lucania Platforms (supported by the available biostatigraphy). A consequence of this correlation is that the Petina/Sorrento Formations of the Campania-Lucania Platform are broadly time-equivalent with the Calcari di Monte Cavallo of the Friuli Platform (Calcareniti del Molassa of Robson, 1989). If the correlation and its limits are correct, it appears that the sedimentation rate during deposition of the carbonates containing the first relatively rapid $\delta^{13}C$ positive excursion at the Raia del Pedale (Campania-Lucania) was roughly equivalent to that on the Friuli Platform. However, the sedimentation rate at the Raia del Pedale during the deposition of carbonates with the second broad positive excursion was approximately 3 times that on the Friuli Platform. Blue lines on the strontium-isotope profiles are an approximate line of best fit along the minimum margin of values (after Burke *et al.*, 1982), and on the carbon-isotope profiles are five-point moving averages.

excursions over this period: the first appears to be between the +1230 and +1330 m level, and the second, which is less obvious to identify, between the +1330 and +1400 m level.

However, the trends recorded by the two strontium-isotope profiles do not appear to closely match: samples from the Raia del Pedale section show a trough of relatively less radiogenic values, whereas those from the Val Cellina section show a relatively 'flat' profile. These strontium-isotope trends are discussed in relation to the trends of reference isotope profiles in ***5.2***.

If the carbon-isotope correlations are correct, the Petina and Sorrento Formations of the Campania–Lucania Platform are time-equivalent to the Calcari di Monte Cavallo (Cuvillier *et al.*, 1968) / Calcareniti del Molassa (Robson, 1989) of the Friuli Platform. Although the Petina Formation has been interpreted as representative of prograding intertidal flats (Robson, 1989) and there seems to be no direct equivalent of this lithotype in the Val Cellina section (Friuli) at this level, both the rudist-bearing Calcari di Monte Cavallo and Sorrento Formations have been interpreted to represent relatively open-marine back-reef lagoons. It should be noted that the biostratigraphy and chemostratigraphy of the increasingly condensed Friuli Platform is relatively inaccurate at this level, due to the low sampling density. Despite this, the above correlation leads to the conclusion that the accumulation rate on both platforms was comparable during Cenomanian–Turonian time but from Turonian–Santonian time the Campania–Lucania Platform sedimentation rate was up to 3 times that on the Friuli platform (see ***5.3*** for further detail on accumulation rates).

5.2 Global correlations to other facies types

Triassic–Tertiary composite carbon- and strontium-isotope profiles of Italian carbonate platforms allow chemostratigraphic correlations with other biostratigraphically calibrated and globally distributed sections. These correlations improve dating of the shallow-water carbonates, and further facilitate the comparison of facies changes on Tethyan platforms with those (as well as other proxy data) observed from varying depositional environments of the same period (ranging from the deep-marine to the terrestrial realm). As a consequence,

interpretations on the response of these carbonate platforms to observed global events can be made (see ***Chapter 6***).

Figure 5.iv(A) illustrates the complete collection of the most stratigraphically significant isotopic profiles of Jurassic–Tertiary Italian carbonate platforms that have resulted from this study. The strontium- and carbon-isotope profiles of the three respective platforms are correlated and displayed in stratigraphic sequence (Early Jurassic–Tertiary, although missing the Bajocian–Oxfordian Stages). Time is once again constrained by the low-resolution (up to stage level) biostratigraphy of the carbonate platforms, but it should be noted that stage durations are not depicted in proportion to their proposed relative durations. The *x*-scale is instead illustrated in proportions of vertical thickness (metres) of the respective individual platform sections (see Figures 5.i and 5.iii). For a very general visual comparison, the Jurassic–Early Cretaceous belemnite isotopic data (from globally distributed localities) compiled by Gröcke (2001) and Jenkyns *et al.* (2002), are displayed alongside the Italian carbonate-platform data of this study (Figure 5.iv(B)).

It is immediately apparent that the $^{87}Sr/^{86}Sr$ and $\delta^{13}C$ trends displayed in the reference curves and the platform carbonates are similar and can be correlated. In particular, the Pliensbachian–Toarcian strontium-isotope 'trough' in values and the synchronous negative–positive carbon-isotope excursions are easily identified in both the belemnite and shallow-water carbonate profiles. The Aalenian–Bajocian negative carbon-isotope excursion from the Campania–Lucania Platform (?and the topmost Trento platform) also appears to be reproduced in the belemnite data. Characteristic carbon- and strontium-isotope trends for the Oxfordian–Kimmeridgian belemnite curves of Gröcke (2001) and Jenkyns *et al.* (2002) are also reflected in those of the Friuli Platform: relatively low strontium-isotope values and a broad positive carbon-isotope excursion (Callovian–Oxfordian). From late Oxfordian–early Tithonian times, the belemnite carbon-isotope curve shows a pronounced depletion in ^{13}C, which is also seen in the Kimmeridgian–Portlandian of the Friuli curve. The Berriasian–Hauterivian portion of the $\delta^{13}C$ profiles is less easy to correlate; the Barremian–Aptian negative excursion is not obvious in the belemnite data, and the Aptian positive excursion seen in the Jones (1992) data is not reproduced in the carbonate-platform data. However, the Kimmeridgian–Aptian strontium-

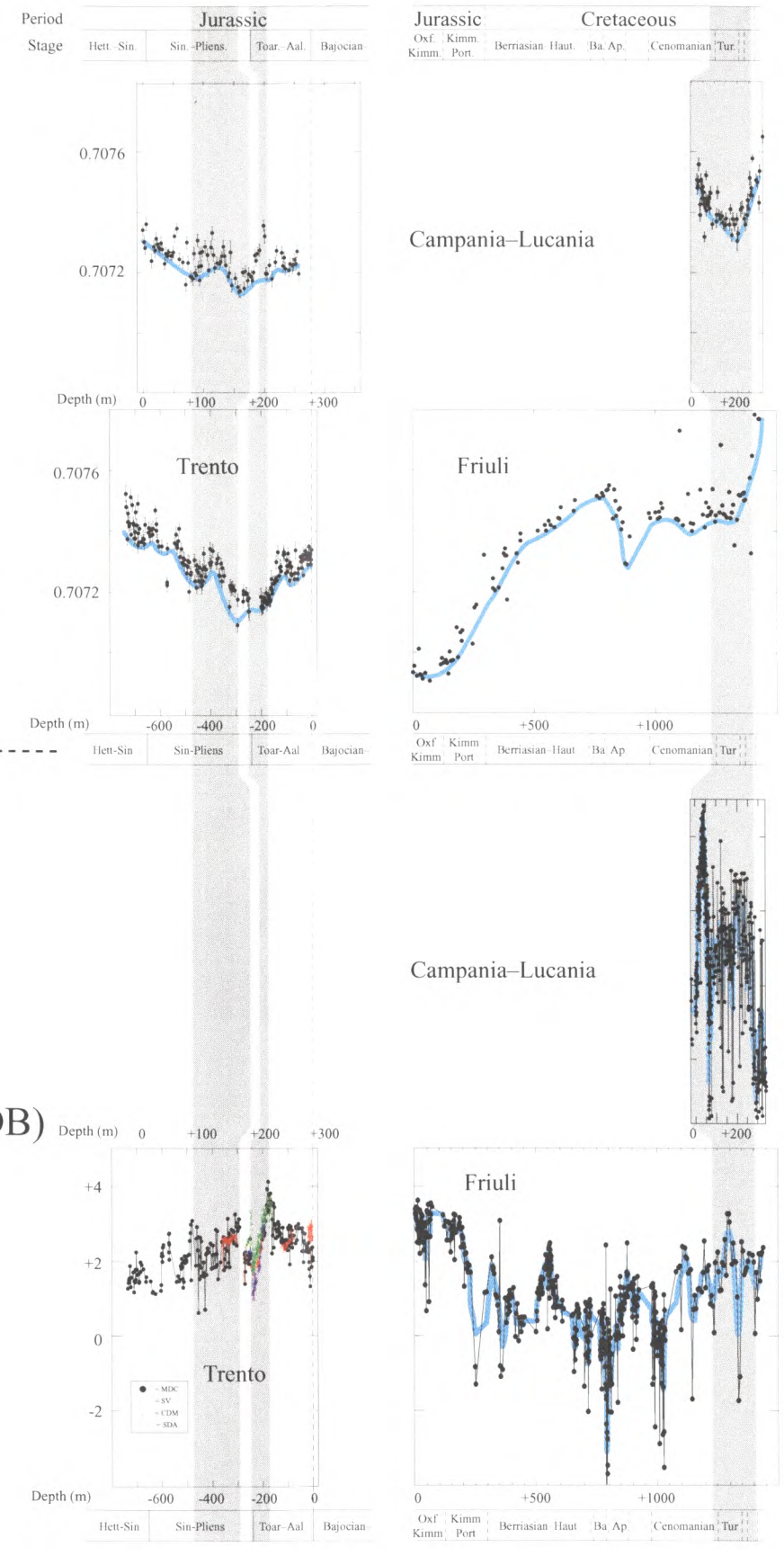

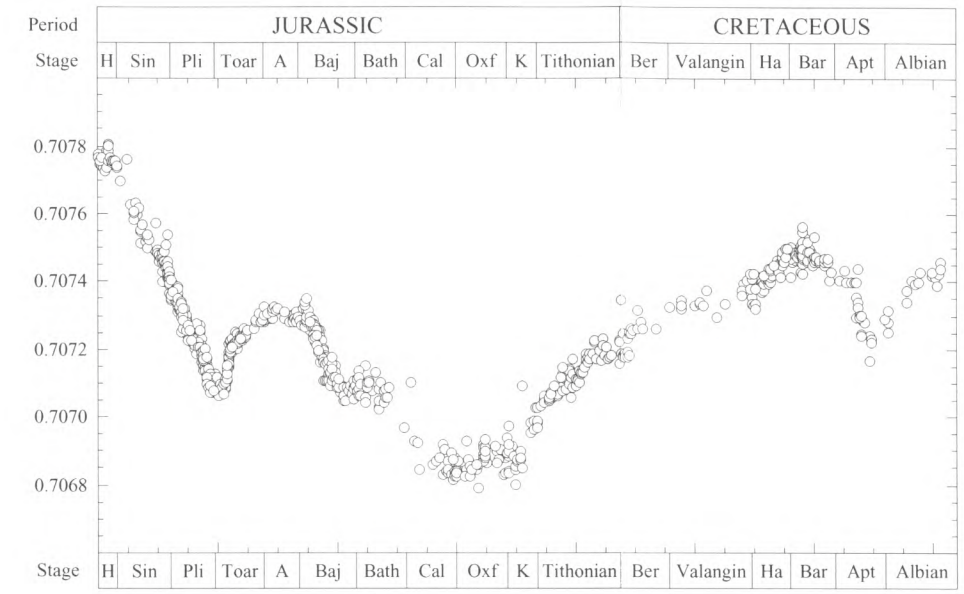

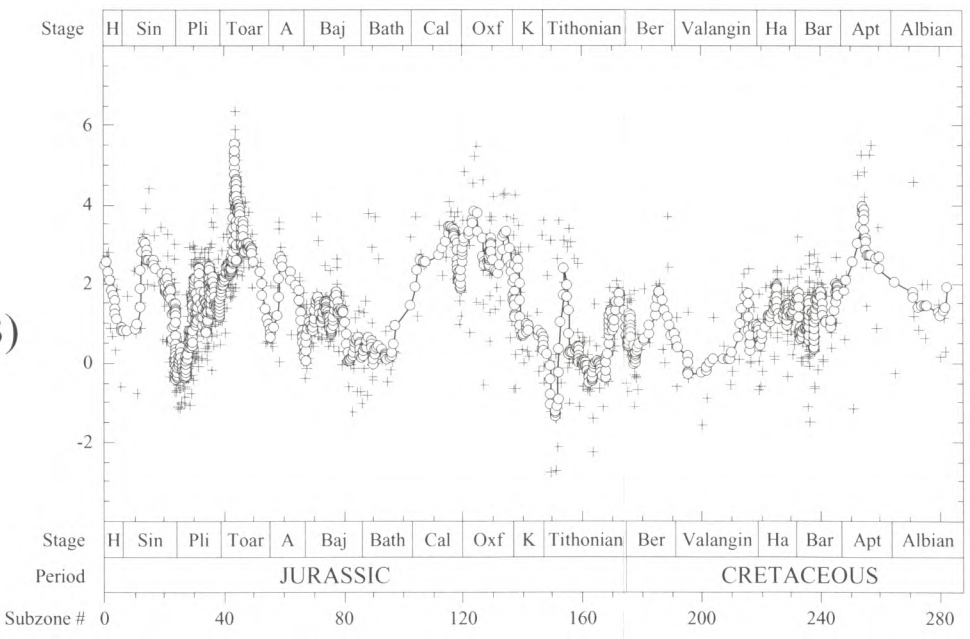

Figure 5.iv. **A**. Correlation of all the stratigraphically significant carbon- and strontium-isotope data of the Jurassic and Cretaceous Italian carbonate platforms obtained by this study. All age is constrained from the available biostratigraphy of previous workers as described in Chapters 2, 3 and 4 (*x*-scales are still in the metric proportions of earlier figures). **B.** Jurassic and Early Cretaceous belemnite isotopic data from Gröcke, 2001 (compiled from Jones *et al.,* 1994a, b; Parkinson, 1994; Podlaha *et al.,* 1998; McArthur *et al.,* 2000a; Gröcke, 2001; Jenkyns *et al.,* 2002a; Price and Gröcke, 2002). Open circles on the belemnite curves represent a 5-pt running median with a 5-pt running mean passing through it. Blue lines as on previous diagrams.

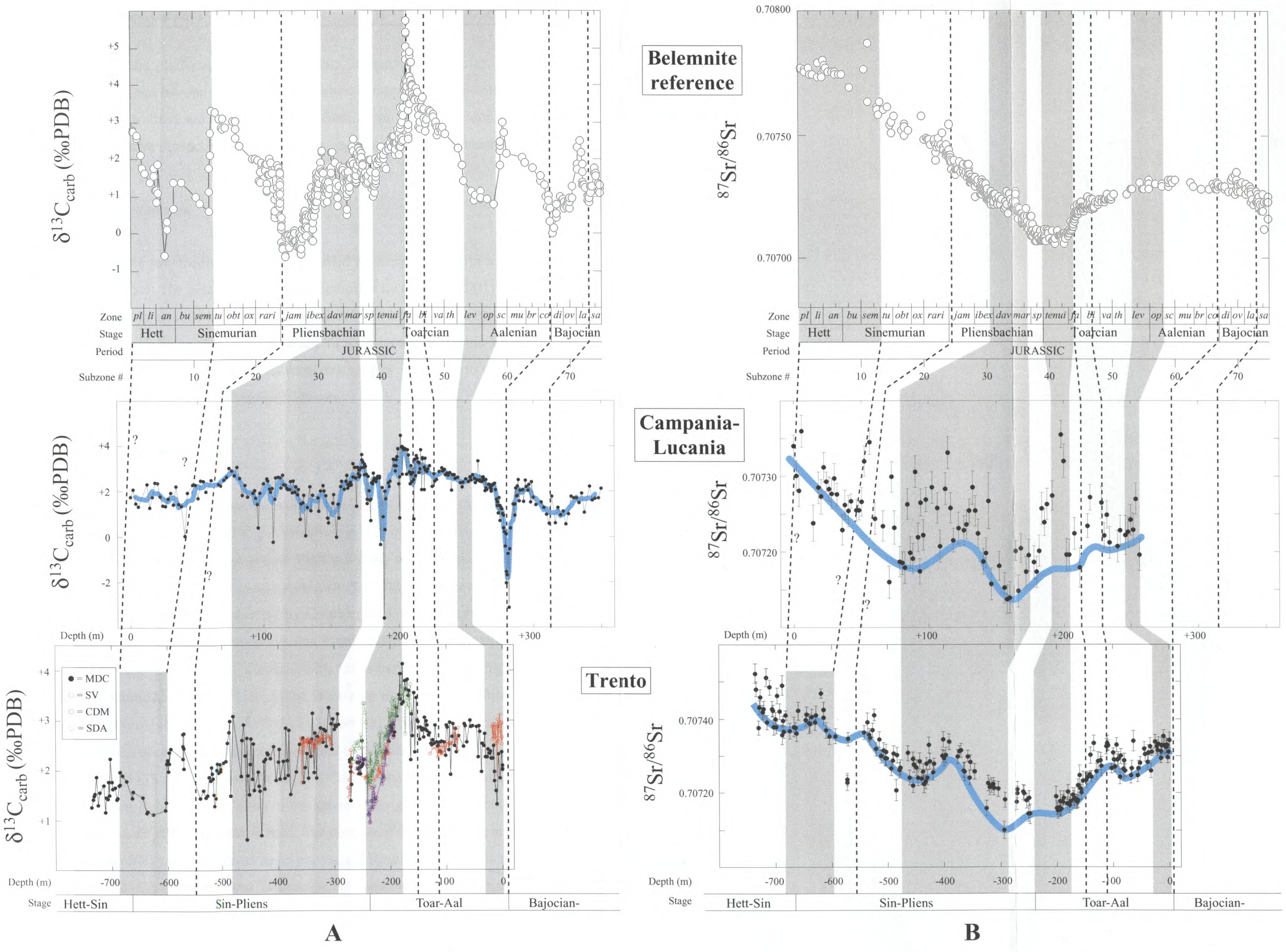

Figure 5.v. **A**. Correlation of the Early–Mid Jurassic carbon-isotope profiles of the Trento and Campania-Lucania Platforms with the carbon-isotope data of belemnites from Jones *et al.* (1994a, b), Parkinson (1994), Podlaha *et al.* (1998), McArthur *et al.* (2000a), Gröcke (2001) and Jenkyns *et al.* (2002a). **B.** Correlation of Early Jurassic strontium-isotope data from the Trento and Campania-Lucania Platforms with that from the same above-listed references. The correlation lines/shaded areas used in **B** are transposed directly from **A**.

isotope curve trends of the platform and belemnite data are strikingly similar. Because the belemnite data do not extend beyond the Albian, this general comparison of profiles cannot be extended further. However, there are more detailed correlations in this chapter (up to sub-zonal level) for intervals with more distinctive isotope profiles, including the Cenomanian–Tertiary.

5.2.1 Trento / Campania–Lucania

Direct correlations are made between Early–Mid Jurassic belemnite and platform-carbonate data in Figure 5.v. The belemnite data were compiled by Gröcke (2001) and Jenkyns *et al.* (2002), after Jones *et al.* (1994a,b), Podlaha *et al.* (1998), McArthur *et al.* (2000a), and Gröcke (2001). As the belemnite data are displayed in a chronostratigraphic matrix, these correlations allow the application of a high-resolution stratigraphy, in places to subzonal level, to the Trento and Campania–Lucania Carbonate Platforms.

5.2.1.1 Low-resolution correlation

Figure 5.v(A) illustrates the carbon-isotope correlations between the belemnite and platform-carbonate data. The first justifiable correlation is that of a negative carbon-isotope excursion observed in the belemnite and Trento Platform data, which is dated as occurring during the *planorbis–semicostatum* Zone (approximately Hettangian–Sinemurian Stages), originally by Jones (1992), and later re-asserted by Gröcke (2001) and Jenkyns *et al.* (2002a). Following this $\delta^{13}C$ negative excursion, belemnite and Trento Platform data illustrate a positive excursion dated as *turneri–obtusum* Zone (Jones, 1992), and a further relatively rapid decrease in $\delta^{13}C$ dated as Sinemurian–Pliensbachian Stage boundary (seen in belemnite data from English, German and Portuguese sections; Jenkyns *et al.*, 2002a). The relatively negative trough in carbon-isotope values, observed in both the Trento and Campania–Lucania Platforms at -300 to -480 m and +75 and +175 m respectively, when correlated to the belemnite data, suggests an age that covers *luridum* Subzone, *ibex* Zone to the *subnodosus–gibbosus* Subzone boundary, and the *margaritatus* Zone (Pliensbachian Stage). The positive $\delta^{13}C$ excursions at the top and bottom (in vertical profile) of this interval have previously been recognised as the *ibex* and *margaritatus* positive $\delta^{13}C$ excursions from Tethyan pelagic sediments and English belemnites

(Jenkyns and Clayton, 1986; Jenkyns, 1988; Jones, 1992; Morettini *et al.*, 2002). Following the *margaritatus*-Zone maximum there is a relative $\delta^{13}C$ minimum in the *spinatum* Zone, latest Pliensbachian (Jones, 1992; Jenkyns and Clayton, 1997; Gröcke, 2001), which is also apparent from the Campania–Lucania and Trento Platform data (the +175 and –270 m levels respectively). This *spinatum*-Zone minimum is immediately followed by a *tenuicostatum*-Zone increase in $\delta^{13}C$, and this trend can be recognised in data obtained from many sections in a range of facies (e.g. Jones, 1992; Jimenez *et al.*, 1996; Jenkyns and Clayton, 1997; Duarte, 1998; Hesselbo *et al.*, 2000; McArthur *et al.*, 2000a; Gröcke, 2001; Jenkyns *et al.*, 2001). The pronounced negative *tenuicostatum–falciferum*-Zone boundary carbon-isotope excursion has likewise been recognised from widely varied locations and facies, and can be identified at the –240 and +185 m levels on the Trento and Campania–Lucania Platforms respectively. The minimum is dated as occurring in the *exaratum* Subzone, *falciferum* Zone, as is the subsequent increase in carbon-isotope values that leads into the positive carbon-isotope excursion (Jenkyns and Clayton, 1997; Hesselbo *et al.*, 2000; Jenkyns *et al.*, 2001). Jenkyns and Clayton (1997) register the $\delta^{13}C$ maximum as *exaratum–falciferum* Subzone boundary, which correlates with the –178 and +200 m levels on the Trento and Campania–Lucania Platforms respectively. Within the Toarcian positive excursion in the belemnite data there are two excursions to relatively depleted $\delta^{13}C$ values. These can both be correlated to similar excursions on the Trento and Campania–Lucania Platforms. The next most obvious belemnite-profile feature that can be correlated with the carbonate-platform chemostratigraphy is that of the Toarcian–Aalenian-boundary minimum. The condensed nature of the Aalenian interval of the Trento platform is well documented, and Sturani (1964) places the Toarcian–Aalenian boundary at only three metres below the contact of the San Vigilio Oolite with the pelagic Rosso Ammonitico (-3 m at the San Vigilio section). The Aalenian–Bajocian boundary negative excursion is another correlatable 'event' seen in both the composite belemnite data and the Campania–Lucania platform carbonates (+281.6 m). However, this feature is not recorded on the Trento Platform due to it having drowned by late Aalenian time. The *laeviuscula–sauzei*-Zone boundary negative excursion is the final correlatable interval between the belemnite data and the Campania–Lucania platform carbonate (+325 m).

In order to help verify the above-described carbon-isotope correlations, the tie-lines/shaded areas were reproduced exactly on the equivalent belemnite and platform strontium-isotope profiles (Figure 5.v(B)). If these $\delta^{13}C$-derived tie-lines are supported by similarities in the trends of the strontium-isotope profiles, this is substantial independent evidence that supports the application of the chronostratigraphic framework onto the Italian platforms. The Hettangian and Sinemurian correlations cannot be unequivocally supported by the strontium-isotope data, because there are no prominent curve inflexions in the belemniite strontium-isotope profile. There are, however, inflexions in the platform-carbonate strontium-isotope curve (saw-tooth), which are not apparent in the reference skeletal-calcite-derived strontium-isotope curves. The most likely explanation for this is that any increase in background clay levels will result in more radiogenic isotope values from analyses of bulk carbonate. However, one major 'saw-tooth' feature is reproducible in reference curves, namely that in the *davoei* Zone (Jones and Jenkyns, 2001). In the *davoei* Zone there is a levelling-off of strontium-isotope values, and even a slight increase until the *davoei–margaritatus* Zone boundary before a further rapid decrease in values during the *margaritatus* Zone. The same feature is clearly recognisable in the strontium-isotope profiles of the Campania–Lucania and Trento Platforms. The second shaded-area tie-point on Figure 5.v(B) (working upsection) corresponds to the *ibex–margaritatus* Zone as shown in the carbon-isotope profiles (see above). After the *ibex–davoei* Zone boundary both the reference and platform-carbonate strontium-isotope profiles flatten (the -478 and +75 m levels on the Trento and Campania–Lucania Platforms respectively), followed by more radiogenic values giving a maximum (the -400 and +130 m levels respectively). This maximum is at the *davoei–margaritatus* Zone boundary, and the ensuing decrease in isotope values occurs during the *margaritatus* Zone (-400 to –300 m and +130 to +165 m levels respectively). Levels –300 and +165 to +175 m on the Trento and Campania–Lucania Platforms are also correlated to the *margaritatus*-Zone positive excursion on the carbon-isotope profiles (Figure 5.v(A)).

The *tenuicostatum–falciferum*-Zone tie-line (shaded) between the belemnite and carbonate-platform carbon-isotope profile also correlates the strontium-isotope profiles relatively well (though data over this interval from both platforms are sparse). The late Pliensbachian–early Toarcian strontium-isotope best-fit profiles compare well with the (Jones *et*

al., 1994b) curve for the same period (i.e. sharp *margaritatus*-Zone fall in values into a *spinatum*-Zone minimum, followed by a *tenuicostatum*-Zone step-up, before a sharp rise in values in the *falciferum* Zone). The sharp *falciferum*-Zone rise in strontium-isotope values, and subsequent inflexion to less steeply rising values, do not appear to correlate closely with the carbonate-platform profiles. However, the $\delta^{13}C$ correlation indicates that there may be a hiatus or condensed interval in the belemnite profile (the tie-lines converge at the *exaratum–falciferum*-Subzone boundary), which has been discussed by previous authors (regarding the Yorkshire reference sections; Jones *et al.*, 1994b; McArthur *et al.*, 2000a; Jones and Jenkyns, 2001; Jenkyns *et al.*, 2002a).

The use of the carbonate-platform strontium-isotope profiles ends with these relatively broad-scale correlations. In general, the strontium-isotope profiles are less useful for high-resolution correlation (c.f. carbon isotopes) given the nature of the broad changes in the curve (and the relative high amounts of scatter observed in samples from the Campania–Lucania Platform). However, the strontium-isotope profiles are of considerable importance in supporting the carbon-isotope and biostratigraphic correlations (especially since they are less prone to diagenetic modification than carbon- and oxygen-isotopes; Jenkyns and Wilson, 1999; McArthur *et al.*, 2000a), and they are also useful in indicating potential stratigraphic gaps or condensed intervals by the nature of the low-frequency curve changes (i.e. rapid shifts are unlikely unless there is a hiatus/condensed level; Jones *et al.*, 1994b; McArthur *et al.*, 2000a; Jones and Jenkyns, 2001; Jenkyns *et al.*, 2002a).

5.2.1.2 High-resolution correlation

In addition to the broad-scale correlations described above (Figure 5.v), where $\delta^{13}C$ profiles are particularly pronounced, distinctive and well described in the literature, more detailed correlations (up to the level of ammonite subzones) of the carbon-isotope profiles can be undertaken. Figure 5.vi illustrates the detailed carbon-isotope profile correlation of the Pliensbachian–Toarcian interval of the Trento and Campania–Lucania Platforms with that of the Mochras-Farm-Borehole (Wales) data of Jenkyns *et al.* (2001). The platform-carbonate data can be correlated with the Winterborne Kingston, Mochras, Hawsker Bottoms and Dogna datasets

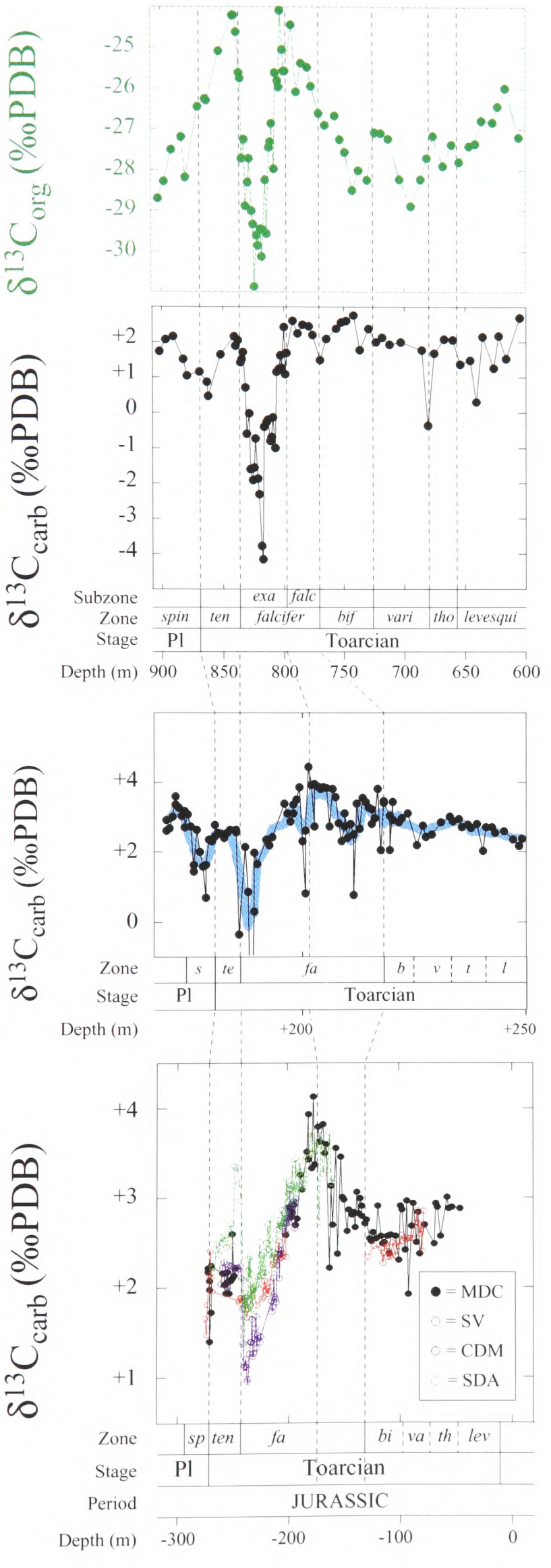

North European reference curves (Mochras Borehole)

Campania–Lucania Platform curve

Trento Platform composite curve

Figure 5.vi. Detailed correlation of Pliensbachian–Toarcian carbon-isotope data of the Trento and Campania–Lucania Platforms with north European carbonate- and organic-$\delta^{13}C$ data of Jenkyns *et al.* (2001).

of Jenkyns *et al.* (2001). Although the Hawsker Bottoms (Yorkshire, England) data are most well-constrained by ammonite biostratigraphy (illustrated in Figure 6.i), the Mochras-Farm-Borehole data are shown in Figure 5.vi because the profile ranges over a reasonably greater stratigraphic interval and illustrates very similar trends to the carbonate-platform profile. The pronounced negative followed by positive excursions are dated as occurring in the *exaratum–falciferum* Subzones, in the *falciferum* Zone of the Toarcian (e.g. Hesselbo *et al.*, 2000; McArthur *et al.*, 2000a; Gröcke, 2001; Jenkyns *et al.*, 2001), and these distinctive excursions are reproduced in the Tethyan shallow-water platform carbonates of this study. Therefore, the dating framework of north European ammonite-subzones of Hawsker Bottoms, Yorkshire can successfully be applied to the poorly constrained shallow-water platform carbonates of Italy.

5.2.1.3 Summary

Figures 5.vii and 5.viii summarise the improvements made to the dating of the Trento and Campania–Lucania Platforms respectively by using chemostratigraphic correlations to other biostratigraphically well-constrained Lower Jurassic sections, as described above. Absolute ages for the Early Jurassic timescale are constrained by Pàlfy *et al.* (2000b). ***Chapter 6*** discusses the application of these correlations (further to the refinement in dating described above), by relating other characteristic facies and proxy changes to physical phenomena witnessed in the carbonate-platform facies.

5.2.2 Friuli / Campania–Lucania

The Late Jurassic–Tertiary carbon- and strontium-isotope profiles of the Friuli and Campania–Lucania Platforms can be correlated to globally distributed deeper-water-facies/belemnite reference curves allowing an ammonite-subzonal biostratigraphic dating framework to be applied to the otherwise relatively poorly constrained platform carbonates.

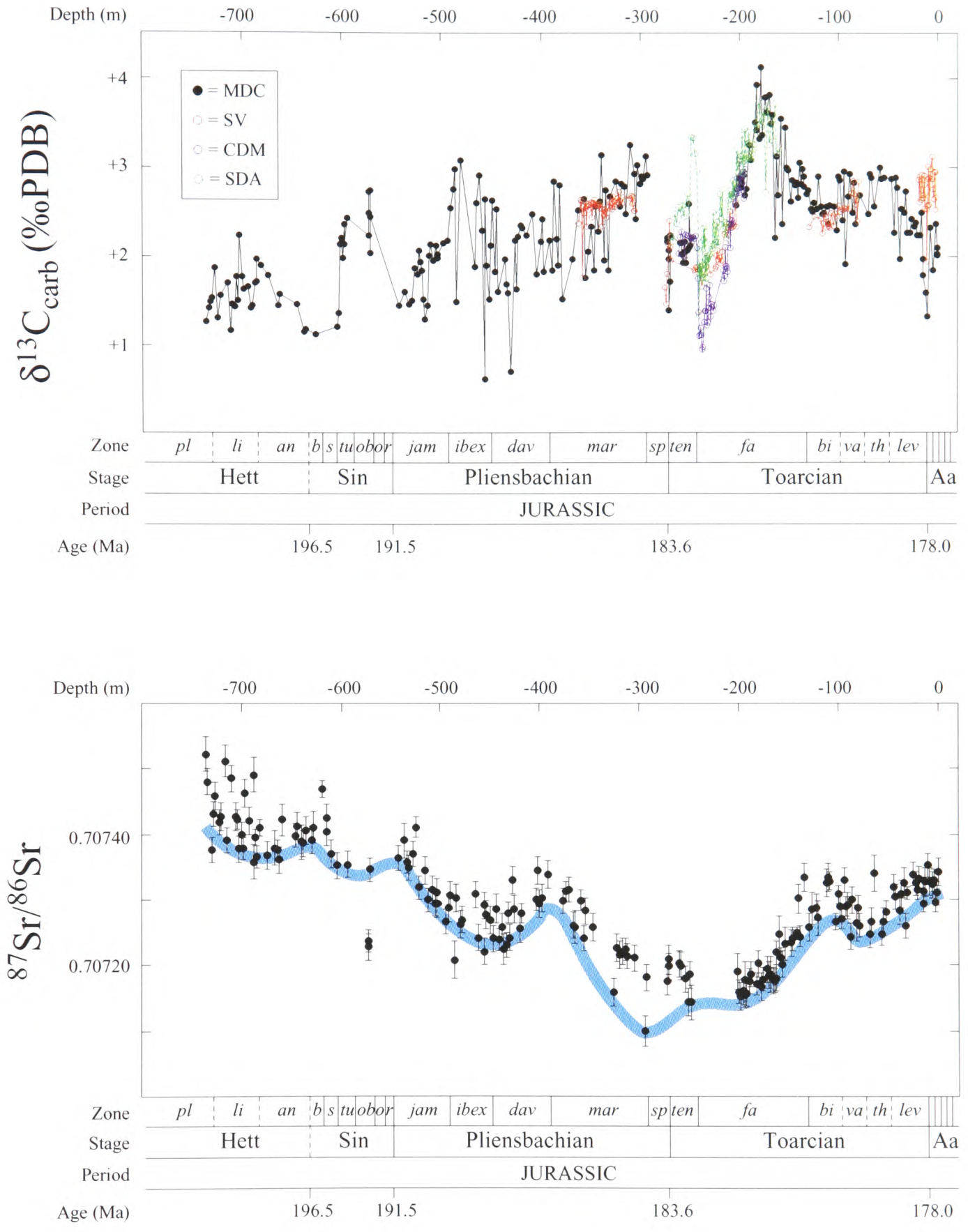

Figure 5.vii. Summary diagram of carbon- and strontium-isotope profiles of the Lower Jurassic of the Trento Platform, which have been chemostratigraphically correlated to biostratigraphically well-constrained sections. The consequent dating agrees with previous biostratigraphic work, but is at higher resolution. Absolute age (Ma) ia after Pàlfy *et al.* (2000b).

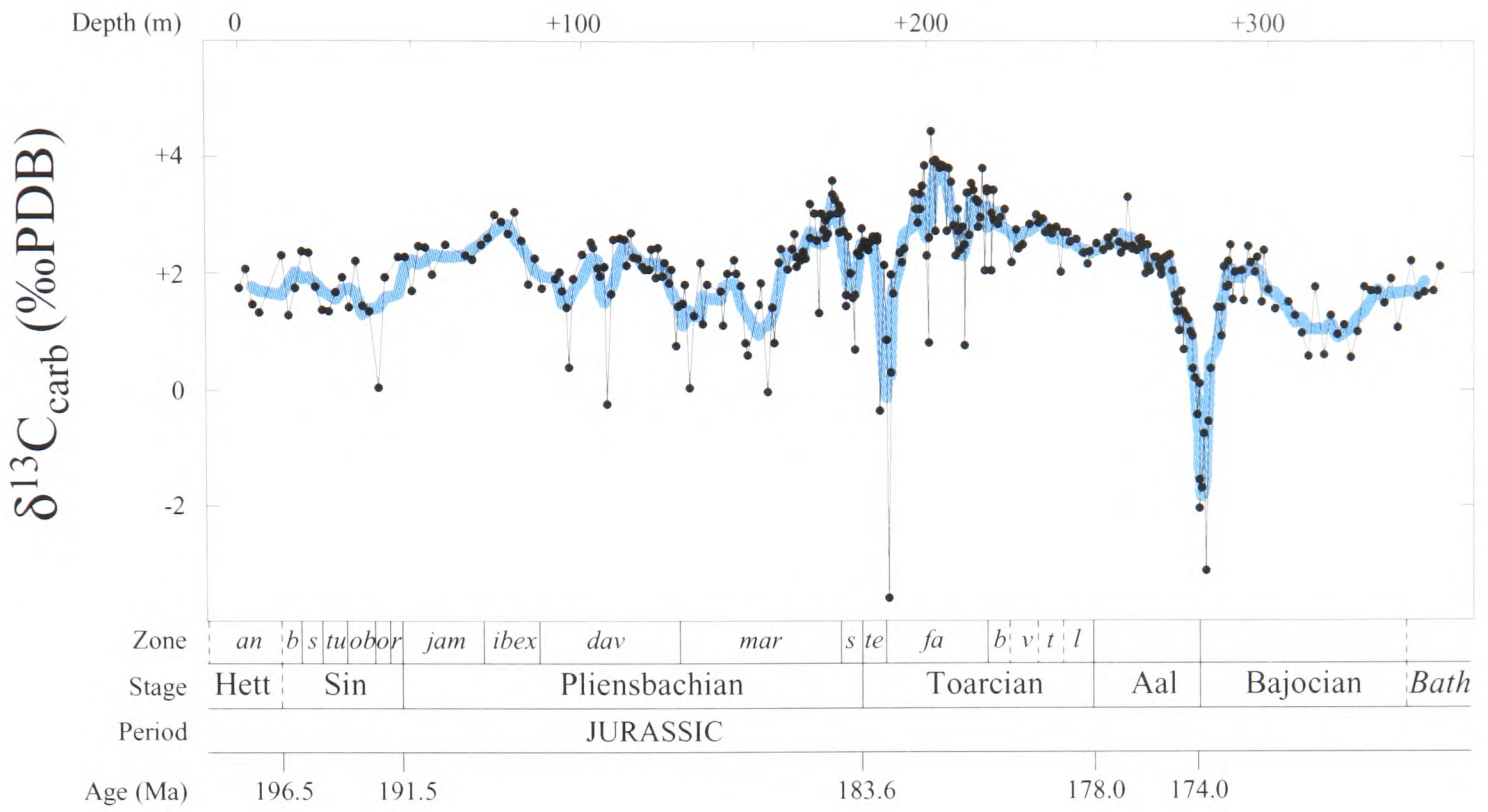

Figure 5.viii. Summary diagram of carbon- and strontium-isotope profiles of the Lower Jurassic of the Campania–Lucania Platform, which have been chemostratigraphically correlated to biostratigraphically well-constrained sections. The consequent dating agrees with previous biostratigraphic work, but at higher resolution. Stage boundary ages are after Pàlfy *et al.* (2000b).

5.2.2.1 Low-resolution correlation

In much the same way as described above, Figures 5.ix(A) and (B) illustrate the carbon- and strontium-isotope data of the Friuli and Campania–Lucania Platforms correlated with selected reference curves compiled from varying sources (particularly distinctive portions of the profiles are also further discussed in detail following the general correlations of Figure 5.ix). The 'belemnite reference' $\delta^{13}C$ curve in Figure 5.ix(A) is modified after Gröcke (2001), who collated data from Jones *et al.* (1994a,b), Podlaha *et al.* (1998), McArthur *et al.* (2000a), and Gröcke (2001), from samples ranging in age from Callovian (Late Jurassic)–Albian (Early Cretaceous). The 'composite reference' carbon-isotope profile assembled from data published by Lini *et al.* (1992), Jenkyns *et al.* (1994), Menegatti *et al.* (1998), Bralower *et al.* (1999), Erba *et al.* (1999) and Voigt (2000) was compiled by Wissler (*pers. comm.).* The Wissler reference curve covers the interval from Berriasian (Early Cretaceous)–Maastrichtian (Late Cretaceous). The strontium-isotope 'composite reference' curve illustrated in Figure 5.ix(B) is modified after Jones and Jenkyns (2001) who compiled data from Hess *et al.* (1986), McArthur *et al.* (1993), Jones *et al.* (1994a,b), and Bralower *et al.* (1997), and covers the interval from Oxfordian (Late Jurassic)–Maastrichtian. The tie-line/shaded area correlations on Figure 5.ix(B) are transposed from Figure 5.ix(A) to help verify these carbon-isotope-based correlations.

The Late Jurassic interval of the Friuli Platform carbon-isotope profile correlates well with the broad, relatively ^{13}C-enriched Oxfordian–Kimeridgian portion of the belemnite reference curve compiled by Gröcke (2001). The Kimmeridgian–Tithonian transition witnesses a decrease in $\delta^{13}C$ and, because the same trend is observed in the Portlandian of the section through the Friuli Platform, this interval can be better constrained. Over the Tithonian–Berriasian, a positive $\delta^{13}C$ excursion is registered in the belemnite data, and this has been tentatively correlated with that observed at the +400 m level in the section through the Friuli Platform (biostratigraphical control is very poor in the Portlandian–Barremian interval in the Friuli Platform). The late Berriasian positive excursion observable in the belemnite curve (but not clearly apparent in the Wissler composite reference curve) is not clearly recognisable, unless it is incorporated into what has been tentatively described as the Tithonian–Berriasian positive $\delta^{13}C$ excursion (possibly due to a condensed interval).

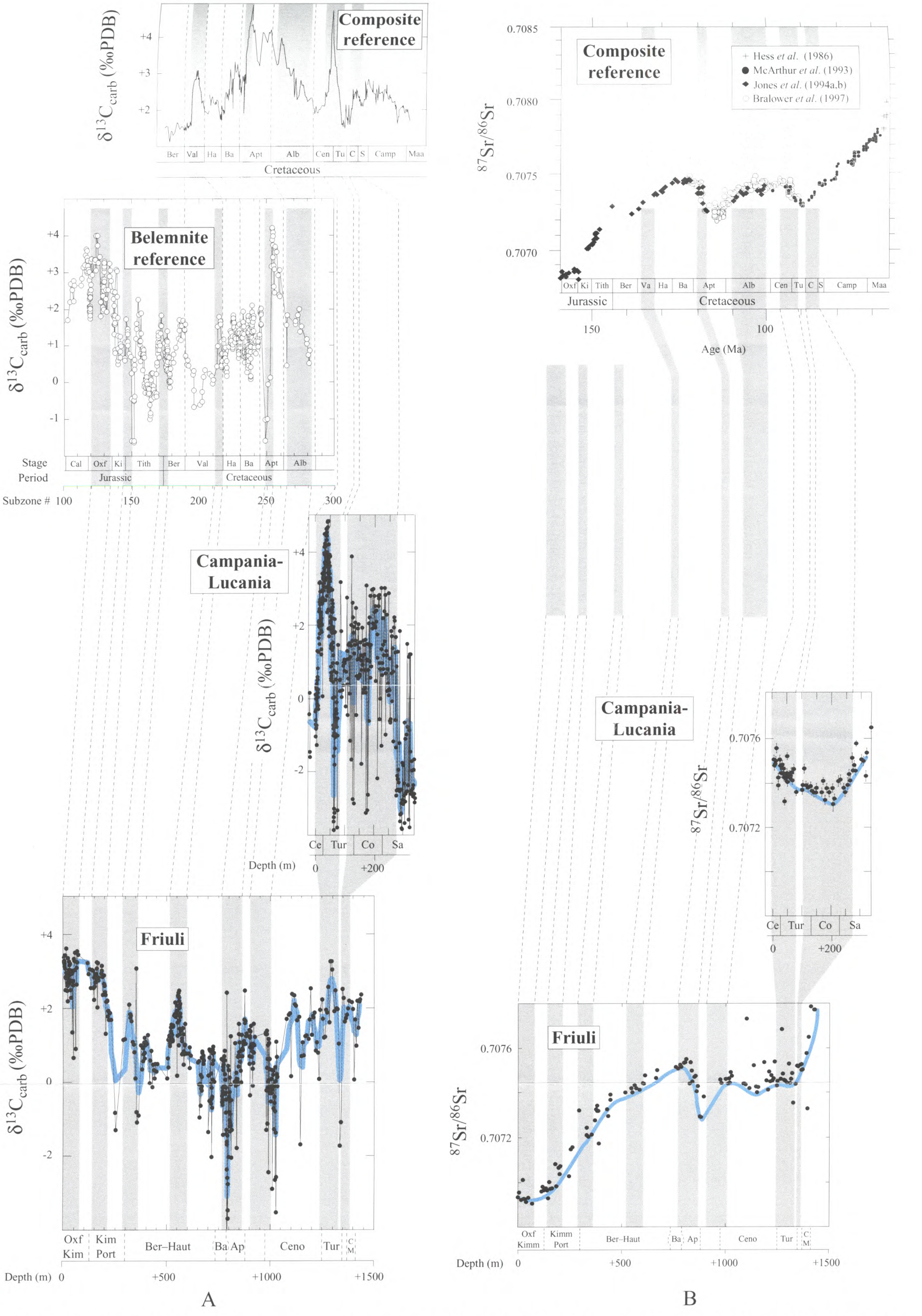

Figure 5.ix. **A**. Correlation of the Late Jurassic-Tertiary carbon-isotope profiles of the Friuli and Campania-Lucania Platforms with: i) belemnite carbon-isotope data of Jones *et al.* (1994a,b), Parkinson (1994), Podlaha *et al.* (1998), McArthur *et al.* (2000a), and Gröcke (2001); ii) various composite $\delta^{13}C$ data compiled by Wissler (2001) from Lini *et al.* (1992), Menegatti *et al.* (1998), Erba *et al.* (1999), Bralower *et al.* (1999), Voigt (2000), Jenkyns *et al.* (1994). **B.** Correlation of Late Jurassic–Tertiary strontium-isotope data from the Friuli and Campania-Lucania Platforms with composite reference data from Jones and Jenkyns (2001). The correlation lines/shaded areas used in **B** are transposed directly from **A**.

The subsequent pronounced positive isotope excursion that reaches a maximum at the +555 m level in the section through the Friuli Platform is very distinctive, and is interpreted to be the Valanginian–Hauterivian excursion as described in detail as a potential global phenomenon associated with regional deposition of black shales (Coplen and Schlanger, 1973; Douglas and Savin, 1973; Robertson and Bliefnick, 1983; Cotillon and Rio, 1984; Patton *et al.*, 1984; Lini *et al.*, 1992; Channell *et al.*, 1993; Weissert *et al.*, 1998; van de Schootbrugge *et al.*, 2000; Bralower *et al.*, 2002). The Valanginian–Hauterivian positive excursion is not well represented in the belemnite data due to extreme condensation in the Cleveland and Volga Basins (England and Russia respectively) at this level, but despite this, a relatively short-duration maximum is still present.

The subsequent most pronounced excursion is the relatively negative isotope value shift that occurs between the +775 and +795 m levels in the Friuli section, which is known to be approximately at the Barremian–Aptian boundary (***3.1.1***). It is reasonable to assume that this isotope shift represents the negative $\delta^{13}C$ excursion of the early Aptian, which is globally reproducible from the marine and terrestrial realms (e.g. Bralower *et al.*, 1998; Menegatti *et al.*, 1998; Erba *et al.*, 1999; Gröcke *et al.*, 1999; Jenkyns and Wilson, 1999; Masse *et al.*, 1999; Jahren *et al.*, 2001; Wissler, 2001). However, given the above, there is no subsequent candidate in the Friuli Platform for the positive carbon-isotope excursion known to occur in the Aptian, which likewise has proved globally reproducible. Values briefly climb as high as those found in the Valanginian–Hauterivian maximum and so, it is possible that this level represents the positive excursion but is so condensed that little record remains. This hypothesis is potentially supported by the presence of a positive excursion in the carbon-isotope record between the +900 and +1000 m levels (which appears to be bounded above and below – in vertical profile – by negative $\delta^{13}C$ excursions). It is possible that this maximum in isotope values registers the presence of the early Albian positive excursion and the negative preceding it could therefore potentially be correlated with the late Aptian negative excursion illustrated in the Wissler composite reference curve (i.e. the data from Mexican hemipelagic sections of Bralower *et al.*, 1999), and also the curves from the Pacific Guyots given by Jenkyns (1995a). The negative excursion above the potential early Albian positive is found in an interval that is dated as early

Cenomanian by biostratigraphic analyses (the +1000 to +1050 m level). This negative excursion would correlate relatively well with the ^{13}C-depleted isotope ratios illustrated by the Wissler compilation for this level.

The positive $\delta^{13}C$ excursion at the +1100 m level in the Friuli Platform section is taken as the mid-Cenomanian positive excursion described from the English Chalk and Italian Scaglia by Jenkyns *et al.* (1994). Both platform and pelagic facies show a subsequent positive excursion (at the +1195 m level and *C.guerangeri* ammonite zone respectively), before a more pronounced positive excursion, which can also be clearly observed in the profile from the Campania–Lucania Platform. Chemostratigraphic profiles ($\delta^{13}C$) from numerous locations indicate that this major four-pronged $\delta^{13}C$ positive excursion (see Figure 5.xiv and 5.xv), discovered in marine and terrestrial records, occurs at the Cenomanian–Turonian Stage boundary (Scholle and Arthur, 1980; Pratt and Threlkeld, 1984; Schlanger *et al.*, 1987; Thurow *et al.*, 1992; Gale *et al.*, 1993; Jenkyns *et al.*, 1994; Hasegawa, 1997; Crespo de Cabrera *et al.*, 1999; Stoll and Schrag, 2000; Voigt, 2000; Jenkyns *et al.*, 2002b). This pronounced isotope maximum is followed by an equally pronounced minimum, before the $\delta^{13}C$ curve rises into a relatively positive broad plateau, dated as Coniacian–Santonian from the Campania–Lucania Platform biostratigraphy (Robson, 1989) and, more reliably, from planktonic biota in pelagic sections (Jenkyns *et al.*, 1994; Stoll and Schrag, 2000). Following a Santonian minimum on the Campania–Lucania Platform, there are few data left to correlate. Data above this $\delta^{13}C$ minimum in the section through the Friuli Platform become very condensed and, with a relatively low sampling density real trends are difficult to discern (n.b. only a 'pilot study' was possible above +1035 m, as the section is now inaccessible).

In order to verify the correlations made using the carbon-isotope profiles, the tie-lines/shaded areas from Figure 5.ix(A) are transposed onto the platform (Friuli and Campania–Lucania) and reference strontium-isotope profiles in Figure 5.ix (B). It is immediately apparent that the broad-scale trends of the increasingly radiogenic strontium-isotope curve for the Oxfordian–Barremian correlate extremely well with the composite profile of Jones and Jenkyns (2001). In a similar fashion, the drop to less radiogenic values in the Aptian is clearly apparent in data from both the carbonate platform and skeletal calcite. In

particular, the very low Oxfordian–Kimmeridgian strontium-isotope values and the relatively radiogenic Barremian–Aptian values (with the marked Aptian inflexion to less radiogenic values) provide firm support for the biostratigraphic and carbon-isotope correlation at these intervals. Consequently, the potentially controversial correlation between the negative carbon-isotope excursion at the +790 m level and the early Aptian negative excursion is supported. However, although the Cenomanian–Coniacian absolute strontium-isotope values of the Friuli Platform are in the correct range to correlate with those of the Albian–Cenomanian reference curve, the Cenomanian–Turonian drop to less radiogenic values is not observed. Instead the profile remains relatively flat from Cenomanian–Coniacian, before a sharp rise to more radiogenic values, which can be correlated to the Late Cretaceous strontium-isotope reference profile (although condensation on the Friuli Platform at this level makes this rise appear very rapid). However, the drop to less radiogenic $^{87}Sr/^{86}Sr$ values observed in the Cenomanian–Turonian interval of the reference profile is observed in the strontium-isotope profile from the section through the Campania–Lucania Platfrom. This distinctive trough feature of the strontium-isotope profile supports evidence from the $\delta^{13}C$ record, that this level in the Campania–Lucania Platform is Cenomanian–Turonian boundary in age.

It is conceivable that diagenetic modification of Cenomanian–Turonian levels in the section through the Friuli Platform has resulted in an increase in strontium-isotope values but with little effect on carbon-isotope values. However, strontium-isotope signals are generally regarded as more resistant to alteration than those of carbon- and oxygen-isotopes (McArthur *et al.*, 2000b). It is also possible that the 'vital effect' of the rudist skeletal debris at this interval has had some unquantifiable effect on the strontium-isotope profile. Generally, however, the carbon-isotope correlations of the carbonates from the Friuli and Campania–Lucania Platforms are supported by both the strontium-isotope profiles and the available biostratigraphy.

5.2.2.2 High-resolution correlation

The Oxfordian–Tithonian, Valanginian–Hauterivian, Barremian–Aptian and Cenomanian–Santonian carbon-isotope profiles of the Friuli and Campania–Lucania Platforms are very distinctive and some of the trends displayed have been globally recognised and

described. It is therefore possible to correlate these intervals at higher resolution than outlined above, and such correlations follow.

Oxfordian–Berriasian

Figure 5.x illustrates the Oxfordian–Berriasian portion of the carbon-isotope profile of the Friuli Platform (as dated by biostratigraphy) correlated with another profile from the same interval of time, but produced from hemipelagic sections of north Tethyan origin (Weissert and Mohr, 1996). First appearances appear to be encouraging in that there are some clear similarities between the two curves. In particular, relatively ^{13}C-depleted isotope values in the Oxfordian Stage (*transversarium* Zone; Weissert and Mohr, 1996) can be loosely correlated, although without complete profiles for the entire Oxfordian, such a correlation could be subject to error. The relatively high $\delta^{13}C$ values at the Kimmeridgian–Tithonian-Stage boundary can be correlated, and these occur below a subsequent depletion in both profiles. The two data-points at the +230 and +245 m levels are extremely negative related to those directly above and below, and their isotope ratios may have been subject to post-depositional modification. However, the relatively high $\delta^{13}C$ values at the Tithonian–Berriasian-Stage boundary have been correlated and, although this is only registered by a single datum point in the North Tethyan section, the correlation is also substantiated by the available biostratigraphy of both sections.

Valanginian–Hauterivian

Figure 5.xi illustrates the detailed correlation between the +500 to +650 m levels (Berriasian–Hauterivian according to the available biostratigraphy) of the Friuli Platform and the Valanginian–Barremian pelagic reference $\delta^{13}C$ profile of Lini *et al.* (1992). The two profiles both display a clear relative maximum in $\delta^{13}C$ followed by a quasi-symmetrical depletion. A subsequent minimum in carbon-isotope values has also been correlated (the +650 m level on the Friuli Platform and Hauterivian–Barremian Stage boundary (*L. bollii* nannofossil zone) of Lini *et al.* (1992).

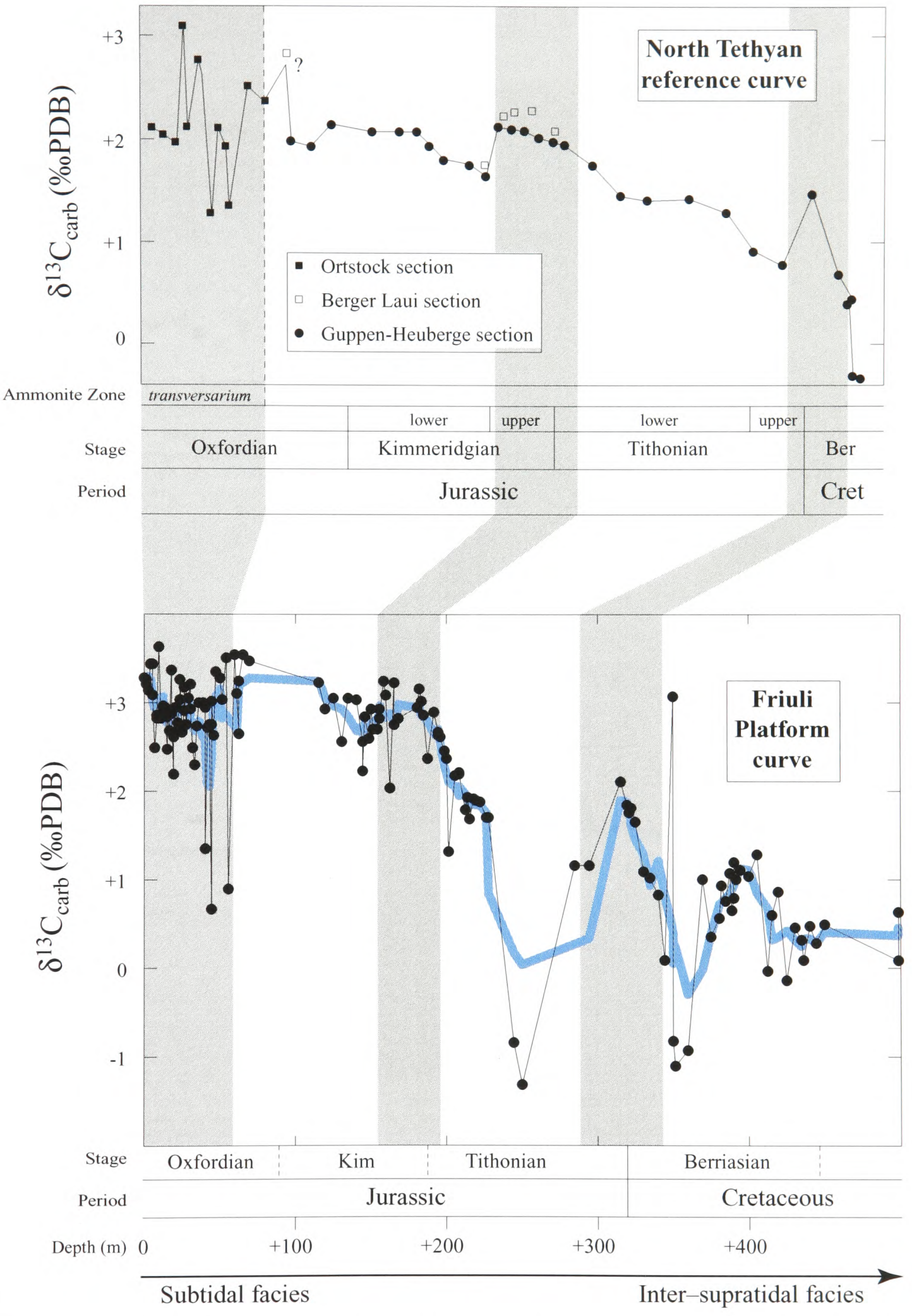

Figure 5.x. Correlation between the reference carbon-isotope profile of north Tethyan hemipelagic sediments (Weissert and Mohr, 1996) and that of the lower 500 m of the Upper Jurassic Friuli Platform section (Val Cellina). Note that the Tithonian–Berriasian correlation is based on the available biostratigraphy for the Friuli Platform.

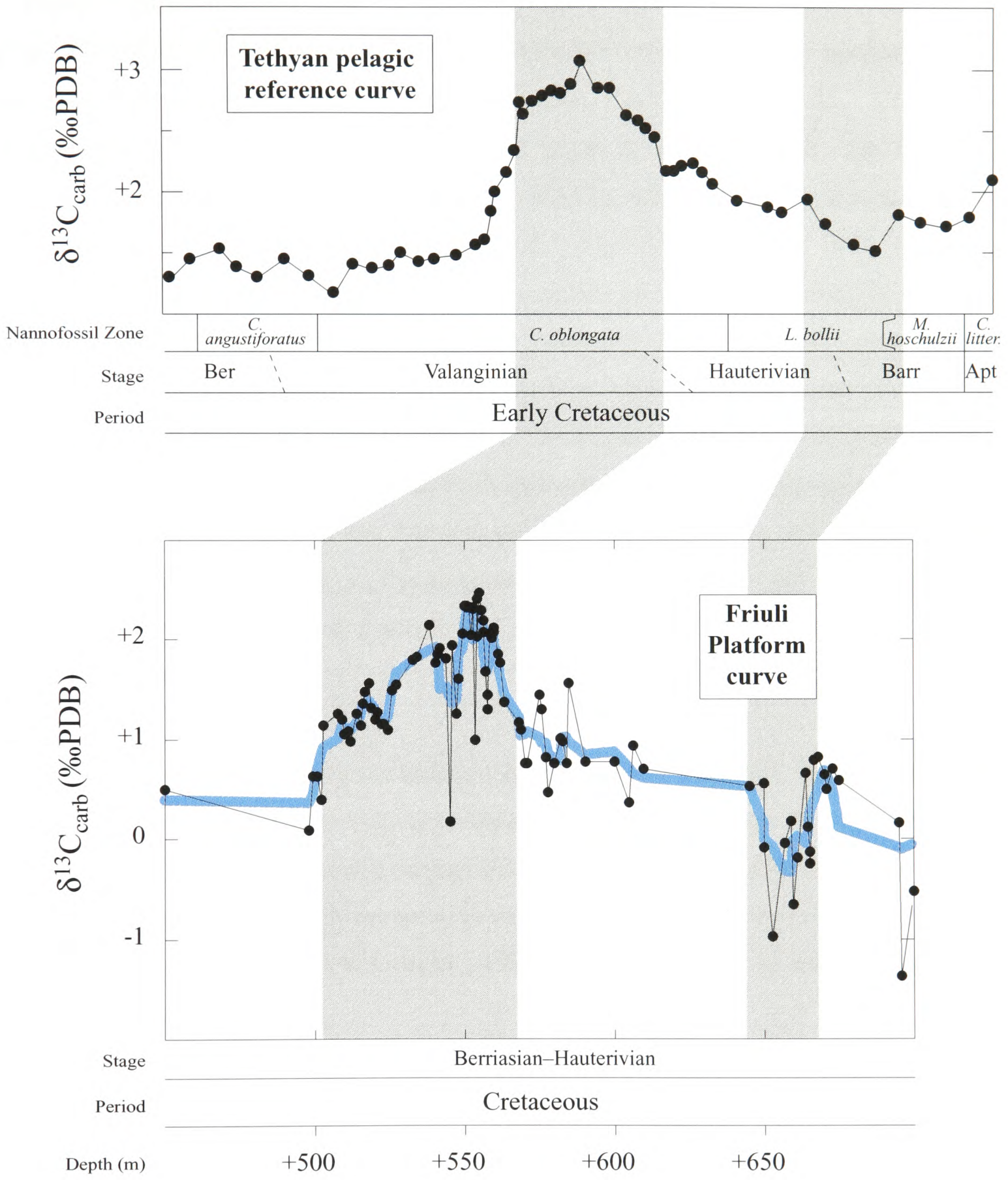

Figure 5.xi. Correlation between the reference Tethyan pelagic carbon-isotope profile of Lini *et al.* (1992) and the carbon-isotope profile of the Lower Cretaceous Friuli Platform section (Val Cellina).

Barremian–Albian

Figure 5.xii illustrates a platform–basin correlation between Barremian–Albian carbon-isotope profiles of the Friuli Platform (crudely dated by biostratigraphy) and a southern Tethyan pelagic reference section (Cismon, Southern Alps, Italy; Erba *et al.*, 1999). The Barremian–Aptian (shaded area) of both profiles appear to correlate well: late Barremian (platform)/early Aptian (Cismon) rise in $\delta^{13}C$, followed by relatively rapid coherent negative isotope value shift, in turn followed by a sharp return to background values and a subsequent gradual depletion in $\delta^{13}C$ values. If correct, this correlation allows the attribution of a notional *G. blowi–L. Cabri* planktonic-foraminferal-zone boundary to the shallow-water platform carbonates, which indicates that the Barremian–Aptian boundary (designated on the Friuli Platform biostratigraphy by the appearance of *S. dinarica*), is positioned slightly too high stratigraphically. However, the nature of the Fiuli Platform profile above this correlated interval does not closely resemble that of the Tethyan pelagic reference curve. Although the Friuli profile exhibits a gradual rise in $\delta^{13}C$, the maximum values obtained are not truly reflective of those observed in the early Aptian positive $\delta^{13}C$ excursions from the reference sections (i.e. attaining values of at least +4 ‰).

It is therefore suggested that the carbon-isotope signal of the Friuli Platform was either 'dampened' over the post-negative-excursion Aptian interval (e.g. because the platform became restricted from the open-marine realm during this period resulting in a locally derived signal affected by processes such as high evaporation and organic-matter decay (Brasier and Green, 1993; Patterson and Walter, 1994; Grötsch, 1998), or alternatively is missing due to the presence of a hiatus in the section.

Cenomanian–Santonian

The biostratigraphically-constrained Cenomanian–Santonian $\delta^{13}C$ profile of the Friuli Platform (Campanian–Tertiary is too condensed and sampling too infrequent for high-resolution correlation) is correlated to the equivalent pelagic reference profile of the English Chalk in Figure 5.xiii. The mid-Cenomanian 'highs' (which follow the Albian–Cenomanian-Stage

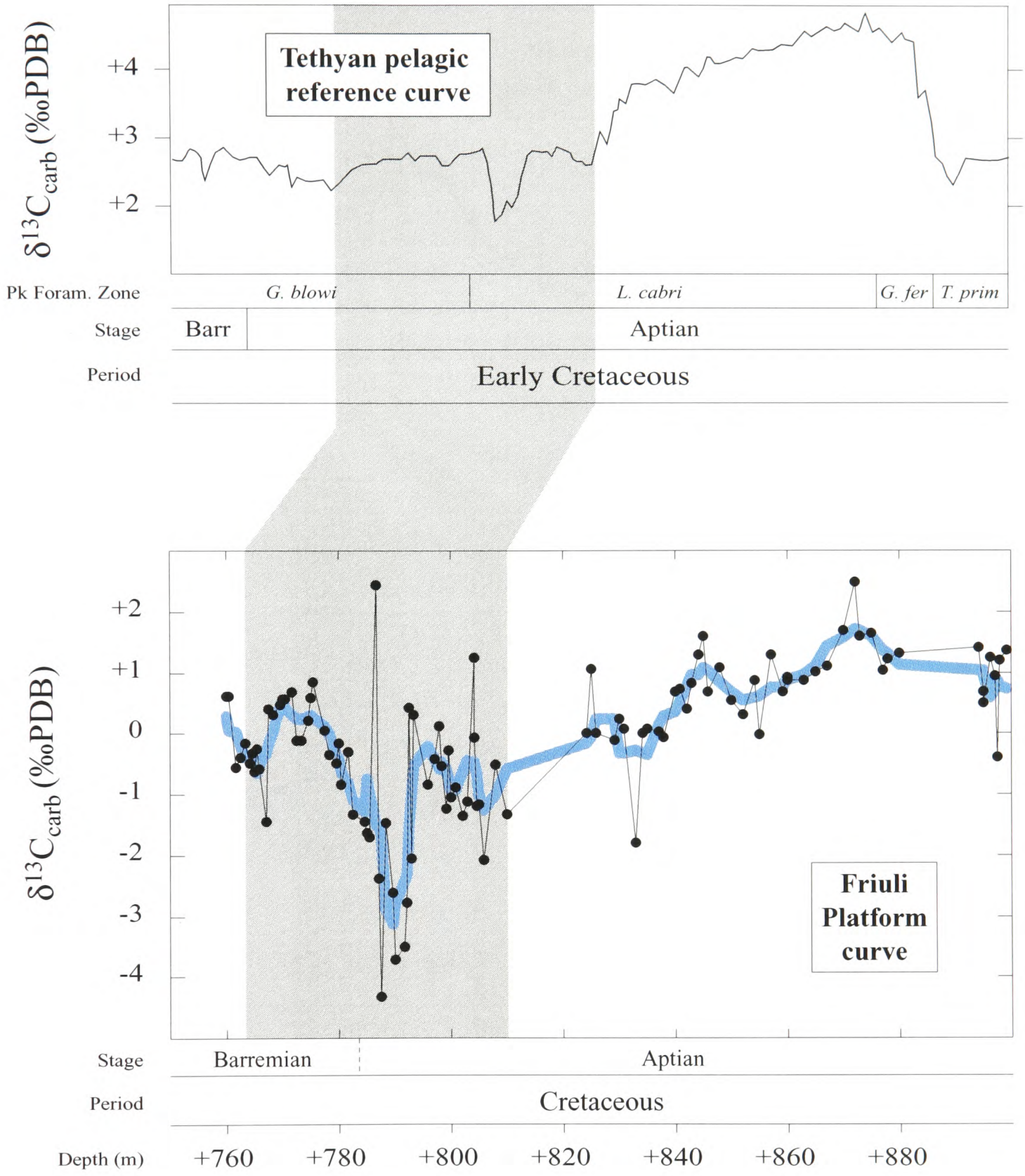

Figure 5.xii. Correlation between the Barremian–Aptian (biostratigraphically constrained) carbon-isotope profile of the Friuli Platform (Val Cellina section) and the Cismon pelagic reference curve of Erba *et al.* (1999).

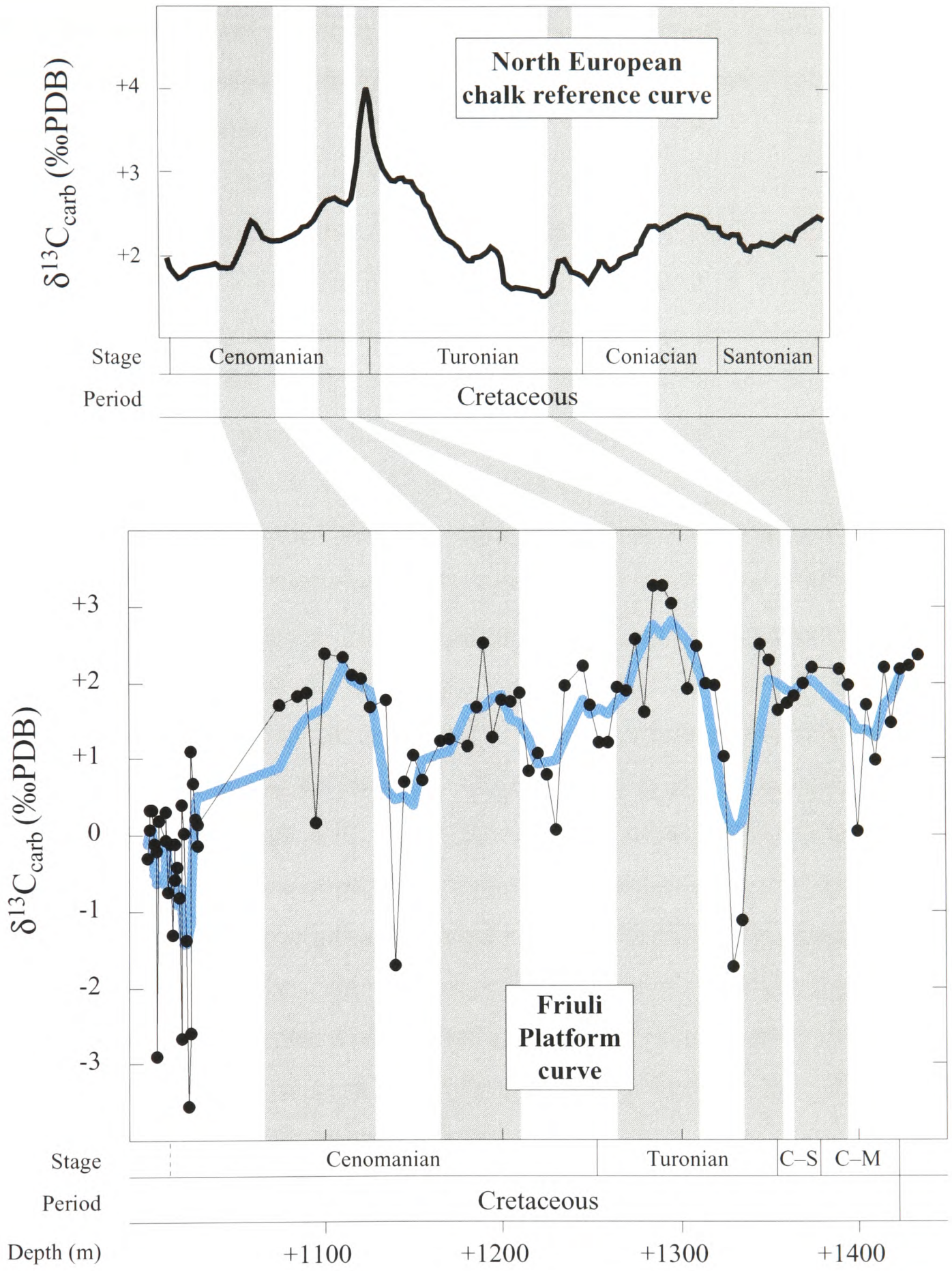

Figure 5.xiii. Detailed correlation of carbon-isotope data from Cenomanian–Tertiary age of the Friuli Platform (dated here with biostratigraphy) with the reference data of Jenkyns *et al.* (1994). C–S = Coniacian–Santonian; C–M = Campanian–Maastrichtain.

boundary 'low') in isotope values are correlated, as are the more minor maxima preceding the major Cenomanian–Turonian positive excursions. The late Turonian positive excursions are correlated on the basis of biostratigraphy, and the Coniacian–Santonian positive plateau is also tentatively correlated, but the few data available at this level in the Friuli Platform make such a correlation relatively unreliable.

Figure 5.xiv illustrates the Cenomanian–Santonian $\delta^{13}C$ correlation of the Campania–Lucania Platform with that of the Chalk reference curve of Jenkyns *et al.*, (1994). The most striking similarity between the two profiles is between the Cenomanian–Turonian positive $\delta^{13}C$ excursion of the Chalk and the positive excursion that has been dated as early Turonian with the available platform biostratigraphy (Robson, 1989). The implication of this chemostratigraphic correlation is that the original Cenomanian–Turonian-Stage boundary placement of Robson (1989) on the Campania–Lucania Platform is approximately 30 m too low stratigraphically. The lack of stratigraphically extensive relatively low $\delta^{13}C$ isotope values immediately above the Cenomanian– Turonian positive $\delta^{13}C$ excursion (compared to the data of Jenkyns, 1994), indicates that the sediments representing this interval of time in the Campania–Lucania Platform may be condensed or contain a hiatus (possibly related to the presence of intraclastic breccias between the +80 and +120 m levels; ***4.1.2*** and ***6.2.6***). The broad plateau of relatively high $\delta^{13}C$ values between the +100 and +280 m levels of the Campania–Lucania Platform is interpreted to represent that observed in the chalk data which initiates in the late Turonian, continues through the Coniacian before dropping to lower $\delta^{13}C$ values in the mid-Santonian. These characteristics and the intervals in which they occur (dated by Robson's (1989) biostratigraphic analyses) are approximately replicated by the data from the Campania–Lucania Platform, although relatively high scatter between the +80 and +300 m levels obscures some of the higher-resolution trends.

Figure 5.xv illustrates a detail of the correlation between the Cenomanian–Turonian positive $\delta^{13}C$ excursions of the Chalk reference profile of Jenkyns *et al.* (1994) and the shallow-water carbonates of the Campania–Lucania Platform. At this scale, the distinctive 'four-pronged' positive excursion (maxima A–D) of the Cenomanian–Turonian boundary reference curves can be correlated in detail, and Figure 5.xv illustrates that even these detailed

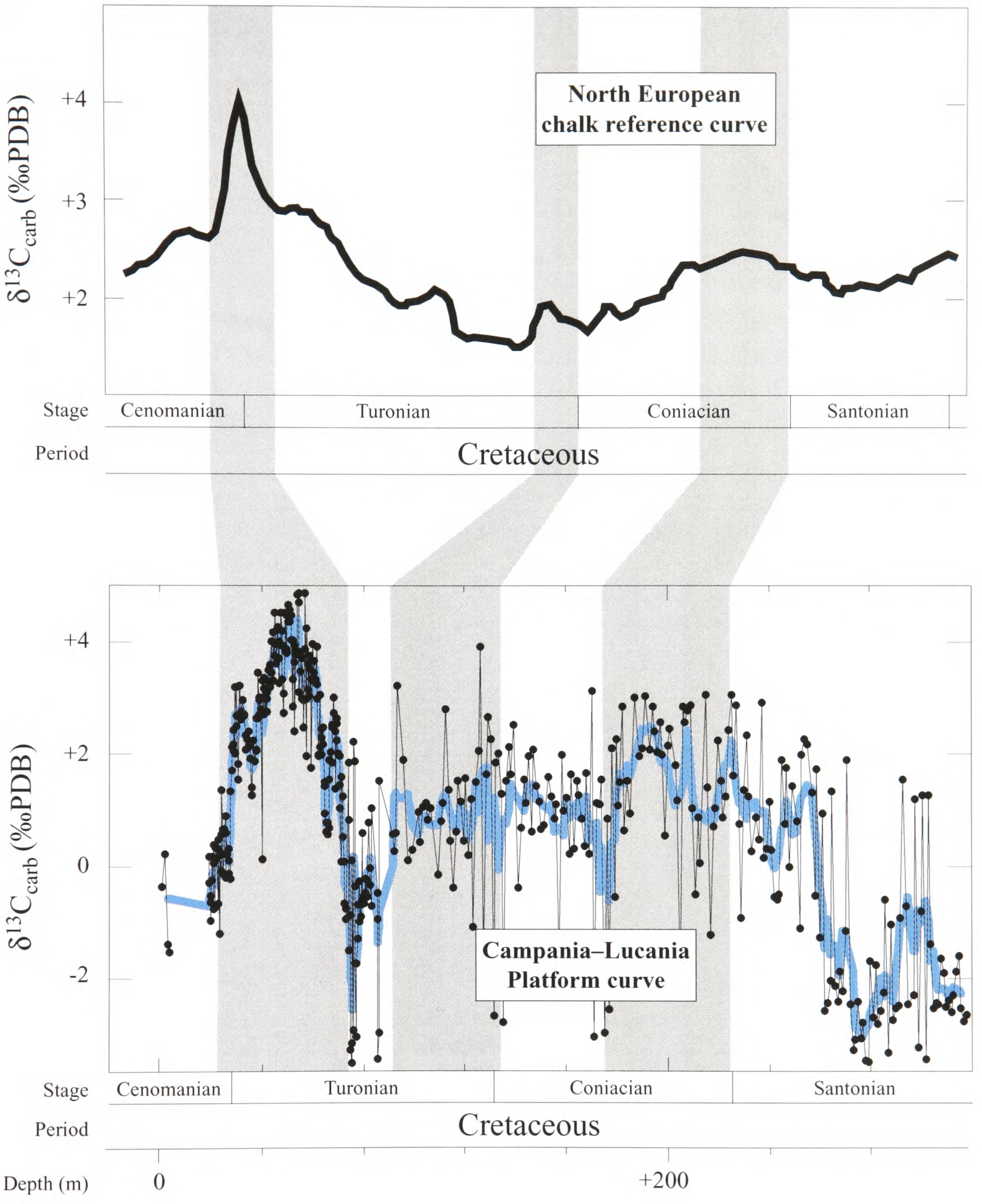

Figure 5.xiv. Correlation of the carbon-isotope profile of the Cenomanian–Santonian of the Campania–Lucania Platform (Raia del Pedale section biostratigraphically dated by Robson, 1989) with the reference data of Jenkyns *et al.* (1994) from the English Chalk.

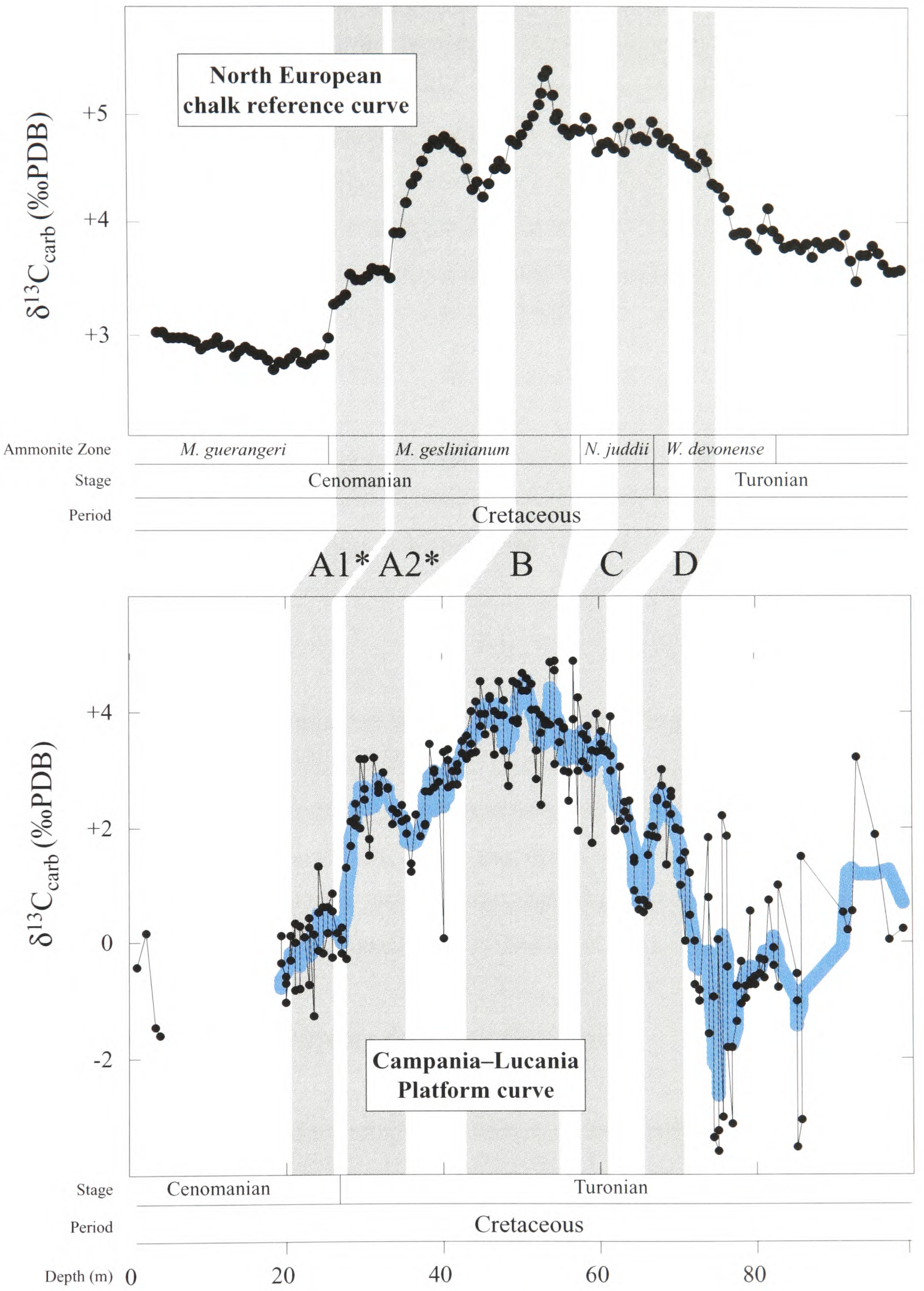

Figure 5.xv. High-resolution carbon-isotope correlation between the shallow-water carbonates of the Campania–Lucania Platform (dated here by biostratigraphy) and the reference chalk profile of Jenkyns *et al.* (2002b). A–D distinguishes the four-prongs of the positive $\delta^{13}C$ excursion of the Cenomanian–Turonian boundary. [* after Jenkyns *et al.* (2002b)].

characteristics are clearly replicated in the platform-carbonate isotope data. Very recently, Jenkyns *et al.* (2002b) have suggested that 'maximum-A' should become 'A2' allowing the addition of a further reproducible maximum: 'A1'. This maximum occurs as a plateau in $\delta^{13}C$ values before the rise into the main excursion, and is here suggested to be present between the +20 and+30 m levels in the Campania–Lucania Platform section (Raia del Pedale). The Cenomanian–Turonian Stage boundary is traditionally placed at the level of the 'C' maximum, which is the *N. juddii–W. devonense* ammonite-zone boundary in northern Europe and the base of the *W. devonense* ammonite zone in North America (Gale *et al.*, 1993; Jenkyns *et al.*, 1994; Kennedy *et al.*, 2000; Jenkyns *et al.*, 2002b).

These correlations therefore result in the ammonite-zone biostratigraphy of northern Europe being applied to the shallow-water Campania–Lucania Platform, which had previously been dated by Robson (1989) only to stage-boundary level.

5.2.2.3 Summary

Figures 5.xvi and 5.xvii summarise the improvements in dating that the application of chemostratigraphic correlations (from reference sections that have been constrained biostratigraphically to the carbonate-platform sections) have made to the Late Jurassic–Tertiary shallow-water carbonate platforms of Italy. Stage boundaries have been re-positioned where chemostratitigraphic analysis indicates that the previous biostratigraphy may be incorrect. Absolute ages in these figures are those determined by Gradstein *et al.* (1995).

5.3 Accumulation rates of Tethyan carbonate platforms

Application of the new chronostratigraphic frameworks to Tethyan carbonate platforms allows calculation of absolute stage-by-stage accumulation rates of their shallow-water carbonate (note that there are no corrections for compaction in this study).

Absolute rates of accumulation for each stage of the platforms studied were calculated and are illustrated in tabular form in Figure 5.xviii. Although it is inevitable that there will be

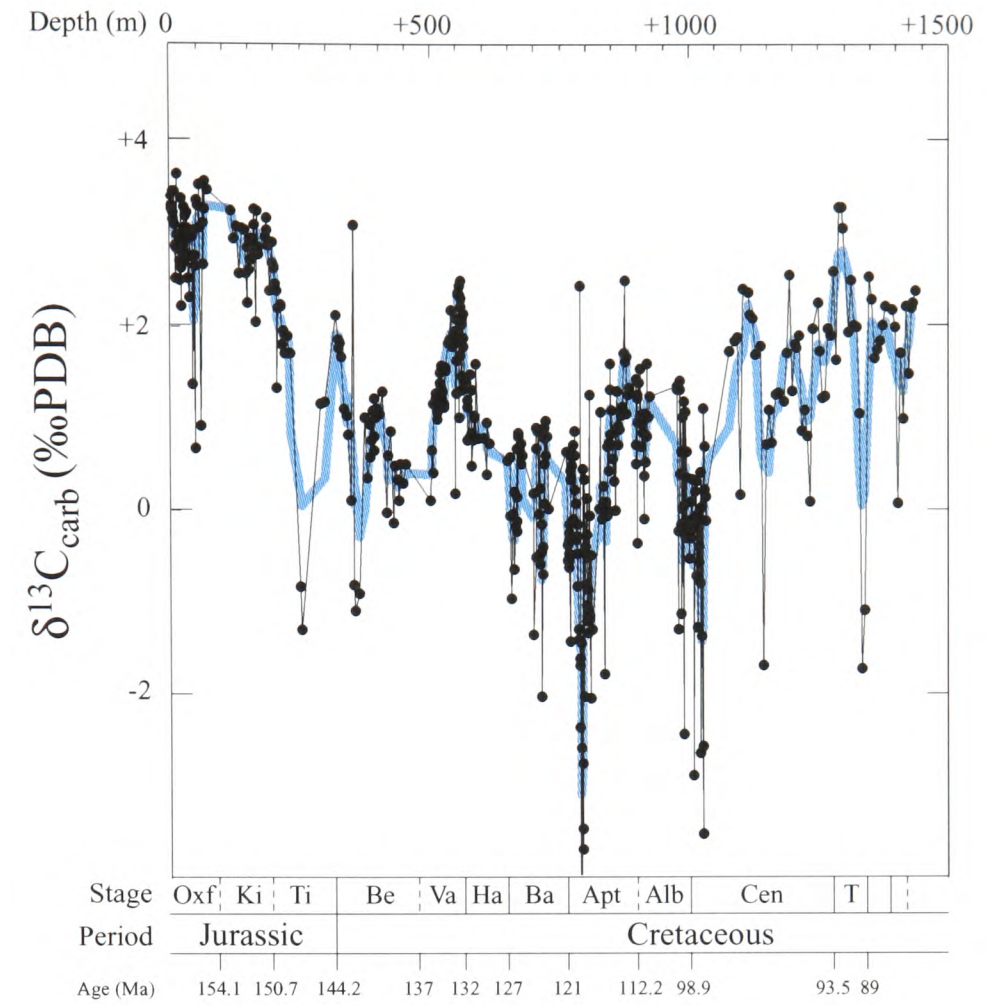

Figure 5.xvi. Summary diagram of carbon- and strontium-isotope profiles of the Upper Jurassic–Tertiary of the Friuli Platform, which have been chemostratigraphically correlated with sections well constrained by biostratigraphy. The consequent dating agrees with previous biostratigraphic work, but at increased resolution. Absolute ages are taken from Gradstein *et al.* (1995).

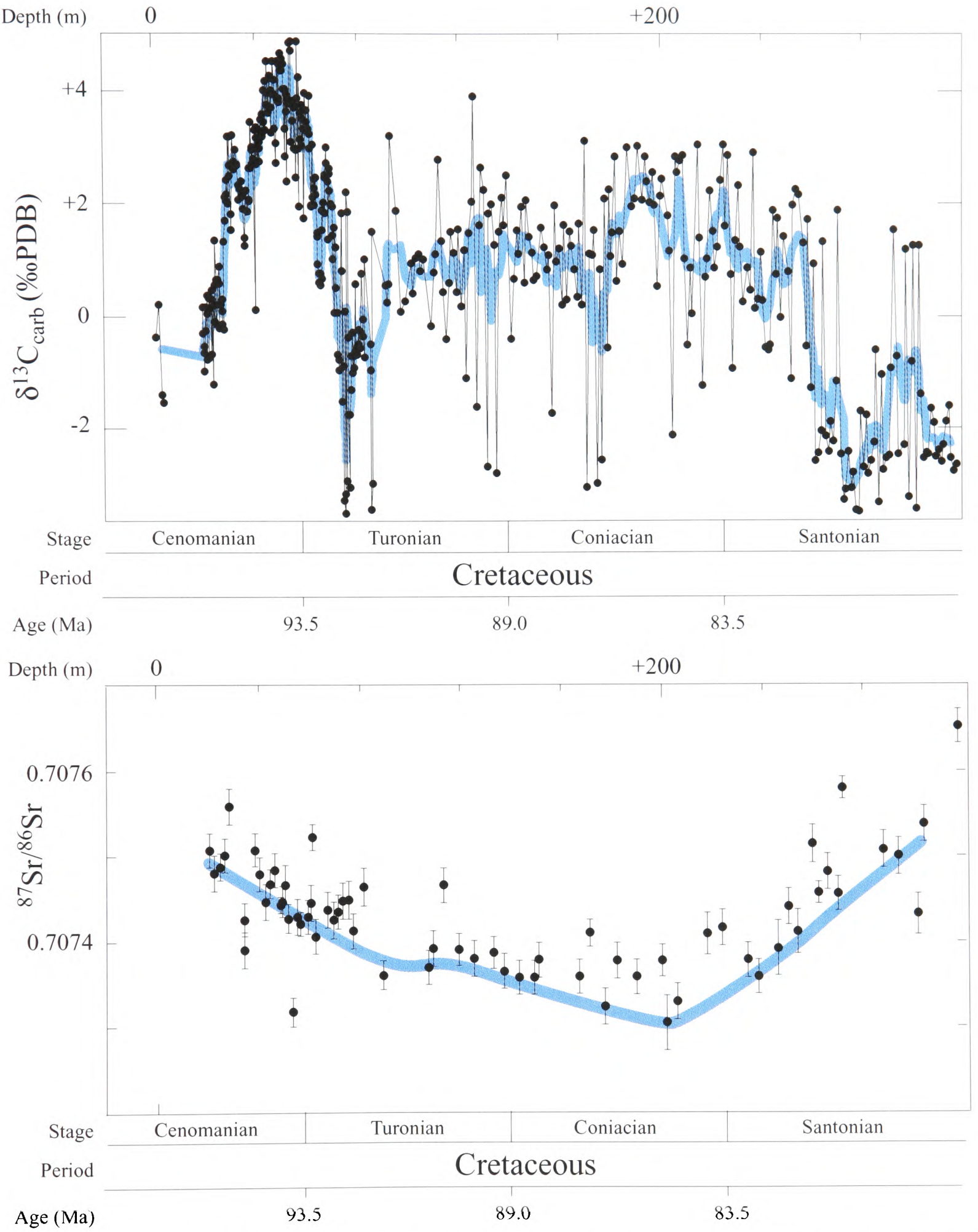

Figure 5.xvii. Summary diagram of the carbon- and strontium-isotope profiles of the Upper Cretaceous of the Campania–Lucania Platform, which has been correlated with a reference section from northern Europe that is biostratigraphically contrained. The consequent improvement in the resolution of dating still broadly agrees with the available shallow-water carbonate biostratigraphy for the section (Robson, 1989). Absolute ages are taken from Gradstein *et al.* (1995).

System	Stage	Age (Ma)*	Italian carbonate platform accumulation rate (m/my)		
			Trento	Campania–Lucania	Friuli
Cretaceous	Maastrichtian	71.3			2
	Campanian	83.5			2
	Santonian	85.8		>43	9
	Coniacian	89.0		25	9
	Turonian	93.5		19	13
	Cenomanian	98.9		>10	52
	Albian	112.2			8
	Aptian	121.0			14
	Barremian	127.0			19
	Hauterivian	132.0			18
	Valanginian	137.0			18
	Berriasian	144.2			22
Jurassic	Tithonian	150.5			19
	Kimmeridgian	154.7			26
	Oxfordian	156.5			?
	Callovian	160.4			
	Bathonian	166.0			
	Bajocian	174.0		?	
	Aalenian	178.0	1	8	
	Toarcian	183.6	48	13	
	Pliensbachian	191.5	35	16	
	Sinemurian	196.5	13	?	
	Hettangian	199.6	?	?	

*Hettangian–Kimmeridgian after Pàlfy *et al.* (2000b). Tithonian–Maastrichtian after Gradstein *et al.* (1995).

Figure 5.xviii. Approximate accumulation rates for the three Italian shallow-water carbonate platforms analysed in this study. 199.6 Ma is the absolute age of the base of the Hettangian Stage. ">" indicates that, where full stages are incompletely exposed, only a minimum accumulation rate can be calculated.

some degree of error associated with these estimated accumulation rates, potentially significant interpretations can be made on carbonate-platfrom accumulation dynamics during periods of global oceanographic change. The rates calculated can also be compared to other platform accumulation rates described in the literature. Bosscher and Schlager (1993) also review Phanerozoic rates of carbonate-platform accumulation in detail, and in summary format; these, and other rates from Schlager (1981) and the individual authors listed, are given below (note that time scale is after Harland *et al.*, 1982):

1) Triassic–Tertiary:
   Apenninic platform = 10–100 m/my (D'Argenio *et al.*, 1975b)
2) Early Jurassic:
   Friuli Platform = 130 m/my (Winterer and Bosellini, 1981)
   Trento Platform = 50 m/my (Winterer and Bosellini, 1981)
   Apennines = 32 m/my (D'Argenio *et al.*, 1975b)
3) Middle Jurassic:
   Apennines = 18.2 m/my (D'Argenio *et al.*, 1975b)
4) Late Jurassic:
   Friuli Platform = 30–45 m/my (Winterer and Bosellini, 1981)
   North Africa = 84.2 m/my (Wilson, 1975)
   Morocco = 89.5 m/my (Ranke *et al.*, 1982)
   Caucasus = 105.3 m/my (Beznosov *et al.*, 1978)
5) Early Cretaceous:
   Friuli Platform = 10–18 m/my (Winterer and Bosellini, 1981)
   Florida = 64.5 m/my (Owens, 1983)
   Bahamas = 25.7 m/my (Goodell and Garman, 1969)
   Middle East = 21.5 m/my (Murris, 1980)
6) Late Cretaceous:
   Mexico (Alb–Cen) = 60–90 m/my (Enos, 1977)
   Latium, Italy (Cen) = 46.2 m/my (Carbone and Sirna, 1981)
   Bahamas = 17.8 m/my (Goodell and Garman, 1969)

Although only given as examples due to the problems of extracting significant global interpretations from regionally influenced systems, the above data correspond relatively well with those accumulation rates calculated for the three platforms in this study: they all fall within the minimum–maximum range of 10–130 m/my. It should be noted that absolute accumulation-rate comparisons of geographically widespread platforms will not always provide significant results because there are so many varying local and regional controls on accumulation rates. Long-term trends show more useful information, but there are problems attaining the necessary degree of resolution and detailed descriptions of the long-lived platforms. However, comparisons with neighbouring platforms, or with accumulation rates obtained for the same platforms from earlier workers, can prove a profitable exercise.

The value of 50 m/my for the Early Jurassic Trento Platform from Winterer and Bosellini (1981) is a very close estimate to 48 m/my calculated here for the Toarcian. However, the average for the Early Jurassic in this study would be lower, because accumulation rates were highest during the Toarcian presumably as a result of prolonged high eustatic sea level and rapid subsidence necessitating rapid rates of accumulation for platform survival (e.g. Hallam, 1981; Winterer and Bosellini, 1981). Indeed, it has been observed that periods with high incidences of platform drowning coincide with highs in accumulation rates (Bosscher and Schlager, 1993; Schlager, 1989). The Campania–Lucania Platform, however, does not share as close a comparison with the 32 m/my accumulation rate suggested by D'Argenio *et al.* (1975b). This is a very general rate, however (including the Hettangian and Sinemurian Stages), and so it is possible that the Monte Sorgenza section is recording an anomalously low value from the average trend obtained for all of the platforms that comprise the 'Apeninnic Platform'. However, from the data calculated by this study alone, it is clear that the Campania–Lucania Platform must have experienced much lower rates of subsidence than the Trento Platform (discounting the effects of off-platform sediment transport) because accumulation rates appear to have been 2–3.5 times lower in the latter (Figure 5.xviii). It is interesting to note that Aalenian accumulation rates show a marked drop on both the Campania–Lucania Platform and on the Trento Platform (***6.1.2***).

Winterer and Bosellini (1981) suggest that the rate of carbonate accumulation for the Friuli Platform during the Late Jurassic was between 30–45 m/my. However, rates calculated in this study for the Friuli Platform reach as high as 26 m/my in the Kimmeridgian (it is possible that they were higher in the Oxfordian), and 19 m/my for the Tithonian. It is possible that decreasing platform accumulation rates at this time are related to falling sea level and other oceanographic/carbon-cycle changes in the Tithonian (Weissert and Channell, 1989). For instance, a fall in sea level could have considerably hindered sedimentation on the Friuli-Platform due to the decrease in available shelf and accommodation space (Weissert and Channell, 1989). Weissert *et al.* (1998) indicate that Tethyan platform growth increased during the Berriasian, before a sharp decrease in accumulation rate during the Valanginian, followed by gradual increase in the rate of platform growth until the latest Barremian. The calculated accumulation rates of this study demonstrate the same trend, because rates decrease from 22 to 18 m/my from the Berriasian–Valanginian, before rising to 19 m/my in the Barremian. Likewise, both the data of this study and that of Weissert *et al.* (1998) show a pronounced drop in carbonate accumulation in the Aptian, and growth of the Friuli Platform went on into further decline in the Albian (whereas other Tethyan platforms showed some recovery). If this discrepancy is real (i.e. if there is no mistake in the ascribed longevity of the Friuli-Platform Albian), it is possible that the Friuli Platform faced other local environmental stresses during this period of time. It is encouraging to note that the 10–18 m/my Early Cretaceous accumulation rate of the Friuli Platform, as suggested by Winterer and Bosellini (1981), is so close to those calculated in this study, which range from 8–22 m/my (Albian and Berriasian respectively).

The Cenomanian carbonate accumulation rate on the Friuli Platform is calculated to be 52 m/my (whereas that on the Campania–Lucania Platform was at least 10 m/my – the Cenomanian is only partially exposed at the Raia del Pedale section). Enos (1977) suggested that the Golden Lane Platform (central Mexico) accumulated at a rate of between 60–90 m/my during the Albian–Cenomanian, which is similar, at its lowest limit, to those calculated for the Friuli Platform at the same interval. Once again, it is likely that for carbonate platforms to survive this period of rising eustatic sea level (i.e. not drown) and widespread oceanographic change, they would need high rates of accumulation (Schlager, 1989; Bosscher and Schlager,

1993). It must also be noted that local changes in subsidence may also play crucial roles in amplifying or dampening the affect of eustatic sea-level change. However, whilst accumulation rates on the Fruili Platform decreased during Turonian–Maastrictian time the Campania–Lucania Platform experienced increasing rates of growth, reaching at least 43 m/my in the Santonian (minimum value given as the Santonian is not fully exposed at the Raia del Pedale section).

In general, the accumulation rates of the Trento, Friuli and Campania–Lucania Platforms that were calculated in this study (as a result of chemostratigraphic dating) agree with those general rates suggested by previous authors. Indeed, even at higher levels of resolution, some of the trends of platform growth and decline described here match very closely those given by previous authors.

5.3.1 Accumulation rates over intervals with pronounced isotope excursions

Where recognised $\delta^{13}C$ excursions (i.e. by correlation) from the carbonate platforms have been constrained using reference sections/profiles, it is possible to calculate estimates for carbonate accumulation rates in very high resolution.

Early Toarcian

In the Yorkshire reference sections for the early Toarcian, the length of time from the beginning of the negative $\delta^{13}C$ excursion until the maximum of the positive $\delta^{13}C$ excursion can be calculated at approximately 175 ky using the 'annual laminae' method adopted by Hesselbo *et al.* (2000). This period of time calculated from the Yorkshire sections is equivalent to an approximately 40-m-thickness of carbonate deposited at the Sega d'Ala on the Trento Platform. This means that the accumulation rate at the Sega d'Ala, during what is predominantly the *exaratum* Subzone, was approximately 230 m/my. The same period of time is roughly equivalent to a 17-m thickness of carbonate in the Monte Sorgenza section of the Campania–Lucania Platform. The accumulation rate for this locality on the Campania–Lucania Platform during the *exaratum* Subzone therefore calculates to be 100 m/my. McArthur *et al.*

(2000) suggest that the duration of the *exaratum* Subzone was 1.1 my, using rates of change of strontium-isotope ratios as a tool for their calculation. If correct, the accumulation rates on the Trento and Campania–Lucania Platforms during the *exaratum* Subzone have to be modified to 35 and 15 m/my respectively. Additionally, if it is assumed that the cyclically bedded Upper Tenno Formation of the Colma di Malcesine section (Trento Platform) is a result of Milankovitch cyclicity on a precessional scale, beds of approximately 20-cm thickness represent approximately 20 ky. Some of these beds appear to be 'bundled' into packages of five (?the first eccentricity mode), each approximately 1-m thick. This formation is clearly exposed between +10 and +36 m in the Colma di Malcesine section (in terms of the $\delta^{13}C$ profile, this represents a segment from just above the *exaratum*-Zone minimum to just below the *exaratum–falciferum* Subzone boundary, or $\delta^{13}C$ maximum). This results in a 2.5-my duration for only a fraction of the *exaratum* Subzone (approximately half in terms of the Jet Rock thickness in the Yorkshire reference sections; Hesselbo *et al*, 2000; Jenkyns *et al.*, 2001). For this duration, calculated using a very basic application of Milankovitch theory, to be correct, the accumulation rate on the Trento Pltaform at this time would have to have been approximately 10 m/my (possible reflecting the 'unhealthy' state of the platform at this time?).

The 230 m/my calculated accumulation rate for the Trento Platform during the *exaratum* Subzone is at the upper limits of possibility for platform-carbonate accumulation (Schlager, 1981). If the *exaratum* Subzone represents a period of eustatic sea-level rise, then the Trento Platform may have been 'forced' to increase input of carbonate to fill the increasingly available accommodation space (and not drown). However, if the Trento Platform is believed to have been 'unhealthy' during this period (as suggested by the facies; ***Chapter 6***), then it is unlikely that carbonate could be produced in such abundance. Therefore, it is more likely that the duration of time calculated for the *exaratum* Subzone using the 'annual laminae' method on the Jet Rock of Yorkshire results in too short a period of time (i.e. the laminae are not annual). Other data suggest that the *exaratum* Subzone lasted longer than 1 my (McArthur *et al*, 2000), and possibly at least 2.5 my (see above). Although the duration of the *exaratum* Subzone may have been underestimated, the negative $\delta^{13}C$ excursion (associated with methane release from clathrates) still appears to be a rapid event (over a 3-m thickness in the Sega d'Ala section on the Trento Platform). Unfortunately the accumulation rate for the Basal Tenno calcareous shales

cannot be estimated. However, assuming that carbonate accumulation rates for the Basal Tenno Formation range between 35–230 m/my (using the McArthur *et al.* (2000) and Hesselbo *et al.* (2000) durations for the *exaratum* Subzone respectively: see above), it is possible to estimate the length of time over which the negative $\delta^{13}C$ excursion occurred. In the Sega d'Ala section, the negative $\delta^{13}C$ excursion initiates between –3 and –2 m, and reaches a minimum at +0.4 m. Therefore, the excursion occurs over between 2.4 and 3.4 m, and this results in a duration of the negative $\delta^{13}C$ excursion of between 10–100 ka. If it is believed that: 1) the 'annual laminae' method of calibrating the Jet Rock gives underestimates in duration calculations; and 2) the Basal Tenno Formation represents a more 'unhealthy' state of the Trento Platform carbonate factory than the Upper Tenno (meaning accumulation rates are more likely to range at the lower limits of calculations that average both Tenno Formation accumulation rates; ***Chapter 6***), it is more likely that the duration of the negative $\delta^{13}C$ excursion is also at the lower limits of the 10–100 ky range. It is therefore still consistent that the negative $\delta^{13}C$ excursion was a relatively 'catastrophic' event, caused by the dissociation of methane from clathrates.

Valanginian–Hauterivian

The duration of the Valanginian–Hauterivian positive $\delta^{13}C$ excursion was estimated by Lini *et al.* (1992) and Channell *et al.* (1993) to be approximately 5 my. This equates to a 100-m thickness of shallow-water carbonate in the Val Cellina section of the Friuli Platform. If correct, these figures mean that carbonate was accumulating at a rate of 20 m/my in this area of the Friuli Platform during that time. This figure is consistent with stage-by-stage accumulation rate calculations for the Lower Cretaceous of the Friuli Platform (Figure 5.xviii), which is further evidence that the Friuli Platform was relatively unaffected by changing oceanographic conditions during the Valanginian–Hauterivian (and the rest of the Early Cretaceous).

Early Aptian

Cyclostratigraphic analysis of the Selli Black Shale in the Umbria–Marche Basin of Italy led Fiet (2000) to estimate that the period of time represented by this level is approximately 400 ky. However, it is difficult to correlate to a 'Selli-equivalent' level in the Val Cellina section of

the Friuli Platform, as the $\delta^{13}C$ isotope signal appears not to register the 'open-ocean' signal that can be identified in reference sections. Assuming that the length of time represented by the negative $\delta^{13}C$ excursion associated with the 'Selli Event' (*G. blowi* Zone) is a fraction of the 400 ky estimated for the black shale, it is possible to grossly estimate an accumulation rate for the Friuli Platform in the early Aptian. By extrapolation, the negative $\delta^{13}C$ excursion of the Cismon reference section appears to be equivalent to approximately one tenth of the thickness of the black shale, and so approximately 40 ky (Menegatti *et al.,* 1998). The $\delta^{13}C$ excursion in the Val Cellina section is over a 25-m thickness of platform carbonate (+770 to +795 m), and so an accumulation rate of 625 m/my is calculated. Because this accumulation rate far exceeds what is reasonable for a shallow-water carbonate platform (Phanerozoic maximum ~ 2–300 m/my; Schlager, 1981), the same calculation can be applied working 'backwards': what length of time is reasonable to accumulate 25 m of carbonate within the accumulation rate limits of 20–200 m/my? This process results in a duration for negative $\delta^{13}C$ excursion to range between 0.1–1 my. The shift to more negative values in the excursion occurs over a 15-m thickness of carbonate in the Val Cellina, which equates to 75–750 ka.

However, working with so much uncertainty regarding the lower Aptian interval of the Val Cellina section of the Friuli Platform, inputs for the calculations on accumulation rates/durations are prone to a high degree of error, and so results are of very limited significance.

Cenomanian–Turonian

There is a range of estimated durations in the literature for the "Cenomanian–Turonian Boundary Event": from 0.25 to 0.8 my (Paul *et al.,* 1994 and Arthur *et al.*, 1988 respectively). However, the most often calculated duration is that of between 0.4–0.5 my (e.g. Arthur *et al*, 1988; Kuhnt *et al.,* 1990; Caron *et al.*, 1999; Paul *et al.*, 1999). The positive $\delta^{13}C$ excursion associated with the Cenomanian–Turonian boundary is found between the +20 and +70 m levels of the Raia del Pedale section, Campania–Lucania Platform. Therefore, the estimated accumulation rate for shallow-water carbonates on the Campania–Lucania Platform at this time is approximately 100–125 m/my. This accumulation rate is relatively high on comparison with

the stage-by-stage estimates calculated for the Campania–Lucania (and Friuli) Platform during the Cenomanian–Santonian (Figure 5.xviii), but with indications of flooding (planktonic foraminifera) it is likely that accumulation rates increased at Cenomanian–Turonian boundary time to match an increase in accommodation space.

Figure 5.xix summarises the accumulation rates calculated for the major $\delta^{13}C$ excursion intervals identified in each of the shallow-water carbonate platforms:

	Italian carbonate platform accumulation rate (m/my)		
$\delta^{13}C$ excursion interval	**Trento**	**Friuli**	**Campania–Lucania**
early Toarcian (*exaratum)*	35–230		15–100
Valanginian–Hauterivian		20	
early Aptian		(?625)	
Cenomanian–Turonian			100-125

Figure 5.xix. Accumulation rates over recognised $\delta^{13}C$ excursions for the shallow-water carbonate platforms studied. Durations of $\delta^{13}C$ excursions are taken from estimations suggested in the literature (see text).

Chapter 6: Carbonate platform response to global change

Chapter 6: The response of carbonate platforms to periods of major oceanographic change

6.1 $\delta^{18}O$ as a proxy for palaeotemperature

The oxygen-isotope ratio ($\delta^{18}O$) of skeletal calcite (e.g. foraminifera, belemnites, bivalves) is dependent upon the temperature of the water from which it is precipitated, but it is also controlled by the $\delta^{18}O$ ratio of seawater (dependent on global ice volume and the Precipitation-Evaporation (P-E) balance of the local water mass); vital effects of the precipitating organism; and variations in pH and alkalinity (e.g. Urey, 1947; Emiliani, 1954; Klein *et al.*, 1997; Spero *et al.*, 1997; Clarke and Jenkyns, 1999; Crowley and Zachos, 2000; Pearson *et al.*, 2001; Wilson *et al.*, 2002). Post-depositional modification of the shell material may also affect primary isotope ratios, and it is with relative ease (compared to other isotopic systems) that $\delta^{18}O$ signals are altered due to the high ratio of oxygen in pore-fluid (H_20) to oxygen in primary carbonate (CO_3).

There is a paucity of reliable and high-resolution palaeotemperature data for Jurassic–Cretaceous OAE's and other relatively minor perturbations in the global carbon cycle. However, palaeotemperature data from belemnites (Mg/Ca and $\delta^{18}O$) taken from the Pliensbachian–Toarcian interval has allowed speculation on palaeotemperature trends during this period (Jones, 1992; McArthur *et al.*, 2000a; Bailey *et al.*, 2001; Gröcke, 2001; Rosales *et al.*, 2001; Jenkyns *et al.*, 2002a). Because there is a regional coherence between two independent palaeotemperature proxies (from two localities: northwest Europe and Spain), interpretations based on the data can be more confident (***6.2.1***).

Figures 6.i, 6.ii, 6.iii and 6.iv illustrate $\delta^{18}O$ profiles of shallow-water carbonates from sections through the Trento Platform (***2.2.3*** and ***2.3***). The $\delta^{18}O$ profile of Madonna della Corona illustrates a relatively coherent increase follow by decrease in $\delta^{18}O$ values over the Pliensbachian–Toarcian Stage boundary (Figure 6.i). Assuming that the $\delta^{18}O$ signal represents

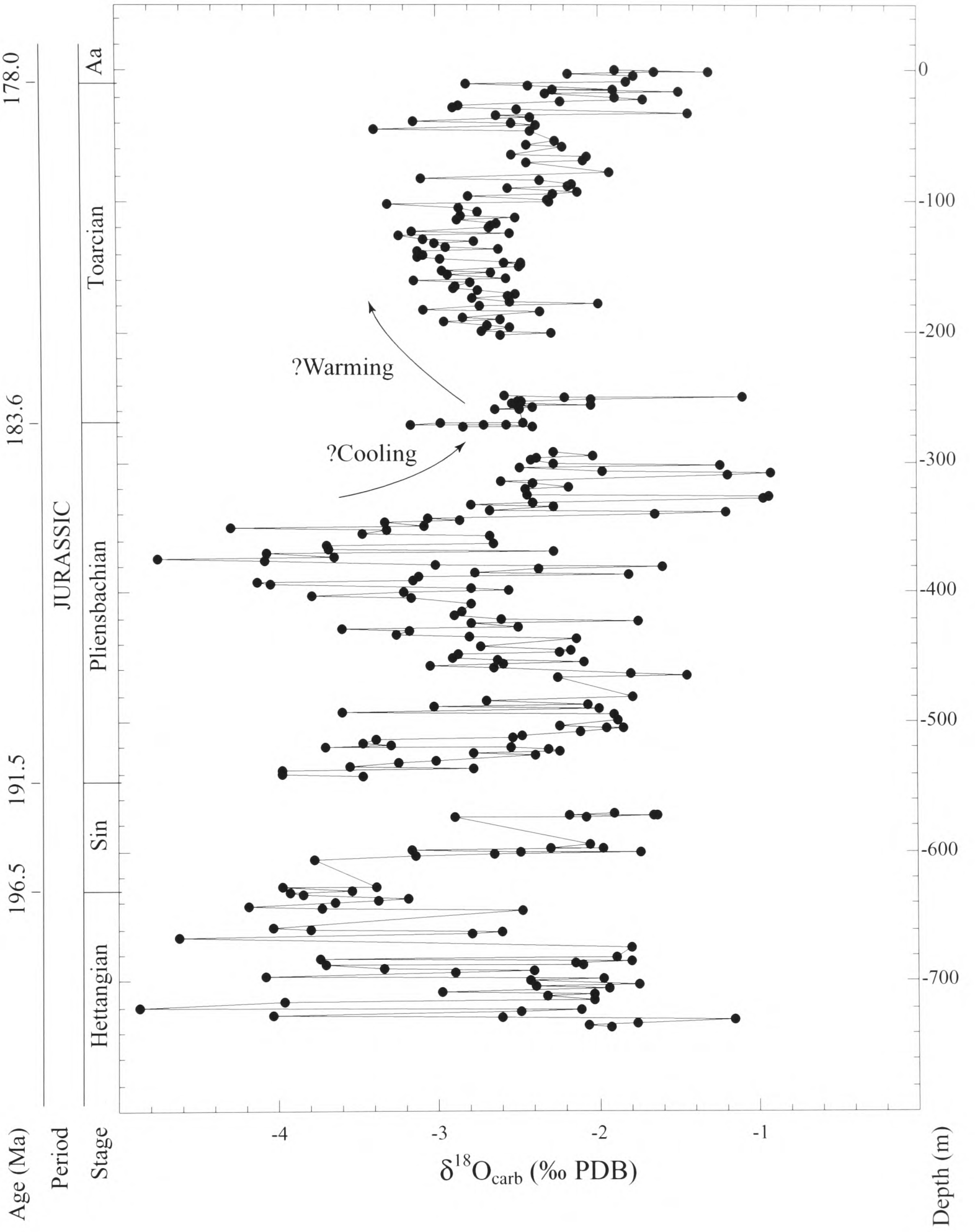

Figure 6.i. Oxygen-isotope profile of the Madonna della Corona section, Trento Platform. Ages are inferred from chemostratigraphic correlation (see Chapter 5). Interpretations on significant palaeotemperature trends are indicated with arrows. Age (Ma) after Pàlfy *et al.* (2000b).

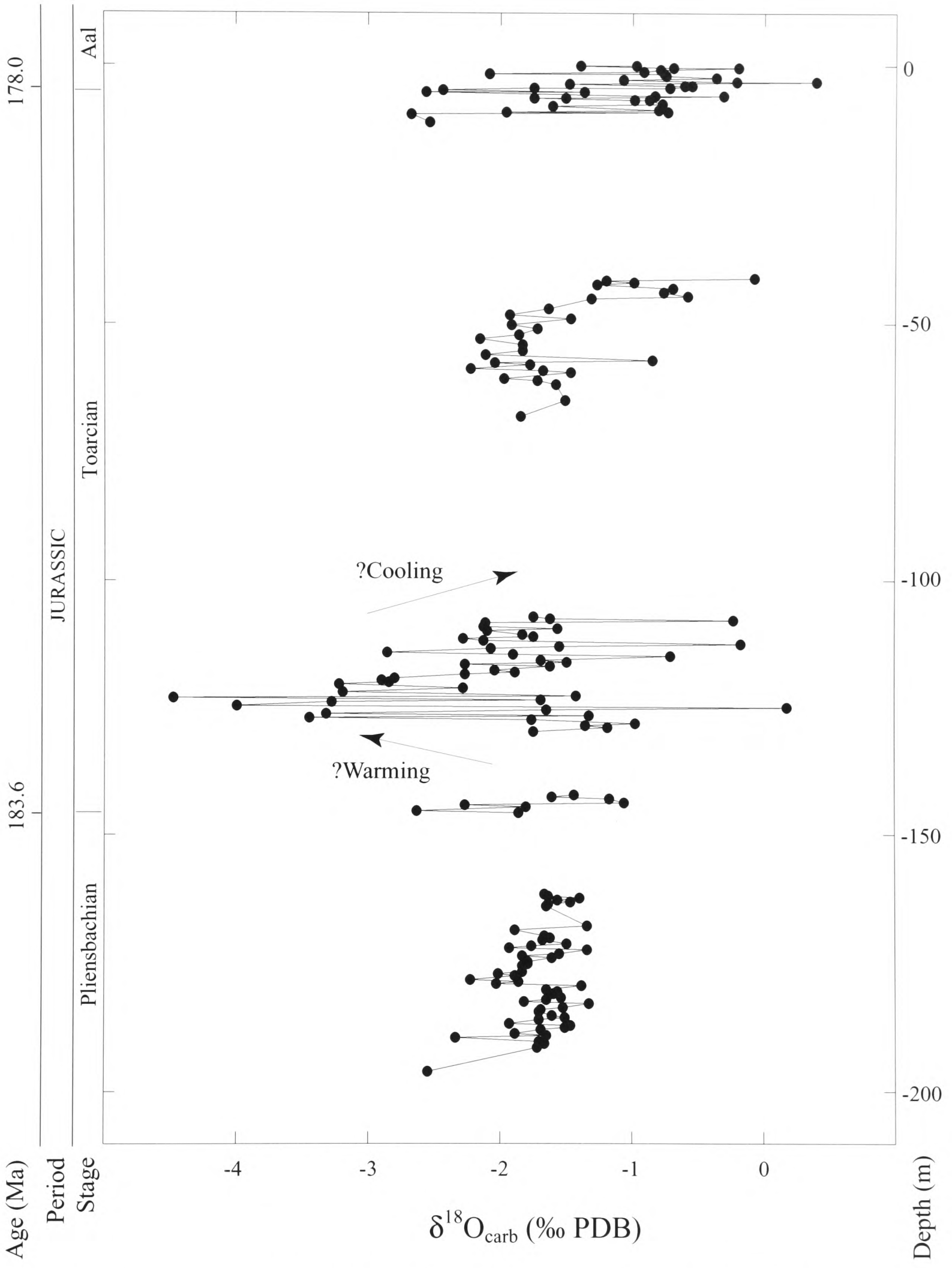

Figure 6.ii. Oxygen-isotope profile of the San Vigilio section, Trento Platform. Ages are inferred from chemostratigraphic correlation (see Chapter 5). Interpretations on significant palaeotemperature trends are indicated with arrows. Age (Ma) after Pàlfy *et al.* (2000b).

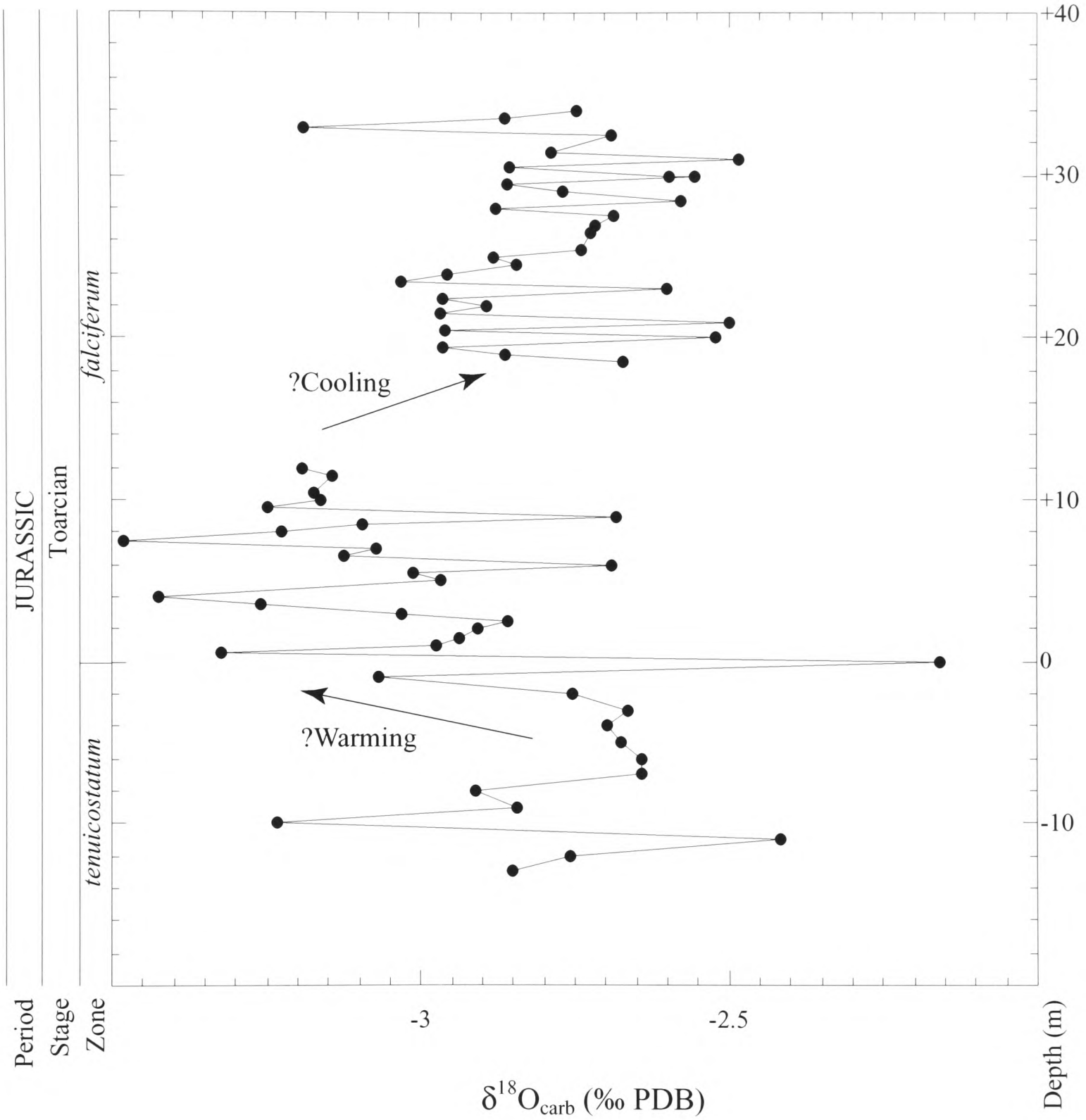

Figure 6.iii. Oxygen-isotope profile of the Colma di Malcesine section, Trento Platform. Ages are inferred from chemostratigraphic correlation (see Chapter 5). Interpretations on significant palaeotemperature trends are indicated with arrows. Age (Ma) after Pàlfy *et al*. (2000b).

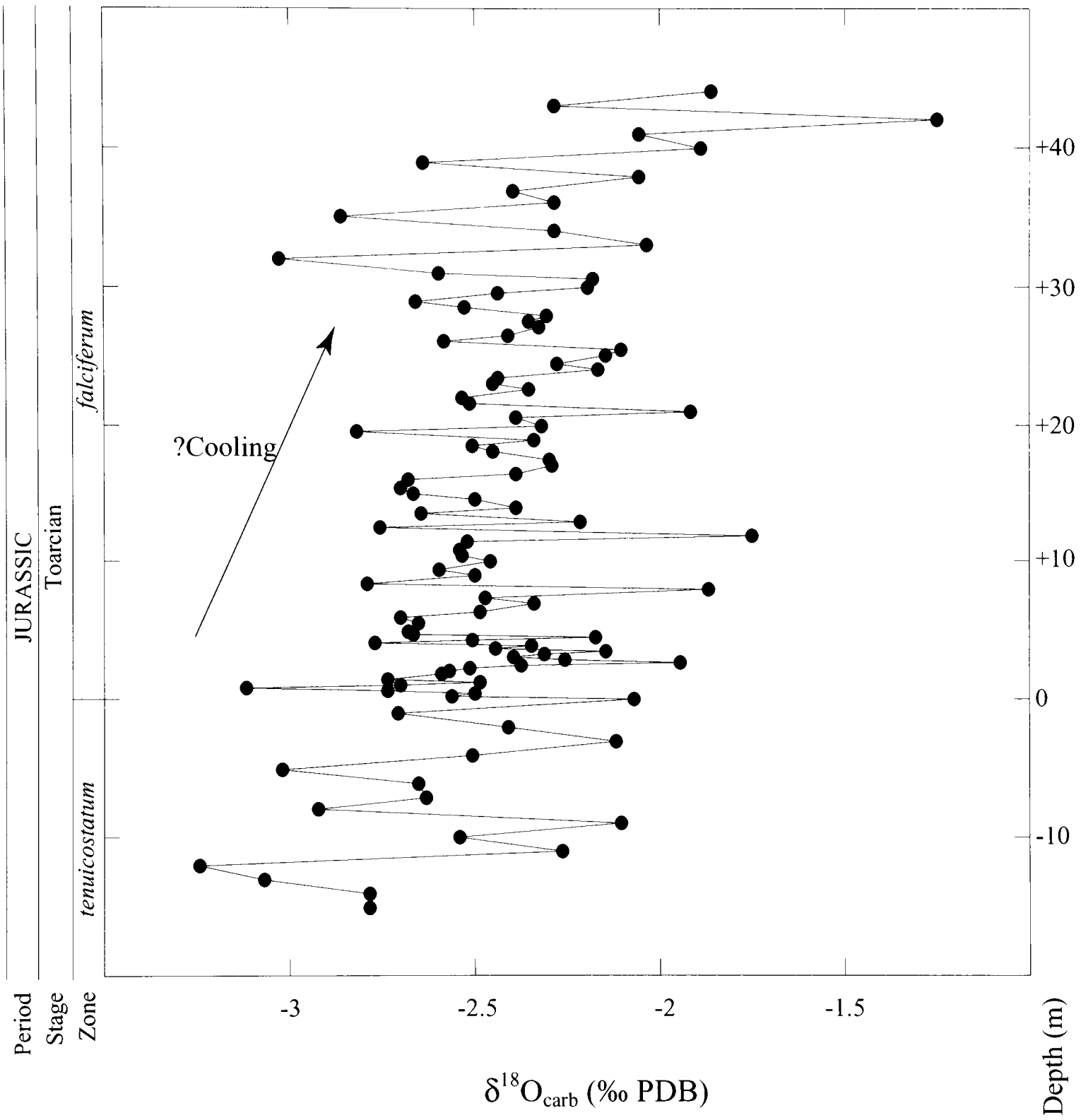

Figure 6.iv. Oxygen-isotope profile of the Sega d'Ala section, Trento Platform. Ages are inferred from chemostratigraphic correlation (see Chapter 5). Interpretations on significant palaeotemperature trends are indicated with arrows. Age (Ma) after Pàlfy *et al.* (2000b).

changes in palaeotemperature, the trends can be taken to represent a relative cooling in the late Pliensbachian followed by warming in the Toarcian. The $\delta^{18}O$ profiles from San Vigilio and Colma di Malcesine both display a shift to more negative values (indicative of palaeotemperature increase) coincident with the transition to shaly facies (Basal Tenno Formation; Figures 6.ii and 6.iii). However, the Sega d'Ala profile shows a scattered but gradually increasing trend during the Toarcian, which signifies gradual cooling (Figure 6.iv). Therefore, $\delta^{18}O$ profiles from Madonna della Corona, San Vigilio and Colma di Malcesine possibly represent a relatively cool period during the late Pliensbachian followed by warming into the Toarcian that is, to a certain extent, correlatable with reference $\delta^{18}O$ and Mg/Ca profiles from belemnites (Figure 6.viii; McArthur *et al.*, 2000a; Bailey *et al.*, 2001; Rosales *et al.*, 2001). In addition to these proxy data, there is evidence of cooling in the Pliensbachian Stage registered by the relatively frequent occurrence in the sedimentary record of glendonites and deposits with affinities to glacial tillites and dropstones (Price, 1999).

Over a longer timescale, the $\delta^{18}O$ profile of samples from the Madonna della Corona section displays scattered values over the lower 500 m of section (Figure 6.i). However, the profile does not show the general increasing trend from Hettangian–Bajocian that is displayed in the belemnite data of Jenkyns *et al.* (2002a), although it should be noted that palaeotemperature trends may not be the same at all palaeolatitudes.

The $\delta^{18}O$ profile of the Pliensbachian–Toarcian interval from the section through the Campania–Lucania Platform (approximately the +150 to +250 m level of the Monte Sorgenza section; Figure 6.v) can also be compared to belemnite reference data (McArthur *et al.*, 2000a; Figure 6.ix) and data from the Trento Platform. Data over the most critical interval (Pliensbachian–Toarcian Stages) are scattered due to the presence of a fault plane with observed post-depositional sediment–fluid interactions (***4.3***). However, a relative increase in isotope values in the late Pliensbachian is followed by a 1 ‰ negative shift in oxygen-isotope values over the Pliensbachian–Toarcian Stage boundary. This $\delta^{18}O$ signal may represent a cooling followed by warming (in terms of palaeotemperature) and is correlatable with similar trends observed in equivalent intervals from the Trento Platform (Madonna della Corona, San Vigilio

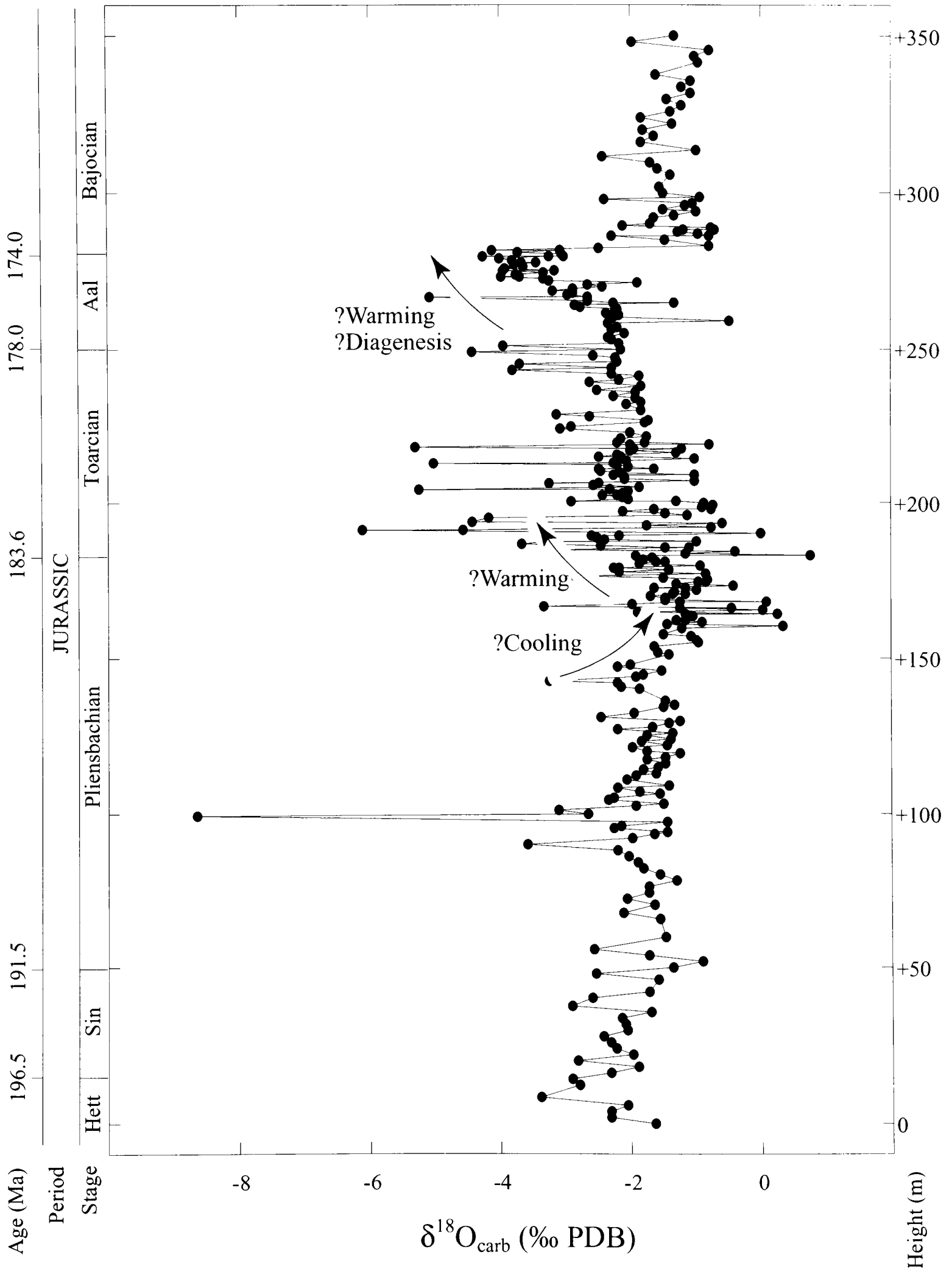

Figure 6.v. Oxygen-isotope profile of the Monte Sorgenza section. Interpretations on significant palaeotemperature trends are indicated with arrows. Age is determined by chemostratigraphic correlation (see Chapter 5). Age (Ma) after Pàlfy *et al.* (2000b)

and Colma di Malcesine sections; see above) and reference belemnite data (Figure 6.ix; McArthur *et al.*, 2000a; Rosales *et al.*, 2001).

Due to problems interpreting the Aalenian–Bajocian levels of the Monte Sorgenza section (related to uncertainty regarding diagenetic alteration), no detailed analysis of $\delta^{18}O$ data from this interval is made (***4.3***). However, if the negative $\delta^{18}O$ excursion is not the result of diagenetic modification, it may signify a period of warming over this interval. Taken as a whole, the $\delta^{18}O$ profile of the Monte Sorgenza section (Campania–Lucania Platform) illustrates a very slight gradual increase from base to top, but not to the extent of the belemnite data illustrated by Jenkyns *et al.* (2002a) for the Hettangian–Bajocian (with which this section has been correlated using carbon-isotope stratigraphy; ***5.2.1***).

Figure 6.vi illustrates the complete $\delta^{18}O$ profile of the Upper Jurassic–Tertiary interval from the Val Cellina section through the Friuli Platform. The data here are too scattered over most of the section for detailed analysis and interpretation. Comparison with the belemnite $\delta^{18}O$ profiles of Gröcke (2001) and Podlaha *et al.* (1998) and the pelagic fine-fraction and bulk sediments of Clarke and Jenkyns (1999) and Jenkyns *et al.* (1994), shows few correlatable points. In particular, there is no Oxfordian–Kimmeridgian minimum, Valanginian–Hauterivian maximum or Aptian minimum that can be recognised in the data from the Friuli Platform. However, there does appear to be mid-Cenomanian and Cenomanian–Turonian minima in $\delta^{18}O$ values. Interpreted in terms of palaeotemperatures, these minima represent periods of warming followed by cooling. A similar minimum in $\delta^{18}O$ values during the Cenomanian–Turonian interval has been observed by Clarke and Jenkyns (1999) and Jenkyns *et al.* (1994), however, there is no evidence of a mid-Cenomanian negative (although there does appear to be a minimum at the Albian–Cenomanian Stage boundary in the reference data, which may correlate to the relatively poorly dated "mid-Cenomanian" of the Val Cellina section). However, over levels where data/sample recovery is good in the Val Cellina section, there are few recognisable $\delta^{18}O$ trends and so, due to these difficulties, data from the Val Cellina are taken as being of little value.

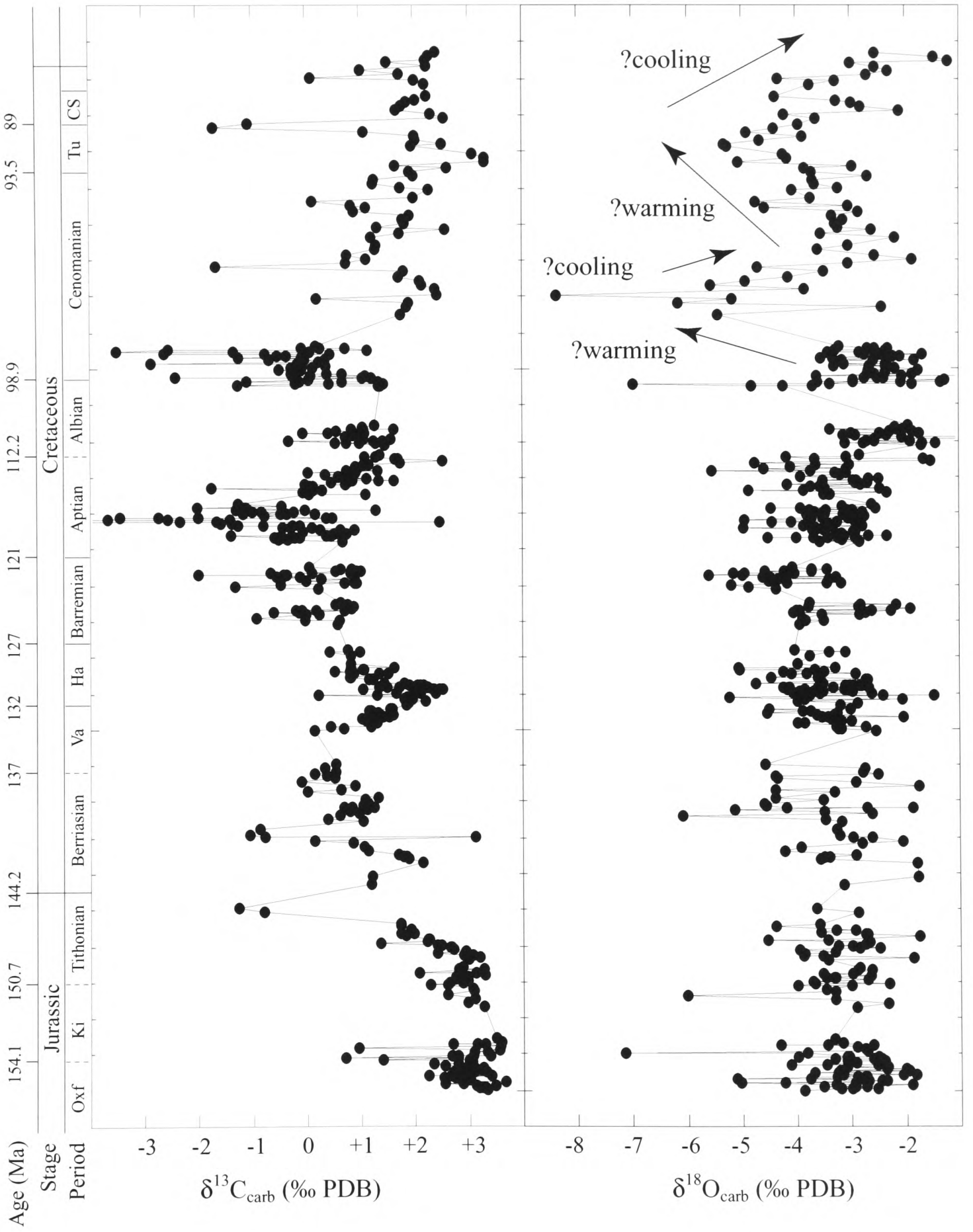

Figure 6.vi. Petrographically screened carbon- and oxygen-isotope profiles of the Val Cellina section, Friuli Platform. Age is determined by chemostratigraphic correlation (see Chapter 5). Interpretations on significant palaeotemperature trends are indicated with arrows. Oxf = Oxfordian; Ki = Kimmeridgian; Va = Valanginian; Ha = Hauterivian; Tu = Turonian; CS = Coniacian – Santonian. Age (Ma) after Gradstein *et al.* (1995).

Disregarding the clearly modified $\delta^{18}O$ signal from the base of the Raia del Pedale section through the Campania–Lucania Platform (recognised by anomalous values from the +4 to +18 m level associated with clear dolomite recrystallisation; ***4.3***), it is apparent that there is a 'trough' in values between the 0 and +80 m levels (Figure 6.vii). This negative excursion (indicating a relative increase followed by decreased palaeotemperature) is correlatable with negative $\delta^{18}O$ excursions observed in fine-fraction and bulk-sediment data from the Cenomanian–Turonian period (Jenkyns *et al.*, 1994; Clarke and Jenkyns, 1999). However, the upper 240 m of section display few pronounced trends, and are not correlatable.

In summary: $\delta^{18}O$ data from shallow-water carbonates produces trends that are scattered, and only infrequently correlatable with reference datasets from pelagic sections. Therefore these data are not deemed a reliable independent indicator of palaeotemperature. As discussed in ***1.4.3***, ***2.3***, ***3.3***, and ***4.3***, this limited reliability is related to the ease in which diagenesis can modify primary $\delta^{18}O$ signals due to the high ratio of oxygen in pore waters to oxygen in calcareous sediment (as opposed to carbon or strontium; Scholle and Arthur, 1980). Significant syn-depositional effects that could modify open-ocean $\delta^{18}O$ signals of shallow-water carbonates are: 1) restricted lagoonal temperature extremes; 2) lagoonal evaporation; and 3) dilution by ^{16}O-enriched fluvial waters (Allan and Matthews, 1982; Brasier and Green, 1993). However, in some sections open-ocean $\delta^{18}O$ trends appear to be registered in the shallow-water carbonates (generally over those intervals characterised by OAE's).

6.2 Records of major oceanographic change from Tethyan carbonate platforms

High-resolution correlation of reference and carbonate-platform chemostratigraphic profiles has facilitated the application of North European and Tethyan biostratigraphic frameworks onto poorly constrained Tethyan platform carbonates. This correlative technique also allows comparisons of carbonate-platform facies with other geographically distributed facies (and their various proxies) that cover similar intervals of time. The early Toarcian, Aptian–Albian (OAE's 1a–1d), Cenomanian–Turonian (OAE 2) and Coniacian–Santonian (OAE 3) Oceanic Anoxic Events (Schlanger and Jenkyns, 1976; Arthur *et al.*, 1990; Erbacher *et al.*, 1996), and other periods of significant perturbation in the global carbon-cycle

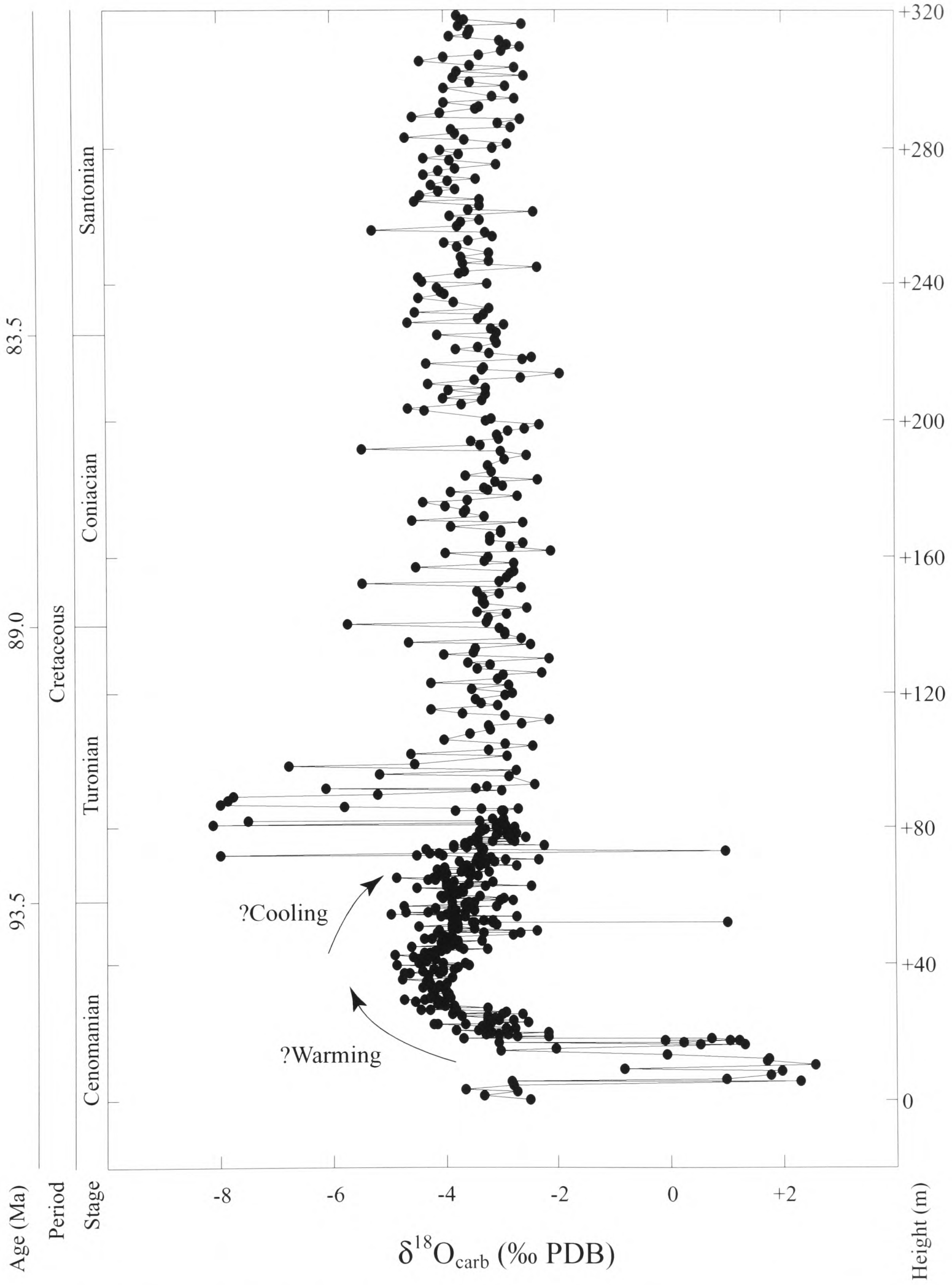

Figure 6.vii. Oxygen-isotope profile of the Raia del Pedale section, Campania–Lucania Platform. Age is determined by chemostratigraphic correlation (see Chapter 5). Interpretations on significant palaeotemperature trends are indicated with arrows. Age (Ma) after Gradstein *et al.* (1995).

(Aalenian–Bajocian, Oxfordian–Tithonian, Valanginian–Hauterivian) have been identified in sections through Tethyan carbonate platforms (***Chapter 5***). All of these periods of time are well known for widespread accumulations of deep-water black shales, and so it is possible to compare how these deep-water facies relate to carbonate-platform sequences. These comparisons highlight the nature in which Jurassic and Cretaceous carbonate platforms responded to the causative mechanisms responsible for widespread (and sometimes global) deep- and mid-water anoxia (Sinninghe-Damste and Koester, 1998).

6.2.1 The early Toarcian Oceanic Anoxic Event

The early Toarcian oceanic anoxic event (Jenkyns, 1988) was registered by a distinctive global sedimentary record characterised by an interval with: elevated organic-carbon levels; a carbon-isotope negative followed by positive excursion ($\delta^{13}C_{carb}$, $\delta^{13}C_{org}$); a nitrogen-isotope ($\delta^{15}N$) positive excursion; a shift in strontium-isotope ($^{86}Sr/^{86}Sr$) ratios to more radiogenic values (McArthur *et al.*, 2000a; Jenkyns *et al.*, 2001; Jones and Jenkyns, 2001; Jenkyns *et al.*, 2002a); and a globally significant mass extinction event (e.g. Hallam, 1961, 1986; Aberhan and Fürsich, 1996; Hallam and Wignall, 1996). Distinctive lower Toarcian organic carbon-rich black shales have been documented from northern and southern Europe, North Africa, Madagascar, North and South America, Australia and across Asia (Jenkyns *et al.*, 2002a).

Chemostratigraphic correlation between reference sections and carbonate platform sections (Campania–Lucania and Trento) of the negative followed by positive $\delta^{13}C$ isotope excursion characteristic of the early Toarcian (supported by strontium-isotope stratigraphy and biostratigraphy; ***5.2.1***), allowed the comparison of these time equivalent facies. These facies comparisons allow the identification of causative mechanisms that could have potentially affected the global ocean–atmosphere system (Hesselbo *et al.,* 2000 and references therein).

Comments on the reference sections

Figures 6.viii (A) and 6.ix (A) illustrate published chemostratigraphic profiles ($\delta^{13}C_{carb}$, $\delta^{18}O$, Mg/Ca, $\delta^{13}C_{org}$, wt% TOC; McArthur *et al.*, 2000a; Jenkyns *et al.*, 2001) and graphic log (Hesselbo and Jenkyns, 1998) from the lower Toarcian of the epicontinental Cleveland Basin in Yorkshire, England. Together, these data give the highest resolution record to date of the sequence of climatic, oceanic and biological events that characterised the early Toarcian.

The Yorkshire reference data are illustrated above $\delta^{13}C_{carb}$ profiles and graphic logs of the lower Toarcian from shallow-water carbonates of the Trento and Campania–Lucania Platform (Figures 6.viii and 6.ix (B)), which were accurately correlated with the Mochras Borehole reference data of Jenkyns *et al.* (2001) in Figure 5.vi. The belemnite $\delta^{18}O$ and Mg/Ca profiles, whose trends are also displayed in the Tethyan data of Rosales *et al.* (2001), are included in Figures 6.viii (A) and 6.ix (A) as potential independent proxies for palaeotemperature over the *tenuicostatum* and *falciferum* Zones (e.g. McArthur *et al.*, 2000a; Gröcke, 2001; Jenkyns *et al.*, 2002a). The significance of $\delta^{18}O$ from belemnites as a palaeotemperature proxy is problematic because belemnites are extinct and the temperature response of their skeletal calcite cannot be calibrated (vital effects, variable levels of habitation in the water-column as well as evaporation–precipitation balance of local sea-water may all cause non-quantifiable deviation from average equilibrium $\delta^{18}O$ values). However, because two independent palaeotemperature proxies ($\delta^{18}O$ and Mg/Ca) from northern England (McArthur *et al.*, 2000a) and northern Spain (Rosales *et al.*, 2001) follow a similar pattern, these trends are interpreted as real.

The study of the Yorkshire data at such high resolution highlights a sequence of events leading into and out of the period of Toarcian oceanic anoxia. The initiation of the $\delta^{13}C_{org}$ decrease in values (mid-*semicelatum* Subzone) is concomitant with the initiation of a rise in wt% TOC. The palaeotemperature proxies ($\delta^{18}O$, Mg/Ca) also indicate a synchronous increase in temperature from the early-*semicelatum* Subzone (the $\delta^{13}C_{carb}$ profile is too scattered over the *semicelatum*–lower *exaratum*-Subzone section for reliable interpretation). The above trends continue until the upper *semicelatum* Subzone, where a pronounced negative $\delta^{13}C_{org}$ shift is

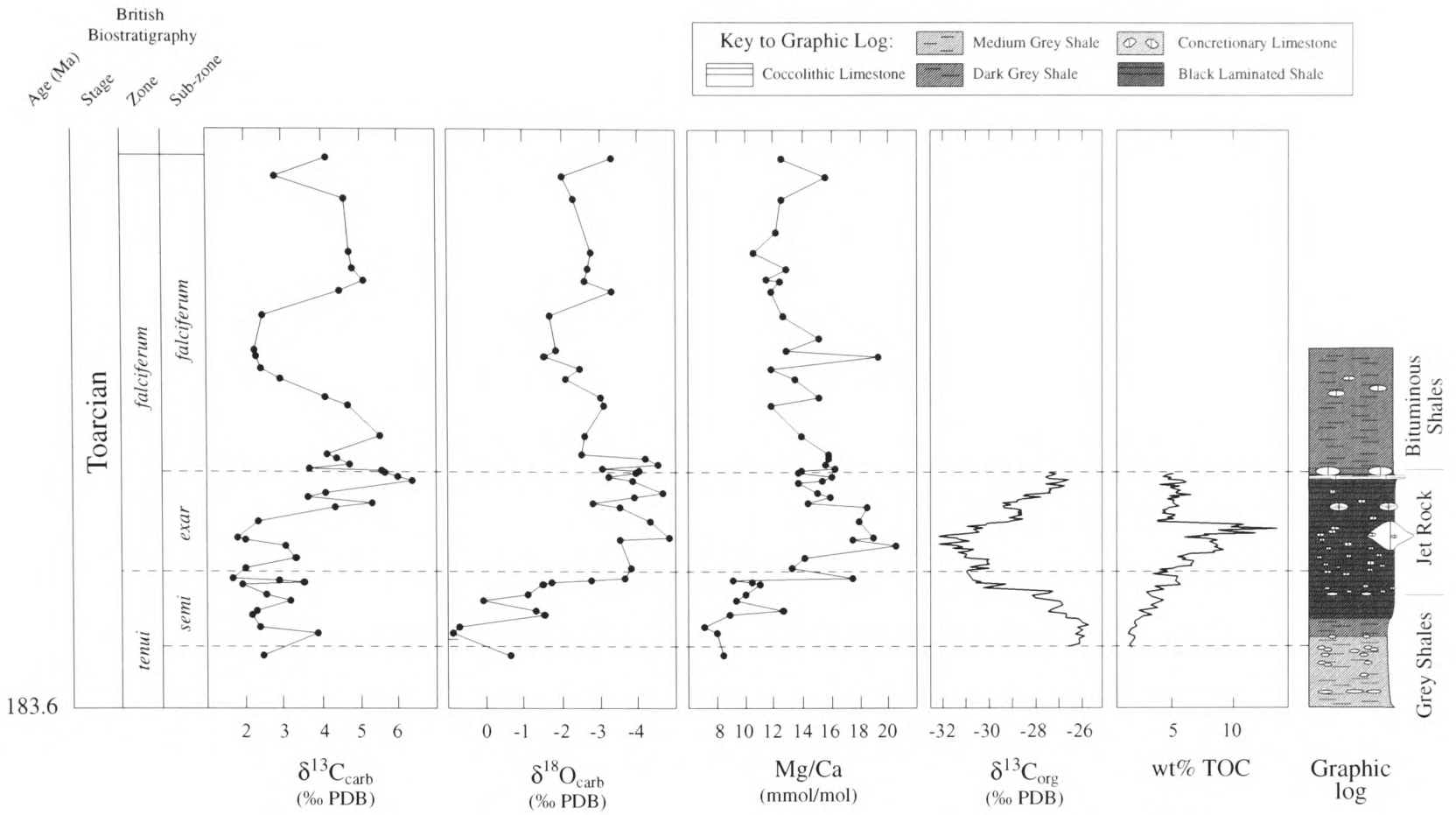

A - Yorkshire reference

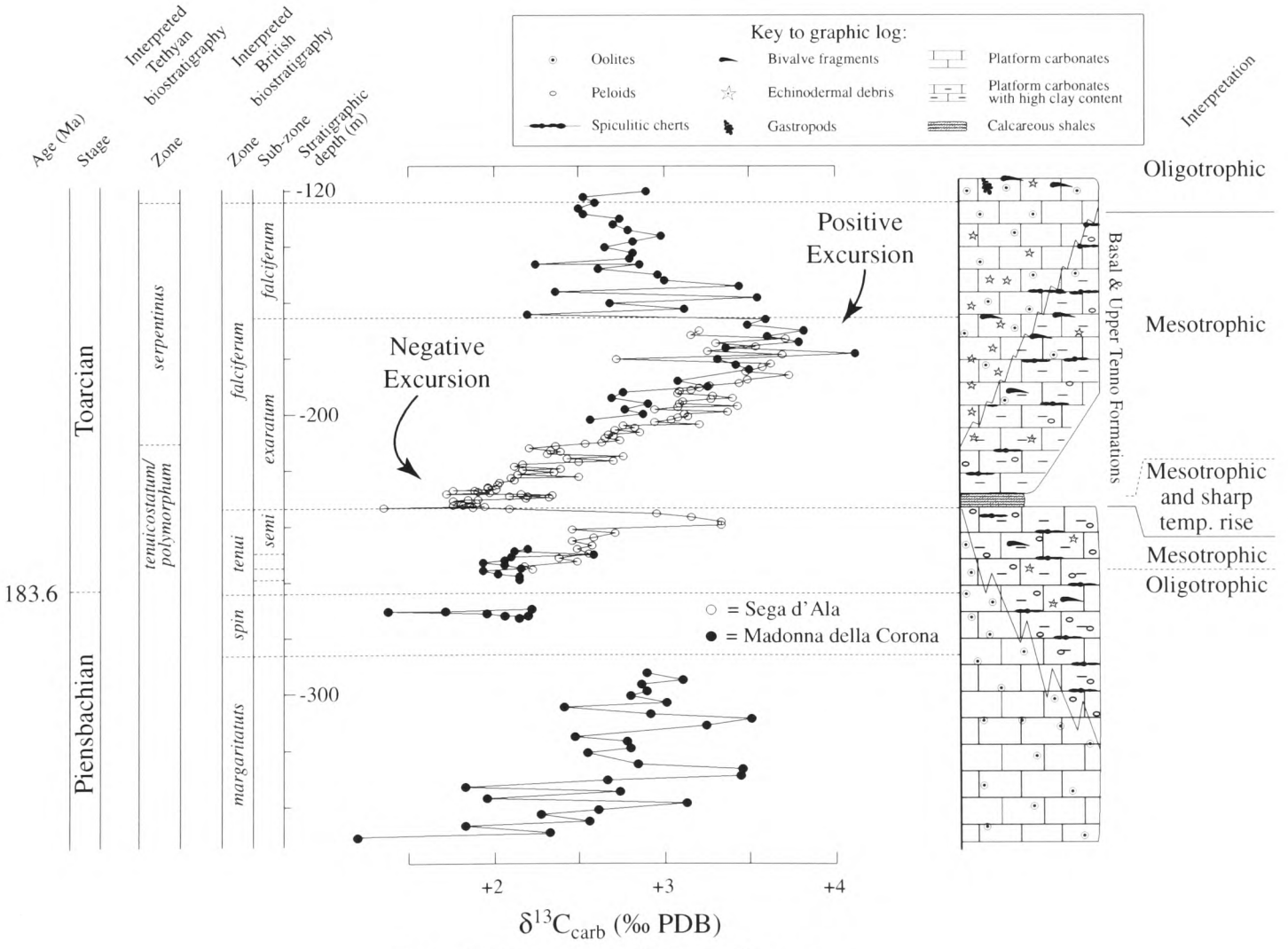

B - Trento Platform

Figure 6.viii. Comparison between early Toarcian reference chemostratigraphic data from epicontinental basinal facies of Yorkshire, England (**A**; Jenkyns *et al.*,2001; McArthur *et al.*,2000a; Hesselbo and Jenkyns, 1998), and $\delta^{13}C$ profile and graphic log of the Trento Platform, Italy (**B**) . Age (Ma) after Pàlfy *et al.* (2000b).

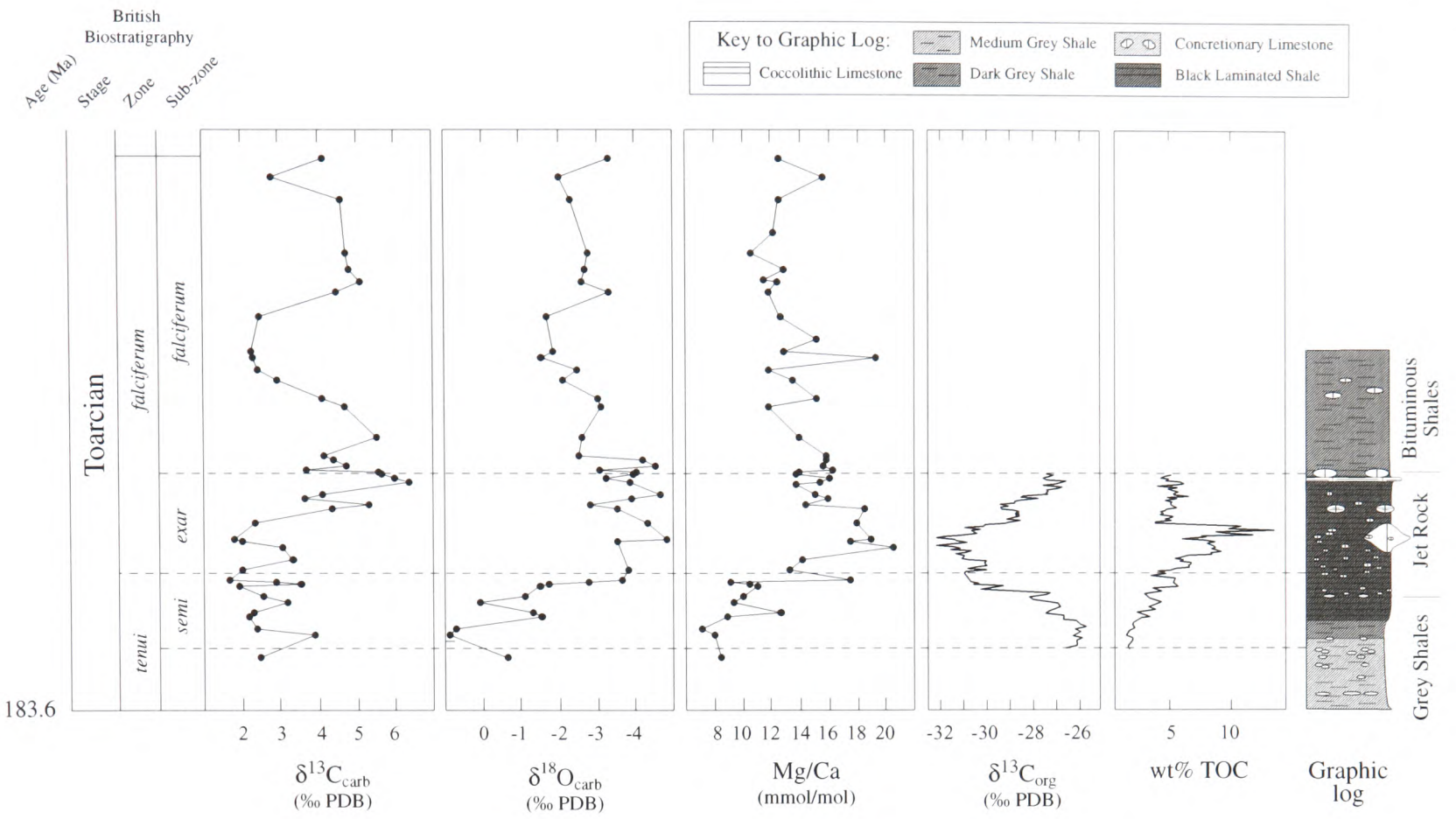

A - Yorkshire reference

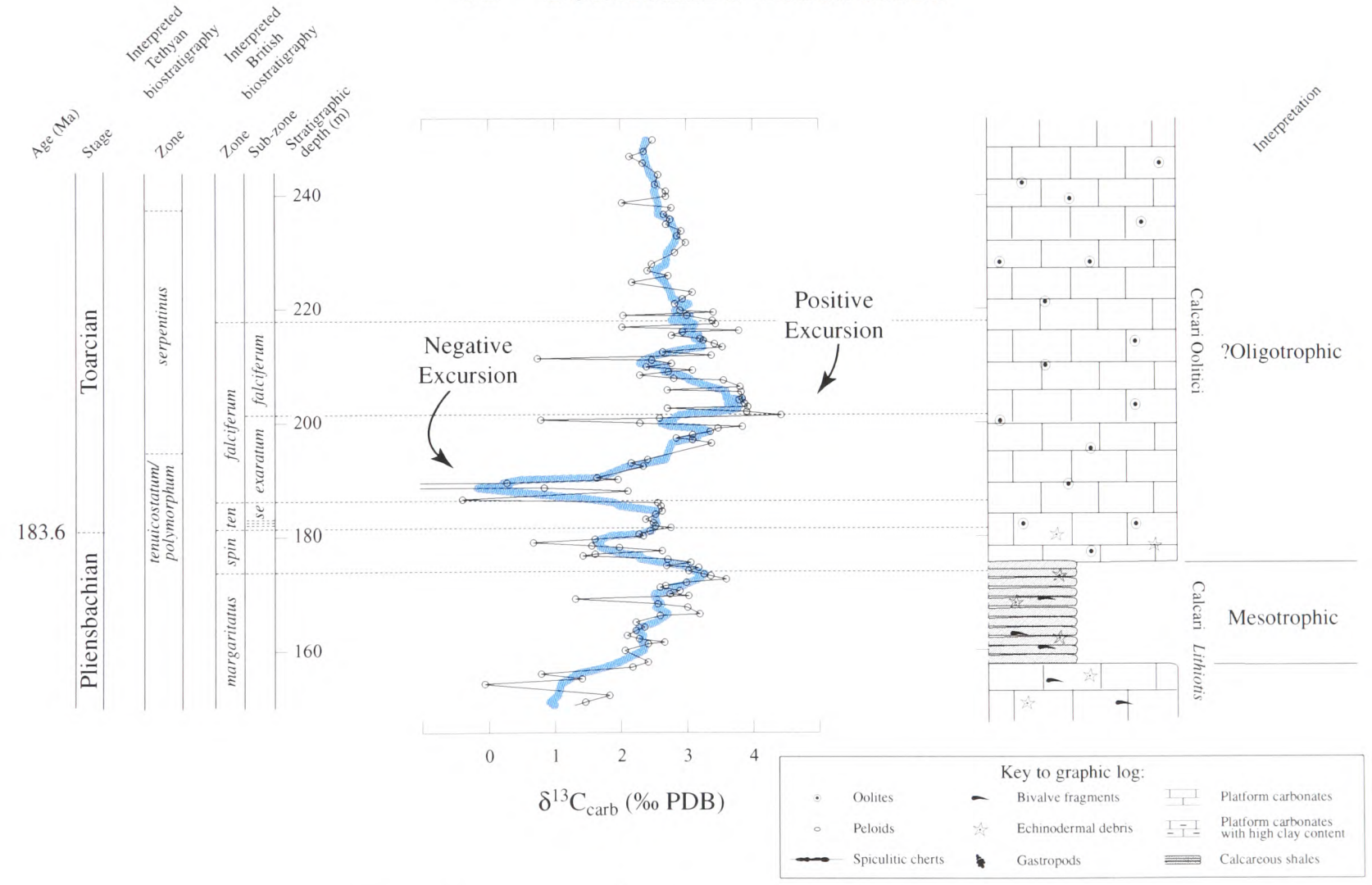

B - Campania–Lucania Platform

Figure 6.ix. Comparison between Pliensbachian–Toarcian reference chemostratigraphic data of epicontinental basinal facies of Yorkshire, England (**A**; Jenkyns *et al.*,2001; McArthur *et al.*,2000a; Hesselbo and Jenkyns, 1998) and $\delta^{13}C$ profile and graphic log of the Campania–Lucania Platform, Italy (**B**) . Age (Ma) after Pàlfy *et al.* (2000b).

registered, synchronous with an equally sharp rise in palaeotemperature (clearly visible in the $\delta^{18}O$ profile, but there is limited scatter in the Mg/Ca profile at this level). This abrupt negative excursion, which punctuates the rising $\delta^{13}C_{carb}$ isotope trend of the Mochras Borehole and the Trento and Campania–Lucania Platforms (Figure 5.vi), has been attributed to the dissociation of gas hydrates with an associated sharp temperature increase resulting from greenhouse conditions that followed the rapid oxidation of methane to carbon dioxide (Hesselbo et al., 2000). However, major input of CO_2 into the atmosphere from Karoo–Ferrar igneous activity is an alternative or additional mechanism for global warming over a longer timescale (Pàlfy and Smith, 2000). Beerling *et al.* (2002) quantify atmospheric CO_2 level rise and global climatic warming during the early Toarcian OAE at 900 ppmv and ~3°C, respectively. Wt% TOC continues to rise in a relatively linear trend over the level of the rapid $\delta^{13}C_{org}$ negative excursion. Following the negative shift, isotope ratios continue to fall gradually until they reach a minimum in the lower–mid-*exaratum* Subzone, in the *falciferum* Zone. The temperature proxy profiles likewise continue to rise gradually, reaching maxima at the same level (lower–mid-*exaratum* Subzone), whereas wt% TOC values also register a maximum in the mid-*exaratum* Subzone. It should also be noted that $^{87}Sr/^{86}Sr$ values become increasingly radiogenic upwards from the *semicelatum–exaratum*-Subzone boundary (not illustrated; Jones *et al.*, 1994b; McArthur *et al.*, 2000a; Jenkyns *et al.*, 2002a). Above this interval, both the $\delta^{13}C_{carb}$ and $\delta^{13}C_{org}$ profiles display relative heavy values as both curves progress into the subsequent positive excursion (maximum dated as *exaratum–falciferum*-Subzone boundary; Jenkyns and Clayton, 1997). This rise in $\delta^{13}C$ is mirrored by falling palaeotemperature, a pronounced drop in wt% TOC levels, and a flattening of the $^{87}Sr/^{86}Sr$ profile.

The impact on the Trento Platform

Föllmi *et al.* (1994) document the response of north Tethyan carbonate platforms to Early Cretaceous environmental 'events'. The authors use particular carbonate facies associations to interpret the necessary trophic state of surface waters at the time of deposition of the facies concerned. The evolution in the general state of health of the carbonate platform is therefore ascertained. Specifically, the following facies and interpretations on carbonate-platform health are suggested:

i) *Coral–Oolite carbonate production*: oligotrophic conditions and relatively healthy platform

ii) *Crinoid–Bryozoan carbonate production:* mesotrophic conditions (encouraging suspension feeders – e.g. crinoids, bivalves and silicosponges) and less healthy platform conditions

iii) *Platform destruction and condensation:* eutrophic conditions and platform demise

This interpretation of these carbonate facies can be applied to the Pliensbachian–Toarcian interval of the Trento Platform. Figure 6.viii (B) illustrates the $\delta^{13}C_{carb}$ profile and graphic log of the lower Toarcian of the Trento Platform ($\delta^{13}C_{carb}$ profiles of only the relatively complete Madonna della Corona and Sega d'Ala sections are displayed for reasons of clarity). There is a marked symmetry in the sequence of facies changes in the Toarcian section of the Trento Platform from shallow-water oolitic carbonate, to thin-bedded cherty limestone, to calcareous shale, to thin-bedded cherty limestone and back to massive-bedded oolite. This sequence of facies is mirrored in the $\delta^{13}C_{carb}$ record by an initial increase, sharp decrease and subsequent increase before a return to background carbon-isotope values. The rising $\delta^{13}C_{carb}$ values over the *tenuicostatum* Zone of the early Toarcian (seen regionally across Europe; e.g. Jenkyns and Clayton, 1997; Jenkyns et al., 2001), coincident with a gradual rise in temperature and increasing wt% TOC, are registered in the platform-carbonate record by a change in facies from well-washed oolite to clay-rich limestone with sponge-derived cherts (an increase in abundance of filter-feeders reflecting mesotrophic–eutrophic shallow-marine conditions; Föllmi *et al.*, 1994). The re-established increase in values rising into a positive $\delta^{13}C_{carb}$ isotope excursion, with coincident wt% TOC and $\delta^{15}N$ maxima, is represented in the Trento Platform succession by a return to thin-bedded limestone with sponge-derived chert, signifying a return to mesotrophic–eutrophic conditions (Föllmi *et al.*, 1994). Widespread oligotrophic conditions are believed to have returned by the latest *falciferum* Zone of the Toarcian when temperature and nutrient levels had stabilised.

Maximum devastation of carbonate producers on the Trento Platform occurred synchronously with the $\delta^{13}C_{carb}$ / $\delta^{13}C_{org}$ negative excursion registered in the late *semicelatum* Subzone in northern and southern Europe. If methane dissociation were responsible for the $\delta^{13}C_{carb}$ / $\delta^{13}C_{org}$ negative excursion, evidence of associated temperature and pCO_2 increases would be expected. Beerling *et al.* (2002) suggest a 900 ppmv increase in atmospheric CO_2 levels and an ~3°C global temperature increase during the early Toarcian. Previous authors have proposed that temperature increase has caused recent and ancient carbonate-platform crises (see below; Jokiel and Coles, 1977, 1990; Goreau and Hayes, 1994; Strong *et al.*, 1998; Jenkyns and Wilson, 1999; Glynn, 2000; Goreau *et al.*, 2000; Wellington *et al.*, 2001), and increased input of CO_2 into the ocean-atmosphere system may also be detrimental to shallow-marine carbonate factories (Kleypas *et al.*, 1999; Gattuso and Buddemeier, 2000).

Directly below and above the calcareous shales in the Trento Platform (*exaratum* Subzone), clay-rich limestones with spiculite (*semicelatum* and *exaratum–falciferum* Subzones) were deposited. The Yorkshire reference section of Jenkyns *et al.* (2001) and McArthur *et al.* (2000) illustrates a *semicelatum–falciferum* Subzone increase in $^{87}Sr/^{86}Sr$, wt% TOC and $\delta^{15}N$ values (Figure 6.viii). The latter two parameters reach maxima in the Belluno Trough (adjacent to the Trento Platform) and the Cleveland Basin, Yorkshire in the mid-*exaratum* Subzone (Jenkyns *et al.*, 2001). Widespread wt% TOC maxima in the early Toarcian have been interpreted as the result of increased productivity. Maxima in $\delta^{15}N$ are thought to reflect regional upwelling, high productivity, generation of suboxic water masses and consequent denitrification, the isotopic signature of which was transferred into organic-rich sediment (Jenkyns *et al.*, 2001). These $\delta^{15}N$ and wt% TOC maxima hence denote regional elevated nutrient levels, possibly attributed to increased rates of continental weathering as expressed by rising sea-water $^{87}Sr/^{86}Sr$ values in the *exaratum* Subzone, and in turn related to high temperature/CO_2 and an increased hydrological cycle. Supporting this contention is the levelling-off of $^{87}Sr/^{86}Sr$ values in the *falciferum* Subzone concurrent with temperature stabilisation and the decrease in $\delta^{13}C$ values after the maximum. Elevated nutrients and the increasingly mesotrophic conditions from the early *semicelatum* Subzone to *falciferum* Zone apparently restricted carbonate production and ensured the invasion of abundant filter-feeders

(including siliceous sponges) on the Trento Platform during the early Toarcian Oceanic Anoxic Event (c.f. Hallock and Schlager, 1986; Föllmi *et al.*, 1994; Glynn, 2000).

In summary: it appears that maximum devastation of the Trento Platform occurred during a period of rapid temperature increase (mesotrophic conditions and temperature increase), whilst background high nutrient levels forced clay- and sponge-rich limestone deposition, at what appears to be the expense of 'healthy' carbonate producers.

The impact on the Campania–Lucania Platform

Figure 6.ix (B) illustrates the $\delta^{13}C_{carb}$ profile and graphic log of the upper Pliensbachian–Toarcian interval of a section through the Campania–Lucania Platform. It is clear that, although the carbon-isotope profile is strikingly similar to that of the Trento Platform (and reference curves; Figure 5.vi), the nature of the facies in the Campania–Lucania Platform over the interval in question is different.

The Calcari à *Lithiotis* Formation of the Campania–Lucania Platform is broadly equivalent to the Calcari Grigi of the Trento Platform (***5.1.1***, Figure 5.ii and Bosellini and Broglio Loriga, 1971). In particular, the upper shaly horizons of the Calcari à *Lithiotis* appear time-equivalent with the initiation in deposition of the Misone Formation at Madonna della Corona on the Trento Platform (i.e. *margaritatus* Zone). Although there is a relatively minor $\delta^{13}C$ excursion to heavier values in the *margaritatus* Zone (Jenkyns and Clayton, 1986; Jones, 1992), there is little evidence in the global sedimentary record for widespread accumulation of black shales at this time. Likewise, there is little evidence for widespread demise and/or environmental stressing of carbonate platforms in the *margaritatus* Zone and so, it follows that the shaly levels of the Misone Formation and the Calacari à *Lithiotis* represent a local/regional phenomenon that forced a decline in carbonate accumulation. Comparing the Misone and Upper Tenno Formations of the Trento Platform and recognising that they are a similar lithotype, it is reasonable to suggest that they formed under similar environmental conditions. As suggested for the Upper Tenno Formation (see above), these conditions could have included relatively

high nutrient levels that acted as an environmental stress on the Trento and Campania–Lucania Platforms during the late Pliensbachian (*margaritatus* Zone).

Coincident with the decrease in $\delta^{13}C_{carb}$ ratios from *margaritatus–spinatum* Zone in the section through the Campania–Lucania Platform, is a marked facies transition from calcareous shales / rhythmically bedded micritic limestones to massive-bedded oosparite. This oolitic facies continues without significant facies change throughout the negative and positive $\delta^{13}C_{carb}$ shifts associated with the oae.

Petrographic analyses reveal that the lower levels of the oolite formation consist of typical radial primary calcite ooids set in a sparry-calcite cement. However, stratigraphically higher up in the Calcari à Oolitici Formation, the ooids become darker (micritic) and have a more predominant concentric structure. There is also an apparent bimodalism between relatively large micritic and concentrically laminated ooids, and smaller interstice-filling ooids with a similar nature. These ooids could either be heavily micritised "normal" ooids or, alternatively, "pelagic" ooids (micro-oncolites), which are believed to form by cyano-bacterial accretion in relatively deeper water than usual for typical "Bahamian-oolite" formation (Jenkyns, 1972). The sparry-calcite cement throughout the oolite indicates that high-turbidity was a factor at play at the time of deposition, which is significant when considered that above and below the oolite body are deposits suggestive of slack-water lagoonal environments (Calcari à *Lithiotis* and the Calcari Maculati Formations; ***4.1.1***). It is therefore reasonable to believe that the Calcari Oolitici Formation represents a period of relatively deep water, because the facies in the Monte Sorgenza section became more marginal, before a return to lagoonal (and later peritidal) conditions (i.e. a transition from lagoon to oolite sand barrier to lagoon).

In general, it appears that the Campania–Lucania Platform suffered few adverse consequences as a result of the early Toarcian Oceanic Anoxic Event and all of the global environmental stresses associated with it.

Discussion

Because the Trento and Campania–Lucania Platforms responded in different ways to what must have been similar global environmental stresses during the early Toarcian Oceanic Anoxic Event, local/regional marine environments surrounding the platforms must have varied. Understanding why similar ecological systems in differing localities respond to global temperature, nutrient, sea level and pCO_2 changes (and possibly other mechanisms) differently is difficult without clear high-resolution data from well-understood proxies. However, in such circumstances where this information is not sufficiently available, the application of Lyell's famous mantra: "The present is the key to the past", can provide additional information. In this instance, the modern-world equivalents of global carbonate-platform crises need to be investigated. The most understood of such phenomena at present are Global Coral Bleaching Events (affecting corals, sea anemones, zoanthids, giant clams, benthic foraminifera, and many other zooxanthellate invertebrates; I.S.R.S., 1998), which have been intensively studied over the last decade.

Glynn (2000) suggests that tropical zooxanthellate reef species are more vulnerable to rising than falling temperatures (i.e at present, a rise in temperature of only 2–3°C is necessary for deleterious effect, compared to a fall of 8–10°C). Evidence from the modern oceans suggests that temperature is the dominant factor responsible for events of global coral demise (the result of "bleaching"; e.g. "1998 Global Bleaching Event"), and that positive sea-surface temperature (SST) anomalies are responsible for causing "bleaching hotspots" ("SST anomalies that approximate or exceed by 1.0°C or more the SST expected climatologically during the warmest month of the year"; Goreau *et al.*, 2000). For example, the most recent and most understood coral demise event: the "1998 Global Bleaching Event", was characterised by unprecedented elevations in SST due to a severe El Niño Southern Oscillation (ENSO) combined with the effect of the Indian Ocean's 11-year oscillation and northern hemisphere tropical warming (Goreau *et al.*, 2000). Locally, coral mortality reached 70–99% (Mozambique, Kenya, Qatar, India, Sri Lanka, Maldives, Seychelles, Chagos, Western Australia, Japan), with the lowest mortality rates found in the most stressed habitats. This counter-intuitive observation is the consequence of very complex interactions of various environmental conditions and their

results on carbonate producers. For example: upwelling waters rich in nutrients can, in some instances, protect carbonate producers from severe mortality (resulting from temperature-induced bleaching), because of the cooling effect of the deep water that is upwelled (this indicates that temperature effects are the dominant control on carbonate accumulation rates in the modern world; Goreau *et al*, 2000). None of the coral species that have experienced regional extinction as a result of bleaching events in the last two decades have reappeared in the subsequent fifteen years (Glynn, 2000). It is therefore apparent over the timescales studied that only prolonged and protracted high SST's have devastating global effects on carbonate-producing systems (other detrimental factors act on local-scales only). Without new growth, reef frameworks are soon destroyed by bioeroders and carbonate production is out-weighed by erosion and subsidence (Hallock, 1988).

Applying this approach is not completely foolproof: it is possible that ancient environments experienced different phenomena than those encountered in the modern world. The most obvious caveat is that during the early Toarcian OAE elevated nutrient levels are believed to have been present in the global ocean, allowing high planktonic productivity and thus promoting oceanic anoxia (e.g. Jenkyns *et al.*, 2002a). Current understanding is that ancient carbonate-platform crises are primarily the result of elevated nutrient levels (Hallock and Schlager, 1986; Hallock, 1988; Zempolich, 1993; Föllmi *et al.*, 1994; Weissert *et al.*, 1998). The interpretation that rhythmically bedded pelletal limestones with spiculitic cherts (Misone and Upper Tenno Formations in the Trento Platform) are derived from carbonate production in nutrient-stressed waters is consistent with this hypothesis (see above; Föllmi *et al.*, 1994). However, it is also important to consider the role of temperature on the demise of carbonate platforms, especially in light of knowledge on modern global bleaching events and new data that suggests that there is synchroneity between platform devastation and pronounced temperature increase in the early Toarcian (see above).

Further evidence that temperature-related demise of carbonate production in the modern world is an applicable model for the early Toarcian comes from indications that recent global coral bleaching events have negligible effects on carbonate producers located in regions of upwelling (cool-water circulation) or high turbidity (Goreau *et al.*, 2000). Therefore, although

global environmental (temperature-related) stresses are acting over the period of these events, there is a regionally varying response by carbonate-producing organisms dependent on their local environment, as observed in the Toarcian. Föllmi *et al.* (1994) and Weissert *et al.* (1998) also discuss the immunity of carbonate platforms to global oceanographic events in the Early Cretaceous (***6.2.4*** and ***6.2.5***). The authors conclude that platforms isolated from the continents and ocean currents that may cause environmental stress (e.g. upwelling) are likely to be unaffected by the degradative factors that may harm other platforms during these periods. Their examples of isolated platforms are those located on the Adria Plate. If this were the case, the Campania–Lucania Platform (?and Friuli Platform) was not only isolated from continental influences but may also have been the recipient of cool-water circulation and/or highly turbid surface waters. This isolation would leave the carbonate platform relatively sheltered from the prevailing environmental temperature and/or nutrient stresses.

Another potentially significant factor that may have contributed to the Campania–Lucania Platform suffering less observable deterioration than the Trento Platform in the early Toarcian is the difference in accumulation rate. As discussed in ***5.3***, the average carbonate accumulation rate on the Trento Platform was approximately 2.5 times that on the Campania–Lucania Platform during the Early Jurassic. Assuming that higher accumulation rates reflect higher subsidence/lower off-platform sediment transport rates, this would amplify the effect of any environmental stresses on the Trento Platform because, all other factors being equal, it would still require more growth to keep up with sea level than was the case with the Campania–Lucania Platform.

To summarise: the prevailing oceanographic conditions during the early Toarcian OAE resulted in widespread carbonate-platform drowning (e.g. Sicily, Morocco, Tunisia, Greece, Spain; Bernoulli and Jenkyns, 1974), 'partial drowning' (e.g. Trento Platform; Barbujani *et al.*, 1986; Cobianchi and Picotti, 2001), and locally there were only negligible effects on carbonate platforms (e.g. Campania–Lucania, Friuli, Yugoslav Platforms; Aubouin, 1963; Davey, 1994; Violante, 2000). Figure 6.x illustrates the application of the carbonate-platform model that hypothesizes temperature-triggered devastation to carbonate platforms of the early Toarcian.

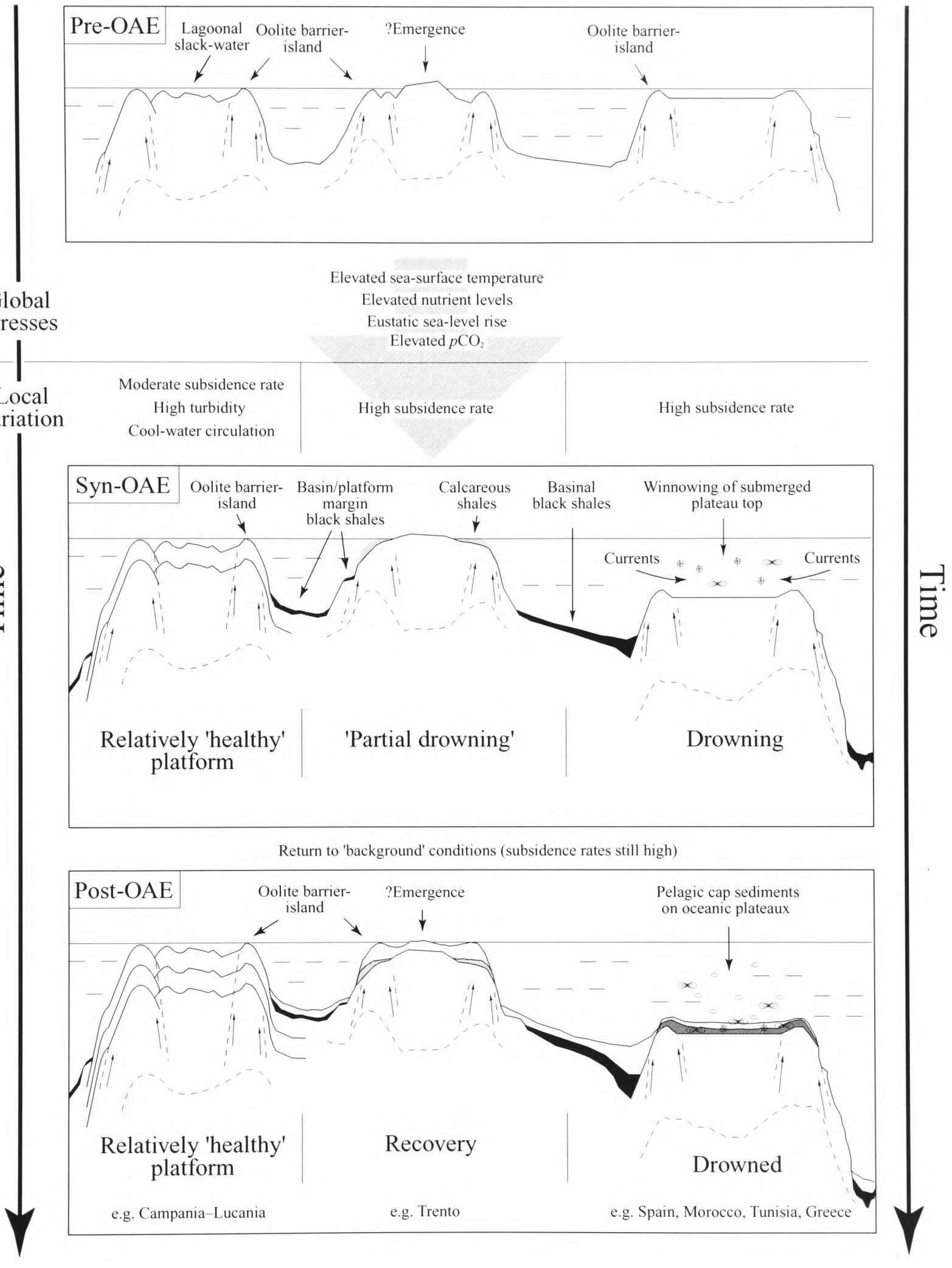

Figure 6.x. Variations in carbonate-platform responses to the early Toarcian Oceanic Anoxic Event and its postulated global forcing mechanisms are partially dependent on local environmental controls.

6.2.2 The Aalenian–Bajocian

The Aalenian–Bajocian (Middle Jurassic) is recognised as a period of time characterised in the sedimentary record by distinctive negative and positive carbon-isotope shifts. The negative carbon-isotope excursion that is observed at the Aalenian–Bajocian-Stage boundary (174 Ma; Pàlfy *et al.*, 2000b) is relatively long-lived (c.f. early Toarcian/Aptian negative excursions) and is followed by a positive excursion in the mid-Bajocian (~170 Ma; Pàlfy *et al.*, 2000b; Hesselbo *et al.*, *In Press*). These distinctive $\delta^{13}C$ trends are registered in Tethyan pelagic facies (Figure 6.xi; Bartolini *et al.*, 1999; Bartolini and Cecca, 1999; Morettini *et al.*, 2002), Italian redeposited calcitic ooids (not shown; Zempolich and Erba, 1999), Portuguese and Scottish belemnites (Figure 6.xi; Gröcke, 2001; Jenkyns *et al.*, 2002a) and terrestrial organic carbon (wood) from northern England (Figure 6.xi; Hesselbo *et al.*, *In Press*). Some datasets also display an Aalenian (*murchisonae* Zone) positive excursion, preceding the Aalenian-Bajocian negative discussed above (Figure 6.xi; Bartolini *et al.*, 1999; Jenkyns *et al.*, 2002a).

Comments on the reference sections

It can be observed from Figure 6.xi (after Hesselbo *et al.*, *In Press*) that the pelagic carbonate section from Terminelletto (Umbria–Marche, Italy; Bartolini *et al.*, 1999) offers the most coherent $\delta^{13}C$ dataset of the reference sections: the Aalenian–Bajocian negative followed by mid-Bajocian positive excursions can be clearly identified. It is notable that the neighbouring Presale section of Bartolini and Cecca (1999) is not confidently calibrated to the standard ammonite biostratigraphy, and so the negative excursion in the mid–upper Aalenian is likely to be the same Aalenian–Bajocian boundary negative excursion detailed in the other reference sections. Fossil-wood data of Hesselbo *et al.* (*In Press*) likewise illustrate relatively depleted $\delta^{13}C$ ratios at the Aalenian–Bajocian boundary, with a subsequent positive excursion in the mid-Bajocian (although depositional rates are believed to be episodic causing condensed excursion intervals; Hesselbo *et al.*, *In Press*). Portuguese and Scottish belemnite data also show isotopically light carbon-isotope ratios in Aalenian–Bajocian / lower Bajocian levels (Gröcke, 2001; Jenkyns *et al.*, 2002a).

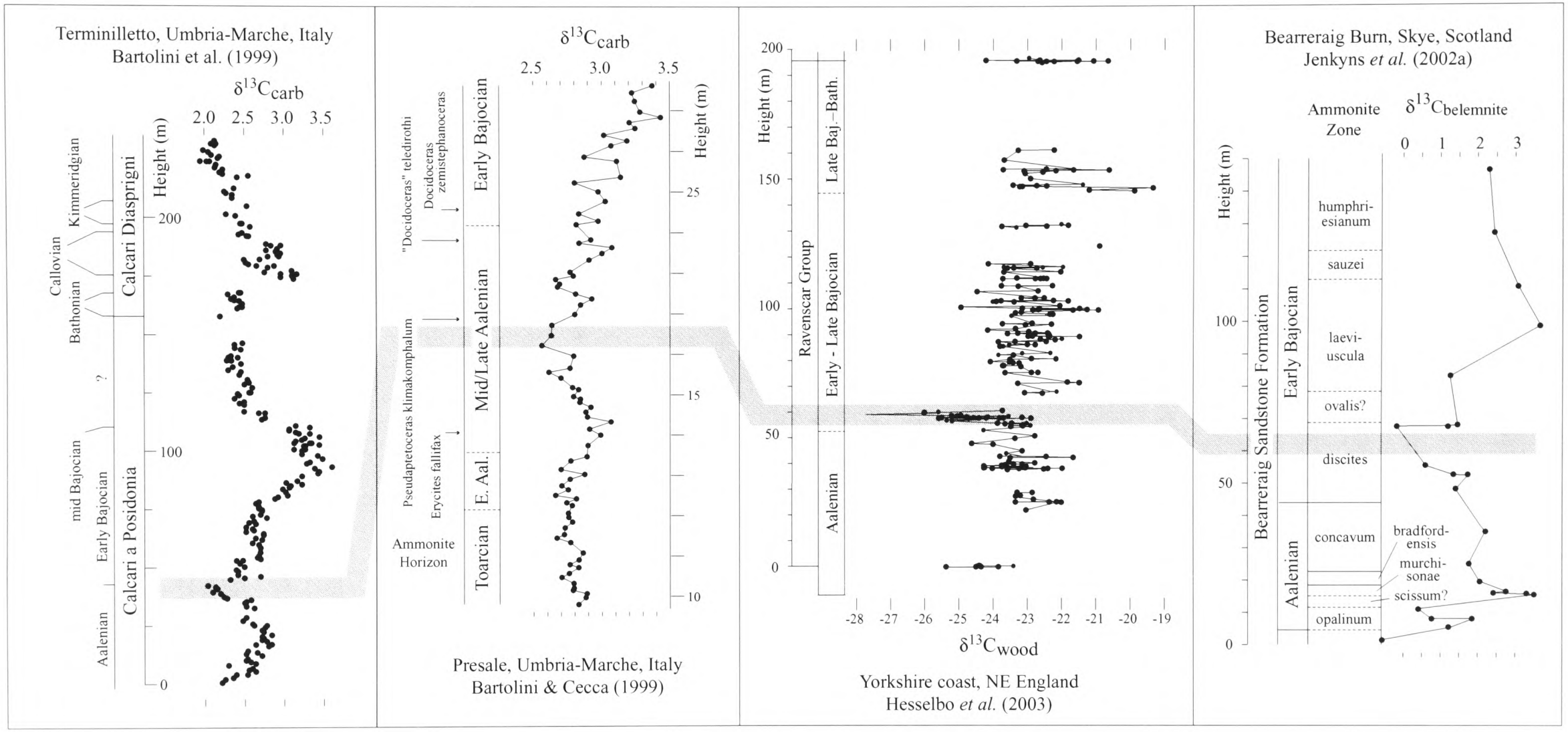

Figure 6.xi. Middle Jurassic reference $\delta^{13}C$ data from Italian pelagic carbonates (Bartolini *et al.*, 1999; Bartolini & Cecca, 1999) , Scottish belemnites (Jenkyns *et al.*, 2002a), and English fossil wood (Hesselbo *et al.*, *In Press*).

The change in wood-type (charcoal–coal) found in the Ravenscar Group, Yorkshire, England pre- and post-negative $\delta^{13}C$ excursion, is interpreted by Hesselbo *et al.* (*In Press*) to indicate a transition from arid to humid climates (charcoal formation, which results from wild-fires, necessitates arid conditions). The data from the Ravenscar Group also suggest a pCO_2 increase coincident with the negative excursion followed by decreasing pCO_2, as discerned from leaf stomatal indices (these data cannot be heavily relied upon, however, due to inconsistencies with previously collected material and poor stratigraphic resolution; Hesselbo *et al.*, *In Press*).

Tethyan pelagic successions of Umbria–Marche, Italy record a lower Bajocian onset in biosiliceous (radiolarian) sedimentation, a carbonate depositional hiatus on Apenninic "swells", and a pronounced reduction in biodiversity (Bartolini and Cecca, 1999). The authors interpret these events as the "manifestation of a carbonate productivity crisis, induced by...eutrophication...", itself the result of "greenhouse" climate. Because shifts in $\delta^{13}C$ are believed to represent changes in the partitioning of the global organic-carbon/carbonate-carbon reservoirs (e.g. Weissert *et al.*, 1998) and there is no evidence for widespread organic-rich shale deposition during this interval, it is concluded by the authors that a decrease in carbonate production is responsible for driving the mid-Bajocian $\delta^{13}C$ record to relatively high values (Bartolini *et al.*, 1996; Bartolini and Cecca, 1999).

Impact on the Trento Platform

Because the Aalenian interval is condensed on the Trento Platform (Sturani, 1964) and shallow-water carbonate deposition ceased at approximately the Aalenian–Bajocian Stage boundary, it is not possible to correlate confidently carbon-isotope signals from this period of time (although biostratigraphic constraint using ammonites is very good; Sturani, 1964).

Initially, drowning of the Trento Platform was suggested to be the result of a rapid subsidence event (e.g. Bosellini and Winterer, 1975; Bosellini *et al.*, 1981). However, analysis of the eastern margin of the platform and the identification of shallow-water components in the overlying Rosso Ammonitico has led a later author to suggest that drowning occurred at shallow depths and resulted from eutrophication of surface waters (Zempolich, 1993). This hypothesis is

consistent with similar claims of eutrophic environmental conditions in the Umbria–Marche Basin at this time (Bartolini and Cecca, 1999). In general, the San Vigilio Oolite–Rosso Ammonitico facies contact appears relatively transitional in nature: the presence of Aalenian ammonites and pink-stained oolite, condensed in nature with hardgrounds and ferro-manganese crusts (registering a series of hiatuses) suggests decreasing sedimentation rate and increasing pelagic conditions leading to the ultimate drowning of the carbonate platform. Further evidence of ooids, oncolites, stromatolites and wave-rippled coquinas in the "drowning facies", and analogies to modern drowned platforms, support the hypothesis that drowning occurred in relatively shallow water that was rich in nutrients but deficient in oxygen (Zempolich, 1993). Although drowning of the Trento Platform due to eutrophication may agree with the interpretation of environmental conditions outlined above for the Umbria–Marche Basin in the Aalenian–Bajocian (Bartolini *et al.*, 1999; Bartolini and Cecca, 1999; Morettini *et al.*, 2002), there is a significant contrast: on the Trento Plateau, carbonate deposition continued post-Aalenian in pelagic facies (locally after a Bajocian hiatus; Sturani, 1964). The calcareous pelagic sediments that were deposited after drowning of the carbonate platform are termed the Rosso Ammonitico (although radiolarian cherts develop in the Rosso Ammonitico Medio, which is Callovian–Oxfordian in age; Baumgartner *et al.*, 1995; Clari and Martire, 1996). However, it is suggested that in Umbria–Marche there was a "carbonate crisis" in deposition that led to positive $\delta^{13}C$ excursions being registered in global carbon-isotope records (see above).

Impact on the Campania–Lucania Platform

$\delta^{13}C$ data from a section through the Campania–Lucania Platform (Figure 5.v) can be correlated with a compilation of belemnite data of Gröcke (2001) and Jenkyns *et al.* (2002a). Particularly distinctive are the negative $\delta^{13}C$ excursion dated as Aalenian–Bajocian boundary (174 Ma; Pàlfy *et al.*, 2000b), and the approximately mid-Bajocian positive excursion (170 Ma; Pàlfy *et al.*, 2000b; Hesselbo *et al.*, *In Press*). Also significant in the Campania–Lucania Platform (the +260 m level of the Monte Sorgenza section), is a positive $\delta^{13}C$ excursion registered in the Aalenian, which could potentially correlate with the positive excursion also seen in the belemnite data (Figures 5.v and 6.xi).

The Campania-Lucania Platform did not appear to be as severely affected as neighbouring areas of carbonate production (Trento Platform and Umbria–Marche Basin) by the carbon-cycle perturbation in the Aalenian–Bajocian. However, there was a significant facies change recorded at what is believed to be approximately the Aalenian–Bajocian boundary by biostratigraphy (Violante, 2000) and chemostratigraphy (***5.2.1*** and Figure 5.v). The facies change from oolite to cyclically bedded micritic limestones of peritidal nature (***4.1***) is indicative of carbonate-platform progradation due to relative sea-level highstand. The pronounced nature of the negative $\delta^{13}C$ excursion (and negative $\delta^{18}O$ excursion; Figure 6.v) suggests diagenetic modification may be significant at this level, but it should also be noted that there is a coherent return to background $\delta^{13}C$ values following the facies change (as opposed to a sharp one datum-point shift), so causative mechanisms for the distinct isotope and facies character *other than diagenesis* cannot be discounted (***4.3***). There are also distinct similarities between the condensed, pink nature of the upper levels of the Calcari à Oolitici (Campania–Lucania) and the San Vigilio Oolite (Trento). It is therefore possible that the same palaeoecological changes that resulted in the drawn-out drowning of the Trento Platform (due to eutrophication); the arid–humid climate change interpreted from characteristics of the Ravenscar Group of Yorkshire, England; and the onset of biosiliceous sedimentation at the expense of carbonate sedimentation (due to eutrophication) in Umbria–Marche, Italy, is also related to the oolite–cyclically-bedded micrite facies transition observed on the Campania–Lucania Platform. This casusative mechanism was not severe enough, however, to drown the platform. It is therefore reasonable to suggest that other local factors amplified the crisis in the Trento region at this time or, alternatively, local factors shielded the Campania–Lucania Platform.

Discussion

The fact that carbonate deposition does not appear to have ceased on a global, or even multi-regional scale, in the Aalenian–Bajocian means that it is unlikely that the reported 'carbonate crisis' in Umbria–Marche (and parts of the Trento Platform) could drive positive shifts in the global $\delta^{13}C$ record. It should also be noted that it would require an extremely large carbonate depositional change to affect the global carbon-isotope curve compared to organic-

carbon or methane reservoir changes (because of their respective average carbon-isotope values).

Previous authors have suggested that increased magmatism in the Aalenian–Bajocian may be the driving mechanism for all of the suggested environmental changes and observed isotopic shifts described above. In particular, the birth of the Pacific Plate, major subduction-related volcanism, continental deformation around the margins of Pangaea and ocean-spreading of Alpine Tethys have all been invoked to explain those changes above as well as the high eustatic sea level and initiation in the decrease of strontium-isotope ratios to less radiogenic values observed at this time (Figure 5.iv; Bartolini and Cecca, 1999; Bartolini and Larson, 2001; Gröcke, 2001; Hallam, 2001; Hesselbo *et al.*, *In Press*). These mechanisms support the observed geological phenomenon because increased mantle-derived magmatic activity would have induced greenhouse conditions by releasing CO_2, which would increase the hydrological cycle (arid to humid; Hesselbo *et al.*, *In Press*) and so supply increased levels of nutrients to the oceans in run-off. This chain of events could result in (meso-) eutrophication of surface waters. These proposed tectonic mechanisms are further supported by evidence that the observed facies and isotopic changes all occur gradually over relatively long periods of time (Hesselbo *et al.*, *In Press*).

Disregarding the possibility of relatively rapid methane dissociation, prolonged release of large volumes of isotopically light CO_2 is the most likely mechanism for forcing the gradual decrease of $\delta^{13}C$ values at the Aalenian–Bajocian boundary. However, the lack in accumulation of extensive Bajocian black-shales coupled with a lack of evidence for reduction in carbonate production that could drive a pronounced increase in $\delta^{13}C$ values during the mid-Bajocian results in this period of time remaining enigmatic in terms of mechanisms responsible for positive shifts in the $\delta^{13}C$ record.

6.2.3 The Oxfordian–Tithonian

Comments on the reference sections

Weissert and Mohr (1996) provide an excellent review of carbon cycling in the Late

Jurassic (Oxfordian–Tithonian), in which they detail that this interval is characterised by a $\delta^{13}C$ record that on a broad-scale displays decreasing isotope values from approximately +3‰ to +1‰. However, there is a relatively major positive excursion in the mid–upper Oxfordian and another two more minor excursions to more positive values in the upper Kimmeridgian and mid-Tithonian (Figure 6.xii). Later work on sections through the northern Tethys margin and the Polish Jura, by Padden *et al.* (2001) and Wierzbowski (2002) respectively, has added further detail to the Oxfordian carbon-isotope record. The former describe a negative $\delta^{13}C$ excursion in the *transversarium*-Zone (mid-Oxfordian) attributed to methane release from gas hydrates. Morgans-Bell *et al.* (2001) have also described a positive $\delta^{13}C_{org}$ excursion in the mid-*eudoxus* Zone (Kimmeridgian). The Upper Jurassic sedimentary record is characterised by the presence of widespread (but not globally distributed; Jenkyns, 1996) organic-rich black shales: some of the more significant sinks of organic-rich sediments were the Siberian Basin, the North Sea, the North American Gulf Coast, and the Arabian Shield (Weissert and Mohr, 1996). Occurences of these organic-rich sediments are particularly concentrated at upper Oxfordian, Kimmeridgian and lower Tithonian levels and their formation is believed to relate predominantly to high productivity and/or poor oceanic circulation during periods of high relative sea level (Jenkyns, 1996; Weissert and Mohr, 1996).

Weissert and Mohr (1996) also conclude that the relatively good health of European, Asian and Arabian reef provinces during the Kimmeridgian–Tithonian (as opposed to the Oxfordian when sponge reefs replaced carbonate producers in northern Tethys as a result of eutrophication; Leinfelder, 1993) buffered what would otherwise have been major carbon-isotope maxima responding to widespread deposition of organic-rich sediment. In this way, the authors justify the difference between the pronounced Oxfordian positive and the later two less pronounced excursions.

Impact on the Friuli Platform

Figure 6.xii illustrates the $\delta^{13}C$ correlation between the north Tethyan reference curve of Weissert and Mohr (1996) and the Friuli Platform profile. The available biostratigraphy further supports the claim that the lower 300 m of the Friuli Platform ranges in age from

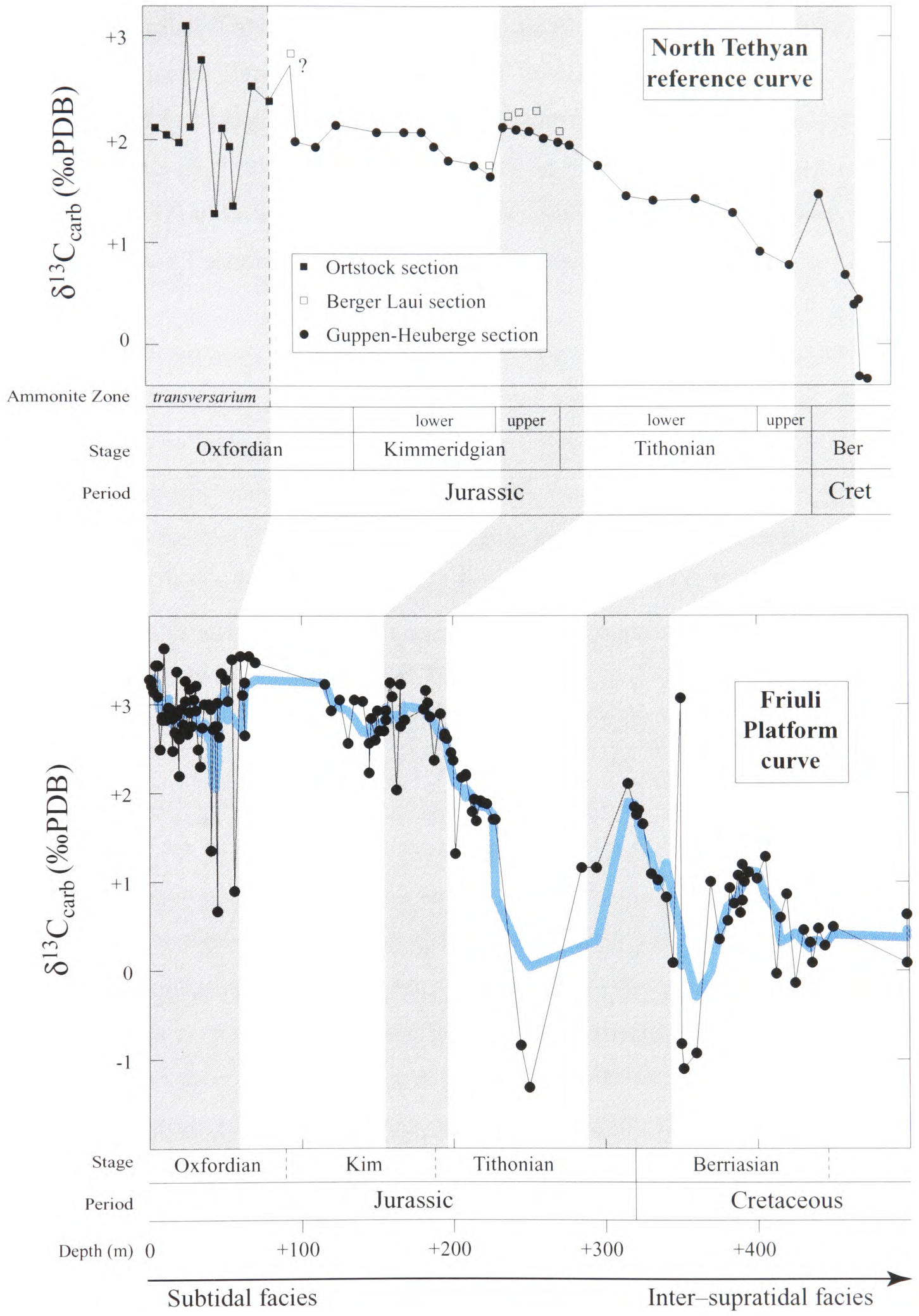

Figure 6.xii. Correlation between the reference carbon-isotope profile of north Tethyan hemipelagic sediments (Weissert and Mohr, 1996) and that of the lower 500 m of the Upper Jurassic Friuli Platform section (Val Cellina). Note that the Tithonian–Berriasian correlation is based on the available biostratigraphy for the Friuli Platform.

Oxfordian–Tithonian. Although there is no exposure of pre-Oxfordian carbonates in the Friuli Platform, those Oxfordian–Tithonian facies that are exposed have been interpreted to reflect: 1) intertidal platform facies deposited at a depth of 10–15 m (Cuvillier *et al.*, 1968); 2) sub–supratidal facies that range in depositional style from biomicritic limestone representing lagoonal environments (3–5 m water depth; from the 0 to +215 m levels / Oxfordian to lower Tithonian; Ghetti, 1987) to Lofer Cylic limestones indicative of the inter–supratidal zones (the +215 to +350 m levels / Tithonian to Berriasian; Fischer, 1964; Ghetti, 1987).

Although sedimentation patterns changed over this interval, the changes are not of an extent to be related reliably to global environmental stresses, because small changes in depositional style can be forced by relatively minor local factors. However, there does appear to be a general transition from subtidal to increasingly inter–supratidal zone facies over the lower 300 m of section in the Val Cellina section (possibly related to a change from fault-related subsidence to thermal subsidence in the evolution of Tethyan rifting). This indicates either a slowing rate of rise in relative sea level or the onset of more conducive conditions for platform growth at this locality between Oxfordian and Tithonian times.

Discussion

Because there are no pronounced facies changes associated with the relatively high $\delta^{13}C$ values in the carbon-isotope profile of the Oxfordian–Tithonian interval, it is suggested that the Friuli Platform was relatively sheltered from the potentially degradative factors responsible for organic-carbon accumulation. Regarding sea level, an Oxfordian (*transversarium/glosense* Zone) transgression is very well documented from a geographically widespread area: Jenkyns (1996), and references therein, document stratigraphic evidence for Oxfordian-Stage flooding from the Balearics, Morocco, southern Spain, northeastern Spain, northern Switzerland, Paris Basin, Poland, England, Scotland, North Sea, Greenland, Russia, Alaska, Himalayas, Pakistan and the Gulf of Mexico. Jenkyns (1996), Weissert and Channell (1989), and Weissert and Mohr (1996) recognise the significance of a coincident Oxfordian sea-level trangression and positive carbon-isotope excursion, but Weissert and Mohr (1996) go on to note that the subsequent drop in isotope values in the Tithonian also correlates with falling sea level. Direct facies interpretations that suggest either a decrease in the rates of sea-level rise or better growth

conditions for carbonate platforms (i.e. subtidal–intertidal facies transition) during the Oxfordian–Tithonian of the Friuli Platform can likewise be correlated to a transition from 'high' to 'low' $\delta^{13}C$ trends in the shallow-water carbonates.

6.2.4 The Valanginian–Hauterivian

Comments on the reference sections

Reference sections of Tethyan pelagic sediments that have been biostratigraphically and magnetstratigraphically calibrated provide distinctive $\delta^{13}C_{carb}$ and $\delta^{13}C_{org}$ profiles of the positive isotope excursion in the Valanginian–Hauterivian interval (Figure 5.xi; Lini *et al.*, 1992; Channell *et al.*, 1993; Michalík *et al.*, 1995; Weissert *et al.*, 1998; Hennig *et al.*, 1999; Föllmi *et al*, 1994; van de Schootbrugge *et al.*, 2000; Wortmann and Weissert, 2000). These reference carbon-isotope profiles have further been correlated to profiles obtained from sections in the Gulf of Mexico, the western North Atlantic and the Central Pacific (Lini *et al.*, 1992). The isotope excursion itself is therefore considered as a global oceanographic phenomenon. The Valanginian–Hauterivian pelagic sedimentary record shows widespread organic-rich sediment deposition. Localities with black shales deposited in the Valanginian–Hauterivian include the Southern Alps (Lombardian Basin), the Blake Bahama Formation and North Atlantic, the Galicia Margin, the Gulf of Mexico, offshore Morocco, east Antarctica (Lini *et al.*, 1992), and the Pacific Basin (Bralower *et al.*, 2002). Although accumulations of organic-rich black shales are not as ubiquotously distributed as in the early Toarcian, early Aptian and Cenomanian–Turonian intervals, they are widespread in the Valanginian–Hauterivian, and provide further evidence of a major carbon-cycle perturbation at this time.

Lini *et al.* (1992) provide the most recent review of palaeoenvironmental conditions in the Valanginian–Hauterivian interval and their relation to the carbon cycle. They document a greenhouse climate that was the result of elevated inputs of tectonically derived CO_2, which caused an intensification of the hydrological cycle and continental weathering rates. Consequently, a rise in nutrient levels in the oceans from runoff caused primary productivity increases leading to the preservation of organic-rich sediments (i.e. black shales). Increased

carbon burial was suggested to act as a negative feedback mechanism by drawing CO_2 out of the atmosphere into the sediment sink (deposited as organic carbon), which eventually returned the system to environmental conditions similar to those experienced pre-Valanginian–Hauterivian.

In ***6.2.1***, the Föllmi *et al.* (1994) method of carbonate facies interpretation is described and employed to discuss the significance of facies associations from the Pliensbachian–Toarcian interval in the Trento Platform. This interpretational model was first devised by Föllmi *et al.* (1994) to explain Lower Cretaceous platform successions from the north Tethyan margin. In particular, facies interpreted to represent mesotrophic and eutrophic conditions (crinoid–bryozoan and condensed phosphatic intervals respectively) were found at Valanginian–Hauterivian levels, and these indicators are believed to represent 'unhealthy' conditions on the north Tethyan carbonate platforms during this period. Because these intervals of platform demise are associated with the Valanginian–Hauterivian positive carbon-isotope excursion, Föllmi *et al.* (1994) and Weissert *et al.* (1998) suggest that the mechanisms that caused widespread ocean anoxia and carbon-cycle perturbation were also responsible (directly or indirectly) for platform drowning on the north Tethyan margin. Other platforms that drowned during the Valanginian–Hauterivian include those along the African margin, the American Atlantic margin and on the Arabian Peninsula (Weissert *et al.*, 1998 and references therein). However, Föllmi *et al.* (1994) go on to admit that not all carbonate platforms were affected in this way, and those platforms that were immune to environmental stresses were "isolated, clean platforms, which were remote from continents and did not experience the presence of impinging oxygen-minimum zones, upwelling nutrient-rich waters and the like".

Impact on the Friuli Platform

From chemostratigraphic correlations between reference isotope profiles and the Friuli Platform, it is concluded that the $\delta^{13}C$ positive excursion in the Valanginian–Hauterivian can be observed between the +500 and +600 m levels in the Val Cellina section, Friuli Platform (Figures 5.ix and 5.xi). Cuvillier *et al.* (1968), Ghetti (1987) and Ghetti and Brigatti (1991) interpret the carbonate facies over this interval to represent marine environments that were

restricted and intertidal in nature with deposition occurring in a maximum depth of between 1–5 m. Periodic subaerial exposure led to the formation of birdseye, mud-crack and green-clay horizon (***3.1*** and ***3.1.1***). In this study, a clay-rich interval that is 50-cm thick and is eroded back at outcrop was discovered coincident with the apex of the $\delta^{13}C$ maximum (the +550 m level in the Val Cellina section). However, this interval is presumably the result of the same exposure-related effects that caused the other green argillaceous intervals (Ghetti and Brigatti, 1991).

Discussion

As in Oxfordian–Tithonian levels of the Friuli Platform, there is no major depositional-style change over the Valanginian–Hauterivian interval. The Friuli Platform appears to have been relatively 'immune' to Valanginian–Hauterivian oceanographic events that affected the north Tethyan platforms. It is likely, therefore, that the Friuli Platform matches the Föllmi *et al.* (1994) description of an isolated platform shielded from continentally-derived environmental stresses and nutrient-rich water circulation (c.f. Campania–Lucania Platform during the Toarcian).

6.2.5 The Aptian–Albian Oceanic Anoxic Events

Comments on the reference sections

The Aptian–Albian oceanic anoxic events (OAE's 1a–1d; Arthur *et al.*, 1990; Erbacher *et al.*, 1996) are very well documented from an extensive dataset of globally distributed localities and varying facies types (marine–terrestrial). The early Aptian OAE (1a, Livello Selli) is believed to have been a global phenomenon, whereas the later OAE's in the series are more generally regarded as being widespread, as opposed to global in extent. In general, these OAE's are charcterised by intervals with elevated wt% TOC (e.g. Schlanger and Jenkyns, 1976; Arthur *et al.*, 1990; Bralower *et al.*, 1994); a negative followed by positive carbon-isotope excursion in lower Aptian intervals and an Albian series of positive excursions (in terrestrial and marine facies; e.g. Scholle and Arthur, 1980; Erbacher *et al.*, 1996; Ferreri, 1997; Menegatti *et al.*, 1998; Weissert *et al.*, 1998; Bralower *et al.*, 1999; Erba *et al.*, 1999; Gröcke *et al.*, 1999;

Jenkyns and Wilson, 1999; Masse *et al.*, 1999; Jahren *et al.*, 2001); an Aptian strontium-isotope value shift to less radiogenic values followed by a return to more radiogenic values in the Albian (e.g. Jones *et al.*, 1994a; Bralower *et al.*, 1997; Jenkyns and Wilson, 1999; Jones and Jenkyns, 2001; Price and Gröcke, 2002); and an early Aptian "nannoconid crisis" (Erba, 1994).

Due to the various consequences of the OAE's, diagnosing the prevailing forcing mechanisms remains controversial. However, a mechanism generally accepted for promoting greenhouse conditions and an intensification of the hydrological cycle during this period is related to a significant increase in the rate of sea-floor spreading and basaltic plateau volcanism, which released large volumes of mantle-derived CO_2 into the atmosphere (e.g. Larson, 1991a, b; Erba, 1994; Jenkyns and Wilson, 1999; Larson and Erba, 1999). However, it has also been suggested that a significant release of methane from gas hydrates occurred in the early Aptian, and evidence for this is registered by a pronounced negative shift in global marine and terrestrial carbon-isotope profiles (Menegatti *et al.*, 1998; Erba *et al.*, 1999; Gröcke *et al.*, 1999; Jahren *et al.*, 2001). It is this negative $\delta^{13}C$ excursion that is coincident with the global deposition of organic-rich black shale. Therefore, the early Aptian OAE 1a shares some similarities with the early Toarcian OAE (***6.2.1***; Beerling *et al.*, 2001).

$\delta^{13}C$ profiles from Barremian–Albian levels of shallow-water carbonates are also relatively abundant (Vahrenkamp, 1996; Ferreri, 1997; Grötsch, 1998; Masse *et al.*, 1999; Wissler *et al.*, 1999; Wissler, 2001; Wissler *et al.*, 2002). Although the carbonate platforms investigated by the above authors did not drown during the OAE's, widespread platform drowning is documented for the Aptian–Albian (e.g. Simo *et al.*, 1993; Weissert *et al.*, 1998). Platforms that drowned during the Aptian–Albian interval include those located in Mexico and along the northeastern North American margin (Weissert *et al.*, 1998). Weissert *et al.* (1998) suggest that "contemporaneous black shale deposits and drowned carbonate platforms therefore reflect the contrasting response of the marine organic and carbonate carbon pumps to nutrient-enhanced phytoplankton productivity". The authors even specify that carbonate platforms located on river-influenced coastlines were particularly vulnerable to nutrient-induced stress and therefore drowning (northern and southwestern Tethyan margins and northeastern America; Jansa, 1993). However, those carbonate platforms located on the Adria microplate were little

affected by continental influences and maintained growth through this period of eustatic sea-level rise (Haq *et al.*, 1987; Föllmi *et al.*, 1994).

Impact on the Friuli Platform

Figure 5.xii illustrates the $\delta^{13}C$ correlation of Barremian–Aptian profiles between a Tethyan pelagic reference section (Erba *et al.*, 1999) and the section through the Friuli Platform (Val Cellina). The association of the isotope profile from the Friuli Platform section with a graphic log of the shallow-water carbonates is illustrated in Figure 6.xiii. As discussed in ***5.2.2.2***, without a recognisable isotope trend that can be confidently correlated with the positive $\delta^{13}C$ excursions from the Aptian and Albian, there is little significance in a detailed analysis of platform responses during this time. However, it is believed that the negative $\delta^{13}C$ excursion in the lower Aptian is registered in the shallow-water carbonates of the Friuli Platform. Regardless of this fact, however, the carbonate platform appears to have been little influenced by the global oceanographic conditions that had developed at this time (D'Argenio *et al.*, 1992; Föllmi *et al.*, 1994; Weissert *et al.*, 1998). However, it is potentially significant that there is an apparent association of green argillaceous levels with the beginning of the negative $\delta^{13}C$ excursion. With no exposure below the +760 m level, however, it is difficult to say whether this represents a real increase in the frequency of green clay levels around this level, or whether the +760 to +770 m level records a temporary respite from conditions that had begun lower down in the section, which is not exposed (the +720 to +760 m level).

Also, it is clear that the positive $\delta^{13}C$ excursion in the lower Aptian is not represented in the $\delta^{13}C$ profile, and so it must be concluded that: 1) there is missing section due to a hiatus; 2) the primary isotope signal has been modified by diagenesis; or 3) the depositional environment in which this level of the carbonate platform was deposited became restricted and ceased to record the isotope signal of the open ocean (Brasier and Green, 1993; Grötsch, 1998). It is believed that the last of these possibilities is the most likely because there is no evidence for major hiatus in the section and, it is concluded that diagenetic modification would have resulted in very negative and/or scattered carbon- and oxygen-isotope signals, which is not the case here. However, restricted conditions are believed to have only been ephemeral, as by approximately

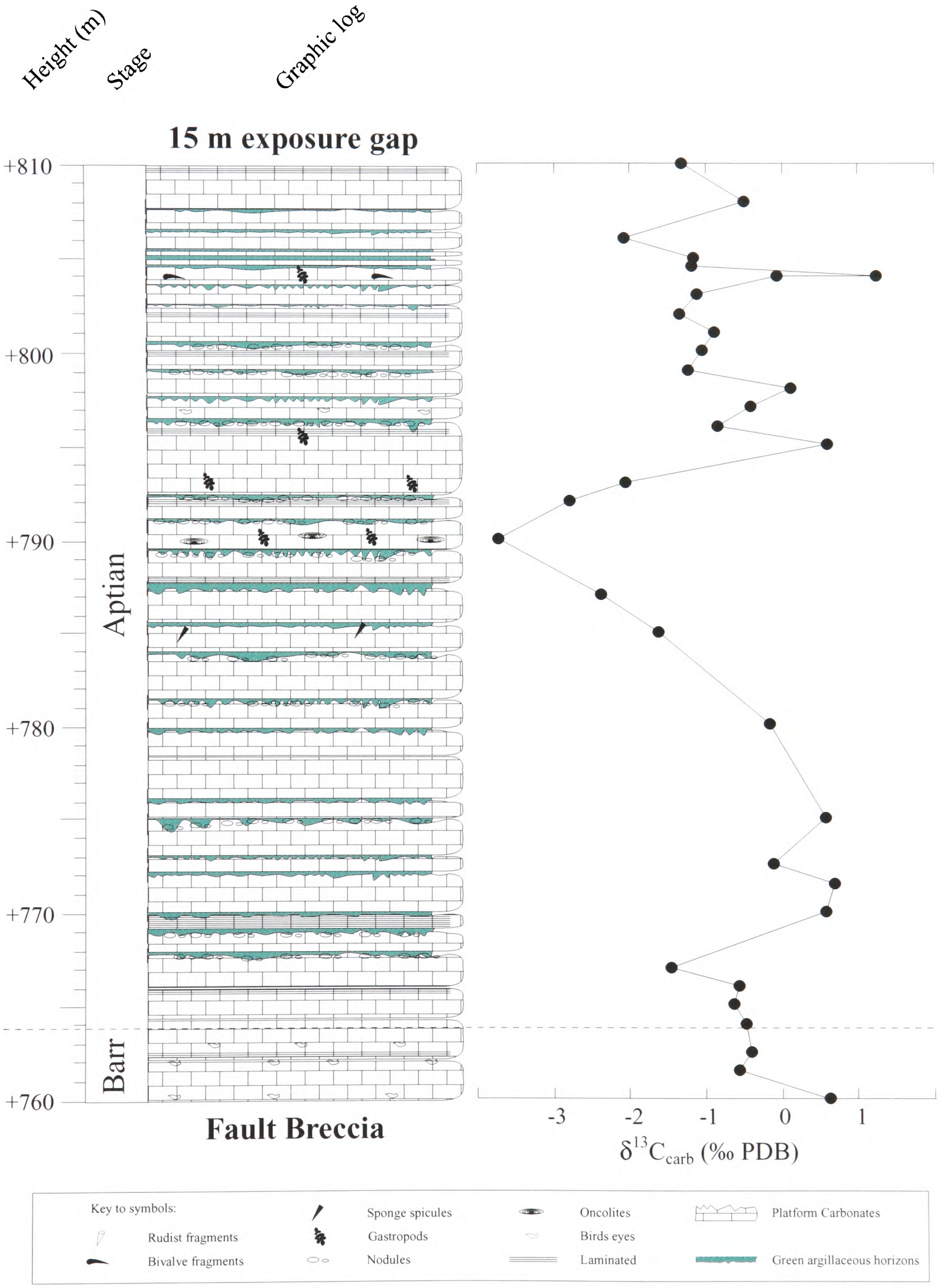

Figure 6.xiii. Detailed stratigraphic log and carbon-isotope profile of the +760 to +810 m levels of platform carbonate in the Val Cellina section, Friuli Platform. The position of the Barremian (Barr)–Aptian Stage boundary is based on chemostratigraphic correlation.

the Albian–Cenomanian Stage boundary (the +1000m level in the section), correlations of the $\delta^{13}C$ profile from the shallow-water carbonates to reference curves can be achieved once more (Figure 5.ix).

In summary: Barremian–Aptian levels of the section through the Friuli Platform (Val Cellina) are, in this instance, difficult to correlate because of problems resulting from exposure gaps and possible restricted conditions at the time of deposition. However, the negative $\delta^{13}C$ excursion from lower Aptian levels is confidently correlated and, although following this 'event' absolute values do not reach as high as encountered in the reference sections, the elevated $\delta^{13}C$ values between the +820 and +900 m levels are similar to that of the reference data. It is believed, however, that there may have been a general 'dampening' of the primary isotope signal due to platform restriction at the time of deposition (e.g. Grötsch, 1998; Davey and Jenkyns, 1999).

Discussion

It is concluded that the Friuli Platform was, broadly speaking, immume to the global oceanographic events of the Barremian–Albian period, which were so detrimental to other carbonate platforms in Tethys and elsewhere (see above).

The persistance of cyclic intertidal facies between the +770 and +810 m levels is indicative of relative sea-level rise, and is compatible with the general view of eustatic sea-level rise in the early Aptian (coincident with the negative $\delta^{13}C$ excursion: Gröcke *et al.*, 1999). Falling sea level later in the Aptian has been associated with the $\delta^{13}C$ positive excursion (Gröcke *et al.*, 1999), and if justified, this is another potential cause for the lack in positive isotope excursion on the Friuli Platform: falling sea level may have resulted in non-deposition/restriction on the Friuli Platform during this period.

6.2.6 The Cenomanian–Turonian Oceanic Anoxic Event

Comments on the reference sections

The Cenomanian–Turonian (Late Cretaceous) Oceanic Anoxic Event (OAE 2, Bonarelli Event) is recognised as being a global phenomenon characterised by intervals with elevated wt% TOC (e.g. Schlanger and Jenkyns, 1976; Jenkyns, 1980; Schlanger *et al.*, 1987; Arthur *et al.*, 1990); a four-pronged positive carbon-isotope excursion (in terrestrial and marine facies; e.g. Scholle and Arthur, 1980; Pratt and Threlkeld, 1984; Hilbrecht and Hoefs, 1986; Corfield *et al.*, 1991; Thurow *et al.*, 1992; Gale *et al.*, 1993; Jenkyns *et al.*, 1994; Valladares *et al.*, 1996; Hasegawa, 1997; Crespo de Cabrera *et al.*, 1999; Davey and Jenkyns, 1999; Hasegawa and Hatsugai, 2000; Stoll and Schrag, 2000); a shift in strontium-isotope values to less radiogenic values followed by a return to more radiogenic values beginning in the late Turonian (e.g. Jones *et al.*, 1994a; Bralower *et al.*, 1997; Jenkyns and Wilson, 1999; Jones and Jenkyns, 2001); a modest extinction event in the upper Cenomanian (e.g. Jarvis *et al.*, 1988; Harries, 1993; Hallam and Wignall, 1996); widespread drowning of carbonate platforms (e.g. Philip and Airaud, 1991; Simo *et al.*, 1993; Drzewiecki and Simo, 1997); global first-order eustatic sea-level highstand (Haq *et al.*, 1987); a palaeotemperature maximum (Jenkyns *et al.*, 1994; Clarke and Jenkyns, 1999; Huber *et al.*, 2002; Wilson *et al.*, 2002); and widespread chalk sedimentation on continental shelves (e.g. Hancock and Kauffman, 1979; Scholle and Arthur, 1980; Jenkyns *et al.*, 1994). Organic-rich black shales are globally distributed and in particular have been found in northern and southern Europe, Africa, North and South America, western Australia and the Pacific and Atlantic Basins (Jenkyns *et al.*, 1994 and references therein).

Oxygen-isotope data compiled from Cenomanian–Turonian sections through the English Chalk and the Exmouth Plateau (western Australia) register a pronounced warming through the Cenomanian, and a subsequent Turonian cooling (Jenkyns *et al.*, 1994; Clarke and Jenkyns, 1999). Modelling suggests that the extensive and prolonged drawdown of CO_2 into organic-rich sediments in the late Cenomanian resulted in the breach of a climatic threshold, resulting in global cooling and a return to pre-OAE conditions (Arthur *et al.*, 1988; Jenkyns *et al.*, 1994). Jones and Jenkyns (2001) conclude that pulses of major hydrothermal activity (most likely

caused by increased ocean-crust production, but also associated with oceanic plateau emplacement) were reposnsible for the three negative strontium-isotope excursions associated with the major Mesozoic OAE's (early Toarcian, early Aptian and Cenomanian–Turonian boundary). The authors suggest that this increased hydrothermal activity was responsible for increased pCO_2 during these periods, driving global warming, intensification of the hydrological cycle, increased weathering and nutrient input into the oceans. These processes resulted in high oceanic productivity and organic-carbon preservation in marine sediments. The major difficulty in assessing this theory for the Cenomanian–Turonian OAE is that crust formation at this time occurred in the Cretaceous Long Normal magnetic chron (Aptian–Santonian), making accurate dating of oceanic-crust formation very difficult. However, it has been suggested that formation of the Caribbean and parts of the Ontong–Java oceanic plateaus took place synchronously with the Cenomanian–Turonian OAE (Sinton and Duncan, 1997; Jones and Jenkyns, 2001).

Davey and Jenkyns (1999) detail the litho- and chemostratigraphy of the peri-Adriatic carbonate platform of Croatia. Not only does this carbonate platform register the reproducible positive $\delta^{13}C$ excursion at the Cenomanian–Turonian boundary, but there is also a coincident facies change to the distinctive Sveti Duh Formation: a nodular lime mudstone, locally with some organic matter, planktonic foraminifera, calcispheres, radiolarian-derived cherts, well-preserved fish fossils and locally Turonian ammonites (Jenkyns, 1991). This formation represents increased oceanic influence on the carbonate platform during Cenomanian–Turonian boundary time, when sea-level rise outstripped platform accumulation (Gusic and Jelanska, 1993; Davey and Jenkyns, 1999). However, this phenomenon was not enough to fully drown the carbonate platform, which persisted for the remainder of the Cretaceous.

Another carbonate platform that developed during the Cenomanian–Campanian interval is the Iberian Platform (Valladares *et al.*, 1996). A positive $\delta^{13}C$ excursion is registered at the Cenomanian–Turonian boundary in these shallow-water carbonates and is coincident with the introduction of planktonic foraminifera and calcispheres into the sediment. This is therefore further evidence that flooding of carbonate platforms occurred during the same interval as the Cenomanian–Turonian OAE (as registered by the $\delta^{13}C$ excursion), but it did not necessarily result in platform drowning.

Impact on the Friuli Platform

Figure 5.xiii illustrates the $\delta^{13}C$ correlation between the Cenomanian–Turonian levels of the chalk reference curve and the Friuli Platform profile. Highlighted are the positive excursions from the mid-Cenomanian and Cenomanian–Turonian boundary (both associated with drowning of carbonate platforms; Simo *et al.*, 1993). The facies over this level in the section through the Friuli Platform record rudist-bearing limestones with planktonic foraminifera and other benthic organisms (***3.1***). The presence of planktonic foraminifera indicates an increased oceanic influence on the Friuli Platform at this time. Further detailed lithostratigraphic studies were not possible on these levels of the Val Cellina section, as they are no longer accessible.

Impact on the Campania–Lucania Platform

All four reproducible maxima (A–D) associated with the positive $\delta^{13}C$ excursion at the Cenomanian–Turonian boundary are recognised in the carbon-isotope profile of the section through the Campania–Lucania Platform (Figure 5.xv). The available biostratigraphy of the platform carbonates (Robson, 1989) and correlation of the reference strontium-isotope profile with that from the section through the Campania–Lucania Platform also support the contention that these levels are Cenomanian–Turonian in age (Figure 5.ix). This evidence allows a confident facies comparison of these levels in the carbonate platform with those in the reference sections. Similar to the Friuli Platform, the Campania–Lucania Platform generally comprises micritic facies dominated by rudists and benthic foraminifera as bioclasts. There are also rare planktonic foraminifera recognised in this study in levels that have been dated as Turonian (***4.1.2***), and this is consistent with the flooding characteristics described from the Dinaric Platform for the same time period (see above). In addition to these characteristics, there are also levels in the Campania–Lucania Platform that are relatively rich in organic matter (***4.2.4*** and Figure 4.vii). There is a particular concentration of these organic-rich levels coincident with the positive $\delta^{13}C$ excursion at the Cenomanian–Turonian boundary (between the +40 to +80 m levels). The facies between the +80 and +120 m levels in the section through the

Campania–Lucania Platform (Turonian) are generally intraclastic/brecciated in nature: the likely result of storm-influence on deposition of the platform carbonate at this time.

Discussion

Platform accumulation rates (***5.3***) indicate that the Friuli Platform was relatively 'healthy' during this period. The rudist-reef ecosystem therefore produced enough carbonate to keep up with the rapidly increasing accommodation space that must have resulted from the sea-level rise that was experienced at this time. However, the occurrence of planktonic biota amongst grains of shallow-water affinity indicate platform flooding occurred in a similar way to that observed on the Dinaric Platform (see above), although with less obvious detrimental effects in the Friuli region. There are no signs of 'partial drowning' on the Friuli Platform, and so it was presumably more 'immune' to OAE-related stresses than the Dinaric Platform. A suggestion that could account for this phenomenon is that the Friuli Platform was on the margin of open ocean, whereas the Dinaric Platform bordered a potentially restricted Marche–Umbrian–Adriatic deep-water basin where oceanic anoxia was more acute (the black shales of the Adriatic Bonarelli Horizon are amongst the most carbon-rich that have been reported from this time; Jenkyns, 1991).

Although three peri–Adriatic carbonate platforms (Friuli, Campania–Lucania and Dinaric) are predominantly composed of rudist-derived limestone and display increased oceanic character during the Cenomanian–Turonian, the Campania–Lucania Platform shares more obvious similarities with the Dinaric Platform than with the Friuli Platform. This similarity is a function of the intercalated carbon-rich levels found within these two platforms (i.e. the Sorrento Formation of Italy appears equivalent, and similar, to the Sveti Duh Formation of Croatia). It is possible, therefore, that the Campania–Lucania Platform suffered in a similar fashion to the Dinaric Platform during this period: rapid transgression and an 'inflated' oxygen-minimum zone induced the carrying of deoxygenated water onto the platform (Jenkyns, 1991).

However, as none of the above carbonate platforms suffered to the extent that they drowned during this period, they must have been relatively isolated from some of the more

severe effects generated by the OAE. If this hypothesis is correct, it may be significant that the Campania–Lucania and Dinaric Platforms were both locally exposed to what must have been nutrient-rich water (in the oxygen-minimum zone), but without any noticeable effect on their carbonate accumulation rate. A similar phenomenon has been observed on Resolution Guyot in the Pacific Ocean: organic-rich levels are recorded in the lower Aptian (registering the presence of nutrient-rich/de-oxygenated waters at the time of deposition), but the guyot continued to grow and accumulate shallow-water carbonate (Wilson *et al.*, 1998; Jenkyns and Wilson, 1999). Jenkyns and Wilson (1999) suggest that high sea-surface temperatures in equatorial waters (>30°C) are in fact the dominant mechanism responsible for Pacific guyot drowning, and not elevated nutrient levels. It is possible to conclude, therefore, that nutrient-rich waters were not capable of drowning the Dinaric and Campania–Lucania Platforms during the Cenomanian–Turonian interval. Lacking other mechanisms capable of platform devastation on a global scale, it is suggested that the palaeotemperature maximum at the Cenomanian–Turonian boundary could have been responsible for widespread drowning at this time (***6.2.1*** and ***6.3***; Jenkyns *et al.*, 1994; Clarke and Jenkyns, 1999; Glynn, 2000; Goreau *et al.*, 2000).

6.2.7 The Coniacian–Santonian Oceanic Anoxic Event

Comments on the reference sections

The Coniacian–Santonian Oceanic Anoxic Event (OAE 3) is less well documented in the literature than the other Jurassic and Cretaceous OAE's, but was first described as a potential OAE candidate by Arthur and Schlanger (1979), Jenkyns (1980), and Arthur *et al.* (1990). OAE 3 is characterised by a shift in $\delta^{13}C$ to more positive values (Scholle and Arthur, 1980; Corfield *et al.*, 1991; Jenkyns *et al.*, 1994; Crespo de Cabrera *et al.*, 1999; Stoll and Schrag, 2000); widespread development of organic-rich black-shales (northwest and southwest African margin, northern South America, and the Western Interior Seaway of North America; Arthur *et al.*, 1990; Jenkyns *et al.*, 1994); a potential maximum in palaeotemperature (Clarke and Jenkyns, 1999); and a strontium-isotope shift to more radiogenic values (Jones *et al.*, 1994a; Jones and Jenkyns, 2001). Generally, palaeoclimatic and palaeoceanographic conditions

are believed to be similar to those experienced during the Cenomanian–Turonian OAE, and so less time is dwelt on reviewing these (see ***6.2.6***). However, it should be noted that there was further widespread drowning of carbonate platforms at this time (e.g. Mexico, Brazil, Tunisia; Simo *et al.*, 1993).

Impact on the Friuli Platform

As discussed in ***5.2.2.2*** and ***5.3***, the post-Turonian levels of the section through the Friuli Platform become increasingly condensed, and with low frequency sampling (due to inaccessibility after the initial pilot study) correlation of these intervals is difficult and of little significance. It can be noted that, as with the Cenomanian–Turonian OAE, facies are dominated by rudist-derived limestones with planktonic foraminifera, indicative of platform flooding (***6.2.6***).

Impact on the Campania–Lucania Platform

Figure 5.xiv illustrates the correlation of the Coniacian–Santonian $\delta^{13}C$ profile of the Campania–Lucania Platform to the chalk reference curves of Jenkyns *et al.* (1994). The carbonate platform does not appear to be condensed in the Coniacian–Santonian (***5.3***), but instead the Sorrento Formation continued to be deposited in much the same style as during the Cenomanian–Turonian interval. Coincident with the broad positive $\delta^{13}C$ 'plateau' are a series of organic-rich carbonate levels (the +120, +170's, +200's and +225 m levels; Figure 4.xxv). The fact that these organic-rich levels are locally associated with relatively depleted $\delta^{13}C$ ratios may be a factor in the organic-carbon content of the bulk-rock samples (it is possible not all organic carbon was eliminated from the analyses). Associated with the final decrease in isotope values at the top of the section is the disappearance of organic carbon-rich levels from the Raia del Pedale section.

Discussion

Palaeoenvironmental conditions appear to have remained similar during the Cenomanian–Santonian interval on the Friuli and Campania–Lucania Platforms. In particular, the late Turonian–Santonian period witnessed the return of those environments which resulted in emplacement of organic-rich carbonate onto the Campania–Lucania Platform (***6.2.6***; Jenkyns, 1991; Davey and Jenkyns, 1999). The carbonate platform does not appear to have suffered in terms of its accumulation rate (***5.3***), and carried on growing throughout the rest of the Santonian. If the Campania–Lucania Platform was not in a "nutrient-shadow" during the Cenomanian–Turonian interval (as registered by the presence of organic-rich facies), the elevated nutrient levels alone were not capable of drowning the platform. Therefore, as in the Cenomanian–Turoninan interval, it is possible that shielding from high sea-surface temperatures may have been the reason the platform did not drown.

6.3 Concluding remarks

With such a large database of causes, effects and platform responses of/to periods of major perturbation in the carbon cycle, it is possible to delimit the common factors between each 'event'. In particular, it is understood that all periods of widespread/global devastation of carbonate platforms occurred at times with the following characteristics: high eustatic sea level; positive $\delta^{13}C$ excursions; elevated pCO_2; high hydrothermal/volcanic activity; elevated marine primary productivity/organic-carbon burial; relatively high palaeotemperatures; and elevated continental weathering rates/relatively intense hydrological cycle. Further associated characteristics that are not observed during all events are: possible records of methane-hydrate dissociation (as registered by pronounced negative excursions in $\delta^{13}C$ records); shifts in strontium isotope values to less radiogenic values; and carbonate precipitation crises.

The triggers of each of the events, the combination and relative significance of the above-listed characteristics and the way in which they manifested themselves to cause global disruption of the palaeooceanographic/palaeoatmospheric realms varied and are very complex. Not only did each event vary in terms of its driving mechanisms, there were also 'internal'

regional variations in effects when each event is considered individually. In other words, the immunity of platforms to the consequences of these global perturbations varied, depending on the local environment of each individual platform. This same phenomenon of platform 'immunity' is witnessed in the modern world during Global Coral Bleaching Events (***6.2.1***; Goreau *et al.*, 2000).

To drown a carbonate platform completely, it appears that the oceans must be preconditioned: rising relative sea level (in most cases eustatic) is necessary to ensure that carbonate producers that have succumbed to environmental stresses cannot regain the necessary 'footing' for rejuvenation. However, evidence shows that rising sea level acting alone (in a greenhouse world), and not in concert with other environmental stresses, is not capable of drowning a 'healthy' carbonate platform, as rates of platform growth can outstrip all rates of relative sea-level rise (Schlager, 1981).

There are numerous environmental stresses responsible for the degradation of carbonate platforms in the modern world. Goreau (1992) lists the following: "overgrowth by algae, sponges and soft corals; eutrophication by sewage nutrients; reduced herbivory due to overfishing and natural causes; hurricanes; sedimentation; diver and boat damage; and coral bleaching". The length of this list is a function of the sensitivity of reef ecosystems to oceanographic conditions. However, in terms of global mortality, the only factor that can act on this scale in the modern world is bleaching related to sea-surface temperature increases during El Niño Southern Oscillations (Goreau *et al.*, 2000). Despite this evidence, mechanisms for global demise of carbonate platforms in the ancient world have focussed almost singularly on nutrient-related mortality (e.g. Hallock, 1988; Zempolich, 1993; Föllmi *et al.*, 1994; Weissert *et al.*, 1998; Cobianchi and Picotti, 2001). However, Schlager (1981), Wilson *et al.* (1998), Jenkyns and Wilson (1999), and Glynn (2000) have all discussed the potential role of palaeotemperature in the demise of ancient carbonate platforms. The limiting factor regarding temperature-related hypotheses of drowning appears to be the abundance of nutrient-level proxy data and the paucity of high-resolution temperature-proxy data over the intervals in question. However, this situation is changing with evidence that platforms do not always drown when both sea-level rises are rapid and sea-water nutrient levels are high. This scenario is

demonstrated by platforms with organic-rich intervals (derived from nutrient-rich/de-oxygenated water) whose growth potentials were not severely affected and were still evidently 'healthy' (***6.2.1***, ***6.2.6***, ***6.2.7***; Wilson *et al.*, 1998; Jenkyns and Wilson, 1999). The implication of this phenomenon is that these platforms were not in a 'nutrient-shadow' zone yet did not drown, and so were potentially in a 'high sea-surface-temperature shadow' zone. Also, with increasing resolution and reliability of temperature-proxy data (e.g. belemnite Mg/Ca and $\delta^{18}O$ data from the Pliensbachian–Toarcian interval: McArthur *et al.*, 2000a; Bailey *et al.*, 2001; Rosales *et al.*, 2001), increasingly direct evidence for the relationship between temperature increases and platform devastation is coming to light (***6.2.1***).

Chapter 7: Conclusions

Chapter 7: Conclusions

The chemostratigraphic frameworks developed in this study have increased the precision of dating of poorly constrained shallow-water carbonate platforms in Italy. This increase in precision has been achieved by chemostratigraphic correlation with sections that are well constrained by biostratigraphy. The high-resolution correlation of platforms to other facies has also allowed comparison of changes in carbonate-platform facies with those of other sections and their available proxy data.

The method of chemostratigraphic correlation is limited by the effects of diagenetic modification of primary isotope signals: a phenomenon that is especially prevalent in shallow-water carbonates. To combat this problem, screening of samples by petrographic analysis was employed: samples with obvious signs of recrystallisation were rejected. In addition, a more analytical/quantitative procedure of screening has been devised that removes carbon-isotope data obtained from those samples with 'anomalous' oxygen-isotope values. In general, strontium-isotope values of samples taken from the Trento and Friuli Platforms were coherent and produced reproducible trends that could be correlated with reference sections. Strontium-isotope data of samples taken from the Lower Jurassic of the Campania–Lucania Platform were more variable, although remnants of a primary isotope signal are still discernible.

Carbon-isotope data of samples taken from the Trento Platform gave reproducible signals over critical intervals, and scatter not removed by screening using oxygen-isotope data is assumed to result from the presence of abundant skeletal material. In general, carbon-isotope data of samples taken from the Friuli Platform display reproducible trends, although there are intervals with anomalously negative values; and trends for the Aptian–Cenomanian indicate that platform restriction may have been a factor at that time (as they do not register the open-marine signature that has been globally recognised for this period). Lower Jurassic carbon-isotope signals obtained from samples taken from the Campania–Lucania Platform are generally coherent and display reproducible trends but, at intervals where post-depositional fluid interaction and crystal replacement are apparent, anomalously negative values are registered. The carbon-isotope record obtained from samples taken from the section through the

Cenomanian–Turonian boundary interval of the Campania–Lucania Platform is well preserved and coherent in nature. Consequently, the profile can be accurately correlated with reference data from pelagic sections. However, where there is evidence of dolomite replacement and concentrated bioclastic debris, the signal becomes less coherent. It is important to note that carbon- and oxygen-isotope signals from the shallow-water carbonates analysed are generally more coherent over levels known to represent periods of carbon-cycle perturbation (in particular the Toarcian and Cenomanian–Turonian). This observation could be a function of reduced meteoric diagenesis at these levels due to elevated sea levels during periods of deposition.

Chemostratigraphic frameworks are only useful in refining relative age specifications of carbonate platforms when sections analysed are of extensive vertical thickness (i.e. > 50 m), unless biostratigraphic constraint is particularly good and/or facies are particularly distinctive (e.g. Toarcian interval in the Trento Platform). Biostratigraphic and lithostratigraphic background is an integral part of the chemostratigraphic approach used in this study. Strontium-isotope stratigraphy has also been employed where possible because, although the technique only offers broad-ranged trends for correlation, strontium-isotope ratios appear to be the most diagenetically robust proxy used in this study.

In summary, chemostratigraphic analysis of shallow-water carbonates would benefit from a more cohesive, consistently reliable and thorough method of diagenetic screening, which will most likely be related to a greater understanding of oxygen-isotope records (or possibly trace-element ratios). However, with well-defined and calibrated reference curves already available for correlation, those platform carbon-isotope and strontium-isotope records with reproducible trends are valuable assets. The expanded nature of sedimentary records through carbonate platforms provides increased resolution of critical isotopic trends and facies characteristics (e.g. the Cenomanian–Turonian interval of the Campania–Lucania Platform). With tighter stratigraphic constraint, carbonate platforms become much more valuable when assessing past climatic and oceanographic conditions. Advances in high-resolution dating of a rock type so intrinsically linked to the carbon cycle, relative sea level and the environmental conditions in which it prevailed, offer an invaluable resource for insight into what, up to now, has proved a relatively enigmatic system.

References

References

Aberhan, M., Fürsich, F. T., 1996. Diversity analysis of Lower Jurassic bivalves of the Andean Basin and Pliensbachian–Toarcian mass extinction. *Lethaia*, **v.** 29, pp. 181-195.

Accarie, H., Emmanuel, L., Robaszynski, F., Baudin, F., Amedro, F., Caron, M., Deconinck, J. F., 1996. La Geochimie isotopique du carbone ($\delta^{13}C$) comme outil stratigraphique; application a la limite Cenomanien/ Turonien en Tunisie centrale. *Comptes Rendus de l'Academie des Sciences, Serie II. Sciences de la Terre et des Planetes*, **v.** 322, pp. 579-586.

AGIP, 1959. Relazione geologica e mineraria sulla Pianura Padana. *Accadamia Nazionale Lincei Roma*, **v.** 3, pp. 63-559.

Allan, J. R., Matthews, R. K., 1982. Isotope signature associated with early meteoric diagenesis. *Sedimentology*, **v.** 29, pp. 797-817.

Anderson, T. F., Popp, B. N., Williams, A. C., Ho, L. Z., Hudson, J. D., 1994. The stable isotopic records of fossils from the Peterborough Member, Oxford Clay Formation (Jurassic), UK; palaeoenvironmental implications. *In* Hudson, J. D., (*ed.*). Oxford Clay studies.: Geological Society of London, London, **v.** 151 Part 1, pp. 125-138.

Argand, E., 1924. La tectonique de l'Asie. *Proceedings of the International Geological Congress*, **v.** 13, pp. 171-372.

Arthur, M. A., Schlanger, S. O., 1979. Cretaceous "oceanic anoxic events" as causal factors in development of reef-reservoired giant oil fields. *American Association of Petroleum Geologists Bulletin*, **v.** 63, pp. 870-885.

Arthur, M. A., Dean, W. E., Schlanger, S. O., 1985. Variations in the global carbon cycle during the Cretaceous related to climate, volcanism, and changes in atmospheric CO_2. *In* Sundquist Eric, T., Broecker Wallace, S., (*eds.*). The carbon cycle and atmospheric CO_2 ; natural variations Archean to present.: Geophysical Monograph: American Geophysical Union, Washington, DC, United States, **v.** 32, pp. 504-529.

Arthur, M. A., Dean, W. E., Pratt, L. M., 1988. Geochemical and climatic effects of increased marine organic carbon burial at the Cenomanian/Turonian boundary. *Nature*, **v.** 335, pp. 714-717.

Arthur, M. A., Jenkyns, H. C., Brumsack, H. J., Schlanger, S. O., 1990. Stratigraphy, geochemistry, and paleo-oceanography of organic carbon-rich Cretaceous sequences. *In* Ginsburg, R. N., Beaudoin, B., (*eds.*). Cretaceous resources, events and rhythms; background and plans for research.: NATO ASI Series. Series C: Mathematical and Physical Sciences: D. Reidel, Dordrecht-Boston, **v.** 304, pp. 75-119.

Aubouin, J., 1963. Essai sur la paléogéographie post-triassique et l'évolution secondaire et tertiaire du versant sud des Alps Orientales. (Alpes Méridionales; Lombardie et Venétie, Italie; Slovénie occidentale, Yugoslavie). *Bulletin de la Sociéte Géologique de France*, **v.** 7, pp. 730-766.

Bailey, T., Rosenthal, Y., Falkowski, P., 2001, The Toarcian Oceanic Anoxic Event: New insights into rapid climate change from multi-element proxies: *Eos. Trans. AGU*, 82(47) Fall Meeting Suppl., Abstract PP31B-12

Bailey, T. R., McArthur, J. M., Prince, H., Thirlwall, M. F., 2000. Dissolution methods for strontium isotope stratigraphy: Whole rock analysis. *Chemical Geology*, **v.** 167, pp. 313-319.

Balog, A., 1995, Milankovitch-driven cyclicity and climate-controlled dolomitization of a Late Triassic carbonate platform, Hungary [PhD thesis]: Virginia Polytechnic Institute and State University, Virginia.

Balog, A., Read, J. F., Haas, J., 1999. Climate-controlled early dolomite, Late Triassic cyclic platform carbonates, Hungary. *Journal of Sedimentary Research*, **v.** 69, pp. 267-282.

Barbujani, C., Bosellini, A., Sarti, M., 1986. L'oolite di San Vigilio nel Monte Baldo (Giurassico, Prealpi Venete). *Annali dell'Università di Ferrara*, **v.** 9, pp. 20-47.

Bartolini, A., Baumgartner, P. O., Hunziker, J. C., 1996. Middle and Late Jurassic carbon-stable-isotope stratigraphy and radiolarite sedimentation of the Umbria-Marche Basin (Central Italy). *Eclogae Geologicae Helvetiae*, **v.** 89, pp. 831-879.

Bartolini, A., Baumgartner, P. O., Guex, J., 1999. Middle and Late Jurassic radiolarian palaeoecology versus carbon-isotope stratigraphy. *Palaeogeography, Palaeoclimatology, Palaeoecology*, **v.** 145, pp. 43-60.

Bartolini, A., Cecca, F., 1999. 20 My hiatus in the Jurassic of Umbria-Marche Apennines (Italy): Carbonate crisis due to eutrophication. *Comptes Rendus de l'Academie de Sciences Serie-IIa: Sciences de la Terre et des Planetes*, **v.** 329, pp. 587-595.

Bartolini, A., Larson, R. L., 2001. Pacific microplate and the Pangaea supercontinent in the Early to Middle Jurassic. *Geology*, **v.** 29, pp. 735-738.

Baumgartner, P. O., Martire, L., Gorican, S., O'Dogherty, L., Erba, E., Pillevuit, A., 1995. New Middle and Upper Jurassic radiolarian assemblages co-occurring with ammonites and nannofossils from the Southern Alps (Northern Italy). *In* Baumgartner, P. O., et al., (*eds.*). Middle Jurassic to Lower Cretaceous Radiolarian of Tethys: Occurrences, Systematics, Biochronology: International Association of Radiolarian Paleontologists, Lausanne, **v.** 23, pp. 737-750.

Beccarelli-Bauck, L., 1988. Oolite di Massone e Oolite di S. Vigilio: considerazioni su due litosomi oolitici della regione baldense-gardesena (Prov. Trento e Verona). *Arbeiten aus dem Institut fuer Geologie und Palaeontologie an der Universitaet Stuttgart*, **v.** 84, pp. 199-205.

Beerling, D. J., Lomas, M. R., Gröcke, D. R., 2002. On the nature of methane gas-hydrate dissociation during the Toarcian and Aptian Oceanic Anoxic Events. *American Journal of Science*, **v.** 302, pp. 28-49.

Berner, R. A., 1999. A new look at the long-term carbon cycle. *GSA Today*, **v.** 9, pp. 1-6.

Bernoulli, D., 1972. North Atlantic and Mediterranean Mesozoic facies: a comparison. *In* Hollister, C. D., et al., (*eds.*). Deep Sea Drillng Programme Initial Reports, **v.** 11, pp. 801-822.

Bernoulli, D., Laubscher, H. P., 1972. The palinspatic problem of the Hellenides. *Eclogae Geologicae Helvetiae*, **v.** 63, pp. 609-621.

Bernoulli, D., Jenkyns, H. C., 1974. Alpine, Mediterranean, and central Atlantic Mesozoic facies in relation to the early evolution of the Tethys. Modern and Ancient Geosynclinal Sedimentation; Deep-sea pelagic sediments and ophiolite assemblages.: *SEPM Special Publication*, **v.** 19, pp. 129-160.

Bernoulli, D., Caron, C., Homewood, P., Kalin, O.,van Stuijvenberg, J., 1979. Evolution of continental margins in the Alps. *Schweizerische Mineralogische und Petrographische Mitteilungen*, **v.** 59, pp. 165-170.

Bernoulli, D., 2001. Mesozoic–Tertiary carbonate platforms, slopes and basins of the external Apennines and Sicily. *In* Vai, G. B., Martini, I. P., (*eds.*). Anatomy of an Orogen: the Apennines and Adjacent Mediterranean Basins: Kluwer Academic Publishers pp. 307-326.

Beznosov, N. V., Gorbatchik, T. N., Mikhailova, I. A., Pergament, M. A., 1978. Soviet Union. *In* Moulade, M., Nairn Alan, E. M., (*eds.*). The Phanerozoic Geology of the World: Elsevier, Amsterdam, **v.** I: The Mesozoic, pp. 529.

Bolin, B., 1970. The Carbon Cycle. *Scientific American*, **v.** 223, pp. 125-132.

Bosellini, A., 1967. La tematica deposizionale della Dolomia Principale (Dolomiti e Prealpi Venete). *Bollettino della Societa Geologica Italiana*, **v.** 86, pp. 133-169.

Bosellini, A., Broglio Loriga, C., 1971. I Calcari Grigi di Rotzo (Giurassico inferiore, altopiano di Asiago) e loro inquadramento nella paleogeografia e nelle evoluzione tettono-sedimentaria nelle Prealpi Venete. *Annali dell'Universita di Ferrara*, **v.** 5, pp. 1-61.

Bosellini, A., 1972. Paleoecologia del calcari a "*Lithiotis*" (Giurassico inferiore, Prealpi Venete). *Rivista Italiana di Paleontologia e Stratigrafia*, **v.** 78, pp. 441-466.

---, 1973. Modello geodinamico e paleontettonico delle Alpi Meridionali durante il Giurassico-Cretacico. Sue possibili applicazioni agli Appennini. *In* Accordi, B., (*eds.*). Moderne Vedute sulla Geologia dell'Appennini: Accadamia Nationale Lincei, **v.** 183, pp. 163-205.

Bosellini, A., Winterer, E. L., 1975. Pelagic limestone and radiolarite of the tethyan Mesozoic: a genetic model. *Geology*, **v.** 3, pp. 279-282.

Bosellini, A., Masetti, D., Sarti, M., 1981. A Jurassic "Tongue of the Ocean" infilled with oolitic sands; the Belluno Trough, Venetian Alps, Italy. *In* Cita, M. B., Ryan, W. B. F., (*eds.*). Carbonate Platforms of the Passive-Type Continental Margins.: Marine Geology: Elsevier, Amsterdam, Netherlands, **v.** 44, pp. 59-95.

Bosellini, A., Hardie, L. A., 1985. Facies e Cicli della Dolomia Principale della Alpi Venete. *Memorie della Società Geologica Italiana*, **v.** 30, pp. 245-266.

Bosellini, A., 1989. Dynamics of Tethyan carbonate platforms. *In* Crevello Paul, D., et al.,(*eds.*). Controls on Carbonate Platform and Basin Development.: Society of Economic Paleontologists and Mineralogists, Special Publication, Tulsa, OK, United States, **v.** 44, pp. 3-13.

---, *In Press*. Dinosaurs "re-write" the geodynamics of the eastern Mediterranean and the paleogeography of the Apulia Platform. *Earth Science Reviews*, **v.** 1251.

Bosscher, H., Schlager, W., 1993. Accumulation rates of carbonate platforms. *Journal of Geology*, **v.** 101, pp. 345-355.

Bralower, T. J., Arthur, M. A., Leckie, R. M., Sliter, W. V., Allard, D. J., Schlanger, S. O., 1994. Timing and paleoceanography of oceanic dysoxia/anoxia in the late Barremian to early Aptian (Early Cretaceous). *Palaios*, **v.** 9, pp. 335-369.

Bralower, T. J., Fullagar, P. D., Paull, C. K., Dwyer, G. S., Leckie, R. M., 1997. Mid-Cretaceous strontium-isotope stratigraphy of deep-sea sections. *Geological Society of America Bulletin*, **v.** 109, pp. 1421-1442.

Bralower, T. J., Cobabe, E. A., Clement, B. M., Longoria, J. F., Sliter, W. V., 1998. Were the Aptian-Albian oceanic anoxic events global in extent? Evidence from northeastern Mexican sections. Geological Society of America, 1998 annual meeting.: Abstracts with Programs: Geological Society of America (GSA), Boulder, CO, United States, **v.** 30; 7, pp. 52-53.

Bralower, T. J., CoBabe, E., Clement, B., Sliter, W. V., Osburn, C. L., Longoria, J., 1999. The record of global change in Mid-Cretaceous (Barremian-Albian) sections from the Sierra Madre, northeastern Mexico. *In* Huber, B. T., et al., (*eds.*). Journal of Foraminiferal Research, **v.** 29; 4, pp. 418-437.

Bralower, T. J., Premoli-Silva, I., Malone, M. J., and the Shipboard Scientific Party, 2002. Leg 198 Preliminary Report. ODP Preliminary Report, 98 (online). Available from World Wide Web: http://www-odp.tamu.edu/publications/prelim/198 prel/198PREL.PDF

Brasier, M. D., Green, O. R., 1993. Winners and losers: stable isotopes and microhabitats of living Archaiadae and Eocene Nummulites (larger foraminifera). *Marine Micropaleontology*, **v.** 20, pp. 267-276.

Broecker, W. S., Peng, T. H., 1982. Tracers in the Sea: Eldigio Press, Palisades, New York, 690 pp.

Bruni, R., *Unpubl.*, [PhD thesis]: University of Ancona, Ancona.

Buchardt, B., 1978. Oxygen-isotope palaeotemperatures from the Tertiary period in the North Sea area. *Nature*, **v.** 275, pp. 121-123.

Burchell, M., 1989, Organic-rich sediments of a young rifted continental margin - the Rhaetic of western Tethys [PhD thesis]: University of Oxford, Oxford.

Burchell, M., Stefani, M., Masetti, D., 1990. Cyclic sedimentation in the Southern Alpine Rhaetic: the importance of climate and eustatsy in controlling platform–basin interactions. *Sedimentology*, **v.** 37, pp. 795-815.

Burke, W. H., Denison, R. E., Hetherington, E. A., Koepnick, R. B., Nelson, H. F., Otto, J. B., 1982. Variation of seawater Sr^{87}-Sr^{86} throughout Phanerozoic time. *Geology*, **v.** 10, pp. 516-519.

Cadet, J. P., 1975. Sur la géologie des confins méridionaux de la Bosnie at de la Serbie: mise en évidence de la nappe de Seurec (région de Visegrad et Rogatica, Yugoslavie). *Bulletin de la Sociéte Géologique de France*, **v.** 7, pp. 967-972.

Carannante, G., Carbone, F., Catenacci, V., Simone, L., 1978. I carbonati triassici dei Monti Aurunci; facies deposizionali e diagenetiche. *Bollettino della Societa Geologica Italiana*, **v.** 97, pp. 687-698.

Carbone, F., Sirna, G., 1981. Upper Cretaceous reef models from Rocca di Cave and adjacent areas in Latium, central Italy. *In* Toomey, D. F., (*eds.*). European Fossil Reef Models: Society of Economic Paleontologists and Mineralogists Special Publication, **v.** 30, pp. 427-445.

Castellarin, A., 1972. Evoluzione paleotettonica sinsedimentaria del limite tra piattaforma Veneta è bacino Lombardo, à nord di Riva del Garda. *Giornale di Geologia*, **v.** 38, pp. 11-212.

Catalano, R., Channell, J. E. T., D'Argenio, B., Napoleone, G., 1976. Mesozoic palaeogeography of the Southern Apennines and Sicily. *Memorie della Società Geologica Italiana*, **v.** 15, pp. 95-118.

Celet, P., 1977. The Dinaric and Aegean arcs: the geology of the Adriatic. *In* Nairn, A. E. M., et al.,(*eds.*). The Ocean Basins and Margins: Plenum, New York, v. 4A, pp. 215-261.

Channell, J. E. T., 1976. Umbrian palaeomagnetism and the concept of the African-Adriatic Promontory. *Memorie della Società Geologica Italiana*, **v.** 15, pp. 119-128.

Channell, J. E. T., D'Argenio, B., Horváth, F., 1979. Adria, the African Promontory, in Mesozoic Mediterranean palaeogeography. *Earth Science Reviews*, **v.** 15, pp. 213-292.

Channell, J. E. T., Erba, E., Lini, A., 1993. Magnetostratigraphic calibration of the Late Valanginian carbon-isotope event in pelagic limestones from Northern Italy and Switzerland. *Earth and Planetary Science Letters*, **v.** 118, pp. 145-166.

Chiocchini, M., Farinacci, A., Mancinelli, A., Molinari, V., Potetti, M., 1994. Biostratigrafia a foraminiferi, dasicladali e calpionelle delle successioni carbonatiche mesozoiche dell'Apennino centrale (Italia). *In* Mancinelli, A.,(*eds.*). Biostratigrafia dell'Italia Centrale: Instituto di Geologia dell' Universita di Camerino, Camerino, Italy, **v.** A, pp. 9-129.

Clari, P. A., Martire, L., 1996. Interplay of cementation, mechanical compaction, and chemical compaction in nodular limestones of the Rosso Ammonitico Veronese (Middle-Upper Jurassic, northeastern Italy). *Journal of Sedimentary Research*, **v.** 66, pp. 447-458.

Clarke, L. J., Jenkyns, H. C., 1999. New oxygen-isotope evidence for long-term Cretaceous climatic change in the Southern Hemisphere. *Geology*, **v.** 27, pp. 699-702.

Cobianchi, M., Picotti, V., 2001. Sedimentary and biological response to sea level and paleocaeanographic changes of a Lower–Middle Jurassic Tethyan platform margin (Southern Alps, Italy). *Palaeogeography, Palaeoclimatology, Palaeoecology*, **v.** 169, pp. 219-244.

Coplen, T. B., Schlanger, S. O., 1973. Oxygen- and carbon-isotope studies of carbonate sediments from site 167, Magellan Rise, Leg 17. *Initial Reports of the Deep Sea Drilling Project*, **v.** 17, pp. 505-509.

Corfield, R. M., Cartlidge, J. E., Premoli-Silva, I., Housley, R. A., 1991. Oxygen- and carbon-isotope stratigraphy of the Palaeogene and Cretaceous limestones in the Bottacione Gorge and the Contessa Highway sections, Umbria, Italy. *Terra Nova*, **v.** 3, pp. 414-422.

Cotillon, P., Rio, M., 1984. Cyclic sedimentation in the Cretaceous of Deep Sea Drilling Project Sites 535 and 540 (Gulf of Mexico), 534 (Central Atlantic), and in the Vocontian Basin (France). *Initial Reports of the Deep Sea Drilling Project*, **v.** 77, pp. 339-376.

Cousin, M., 1963. Sur la stratigraphie et la paleogeographie du Frioul occidental: Le Val Cellina (Alpes meridionales, Udine, Italie). *Bulletin de la Sociéte Géologique de France*, **v.** 5, pp. 1085-1092.

---, 1964. Contribution a l'étude géoloogique des Préalpes carniques orientales (Alpes méridionales, province d'Udine, Italie). *Bulletin de la Sociéte Géologique de France*, **v.** 5, pp. 809-820.

Cousin, M., Fourcade, E., 1982. Les facies cretaces de la plate-forme Frioulano-karstique et leur environnement paleogeographique (Alpes Meridionales et Dinarides). *In* Cotillon, P., Philip, J., (*eds.*). Symposium sur "Les facies de plate-forme du Cretace dans le domaine mesogeen": Academic Press, London, United Kingdom, **v.** 3, pp. 113-123.

Craig, H., 1957. Isotopic standards for carbon and oxygen and correction factors for mass-spectrometric analysis of carbon dioxide. *Geochimica et Cosmochimica Acta*, **v.** 12, pp. 133-149.

Crespo de Cabrera, S., Sliter, W. V., Jarvis, I., 1999. Integrated foraminiferal biostratigraphy and chemostratigraphy of the Querecual Formation (Cretaceous), Eastern Venezuela. *In* Huber, B. T., et al., (*eds.*). Paleoecological and Geochemical Signatures of Cretaceous Anoxic Events: a tribute to William V. Sliter: Journal of Foraminiferal Research: Cushman Foundation for Foraminiferal Research, Ithaca, NY, United States, **v.** 29, pp. 487-499.

Crowell, J. C., 1982. Continental glaciation through geologic time. Climate in Earth History: National Academy Press, Washington D.C. pp. 77-82.

Crowley, T. J., Zachos, J. C., 2000. Comparison of zonal temperature profiles for past warm time periods. *In* Huber, B. T., et al., (*eds.*). Warm Climates in Earth History: Cambridge University Press, Cambridge pp. 50-76.

Cuif, J. P., Gautret, P., 1991. Étude de la repartition des principaux types de démosponges depuis le Permien. Hypothese d'une incidence des conditions océanographiques sur le biominéralisation carbonaté des spongiaires. *Bulletin de la Sociéte Géologique de France*, **v.** 162, pp. 875-886.

Curiale, J. A., 1994. Geochemical anomalies at the Cenomanian–Turonian boundary, northwest New Mexico. *In* Telnaes, N., et al., (*eds.*). Advances in Organic Geochemistry: Pergamon International, Oxford-New York,, **v.** 22, pp. 487-500.

Cuvillier, J., Foury, G., Morano, A. P., 1968. Foraminiferes nouveaux du jurassique superieur du val Cellina (Frioul occidental, Italie). *Geologica Romana*, **v.** 7, pp. 141-155.

D'Argenio, B., 1969. Central and Southern Italy Cretaceous bauxites: stratigraphy and paleogeography. *Annals of the Institute of Geological Publications Hungary*, **v.** 54, pp. 221-233.

D'Argenio, B., Radoicic, R., Sgrosso, I., 1971. A paleogeographic section through the Italo-Dinaric external zones during Jurassic and Cretaceous times. *Nafta, Zagreb*, **v.** 22, pp. 195-207.

D'Argenio, B., 1974. Le piattaforme carbonatiche periadriatiche. Una rassegna di problemi nel quadro geodinamico mesozoico dell'area mediterrenea. *Memorie della Società Geologica Italiana*, **v.** 13, pp. 137-159.

D'Argenio, B., De Castro, P., Emiliani, C., Simone, L., 1975a. Bahamian and Apenninic limestones of identical lithofacies and age. *American Association of Petroleum Geologists Bulletin*, **v.** 59, pp. 524-530.

D'Argenio, B., Pescatore, T., Scandone, P., 1975b. Structural pattern of the Campania–Lucania Apennines. *Quaderni de 'La Richerche Scientifica*, **v.** 90, pp. 313-327.

D'Argenio, B., Ferreri, V., Raspini, A., 1992. A cm-scale study of shallow water Cretaceous deposits formed under high-frequency eustatic regime. Monti di Sarno (southern Italy). A sedimentologic approach to microstratigraphy. *Bollettino della Societa Geologica Italiana*, **v.** 111, pp. 399-407.

D'Argenio, B., Ferreri, V., Weissert, H., Amodio, S., Buonocunto, F., Wissler, L., *In Press*. Orbital chronostratigraphy and C-isotope stratigraphy in regional to global correlation Lower Cretaceous carbonate platforms of southern Italy. *Journal of the Geological Society [London].*

Davey, S. D., 1994, Evolution of Mesozoic carbonate platforms of the Adriatic [PhD thesis]: University of Wales, Cardiff.

Davey, S. D., Jenkyns, H. C., 1999. Carbon-isotope stratigraphy of shallow-water limestones and implications for the timing of Late Cretaceous sea-level rise and anoxic events (Cenomanian-Turonian of the peri-Adriatic carbonate platform, Croatia). *Eclogae Geologicae Helvetiae*, **v.** 92, pp. 163-170.

Dercourt, J., 1972. The Canadian Cordillera, the Hellenides, and the sea-floor-spreading theory. *Canadian Journal of Earth Sciences*, **v.** 9, pp. 709.

Dercourt, J., Zonenshain, L. P., Ricou, L. E., Kazmin, V. G., Le, P. X., Knipper, A. L., Grandjacquet, C., Sbortshikov, I. M., Geyssant, J., Lepvrier, C., Pechersky, D. H., Boulin, J., Sibuet, J. C., Savostin, L. A., Sorokhtin, O., Westphal, M., Bazhenov, M. L., Lauer, J. P., Biju, D. B., 1986. Geological evolution of the Tethys belt from the Atlantic to the Pamirs since the Lias. *In* Aubouin, J., et al., (*eds.*). Evolution of the Tethys: Tectonophysics: Elsevier, Amsterdam, Netherlands, **v.** 123, pp. 241-315.

Dewey, J. F., Pitman, J. F., Ryan, W. B. F., Bonnin, J., 1973. Plate tectonics and the evolution of the Alpine system. *Geological Society of America Bulletin*, **v.** 84, pp. 3137-3180.

Dewey, J. F., Pitman, J. F., 1998. Sea-level changes: mechanisms. magnitudes and rates. *In* Pindell, J. L., Drake, C., (*eds.*). Paleogeographic Evolution and Non-Glacial Eustasy, Northern South America: Society of Economic Paleontologists and Mineralogists Special Publication, Tulsa, OK, United States, **v.** 58, pp. 1-16.

Dickens, G. R., O'Neil, J. R., Rea, D. K., Owen, R. M., 1995. Dissociation of oceanic methane hydrate as a cause of the carbon isotope excursion at the end of the Paleocene. *Paleoceanography*, **v.** 10, pp. 965-971.

Ditchfield, P. W., 1997. High northern palaeolatitude Jurassic-Cretaceous palaeotemperature variation; new data from Kong Karls Land, Svalbard. *Palaeogeography, Palaeoclimatology, Palaeoecology*, **v.** 130, pp. 163-175.

Douglas, R. G., Savin, S. M., 1973. Oxygen- and carbon-isotope anlyses of Cretaceous and Tertiary foraminifera from the central North Pacific. *Initial Reports of the Deep Sea Drilling Project*, **v.** 17, pp. 591-605.

Drzewiecki, P., Simo, J. A., 1997. Carbonate platform drowning and oceanic anoxic events on a mid-Cretaceous carbonate platform, south-central Pyrenees, Spain. *Journal of Sedimentary Research*, **v.** 67, pp. 698-714.

Duarte, L. V., 1998. Clay minerals and geochemical evolution in the Toarcian-lower Aalenian of the Lusitanian Basin (Portugal). *Cuadernos de Geologìa Ibèrica*, **v.** 24, pp. 69-98.

Elderfield, H., Gieskes, J. M., 1982. Sr isotopes in interstitial waters of marine sediments from Deep Sea Drilling Project cores. *Nature*, **v.** 300, pp. 493-497.

Emery, D., Dickson, J. A. D., Smalley, P. C., 1987. The strontium isotopic composition and origin of burial cements in the Lincolnshire Limestone (Bajocian) of central Lincolnshire, England. *Sedimentology*, **v.** 34, pp. 795-806.

Emiliani, C., 1954. Depth habitats of some species of pelagic foraminifera as indicated by oxygen isotope ratios. *American Journal of Science*, **v.** 252, pp. 149-158.

Enos, P., 1977. Tamabra limestone of the Poza Rica trend, Cretaceous, Mexico. *In* Cook, H. E.,Enos, p.,(*eds.*). Deep-Water Carbonate Environments: Society of Economic Paleontologists and Mineralogists Special Publication, Tulsa, OK, United States, **v.** 25, pp. 273-314.

Erba, E., 1994. Nannofossils and "superplumes": the Early Aptian nannoconid crisis. *Paleoceanography*, **v.** 3, pp. 484-501.

Erba, E., Channell, J. E. T., Claps, M., Jones, C., Larson, R., Opdyke, B., Premoli, S. I., Riva, A., Salvini, G., Torricelli, S., 1999. Integrated stratigraphy of the Cismon Apticore (southern Alps, Italy); a "reference section" for the Barremian-Aptian interval at low latitudes. *In* Huber, B. T., et al., (*eds.*). Paleoecological and Geochemical Signatures of Cretaceous Anoxic Events; a tribute to William V. Sliter.: Cushman Foundation for Foraminiferal Research, Ithaca, NY, United States, **v.** 29, pp. 371-391.

Erbacher, J., Thurow, J., Littke, R., 1996. Evolution patterns of radiolaria and organic matter variations; a new approach to identify sea-level changes in mid-Cretaceous pelagic environments. *Geology*, **v.** 24, pp. 499-502.

Erbacher, J., Thurow, J., 1997. Influence of oceanic anoxic events on the evolution of mid-Cretaceous radiolaria in the North Atlantic and western Tethys. *In* Takahashi, K.,Lazarus, D., (*eds.*). InterRad VII.: Elsevier, Amsterdam, Netherlands, **v.** 30, pp. 139-158.

Ferasin, F., 1958. Il complesso di scogliera cretaceo nel Veneto centro-orientale. *Memorie degli Instituti di Geologia e Mineralogia dell'Universita di Padova*, **v.** 21, pp. 58.

Ferreri, V., Weissert, H., D'Argenio, B., Buonocunto, F. P., 1997. Carbon isotope stratigraphy: a tool for basin to carbonate platform correlation. *Terra Nova*, **v.** 9, pp. 57-61.

Fiet, N., 2000. Calibrage temporel de l'Aptien et des sous-etages associes par une approche cyclostratigraphique appliquee a la serie pelagique de Marches-Ombrie (Italie centrale). *Bulletin de la Societe Geologique de France*, 171, pp. 103-113.

Fischer, A. G., 1964. The Lofer Cyclothems of the Alpine Triassic. *In* Merriam, D. F., (*eds.*). Symposium on Cyclic Sedimentation: Bulletin of the Geological Survey Kansas, **v.** 169, pp. 107-149.

Föllmi, K. B., Weissert, H., Bisping, M., Funk, H., 1994. Phosphogenesis, carbon-isotope stratigraphy, and carbonate-platform evolution along the Lower Cretaceous northern Tethyan margin. *Geological Society of America Bulletin*, **v.** 106, pp. 729-746.

Frakes, L. A., Francis, J. E.,Syktus, J. I., 1992. Climate modes of the Phanerozoic: Cambridge University Press, Cambridge, 274 pp.

Freund, R. M., Goldberg, T., Weissbrod, Y., Druckmann, Derin, B., 1975. The Triassic–Jurassic structure of Israel and its relation to the origin of the eastern Mediterranean. *Geological Survey of Israel Bulletin*, **v.** 65, pp. 1-26.

Gaetani, M., 1975. Jurassic stratigraphy of the Southern Alps; a review. *In* Squyres, C. H.,(*eds.*). Geology of Italy; **v.** I.: Earth Science Society of the Libyan Arab Republic, Tripoli, Libya pp. 377-402.

Gale, A. S., Jenkyns, H. C., Kennedy, W. J., Corfield, R. M., 1993. Chemostratigraphy versus biostratigraphy: data from around the Cenomanian–Turonian boundary. Jou*rnal of the Geological Society [London],* **v.** 150, pp. 29-32.

Gattuso, J. P., Buddemeier, R. W., 2000. Ocean biogeochemistry; calcification and CO_2. *Nature,* **v.** 407, pp. 311-313.

Geyer, O. F., Gohner, D., Krautter, M., 1986. Die obertriassiche bis alttertiäre Schichtfolge der Trento–Schwelle (Südalpen) unter besonderer Berücksichtigung Jurassicher Formationen. *Jahresberichte und Mitteilungen des Oberrheinischen Geologischen Vereines*, **v.** 68, pp. 129-176.

Ghetti, S., 1987, Evoluzione cretacica del margine occidentale della Piattaforma Friulana [PhD thesis]: University of Ferrara, Ferrara.

Ghetti, S., Brigatti, M. F., 1991. Mineralogy of Cretaceous green clay levels (Friuli Platform, southern Alps, Italy); relationships to the depositional environment. *Neues Jahrbuch fuer Geologie und Palaeontologie. Monatshefte*, **v.** 1991, pp. 489-504.

Gill, W. D., 1965. The Mediterranean Basin. Salt basins around Africa: Institute of Petroleum, London pp. 101-111.

Glynn, P. W., 2000. El Niño-Southern Oscillation mass mortalities of reef corals: a model of high temperature marine extinctions. *In* Insalaco, E., et al.,(*eds.*). Carbonate Platform Systems: components and interactions: Geological Society Special Publication, London, **v.** 178, pp. 117-133.

Goodell, H. G., Garman, R. K., 1969. Carbonate geochemistry of Superior deep test well, Andros Island, Bahamas. *American Association of Petroleum Geologists Bulletin*, **v.** 53, pp. 513-536.

Goreau, T. J., 1992. Bleaching and reef community change in Jamaica: 1951-1991. *American Zoologist*, **v.** 32, pp. 683-695.

Goreau, T. J., Hayes, R. L., 1994. Coral Bleaching and Ocean "Hot Spots". *Ambio*, **v.** 23, pp. 176-180.

Goreau, T. J., McClanahan, T., Hayes, R. L., Strong, A. E., 2000. Conservation of coral reefs after the 1998 Global Bleaching Event. *Conservation Biology*, **v.** 14, pp. 5-15.

Gradstein, F. M., Agterberg, F. P., Ogg, J. G., Hardenbol, J., van Veen, P., Thierry, J., Huang, Z., 1995. A Triassic, Jurassic and Cretaceous time scale. *In* Berggren, W. A., et al., (*eds.*). Geochronology, Time Scales and Global Stratigraphic Correlation: Society of Economic Paleontologists and Mineralogists Special Publication, **v.** 54, pp. 95-126.

Graziano, R., 1999. The Early Cretaceous drowning unconformities of the Apulia carbonate platform (Gargano Promontory, southern Italy): local fingerprints of global palaeoceanographic events. *Terra Nova*, **v.** 11, pp. 245-250.

Grigg, R. W., 1982. Darwin Point: a threshold for atoll formation. *Coral Reefs*, **v.** 1, pp. 29-34.

Gröcke, D. R., Hesselbo, S. P., Jenkyns, H. C., 1999. Carbon-isotope composition of Lower Cretaceous fossil wood: ocean-atmosphere chemistry and relation to sea-level change. *Geology*, **v.** 27, pp. 155-158.

Gröcke, D. R., 2001, Isotope Stratigraphy and Ocean-Atmosphere Interactions in the Jurassic and Early Cretaceous [D. Phil. thesis]: Univeristy of Oxford, Oxford.

Gross, M. G., 1964. Variations in the $^{18}O/^{16}O$ and $^{13}C/^{12}C$ ratios of diagenetically altered limestones in the Bermuda Islands. *Journal of Geology*, **v.** 72, pp. 170-194.

Grötsch, J., Billing, I., Vahrenkamp, V. C., 1998. Carbon-isotope stratigraphy in shallow-water carbonates: implications for Cretaceous black-shale deposition. *Sedimentology*, **v.** 45, pp. 623-634.

Gusic, I., Jelanska, V., 1993. Upper Cenomanian–Lower Turonian sea-level rise and its consequences on the Adriatic/Dinaric carbonate platform. *Geologische Rundschau*, **v.** 82, pp. 676-686.

Haas, J., 1988. Upper Triassic carbonate platform evolution in the Transdanubian mid-mountains. *Acta Geologica Hungarica*, **v.** 31, pp. 299-312.

Hallam, A., 1961. Cyclothems, transgressions and faunal change in the Lias of northwest Europe. *Transactions of the Edinburgh Geological Society*, **v.** 18, pp. 132-174.

---, 1981. A revised sea-level curve for the Early Jurassic. *Journal of the Geological Society [London]*, **v.** 138, pp. 735-743.

Hallam, A., El Shaarawy, Z., 1982. Salinity reduction of the end-Triassic sea from the Alpine region into northwestern Europe. *Lethaia*, **v.** 15, pp. 169-178.

Hallam, A., 1986. The Pliensbachian and Tithonian extinction events. *Nature*, **v.** 308, pp. 686-687.

---, 1992. Phanerozoic Sea-Level Changes: Columbia University Press, New York.

Hallam, A.,Wignall, P. B., 1996. Mass Extinctions and their Aftermath: Oxford University Press, Oxford.

Hallam, A., 1997. Estimates of the amount and rate of sea-level change across the Rhaetian-Hettangian and Pliensbachian-Toarcian boundaries (Latest Triassic to Early Jurassic). *Journal of the Geological Society [London]*, **v.** 154 Part 5, pp. 773-779.

---, 2001. A review of the broad pattern of Jurassic sea-level changes and their possible causes in the light of current knowledge. *Palaeogeography, Palaeoclimatology, Palaeoecology*, **v.** 167, pp. 23-37.

Hallock, P., Schlager, W., 1986. Nutrient excess and the demise of coral reefs and carbonate platforms. *Palaios*, **v.** 1, pp. 389-398.

Hallock, P., 1988. The role of nutrient availability in bioerosion: consequences to carbonate buildups. *Palaeogeography, Palaeoclimatology, Palaeoecology*, **v.** 63, pp. 275-291.

Hancock, J. M., Kauffman, E. G., 1979. The great transgressions of the Late Cretaceous. *Journal of the Geological Society [London]*, **v.** 136, pp. 175-186.

Haq, B. U., Hardenbol, J., Vail, P. R., 1987. Chronology of fluctuating sea levels since the Triassic. *Science*, **v.** 235, pp. 1156-1167.

---, 1988. Mesozoic and Cenozoic chronostratigraphy and cycles of sea-level change. *In* Wilgus Cheryl, K., et al., (*eds.*). Sea-Level Changes; an integrated approach.: Society of Economic Paleontologists and Mineralogists Special Publication, Tulsa, OK, United States, **v.** 42, pp. 72-108.

Hardie, L. A., Bosellini, A., Goldhammer, R. K., 1986. Repeated subaerial exposure of subtidal carbonate platforms, Triassic, northern Italy: evidence for high frequency sea level oscillations on a 10,000 year scale. *Paleoceanography*, **v.** 1, pp. 447-457.

Harland, W. B., Cox, A. V., Llewellyn, P. G., Pickton, C. A. G., Smith, A. G., Walters, R., 1982. A Geologic Time Scale: Cambridge University Press, Cambridge, 131 pp.

Harries, P. J., 1993. Dynamics of survival following the Cenomanian–Turonian (Upper Cretaceous) mass extinction event. *Cretaceous Research*, **v.** 14, pp. 563-583.

Hasegawa, T., 1997. Cenomanian–Turonian carbon-isotope events recorded in terrestrial organic matter from northern Japan. *Palaeogeography, Palaeoclimatology, Palaeoecology*, **v.** 130, pp. 251-273.

Hasegawa, T., Hatsugai, T., 2000. Carbon-isotope stratigraphy and its chronostratigraphic significance for the Cretaceous Yezo Group, Kotanbetsu area, Hokkaido, Japan. *Paleontological Research*, **v.** 4, pp. 95-106.

Hennig, S., Weissert, H., Bulot, L. G., 1999. C-isotope stratigraphy, a calibration tool between ammonite- and magnetostratigraphy: the Valanginian–Hauterivian transition. *Geologica Carpathica*, **v.** 50, pp. 91-96.

Hess, J., Bender, M. L., Schilling, J.-G., 1986. Evolution of the ratio of strontium-87 to strontium-86 in seawater from Cretaceous to present. *Science*, **v.** 231, pp. 979-984.

Hesselbo, S. P., Jenkyns, H. C., 1998. British Lower Jurassic sequence stratigraphy. *In* de Graciansky, P. C., et al., (*eds.*). Mesozoic and Cenozoic Sequence Stratigraphy of European Basins: Society of Economic Paleontologists and Mineralogists Special Publication, Tulsa, OK, United States, **v.** 60, pp. 561-581.

Hesselbo, S. P., Gröcke, D. R., Jenkyns, H. C., Bjerrum, C. J., Farrimond, P., Morgans Bell, H. S., Green, O. R., 2000. Massive dissociation of gas hydrate during a Jurassic oceanic anoxic event. *Nature*, **v.** 406, pp. 392-395.

Hesselbo, S. P., Robinson, S. A., Surlyk, F., Piasecki, S., 2002. Terrestrial and marine extinction at the Triassic–Jurassic boundary synchronized with major carbon-cycle perturbation: a link to initiation of massive volcanism? *Geology*, **v.** 30, pp. 251-254.

Hesselbo, S. P., Morgans Bell, H. S., McElwain, J. C., Rees, P. M., Robinson, S. A., *In Press*. A carbon-cycle perturbation in the Middle Jurassic and accompanying changes in the terrestrial palaeoenvironment. *Journal of Geology*.

Hilbrecht, H., Hoefs, J., 1986. Geochemical and palaeontological studies of the $\delta^{13}C$ anomaly in Boreal and North Tethyan Cenomanian–Turonian sediments in Germany and adjacent areas. *Palaeogeography, Palaeoclimatology, Palaeoecology*, **v.** 53, pp. 169-189.

Hodell, D. A., Mueller, P. A., McKenzie, J. A., Mead, G. A., 1989. Strontium isotope stratigraphy and geochemistry of the late Neogene ocean. *Earth and Planetary Science Letters*, **v.** 92, pp. 165-178.

Hodell, D. A., Mead, G. A., Mueller, P. A., 1990. Variation in the strontium isotopic composition of seawater (8 Ma to present); implications for chemical weathering rates and dissolved fluxes to the oceans. *Chemical Geology; Isotope Geoscience Section*, **v.** 80, pp. 291-307.

Hofbauer, G., 1985. Stratigraphie, Fazies und Tectonik am SW-Rand des Parnassos-Kiona Gebirge (Mittel-griechland). *Erlanger Geologische Abhandlungen*, **v.** 112, pp. 11-45.

Hollander, D. J., Bessereau, G., Belin, S., Huc, A. Y., Houzay, J. P., 1991. Organic matter in the early Toarcian shales, Paris Basin, France; a response to environmental changes. *Revue de l'Institut Francais du Petrole*, **v.** 46, pp. 543-562.

Hsü, K. J., 1977. Tectonic evolution of the Mediterranean basins. *In* Nairn, A. E. M., et al.,(*eds.*). The Ocean Basins and Margins: Plenum, New York, **v.** 4A, pp. 29-75.

Huber, B. T., Norris, R. D., MacLeod, K. S., 2002. Deep-sea paleotemperature record of extreme warmth during the Cretaceous. *Geology*, **v.** 30, pp. 123-126.

Iannace, A., Frisia, S., 1994. Changing dolomitization styles from Norian to Rhaetian in the southern Tethys realm. *In* Purser, B., et al., (*eds.*). Dolomites; a volume in honour of Dolomieu.: Special Publication of the International Association of Sedimentologists: Blackwell, Oxford, **v.** 21, pp. 75-89.

I.S.R.S., 1998. International Society for Reef Studies. Statement on Bleaching. *Reef Encounter*, **v.** 24, pp. 19.

Jadoul, F., Berra, F., Frisia, S., 1992. Stratigraphic and paleogeographic evolution of a carbonate platform in an extensional tectonic regime; the example of the Dolomia Principale in Lombardy (Italy). *Rivista Italiana di Paleontologia e Stratigrafia*, **v.** 98, pp. 29-43.

Jahren, A. H., Arens, N. C., 1998, Methane hydrate dissociation implicated in Aptian OAE events: Geological Society of America Annual Meeting, Abstract Volume 30, pp. 53.

Jahren, A. H., Arens, N. C., Sarmiento, G., Guerrero, J., Amundson, R., 2001. Terrestrial record of methane-hydrate dissociation in the Early Cretaceous. *Geology*, **v.** 29, pp. 159-162.

Jansa, L. F., 1993. Early Cretaceous carbonate platforms of the northeastern American margin. *American Association of Petroleum Geologists Memoi*r, **v.** 56, pp. 111-126.

Jarvis, I., Carson, G. A., Cooper, M. K. E., Hart, M. B., Leary, P., Tocher, B. A., Horne, D., Rosenfeld, A., 1988. Microfossil assemblages and the Cenomanian–Turonian (Late Cretaceous) Oceanic Anoxic Event. *Cretaceous Research*, **v.** 9, pp. 3-103.

Jenkyns, H. C., 1972. Pelagic "oolites" from the Tethyan Jurassic. *Journal of Geology*, **v.** 80, pp. 21-23.

---, 1974. Origin of red nodular limestones (Ammonitico Rosso, Knollenkalke) in the Mediterranean Jurassic; a diagenetic model. *Special Publication of the International Association of Sedimentologists*: Blackwell Science, Oxford, **v.** 1, pp. 249-271.

---, 1980. Cretaceous oceanic anoxic events: from continents to oceans. *Journal of the Geological Society [London]*, **v.** 137, pp. 171-188.

---, 1985. The Early Toarcian and Cenomanian–Turonian anoxic events in Europe; comparison and contrasts. *Geologische Rundschau*, **v.** 74, pp. 505-518.

Jenkyns, H. C., Clayton, C. J., 1986. Black shales and carbon isotopes in pelagic sediments from the Tethyan Lower Jurassic. *Sedimentology*, **v.** 33, pp. 87-106.

Jenkyns, H. C., 1988. The early Toarcian (Jurassic) anoxic event: stratigraphic, sedimentary, and geochemical evidence. *American Journal of Science*, **v.** 288, pp. 101-151.

---, 1991. Impact of Cretaceous sea level rise and anoxic events on the Mesozoic carbonate platform of Yugoslavia. *American Association of Petroleum Geologists Bulletin*, **v.** 75, pp. 1007-1017.

Jenkyns, H. C., Gale, A. S., Corfield, R. M., 1994. Carbon- and oxygen-isotope stratigraphy of the English Chalk and Italian Scaglia and its palaeoclimatic significance. *Geological Magazine*, **v.** 131, pp. 1-34.

Jenkyns, H. C., 1995a. Carbon-isotope stratigraphy and paleoceanographic significance of the Lower Cretaceous shallow-water carbonates of Resolution Guyot, Mid-Pacific Mountains. *In* Winterer, E. L., et al., (*eds.*). Proceedings of the Ocean Drilling Program; scientific results, **v.** 143, pp. 99-104.

---, 1996. Relative sea-level change and carbon isotopes: data from the Upper Jurassic (Oxfordian) of central and Southern Europe. *Terra Nova*, **v.** 8, pp. 75-85.

Jenkyns, H. C., Clayton, C. J., 1997. Lower Jurassic epicontinental carbonates and mudstones from England and Wales; chemostratigraphic signals and the early Toarcian anoxic event. *Sedimentology*, **v.** 44, pp. 687-706.

Jenkyns, H. C., 1999. Mesozoic anoxic events and palaeoclimate. *Zentralblatt für Geologie und Palaontologie Teil I*, **v.** 1997, pp. 943-949.

Jenkyns, H. C., Wilson, P. A., 1999. Stratigraphy, paleoceanography, and evolution of Cretaceous Pacific guyots: relics from a greenhouse earth. *American Journal of Science*, **v.** 299, pp. 341-392.

Jenkyns, H. C., Gröcke, D. R., Hesselbo, S. P., 2001. Nitrogen isotope evidence for water mass denitrification during the early Toarcian (Jurassic) oceanic anoxic event. *Paleoceanography*, **v.** 16, pp. 1-11.

Jenkyns, H. C., Jones, C. E., Gröcke, D. R., Hesselbo, S. P., Parkinson, D. N., 2002a. Chemostratigraphy of the Jurassic system: applications, limitations and implications for palaeoceanography. *Journal of the Geological Society [London]*, **v.** 159, pp. 351-378.

Jenkyns, H. C., Tsikos, H., C. T.-Net Group, 2002b. The Cenomanian–Turonian Oceanic Anoxic Event: crystallizing the concept: Workshop on Cretaceous Ocean Dynamics and Climate, Florissant, Co., USA. Abstract Volume pp. 43.

Jenkyns, H. C., Paull, C. K., Cummins, D. I., Fullagar, P. D., 1995b. Strontium isotope statigraphy of Lower Cretaceous atoll carbonates in the Mid-Pacific Mountains. *In* Winterer, E. L., Sager, W. W., Firth, J. V., and Sinton, J. M., (*eds.*). Proceedings of the Ocean Drilling Program, Scientific Results, **v.** 143, pp. 89-97.

Jimenez, A. P., Jimenez, de C. C., Rivas, P., Vera, J. A., 1996. The early Toarcian anoxic event in the westernmost Tethys (Subbetic); paleogeographic and paleobiogeographic significance. *Journal of Geology*, **v.** 104, pp. 399-416.

Jokiel, P. L., Coles, S. L., 1977. Effect of temperature on the growth and mortality of Hawaiian reef corals. *Marine Biology*, **v.** 43, pp. 201-208.

---, 1990. Response of Hawaiian and other Indo-Pacific reef corals to elevated temperature. *Coral Reefs*, **v.** 8, pp. 155-162.

Jones, C. E., 1992, Strontium isotopes in early Jurassic and Cretaceous sea water [D.Phil. thesis]: University of Oxford, Oxford.

Jones, C. E., Jenkyns, H. C., Coe, A. L., Hesselbo, S. P., 1994a. Strontium isotopic variations in Jurassic and Cretaceous seawater. *Geochimica et Cosmochimica Acta*, **v.** 58, pp. 3061-3074.

Jones, C. E., Jenkyns, H. C., Hesselbo, S. P., 1994b. Strontium isotopes in early Jurassic seawater. *Geochimica et Cosmochimica Acta*, **v.** 58, pp. 1285-1301.

Jones, C. E., Jenkyns, H. C., 2001. Seawater strontium isotopes, oceanic anoxic events, and seafloor hydrothermal activity in the Jurassic and Cretaceous. *American Journal of Science*, **v.** 301, pp. 112-149.

Kastner, M., Elderfield, H., Martin, J. B., Suess, E., Kvenvolden, K. A., Garrison, R. E., 1990. Diagenesis and interstitial-water chemistry at the Peruvian continental margin; major constituents and strontium isotopes. *In* Suess, E., et al., (*eds.*). Proceedings of the Ocean Drilling Program, Scientific Results, **v.** 112, pp. 413-440.

Kemper, E., 1987. Das klima der Kriede-Zeit. *Geologisches Jahrbuch*, **v.** 96A, pp. 5-185.

Kennedy, W. J., Walaszczyk, I., Cobban, W. A., 2000. Pueblo, Colorado, USA, candidate Global Boundary Stratotype Section and Point for the base of the Turonian Stage of the Cretaceous, and for the base of the middle Turonian Substage, with a revision of the Inoceramidae (Bivalvia). *Acta Geologica Polonica*, **v.** 50, pp. 295-334.

Klein, R. T., Lohmann, K. C., Kennedy, G. L., 1997. Elemental and isotopic proxies of paleotemperature and paleosalinity: climate reconstruction of the marginal northeast Pacific ca. 80ka. *Geology*, **v.** 25, pp. 363-366.

Kleypas, J. A., Buddemmeier, R. W., Archer, D., Gattuso, J.-P., Langdon, C., Opdyke, B. N., 1999. Geochemical consequences of increased atmospheric carbon dioxide on coral reefs. *Science*, **v.** 284, pp. 118-120.

Koepnick, R. B., Denison, R. E., Burke, W. H., Hetherington, E. A., Dahl, D. A., 1990. Construction of the Triassic and Jurassic portion of the Phanerozoic curve of seawater $^{87}Sr/^{86}Sr$. *Chemical Geology*, **v.** 80, pp. 327-349.

Krautter, M., 1987. "Massone-Oolith" und "Giallo di Mori" im Unterjura der Trento-Plattform (Suedalpen). *Neues Jahrbuch fuer Geologie und Palaeontologie. Monatshefte*, **v.** 1987, pp. 204-212.

Kuhnt, W., Herbin, J. P., Thurow, J., Wiedmann, J., 1990. Distribution of Cenomanian–Turonian organic facies in the western Mediterranean and along the adjacent Atlantic margin. *In* Huc, A. Y., (*eds.*). Deposition of Organic Facies.: American Association of Petroleum Geologists, Tulsa, OK, United States, **v.** 30, pp. 133-160.

Kump, L. R., Arthur, M. A., 1999. Interpreting carbon-isotope excursions: carbonates and organic matter. *Chemical Geology.*, **v.** 161, pp. 181-198.

Küspert, W., 1982. Environmental changes during oil shale deposition as deduced from stable-isotope ratios. *In* Einsele, G.,Seilacher, A., (*eds.*). Cyclic and Event Stratification: Springer-Verlag, New York pp. 482-501.

Lamolda, M. A., Gorostidi, A., Paul, C. R. C., 1994. Quantitative estimates of calcareous nannofossil changes across the Plenus Marls (latest Cenomanian), Dover, England; implications for the generation of the Cenomanian–Turonian boundary event. *Cretaceous Research*, **v.** 15, pp. 143-164.

Larson, R. L., 1991a. Latest pulse of earth: evidence for a mid-Cretaceous Superplume. *Geology*, **v.** 19, pp. 547-550.

---, 1991b. Geological consequences of superplumes. *Geology*, **v.** 19, pp. 963-966.

Larson, R. L., Erba, E., 1999. Onset of the mid-Cretaceous greenhouse in the Barremian–Aptian: igneous events and the biological, sedimentary, and geochemical responses. *Paleoceanography*, **v.** 14, pp. 663-678.

Laubscher, H. P., Bernoulli, D., 1977. Mediterranean and Tethys. *In* Nairn, A. E. M., et al.,(*eds.*). The Ocean Margins and Basins: Plenum, New York, **v.** 4A, pp. 1-28.

Leinfelder, R. R., 1993. Upper Jurassic reef types and controlling factors. *Profil*, **v.** 5, pp. 1-45.

Lemoine, M., 1983. Rifting and early drifting: Mesozoic Central Atlantic and Ligurian Tethys. *In* Sheridan, R. E., et al., (*eds.*). Initial Reports of the Deep Sea Drilling Programme, **v.** 76, pp. 885-895.

Lini, A., Weissert, H., Erba, E., 1992. The Valanginian carbon isotope event: a first episode of greenhouse climate conditions during the Cretaceous. *Terra Nova*, **v.** 4, pp. 374-384.

Luciani, V., Cobianchi, M., Jenkyns, H. C., 2001. Biotic and geochemical response to anoxic events: the Aptian pelagic succession of the Gargano Promontory (southern Italy). *Geological Magazine*, **v.** 138, pp. 277-298.

Manatschal, G., Bernoulli, D., 1999. Architecture and tectonic evolution of nonvolcanic margins: present day Galicia and ancient Adria. *Tectonics*, **v.** 18, pp. 1099-1119.

Marconi, M., Wezel, F. C., Longinelli, A., 1994. A stable isotope study of a calcareous-black shale series from the Barremian-Aptian of the Northern Apennines, Umbro-Marchean Succession, Italy. *Mineralogica et Petrographica Acta*, **v.** 37, pp. 211-218.

Marzoli, A., Renne, P. R., Piccirillo, E. M., Ernesto, M., Bellieni, G., De Min, A., 1999. Extensive 200-million-year-old continental flood basalts of the Central Atlantic magmatic province. *Science*, **v.** 284, pp. 616-618.

Masse, J. P., El, A. A., Erlenkeuser, H., 1999. Isotope stratigraphy $\delta^{13}C$ of the lower Aptian from Provence (SE France): application to platform/basin correlations. *Eclogae Geologicae Helvetiae*, **v.** 92, pp. 259-263.

McArthur, J. M., Thirlwall, M. F., Gale, A. S., Kennedy, W. J., Burnett, J. A., Mattey, D., Lord, A. R., 1993. Strontium-isotope stratigraphy for the Late Cretaceous: a refinement based on the English Chalk. *In* Hailwood, E.,Kidd, R., (*eds.*). High Resolution Stratigraphy: Geological Society of London Special Publication, **v.** 70, pp. 195-209.

McArthur, J. M., Donovan, D. T., Thirlwall, M. F., Fouke, B. W., Mattey, D., 2000a. Strontium isotope profile of the early Toarcian (Jurassic) oceanic anoxic event, the duration of ammonite biozones, and belemnite palaeotemperatures. *Earth and Planetary Science Letters*, **v.** 179, pp. 269-285.

McArthur, J. M., Norton, N., Thirlwall, M. F., 2000b. Strontium isotope stratigraphy of the Aalenian/Bajocian Auxiliary Stratotype Point at Bearreraig, Isle of Skye, NW Scotland. *GeoResearch Forum*, **v.** 6, pp. 137-144.

McHone, J. G., 1996. Broad-terrane Jurassic flood basalts across northeastern North America. *Geology*, **v.** 24, pp. 319-322.

Menegatti, A. P., Weissert, H., Brown, R. S., Tyson, R. V., Farrimond, P., Strasser, A., Caron, M., 1998. High-resolution $\delta^{13}C$ stratigraphy through the early Aptian 'Livello Selli' of the Alpine Tethys. *Paleoceanography*, **v.** 13, pp. 530-545.

Michalík, J., 1980. A paleoenvironmental and paleoecological analysis of the west Carpathians part of the Northern Tethyan nearshore region in the latest Triassic time. *Rivista Italiana di Paleontologia e Stratigrafia*, v. 85, pp. 1047-1064.

Michalík, J., Reháková, D., Hladíková, J., Lintnerová, O., 1995. Lithological and biological indicators of orbital changes in Tithonian and Lower Cretaceous sequences, Western Carpathians, Slovakia. *Geologica Carpathica*, v. 46, pp. 161-174.

Morettini, E., Santantonio, M., Bartolini, A., Cecca, F., Baumgartner, P. O., Hunziker, J. C., 2002. Carbon isotope stratigraphy and carbonate production during Early–Middle Jurassic: examples from the Umbria–Marche–Sabina Apennines (central Italy). *Palaeogeography, Palaeoclimatology, Palaeoecology*, v. 184, pp. 251-273.

Morgans-Bell, H. S., Coe, A. L., Hesselbo, S. P., Jenkyns, H. C., Weedon, G. P., Marshall, J. E. A., Tyson, R. V., Williams, C. J., 2001. Integrated stratigraphy of the Kimmeridge Clay Formation (Upper Jurassic) based on exposures and boreholes in south Dorset, UK. *Geological Magazine*, v. 138, pp. 511-539.

Murris, R. J., 1980. Middle East: stratigraphic evolution and oil habitat. *American Association of Petroleum Geologists Bulletin*, v. 64, pp. 597-618.

Owens, J. P., 1983. The northwest Atlantic Ocean margin. *In* Moulade, M.,Nairn Alan, E. M., (*eds.*). The Phanerozoic Geology of the World: Elsevier, Amsterdam, v. II: The Mesozoic, pp. 33-60.

Padden, M., Weissert, H., de Rafelis, M., 2001. Evidence for Late Jurassic release of methane from gas hydrate. *Geology*, v. 29, pp. 223-226.

Pàlfy, J., Mortensen, J. K., Carter, E. S., Smith, P. L., Friedman, R. M., Tipper, H. W., 2000a. Timing of the end-Triassic mass extinction: first on land, then in the sea? *Geology*, v. 28, pp. 39-42.

Pàlfy, J., Smith, P. L., 2000. Synchrony between Early Jurassic extinction, oceanic anoxic event, and the Karoo–Ferrar flood basalt volcanism. *Geology*, v. 28, pp. 747-750.

Pàlfy, J., Smith, P. L., Mortensen, J. K., 2000b. A U–Pb and $^{40}Ar/^{39}Ar$ time scale for the Jurassic. *Canadian Journal of Earth Sciences*, v. 37, pp. 923-944.

Pàlfy, J., Demény, A., Hass, J., Hetényi, M., Orchard, M. J., Veto, I., 2001. Carbon-isotope anomaly and other geochemical changes at the Triassic-Jurassic bounday from a marine section in Hungary. *Geology*, v. 29, pp. 1047-1050.

Palmer, M. R., Elderfield, H., 1985. Sr isotope composition of sea water over the past 75 Myr. *Nature*, v. 314, pp. 526-528.

Palmer, M. R., Edmond, J. M., 1989. The strontium isotope budget of the modern ocean. *Earth and Planetary Science Letters*, v. 92, pp. 11-26.

Patterson, W. P., Walter, L. M., 1994. Depletion of ^{13}C in seawater ΣCO_2 on modern carbonate platforms: significance for the carbon isotopic record of carbonates. *Geology*, v. 22, pp. 885-888.

Patton, J. W., Choquette, P., Guennel, G. K., Kaltenback, A. J., Moore, A., 1984. Organic geochemistry and sedimentology of lower to mid-Cretaceous deep-sea carbonates, sites 535 and 540, Leg 77. *Initial Reports of the Deep Sea Drilling Project*, v. 77, pp. 417-443.

Paul, C. R. C., Mitchell, S. F., Lamolda, M. A., Gorostidu, A., 1994. The Cenomanian–Turonian Boundary Event in northern Spain. *Geological Magazine*, v. 131, pp. 801-817.

Pearson, P. N., Ditchfield, P. W., Singano, J., Harcourt-Brown, K. G., Nicholas, C. J., Olsson, R. K., Shackleton, N. J., Hall, M. A., 2001. Warm tropical sea surface temperatures in the Late Cretaceous and Eocene epochs. *Nature*, **v.** 413, pp. 481-487.

Philip, J. M., Airaud, C. C., 1991. The demise of the rudist-bearing carbonate platforms at the Cenomanian/ Turonian boundary; a global control. *In* Montaggioni, L. F., Macintyre, I. G., (*eds.*). Reefs as Recorders of Environmental Changes.: Springer International, Berlin-Heidelberg-New York, v. 10, pp. 115-125.

Picotti, V., Cobianchi, M., 1996. Jurassic periplatform sequences of the eastern Lombardian Basin (Southern Alps): the deep-sea record of the tectonic evolution, growth and demise history of a carbonate platform. *Memorie di Scienze Geologiche, Padova*, **v.** 48, pp. 171-219.

Podlaha, O. G., Mutterlose, J., Veizer, J., 1998. Preservation of $\delta^{18}O$ and $\delta^{13}C$ in belemnite rostra from the Jurassic/ Early Cretaceous successions. *American Journal of Science*, **v.** 298, pp. 324-347.

Pratt, L. M., Threlkeld, C. N., 1984. Stratigraphic significance of $^{13}C/^{12}C$ ratios in mid-Cretaceous rocks on the Western Interior, U.S.A. *In* Stott, D. F., Glass, D. J., (*eds.*). The Mesozoic of Middle North America.: Canadian Society of Petroleum Geologists, Calgary, Ab., Canada, **v.** 9, pp. 305-312.

Price, G. D., 1999. The evidence and implications of polar ice during the Mesozoic. *Earth Science Reviews*, **v.** 48, pp.183-210.

Price, G. D., Gröcke, D. R., 2002. Strontium-isotope straigraphy and oxygen- and carbon-isotope variation during the Middle Jurassic–Early Cretaceous of the Falkland Plateau, South Atlantic. *Palaeogeography, Palaeoclimatology, Palaeoecology*, **v.** 183, pp. 209-222.

Qing, H., Bosence, D. W. J., Rose, E. P. F., 2001. Dolomitization by penesaline sea water in early Jurassic peritidal platform carbonates, Gibraltar, western Mediterranean. *Sedimentology*, **v.** 48, pp. 153-163.

Ranke, U., von Rad, U., Wissmann, G., 1982. Stratigraphy, facies, and tectonic development of the on- and offshore Aiun–Tarfaya Basin - a review. *In* von Rad, U., (*eds.*). Geology of the Northwest African Continental Margin: Springer-Verlag, Berlin pp. 86-105.

Richter, F. M., DePaolo, D. J., 1987. Numerical models for diagenesis and the Neogene Sr isotopic evolution of seawater from DSDP Site 590B. *Earth and Planetary Science Letters*, **v.** 83, pp. 27-38.

---, 1988. Diagenesis and Sr isotopic evolution of seawater using data from DSDP 590B and 575. *Earth and Planetary Science Letters*, **v.** 90, pp. 382-394.

Robertson, A. H. F., Bliefnick, D. M., 1983. Sedimentology and origin of Lower Cretaceous pelagic carbonates and redeposited clastics, Blake–Bahama Formation, Deep Sea Drilling Project Site 534, western equatorial Atlantic. *Initial Reports of the Deep Sea Drilling Project*, **v.** 76, pp. 795-820.

Robson, J., 1989, Stratigraphy and Sedimentology of Late Mesozoic Platform Carbonates, Southern Italy [PhD thesis]: Kingston Polytechnic, Kingston-Upon-Thames.

Rosales, I., Quesada, S., Robles, S., 2001. Primary and diagenetic isotopic signals in fossils and hemipelagic carbonates: the Lower Jurassic of northern Spain. *Sedimentology*, **v.** 48, pp. 1149-1169.

Sælen, G., Doyle, P., Talbot, M. R., 1996. Stable isotope analysis of belemnite rostra from the Whitby Mudstone Formation, England: surface water conditions during deposition of a marine balck shale. *Palaios*, **v.** 11, pp. 97-117.

Sandberg, P. A., 1983. An oscillating trend in Phanerozoic non-skeletal carbonate mineralogy. *Nature*, **v.** 305, pp. 19-22.

Sarti, M., Bosellini, A., Winterer, E. L., 1992. Basin geometry and architecture of a Tethyan passive margin, Southern Alps, Italy: implications for rifting mechanisms. *American Association of Petroleum Geologists Memoir*, **v.** 53, pp. 241-258.

Sartorio, D., 1986. Caprinid patch reef in the Cansiglio inner platform carbonate sequence (Southern Alps); a record of the earliest Aptian marine transgression. *Rivista Italiana di Paleontologia e Stratigrafia*, **v.** 92, pp. 383-399.

---, 1987. Reef and open episodes on a carbonate platform margin from Malm to Cenomanian: the Cansiglio example (Southern Alps). *Memorie della Società Geologica Italiana*, **v.** 40, pp. 91-97.

Schlager, W., 1981. The paradox of drowned reefs and carbonate platforms. *Geological Society of America Bulletin*, **v.** 92, pp. 1197-1211.

---, 1989. Drowning unconformities on carbonate platforms. *In* Crevello, P. D., (*ed.*). Controls on Carbonate Platform and Basin Development: Society of Economic Paleontologists and Mineralogists Special Publication, Tulsa, OK, United States, **v.** 44, pp. 15-25.

Schlanger, S. O., Jenkyns, H. C., 1976. Cretaceous oceanic anoxic events; causes and consequences. *Geologie en Mijnbouw*, **v.** 55, pp. 179-184.

Schlanger, S. O., 1986. High frequency sea-level fluctuations in Cretaceous time: an emerging geophysical problem. *In* Hsü, K. J., (*ed.*). Mesozoic and Cenozoic oceans: American Geophysical Union/Geological Society of America Geodynamics Series, **v.** 15, pp. 61-74.

Schlanger, S. O., Arthur, M. A., Jenkyns, H. C., Scholle, P. A., 1987. The Cenomanian–Turonian Oceanic Anoxic Event, I. Stratigraphy and distribution of organic carbon-rich beds and the Marine $\delta^{13}C$ excursion. Geological Society Special Publication, London, **v.** 26, pp. 371-399.

Scholle, P. A., Kling, S. A., 1972. Southern British Honduras; lagoonal coccolith ooze. *Journal of Sedimentary Petrology*, **v.** 42, pp. 195-204.

Scholle, P. A., Arthur, M. A., 1980. Carbon isotope fluctuations in Cretaceous pelagic limestones: potential stratigraphic and petroleum exploration tool. *American Association of Petroleum Geologists Bulletin*, **v.** 64, pp. 67-87.

Simo, J. A., Scott, R. W., Masse, J. P., 1993. Cretaceous carbonate platforms: an overview. In Simo, T.,(eds.). Cretaceous Carbonate Platforms: *American Association of Petroleum Geologists Memoir*, **v.** 56, pp. 1-14.

Sinninghe-Damste, J. S., Koester, J., 1998. A euxinic southern North Atlantic Ocean during the Cenomanian/ Turonian oceanic anoxic event. *Earth and Planetary Science Letters*, **v.** 158, pp. 165-173.

Sinton, C. W., Duncan, R. A., 1997. Potential links between oceanic plateau volcanism abd global ocean anoxia at the Cenomanian–Turonian boundary. *Economic Geology*, **v.** 92, pp. 234-246.

Smith, A. G., Smith, D. G., Funnell, B. M., 1994. Atlas of Mesozoic and Cenozoic coastlines: Cambridge University Press.

Spero, H. J., Bijma, J., Lea, D. W., Bemis, B. E., 1997. Effect of seawater carbonate concentration on foraminiferal carbon and oxygen isotopes. *Nature*, **v.** 390, pp. 497-500.

Stampfli, G. M., Borel, G. D., 2002. A plate tectonic model for the Paleozoic and Mesozoic constrained by dynamic plate boundaries and restored synthetic oceanic isochrons. *Earth and Planetary Science Letters*, **v.** 196, pp. 17-33.

Stanley, S. M., Hardie, L. A., 1998. Secular oscillations in the carbonate mineralogy of reef-building and sediment-producing organisms driven by tectonically forced shifts in seawater chemistry. *Palaeogeography, Palaeoclimatology, Palaeoecology*, **v**. 144, pp. 3-19.

Stefani, M., Burchell, M., 1989. Upper Triassic (Rhaetic) argillaceous sequences in northern Italy: depositional dynamics and source potential. *In* Huc, A. Y., (*eds.*). Deposition of Organic Facies: American Association of Petroleum Geologists, Tulsa, OK, United States, **v**. 30, pp. 93-106.

Stoll, H. M., Schrag, D. P., 2000. High-resolution stable isotope records from the Upper Cretaceous rocks of Italy and Spain: glacial episodes in a greenhouse planet? *Geological Society of America Bulletin*, **v**. 112, pp. 308-319.

Strong, A. E., Goreau, T. J., Hayes, R. L., 1998. Ocean Hot Spots and coral reef bleaching. *Reef Encounter*, **v**. 24, pp. 20-22.

Sturani, C., 1964. La successione delle fauna ad ammoniti nelle formazione Medio Giurassiche delle Prealpi Venete occidentali. *Memorie degli Istituto di Geologia e Mineralogia dell'Universita di Padova*, **v**. 24, pp. 24.

---, 1971. Ammonites and stratigraphy of the Posidonia alpina beds of the Venetian Alps. *Memorie degli Istituto di Geologia e Mineralogia dell'Universita di Padova*, **v**. 24, pp. 1-63.

Thurow, J., Brumsack, H.-J., Rullkotter, J., Littke, R.,Meyers, P., 1992. The Cenomanian/Turonian Boundary Event in the Indian Ocean - a key to the global picture. *In* Duncan, R. A., et al., (*eds.*). Synthesis of Results from Scientific Drilling in the Indian Ocean: Amererican Geophysical Union Monograph, **v**. 70, pp. 253-273.

Urey, H. C., 1947. The thermodyamic properties of isotopic substances. *Journal of the Chemistry Society*, **v**. 1947, pp. 562-581.

Vahrenkamp, V. C., 1996. Carbon Isotope Stratigraphy of the Upper Kharaib and Shaiba Formations: Implications for the Early Cretaceous Evolution of the Arabian Gulf Region. *American Association of Petroleum Geologists Bulletin*, **v**. 80, pp. 647-662.

Valladares, I., Recio, C., Lendinez, A., 1996. Sequence stratigraphy and stable isotopes ($\delta^{13}C$, $\delta^{18}O$) of the Late Cretaceous carbonate ramp of the western margin of the Iberian Chain (Soria, Spain). *Sedimentary Geology*, **v**. 105, pp. 11-28.

van de Schootbrugge, B., Föllmi, K. B., Bulot, L. G.,Burns, S. J., 2000. Paleoceanographic changes during the Early Cretaceous (Valanginian–Hauterivian): evidence from oxygen and carbon stable isotopes. *Earth and Planetary Science Letters*, **v**. 181, pp. 15-31.

Veizer, J., 1983. Trace elements and isotopes in sedimentary carbonates. *In* Reeder, R. J., (*ed.*). Carbonates: Mineralogy and Chemistry: Mineralogical Society of America, Washington D.C., **v**. 11.

Veizer, J., Ala, D., Azmy, K., Bruckschen, P., Buhl, D., Bruhn, F., Carden, G. A. F., Diener, A., Ebneth, S., Godderis, Y., Jasper, T., Korte, C., Pawellek, F., Podlaha, O. G., Strauss, H., 2000. $^{87}Sr/^{86}Sr$, $\delta^{13}C$ and $\delta^{18}O$ evolution of Phanerozoic seawater. *Chemical Geology*, **v**. 161, pp. 59-88.

Violante, C., 2000, Flooding unconformities at Lias–Dogger boundary in carbonate platform deposits. Aurunci Mountains, Central Apennines (Italy): Società geologica Italiana Conference, 80th Summer Reunion, Trieste, 6-8th September, Abstract Volume, pp. 464-464.

Voigt, S., 2000. Cenomanian–Turonian composite $\delta^{13}C$ curve for Western and Central Europe; the role of organic and inorganic carbon fluxes. *Palaeogeography, Palaeoclimatology, Palaeoecology*, **v**. 160, pp. 91-104.

Ward, P. D., Haggart, J. W., Carter, E. S., Wilbur, D., Tipper, H. W., Evans, T., 2001. Sudden productivity collapse associated with the Triassic–Jurassic boundary mass extinction. *Science*, **v.** 292, pp. 1148-1151.

Weissert, H., Channell, J. E. T., 1989. Tethyan carbonate carbon isotope stratigraphy across the Jurassic-Cretaceous boundary: an indicator of decelerated global carbon cycling? *Paleoceanography*, **v.** 4, pp. 483-494.

Weissert, H., Lini, A., 1991. Ice age interludes during the time of Cretaceous greenhouse climate? *In* Mueller, D. W., et al., (*eds.*). Controversies in Modern Geology: Evolution of Geological Theories in Sedimentology, Earth History and Tectonics: Academic Press, London, United Kingdom pp. 173-191.

Weissert, H., Mohr, H., 1996. Late Jurassic climate and its impact on carbon cycling. *Palaeogeography, Palaeoclimatology, Palaeoecology*, **v.** 122, pp. 27-43.

Weissert, H., Lini, A., Föllmi, K. B., Kuhn, O., 1998. Correlation of Early Cretaceous carbon isotope stratigraphy and platform drowning events; a possible link? *Palaeogeography, Palaeoclimatology, Palaeoecology*, **v.** 137, pp. 189-203.

Wellington, G. M., Glynn, P. W., Strong, A. E., Navarette, S. A., Wieters, E., Hubbard, D., 2001. Crisis on coral reefs linked to climate change. *EOS*, **v.** 82, pp. 1 & 5.

Wicher, C. A., 1938. Microfauna aus Jura und Kreide insbesondere Nordwest Deutschland. *Abh. Pr. Geol. Landesamt*, **v.** 193, pp. 1-16.

Wickman, F. E., 1948. Isotope ratios, a clue to the age of certain marine sediments. *Journal of Geology*, **v.** 56, pp. 61-66.

Wierzbowski, H., 2002. Detailed oxygen- ans carbon-isotope stratigraphy of the Oxfordian in Central Poland. *International Journal of Earth Sciences (Geol. Rundsch.)*, **v.** 91, pp. 304-314.

Wilson, J. L., 1975. Carbonate Facies in Geologic History: Springer-Verlag, New York, 471 pp.

Wilson, P. A., Jenkyns, H. C., Elderfield, H., Larson, R. L., 1998. The paradox of drowned carbonate platforms and the origin of Cretaceous Pacific Guyots. *Nature*, **v.** 392, pp. 889-894.

Wilson, P. A., Norris, R. D., Cooper, M. J., 2002. Testing the Cretaceous greenhouse hypothesis using glassy foraminiferal calcite from the core of Turonian tropics on Demerara Rise. *Geology*, **v.** 30, pp. 607-610.

Winterer, E. L., Bosellini, A., 1981. Subsidence and sedimentation on Jurassic passive continental margin, Southern Alps, Italy. *American Association of Petroleum Geologists Bulletin*, **v.** 65, pp. 394-421.

Winterer, E. L., Metzler, C. V., Sarti, M., 1991. Neptunian dykes and associated breccias (Southern Alps, Italy and Switzerland): role of gravity sliding in open and closed systems. *Sedimentology*, **v.** 38, pp. 381-404.

Wissler, L., Weissert, H., Menegatti, A., Ferreri, V., D, A. B., Buonocunto, F., Raspini, A., Ammodio, S., 1999. δ^{13}C-stratigraphy in Barremian-Aptian shallow water carbonates of southern Italy. European Union of Geosciences conference abstracts; EUG 10.: Journal of Conference Abstracts: Cambridge Publications, Cambridge, United Kingdom, **v.** 4, pp. 218.

Wissler, L., 2001, Response of Early Cretaceous sedimentary systems to perturbations in global carbon cycling: insights from stratigraphy, sedimentology and geochemical modelling [PhD thesis]: ETH Zurich.

Wissler, L., Weissert, H., Masse, J. P., Bulot, L. G., 2002. Chemostratigraphic correlation of Barremian and lower Aptian ammonite zones and magnetic reversals. *Geologae Rundschau*, **v.** 91, pp. 272-279.

Wood, A. W., 1981. Extensional tectonics and the birth of the Lagonegro Basin (southern Italian Apennines). *Neues Jahrbuch fuer Geologie und Palaeontologie. Abhandlungen*, **v.** 161, pp. 93-131.

Wortmann, U., Weissert, H., 2000. Tying platform drowning to perturbations of the global carbon cycle with a $\delta^{13}C_{org}$ curve from the Valanginian of DSDP Site 416. *Terra Nova*, **v.** 12, pp. 289-294.

Wortmann, U., Weissert, H., Funk, H.,Hauck, J., 2001. Alpine plate kinematics revisited: the Adria problem. *Tectonics*, **v.** 20, pp. 134-147.

Zempolich, W. G., 1993. The drowning succession in Jurassic carbonates of the Venetian Alps, Italy: a record of supercontinent breakup, gradual eustatic rise, and eutrophication of shallow-water environments. *American Association of Petroleum Geologists Memoir*, **v.** 57, pp. 63-105.

Zempolich, W. G., Erba, E., 1999. Sedimentologic and chemostratigraphic recognition of third-order sequences in resedimentated carbonate; the Middle Jurassic Vajont Limestone, Venetian Alps, Italy. *In* Harris, P. M., et al., (*eds.*). Advances in carbonate sequence stratigraphy; application to reservoirs, outcrops and models: Society of Economic Paleontologists and Mineralogists Special Publication, Tulsa, OK, United States, **v.** 63, pp. 335-370.

Ziegler, P. A., 1988. Post-Hercynian plate re-organisation in the Tethys and Arctic-North Atlantic domains. *In* Manspeizer, W., (*eds.*). Triassic Jurassic rifting: developments in Geotectonics: Elsevier, Amsterdam pp. 711-755.

---, 1990. Geological atlas of Western and Central Europe: Shell Internationale Petroleum Maatschappij B.V., The Hague.

Appendix

A1: Methods

A1: Methods

1. Sample Collection

All fieldwork was undertaken as a collaborative effort between the Universities of Oxford and Ancona with additional support from the Instituto di Ricerca "Geomare Sud" for the Monte Sorgenza section, near Naples.

Sections were chosen through knowledge of local geology and regional literature and outcrops were subsequently measured and marked to allow re-sampling at a later date over the critical intervals discovered. Duplicate samples were taken for the section through the Friuli Platform: one each for chemostratigraphic and biostratigraphic analysis (generally carried out in Oxford and Ancona respectively).

2. Chemostratigraphic analysis

2.1 Strontium-isotope analysis

Initially, bulk-rock samples were mechanically cut to shape (approx. $1cm^3$) with a rotating disc-saw and cleaned on a diamond-anvil grinder. The aim of this process was to remove as much diagenetic vein calcite and weathered material as possible, which could affect the primary stable-isotope values recorded upon analysis.

The chemical treatment which followed mechanical cleaning was first described by (Jones *et al.*, 1994b) after the process was successfully developed on belemnites, and has since been used with minor modification for all strontium-isotope analyses carried out on carbonates in the Age & Isotope Laboratory, University of Oxford.

The chemical cleaning and strontium-separation process developed for use on shallow-water carbonate samples is described in detail below. After mechanical cleaning, sample blocks were chemically cleaned of residual carbonate dust by a five minute submersion in ~0.6M HCl in clean FEP beakers placed in an ultrasonic bath. Sample blocks were then rinsed with de-ionised water and left to dry in an oven at 60°C. These chemically treated blocks were subsequently crushed using a percussion mortar and hammer, and then between 160–180 mg of sample powder was weighed into clean, labelled 15ml centrifuge tubes. To the weighed powders, 6ml of ~0.6M HCl was added with the aim of dissolving the powder over the course of a mild reaction whilst additionally minimising the risk of leaching strontium from any residual clays present. This leaching can be a danger with too vigorous a reaction (Bailey *et al.*, 2000). To further dissolve any remaining carbonate, ~6M HCl was added drop-wise to the centrifuge tubes. The solutions were transferred to clean FEP beakers and evaporated in dry-blocks to incipient dryness. The residues were dissolved in 2ml 3.0M HCl, transferred into clean 15ml centrifuge tubes and centrifuged.

1ml of these sample solutions was carefully added drop-wise to cleaned, equilibrated (5ml 3.0M HCl) and calibrated cation exchange columns (0.7x8.5cm resin bed - in water - of 200-400 mesh AG 50W X12 resin). Subsequently, the columns were washed with 1, 1, 2 and 15ml 3.0M HCl, following which sample strontium could be eluted with 9ml 3.0M HCl into FEP beakers. The FEP beakers were placed in dry-blocks once more, and evaporated to dryness. When dry, aqua-regia was added (~5ml 16M HNO_3 and ~2ml ~6M HCl at ~100°c) to eliminate any organic matter which passed unaffected through the above process.

The separated strontium residues were then prepared for analysis of strontium-isotope ratios on a VG Isomass 54E solid-state thermal ionisation mass spectrometer (TIMS). 1ml 1.2M H_3PO_4 was placed in the centre of outgassed single tantalum filaments and then heated by ~1 amp current until the H_3PO_4 beads had been reduced as much as possible in size. The strontium samples were then dissolved in 1ml of ultra-pure de-ionised water, and again the filaments were heated with ~1 amp current to reduce the samples to dryness. The filaments were then heated by increasing the current until they emitted a dull red glow, an indication that remaining organic matter and excess H_3PO_4 had been burnt off. Filaments were then loaded into the turret of the mass spectrometer where they were analysed over the period of three days (on average).

Normalisation of strontium-isotope ratios was carried out using the National Institute of Standards and Technology Standard Reference Material (NIST SRM) 987 value of 0.710250.

2.2 Carbon- and oxygen-isotope analysis of carbonates

Samples powdered using a percussion mortar in the method described above were loaded (approximately 3mg) into thimbles but, to avoid the risk of memory effects, not in stratigraphic order. 10% H_2O_2 was added and left for thirty to sixty minutes to destroy any organic matter present (any longer and the oxygen-isotope ratios are susceptible to alteration). Excess water was then removed by addition of acetone, and the samples were placed in an oven at 60°C to dry. The prepared thimbles and eight Carrara Marble standards (four at the beginning and four at the end of each run) were then loaded onto the carousel of a VG Isogas Series II Prism mass spectrometer. The carbon- and oxygen-isotope results obtained were Craig-corrected (Craig, 1957) to cancel-out any affects to the results from ^{14}C and ^{17}O, and are reported as δ values in per mil (‰) relative to the Pee Dee Belemnite (PDB) standard. Analytical reproducibility of replicate standards for the above process was less than 0.1‰ for both carbon- and oxygen-isotope analyses.

2.3 Carbon-isotope analysis of organic compounds

Samples powdered in the method described above were weighed (as TOC values were low, upto 60 mg of sample was used in each case) and sealed within 8x6 mm steel-foil cups. These were subsequently loaded into an Europa Scientific Limited CN sample converter connected to a 20-20 stable-isotope gas-ratio mass spectrometer at the Archaeology Research Laboratory, University of Oxford and analysed. An internal nylon standard ($\delta^{13}C_{nylon}$=-26.2 ±0.2‰) was used for calibration of the isotope ratios obtained and these were then expressed in standard per mil (‰) notation, PDB. Analytical reproducibility of samples for the above process was better than 0.1‰.

2.4 Total Organic Carbon (TOC) analyses

Four powdered duplicate samples were weighed (two for roasting (2 x 100mg) and two not for roasting (2 x 50mg) – weights varied depending on visual estimates of TOC) into ceramic boats: chosen because they do not contain carbon, which would affect the results. Roasting was carried out in an oven at 450°C for twelve hours to burn-off any organic carbon. CO_2, produced by analysing a pre-roasted boat of sample in a Strohlein Coulomat 702 at 1260°c, was passed through barium perchlorate solution changing its pH. The amount of electricity required, when passed through an electrolytic reagent that returned the solution to its original pH, was a measure of the amount of carbon originally released as CO_2.

After the same procedure was carried out on a non-roasted duplicate sample, and then repeated with the two remaining duplicates, the average difference in the amounts of CO_2 that was produced by the roasted and non-roasted samples gave the amount of Total Organic Carbon in the original sample:

$$\text{Total Organic Carbon} = \text{Carbon}_{\text{Non-Roasted}} - \text{Carbon}_{\text{Roasted}}$$

Data were expressed as a percentage of organic carbon of the total weight (wt% TOC).

3. Other Analyses

3.1 Sample staining

Staining of hand specimens of shallow-water carbonates was used to distinguish between carbonate minerals: primarily calcite and dolomite. Cut and polished sample surfaces were thoroughly cleaned with de-ionised water and then etched in 5M HCl for approximately thirty seconds. After rinsing with de-ionised water, samples were ready for a thirty-second submersion in a weakly acidified Alizarin Red S (0.2 gm/100 ml of 2M HCl) / Potassium Ferricyanide (2.0 gm/100 ml of 2M HCl) combined stain solution, mixed in the ratio A.R.S. : P.F. = 3 : 2.

The following colour changes could be expected for carbonate minerals:

Pink–Red	=	Calcite / Aragonite (depending on crystal orientation)
Mauve–Royal Blue	=	Ferroan Calcite (depending on percentage of iron present)
No Colour Change	=	Dolomite
Pale–Deep Turquoise	=	Ferroan Dolomite (depending on percentage of iron present)

A2: Data tables

Appendix Table 2.1: Madonna della Corona, Trento Platform

n	Sample	Stratigraphic depth (m)	$^{87}Sr/^{86}Sr$	Error	$\delta^{13}C_{carb}$ (‰PDB)	$\delta^{18}O_{carb}$ (‰PDB)	$\delta^{13}C_{org}$ (‰)	TOC (wt %)
1	MDC 0.0	0.0	0.707343	2.1E-05	2.027	-1.89		
2	MDC -0.43	-0.43	0.707310	1.8E-05	2.012	-1.304		
3	MDC -0.65	-0.65			2.093	-1.645		
4	MDC -2.0	-2.0	0.707295	1.3E-05	2.366	-2.181		
5	MDC -3.9	-3.9	0.707330	1.7E-05	1.838	-1.775		
6	MDC -6.0	-6.0	0.707323	2.0E-05				
7	MDC -8.0	-8.0	0.707327	2.1E-05	2.324	-1.821		
8	MDC -10.0	-10.0	0.707352	1.7E-05	1.318	-2.815		
9	MDC -12.0	-12.0	0.707327	2.2E-05	1.581	-2.426		
10	MDC -14.0	-14.0	0.707294	1.3E-05	1.778	-1.898		
11	MDC -14.7	-14.7	0.707313	2.1E-05	1.963	-2.279		
12	MDC -16.0	-16.0			2.481	-1.484		
13	MDC -18.0	-18.0	0.707332	1.8E-05	2.237	-2.323		
14	MDC -20.0	-20.0	0.707316	1.5E-05	2.24	-1.883		
15	MDC -22.0	-22.0	0.707325	1.8E-05	2.378	-1.715		
16	MDC -24.0	-24.0	0.707339	1.8E-05	2.332	-2.227		
17	MDC -26.0	-26.0			2.418	-2.868		
18	MDC -28.0	-28.0			2.255	-2.904		
19	MDC -30.0	-30.0	0.707310	1.0E-05	2.266	-2.501		
20	MDC -32.0	-32.0	0.707260	1.8E-05	2.725	-1.426		
21	MDC -34.0	-34.0	0.707325	2.3E-05	2.491	-2.624		
22	MDC -36.0	-36.0	0.707308	2.1E-05	2.523	-2.412		
23	MDC -38.0	-38.0	0.707283	2.0E-05	1.96	-3.147		
24	MDC -40.0	-40.0			2.774	-2.533		
25	MDC -42.0	-42.0	0.707304	1.9E-05	2.886	-2.385		
26	MDC -44.0	-44.0	0.707320	1.8E-05	2.262	-3.395		
27	MDC -46.0	-46.0			2.864	-2.422		
28	MDC -52.0	-52.0	0.707282	1.6E-05				
29	MDC -54.0	-54.0	0.707267	2.1E-05	2.88	-2.263		
30	MDC -56.0	-56.0	0.707247	1.6E-05	2.861	-2.437		
31	MDC -58.0	-58.0			2.997	-2.223		
32	MDC -64.0	-64.0	0.707340	2.7E-05	2.552	-2.539		
33	MDC -66.0	-66.0	0.707267	2.0E-05	2.887	-2.07		
34	MDC -68.0	-68.0	0.707247	2.1E-05	2.917	-2.092		
35	MDC -70.0	-70.0			2.473	-2.442		
36	MDC -78.0	-78.0	0.707261	1.8E-05	2.681	-1.922		
37	MDC -80.0	-80.0	0.707287	1.9E-05				
38	MDC -82.0	-82.0	0.707264	2.7E-05	2.365	-3.096		
39	MDC -84.0	-84.0			2.819	-2.354		
40	MDC -86.0	-86.0	0.707300	2.0E-05	2.492	-2.164		
41	MDC -88.0	-88.0	0.707244	2.0E-05	2.921	-2.178		
42	MDC -90.0	-90.0	0.707291	2.0E-05	2.676	-2.556		
43	MDC -92.0	-92.0	0.707289	1.5E-05	1.915	-2.119		
44	MDC -94.0	-94.0	0.707330	1.9E-05	2.958	-2.271		
45	MDC -96.0	-96.0	0.707271	1.5E-05	2.405	-2.8		

n	Sample	Stratigraphic depth (m)	$^{87}Sr/^{86}Sr$	Error	$\delta^{13}C_{carb}$ (‰PDB)	$\delta^{18}O_{carb}$ (‰PDB)	$\delta^{13}C_{org}$ (‰)	TOC (wt %)
46	MDC -98.0	-98.0	0.707290	2.0E-05	2.854	-2.308		
47	MDC -100.0	-100.0	0.707308	1.4E-05	2.891	-2.301		
48	MDC -102.0	-102.0	0.707266	1.2E-05	2.295	-3.313		
49	MDC -104.0	-104.0			2.552	-2.86		
50	MDC -108.0	-108.0	0.707328	1.4E-05	2.565	-2.745		
51	MDC -110.0	-110	0.707333	2.1E-05	3.135	-1.377		
52	MDC -112.0	-112.0	0.707325	2.1E-05	2.56	-2.512		
53	MDC -114.0	-114.0			2.491	-2.878		
54	MDC -116.0	-116.0			2.468	-2.623		
55	MDC -118.0	-118.0			2.562	-2.661		
56	MDC -120.0	-120.0	0.707272	2.6E-05	2.896	-2.681		
57	MDC -122.0	-122.0	0.707288	2.0E-05	2.531	-3.156		
58	MDC -124.0	-124.0			2.595	-2.55		
59	MDC -126.0	-126.0	0.707286	2.4E-05	2.495	-3.235		
60	MDC -128.0	-128.0			2.527	-3.091		
61	MDC -130.0	-130.0	0.707258	2.1E-05	2.737	-2.769		
62	MDC -132.0	-132.0			2.703	-3.016		
63	MDC -134.0	-134.0	0.707333	2.1E-05	2.788	-2.941		
64	MDC -135.0	-135.0			2.893	-1.754		
65	MDC -136.0	-136.0			2.985	-2.611		
66	MDC -138.0	-138.0	0.707244	1.6E-05	2.817	-3.117		
67	MDC -139.0	-139.0			3.044	-1.742		
68	MDC -140.0	-140.0	0.707302	2.2E-05	2.654	-3.087		
69	MDC -142.0	-142.0	0.707249	9.5E-06	2.82	-3.122		
70	MDC -144.0	-144.0			2.8	-2.981		
71	MDC -146.0	-146.0	0.707240	1.7E-05	2.855	-2.583		
72	MDC -148.0	-148.0	0.707234	2.0E-05	2.61	-2.48		
73	MDC -150.0	-150.0			2.96	-2.486		
74	MDC -152.0	-152.0			3.001	-2.969		
75	MDC -154.0	-154.0	0.707233	2.5E-05	3.439	-2.668		
76	MDC -156.0	-156.0	0.707201	2.0E-05	2.366	-2.932		
77	MDC -158.0	-158.0	0.707212	1.4E-05	3.544	-2.564		
78	MDC -160.0	-160.0	0.707247	2.7E-05	2.684	-3.142		
79	MDC -162.0	-162.0	0.707219	1.8E-05	3.123	-2.798		
80	MDC -164.0	-164.0	0.707176	1.8E-05	2.199	-2.89		
81	MDC -166.0	-166.0	0.707177	2.0E-05	3.592	-2.894		
82	MDC -168.0	-168.0	0.707186	2.7E-05	3.488	-2.75		
83	MDC -170.0	-170.0	0.707185	2.1E-05	3.816	-2.515		
84	MDC -172.0	-172.0	0.707194	2.0E-05	3.608	-2.558		
85	MDC -174.0	-174.0			3.788	-2.783		
86	MDC -176.0	-176.0	0.707178	1.8E-05	3.367	-2.542		
87	MDC -178.0	-178.0	0.707167	2.1E-05	4.12	-1.993		
88	MDC -180.0	-180.0	0.707202	2.1E-05	3.311	-2.731		
89	MDC -182.0	-182.0	0.707172	1.7E-05	3.422	-3.082		
90	MDC -182.5	-182.5			3.921	-1.337		
91	MDC -184.0	-184.0			3.502	-2.36		
92	MDC -188.0	-188.0	0.707186	1.9E-05	3.081	-2.842		

n	Sample	Stratigraphic depth (m)	$^{87}Sr/^{86}Sr$	Error	$\delta^{13}C_{carb}$ (‰PDB)	$\delta^{18}O_{carb}$ (‰PDB)	$\delta^{13}C_{org}$ (‰)	TOC (wt %)
93	MDC -190.0	-190.0	0.707175	1.9E-05	3.253	-2.6		
94	MDC -192.0	-192.0	0.707156	1.8E-05	2.756	-2.952		
95	MDC -194.0	-194.0	0.707155	2.0E-05	2.691	-2.682		
96	MDC -196.0	-196.0	0.707160	2.0E-05	2.903	-2.543		
97	MDC -197.0	-197.0			2.823	-1.799		
98	MDC -198.0	-198.0	0.707152	2.1E-05	2.766	-2.718		
99	MDC -200.0	-200.0	0.707159	1.8E-05	2.879	-2.293		
100	MDC -202.0	-202.0	0.707190	2.7E-05	2.568	-2.602		
101	MDC -248.0	-248.0	0.707143	2.6E-05	2.199	-2.585		
102	MDC -249	-249	0.707186	2.0E-05	2.115	-2.208		
103	MDC -250.0	-250.0			2.589	-1.089		
104	MDC -251.0	-251.0	0.707144	2.1E-05	2.097	-2.046		
105	MDC -252.0	-252.0			2.058	-2.473		
106	MDC -253.0	-253.0			1.93	-2.504		
107	MDC -254.0	-254.0	0.707179	2.0E-05	2.056	-2.532		
108	MDC -255.0	-255.0			2.158	-2.036		
109	MDC -256.0	-256.0			1.93	-2.498		
110	MDC -257.0	-257.0			2.024	-2.403		
111	MDC -258.0	-258.0	0.707199	2.1E-05	2.149	-2.638		
112	MDC -259.0	-259.0	0.707202	2.1E-05	2.151	-2.484		
113	MDC -269.0	-269.0			2.227	-2.468		
114	MDC -269.5	-269.5	0.707209	2.2E-05	1.718	-2.984		
115	MDC -270.0	-270.0			1.384	-3.173		
116	MDC -270.5	-270.5	0.707198	2.0E-05	1.96	-2.714		
117	MDC -271.0	-271.0			2.067	-2.565		
118	MDC -271.5	-271.5	0.707176	2.1E-05	2.201	-2.409		
119	MDC -272.0	-272.0			2.156	-2.84		
120	MDC -292.0	-292.0	0.707181	2.0E-05	2.905	-2.276		
121	MDC -294.0	-294.0	0.707100	2.3E-05	3.117	-2.03		
122	MDC -296.0	-296.0			2.873	-2.376		
123	MDC -298.0	-298.0			2.899	-2.414		
124	MDC -300.0	-300.0			2.811	-2.278		
125	MDC -302.0	-302.0			3.016	-1.228		
126	MDC -304.0	-304.0	0.707211	2.0E-05	2.418	-2.483		
127	MDC -306.0	-306.0			2.92	-1.968		
128	MDC -308.0	-308.0			3.516	-0.914		
129	MDC -310.0	-310.0			3.254	-1.186		
130	MDC -312.0	-312.0	0.707213	1.9E-05				
131	MDC -314.0	-314.0	0.707224	1.6E-05	2.477	-2.602		
132	MDC -316.0	-316.0	0.707220	2.0E-05	2.785	-2.407		
133	MDC -318.0	-318.0			2.806	-2.185		
134	MDC -320.0	-320.0	0.707215	2.1E-05	2.556	-2.451		
135	MDC -322.0	-322.0	0.707227	2.1E-05				
136	MDC -324.0	-324.0			2.846	-2.444		
137	MDC -326.0	-326.0	0.707158	2.1E-05	3.464	-0.922		
138	MDC -328.0	-328.0			3.454	-0.957		
139	MDC -330.0	-330.0			2.671	-2.406		

n	Sample	Stratigraphic depth (m)	$^{87}Sr/^{86}Sr$	Error	$\delta^{13}C_{carb}$ (‰PDB)	$\delta^{18}O_{carb}$ (‰PDB)	$\delta^{13}C_{org}$ (‰)	TOC (wt %)
140	MDC -332.0	-332.0			1.839	-2.788		
141	MDC -334.0	-334.0			2.741	-2.281		
142	MDC -336.0	-336.0			1.957	-2.68		
143	MDC -338.0	-338.0			3.136	-1.191		
144	MDC -340.0	-340.0			2.614	-1.646		
145	MDC -342.0	-342.0			2.28	-3.066		
146	MDC -344.0	-344.0			2.561	-2.863		
147	MDC -346.0	-346.0	0.707258	2.1E-05	1.832	-3.327		
148	MDC -348.0	-348.0			2.327	-3.086		
149	MDC -350.0	-350.0			1.197	-4.298		
150	MDC -352.0	-352.0			2.051	-3.324		
151	MDC -354.0	-354.0	0.707283	2.0E-05	1.76	-3.479		
152	MDC -356.0	-356.0	0.707241	1.8E-05	2.635	-2.676		
153	MDC -358	-358	0.707299	1.6E-05				
154	MDC -362	-362			2.516	-2.652		
155	MDC -364.0	-364.0	0.707258	2.5E-05	1.385	-3.693		
156	MDC -366.0	-366.0	0.707261	2.1E-05	1.794	-3.679		
157	MDC -368.0	-368.0			1.966	-2.282		
158	MDC -370.0	-370.0	0.707316	1.9E-05	1.127	-4.076		
159	MDC -372.0	-372.0			1.457	-3.653		
160	MDC -374.0	-374.0	0.707312	1.6E-05	0.593	-4.757		
161	MDC -376.0	-376.0	0.707298	2.0E-05	0.963	-4.081		
162	MDC -378.0	-378.0			1.517	-3.021		
163	MDC -380.0	-380.0			2.803	-1.59		
164	MDC -382.0	-382.0			1.896	-2.365		
165	MDC -384.0	-384.0			2.196	-2.771		
166	MDC -386.0	-386.0			2.845	-1.807		
167	MDC -388.0	-388.0			1.846	-3.127		
168	MDC -390.0	-390.0			2.173	-3.158		
169	MDC -392.0	-392.0	0.707338	2.1E-05	1.22	-4.126		
170	MDC -394.0	-394.0			1.125	-4.048		
171	MDC -396.0	-396.0			1.819	-2.797		
172	MDC -398.0	-398.0	0.707303	2.1E-05	2.416	-2.556		
173	MDC -400.0	-400.0	0.707293	2.1E-05	2.168	-3.217		
174	MDC -402.0	-402.0	0.707344	2.1E-05	1.07	-3.788		
175	MDC -404.0	-404.0	0.707300	1.7E-05	1.792	-3.17		
176	MDC -408.0	-408.0			2.479	-2.788		
177	MDC -414.0	-414.0			2.234	-2.851		
178	MDC -418.0	-418.0	0.707279	1.4E-05	2.316	-2.894		
179	MDC -420.0	-420.0	0.707255	2.1E-05	2.344	-2.605		
180	MDC -422.0	-422.0			2.225	-1.746		
181	MDC -424.0	-424.0			1.63	-2.797		
182	MDC -426.0	-426.0	0.707286	2.1E-05	2.181	-2.503		
183	MDC -428.0	-428.0	0.707329	2.1E-05	1.472	-3.599		
184	MDC -430.0	-430.0	0.707242	2.1E-05	0.698	-3.179		
185	MDC -432.0	-432.0	0.707280	1.5E-05	1.58	-3.26		
186	MDC -434.0	-434.0	0.707231	1.9E-05	1.682	-2.806		

n	Sample	Stratigraphic depth (m)	$^{87}Sr/^{86}Sr$	Error	$\delta^{13}C_{carb}$ (‰PDB)	$\delta^{18}O_{carb}$ (‰PDB)	$\delta^{13}C_{org}$ (‰)	TOC (wt %)
187	MDC -436.0	-436.0	0.707224	2.3E-05	1.972	-2.134		
188	MDC -438.0	-438.0	0.707258	2.1E-05				
189	MDC -440.0	-440.0	0.707239	1.6E-05				
190	MDC -442.0	-442.0			1.601	-2.731		
191	MDC -444.0	-444.0	0.707286	2.2E-05	2.524	-2.171		
192	MDC -446.0	-446.0	0.707240	2.0E-05	1.829	-2.246		
193	MDC -448.0	-448.0			2.626	-2.878		
194	MDC -450.0	-450.0	0.707269	2.1E-05	2.125	-2.91		
195	MDC -452.0	-452.0			1.51	-2.629		
196	MDC -454.0	-454.0	0.707277	2.1E-05	1.9	-2.092		
197	MDC -455.0	-455.0	0.707291	2.0E-05	2.647	-2.59		
198	MDC -456.0	-456.0	0.707220	2.0E-05	0.619	-3.045		
199	MDC -458.0	-458.0			2.291	-2.657		
200	MDC -462.0	-462.0	0.707242	2.1E-05	2.907	-1.792		
201	MDC -464.0	-464.0	0.707308	2.0E-05	2.604	-1.439		
202	MDC -466.0	-466.0			1.875	-2.248		
203	MDC -478.0	-478.0	0.707269	2.0E-05				
204	MDC -480	-480	0.707262	2.1E-05	3.075	-1.788		
205	MDC -484	-484	0.707302	2.1E-05	1.488	-2.703		
206	MDC -486	-486	0.707208	2.8E-05	2.985	-2.067		
207	MDC -488.0	-488.0			2.759	-3.033		
208	MDC -490.0	-490.0	0.707307	2.1E-05	2.539	-1.994		
209	MDC -492.0	-492.0	0.707287	2.1E-05	0.738	-3.603		
210	MDC -494.0	-494.0	0.707267	1.9E-05	2.178	-1.9		
211	MDC -498.0	-498.0			2.148	-1.874		
212	MDC -503.0	-503.0	0.707294	2.1E-05	2.023	-2.243		
213	MDC -504.0	-504.0	0.707311	2.1E-05	1.985	-1.942		
214	MDC -505.0	-505.0	0.707293	1.9E-05	2.115	-1.839		
215	MDC -508.0	-508.0	0.707315	2.1E-05	1.948	-2.112		
216	MDC -510.0	-510.0			2.128	-2.47		
217	MDC -512.0	-512.0	0.707300	1.8E-05	2.007	-2.535		
218	MDC -514.0	-514.0			1.449	-3.39		
219	MDC -516.0	-516.0	0.707344	2.1E-05	1.294	-3.477		
220	MDC -518.0	-518.0			1.509	-3.3		
221	MDC -520.0	-520.0			1.846	-2.55		
222	MDC -521.0	-521.0	0.707319	1.8E-05	1.933	-2.306		
223	MDC -522.0	-522.0			2.063	-2.244		
224	MDC -524.0	-524.0	0.707411	1.6E-05	1.8	-2.785		
225	MDC -526.0	-526.0			1.868	-2.394		
226	MDC -528.0	-528.0	0.707369	1.9E-05				
227	MDC -530.0	-530.0			1.502	-3.021		
228	MDC -532.0	-532.0	0.707348	1.9E-05	1.456	-3.25		
229	MDC -534.0	-534.0	0.707357	1.7E-05	1.165	-3.555		
230	MDC -536.0	-536.0	0.707390	2.7E-05	1.602	-2.779		
231	MDC -538.0	-538.0			1.426	-3.983		
232	MDC -540.0	-540.0			1.042	-3.98		
233	MDC -542.0	-542.0	0.707364	1.9E-05	1.447	-3.468		

n	Sample	Stratigraphic depth (m)	$^{87}Sr/^{86}Sr$	Error	$\delta^{13}C_{carb}$ (‰PDB)	$\delta^{18}O_{carb}$ (‰PDB)	$\delta^{13}C_{org}$ (‰)	TOC (wt %)
234	MDC -571.0	-571.0	0.707346	1.8E-05	2.448	-1.898		
235	MDC -571.5	-571.5			2.032	-2.186		
236	MDC -572.0	-572.0	0.707228	2.0E-05	2.737	-1.659		
237	MDC -572.5	-572.5	0.707237	1.7E-05	2.72	-1.636		
238	MDC -573.0	-573.0			2.488	-2.076		
239	MDC -573.5	-573.5			2.232	-2.901		
240	MDC -594.0	-594.0	0.707354	2.0E-05	2.436	-2.05		
241	MDC -597.0	-597.0			2.131	-2.3		
242	MDC -598.0	-598.0			2.359	-1.967		
243	MDC -599.0	-599.0			1.984	-3.166		
244	MDC -600.0	-600.0			2.153	-2.492		
245	MDC -601.0	-601.0			2.211	-1.741		
246	MDC -602.0	-602.0			2.14	-2.65		
247	MDC -603.0	-603.0			1.354	-3.142		
248	MDC -604.0	-604.0	0.707352	2.0E-05	1.211	-3.146		
249	MDC -606.0	-606.0			1.576	-3.776		
250	MDC -610.0	-610.0	0.707369	2.1E-05				
251	MDC -614.0	-614.0	0.707403	2.0E-05				
252	MDC -615.0	-615.0	0.707424	2.1E-05				
253	MDC -618.5	-618.5	0.707469	1.3E-05				
254	MDC -627.0	-627.0			1.121	-3.393		
255	MDC -628	-628	0.707411	2.5E-05	0.459	-3.976		
256	MDC -630	-630	0.707391	2.2E-05	1.136	-3.544		
257	MDC -632	-632			-0.877	-3.933		
258	MDC -634	-634			0.642	-3.845		
259	MDC -636.0	-636.0	0.707406	2.1E-05	1.181	-3.187		
260	MDC -638.0	-638.0	0.707386	2.0E-05	1.151	-3.384		
261	MDC -640.0	-640.0	0.707388	2.7E-05	1.102	-3.646		
262	MDC -642.0	-642.0			1.63	-4.192		
263	MDC -644.0	-644.0	0.707412	2.1E-05	1.24	-3.733		
264	MDC -645.0	-645.0			1.452	-2.475		
265	MDC -646.0	-646.0	0.707398	1.8E-05				
266	MDC -658.5	-658.5	0.707422	2.4E-05	0.752	-4.033		
267	MDC -660.0	-660.0			1.116	-3.802		
268	MDC -662.0	-662.0	0.707361	2.0E-05	1.573	-2.608		
269	MDC -664.0	-664.0	0.707377	1.3E-05	1.446	-2.787		
270	MDC -666.0	-666.0	0.707379	2.6E-05	1.709	-4.627		
271	MDC -674.0	-674.0	0.707368	2.1E-05	1.776	-1.794		
272	MDC -682.0	-682.0	0.707410	1.2E-05	1.891	-1.886		
273	MDC -683.0	-683.0			2.009	-3.739		
274	MDC -685.0	-685.0	0.707365	1.7E-05	1.964	-1.793		
275	MDC -686.0	-686.0	0.707395	1.3E-05	1.716	-2.148		
276	MDC -687.0	-687.0	0.707491	2.7E-05	1.699	-2.097		
277	MDC -688.0	-688.0	0.707358	2.6E-05	1.837	-3.704		
278	MDC -690.0	-690.0			1.442	-3.346		
279	MDC -692.0	-692.0	0.707421	2.1E-05	1.423	-2.406		
280	MDC -694.0	-694.0			1.656	-2.896		

n	Sample	Stratigraphic depth (m)	$^{87}Sr/^{86}Sr$	Error	$\delta^{13}C_{carb}$ (‰PDB)	$\delta^{18}O_{carb}$ (‰PDB)	$\delta^{13}C_{org}$ (‰)	TOC (wt %)
281	MDC -696.0	-696.0	0.707463	2.1E-05	1.885	-4.085		
282	MDC -698.0	-698.0	0.707378	1.7E-05	1.626	-1.971		
283	MDC -700.0	-700.0	0.707400	1.8E-05	1.774	-2.433		
284	MDC -703.0	-703.0	0.707378	2.0E-05	2.229	-1.751		
285	MDC -704.0	-704.0	0.707422	1.5E-05	1.505	-2.392		
286	MDC -706.0	-706.0	0.707427	2.1E-05	1.773	-1.937		
287	MDC -708.0	-708.0			1.429	-2.985		
288	MDC -710.0	-710.0	0.707485	2.1E-05	1.463	-2.03		
289	MDC -712.0	-712.0			1.157	-2.327		
290	MDC -714.0	-714.0	0.707391	2.0E-05	1.703	-2.024		
291	MDC -716.0	-716.0	0.707512	2.4E-05	1.396	-3.966		
292	MDC -720.0	-720.0	0.707426	2.1E-05	1.394	-4.867		
293	MDC -722.0	-722.0	0.707419	1.9E-05	1.555	-2.112		
294	MDC -724.0	-724.0			1.3	-2.484		
295	MDC -726.0	-726.0	0.707458	2.1E-05	1.814	-4.034		
296	MDC -728.0	-728.0	0.707431	1.9E-05	1.872	-2.607		
297	MDC -730.0	-730.0	0.707377	1.9E-05	1.533	-1.148		
298	MDC -732.0	-732.0			1.486	-1.765		
299	MDC -734.0	-734.0	0.707480	2.0E-05	1.414	-2.066		
300	MDC -736.0	-736.0	0.707523	2.7E-05	1.267	-1.924		

Appendix Table 2.2: San Vigilio, Trento Platform

n	Sample	Stratigraphic depth (m)	$^{87}Sr/^{86}Sr$	Error	$\delta^{13}C_{carb}$ (‰PDB)	$\delta^{18}O_{carb}$ (‰PDB)	Carbonate (‰)	TOC (wt%)
1	SV 0.0	0.0	0.707358	1.9E-05	2.655	-0.976		
2	SV -0.2	-0.2			2.522	-1.387		
3	SV -0.43	-0.43			2.939	-0.691		
4	SV -0.6	-0.6			2.9	-0.191		
5	SV -0.9	-0.9	0.707337	1.8E-05	2.941	-0.784		
6	SV -1.25	-1.25			2.635	-0.909		
7	SV -1.6	-1.6			2.749	-2.078		
8	SV -1.8	-1.8			2.865	-0.764		
9	SV -2.0	-2.0			3.112	-0.747		
10	SV -2.5	-2.5			3.109	-0.364		
11	SV -2.7	-2.7			2.971	-1.065		
12	SV -3.0	-3.0			3.036	-0.206		
13	SV -3.2	-3.2	0.707346	1.9E-05	2.655	0.396		
14	SV -3.6	-3.6			2.574	-1.472		
15	SV -3.8	-3.8			2.876	-0.605		
16	SV -4.0	-4.0			3.001	-0.543		
17	SV -4.2	-4.2			2.863	-0.713		
18	SV -4.5	-4.5			2.567	-1.747		
19	SV -4.75	-4.75			1.941	-2.436		
20	SV -5.0	-5.0			2.528	-1.368		
21	SV -5.2	-5.2			2.463	-2.559		
22	SV -5.7	-5.7			2.532	-0.829		
23	SV -6.0	-6.0			2.991	-0.311		
24	SV -6.2	-6.2			2.904	-1.503		
25	SV -6.4	-6.4			2.799	-1.752		
26	SV -6.6	-6.6			2.65	-0.987		
27	SV -6.8	-6.8			2.677	-0.878		
28	SV -7.6	-7.6			2.912	-0.773		
29	SV -7.8	-7.8			2.632	-1.603		
30	SV -8.6	-8.6			2.888	-0.801		
31	SV -8.8	-8.8			2.602	-1.957		
32	SV -9.0	-9.0			2.853	-0.731		
33	SV -9.4	-9.4	0.707342	2.1E-05	2.689	-2.678		
34	SV -10.9	-10.9			2.675	-2.532		
35	SV -41.0	-41.0	0.707343	2.0E-05	2.404	-0.064		
36	SV -41.5	-41.5	0.707281	1.3E-05	2.837	-1.198		
37	SV -42.0	-42.0	0.707365	2.0E-05	2.392	-0.979		
38	SV -42.5	-42.5			2.674	-1.272		
39	SV -43.0	-43.0	0.707325	2.3E-05	2.577	-0.69		
40	SV -44.0	-44.0	0.707291	2.1E-05	2.699	-0.762		
41	SV -44.5	-44.5	0.707264	1.7E-05	2.843	-0.577		
42	SV -45.0	-45.0			2.71	-1.313		
43	SV -47.0	-47.0	0.707293	1.9E-05	2.533	-1.636		
44	SV -48.0	-48.0			2.53	-1.924		
45	SV -49.0	-49.0	0.707353	1.9E-05	2.538	-1.468		

n	Sample	Stratigraphic depth (m)	$^{87}Sr/^{86}Sr$	Error	$\delta^{13}C_{carb}$ (‰PDB)	$\delta^{18}O_{carb}$ (‰PDB)	Carbonate (‰)	TOC (wt%)
46	SV -50.0	-50.0	0.707355	2.1E-05	2.512	-1.913		
47	SV -51.0	-51.0	0.707382	2.1E-05	2.495	-1.711		
48	SV -52.0	-52.0	0.70736	2.5E-05	2.568	-1.855		
49	SV -53.0	-53.0			2.442	-2.158		
50	SV -54.0	-54.0			2.477	-1.831		
51	SV -55.0	-55.0	0.707345	2.1E-05	2.336	-1.831		
52	SV -56.0	-56.0	0.707345	2.1E-05	2.484	-2.118		
53	SV -57.0	-57.0			2.323	-0.838		
54	SV -57.5	-57.5	0.707342	2.0E-05	2.338	-2.045		
55	SV -58.0	-58.0			2.38	-1.774		
56	SV -58.5	-58.5	0.707317	1.3E-05	2.318	-2.224		
57	SV -59.0	-59.0	0.707362	2.1E-05	2.44	-1.678		
58	SV -59.5	-59.5	0.707343	2.2E-05	2.47	-1.461		
59	SV -60.0	-60.0	0.707323	1.9E-05				
60	SV -60.5	-60.5	0.707353	2.0E-05	2.368	-1.975		
61	SV -61.0	-61.0			2.257	-1.712		
62	SV -61.6	-61.6	0.707347	2.1E-05	2.422	-1.571		
63	SV -65.0	-65.0	0.707316	2.1E-05	2.445	-1.513		
64	SV -68.0	-68.0	0.707352	1.7E-05	2.327	-1.851		
65	SV -107.0	-107.0	0.707313	1.6E-05	2.334	-1.746		
66	SV -107.5	-107.5			2.614	-1.624		
67	SV -108.0	-108.0			2.348	-0.227		
68	SV -108.5	-108.5	0.70732	2.1E-05	2.338	-2.116		
69	SV -109.0	-109.0			2.321	-2.127		
70	SV -109.5	-109.5	0.707298	2.1E-05	2.351	-1.564		
71	SV -110.0	-110.0	0.707307	1.6E-05	2.323	-2.092		
72	SV -110.5	-110.5	0.707319	2.0E-05	2.505	-1.832	100	0
73	SV -111.0	-111.0	0.707289	2.3E-05	2.321	-1.745		
74	SV -111.5	-111.5	0.707303	2.0E-05	2.327	-2.278		
75	SV -112.0	-112.0			2.364	-2.119		
76	SV -112.5	-112.5	0.707326	2.0E-05	2.324	-0.164		
77	SV -113.0	-113.0	0.707308	1.3E-05	2.27	-1.555		
78	SV -113.5	-113.5	0.707314	2.0E-05	2.242	-2.076		
79	SV -114.0	-114.0	0.707227	2.1E-05	2.063	-2.857		
80	SV -114.5	-114.5	0.707294	2.3E-05	2.048	-1.905		
81	SV -115.0	-115.0			1.954	-0.707		
82	SV -115.5	-115.5	0.707397	2.1E-05	1.923	-1.691		
83	SV -116.0	-116.0	0.707302	2.1E-05	1.986	-1.492		
84	SV -116.5	-116.5	0.707282	2.1E-05	1.962	-2.264		
85	SV -117.0	-117.0			2.066	-1.622		
86	SV -117.5	-117.5			2.011	-2.043		
87	SV -118.0	-118.0	0.707291	2.1E-05	1.889	-1.884		
88	SV -118.5	-118.5	0.707217	2.0E-05	1.864	-2.273		
89	SV -119.0	-119.0			1.872	-2.795		
90	SV -119.5	-119.5	0.707371	2.0E-05	1.678	-2.906	59.16	0.07
91	SV -120.0	-120.0	0.707328	2.8E-05	1.693	-2.841		
92	SV -120.5	-120.5	0.707329	2.1E-05	1.731	-3.226		

n	Sample	Stratigraphic depth (m)	$^{87}Sr/^{86}Sr$	Error	$\delta^{13}C_{carb}$ (‰PDB)	$\delta^{18}O_{carb}$ (‰PDB)	Carbonate (‰)	TOC (wt%)
93	SV -121.0	-121.0	0.707331	1.8E-05	1.796	-2.277	35.91	0.31
94	SV -121.5	-121.5	0.707415	2.2E-05				
95	SV -122.0	-122.0	0.707455	2.1E-05	1.613	-3.198		
96	SV -122.5	-122.5	0.707327	1.9E-05	1.986	-1.419		
97	SV -123.0	-123.0	0.70741	2.1E-05	1.51	-4.476		
98	SV -123.5	-123.5	0.707372	1.2E-05	1.88	-1.685		
99	SV -124.0	-124.0	0.707261	2.1E-05	1.115	-3.276		
100	SV -124.5	-124.5	0.707327	1.9E-05	1.32	-4.004	97.35	0.09
101	SV -125.0	-125.0	0.707281	1.4E-05	1.76	0.179	47.08	0.11
102	SV -125.5	-125.5	0.707333	2.1E-05	1.663	-1.65	40.48	0
103	SV -126.0	-126.0	0.707333	2.1E-05	1.404	-3.316		
104	SV -126.5	-126.5	0.707333	2.1E-05	1.889	-1.325		
105	SV -127.0	-127.0			1.334	-3.449		
106	SV -127.5	-127.5	0.707345	2.1E-05	1.859	-1.765	97.7	0
107	SV -128.0	-128.0	0.707262	1.9E-05	1.875	-0.973		
108	SV -128.5	-128.5	0.707329	2.0E-05	1.88	-1.354		
109	SV -129.0	-129.0	0.707306	1.9E-05	1.82	-1.189		
110	SV -129.5	-129.5	0.707298	2.1E-05	1.846	-1.744		
111	SV -130.0	-130.0	0.707248	1.9E-05				
112	SV -130.5	-130.5	0.707281	2.0E-05			94.75	0.12
113	SV -142.0	-142.0	0.707293	2.1E-05	1.957	-1.431		
114	SV -142.5	-142.5			2.103	-1.599		
115	SV -143.0	-143.0			2.399	-1.166		
116	SV -143.5	-143.5			2.133	-1.06		
117	SV -144.0	-144.0			1.803	-2.267		
118	SV -144.5	-144.5			1.47	-1.808		
119	SV -145.0	-145.0			1.355	-2.63		
120	SV -145.5	-145.5			1.652	-1.859		
121	SV -161.5	-161.5			2.507	-1.654		
122	SV -162.0	-162.0			2.509	-1.63		
123	SV -162.3	-162.3			2.595	-1.39		
124	SV -162.8	-162.8			2.659	-1.561		
125	SV -163.0	-163.0			2.587	-1.467		
126	SV -163.3	-163.3			2.678	-1.639		
127	SV -163.7	-163.7			2.65	-1.64		
128	SV -167.5	-167.5			2.662	-1.334		
129	SV -168.5	-168.5			2.589	-1.893		
130	SV -169.6	-169.6			2.62	-1.656		
131	SV -170.1	-170.1			2.719	-1.623		
132	SV -170.5	-170.5			2.61	-1.672		
133	SV -171.0	-171.0			2.649	-1.49		
134	SV -171.5	-171.5			2.578	-1.76		
135	SV -172.0	-172.0			2.554	-1.931		
136	SV -172.5	-172.5			2.617	-1.332		
137	SV -173.0	-173.0			2.669	-1.551		
138	SV -173.5	-173.5			2.525	-1.836		
139	SV -174.0	-174.0			2.551	-1.605		

n	Sample	Stratigraphic depth (m)	$^{87}Sr/^{86}Sr$	Error	$\delta^{13}C_{carb}$ (‰PDB)	$\delta^{18}O_{carb}$ (‰PDB)	Carbonate (‰)	TOC (wt%)
140	SV -174.5	-174.5			2.596	-1.781		
141	SV -175.0	-175.0			2.621	-1.79		
142	SV -175.5	-175.5	0.707318	1.6E-05	2.552	-1.833		
143	SV -176.0	-176.0						
144	SV -176.5	-176.5	0.707288	2.2E-05	2.488	-1.835		
145	SV -177.0	-177.0			2.435	-2.007		
146	SV -177.5	-177.5			2.529	-1.888		
147	SV -178.0	-178.0			2.459	-2.22		
148	SV -178.5	-178.5	0.707301	2.2E-05	2.529	-1.863		
149	SV -179.0	-179.0			2.337	-2.033		
150	SV -179.5	-179.5	0.707279	2.1E-05	2.535	-1.38		
151	SV -180.0	-180.0			2.582	-1.652		
152	SV -180.5	-180.5	0.707286	2.4E-05	2.571	-1.565		
153	SV -181	-181	0.707291	2.0E-05	2.565	-1.595		
154	SV -181.5	-181.5			2.579	-1.541		
155	SV -182.0	-182.0	0.707332	2.8E-05	2.561	-1.65		
156	SV -182.5	-182.5	0.707332	2.8E-05	2.524	-1.815		
157	SV -183.0	-183.0			2.634	-1.32		
158	SV -183.5	-183.5			2.602	-1.518		
159	SV -184.0	-184.0			2.582	-1.695		
160	SV -184.5	-184.5	0.707273	2.1E-05	2.44	-1.709		
161	SV -185.0	-185.0			2.601	-1.609		
162	SV -185.5	-185.5			2.572	-1.503		
163	SV -186.0	-186.0			2.586	-1.701		
164	SV -186.5	-186.5	0.707293	3.1E-05	2.518	-1.931		
165	SV -187.0	-187.0			2.559	-1.465		
166	SV -187.5	-187.5	0.707145	1.1E-05	2.33	-1.501		
167	SV -188.0	-188.0			2.6	-1.689		
168	SV -188.5	-188.5	0.707258	2.0E-05	2.486	-1.89		
169	SV -189.0	-189.0			2.563	-1.641		
170	SV -189.5	-189.5			1.756	-2.339		
171	SV -190.0	-190.0			2.615	-1.705		
172	SV -190.5	-190.5	0.707282	2.1E-05	2.634	-1.664		
173	SV -191.0	-191.0						
174	SV -191.5	-191.5	0.707279	2.1E-05	2.369	-1.717		
175	SV -196.0	-196.0			2.364	-2.555		

Appendix Table 2.3: Colma di Malcesine, Trento Platform

n	Sample	Stratigraphic depth (m)	$^{87}Sr/^{86}Sr$	$\delta^{13}C_{carb}$ (‰PDB)	$\delta^{18}O_{carb}$ (‰PDB)	Carbonate (‰)	TOC (wt%)	$\delta^{13}C_{org}$ (‰)
1	CDM 34.0	34.0		3.004	-2.747			
2	CDM 33.5	33.5		2.957	-2.861			
3	CDM 33.0	33.0		2.668	-3.187			
4	CDM 32.5	32.5		2.969	-2.691			
5	CDM 31.5	31.5		2.925	-2.787			
6	CDM 31.0	31.0		2.935	-2.483			
7	CDM 30.5	30.5		2.802	-2.856			
8	CDM 30.0	30.0		3.106	-2.595			
9	CDM 30.0	30.0		2.917	-2.554			
10	CDM 29.5	29.5		2.731	-2.857			
11	CDM 29.0	29.0		2.753	-2.767			
12	CDM 28.5	28.5		2.776	-2.578			
13	CDM 28.0	28.0		2.894	-2.879			
14	CDM 27.5	27.5		2.719	-2.687			
15	CDM 27.0	27.0		2.611	-2.718			
16	CDM 26.5	26.5		2.725	-2.724			
17	CDM 26.0	26.0						
18	CDM 25.5	25.5		2.693	-2.739			
19	CDM 25.0	25.0		2.391	-2.881			
20	CDM 24.5	24.5		2.426	-2.845			
21	CDM 24.0	24.0		2.38	-2.956			
22	CDM 23.5	23.5		2.111	-3.033			
23	CDM 23.0	23.0		2.44	-2.601			
24	CDM 22.5	22.5		2.382	-2.963			
25	CDM 22.0	22.0		2.263	-2.893			
26	CDM 21.5	21.5		1.844	-2.968			
27	CDM 21.0	21.0		1.88	-2.5			
28	CDM 20.5	20.5		1.906	-2.961			
29	CDM 20.0	20.0		2.12	-2.52			
30	CDM 19.5	19.5		1.793	-2.962			
31	CDM 19.0	19.0		1.739	-2.863			
32	CDM 18.5	18.5		1.86	-2.67			
33	CDM 12.0	12.0		1.468	-3.191			
34	CDM 11.5	11.5		1.405	-3.143			
35	CDM 10.5	10.5		1.445	-3.172			
36	CDM 10.0	10.0		1.479	-3.161			
37	CDM 9.5	9.5		1.337	-3.247			
38	CDM 9.0	9.0		1.693	-2.681			
39	CDM 8.5	8.5		1.559	-3.096			
40	CDM 8.0	8.0		1.436	-3.227			
41	CDM 7.5	7.5		1.274	-3.481			
42	CDM 7.0	7.0		1.241	-3.073			
43	CDM 6.5	6.5		1.654	-3.124			
44	CDM 6.0	6.0		1.402	-2.691			
45	CDM 5.5	5.5		1.404	-3.011			

n	Sample	Stratigraphic depth (m)	$^{87}Sr/^{86}Sr$	$\delta^{13}C_{carb}$ (‰PDB)	$\delta^{18}O_{carb}$ (‰PDB)	Carbonate (‰)	TOC (wt%)	$\delta^{13}C_{org}$ (‰)
46	CDM 5.0	5.0		1.272	-2.966			
47	CDM 4.0	4.0		0.992	-3.424			
48	CDM 3.5	3.5		0.963	-3.26			
49	CDM 3.0	3.0		1.126	-3.032			
50	CDM 2.5	2.5		1.209	-2.857	85.75	0	
51	CDM 2.0	2.0		1.132	-2.906	88.67	0.12	-26.92
52	CDM 1.5	1.5		1.118	-2.938	94.5	0.05	
53	CDM 1.0	1.0		1.387	-2.975	88.17	0.05	
54	CDM 0.5	0.5		1.765	-3.322	73.67	0.28	-26.13
55	CDM 0.0	0.0		2.116	-2.156	99.67	0	
56	CDM -1.0	-1.0		2.246	-3.069	99.17	0	
57	CDM -2.0	-2.0		2.218	-2.753	99.75	0	
58	CDM -3.0	-3.0		2.236	-2.665			
59	CDM -4.0	-4.0		2.17	-2.697			
60	CDM -5.0	-5.0		2.236	-2.676			
61	CDM -6.0	-6.0		2.249	-2.643			
62	CDM -7.0	-7.0		2.253	-2.643			
63	CDM -8.0	-8.0		2.259	-2.911			
64	CDM -9.0	-9.0		2.009	-2.842			
65	CDM -10.0	-10.0		2.175	-3.233			
66	CDM -11.0	-11.0		2.297	-2.416			
67	CDM -12.0	-12.0		2.233	-2.756			
68	CDM -13.0	-13.0		2.053	-2.853			

Appendix Table 2.4: Sega d'Ala, Trento Platform

n	Sample	Stratigraphic depth (m)	87Sr/86Sr	$\delta^{13}C_{carb}$ (‰PDB)	$\delta^{18}O_{carb}$ (‰PDB)	$\delta^{13}C_{org}$ (‰)	TOC (wt%)
1	SDA 44.0	44.0		3.21	-1.858		
2	SDA 43.0	43.0		3.158	-2.281		
3	SDA 42.0	42.0		3.716	-1.251		
4	SDA 41.0	41.0		3.301	-2.053		
5	SDA 40.0	40.0		3.535	-1.891		
6	SDA 39.0	39.0		3.259	-2.64		
7	SDA 38.0	38.0		3.69	-2.052		
8	SDA 37.0	37.0		2.723	-2.395		
9	SDA 36.0	36.0		3.625	-2.287		
10	SDA 35.0	35.0		3.572	-2.86		
11	SDA 34.0	34.0		3.482	-2.281		
12	SDA 33.0	33.0		3.736	-2.032		
13	SDA 32.0	32.0		3.493	-3.026		
14	SDA 31.0	31.0		3.438	-2.594		
15	SDA 30.5	30.5		3.261	-2.177		
16	SDA 30.0	30.0		3.203	-2.195		
17	SDA 29.5	29.5		3.161	-2.435		
18	SDA 29.0	29.0		3.087	-2.659		
19	SDA 28.5	28.5		3.085	-2.528		
20	SDA 28.0	28.0		3.285	-2.302		
21	SDA 27.5	27.5		3.403	-2.354		
22	SDA 27.0	27.0		3.272	-2.328		
23	SDA 26.5	26.5		3.112	-2.407		
24	SDA 26.0	26.0		3.095	-2.58		
25	SDA 25.5	25.5		3.433	-2.101		
26	SDA 25.0	25.0		3.078	-2.145		
27	SDA 24.5	24.5		2.946	-2.274		
28	SDA 24.0	24.0		3.369	-2.168		
29	SDA 23.5	23.5		3.122	-2.44		
30	SDA 23.0	23.0		3.137	-2.452		
31	SDA 22.5	22.5		3.079	-2.351		
32	SDA 22.0	22.0		3.04	-2.531		
33	SDA 21.5	21.5		2.949	-2.515		
34	SDA 21.0	21.0		3.207	-1.916		
35	SDA 20.5	20.5		2.756	-2.391		
36	SDA 20.0	20.0		2.824	-2.32		
37	SDA 19.5	19.5		2.708	-2.816		
38	SDA 19.0	19.0		2.857	-2.343		
39	SDA 18.5	18.5		2.672	-2.504		
40	SDA 18.0	18.0		2.704	-2.453		
41	SDA 17.5	17.5		2.653	-2.298		
42	SDA 17.0	17.0		2.742	-2.293		
43	SDA 16.5	16.5		2.633	-2.388		
44	SDA 16.0	16.0		2.533	-2.68		
45	SDA 15.5	15.5		2.365	-2.703		

n	Sample	Stratigraphic depth (m)	87Sr/86Sr	$\delta^{13}C_{carb}$ (‰PDB)	$\delta^{18}O_{carb}$ (‰PDB)	$\delta^{13}C_{org}$ (‰)	TOC (wt%)
46	SDA 15.0	15.0		2.207	-2.669		
47	SDA 14.5	14.5		2.334	-2.498		
48	SDA 14.0	14.0		2.391	-2.39		
49	SDA 13.5	13.5		2.316	-2.647		
50	SDA 13.0	13.0		2.758	-2.216		
51	SDA 12.5	12.5		2.428	-2.76		
52	SDA 12.0	12.0		2.703	-1.749		
53	SDA 11.5	11.5		2.494	-2.523		
54	SDA 11.0	11.0		2.169	-2.54		
55	SDA 10.5	10.5		2.117	-2.536		
56	SDA 10.0	10.0		2.393	-2.459		
57	SDA 9.5	9.5		2.17	-2.597		
58	SDA 9.0	9.0		2.355	-2.503		
59	SDA 8.5	8.5		2.134	-2.789		
60	SDA 8.0	8.0		2.498	-1.869		
61	SDA 7.5	7.5		2.096	-2.469		
62	SDA 7.0	7.0		2.114	-2.339		
63	SDA 6.5	6.5		2.031	-2.487		
64	SDA 6.0	6.0		2.02	-2.702		
65	SDA 5.5	5.5		1.965	-2.652		
66	SDA 5.0	5.0		1.967	-2.678		
67	SDA 4.8	4.8		2.012	-2.665		
68	SDA 4.6	4.6		1.762	-2.173		
69	SDA 4.4	4.4		1.886	-2.51		
70	SDA 4.2	4.2		1.907	-2.768		
71	SDA 4.0	4.0		1.973	-2.35		
72	SDA 3.8	3.8		1.719	-2.444		
73	SDA 3.6	3.6		2.157	-2.148		
74	SDA 3.4	3.4		2.34	-2.309		
75	SDA 3.2	3.2		2.092	-2.398		
76	SDA 3.0	3.0		2.199	-2.255		
77	SDA 2.8	2.8		2.318	-1.944		
78	SDA 2.6	2.6		2.184	-2.374		
79	SDA 2.4	2.4		1.906	-2.514		
80	SDA 2.2	2.2		1.842	-2.568		
81	SDA 2.0	2.0		1.756	-2.593		
82	SDA 1.4	1.4		1.892	-2.738		
83	SDA 1.2	1.2		1.807	-2.487		
84	SDA 1.0	1.0		1.814	-2.704		
85	SDA 0.8	0.8		1.762	-3.12		
86	SDA 0.6	0.6		1.945	-2.733		
87	SDA 0.4	0.4		1.346	-2.499		
88	SDA 0.2	0.2		1.873	-2.563		
89	SDA 0.0	0.0		2.086	-2.072		
90	SDA -1.0	-1.0		2.956	-2.708		
91	SDA -2.0	-2.0		3.155	-2.409		
92	SDA -3.0	-3.0		3.337	-2.115		

n	Sample	Stratigraphic depth (m)	87Sr/86Sr	$\delta^{13}C_{carb}$ (‰PDB)	$\delta^{18}O_{carb}$ (‰PDB)	$\delta^{13}C_{org}$ (‰)	TOC (wt%)
93	SDA -4.0	-4.0		3.338	-2.506		
94	SDA -5.0	-5.0		2.459	-3.018		
95	SDA -6.0	-6.0		2.71	-2.654		
96	SDA -7.0	-7.0		2.589	-2.632		
97	SDA -8.0	-8.0		2.454	-2.926		
98	SDA -9.0	-9.0		2.575	-2.102		
99	SDA -10.0	-10.0		2.489	-2.543		
100	SDA -11.0	-11.0		2.559	-2.265		
101	SDA -12.0	-12.0		2.377	-3.241		
102	SDA -13.0	-13.0		2.487	-3.069		
103	SDA -14.0	-14.0		2.177	-2.787		
104	SDA -15.0	-15.0		2.229	-2.783		

Appendix Table 3.1: Val Cellina, Friuli Platform

n	Sample	Stratigraphic height (m)	$^{87}Sr/^{86}Sr$	Error	$\delta^{13}C_{carb}$ (‰PDB)	$\delta^{18}O_{carb}$ (‰PDB)	$\delta^{13}C_{org}$ (‰)	TOC (wt%)
1	VC 0.0	0.0	0.706930	2.0E-05	3.289	-3.85		
2	VC 1.0	1.0			3.258	-3.177		
3	VC 2.0	2.0			3.208	-2.964		
4	VC 3.0	3.0			3.136	-2.5		
5	VC 4.0	4.0			3.436	-3.492		
6	VC 5.0	5.0	0.706960	2.1E-05	3.436	-2.701		
7	VC 6.0	6.0			3.09	-2.914		
8	VC 7.0	7.0			2.494	-1.866		
9	VC 8.0	8.0			2.828	-3.264		
10	VC 9.0	9.0			2.863	-5.02		
11	VC 10.0	10.0			3.631	-2.923		
12	VC 11.0	11.0			2.825	-4.208		
13	VC 12.0	12.0			2.968	-2.336		
14	VC 13.0	13.0			2.956	-2.43		
15	VC 14.0	14.0			2.954	-2.675		
16	VC 15.0	15.0	0.706920	2.1E-05	2.474	-3.741		
17	VC 16.0	16.0			2.839	-2.788		
18	VC 17.0	17.0			2.684	-5.093		
19	VC 18.0	18.0			2.875	-2.714		
20	VC 19.0	19.0			2.192	-3.259		
21	VC 20.0	20.0			2.662	-3.133		
22	VC 21.0	21.0			2.956	-1.782		
23	VC 22.0	22.0			2.781	-2.026		
24	VC 23.0	23.0			3.036	-3.133		
25	VC 24.0	24.0			3.271	-3.242		
26	VC 25.0	25.0	0.707010	1.9E-05	2.661	-3.662		
27	VC 26.0	26.0			2.921	-1.922		
28	VC 27.0	27.0			3.177	-3.159		
29	VC 28.0	28.0			2.754	-3.201		
30	VC 29.0	29.0			3.049	-1.969		
31	VC 30.0	30.0	0.706930	2.0E-05	3.214	-2.332		
32	VC 31.0	31.0			2.928	-3.063		
33	VC 32.0	32.0			2.493	-2.317		
34	VC 34.0	34.0			2.298	-2.505		
35	VC 35.0	35.0	0.706920	2.3E-05	2.736	-4.105		
36	VC 36.0	36.0			2.997	-3.447		
37	VC 39.0	39.0			3.009	-2.904		
38	VC 40.0	40.0	0.706910	2.0E-05	2.944	-3.055		
39	VC 41.0	41.0			1.357	-2.366		
40	VC 42.0	42.0			2.716	-2.428		
41	VC 43.0	43.0			2.749	-2.583		
42	VC 44.0	44.0			0.661	-3.293		
43	VC 45.0	45.0			3.019	-2.488		
44	VC 46.0	46.0			2.625	-3.974		
45	VC 47.0	47.0			3.345	-3.026		

n	Sample	Stratigraphic height (m)	$^{87}Sr/^{86}Sr$	Error	$\delta^{13}C_{carb}$ (‰PDB)	$\delta^{18}O_{carb}$ (‰PDB)	$\delta^{13}C_{org}$ (‰)	TOC (wt%)
46	VC 50.0	50.0	0.706930	2.8E-05	3.288	-3.794		
47	VC 52.0	52.0			3.044	-7.134		
48	VC 54.0	54.0			3.516	-2.688		
49	VC 56.0	56.0			0.9	-2.724		
50	VC 60.0	60.0			3.537	-2.879		
51	VC 61.0	61.0			3.103	-3.423		
52	VC 63.0	63.0			3.255	-2.585		
53	VC 65.0	65.0			3.544	-3.132		
54	VC 70.0	70.0	0.706910	1.8E-05	3.466	-3.296		
55	VC 115.0	115.0	0.706960	1.5E-05	3.236	-2.885		
56	VC 120.0	120.0	0.706980	1.9E-05	2.927	-2.287		
57	VC 125.0	125.0	0.706970	2.1E-05	3.055	-3.265		
58	VC 130.0	130.0			2.559	-5.995		
59	VC 135.0	135.0	0.706970	2.0E-05	3.045	-3.265		
60	VC 140.0	140.0	0.706960	2.1E-05	3.03	-3.446		
61	VC 144.0	144.0			2.554	-2.969		
62	VC 145.0	145.0	0.706930	2.0E-05	2.228	-3.97		
63	VC 146.0	146.0			2.838	-3.648		
64	VC 148.0	148.0			2.601	-2.273		
65	VC 150.0	150.0	0.707000	1.1E-05	2.934	-3.685		
66	VC 152.0	152.0			2.702	-2.672		
67	VC 154.0	154.0			2.701	-3.27		
68	VC 155.0	155.0	0.706970	2.0E-05	2.929	-3.295		
69	VC 156.0	156.0			2.827	-3.449		
70	VC 158.0	158.0			3.254	-2.606		
71	VC 160.0	160.0			3.089	-3.502		
72	VC 162.0	162.0			2.032	-2.961		
73	VC 165.0	165.0	0.706970	2.1E-05	3.231	-2.588		
74	VC 166.0	166.0			2.753	-2.856		
75	VC 168.0	168.0			2.828	-2.821		
76	VC 180.0	180.0	0.707080	2.0E-05	2.945	-3.398		
77	VC 182.0	182.0			3.159	-1.833		
78	VC 184.0	184.0			3.016	-3.494		
79	VC 185.0	185.0	0.706980	2.0E-05	2.859	-3.85		
80	VC 188.0	188.0			2.366	-3.837		
81	VC 190.0	190.0	0.707000	2.1E-05	2.982	-3.796		
82	VC 192.0	192.0			2.902	-3.262		
83	VC 194.0	194.0			2.675	-3.932		
84	VC 195.0	195.0	0.707060	2.1E-05	2.635	-2.811		
85	VC 196.0	196.0			2.608	-2.442		
86	VC 198.0	198.0			2.452	-2.959		
87	VC 200.0	200.0	0.707040	1.5E-05	2.368	-3.218		
88	VC 202.0	202.0			1.324	-2.708		
89	VC 205.0	205.0	0.707070	1.4E-05	2.185	-2.638		
90	VC 208.0	208.0			2.191	-3.408		
91	VC 212.0	212.0			1.788	-1.705		
92	VC 214.0	214.0			1.934	-2.708		

n	Sample	Stratigraphic height (m)	$^{87}Sr/^{86}Sr$	Error	$\delta^{13}C_{carb}$ (‰PDB)	$\delta^{18}O_{carb}$ (‰PDB)	$\delta^{13}C_{org}$ (‰)	TOC (wt%)
93	VC 215.0	215.0	0.707240	2.1E-05				
94	VC 216.0	216.0			1.683	-2.663		
95	VC 218.0	218.0			1.905	-3.543		
96	VC 220.0	220.0			1.887	-3.25		
97	VC 222.0	222.0			1.871	-2.894		
98	VC 225.0	225.0			1.502	-3.295		
99	VC 226.0	226.0			1.698	-4.366		
100	VC 228.0	228.0			1.697	-3.545		
101	VC 230.0	230.0			0.937	-3.82		
102	VC 245.0	245.0	0.707030	1.6E-05	-0.849	-2.846		
103	VC 250.0	250.0			-1.307	-3.601		
104	VC 255.0	255.0	0.707150	1.3E-05				
105	VC 262.0	262.0	0.707160	2.1E-05				
106	VC 285.0	285.0			1.1535	-3.1104		
107	VC 295.0	295.0	0.707320	1.9E-05	1.165	-1.737		
108	VC 300.0	300.0	0.707210	2.1E-05	-0.145	-3.253		
109	VC 305.0	305.0	0.707190	2.0E-05	1.479	-3.913		
110	VC 310.0	310.0			1.838	-2.99		
111	VC 315.0	315.0			2.11	-1.749		
112	VC 320.0	320.0			1.843	-3.541		
113	VC 321.0	321.0			1.752	-3.465		
114	VC 322.0	322.0			1.805	-3.368		
115	VC 325.0	325.0			1.65	-2.877		
116	VC 330.0	330.0	0.707210	2.1E-05	1.083	-4.192		
117	VC 332.0	332.0	0.707240	2.0E-05				
118	VC 335.0	335.0			1.011	-3.891		
119	VC 340.0	340.0	0.707200	1.3E-05	0.818	-2.756		
120	VC 345.0	345.0			0.095	-2.014		
121	VC 350.0	350.0			-0.832	-2.942		
122	VC 352.0	352.0			-1.104	-3.18		
123	VC 355.0	355.0	0.707210	1.9E-05				
124	VC 360.0	360.0			-0.928	-3.24		
125	VC 370.0	370.0	0.707280	1.9E-05	0.998	-3.148		
126	VC 375.0	375.0	0.707320	1.7E-05	0.344	-3.442		
127	VC 380.0	380.0	0.707340	2.4E-05	0.563	-6.071		
128	VC 382.0	382.0	0.707320	1.9E-05	0.929	-2.567		
129	VC 385.0	385.0			0.749	-3.453		
130	VC 386.0	386.0	0.707320	1.2E-05				
131	VC 387.0	387.0			1.075	-5.109		
132	VC 389.0	389.0			0.647	-2.667		
133	VC 390.0	390.0	0.707170	2.0E-05	0.789	-1.832		
134	VC 392.0	392.0			0.999	-4.53		
135	VC 395.0	395.0			1.098	-4.575		
136	VC 400.0	400.0			1.0337	-3.4725		
137	VC 405.0	405.0			1.283	-4.364		
138	VC 410.0	410.0	0.707340	2.1E-05	1.017	-3.931		
139	VC 413.0	413.0			-0.029	-3.268		

n	Sample	Stratigraphic height (m)	$^{87}Sr/^{86}Sr$	Error	$\delta^{13}C_{carb}$ (‰PDB)	$\delta^{18}O_{carb}$ (‰PDB)	$\delta^{13}C_{org}$ (‰)	TOC (wt%)
140	VC 415.0	415.0			0.5916	-4.3544		
141	VC 420.0	420.0			0.855	-1.705		
142	VC 425.0	425.0			-0.14	-2.875		
143	VC 430.0	430.0	0.707320	2.4E-05	0.463	-4.323		
144	VC 435.0	435.0	0.707300	1.5E-05	0.32344	-4.3579		
145	VC 436.0	436.0			0.094	-2.471		
146	VC 440.0	440.0			0.48091	-2.7536		
147	VC 445.0	445.0	0.707390	2.0E-05	0.284	-2.701		
148	VC 450.0	450.0			0.49415	-4.5444		
149	VC 498.0	498.0			0.089	-2.499		
150	VC 499.0	499.0			0.636	-3.189		
151	VC 500.0	500.0	0.707410	2.6E-05	0.43589	-4.0748		
152	VC 501.0	501.0			0.634	-3.131		
153	VC 502.0	502.0			0.395	-3.228		
154	VC 503.0	503.0			1.15	-2.684		
155	VC 508.0	508.0			1.267	-3.949		
156	VC 509.0	509.0			1.197	-3.808		
157	VC 510.0	510.0			1.049	-2.946		
158	VC 511.0	511.0			1.083	-3.144		
159	VC 512.0	512.0			0.98	-3.323		
160	VC 514.0	514.0			1.261	-3.303		
161	VC 515.0	515.0	0.707400	2.6E-05	1.1459	-3.3896		
162	VC 516.0	516.0			1.368	-3.496		
163	VC 517.0	517.0			1.482	-1.993		
164	VC 518.0	518.0			1.564	-3.275		
165	VC 519.0	519.0			1.319	-3.588		
166	VC 520.0	520.0			1.1975	-3.5899		
167	VC 521.0	521.0			1.279	-3.222		
168	VC 522.0	522.0			1.158	-4.506		
169	VC 523.0	523.0			1.153	-3.859		
170	VC 524.0	524.0			1.106	-3.705		
171	VC 525.0	525.0	0.707430	1.5E-05	1.3062	-3.1017		
172	VC 526.0	526.0			1.497	-4.467		
173	VC 527.0	527.0			1.546	-2.977		
174	VC 533.0	533.0			1.807	-3.164		
175	VC 534.0	534.0			1.833	-2.843		
176	VC 535.0	535.0	0.707400	2.7E-05	1.7131	-3.8102		
177	VC 538.0	538.0			2.16	-3.938		
178	VC 540.0	540.0			1.775	-2.009		
179	VC 541.0	541.0			1.866	-3.823		
180	VC 542.0	542.0			1.917	-3.817		
181	VC 544.0	544.0			1.815	-5.196		
182	VC 545.0	545.0	0.707420	2.0E-05	0.174	-1.427		
183	VC 546.0	546.0			1.944	-3.72		
184	VC 547.0	547.0			1.254	-2.361		
185	VC 548.0	548.0			1.607	-2.573		
186	VC 549.0	549.0			2.061	-4.028		

n	Sample	Stratigraphic height (m)	$^{87}Sr/^{86}Sr$	Error	$\delta^{13}C_{carb}$ (‰PDB)	$\delta^{18}O_{carb}$ (‰PDB)	$\delta^{13}C_{org}$ (‰)	TOC (wt%)
187	VC 550.0	550.0	0.707400	2.1E-05	2.3423	-3.5363		
188	VC 550.5	550.5			2.347	-3.483		
189	VC 551.0	551.0			2.331	-3.904		
190	VC 551.5	551.5			2.324	-3.649		
191	VC 552.0	552.0			2.052	-2.931		
192	VC 552.5	552.5			2.324	-3.524		
193	VC 553.0	553.0			2.31	-3.045		
194	VC 553.5	553.5			0.994	-3.077		
195	VC 554.0	554.0			2.415	-3.006		
196	VC 554.5	554.5			2.036	-4.142		
197	VC 555.0	555.0			2.473	-3.816		
198	VC 555.5	555.5			2.301	-2.966		
199	VC 556.0	556.0			2.192	-4.216		
200	VC 556.5	556.5			2.074	-3.569		
201	VC 557.0	557.0			1.681	-4.096		
202	VC 557.5	557.5			1.304	-3.289		
203	VC 558.0	558.0			1.446	-2.624		
204	VC 558.5	558.5			2.067	-3.061		
205	VC 559.0	559.0			2.02	-2.757		
206	VC 559.5	559.5			2.075	-2.918		
207	VC 560.0	560.0	0.707440	2.0E-05	2.1196	-2.9803		
208	VC 561.0	561.0			1.861	-2.797		
209	VC 562.0	562.0			1.769	-3.474		
210	VC 563.0	563.0			1.382	-4.71		
211	VC 568.0	568.0			1.177	-2.688		
212	VC 569.0	569.0			1.103	-2.644		
213	VC 570.0	570.0	0.707420	2.1E-05	0.761	-3.577		
214	VC 571.0	571.0			0.77	-4.441		
215	VC 575.0	575.0			1.458	-3.776		
216	VC 576.0	576.0			1.301	-4.068		
217	VC 577.0	577.0			0.824	-2.881		
218	VC 578.0	578.0			0.474	-3.467		
219	VC 580.0	580.0			0.759	-4.208		
220	VC 582.0	582.0			1.007	-3.628		
221	VC 583.0	583.0			0.99	-5.021		
222	VC 584.0	584.0			0.771	-5.043		
223	VC 585.0	585.0	0.707410	2.1E-05	1.574	-3.245		
224	VC 590.0	590.0			0.77187	-3.9484		
225	VC 600.0	600.0	0.707440	2.1E-05	0.775	-3.717		
226	VC 605.0	605.0	0.707440	2.1E-05	0.37432	-3.368		
227	VC 606.0	606.0			0.943	-3.073		
228	VC 610.0	610.0	0.707480	1.9E-05	0.70737	-3.9983		
229	VC 645.0	645.0			0.53084	-3.9149		
230	VC 650.0	650.0			0.564	-3.452		
231	VC 650.0	650.0			-0.0796	-3.8045		
232	VC 653.0	653.0			-0.972	-3.849		
233	VC 657.0	657.0			-0.047	-3.487		

n	Sample	Stratigraphic height (m)	$^{87}Sr/^{86}Sr$	Error	$\delta^{13}C_{carb}$ (‰PDB)	$\delta^{18}O_{carb}$ (‰PDB)	$\delta^{13}C_{org}$ (‰)	TOC (wt%)
234	VC 659.0	659.0			0.18	-2.795		
235	VC 660.0	660.0			-0.6602	-4.0295		
236	VC 661.0	661.0			-0.182	-2.692		
237	VC 664.0	664.0			0.665	-2.225		
238	VC 664.5	664.5			0.126	-2.569		
239	VC 665.0	665.0	0.707470	2.0E-05	-0.239	-3.909		
240	VC 665.0	665.0			-0.1318	-3.9665		
241	VC 667.0	667.0			0.79	-1.866		
242	VC 668.0	668.0			0.825	-2.811		
243	VC 670.0	670.0	0.707500	1.4E-05	0.64549	-3.7469		
244	VC 671.0	671.0			0.498	-2.775		
245	VC 673.0	673.0			0.711	-2.126		
246	VC 675.0	675.0			0.58943	-3.7308		
247	VC 695.0	695.0			0.167	-4.342		
248	VC 696.0	696.0			-1.372	-4.843		
249	VC 700.0	700.0			-0.528	-5.167		
250	VC 701.0	701.0			0.653	-3.408		
251	VC 702.0	702.0			0.888	-3.139		
252	VC 703.0	703.0			0.851	-4.141		
253	VC 705.0	705.0	0.707510	2.0E-05	0.373	-5.709		
254	VC 706.0	706.0			-0.062	-4.481		
255	VC 707.0	707.0			0.845	-4.303		
256	VC 708.0	708.0			0.219	-3.358		
257	VC 709.0	709.0			-0.6	-4.591		
258	VC 710.0	710.0			-0.4815	-4.4533		
259	VC 711.0	711.0			-0.168	-3.238		
260	VC 712.0	712.0			-0.473	-4.958		
261	VC 713.0	713.0			-2.049	-4.142		
262	VC 714.0	714.0			-0.412	-5.586		
263	VC 715.0	715.0			-0.7198	-4.9202		
264	VC 716.0	716.0			0.765	-5.129		
265	VC 717.0	717.0			0.489	-4.54		
266	VC 718.0	718.0			0.876	-4.193		
267	VC 719.0	719.0			0.961	-3.693		
268	VC 720.0	720.0			0.58126	-3.3944		
269	VC 722.0	722.0			0.781	-3.686		
270	VC 725.0	725.0			0.0073	-4.0409		
271	VC 760.0	760.0	0.707520	2.0E-05	0.61916	-2.8099		
272	VC 760.5	760.5			0.612	-3.542		
273	VC 761.5	761.5			-0.564	-2.844		
274	VC 762.5	762.5			-0.399	-3.126		
275	VC 763.5	763.5			-0.162	-3.375		
276	VC 764.0	764.0			-0.481	-2.882		
277	VC							
278	VC 765.0	765.0			-0.631	-4.485		
279	VC 765.5	765.5			-0.259	-3.968		
280	VC 766.0	766.0			-0.568	-3.187		

n	Sample	Stratigraphic height (m)	$^{87}Sr/^{86}Sr$	Error	$\delta^{13}C_{carb}$ (‰PDB)	$\delta^{18}O_{carb}$ (‰PDB)	$\delta^{13}C_{org}$ (‰)	TOC (wt%)
281	VC 767.0	767.0			-1.447	-2.631		
282	VC 767.5	767.5			0.415	-2.296		
283	VC 768.5	768.5			0.312	-3.082		
284	VC 769.5	769.5			0.47	-3.133		
285	VC 770.0	770.0	0.707510	1.7E-05	0.57	-3.24		
286	VC 770.5	770.5			0.563	-3.124		
287	VC 771.5	771.5			0.69	-3.148		
288	VC 772.5	772.5			-0.114	-2.916		
289	VC 773.5	773.5			-0.109	-2.884		
290	VC 774.5	774.5			0.209	-3.667		
291	VC 775.0	775.0			0.581	-3.603		
292	VC 775.5	775.5			0.855	-3.459		
293	VC 777.5	777.5			0.06	-4.938		
294	VC 778.5	778.5			-0.334	-3.603		
295	VC 779.5	779.5			-0.487	-3.406		
296	VC 780.0	780.0	0.707530	2.0E-05	-0.1616	-2.7362		
297	VC 780.5	780.5			-0.837	-3.281		
298	VC 781.5	781.5			-0.293	-3.835		
299	VC 782.5	782.5			-1.316	-3.436		
300	VC 784.5	784.5			-1.433	-3.366		
301	VC 785.0	785.0	0.707520	2.1E-05	-1.6295	-3.3708		
302	VC 785.5	785.5			-1.706	-2.875		
303	VC 786.5	786.5			2.432	-4.411		
304	VC 787.0	787.0			-2.376	-3.222		
305	VC 787.5	787.5			-4.316	-4.066		
306	VC 788.5	788.5			-1.456	-2.831		
307	VC 789.5	789.5			-2.603	-3.732		
308	VC 790.0	790.0			-3.7143	-4.924		
309	VC 791.5	791.5			-3.501	-3.676		
310	VC 792.0	792.0			-2.779	-3.473		
311	VC 792.5	792.5			0.433	-2.913		
312	VC 793.0	793.0			-2.054	-2.982		
313	VC 793.5	793.5			0.322	-3.013		
314	VC 795.0	795.0	0.707510	2.0E-05	0.606	-4.218		
315	VC 796.0	796.0			-0.834	-2.7		
316	VC 797.0	797.0			-0.406	-2.778		
317	VC 798.0	798.0			0.122	-3.441		
318	VC 798.5	798.5			-0.524	-3.782		
319	VC 799.0	799.0			-1.228	-3.107		
320	VC 799.5	799.5			-0.272	-2.737		
321	VC 800.0	800.0	0.707530	2.6E-05	-1.0415	-3.4581		
322	VC 801.0	801.0			-0.884	-3.631		
323	VC 802.0	802.0			-1.345	-3.718		
324	VC 803.0	803.0			-1.124	-2.932		
325	VC 804.0	804.0			-0.07	-3.025		
326	VC 804.0	804.0			1.249	-3.422		
327	VC 804.5	804.5			-1.194	-3.882		

n	Sample	Stratigraphic height (m)	$^{87}Sr/^{86}Sr$	Error	$\delta^{13}C_{carb}$ (‰PDB)	$\delta^{18}O_{carb}$ (‰PDB)	$\delta^{13}C_{org}$ (‰)	TOC (wt%)
328	VC 805.0	805.0	0.707540	2.0E-05	-1.1675	-4.4268		
329	VC 806.0	806.0			-2.072	-2.504		
330	VC 808.0	808.0			-0.505	-3.124		
331	VC 810.0	810.0	0.707550	2.0E-05	-1.3166	-2.5726		
332	VC 824.0	824.0			0.008	-3.453		
333	VC 825.0	825.0	0.707440	2.1E-05	1.052	-3.344		
334	VC 826.0	826.0			0	-3.356		
335	VC 829.0	829.0			-0.115	-2.288		
336	VC 830.0	830.0	0.707540	2.0E-05	0.24272	-4.8442		
337	VC 831.0	831.0			0.08	-3.843		
338	VC 833.0	833.0			-1.802	-3.438		
339	VC 834.0	834.0			0.018	-2.421		
340	VC 835.0	835.0	0.707500	2.1E-05	0.073	-3.5285		
341	VC 837.0	837.0			0.019	-3.703		
342	VC 838.0	838.0			-0.074	-2.778		
343	VC 840.0	840.0	0.707450	2.0E-05	0.68011	-4.1304		
344	VC 841.0	841.0			0.723	-2.881		
345	VC 842.0	842.0			0.416	-2.654		
346	VC 843.0	843.0			0.816	-2.919		
347	VC 844.0	844.0			1.296	-2.864		
348	VC 845.0	845.0			1.587	-3.475		
349	VC 846.0	846.0			0.695	-2.442		
350	VC 848.0	848.0			1.075	-2.628		
351	VC 850.0	850.0	0.707470	1.9E-05	0.5427	-3.8959		
352	VC 852.0	852.0			0.302	-3.167		
353	VC 854.0	854.0			0.868	-3.248		
354	VC 855.0	855.0	0.707480	2.1E-05	-0.024	-3.0368		
355	VC 857.0	857.0			1.287	-5.516		
356	VC 859.0	859.0			0.693	-3.707		
357	VC 860.0	860.0	0.707410	2.0E-05	0.88053	-3.0477		
358	VC 860.0	860.0			0.91	-4.574		
359	VC 863.0	863.0			0.868	-4.083		
360	VC 865.0	865.0	0.707430	2.0E-05	1.0065	-3.6166		
361	VC 867.0	867.0			1.114	-2.98		
362	VC 870.0	870.0			1.694	-4.736		
363	VC 872.0	872.0			2.48	-1.48		
364	VC 873.0	873.0			1.589	-1.613		
365	VC 875.0	875.0	0.707290	2.1E-05	1.6465	-3.6309		
366	VC 877.0	877.0			1.04	-4.15		
367	VC 878.0	878.0			1.234	-3.049		
368	VC 880.0	880.0	0.707290	2.0E-05	1.3088	-2.7994		
369	VC 894.0	894.0			1.406	-1.652		
370	VC 895.0	895.0	0.707380	2.1E-05	0.49708	-2.7266		
371	VC 896.1	896.1			1.235	-1.389		
372	VC 897.0	897.0			0.944	-1.629		
373	VC 897.5	897.5			-0.382	-2.674		
374	VC 898.0	898.0			1.202	-1.858		

n	Sample	Stratigraphic height (m)	$^{87}Sr/^{86}Sr$	Error	$\delta^{13}C_{carb}$ (‰PDB)	$\delta^{18}O_{carb}$ (‰PDB)	$\delta^{13}C_{org}$ (‰)	TOC (wt%)
375	VC 899.0	899.0			1.365	-2.523		
376	VC 900.0	900.0			0.334	-1.425		
377	VC 901.0	901.0			1.024	-2.524		
378	VC 902.0	902.0			1.529	-0.502		
379	VC 904.0	904.0			0.682	-2.018		
380	VC 906.0	906.0			0.918	-2.884		
381	VC 907.0	907.0			0.944	-2.302		
382	VC 908.0	908.0			0.822	-3.096		
383	VC 909.0	909.0			-0.119	-2.945		
384	VC 910.0	910.0			1.035	-1.687		
385	VC 911.0	911.0			0.356	-2.434		
386	VC 912.0	912.0			0.507	-2.235		
387	VC 913.0	913.0			0.802	-1.834		
388	VC 915.0	915.0			1.58	-1.993		
389	VC 916.0	916.0			1.02	-2.103		
390	VC 917.0	917.0			0.991	-2.135		
391	VC 920.0	920.0			1.22	-1.894		
392	VC 974.0	974.0			1.328	-4.212		
393	VC 975.0	975.0	0.707460	2.5E-05	1.2887	-3.6592		
394	VC 976.0	976.0			-1.319	-4.789		
395	VC 977.0	977.0			-0.236	-6.974		
396	VC 978.0	978.0			0.382	-1.817		
397	VC 979.0	979.0			1.386	-3.355		
398	VC 980.0	980.0	0.707440	1.7E-05	1.3053	-2.9165		
399	VC 981.0	981.0			0.624	-1.303		
400	VC 982.0	982.0			-0.166	-3.567		
401	VC 983.0	983.0			0.001	-1.219		
402	VC 984.0	984.0			-0.227	-2.921		
403	VC 985.0	985.0			0.994	-2.342		
404	VC 986.0	986.0			-2.465	-2.46		
405	VC 987.0	987.0			1.164	-2.707		
406	VC 988.0	988.0			0.046	-2.006		
407	VC 989.0	989.0			-0.301	-0.854		
408	VC 990.0	990.0			1.0438	-3.5826		
409	VC 991.0	991.0			0.345	-1.819		
410	VC 992.0	992.0			0.613	-2.523		
411	VC 993.0	993.0			-0.309	-2.647		
412	VC 994.0	994.0			-0.2	-2.31		
413	VC 995.0	995.0	0.707460	1.6E-05	-0.8717	-2.6276		
414	VC 997.0	997.0			-0.548	-2.635		
415	VC 998.0	998.0			-0.128	-1.71		
416	VC 1000.0	1000.0	0.707460	2.0E-05	-0.314	-2.1353		
417	VC 1001.0	1001.0			0.075	-2.142		
418	VC 1002.0	1002.0			0.329	-2.606		
419	VC 1003.0	1003.0			0.317	-3.266		
420	VC 1004.0	1004.0			-0.108	-2.314		
421	VC 1005.0	1005.0			-0.1988	-3.0795		

n	Sample	Stratigraphic height (m)	$^{87}Sr/^{86}Sr$	Error	$\delta^{13}C_{carb}$ (‰PDB)	$\delta^{18}O_{carb}$ (‰PDB)	$\delta^{13}C_{org}$ (‰)	TOC (wt%)
422	VC 1006.0	1006.0			-2.905	-2.313		
423	VC 1007.0	1007.0			0.194	-2.298		
424	VC 1010.0	1010.0	0.707440	2.1E-05	-0.08	-3.1188		
425	VC 1011.0	1011.0			0.295	-2.534		
426	VC 1012.0	1012.0			-0.736	-1.788		
427	VC 1013.0	1013.0			-0.123	-3.281		
428	VC 1014.0	1014.0			-1.301	-3.519		
429	VC 1015.0	1015.0	0.707460	2.0E-05	-0.1161	-2.1778		
430	VC 1016.0	1016.0			-0.578	-2.048		
431	VC 1017.0	1017.0			-0.412	-2.286		
432	VC 1018.0	1018.0			-0.814	-1.63		
433	VC 1019.0	1019.0			-2.658	-2.424		
434	VC 1020.0	1020.0	0.707450	2.1E-05	0.39398	-2.7084		
435	VC 1021.0	1021.0			0.022	-2.524		
436	VC 1022.0	1022.0			-1.382	-2.795		
437	VC 1023.0	1023.0			-3.553	-3.375		
438	VC 1024.0	1024.0			-2.596	-3.253		
439	VC 1025.0	1025.0	0.707490	2.0E-05	1.099	-2.318		
440	VC 1026.0	1026.0			0.683	-2.526		
441	VC 1027.0	1027.0			0.211	-2.267		
442	VC 1028.0	1028.0			-0.133	-2.654		
443	VC 1029.0	1029.0			0.14176	-3.1743		
444	VC 1030.0	1030.0	0.707480	1.9E-05				
445	VC 1075.0	1075.0			1.7078	-5.4128		
446	VC 1080.0	1080.0	0.707450	1.7E-05	2.099	-5.2695		
447	VC 1085.0	1085.0	0.707440	1.7E-05	1.8255	-2.388		
448	VC 1090.0	1090.0	0.707440	2.0E-05	1.8627	-6.1429		
449	VC 1095.0	1095.0	0.707440	2.1E-05	0.15603	-5.1443		
450	VC 1100.0	1100.0	0.707730	2.1E-05	2.3814	-8.3812		
451	VC 1105.0	1105.0	0.707480	2.2E-05	1.8167	-5.9516		
452	VC 1110.0	1110.0			2.345	-3.824		
453	VC 1115.0	1115.0	0.707420	2.1E-05	2.097	-5.545		
454	VC 1120.0	1120.0			2.058	-4.911		
455	VC 1125.0	1125.0			1.677	-4.119		
456	VC 1130.0	1130.0			1.563	-4.068		
457	VC 1135.0	1135.0	0.707520	1.9E-05	1.775	-3.459		
458	VC 1140.0	1140.0			-1.701	-4.676		
459	VC 1145.0	1145.0	0.707430	1.9E-05	0.692	-3.015		
460	VC 1150.0	1150.0	0.707400	2.5E-05	1.063	-1.825		
461	VC 1155.0	1155.0	0.707420	2.7E-05	0.717	-2.511		
462	VC 1165.0	1165.0			1.232	-3.572		
463	VC 1170.0	1170.0			1.255	-3.017		
464	VC 1175.0	1175.0	0.707450	1.0E-05	1.369	-4.001		
465	VC 1180.0	1180.0			1.162	-2.153		
466	VC 1185.0	1185.0	0.707540	2.0E-05	1.686	-3.508		
467	VC 1190.0	1190.0			2.539	-2.575		
468	VC 1195.0	1195.0	0.707460	2.0E-05	1.278	-3.194		

n	Sample	Stratigraphic height (m)	$^{87}Sr/^{86}Sr$	Error	$\delta^{13}C_{carb}$ (‰PDB)	$\delta^{18}O_{carb}$ (‰PDB)	$\delta^{13}C_{org}$ (‰)	TOC (wt%)
469	VC 1200.0	1200.0			1.79	-3.247		
470	VC 1205.0	1205.0	0.707410	1.9E-05	1.753	-3.095		
471	VC 1210.0	1210.0	0.707490	2.1E-05	1.879	-3.304		
472	VC 1215.0	1215.0	0.707450	2.7E-05	0.85	-2.813		
473	VC 1220.0	1220.0	0.707480	2.1E-05	1.077	-4.553		
474	VC 1225.0	1225.0	0.707450	2.0E-05	0.792	-3		
475	VC 1230.0	1230.0	0.707460	2.0E-05	0.072	-4.713		
476	VC 1235.0	1235.0	0.707540	2.1E-05	1.963	-3.701		
477	VC 1240.0	1240.0	0.707420	2.1E-05	-0.0202	-3.17		
478	VC 1245.0	1245.0	0.707430	1.6E-05	2.231	-4.038		
479	VC 1250.0	1250.0	0.707450	1.9E-05	1.71	-3.188		
480	VC 1255.0	1255.0			1.21	-3.635		
481	VC 1260.0	1260.0			1.216	-3.668		
482	VC 1265.0	1265.0	0.707460	1.7E-05	1.949	-2.644		
483	VC 1270.0	1270.0	0.707680	2.8E-05	1.885	-3.675		
484	VC 1275.0	1275.0	0.707490	2.2E-05	2.575	-3.816		
485	VC 1280.0	1280.0	0.707460	1.9E-05	1.623	-2.924		
486	VC 1285.0	1285.0	0.707450	2.1E-05	3.272	-5.031		
487	VC 1290.0	1290.0			3.275	-4.131		
488	VC 1295.0	1295.0	0.707450	2.2E-05	3.04	-4.212		
489	VC 1305.0	1305.0	0.707530	2.0E-05	1.925	-5.24		
490	VC 1310.0	1310.0	0.707440	2.4E-05	2.479	-5.294		
491	VC 1315.0	1315.0	0.707460	2.0E-05	1.989	-4.643		
492	VC 1320.0	1320.0	0.707490	2.0E-05	1.971	-3.856		
493	VC 1325.0	1325.0	0.707350	2.1E-05	1.033	-4.88		
494	VC 1330.0	1330.0			-1.738	-4.38		
495	VC 1335.0	1335.0	0.707440	2.0E-05	-1.115	-3.931		
496	VC 1340.0	1340.0	0.707540	2.4E-05	2.328	-3.995		
497	VC 1345.0	1345.0	0.707520	2.0E-05	2.515	-3.602		
498	VC 1350.0	1350.0	0.707520	2.1E-05	2.282	-4.186		
499	VC 1355.0	1355.0			1.63	-2.072		
500	VC 1360.0	1360.0	0.707530	1.4E-05	1.723	-2.778		
501	VC 1365.0	1365.0	0.707500	1.6E-05	1.818	-2.96		
502	VC 1370.0	1370.0	0.707500	2.1E-05	1.997	-3.227		
503	VC 1375.0	1375.0			2.19	-4.366		
504	VC 1390.0	1390.0	0.707580	2.0E-05	2.169	-3.727		
505	VC 1395.0	1395.0	0.707330	2.1E-05	1.965	-3.258		
506	VC 1400.0	1400.0	0.707650	2.0E-05	0.058	-4.304		
507	VC 1405.0	1405.0			1.698	-2.675		
508	VC 1410.0	1410.0	0.707790	2.0E-05	0.985	-2.268		
509	VC 1415.0	1415.0			2.206	-2.523		
510	VC 1420.0	1420.0			1.471	-2.974		
511	VC 1425.0	1425.0	0.707770	1.1E-05	2.174	-1.168		
512	VC 1430.0	1430.0	0.707770	1.8E-05	2.231	-1.43		
513	VC 1435.0	1435.0	0.707810	2.1E-05	2.363	-2.517		

Appendix Table 4.1: Monte Sorgenza, Campania–Lucania Platform

n	Sample	Stratigraphic depth (m)	$^{87}Sr/^{86}Sr$	Error	$\delta^{13}C_{carb}$ (‰PDB)	$\delta^{18}O_{carb}$ (‰PDB)	$\delta^{13}C_{org}$ (‰)	TOC (wt %)
1	MS 0.0	0.0	0.707340	1.5E-05	1.744	-1.629		
2	MS 2.0	2.0	0.707300	2.0E-05	2.075	-2.3		
3	MS 4.0	4.0	0.707280	2.1E-05	1.465	-2.317		
4	MS 6.0	6.0	0.707360	2.1E-05	1.323	-2.054		
5	MS 8.0	8.0			-0.232	-3.366		
6	MS 12.0	12.0			2.323	-2.791		
7	MS 14.0	14.0	0.707240	2.4E-05	1.287	-2.9		
8	MS 16.0	16.0			1.744	-2.307		
9	MS 18.0	18.0	0.707280	2.1E-05	2.392	-1.886		
10	MS 20.0	20.0	0.707270	2.3E-05	2.37	-2.815		
11	MS 22.0	22.0	0.707310	2.0E-05	1.777	-1.966		
12	MS 24.0	24.0	0.707290	1.3E-05	1.387	-2.217		
13	MS 26.0	26.0	0.707280	1.6E-05	1.354	-2.307		
14	MS 28.0	28.0	0.707280	2.0E-05	1.679	-2.416		
15	MS 30.0	30.0	0.707300	2.0E-05	1.935	-2.051		
16	MS 32.0	32.0	0.707280	1.5E-05	1.429	-2.072		
17	MS 34.0	34.0			2.217	-2.129		
18	MS 36.0	36.0	0.707230	2.0E-05	1.459	-1.684		
19	MS 38.0	38.0	0.707260	2.0E-05	1.355	-2.905		
20	MS 40.0	40.0	0.707250	2.1E-05	0.046	-2.598		
21	MS 42.0	42.0	0.707270	9.8E-06	1.947	-1.721		
22	MS 46.0	46.0	0.707260	1.5E-05	2.285	-1.578		
23	MS 48.0	48.0	0.707260	1.3E-05	2.288	-2.542		
24	MS 50.0	50.0	0.707270	1.9E-05	1.698	-1.352		
25	MS 52.0	52.0	0.707320	2.0E-05	2.478	-0.89		
26	MS 54.0	54.0			2.446	-1.709		
27	MS 56.0	56.0	0.707350	1.6E-05	1.989	-2.555		
28	MS 60.0	60.0	0.707240	2.1E-05	2.504	-1.456		
29	MS 66.0	66.0	0.707230	2.0E-05	2.315	-1.556		
30	MS 68.0	68.0			2.237	-2.12		
31	MS 70.0	70.0	0.707160	2.1E-05	2.496	-1.642		
32	MS 72.0	72.0	0.707300	2.0E-05	2.613	-2.048		
33	MS 74.0	74.0	0.707230	2.2E-05	3.03	-1.723		
34	MS 76.0	76.0			2.899	-1.717		
35	MS 78.0	78.0	0.707190	2.0E-05	2.7	-1.291		
36	MS 80.0	80.0	0.707180	1.5E-05	3.073	-1.548		
37	MS 82.0	82.0	0.707180	2.1E-05	2.568	-1.812		
38	MS 84.0	84.0	0.707260	2.0E-05	1.815	-1.873		
39	MS 86.0	86.0	0.707200	2.1E-05	2.266	-2.021		
40	MS 88.0	88.0	0.707190	2.0E-05	1.753	-2.197		
41	MS 90.0	90.0	0.707310	2.1E-05	1.828	-3.588		
42	MS 92.0	92.0	0.707220	1.9E-05	1.91	-1.981		
43	MS 93.0	93.0	0.707170	1.7E-05	2.028	-1.628		
44	MS 94.0	94.0	0.707270	1.8E-05	1.698	-1.429		
45	MS 95.0	95.0			1.419	-2.261		

n	Sample	Stratigraphic depth (m)	$^{87}Sr/^{86}Sr$	Error	$\delta^{13}C_{carb}$ (‰PDB)	$\delta^{18}O_{carb}$ (‰PDB)	$\delta^{13}C_{org}$ (‰)	TOC (wt %)
46	MS 96.0	96.0	0.707220	2.0E-05	0.391	-2.126		
47	MS 97.0	97.0			1.908	-1.446		
48	MS 98.0	98.0	0.707270	1.6E-05				
49	MS 99.0	99.0			1.193	-8.639		
50	MS 100.0	100.0			2.332	-2.647		
51	MS 101.0	101.0			2.21	-3.108		
52	MS 102.0	102.0	0.707280	2.1E-05	2.544	-1.924		
53	MS 103.0	103.0			2.451	-1.502		
54	MS 104.0	104.0			2.1	-2.334		
55	MS 105.0	105.0			1.97	-2.262		
56	MS 106.0	106.0	0.707260	2.0E-05	2.119	-1.542		
57	MS 107.0	107.0			-0.235	-1.864		
58	MS 108.0	108.0	0.707210	2.1E-05	1.67	-2.2		
59	MS 109.0	109.0			2.602	-1.4		
60	MS 111.0	111.0			2.618	-2.047		
61	MS 112.0	112.0	0.707280	2.1E-05	2.593	-1.91		
62	MS 113.0	113.0			2.157	-1.591		
63	MS 114.0	114.0	0.707330	2.1E-05	2.716	-1.797		
64	MS 115.0	115.0			2.293	-1.578		
65	MS 116.0	116.0	0.707260	2.0E-05	2.267	-1.456		
66	MS 117.0	117.0			2.129	-1.735		
67	MS 118.0	118.0	0.707220	1.6E-05	2.093	-1.476		
68	MS 119.0	119.0			2.07	-1.23		
69	MS 120.0	120.0			2.443	-1.738		
70	MS 121.0	121.0			1.933	-1.973		
71	MS 122.0	122.0	0.707230	2.1E-05	2.452	-1.443		
72	MS 123.0	123.0			1.959	-1.841		
73	MS 124.0	124.0			2.206	-1.391		
74	MS 125.0	125.0			1.855	-1.742		
75	MS 126.0	126.0	0.707230	1.9E-05	2.083	-1.358		
76	MS 127.0	127.0			0.772	-2.209		
77	MS 128.0	128.0	0.707240	1.9E-05	1.451	-1.653		
78	MS 129.0	129.0			1.501	-1.402		
79	MS 130.0	130.0	0.707250	1.6E-05	1.822	-1.246		
80	MS 131.0	131.0			0.037	-2.46		
81	MS 132.0	132.0	0.707280	2.2E-05	1.277	-1.937		
82	MS 134.0	134.0	0.707250	2.0E-05	2.195	-1.489		
83	MS 135.0	135.0			1.132	-1.314		
84	MS 136.0	136.0	0.707220	1.9E-05	1.813	-1.472		
85	MS 140.0	140.0	0.707190	1.7E-05	1.708	-1.871		
86	MS 141.0	141.0			1.113	-2.139		
87	MS 142.0	142.0	0.707200	2.0E-05	2.02	-2.194		
88	MS 143.0	143.0			0.374	-3.228		
89	MS 144.0	144.0	0.707270	3.7E-05	2.255	-1.908		
90	MS 145.0	145.0			2.008	-1.804		
91	MS 146.0	146.0	0.707160	2.1E-05	1.797	-1.52		
92	MS 147.0	147.0			0.815	-2.198		

n	Sample	Stratigraphic depth (m)	$^{87}Sr/^{86}Sr$	Error	$\delta^{13}C_{carb}$ (‰PDB)	$\delta^{18}O_{carb}$ (‰PDB)	$\delta^{13}C_{org}$ (‰)	TOC (wt %)
93	MS 148.0	148.0			0.613	-1.986		
94	MS 151.0	151.0			1.479	-1.395		
95	MS 152.0	152.0	0.707180	1.9E-05	1.85	-1.578		
96	MS 154.0	154.0			-0.026	-1.644		
97	MS 155.0	155.0			1.429	-0.969		
98	MS 156.0	156.0	0.707150	2.0E-05	0.824	-0.978		
99	MS 157.0	157.0			2.201	-1.06		
100	MS 158.0	158.0	0.707140	1.9E-05	2.432	-1.496		
101	MS 160.0	160.0	0.707140	2.1E-05	2.084	-1.203		
102	MS 160.5	160.5			2.695	0.338		
103	MS 161.0	161.0			2.428	-1.441		
104	MS 161.5	161.5			2.691	-0.909		
105	MS 162.0	162.0			2.302	-1.29		
106	MS 162.5	162.5			2.124	-1.146		
107	MS 163.5	163.5			2.249	-1.049		
108	MS 164.0	164.0	0.707200	1.3E-05	2.391	-1.16		
109	MS 164.5	164.5			2.67	0.249		
110	MS 165.0	165.0			2.259	-1.885		
111	MS 165.5	165.5			2.809	0.032		
112	MS 166.0	166.0	0.707150	2.1E-05	2.618	-1.245		
113	MS 166.5	166.5			3.214	-0.455		
114	MS 167.0	167.0			2.137	-3.333		
115	MS 167.5	167.5			3.036	-1.973		
116	MS 168.0	168.0	0.707200	1.9E-05	2.585	-1.233		
117	MS 168.5	168.5			3.052	0.081		
118	MS 169.0	169.0			1.328	-1.469		
119	MS 169.5	169.5			3.046	-1.458		
120	MS 170.0	170.0			2.77	-1.686		
121	MS 170.5	170.5			2.924	-1.145		
122	MS 171.0	171.0			2.616	-1.34		
123	MS 171.5	171.5			2.695	-1.314		
124	MS 172.0	172.0	0.707170	2.1E-05	3.021	-0.982		
125	MS 172.5	172.5			3.614	-1.166		
126	MS 173.0	173.0			3.376	-1.622		
127	MS 173.5	173.5			3.285	-0.415		
128	MS 174.0	174.0	0.707190	2.1E-05	3.044	-1.302		
129	MS 174.5	174.5			3.193	-0.967		
130	MS 175.0	175.0			2.715	-0.852		
131	MS 175.5	175.5			3.089	-0.822		
132	MS 176.0	176.0			2.732	-1.492		
133	MS 176.5	176.5			1.451	-2.834		
134	MS 177.0	177.0			1.628	-2.672		
135	MS 177.5	177.5			2.651	-0.847		
136	MS 178.0	178.0	0.707190	2.2E-05	2.007	-2.155		
137	MS 178.5	178.5			1.59	-1.399		
138	MS 179.0	179.0			0.699	-2.162		
139	MS 179.5	179.5			1.631	-2.243		

n	Sample	Stratigraphic depth (m)	$^{87}Sr/^{86}Sr$	Error	$\delta^{13}C_{carb}$ (‰PDB)	$\delta^{18}O_{carb}$ (‰PDB)	$\delta^{13}C_{org}$ (‰)	TOC (wt %)
140	MS 180.0	180.0	0.707170	2.1E-05	2.36	-0.924		
141	MS 180.5	180.5			2.307	-1.844		
142	MS 181.0	181.0			2.463	-1.602		
143	MS 181.5	181.5			2.778	-1.463		
144	MS 182.0	182.0	0.707200	2.1E-05	2.554	-1.79		
145	MS 182.5	182.5			2.525	-1.665		
146	MS 183.0	183.0			2.402	-1.923		
147	MS 183.5	183.5			1.839	0.768		
148	MS 184.0	184.0	0.707260	2.1E-05	2.546	-1.139		
149	MS 184.5	184.5			2.645	-0.4		
150	MS 185.0	185.0			-1.01	-3.147		
151	MS 185.5	185.5			2.636	-1.083		
152	MS 186.0	186.0	0.707240	1.8E-05	2.581	-1.462		
153	MS 186.5	186.5			-0.371	-2.439		
154	MS 187.0	187.0			-1.309	-3.66		
155	MS 187.5	187.5			0.158	-3.289		
156	MS 188.0	188.0	0.707260	2.1E-05	2.141	-0.99		
157	MS 188.5	188.5			0.872	-2.39		
158	MS 189.0	189.0			-3.606	-2.508		
159	MS 189.5	189.5			0.305	-2.584		
160	MS 190.0	190.0			1.982	-2.157		
161	MS 190.5	190.5			1.669	-0.002		
162	MS 191.0	191.0			0.572	-3.362		
163	MS 191.5	191.5			0.392	-6.103		
164	MS 192.0	192.0	0.707270	2.0E-05	0.388	-4.551		
165	MS 192.5	192.5			2.366	-0.745		
166	MS 193.0	193.0			2.191	-1.738		
167	MS 193.5	193.5			2.439	-0.584		
168	MS 194.5	194.5			2.962	-4.414		
169	MS 195.5	195.5			2.994	-4.181		
170	MS 196.5	196.5			3.401	-1.133		
171	MS 197.0	197.0			3.119	-1.458		
172	MS 197.5	197.5			2.869	-2.119		
173	MS 198.0	198.0	0.707360	1.8E-05	3.117	-1.644		
174	MS 198.5	198.5			3.376	-0.771		
175	MS 199.0	199.0			3.509	-0.909		
176	MS 199.5	199.5			3.871	-0.718		
177	MS 200.0	200.0	0.707320	2.2E-05	2.322	-0.864		
178	MS 200.5	200.5			0.82	-1.285		
179	MS 201.0	201.0			2.62	-2.887		
180	MS 201.5	201.5			4.451	-2.024		
181	MS 202.0	202.0	0.707200	2.1E-05	3.942	-2.124		
182	MS 202.5	202.5			2.732	-2.432		
183	MS 203.0	203.0			3.953	-2.187		
184	MS 203.5	203.5			3.898	-2.103		
185	MS 204.0	204.0	0.707200	2.0E-05	3.812	-2.038		
186	MS 204.5	204.5			3.863	-2.299		

n	Sample	Stratigraphic depth (m)	$^{87}Sr/^{86}Sr$	Error	$\delta^{13}C_{carb}$ (‰PDB)	$\delta^{18}O_{carb}$ (‰PDB)	$\delta^{13}C_{org}$ (‰)	TOC (wt %)
187	MS 205.0	205.0			2.299	-5.238		
188	MS 205.5	205.5			3.846	-1.845		
189	MS 206.0	206.0			2.735	-2.571		
190	MS 206.5	206.5			3.826	-2.475		
191	MS 207.0	207.0			1.833	-3.251		
192	MS 207.5	207.5			3.592	-1.007		
193	MS 208.0	208.0	0.707220	2.1E-05	2.837	-2.071		
194	MS 208.5	208.5			2.324	-2.084		
195	MS 209.0	209.0			2.746	-2.254		
196	MS 209.5	209.5			3.114	-1.009		
197	MS 210.0	210.0			2.417	-2.14		
198	MS 210.5	210.5			2.807	-2.441		
199	MS 211.0	211.0			2.503	-2.49		
200	MS 211.5	211.5			0.774	-1.64		
201	MS 212.0	212.0	0.707180	2.6E-05	3.397	-2.04		
202	MS 212.5	212.5			2.663	-2.182		
203	MS 213.0	213.0			2.659	-5.01		
204	MS 213.5	213.5			3.567	-2.24		
205	MS 214.0	214.0			3.446	-2.044		
206	MS 214.5	214.5			3.283	-1.026		
207	MS 215.0	215.0			3.228	-2.13		
208	MS 215.5	215.5			2.803	-2.474		
209	MS 216.0	216.0			2.966	-2.186		
210	MS 216.5	216.5			3.818	-1.303		
211	MS 217.0	217.0			2.047	-1.984		
212	MS 217.5	217.5			3.464	-1.217		
213	MS 218.0	218.0	0.707230	1.6E-05	3.41	-1.943		
214	MS 218.5	218.5			-0.9	-5.301		
215	MS 219.0	219.0			3.039	-1.995		
216	MS 219.5	219.5			3.438	-1.773		
217	MS 220.0	220.0	0.707270	1.7E-05	2.935	-2.196		
218	MS 221.0	221.0			2.855	-2.138		
219	MS 222.0	222.0			2.969	-1.757		
220	MS 223.0	223.0			3.121	-1.99		
221	MS 224.0	224.0			2.564	-3.061		
222	MS 225.0	225.0			2.201	-2.9		
223	MS 226.0	226.0			2.759	-1.759		
224	MS 227.0	227.0			2.428	-1.714		
225	MS 228.0	228.0	0.707270	2.1E-05	2.509	-2.607		
226	MS 229.0	229.0			2.797	-3.119		
227	MS 230.0	230.0	0.707220	1.7E-05	2.853	-1.838		
228	MS 232.0	232.0	0.707250	1.8E-05	3.014	-2.048		
229	MS 233.0	233.0			2.886	-1.821		
230	MS 234.0	234.0	0.707210	2.1E-05	2.953	-1.907		
231	MS 235.0	235.0			2.724	-2.26		
232	MS 236.0	236.0			2.786	-1.92		
233	MS 237.0	237.0			2.689	-2.509		

n	Sample	Stratigraphic depth (m)	$^{87}Sr/^{86}Sr$	Error	$\delta^{13}C_{carb}$ (‰PDB)	$\delta^{18}O_{carb}$ (‰PDB)	$\delta^{13}C_{org}$ (‰)	TOC (wt %)
234	MS 238.0	238.0			2.8	-1.824		
235	MS 239.0	239.0			2.044	-2.605		
236	MS 240.0	240.0	0.707210	2.1E-05	2.715	-2.165		
237	MS 241.0	241.0			2.722	-1.855		
238	MS 242.0	242.0	0.707230	2.0E-05	2.559	-2.278		
239	MS 243.0	243.0			1.633	-3.812		
240	MS 244.0	244.0			2.601	-2.287		
241	MS 245.0	245.0			1.779	-3.699		
242	MS 246.0	246.0	0.707220	2.6E-05	2.362	-2.191		
243	MS 247.0	247.0			2.168	-2.226		
244	MS 248.0	248.0	0.707230	2.0E-05	2.382	-2.551		
245	MS 249.0	249.0			1.606	-4.412		
246	MS 250.0	250.0	0.707240	2.0E-05	2.52	-2.131		
247	MS 251.0	251.0			1.521	-3.953		
248	MS 252.0	252.0	0.707230	2.2E-05	2.4	-2.173		
249	MS 253.0	253.0			2.623	-2.276		
250	MS 254.0	254.0	0.707270	2.1E-05	2.475	-2.34		
251	MS 255.0	255.0			2.708	-2.077		
252	MS 256.0	256.0	0.707200	2.1E-05	2.546	-2.285		
253	MS 257.0	257.0			2.369	-2.206		
254	MS 258.0	258.0			2.479	-2.332		
255	MS 259.0	259.0			3.336	-0.485		
256	MS 260.0	260.0			2.429	-2.31		
257	MS 260.5	260.5			2.481	-2.238		
258	MS 261.0	261.0			2.434	-2.155		
259	MS 261.5	261.5			2.404	-2.351		
260	MS 262.0	262.0			2.605	-2.182		
261	MS 262.5	262.5			2.622	-2.222		
262	MS 263.0	263.0			2.467	-2.191		
263	MS 263.5	263.5			2.508	-2.765		
264	MS 264.0	264.0			2.019	-2.85		
265	MS 264.5	264.5			2.503	-1.324		
266	MS 265.0	265.0			2.14	-2.247		
267	MS 265.5	265.5			2.067	-2.652		
268	MS 266.5	266.5			1.78	-5.078		
269	MS 267.0	267.0			2.284	-2.644		
270	MS 267.5	267.5			2.283	-2.962		
271	MS 268.0	268.0			2.156	-2.872		
272	MS 268.5	268.5			2.084	-2.869		
273	MS 269.0	269.0			1.976	-3.178		
274	MS 269.5	269.5			2.246	-2.878		
275	MS 270.0	270.0			2.302	-2.42		
276	MS 270.5	270.5			2.311	-2.64		
277	MS 271.5	271.5			2.329	-1.88		
278	MS 272.0	272.0			2.053	-3.226		
279	MS 272.5	272.5			1.629	-3.322		
280	MS 273.0	273.0			1.512	-3.979		

n	Sample	Stratigraphic depth (m)	$^{87}Sr/^{86}Sr$	Error	$\delta^{13}C_{carb}$ (‰PDB)	$\delta^{18}O_{carb}$ (‰PDB)	$\delta^{13}C_{org}$ (‰)	TOC (wt %)
281	MS 273.5	273.5			1.365	-3.693		
282	MS 274.0	274.0			1.027	-3.752		
283	MS 274.5	274.5			1.698	-3.321		
284	MS 275.0	275.0			0.7	-3.928		
285	MS 275.5	275.5			1.363	-3.157		
286	MS 276.0	276.0			1.281	-3.927		
287	MS 276.5	276.5			1.218	-3.626		
288	MS 277.0	277.0			0.991	-3.78		
289	MS 277.5	277.5			0.938	-3.428		
290	MS 278.0	278.0			0.365	-3.646		
291	MS 278.5	278.5			0.201	-3.794		
292	MS 279.0	279.0			-0.421	-4.004		
293	MS 279.5	279.5			0.107	-3.247		
294	MS 280.0	280.0			-2.051	-4.241		
295	MS 280.0	280.0			-1.552	-3.016		
296	MS 280.5	280.5			-1.705	-3.029		
297	MS 281.0	281.0			-0.755	-3.73		
298	MS 281.6	281.6			-3.137	-3.078		
299	MS 282.3	282.3			-0.545	-2.488		
300	MS 283.0	283.0			0.373	-0.795		
301	MS 285.0	285.0			1.419	-1.475		
302	MS 286.0	286.0			0.932	-2.288		
303	MS 286.5	286.5			1.416	-0.786		
304	MS 287.0	287.0			2.123	-0.946		
305	MS 287.5	287.5			1.787	-1.27		
306	MS 288.0	288.0			1.8	-1.172		
307	MS 288.5	288.5			2.218	-0.706		
308	MS 289.0	289.0			2.514	-0.757		
309	MS 289.5	289.5			1.573	-2.115		
310	MS 290.0	290.0			2.043	-1.695		
311	MS 292.0	292.0			2.063	-1.637		
312	MS 293.0	293.0			1.543	-1.319		
313	MS 294.0	294.0			2.475	-0.986		
314	MS 295.0	295.0			2.19	-1.488		
315	MS 296.0	296.0			2.032	-1.159		
316	MS 297.0	297.0			2.283	-1.049		
317	MS 298.0	298.0			1.518	-2.383		
318	MS 299.0	299.0			2.405	-0.92		
319	MS 300.0	300.0			1.719	-1.491		
320	MS 302.0	302.0			1.409	-1.55		
321	MS 306.0	306.0			1.529	-1.374		
322	MS 308.0	308.0			1.292	-1.587		
323	MS 310.0	310.0			0.982	-1.683		
324	MS 312.0	312.0			0.586	-2.426		
325	MS 314.0	314.0			1.783	-0.996		
326	MS 316.0	316.0			0.61	-1.843		
327	MS 318.0	318.0			1.276	-1.631		

n	Sample	Stratigraphic depth (m)	$^{87}Sr/^{86}Sr$	Error	$\delta^{13}C_{carb}$ (‰PDB)	$\delta^{18}O_{carb}$ (‰PDB)	$\delta^{13}C_{org}$ (‰)	TOC (wt %)
328	MS 320.0	320.0			0.955	-1.809		
329	MS 322.0	322.0			1.12	-1.352		
330	MS 324.0	324.0			0.564	-1.839		
331	MS 326.0	326.0			0.998	-1.374		
332	MS 328.0	328.0			1.765	-1.222		
333	MS 330.0	330.0			1.717	-1.422		
334	MS 332.0	332.0			1.716	-1.064		
335	MS 334.0	334.0			1.49	-1.209		
336	MS 336.0	336.0			1.91	-1.067		
337	MS 338.0	338.0			1.067	-1.597		
338	MS 342.0	342.0			2.218	-0.961		
339	MS 344.0	344.0			1.621	-1.018		
340	MS 346.0	346.0			1.671	-0.788		
341	MS 348.0	348.0			1.711	-1.956		
342	MS 350.0	350.0			2.133	-1.321		

Appendix Table 4.2: Raia del Pedale, Campania–Lucania Platform

n	Sample	Stratigrahic depth (m)	$^{87}Sr/^{86}Sr$	Error	$\delta^{13}C_{carb}$ (‰ PDB)	$\delta^{18}O_{carb}$ (‰ PDB)	$\delta^{13}C_{org}$ (‰)	TOC (wt %)
1	RDP 0	0			-0.42	-2.494		
2	RDP 1	1			0.154	-3.337		
3	RDP 2	2			-1.468	-2.749		
4	RDP 3	3			-1.6	-3.66		
5	RDP 4	4			-3.565	-2.799		
6	RDP 5	5			0.155	2.309		
7	RDP 5.2	5.2			-2.38	-2.826		
8	RDP 6	6			0.431	0.979		
9	RDP 7	7			0.853	1.783		
10	RDP 8	8			0.152	1.973		
11	RDP 9	9			-1.211	-0.838		
12	RDP 10	10			0.506	2.553		
13	RDP 11	11			0.201	1.693		
14	RDP 12	12			0.997	1.74		
15	RDP 13	13			-0.583	-0.07		
16	RDP 14	14			-0.409	-3.015		
17	RDP 15	15			-0.696	-2.052		
18	RDP 16	16			0.187	1.322		
19	RDP 16.25	16.25			0.653	0.51		
20	RDP 16.5	16.5			-0.056	-3.062		
21	RDP 16.75	16.75			-0.041	0.211		
22	RDP 17	17			0.942	1.03		
23	RDP 17.25	17.25			-0.63	-0.106		
24	RDP 17.5	17.5			-0.05	1.221		
25	RDP 17.75	17.75			-0.259	0.731		
26	RDP 18	18			-0.676	-3.688		
27	RDP 18.25	18.25			0.111	-2.178		
28	RDP 18.5	18.5			-0.368	-2.74		
29	RDP 18.75	18.75			-0.589	-3.056		
30	RDP 19	19	0.707508	2.00E-05	-0.716	-3.278		
31	RDP 19.25	19.25			-1.048	-2.903		
32	RDP 19.5	19.5			0.099	-2.172		
33	RDP 19.75	19.75			-0.321	-3.2		
34	RDP 20	20			0.311	-3.83		
35	RDP 20.25	20.25			-0.003	-3.295		
36	RDP 20.5	20.5			-0.828	-3.435		
37	RDP 20.75	20.75			-0.809	-2.948		
38	RDP 21	21	0.707481	2.10E-05	0.274	-2.782		
39	RDP 21.25	21.25			0.096	-3.346		
40	RDP 21.75	21.75			-0.724	-4.205		
41	RDP 22	22			0.244	-4.149		

n	Sample	Stratigrahic depth (m)	$^{87}Sr/^{86}Sr$	Error	$\delta^{13}C_{carb}$ (‰ PDB)	$\delta^{18}O_{carb}$ (‰ PDB)	$\delta^{13}C_{org}$ (‰)	TOC (wt %)
42	RDP 22.25	22.25			0.406	-3.639		
43	RDP 22.5	22.5			-1.269	-2.543		
44	RDP 22.75	22.75			0.13	-3.18		
45	RDP 23	23	0.707488	1.60E-05	-0.153	-3.063		
46	RDP 23.25	23.25			0.513	-2.787		
47	RDP 23.5	23.5			1.312	-3.261		
48	RDP 23.75	23.75			0.594	-3.119		
49	RDP 24	24			-0.197	-3.259		
50	RDP 24.25	24.25			0.156	-3.711		
51	RDP 24.5	24.5			0.595	-3.249		
52	RDP 24.75	24.75			0.84	-2.988		
53	RDP 25	25	0.707502	2.00E-05	-0.255	-2.62		
54	RDP 25.25	25.25			0.523	-3.883		
55	RDP 25.75	25.75			0.146	-2.941		
56	RDP 26	26			0.242	-3.821		
57	RDP 26.25	26.25			0.036	-4.448		
58	RDP 26.5	26.5			-0.206	-4.288		
59	RDP 26.75	26.75			-0.292	-3.859		
60	RDP 27	27	0.707559	2.10E-05	1.272	-3.269		
61	RDP 27.25	27.25			1.67	-3.842		
62	RDP 27.5	27.5			2.071	-4.002		
63	RDP 27.75	27.75			2.015	-4.139		
64	RDP 28	28			2.129	-4.046		
65	RDP 28.25	28.25			2.38	-4.104		
66	RDP 28.5	28.5			1.973	-4.529		
67	RDP 28.75	28.75			3.164	-4.075		
68	RDP 29	29			2.634	-4.726		
69	RDP 29.25	29.25			3.163	-4.14		
70	RDP 29.5	29.5			2.463	-4.371		
71	RDP 29.75	29.75			1.771	-4.278		
72	RDP 30	30			1.486	-3.919		
73	RDP 30.5	30.5			3.19	-3.947		
74	RDP 30.75	30.75			2.635	-3.957		
75	RDP 31	31			2.568	-4.204		
76	RDP 31.25	31.25			2.726	-3.975		
77	RDP 31.75	31.75			2.935	-3.992		
78	RDP 32	32			2.667	-4.243		
79	RDP 32.5	32.5			2.641	-4.024		
80	RDP 32.75	32.75			2.285	-4.157		
81	RDP 33	33	0.707426	1.90E-05	2.037	-4.402		
82	RDP 33.5	33.5			2.212	-4.115		
83	RDP 33.75	33.75			2.357	-3.973		
84	RDP 34	34			2.092	-4.289		

n	Sample	Stratigrahic depth (m)	$^{87}Sr/^{86}Sr$	Error	$\delta^{13}C_{carb}$ (‰ PDB)	$\delta^{18}O_{carb}$ (‰ PDB)	$\delta^{13}C_{org}$ (‰)	TOC (wt %)
85	RDP 34.5	34.5			2.124	-4.345		
86	RDP 34.75	34.75			1.874	-4.321		
87	RDP 35	35			1.206	-4.76		
88	RDP 35.25	35.25			1.358	-4.302		
89	RDP 36	36			2.191	-3.891		
90	RDP 36.25	36.25			1.828	-4.303		
91	RDP 36.75	36.75			2.031	-4.125		
92	RDP 37	37	0.707508	1.90E-05	2.022	-4.737		
93	RDP 37.25	37.25			2.591	-4.646		
94	RDP 37.5	37.5			2.589	-4.416		
95	RDP 37.75	37.75			3.424	-4.048		
96	RDP 38	38			2.675	-4.229		
97	RDP 38.25	38.25			2.979	-4.05		
98	RDP 38.5	38.5			2.922	-3.847		
99	RDP 39	39	0.707479	2.00E-05	2.754	-3.789		
100	RDP 39.25	39.25			0.072	-4.869		
101	RDP 39.5	39.5			3.272	-3.596		
102	RDP 39.75	39.75			2.669	-4.473		
103	RDP 40	40			3.336	-3.643		
104	RDP 40.25	40.25			3.136	-4.055		
105	RDP 40.5	40.5			2.718	-4.348		
106	RDP 40.75	40.75			2.953	-4.337		
107	RDP 41	41	0.707447	2.10E-05	2.719	-4.18		
108	RDP 41.25	41.25			3.056	-4.471		
109	RDP 41.5	41.5			2.952	-4.476		
110	RDP 41.75	41.75			3.465	-4.264		
111	RDP 42	42			3.255	-4.587		
112	RDP 42.25	42.25			3.173	-4.919		
113	RDP 42.5	42.5			3.567	-4.37		
114	RDP 42.75	42.75			3.976	-4.264		
115	RDP 43	43	0.707468	1.70E-05	3.421	-4.389		
116	RDP 43.25	43.25			3.251	-4.225		
117	RDP 43.5	43.5			3.267	-4.194		
118	RDP 43.75	43.75			4.149	-4.089		
119	RDP 44	44			3.736	-3.27		
120	RDP 44.25	44.25			3.944	-3.683		
121	RDP 44.5	44.5			4.509	-3.991		
122	RDP 44.75	44.75			3.943	-3.766		
123	RDP 45	45	0.707484	2.00E-05	3.59	-4.601		
124	RDP 45.25	45.25			4.189	-3.888		
125	RDP 45.5	45.5			4.248	-3.98		
126	RDP 45.75	45.75			3.241	-4.072		
127	RDP 46	46			3.667	-3.94		

n	Sample	Stratigrahic depth (m)	$^{87}Sr/^{86}Sr$	Error	$\delta^{13}C_{carb}$ (‰ PDB)	$\delta^{18}O_{carb}$ (‰ PDB)	$\delta^{13}C_{org}$ (‰)	TOC (wt %)
128	RDP 46.25	46.25			3.991	-3.914		
129	RDP 46.5	46.5			3.912	-3.345		
130	RDP 46.75	46.75			4.489	-3.787		
131	RDP 47	47	0.707443	9.00E-06	4.179	-4.062		
132	RDP 47.25	47.25			3.905	-4.251		
133	RDP 47.5	47.5			3.298	-4.384		
134	RDP 47.75	47.75			2.695	-4.016		
135	RDP 48	48	0.707447	1.80E-05	3.033	-3.893		
136	RDP 48.25	48.25			3.809	-2.794		
137	RDP 48.5	48.5			4.496	-2.816		
138	RDP 48.75	48.75			3.766	-2.675		
139	RDP 49	49	0.707467	2.30E-05	3.837	-4.148		
140	RDP 49.25	49.25			4.443	-3.316		
141	RDP 49.5	49.5			4.341	-4.103		
142	RDP 49.75	49.75			4.647	-2.362		
143	RDP 50	50	0.707427	1.70E-05	4.545	-3.89		
144	RDP 50.25	50.25			4.343	-3.794		
145	RDP 50.5	50.5			4.543	-3.476		
146	RDP 50.75	50.75			4.464	-3.788		
147	RDP 51	51			4.016	-4.476		
148	RDP 51.25	51.25			2.803	-3.898		
149	RDP 51.5	51.5			4.005	-3.79		
150	RDP 51.65	51.65			3.313	-3.081		
151	RDP 51.75	51.75			3.921	-3.509		
152	RDP 52	52	0.707317	1.70E-05	3.604	-3.475		
153	RDP 52.2	52.2			1.685	1.028		
154	RDP 52.25	52.25			2.353	-3.16		
155	RDP 52.5	52.5			3.742	-3.171		
156	RDP 52.75	52.75			3.825	-3.34		
157	RDP 53	53			3.747	-3.892		
158	RDP 53.25	53.25			4.83	-3.802		
159	RDP 53.5	53.5			4.693	-4.098		
160	RDP 53.75	53.75			4.855	-3.666		
161	RDP 54	54	0.707429	2.10E-05	3.069	-2.73		
162	RDP 54.25	54.25			3.434	-4.966		
163	RDP 54.5	54.5			3.795	-3.999		
164	RDP 54.75	54.75			3.706	-4.713		
165	RDP 55	55	0.707421	1.40E-05	2.959	-4.305	-21.09	
166	RDP 55.25	55.25			3.683	-3.644		
167	RDP 55.5	55.5			2.928	-3.483		
168	RDP 55.75	55.75			2.44	-3.829		
169	RDP 56	56			3.837	-3.896		
170	RDP 56.25	56.25			4.856	-4.184		

n	Sample	Stratigrahic depth (m)	$^{87}Sr/^{86}Sr$	Error	$\delta^{13}C_{carb}$ (‰ PDB)	$\delta^{18}O_{carb}$ (‰ PDB)	$\delta^{13}C_{org}$ (‰)	TOC (wt %)
171	RDP 56.5	56.5			1.917	-3.089		
172	RDP 56.75	56.75			2.953	-3.539		
173	RDP 57	57			4.217	-4.734		
174	RDP 57.25	57.25			3.583	-3.646		
175	RDP 57.5	57.5			3.117	-3.52		
176	RDP 57.75	57.75			3.713	-3.598		
177	RDP 58	58	0.707429	2.00E-05	3.487	-3.499		
178	RDP 58.25	58.25			2.992	-3.899		
179	RDP 58.5	58.5			3.291	-3.042		
180	RDP 58.75	58.75			1.701	-2.81		
181	RDP 59	59	0.707445	2.00E-05	3.276	-4.057		
182	RDP 59.25	59.25			3.934	-2.961		
183	RDP 59.5	59.5			3.41	-3.407		
184	RDP 59.75	59.75			3.621	-4.09		
185	RDP 60	60	0.707523	1.50E-05	3.303	-4.029		
186	RDP 60.25	60.25			3.288	-3.776		
187	RDP 60.5	60.5			3.308	-3.902		
188	RDP 60.75	60.75			3.892	-3.796		
189	RDP 61	61	0.707406	2.10E-05	3.201	-3.708		
190	RDP 61.25	61.25			2.946	-3.676		
191	RDP 61.5	61.5			1.949	-3.864		
192	RDP 61.75	61.75			1.917	-3.706		
193	RDP 62	62			3.019	-4.521		
194	RDP 62.25	62.25			2.075	-3.678		
195	RDP 62.5	62.5			2.414	-3.282		
196	RDP 62.75	62.75			1.94	-3.982		
197	RDP 63	63			2.24	-2.463		
198	RDP 63.25	63.25			2.438	-3.596		
199	RDP 63.5	63.5			2.133	-3.992		
200	RDP 63.75	63.75			1.445	-3.15		
201	RDP 64	64			1.366	-3.844		
202	RDP 64.25	64.25			0.889	-3.994		
203	RDP 64.5	64.5			0.725	-4.179		
204	RDP 64.75	64.75			0.551	-4.301		
205	RDP 65	65			0.502	-4.874		
206	RDP 65.25	65.25			0.719	-4.213		
207	RDP 65.5	65.5			0.634	-3.551		
208	RDP 65.75	65.75			1.848	-4.101		
209	RDP 66	66	0.707437	2.10E-05	1.504	-3.428	-23.37	
210	RDP 66.25	66.25			1.831	-3.578		
211	RDP 66.5	66.5			1.993	-3.972		
212	RDP 66.75	66.75			1.794	-3.224		
213	RDP 67	67			2.432	-3.565		

n	Sample	Stratigrahic depth (m)	$^{87}Sr/^{86}Sr$	Error	$\delta^{13}C_{carb}$ (‰ PDB)	$\delta^{18}O_{carb}$ (‰ PDB)	$\delta^{13}C_{org}$ (‰)	TOC (wt %)
214	RDP 67.25	67.25			2.488	-3.708		
215	RDP 67.5	67.5			2.978	-3.564		
216	RDP 67.75	67.75			2.693	-4.145		
217	RDP 68	68	0.707425	2.20E-05	2.366	-4.004		
218	RDP 68.25	68.25			1.323	-3.58		
219	RDP 68.5	68.5			2.497	-3.636		
220	RDP 68.75	68.75			2.589	-3.388		
221	RDP 69	69			2.201	-2.751		
222	RDP 69.25	69.25			1.962	-3.299		
223	RDP 69.5	69.5			1.942	-3.368		
224	RDP 69.75	69.75			1.922	-3.449		
225	RDP 70	70	0.707435	2.00E-05	1.394	-3.752		
226	RDP 70.25	70.25			0.974	-3.139		
227	RDP 70.5	70.5			0.025	-2.942		
228	RDP 70.75	70.75			1.535	-2.35		
229	RDP 71	71			0.94	-3.312		
230	RDP 71.25	71.25			1.193	-3.183		
231	RDP 71.3	71.3			0.47	-3.427		
232	RDP 71.75	71.75			0.018	-4.064		
233	RDP 72	72	0.707448	2.10E-05	-0.725	-4.493		
234	RDP 72.25	72.25			-0.827	-4.271		
235	RDP 72.5	72.5			-1.023	-4.131		
236	RDP 73	73			3.422	0.977		
237	RDP 73.5	73.5			-1.583	-4.361		
238	RDP 73.5	73.5			1.789	-3.314		
239	RDP 73.75	73.75			0.767	-3.365		
240	RDP 74	74	0.707449	2.20E-05	-0.953	-3.616		
241	RDP 74.25	74.25			-3.372	-3.836		
242	RDP 74.5	74.5			-3.591	-3.861		
243	RDP 74.75	74.75			-3.239	-3.666		
244	RDP 75	75			0.028	-2.237		
245	RDP 75.25	75.25			-3.001	-3.669		
246	RDP 75.5	75.5			2.18	-3.436		
247	RDP 75.75	75.75			1.822	-2.778		
248	RDP 76	76	0.707412	2.10E-05	-0.426	-3.158		
249	RDP 76.25	76.25			-1.811	-3.545		
250	RDP 76.5	76.5			-3.122	-3.441		
251	RDP 76.75	76.75			-1.824	-2.837		
252	RDP 77	77			-1.36	-3.455		
253	RDP 77.25	77.25			-0.752	-2.572		
254	RDP 77.5	77.5			-0.327	-3.09		
255	RDP 77.75	77.75			-1.07	-2.889		
256	RDP 78.25	78.25			-0.764	-2.743		

n	Sample	Stratigrahic depth (m)	$^{87}Sr/^{86}Sr$	Error	$\delta^{13}C_{carb}$ (‰ PDB)	$\delta^{18}O_{carb}$ (‰ PDB)	$\delta^{13}C_{org}$ (‰)	TOC (wt %)
257	RDP 78.5	78.5			-0.963	-3.054		
258	RDP 78.75	78.75			0.529	-2.897		
259	RDP 79	79			-0.74	-3.371		
260	RDP 79.25	79.25			-0.657	-3.382		
261	RDP 79.5	79.5			-0.593	-2.811		
262	RDP 79.75	79.75			-0.746	-3.3		
263	RDP 80	80	0.707464	2.20E-05	-0.291	-2.78		
264	RDP 80.25	80.25			-0.54	-3.11		
265	RDP 80.5	80.5			-0.308	-3.017		
266	RDP 80.75	80.75			-0.613	-2.943		
267	RDP 81	81			-2.168	-8.113		
268	RDP 81.25	81.25			0.725	-3.039		
269	RDP 81.75	81.75			-0.1	-2.974		
270	RDP 82	82			-1.699	-7.507		
271	RDP 82.25	82.25			-0.397	-3.407		
272	RDP 82.5	82.5			-0.777	-3.158		
273	RDP 82.75	82.75			0.985	-2.98		
274	RDP 84.75	84.75			-0.552	-3.004		
275	RDP 85	85			-1.01	-3.803		
276	RDP 85.25	85.25			-3.522	-2.981		
277	RDP 85.5	85.5			-3.061	-2.716		
278	RDP 85.75	85.75			1.473	-3.368		
279	RDP 86	86			0.574	-5.795		
280	RDP 87	87			-1.267	-7.98		
281	RDP 88	88	0.70736	1.70E-5	-0.695	-7.856		
282	RDP 89	89			-2.109	-7.767		
283	RDP 90	90			-0.779	-5.187		
284	RDP 91	91			0.503	-2.997		
285	RDP 91.4	91.4			-0.812	-6.128		
286	RDP 91.5	91.5			0.209	-3.467		
287	RDP 92	92			0.536	-3.255		
288	RDP 93	93			3.1959	-2.4191		
289	RDP 95	95			1.8443	-2.8587		
290	RDP 96	96			-1.425	-5.158		
291	RDP 97	97			0.039	-2.751		
292	RDP 98	98			-3.045	-6.768		
293	RDP 99	99			0.22544	-4.554		
294	RDP 101	101			0.904	-2.892		
295	RDP 102	102			0.36	-4.599		
296	RDP 103	103			1.004	-3.229		
297	RDP 104	104			1.079	-2.43		
298	RDP 105	105			0.759	-2.918		
299	RDP 106	106	0.707391	2.10E-05	0.96949	-4.015		

n	Sample	Stratigrahic depth (m)	$^{87}Sr/^{86}Sr$	Error	$\delta^{13}C_{carb}$ (‰ PDB)	$\delta^{18}O_{carb}$ (‰ PDB)	$\delta^{13}C_{org}$ (‰)	TOC (wt %)
300	RDP 108	108	0.707391	2.10E-05	1.0189	-3.5507		
301	RDP 109	109			-0.224	-3.191		
302	RDP 110	110			0.743	-3.212		
303	RDP 111	111			1.071	-2.647		
304	RDP 112	112	0.707466	2.10E-05	2.7584	-2.1409		
305	RDP 113	113			1.307	-2.935		
306	RDP 114	114			0.38	-3.69		
307	RDP 115	115			-0.456	-4.243		
308	RDP 116	116			0.544	-3.079		
309	RDP 117	117			1.48	-3.356		
310	RDP 118	118	0.70739	1.90E-05	1.092	-3.444		
311	RDP 119	119			0.386	-2.921		
312	RDP 120	120			1.523	-2.816		
313	RDP 121	121			0.127	-3.519		
314	RDP 122	122			1.147	-2.875		
315	RDP 123	123			-1.167	-4.26		
316	RDP 124	124	0.70738	2.10E-05	1.449	-3.061		
317	RDP 125	125			2.017	-2.971		
318	RDP 126	126			3.882	-2.279		
319	RDP 127	127			-1.675	-3.413		
320	RDP 128	128			1.592	-3.211		
321	RDP 129	129			2.633	-3.576		
322	RDP 130	130			2.225	-2.13		
323	RDP 131	131			-2.762	-4.02		
324	RDP 132	132	0.707387	1.90E-05	1.8019	-3.4993		
325	RDP 133	133			1.959	-3.469		
326	RDP 134	134			1.2421	-2.4781		
327	RDP 135	135			-2.878	-4.642		
328	RDP 136	136	0.707365	2.10E-05	1.473	-2.624		
329	RDP 137	137			2.084	-2.94		
330	RDP 138	138			1.579	-2.933		
331	RDP 139	139			2.484	-3.021		
332	RDP 140	140			0.325	-5.71		
333	RDP 141	141			-0.46	-3.252		
334	RDP 142	142	0.707357	2.00E-05	0.616	-3.237	-23.68	
335	RDP 143	143			1.486	-2.913		
336	RDP 144	144			1.0666	-3.4136		
337	RDP 145	145			1.926	-2.531		
338	RDP 146	146			0.549	-3.284		
339	RDP 147	147			2.034	-3.324		
340	RDP 148	148	0.707357	2.00E-05	1.373	-3.317	-22.76	
341	RDP 149	149			1.103	-3.043		
342	RDP 150	150	0.707378	2.10E-05	0.61167	-3.4097	-21.65	

n	Sample	Stratigrahic depth (m)	$^{87}Sr/^{86}Sr$	Error	$\delta^{13}C_{carb}$ (‰ PDB)	$\delta^{18}O_{carb}$ (‰ PDB)	$\delta^{13}C_{org}$ (‰)	TOC (wt %)
343	RDP 151	151			0.681	-2.65		
344	RDP 152	152			2.12	-5.45		
345	RDP 153	153			1.552	-3.036		
346	RDP 154	154			1.193	-2.897		
347	RDP 155	155			0.787	-2.842		
348	RDP 156	156			1.042	-2.761		
349	RDP 157	157			-1.799	-4.517		
350	RDP 158	158			1.937	-2.771		
351	RDP 159	159			0.937	-3.304		
352	RDP 160	160			1.167	-3.234		
353	RDP 161	161			0.152	-3.989		
354	RDP 162	162			1.592	-2.098		
355	RDP 163	163			0.252	-2.838		
356	RDP 164	164			1.473	-2.61		
357	RDP 165	165			1.223	-3.184		
358	RDP 166	166	0.707359	2.00E-05	0.801	-3.21		
359	RDP 167	167			0.296	-2.984		
360	RDP 168	168			1.608	-2.997		
361	RDP 169	169			0.155	-3.869		
362	RDP 170	170	0.70741	1.60E-05	3.0925	-2.6111		
363	RDP 171	171			-3.137	-4.56		
364	RDP 172	172			1.0828	-3.2936		
365	RDP 173	173			1.048	-3.655		
366	RDP 174	174			1.4909	-3.6177		
367	RDP 175	175			-3.063	-3.977		
368	RDP 176	176	0.707323	2.10E-05	0.784	-4.382		
369	RDP 177	177			-2.632	-3.584		
370	RDP 178	178			2.059	-2.703		
371	RDP 179	179			-0.617	-3.891		
372	RDP 180	180			2.228	-3.234		
373	RDP 180.6	180.6			1.019	-3.299		
374	RDP 181	181	0.707377	2.10E-05	1.446	-2.975		
375	RDP 182	182			2.799	-3.081		
376	RDP 183	183			0.568	-2.351		
377	RDP 184	184			1.4794	-3.6247		
378	RDP 185	185			0.884	-3.164		
379	RDP 187	187			2.981	-3.222		
380	RDP 189	189	0.707358	.210E-05	1.915	-2.925		
381	RDP 190	190			2.056	-2.542		
382	RDP 191	191			3.003	-2.988		
383	RDP 192	192			2.5814	-5.4639		
384	RDP 193	193			2.038	-3.357		
385	RDP 194	194			2.807	-3.511		

n	Sample	Stratigrahic depth (m)	$^{87}Sr/^{86}Sr$	Error	$\delta^{13}C_{carb}$ (‰ PDB)	$\delta^{18}O_{carb}$ (‰ PDB)	$\delta^{13}C_{org}$ (‰)	TOC (wt %)
386	RDP 195	195			2.352	-3.031		
387	RDP 196	196			1.986	-3.052		
388	RDP 197	197			2.529	-2.865		
389	RDP 198	198			1.936	-2.574		
390	RDP 199	199	0.707377	1.90E-05	0.496	-2.298		
391	RDP 200	200			2.0954	-3.2757		
392	RDP 201	201	0.707304	3.20E-05	2.407	-3.158		
393	RDP 203	203			1.748	-4.342		
394	RDP 204	204			1.1086	-4.655		
395	RDP 205	205	0.707329	2.10E-05	-2.201	-3.69		
396	RDP 206	206			2.82	-3.32		
397	RDP 207	207			2.517	-4.01		
398	RDP 208	208			2.7314	-3.267		
399	RDP 209	209			2.833	-3.916		
400	RDP 210	210			0.975	-3.275		
401	RDP 211	211			-0.568	-4.287		
402	RDP 212	212			0.818	-3.45		
403	RDP 213	213			-0.014	-2.648		
404	RDP 214	214			0.553	-1.959		
405	RDP 215	215			3.011	-3.318		
406	RDP 216	216			1.343	-3.286		
407	RDP 217	217	0.707409	2.50E-05	-1.305	-4.315		
408	RDP 218	218			0.643	-2.59		
409	RDP 219	219			0.989	-2.441		
410	RDP 220	220			2.1876	-3.1918		
411	RDP 221	221			1.465	-3.796		
412	RDP 222	222			0.817	-3.379		
413	RDP 223	223	0.707416	2.10E-05	1.187	-3.066		
414	RDP 224	224			2.395	-3.095		
415	RDP 225	225			3.032	-4.13		
416	RDP 226	226			1.5731	-3.0483		
417	RDP 227	227			2.832	-3.173		
418	RDP 228	228			0.691	-2.931		
419	RDP 229	229			-0.994	-4.645		
420	RDP 230	230			1.3097	-3.4051		
421	RDP 231	231			2.293	-3.292		
422	RDP 232	232			1.199	-4.517		
423	RDP 233	233	0.707378	2.10E-05	0.195	-3.194		
424	RDP 235	235			0.816	-3.804		
425	RDP 236	236			0.406	-4.431		
426	RDP 237	237	0.707358	2.00E-05	2.872	-3.989		
427	RDP 238	238			0.09	-4.045		
428	RDP 239	239			0.239	-4.115		

n	Sample	Stratigrahic depth (m)	$^{87}Sr/^{86}Sr$	Error	$\delta^{13}C_{carb}$ (‰ PDB)	$\delta^{18}O_{carb}$ (‰ PDB)	$\delta^{13}C_{org}$ (‰)	TOC (wt %)
429	RDP 240	240			1.097	-3.222		
430	RDP 241	241			0.237	-4.391		
431	RDP 242	242			-0.618	-4.458		
432	RDP 243	243			-0.662	-3.713		
433	RDP 244	244			-0.561	-3.626		
434	RDP 245	245	0.707392	3.20E-05	1.848	-2.345		
435	RDP 246	246			0.708	-3.651		
436	RDP 247	247			1.711	-3.193		
437	RDP 248	248			-0.074	-3.698		
438	RDP 249	249	0.707441	2.10E-05	1.367	-3.185		
439	RDP 251	251			0.735	-3.74		
440	RDP 252	252			-1.193	-3.995		
441	RDP 253	253	0.707411	2.60E-05	1.931	-3.56		
442	RDP 254	254			2.228	-3.136		
443	RDP 255	255			2.117	-3.266		
444	RDP 256	256			-0.842	-5.279		
445	RDP 257	257			1.265	-3.76		
446	RDP 258	258			-0.59294	-3.6834		
447	RDP 259	259	0.707514	2.20E-05	1.68	-3.367		
448	RDP 260	260			-1.3349	-3.8741		
449	RDP 261	261	0.707457	1.30E-05	0.892	-2.409		
450	RDP 262	262			-2.656	-3.562		
451	RDP 263	263			-2.511	-3.36		
452	RDP 264	264			-2.113	-4.514		
453	RDP 265	265	0.707482	2.10E-05	1.277	-3.349		
454	RDP 266	266			-2.206	-4.414		
455	RDP 267	267			-2.496	-4.075		
456	RDP 268	268			-1.945	-3.7957		
457	RDP 269	269	0.707456	2.00E-05	-2.304	-4.227		
458	RDP 270	270			-1.22	-3.92		
459	RDP 271	271	0.707580	1.30E-05	1.85	-3.413		
460	RDP 272	272			-2.532	-4.332		
461	RDP 273	273			-3.357	-4.086		
462	RDP 274	274			-3.175	-3.792		
463	RDP 275	275			-2.501	-3.064		
464	RDP 276	276			-3.147	-3.894		
465	RDP 277	277			-2.88	-4.361		
466	RDP 278	278			-3.544	-3.726		
467	RDP 279	279			-3.586	-4.059		
468	RDP 280	280			-1.7568	-3.1414		
469	RDP 281	281			-2.769	-2.854		
470	RDP 282	282			-1.839	-3.616		
471	RDP 283	283			-2.902	-4.66		

n	Sample	Stratigrahic depth (m)	$^{87}Sr/^{86}Sr$	Error	$\delta^{13}C_{carb}$ (‰ PDB)	$\delta^{18}O_{carb}$ (‰ PDB)	$\delta^{13}C_{org}$ (‰)	TOC (wt %)
472	RDP 284	284			-2.662	-3.782		
473	RDP 285	285			-2.323	-3.844		
474	RDP 286	286			-0.671	-2.798		
475	RDP 287	287	0.707508	2.20E-05	-3.418	-3.019		
476	RDP 288	288			-1.103	-2.629		
477	RDP 289	289			-2.826	-4.533		
478	RDP 290	290			-2.6066	-4.0586		
479	RDP 291	291			-2.568	-3.426		
480	RDP 292	292			-0.99533	-3.3703		
481	RDP 293	293	0.707500	2.20E-05	1.498	-3.994		
482	RDP 294	294			-0.787	-2.728		
483	RDP 295	295			-2.537	-3.12		
484	RDP 297	297			-2.38	-3.983		
485	RDP 298	298			1.153	-2.886		
486	RDP 299	299			-3.31	-3.516		
487	RDP 300	300			-0.875	-3.826		
488	RDP 301	301	0.707432	2.40E-05	1.206	-2.555		
489	RDP 302	302			-3.5219	-3.7614		
490	RDP 303	303	0.707538	2.10E-05	1.221	-2.739		
491	RDP 304	304			-1.452	-3.534		
492	RDP 305	305			-2.62	-4.417		
493	RDP 306	306			-2.517	-3.968		
494	RDP 307	307			-2.546	-3.344		
495	RDP 308	308			-1.712	-2.964		
496	RDP 309	309			-1.981	-2.63		
497	RDP 310	310			-2.583	-2.855		
498	RDP 311	311			-2.474	-3.011		
499	RDP 312	312			-2.683	-3.894		
500	RDP 313	313			-2.372	-3.571		
501	RDP 314	314			-1.948	-3.527		
502	RDP 315	315			-1.674	-3.737		
503	RDP 316	316			-2.616	-2.587		
504	RDP 317	317	0.707653	2.00E-05	-2.859	-3.609		
505	RDP 318	318			-2.721	-3.743		

A3: Atlas of photomicrographs

A3.2: Trento photomicrographs

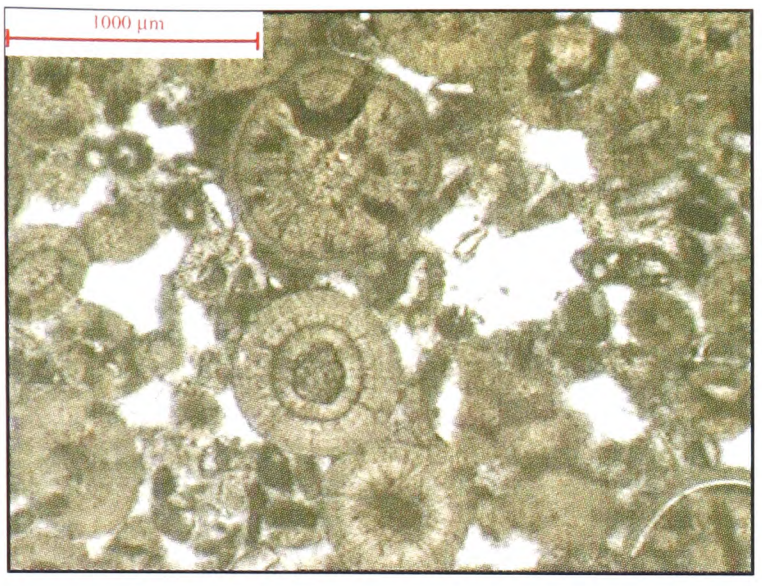

Plate A3.2.i. MDC-0.43 (PPL): Oosparite. Radial calcitic oiids with micritic traces of borings by cyanobacteria. Occasional peloids and bioclastic debris (esp. echinodermal) set in a sparry-calcite cement.

Plate A3.2.ii. MDC-52 (PPL): Biosparite. Assorted bioclasts, including echinoderm plates (echinoid plate with ambulacra shown here), echinoid spines, gastrpods (shown), benthic foraminifera and bivalve shells, and local ooids and peloids set in a sparry-calcite cement.

Plate A3.2.iii. MDC-98 (PPL): Oosparite. Radial calcitic oiids and superficial ooids, locally partially micritised. Occasional peloids and bioclastic debris (esp. echinodermal) set in a sparry-calcite cement (rim and void-filling).

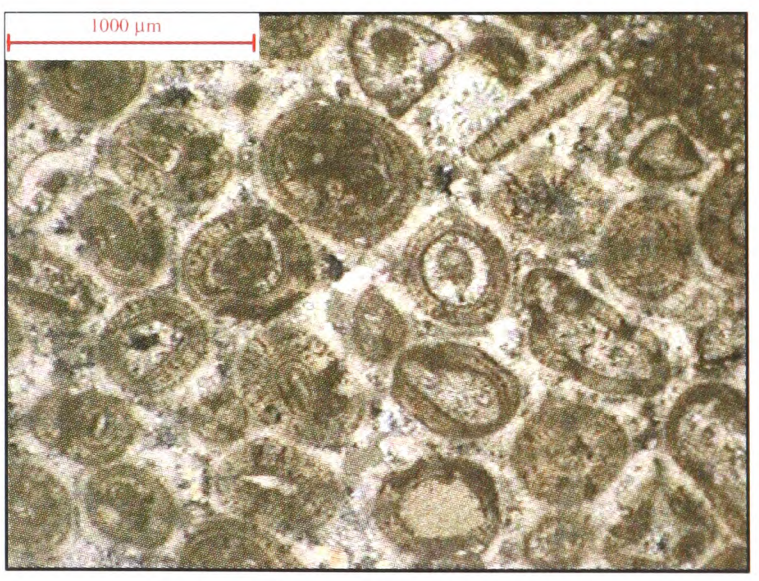

Plate A3.2.iv. MDC-98 (XPL): Oosparite. Radial calcitic oiids and superficial ooids, locally partially micritised. Occasional peloids and bioclastic debris (esp. echinodermal) set in a sparry-calcite cement (rim and void-filling).

Plate A3.2.v. MDC-130 (PPL): Silicified oosparite (chert nodule). Primary radial calcite ooids in sparry-calcite cement are virtually completely silicified in this chert nodule. There are no indications of a Si-source.

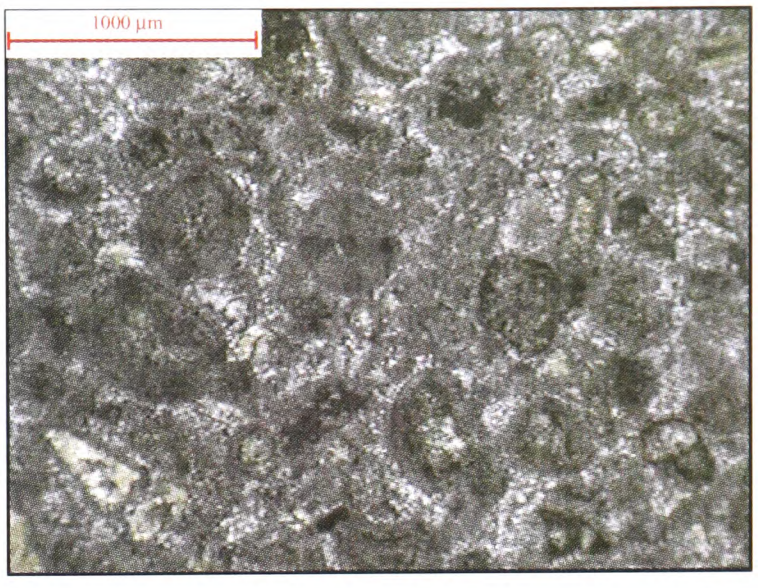

Plate A3.2.vi. MDC-130 (XPL): Silicified oosparite (chert nodule). Primary radial calcite ooids in sparry-calcite cement are virtually completely silicified in this chert nodule. There are no indications of a Si-source.

Plate A3.2.vii. MDC-168 (PPL): Pelmicrite. Peloids and bioclastic debris (echinoderm plates, echinoid spines and bivalves) in a micritic matrix. Partial silicification is locally apparent (here within an echinoderm plate).

Plate A3.2.viii. MDC-168 (XPL): Pelmicrite. Peloids and bioclastic debris (echinoderm plates, echinoid spines and bivalves) in a micritic matrix. Partial silicification is locally apparent (here within an echinoderm plate).

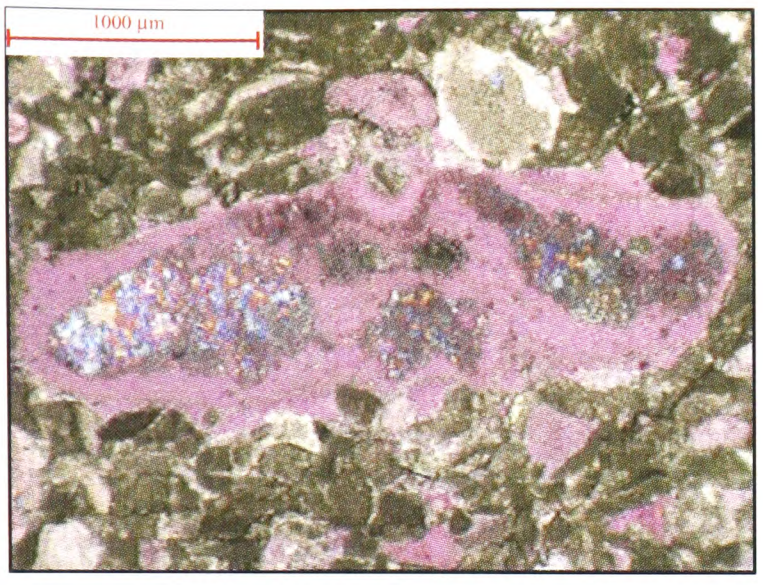

Plate A3.2.ix. MDC-168 (XPL & Tint): Pelmicrite. Peloids and bioclastic debris (echinoderm plates, echinoid spines and bivalves) in a micritic matrix. Partial silicification is locally apparent (here within an echinoderm plate).

Plate A3.2.x. MDC-198 (XPL): Pelmicrite. Predominantly peloid-based clasts, but with assorted benthic foraminifera, bivalve shells and echinoderm skeletal debris (shown here partly silicified), set in a micritic matrix.

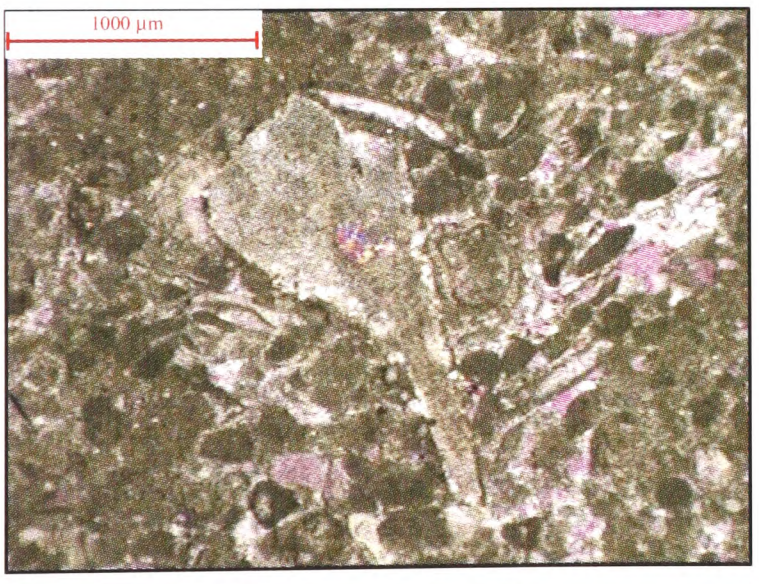

Plate A3.2.xi. MDC-198 (XPL & Tint): Pelmicrite. Predominantly peloid-based clasts, but with assorted benthic foraminifera, bivalve shells and echinoderm skeletal debris (shown here partly silicified), set in a micritic matrix.

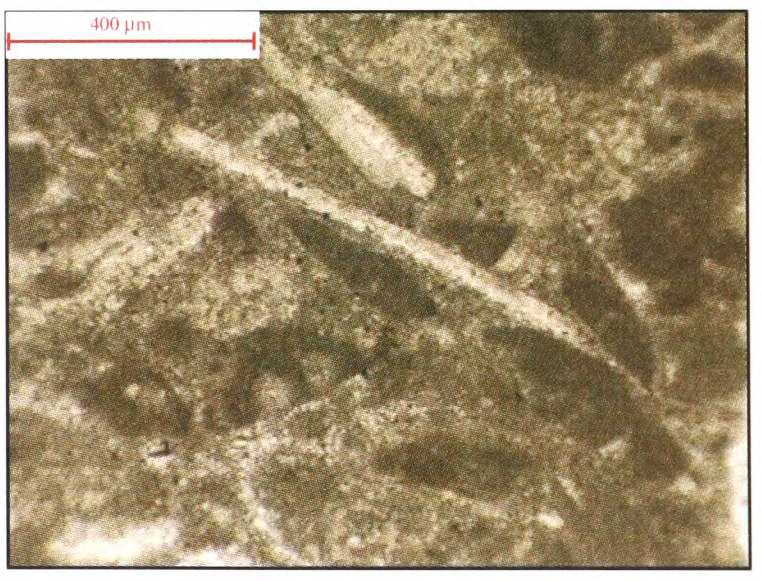

Plate A3.2.xii. MDC-202 (PPL): Pelmicrite. Detail of a sponge spicule (silicic) set within a micritic matrix. Otherwise, petrographically similar to MDC-198.

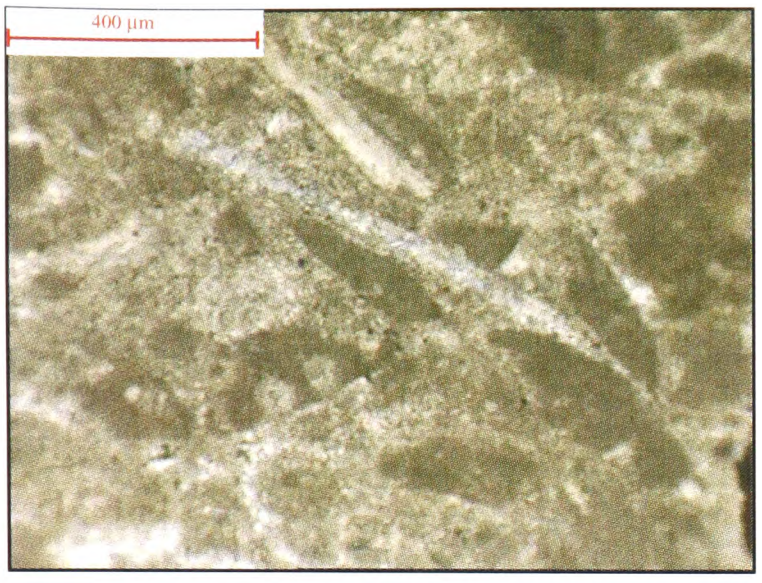

Plate A3.2.xiii. MDC-202 (XPL): Pelmicrite. Detail of a sponge spicule (silicic) set within a micritic matrix. Otherwise, petrographically similar to MDC-198.

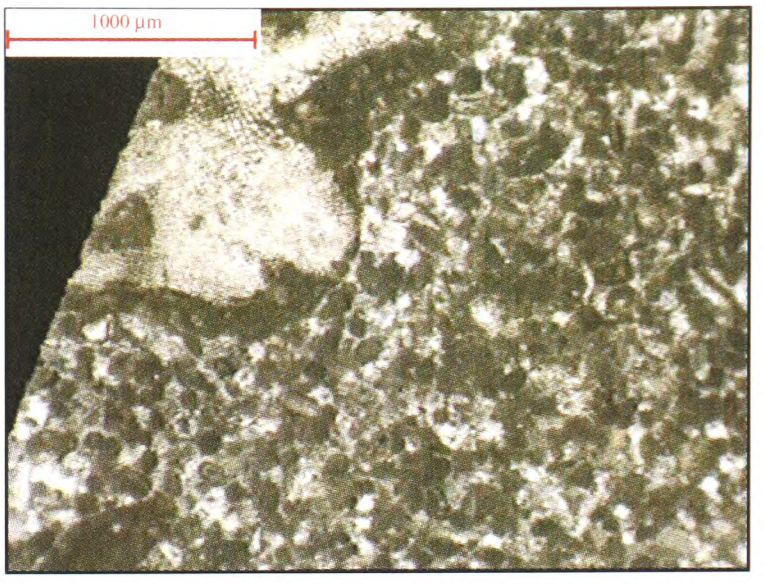

Plate A3.2.xiv. MDC-252 (XPL): Pelsparrite. Rich in peloids with local intraclasts, echinodermal debris (shown here with minor silica replacement) and bivalve shells.

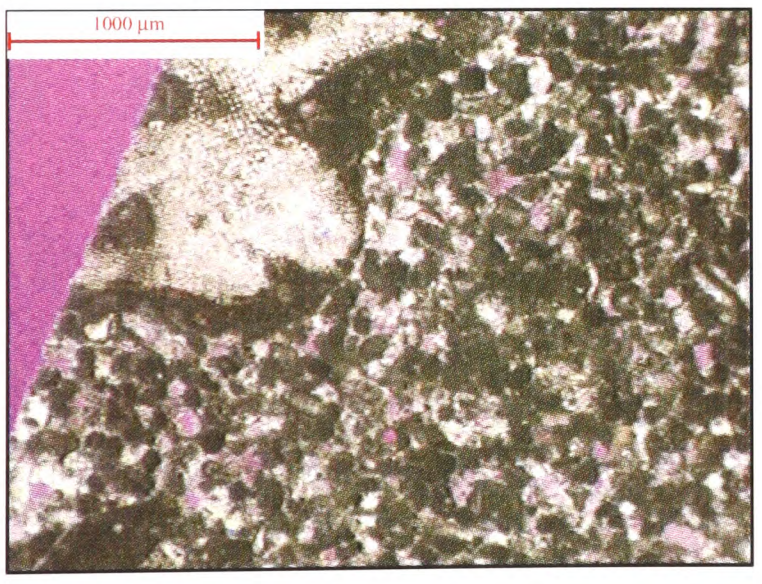

Plate A3.2.xv. MDC-252 (XPL & Tint): Pelsparrite. Rich in peloids with local intraclasts, echinodermal debris (shown here with minor silica replacement) and bivalve shells.

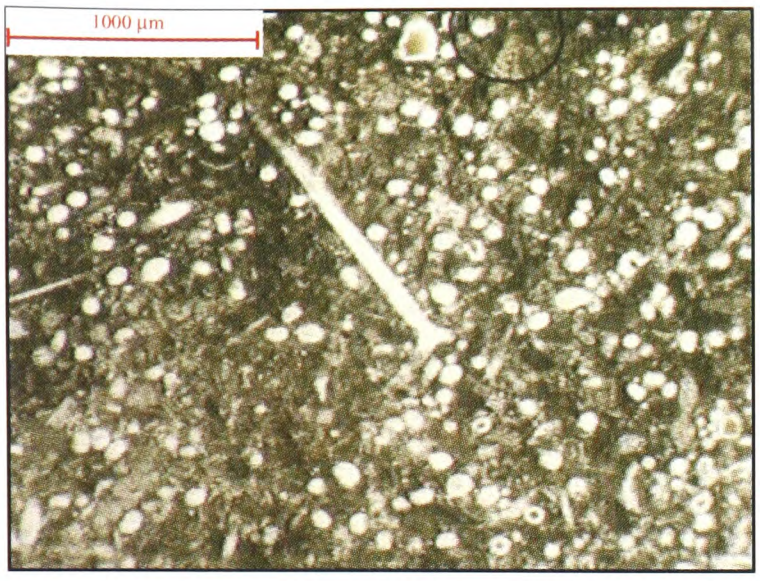

Plate A3.2.xvi. PV-20 (PPL): Biomicrite. Sponge spicules are the only bioclastic constituent of this spiculitic chert nodule.

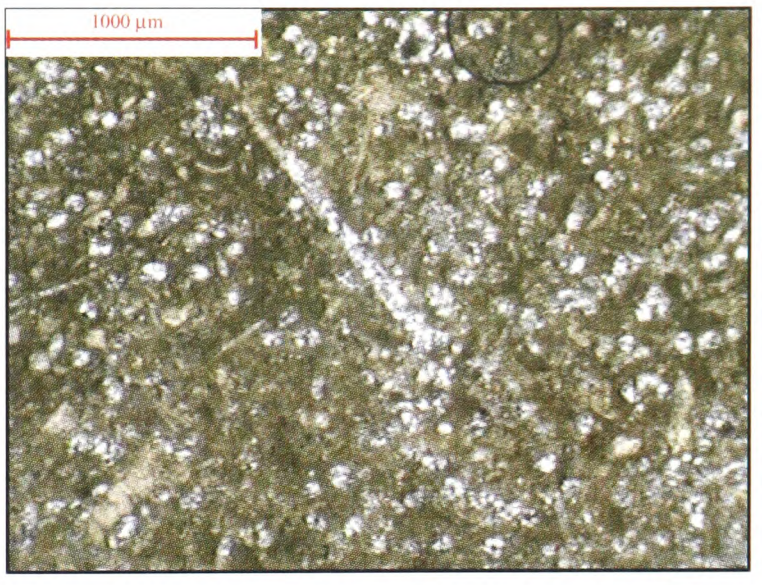

Plate A3.2.xvii. PV-20 (XPL): Biomicrite. Sponge spicules are the only bioclastic constituent of this spiculitic chert nodule.

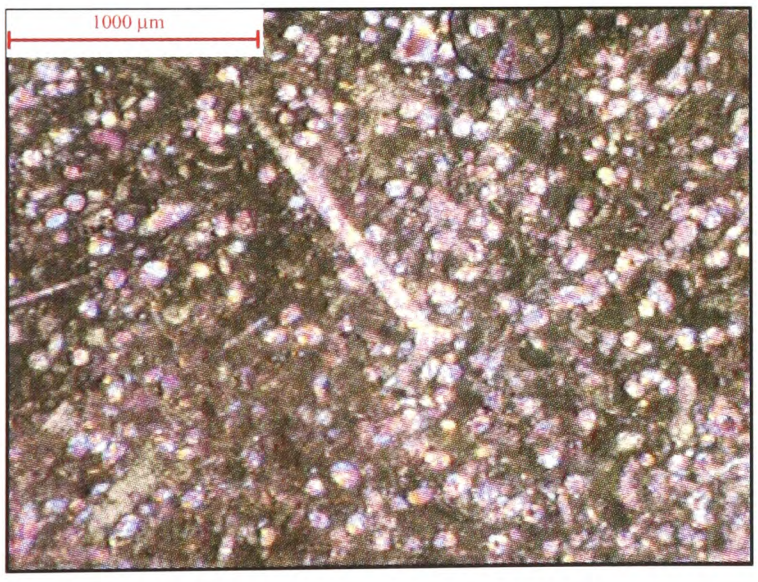

Plate A3.2.xviii. PV-20 (XPL & Tint): Biomicrite. Sponge spicules are the only bioclastic constituent of this spiculitic chert nodule.

Plate A3.2.xix. SVQ-12 (PPL): Silicified oomicrite. This oomicrite is virtually completely replaced by silica forming a chert nodule.

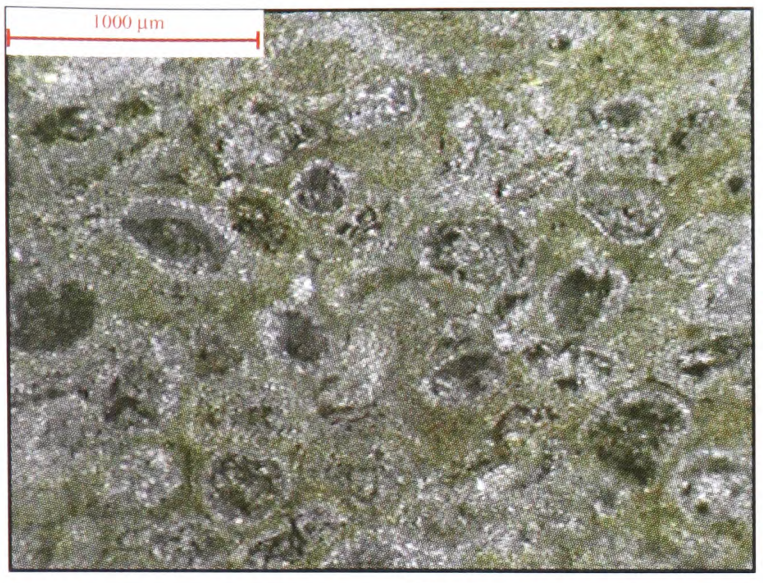

Plate A3.2.xx. SVQ-12 (XPL): Silicified oomicrite. This oomicrite is virtually completely replaced by silica forming a chert nodule.

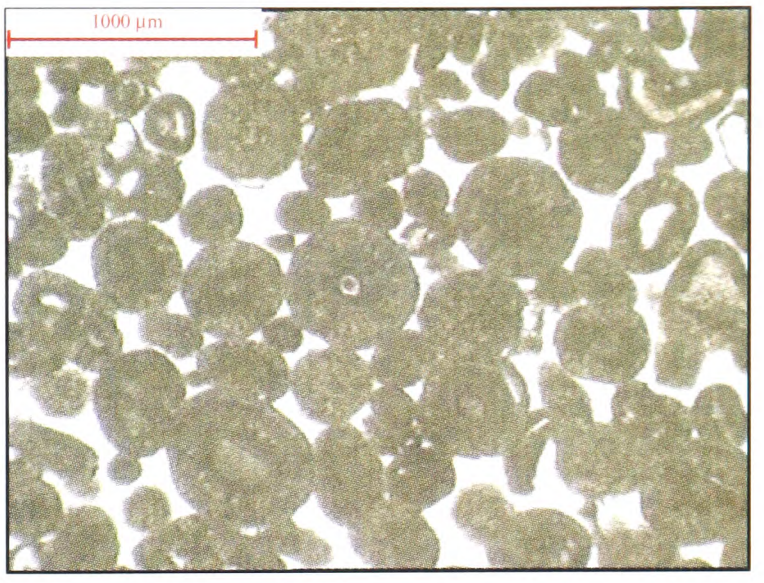

Plate A3.2.xxi. CDM-12 (PPL): Oosparite. Micritised primary radial calcite ooids in a sparry-calcite cement.

Plate A3.2.xxii. CDM 0 (PPL): Oosparite. Increased micrite content compared to those oolites further below the contact, but still cemented with sparry-calcite.

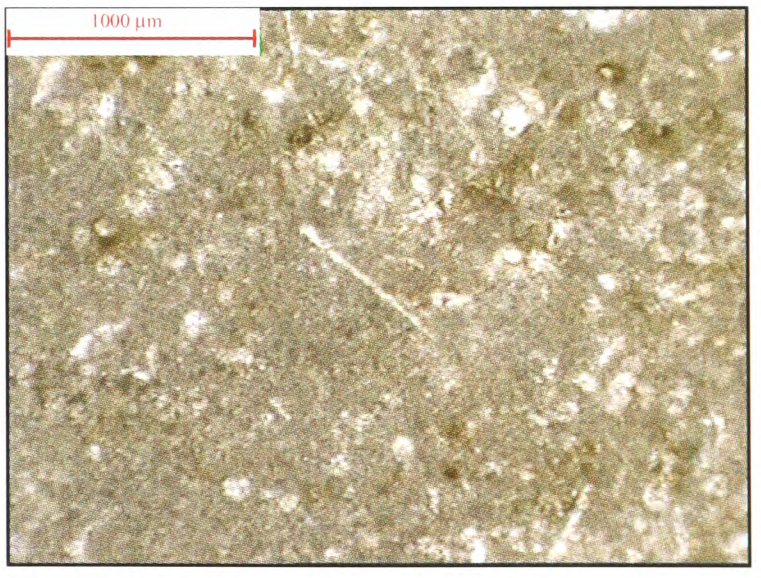

Plate A3.2.xxiii. CDM+1.5 (PPL): Fossiliferous micrite. The bioclasts are wholly represented by sponge spicules (shown).

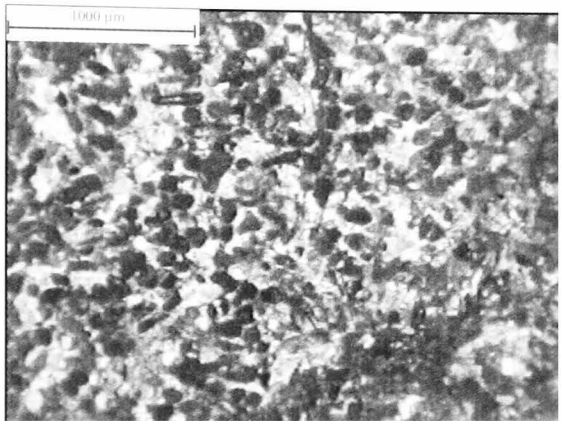

Plate A3.2.xxiv. CDM+9 (PPL): Pelmicrite. Few bioclasts can be observed. Locally, fine sparry-calcite acts as cement (shown).

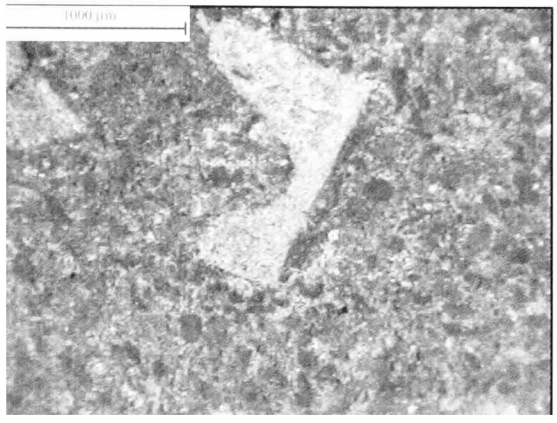

Plate A3.2.xxv. CDM+18.5 (PPL): Pelmicrite. Pelmicrite with echinoderm bioclasts locally silicified (shown).

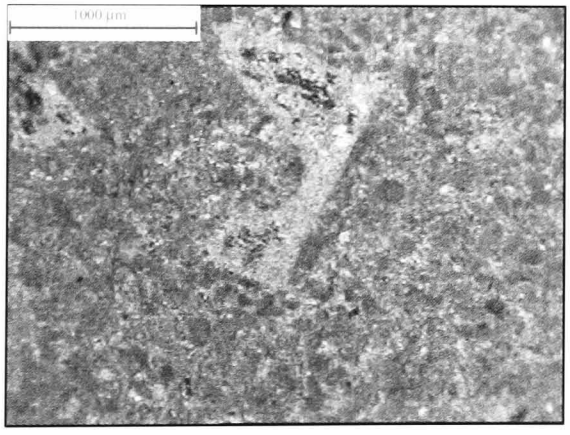

Plate A3.2.xxvi. CDM+18.5 (XPL): Pelmicrite. Pelmicrite with echinoderm bioclasts locally silicified (shown).

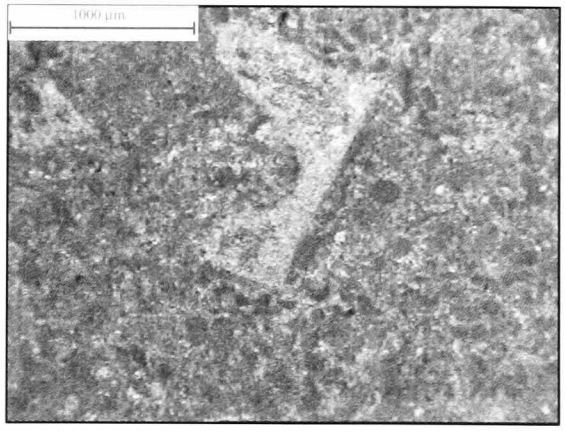

Plate A3.2.xxvii. CDM+18.5 (XPL & Tint): Pelmicrite. Pelmicrite with echinoderm bioclasts locally silicified (shown).

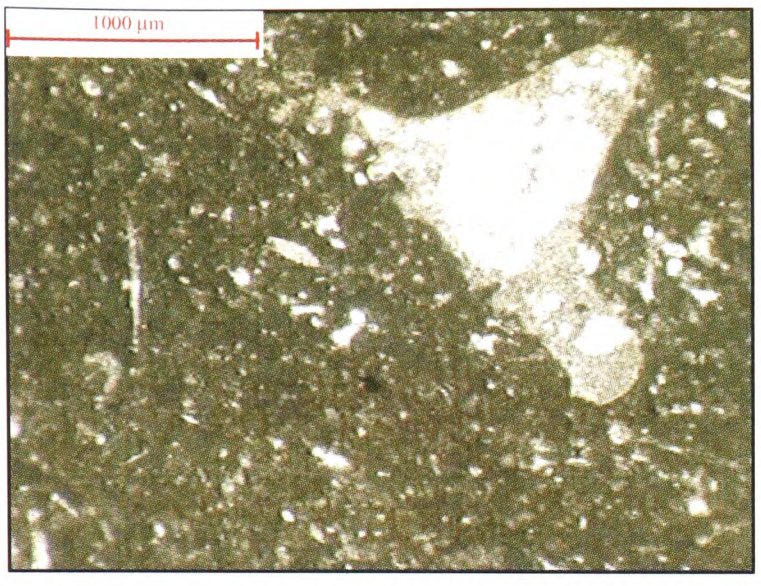

Plate A3.2.xxviii. CDM+19.5 (PPL): Biomicrite. Bioclasts include sponge spicules (shown) and echinoderm fragments, locally silicified (shown).

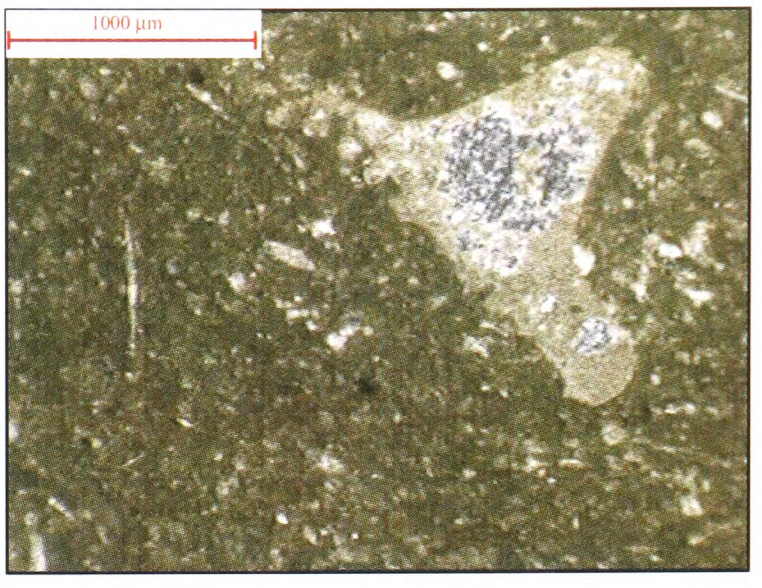

Plate A3.2.xxix. CDM+19.5 (XPL): Biomicrite. Bioclasts include sponge spicules (shown) and echinoderm fragments, locally silicified (shown).

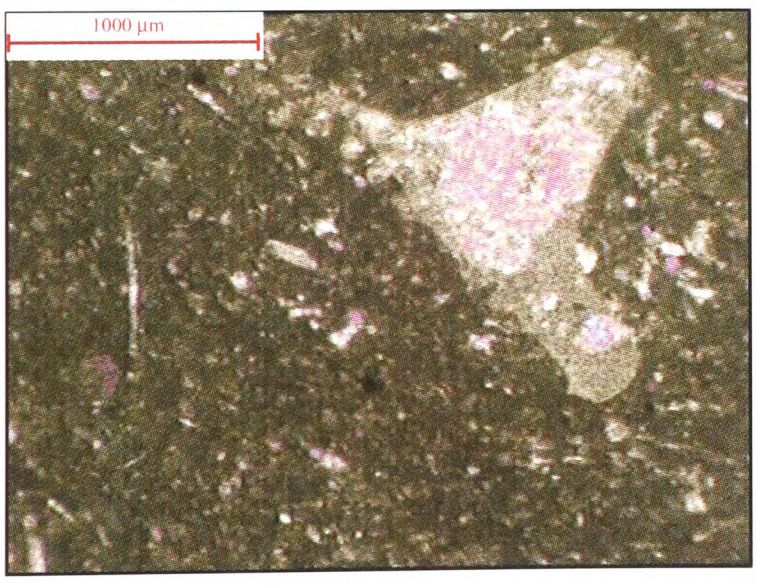

Plate A3.2.xxx. CDM+19.5 (XPL & Tint): Biomicrite. Bioclasts include sponge spicules (shown) and echinoderm fragments, locally silicified (shown).

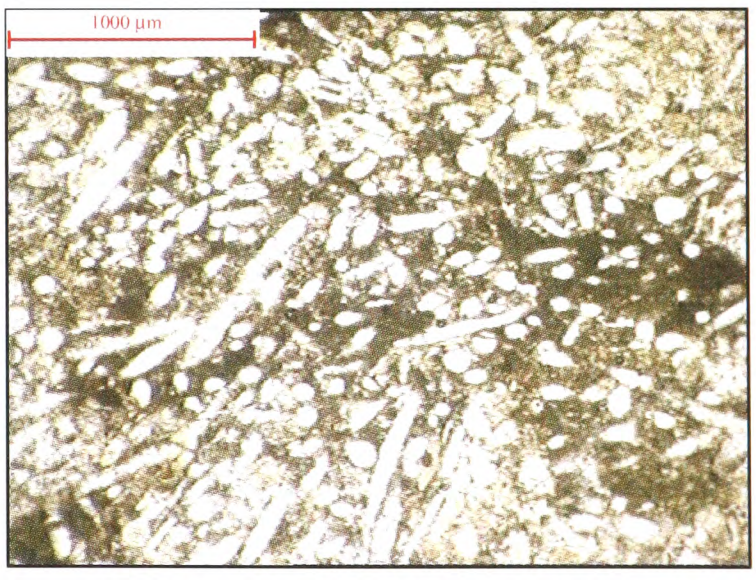

Plate A3.2.xxxi. CDM+21.2 (PPL): Biomicrite. Bioclasts are wholly consituted by sponge spicules in this spiculitic chert nodule.

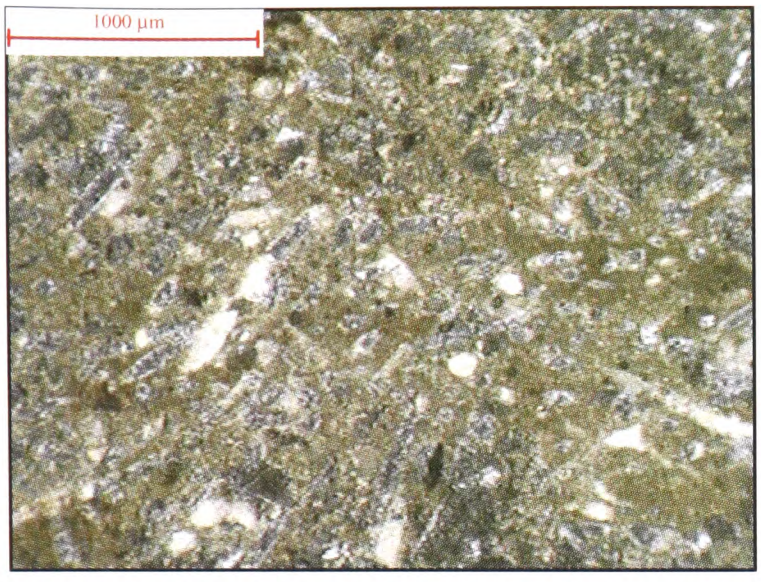

Plate A3.2.xxxii. CDM+21.2 (XPL): Biomicrite. Bioclasts are wholly consituted by sponge spicules in this spiculitic chert nodule.

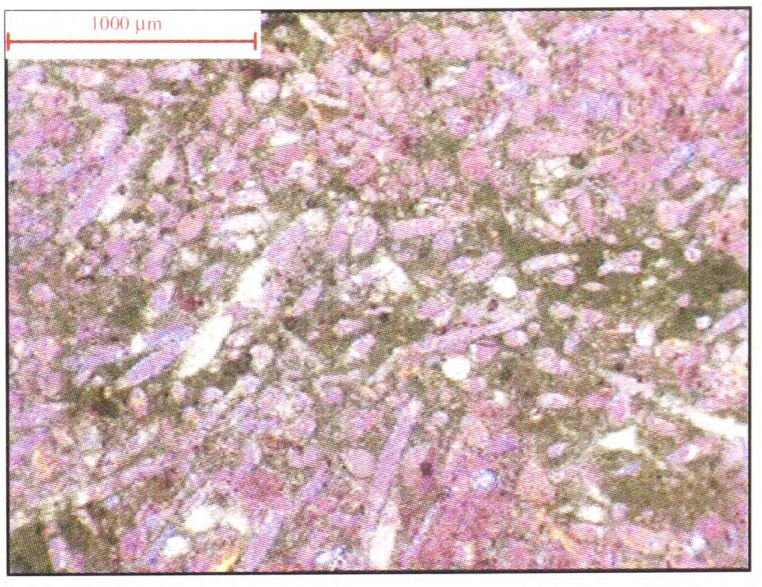

Plate A3.2.xxxiii. CDM+19.5 (XPL & Tint): Biomicrite. Bioclasts are wholly consituted by sponge spicules in this spiculitic chert nodule.

A3.3: Friuli photomicrographs

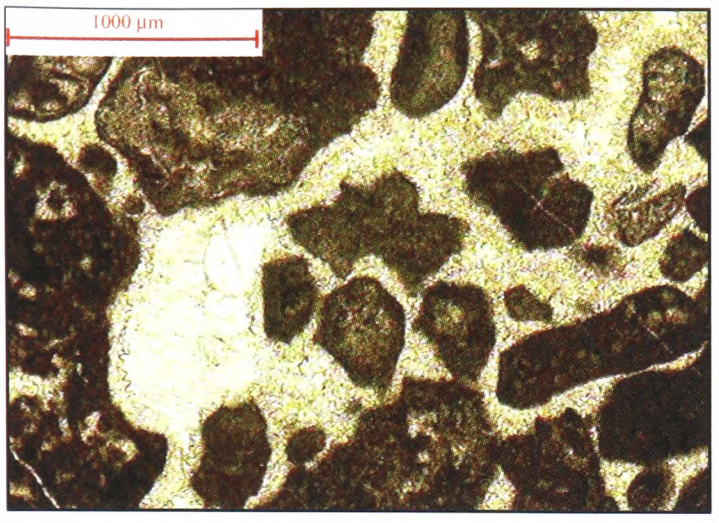

Plate A3.3.i. VC+210 (PPL): Intrasparite. Intraclasts, algae, gastropod fragments and echinoid spines are the major constituents of this grainstone. Two obvious phases of cementation.

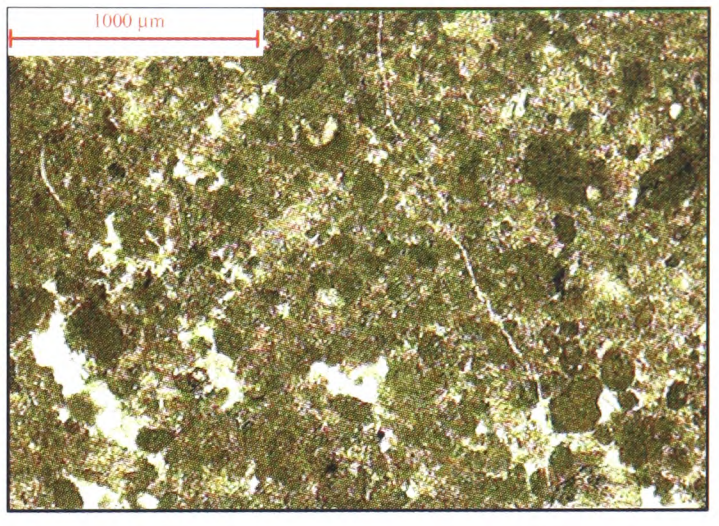

Plate A3.3.ii. VC+230 (PPL): Pelmicrite. Algae and benthic forams are secondary constituents after peloids. Minor void-filling calcite indicates poorly developed birdseye formation.

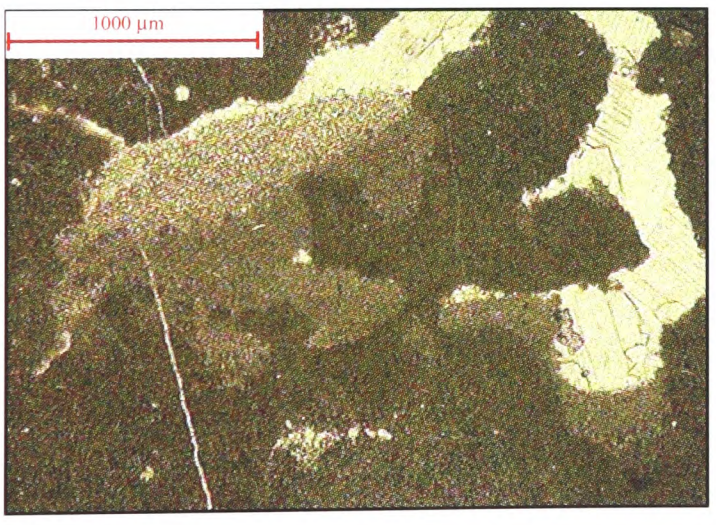

Plate A3.3.iii. VC+245 (PPL): Fossiliferous micrite. This algal bindstone also contains otracods and fenestrae that locally diplay vadose-silt geopetal indicators (pictured).

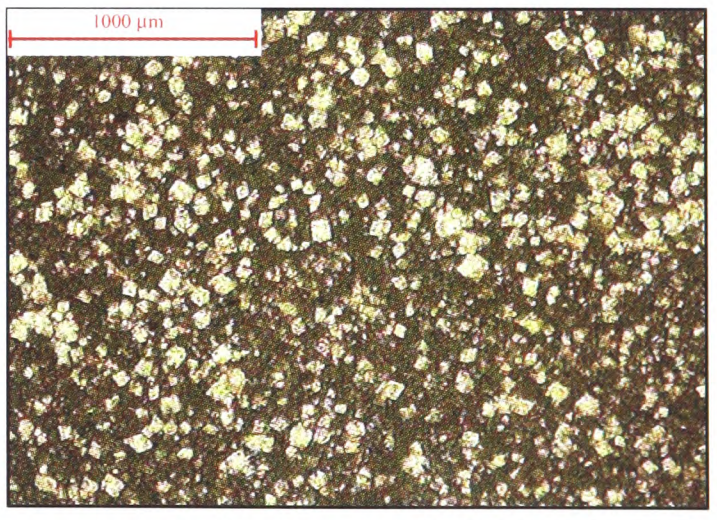

Plate A3.3.iv. VC+265 (PPL): Dolomudstone. Dolomite rhombs are clearly apparent in this micritic matrix.

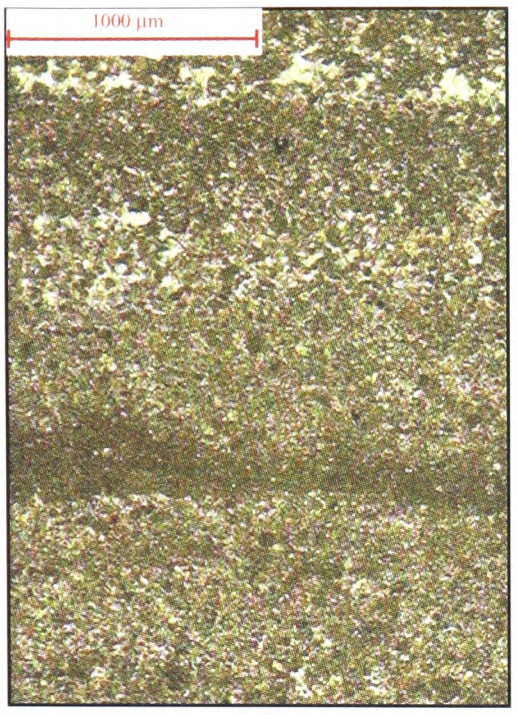

Plate A3.3.v. VC+285 (PPL): Pelmicrite. This packstone is laminated and quasi-stromatolitic in hand-specimen. It also contains benthic foraminifera and ostracods.

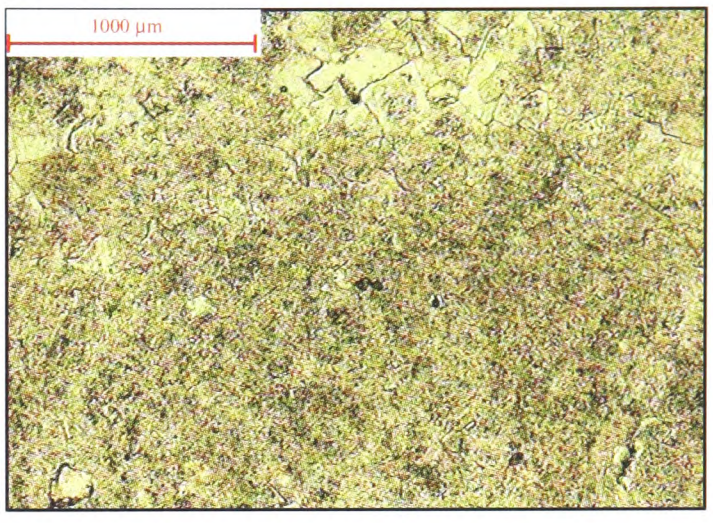

Plate A3.3.vi. VC+410 (PPL): 100% recrystallised. Little primary structure or textures remain after recrystallisation by calcite.

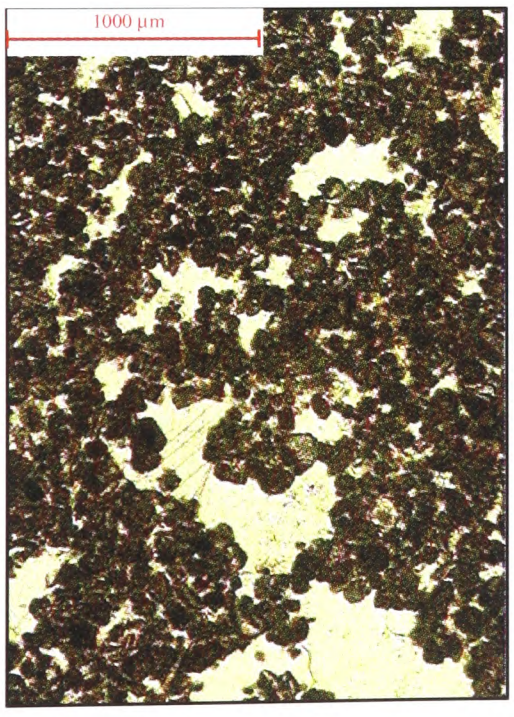

Plate A3.3.vii. VC+585 (PPL): Pelmicrite. This Loferitic pelmicrite contains abundant birseyes (shown), locally with vadose silt and benthic foraminifera are the main bioclastic constituent.

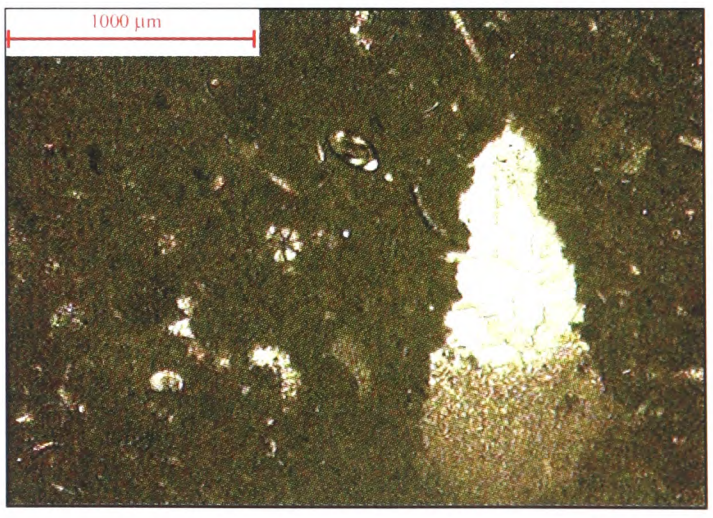

Plate A3.3.viii. VC+650 (PPL): Fossiliferous micrite. Fenestrae with vadose silt (shown), and also rich in benthic foraminifera, osctracods, gastropods and bivalves.

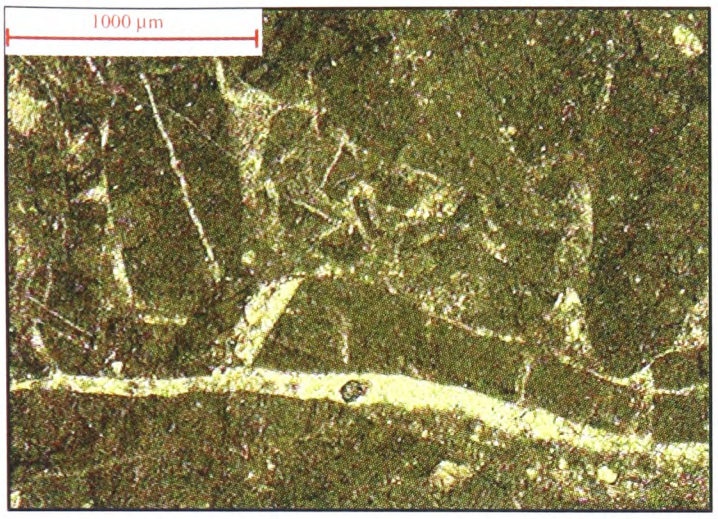

Plate A3.3.ix. VC+705 (PPL): Intramicrite. Microbreccia with localised dolomite along fractures.

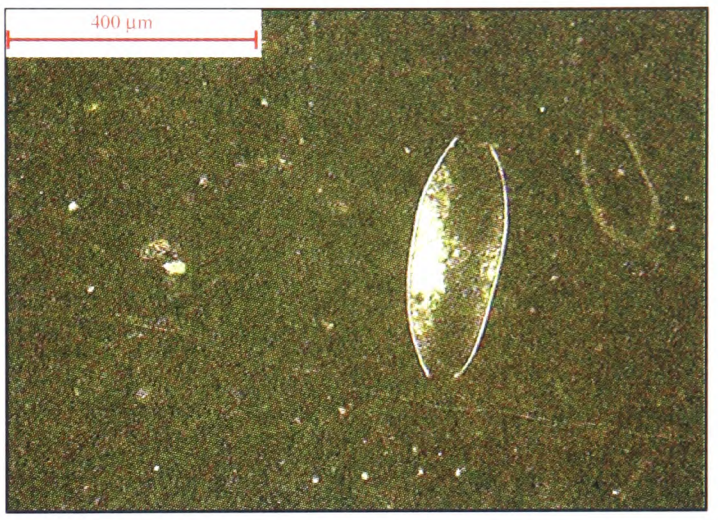

Plate A3.3.x. VC+785 (PPL): Fossiliferous micrite. Ostracods and sponge spicules are the bioclastic constituents, set within a micritic matrix.

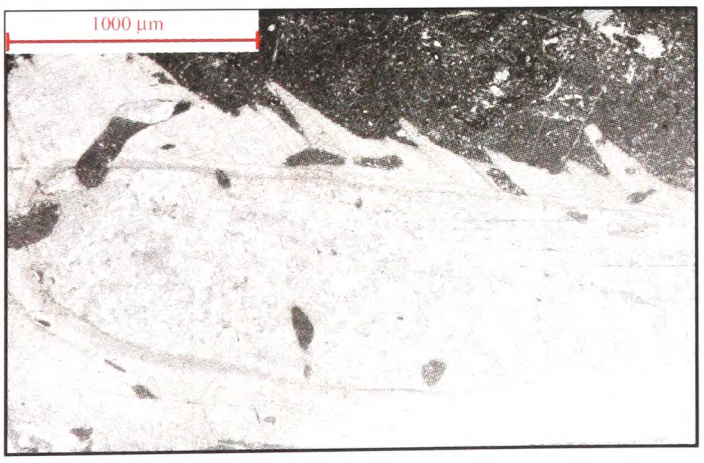

Plate A3.3.xi. VC+1150 (PPL): Biomicrite. This rudstone is packed with rudists, benthic foraminifera and gastropods.

Plate A3.3.xii. VC+1165 (PPL): Biomicrite. This rudstone also contains benthic foraminifera and ostracods.

Plate A3.3.xiii. *Clypeina jurassica.*

Plate A3.3.xiv. *Salpingoporella dinarica.*

Plate A3.3.xv. *Campanellula capuensis.*

Plate A3.3.xvi. *Cuneolina pavonia parva.*

Plate A3.3.xvii. *Chrysalidina gradata.*

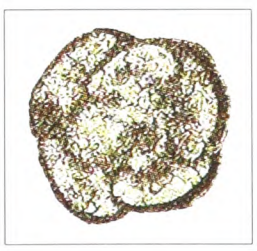

Plate A3.3.xviii. *Accordiella conica.*

Plate A3.3.xix. *Orbitoides tissoti.*

A3.4: Campania–Lucania photomicrographs

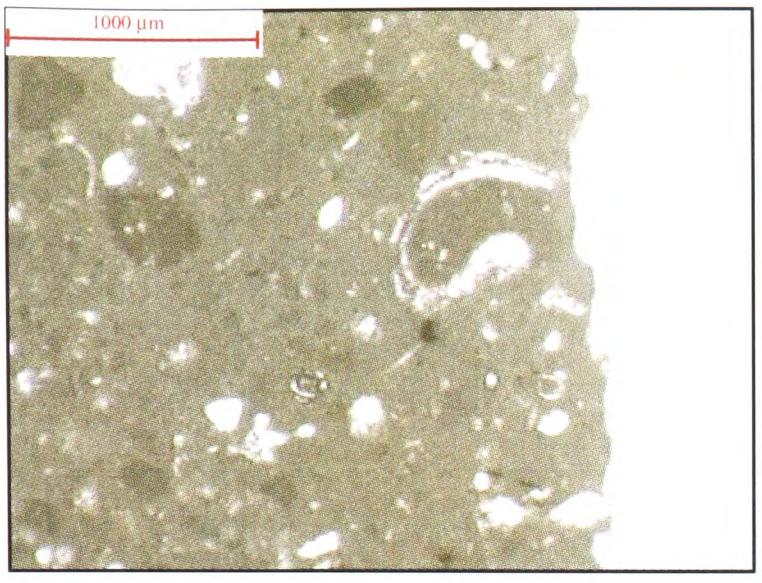

Plate A3.4.i. MS+160.5 (PPL): Biomicrite. Bioclasts include benthic foraminifera, bivalve fragments, and echinodermal debris.

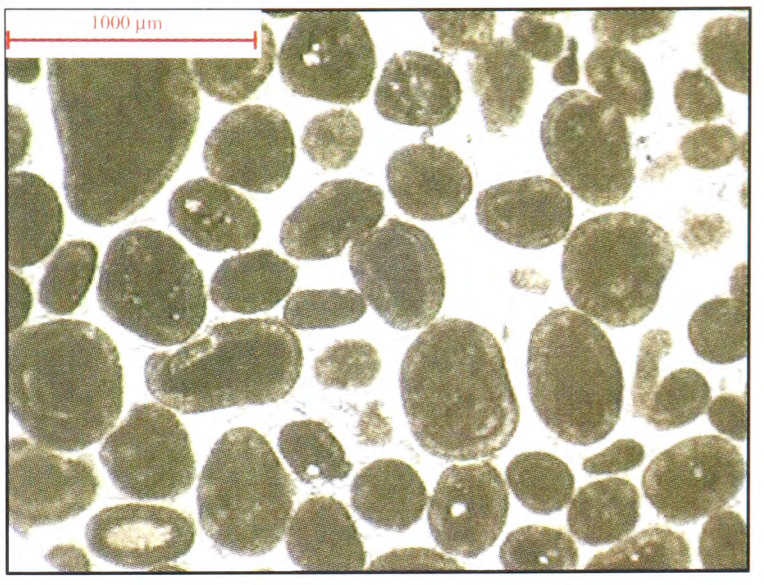

Plate A3.4.ii. MS+177.5 (PPL): Oosparite. Ooids with generally micritic nucleii, and micritised cortices. Floating–point contacts in a sparry-calcite cement (two phases of growth).

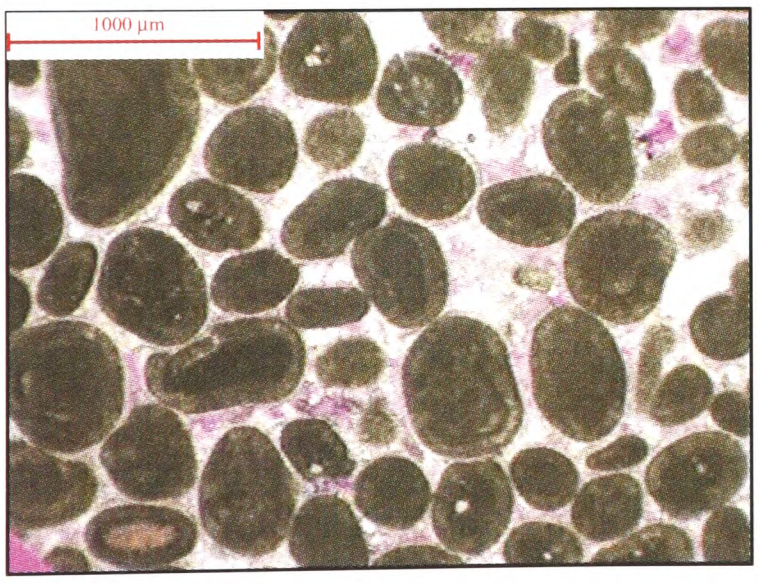

Plate A3.4.iii. MS+177.5 (XPL): Oosparite. Ooids with generally micritic nucleii, and micritised cortices. Floating–point contacts in a sparry-calcite cement (two phases of growth).

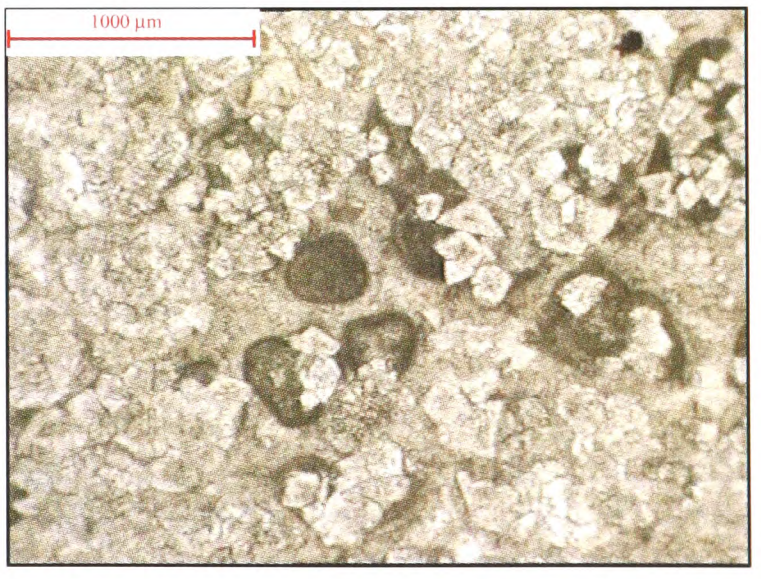

Plate A3.4.iv. MS+183.5 (PPL): Dolomitised oosparite. Micritised ooids in sparry-calcite cement are replaced by pervasive dolomite recrystallisation.

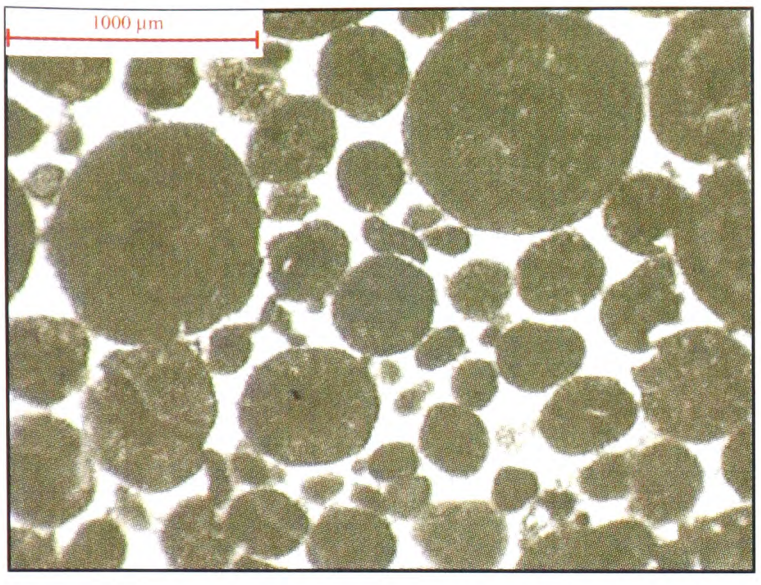

Plate A3.4.v. MS+198.5 (PPL): Oosparite. Micritised ooids (vaguely bimodal size distribution) in a sparry-calcite cement.

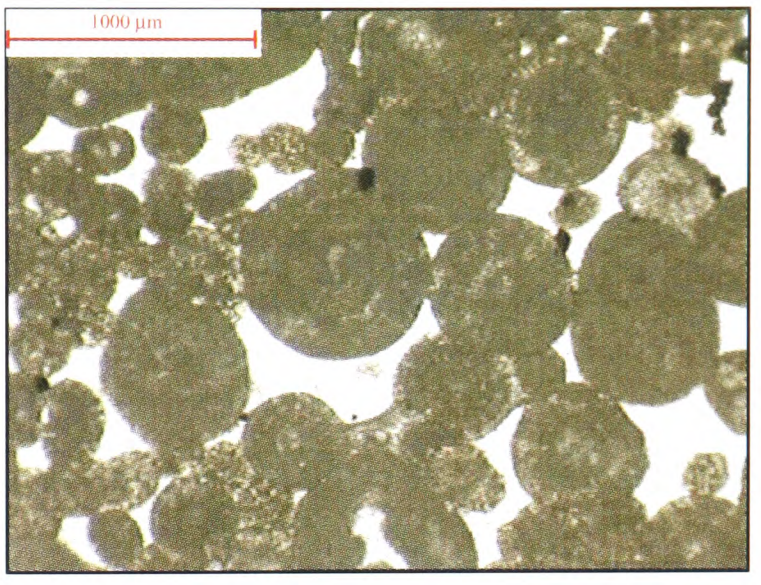

Plate A3.4.vi. MS+280 (PPL): Oosparite. Micritised ooids in a sparry-calcite cement, with localised micritic matrix.

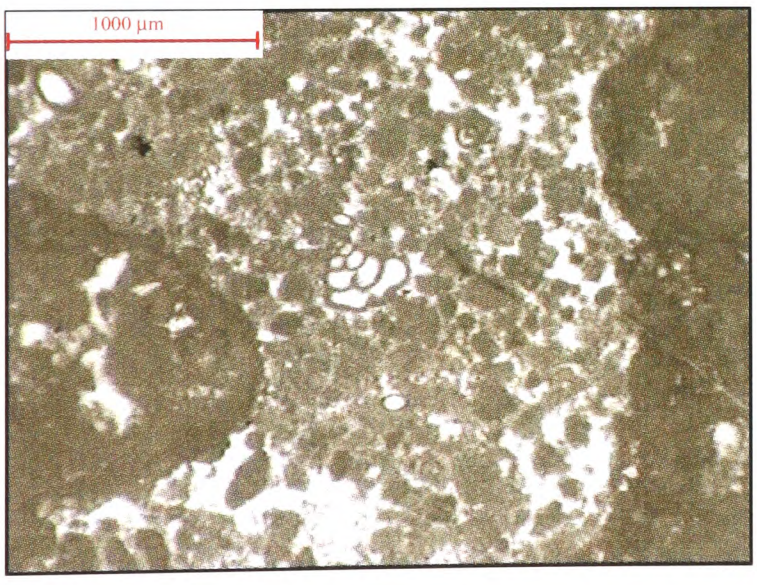

Plate A3.4.vii. MS+283 (PPL): Intramicrite. Micritic intraclasts in a pelmicritic matrix. Benthic foraminifera are abundant, and localised vugs of sparry-calcite appear to represent poorly developed birdseyes.

Plate A3.4.viii. MS+286 (PPL): Fossiliferous micrite. Gastropods, bivalves and benthic foraminifera constitute the bioclastic content.

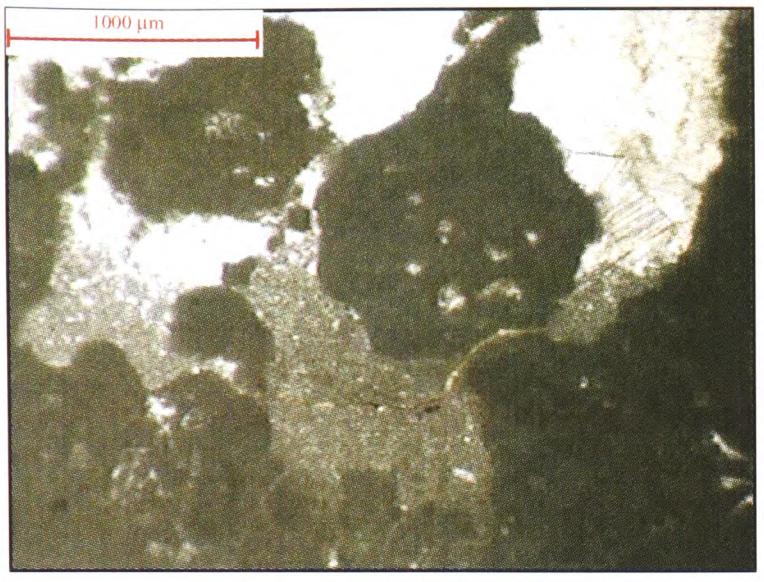

Plate A3.4.ix. MS+293 (PPL): Fossiliferous micrite. Benthic foraminifera, gastropods and bivalves constitute the bioclastic content, and well-developed birdseyes, locally with vadose silt (shown) can be observed.

Plate A3.4.x. RDP+4 (PPL): Dolomitised fossiliferous micrite. Benthic foraminifera wholly constitute the bioclastic content, and localised dolomite replacement is found along veins and as floating rhombs (all shown).

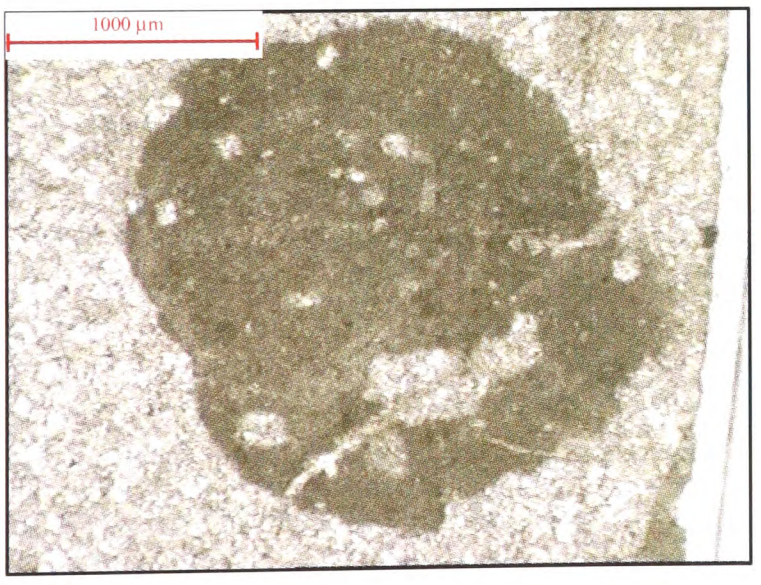

Plate A3.4.xi. RDP+11 (PPL): Dolomitised fossiliferous micrite. Virtually complete pervasive replacemnt of fossiliferous micrite by dolomite.

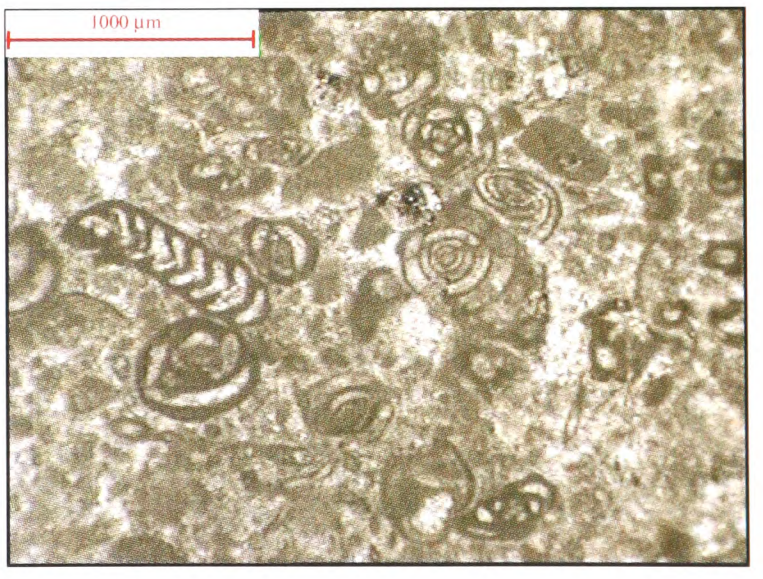

Plate A3.4.xii. RDP+18 (PPL): Biomicrite. Bioclasts consist of benthic foraminifera and localised rudist fragments.

Plate A3.4.xiii. RDP+58.8 (PPL): Fossiliferous micrite. Bioclasts consist of benthic foraminifera. Micrite has localised "crinkly" lamination with organic/ferruginous residue (shown). The former is likely, as samples contain elevated organic-carbon levels.

Plate A3.4.xiv. RDP+81 (PPL): Intramicrite. Intraclasts of fossiliferous micrite (with rare planktonic foraminifera) in a biomicritic matrix (localised peloids also). Benthic foraminifera predominate the bioclastic material.

Plate A3.4.xv. RDP+81 (PPL): Intramicrite. Detail of RDP+81 (x10) illustrating rare planktonic foraminifera (bottom right).

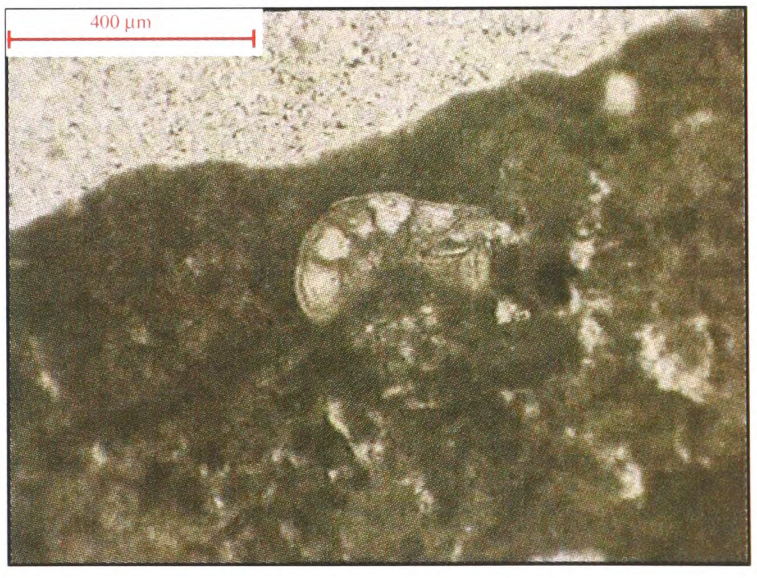

Plate A3.4.xvi. RDP+90.6 (PPL): Intramicrite. Detail of RDP+90.6 (x10) illustrating rare candidate planktonic foraminifera.

A4: Atlas of outcrop photographs

A4.2: Trento outcrop photographs

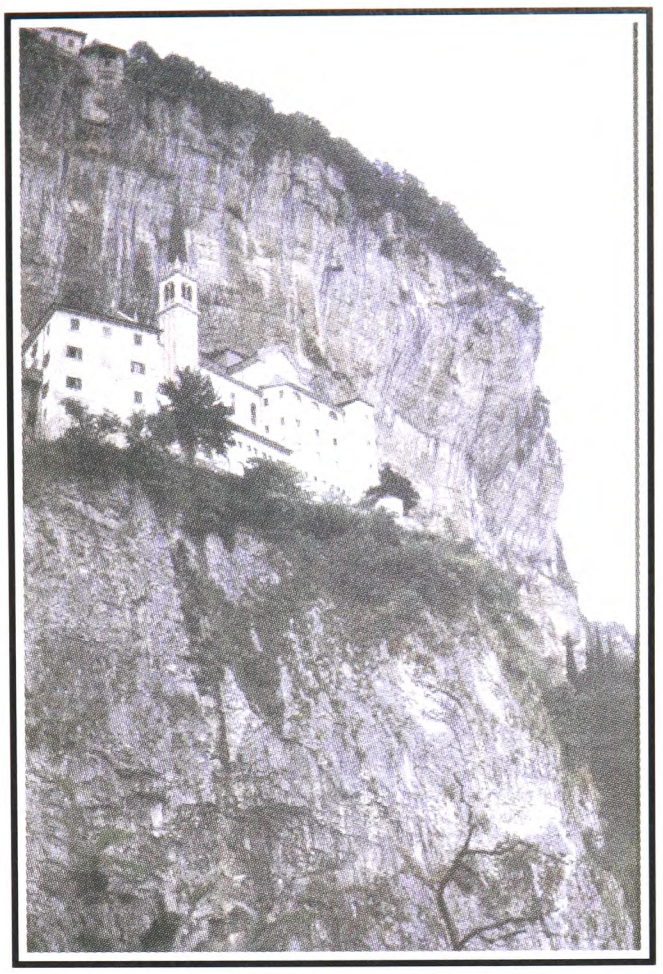

Plate A4.2.i. The Madonna della Corona sanctuary built into the San Vigilio Oolite on what was the western margin of the Trento platform. The contact with the Rosso Ammonitico lies under the tree line at the top of the cliff. The section continues for over 600 m below the level of the photograph.

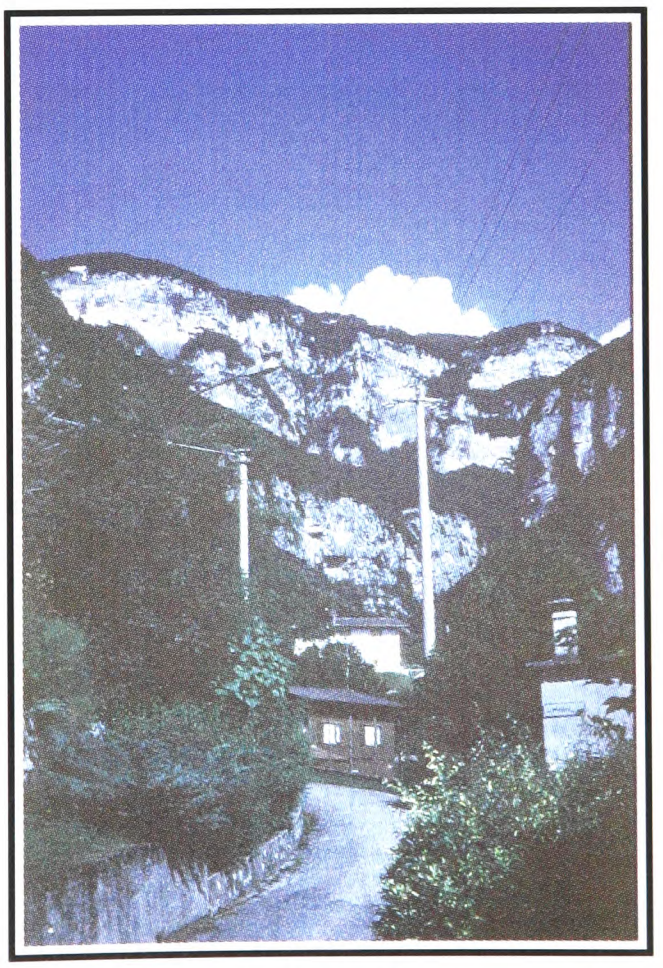

Plate A4.2.ii. The complete Madonna della Corona section as viewed from the town of Brentino, below (the sanctuary can be seen in the top left of the cliff).

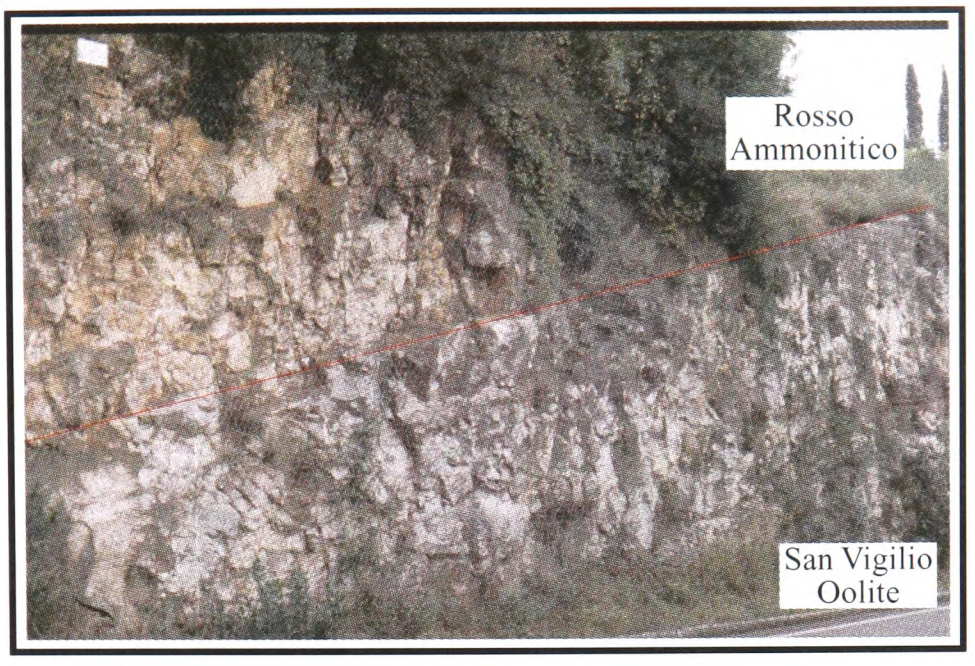

Plate A4.2.iii. The San Vigilio roadside contact between the San Vigilio Oolite and the overlying Rosso Ammonitico. Ammonites found above and below the contact provide the biostratigraphic anchor point for the Trento Platform chemostratigraphic profiles (as dated by Sturani, 1964).

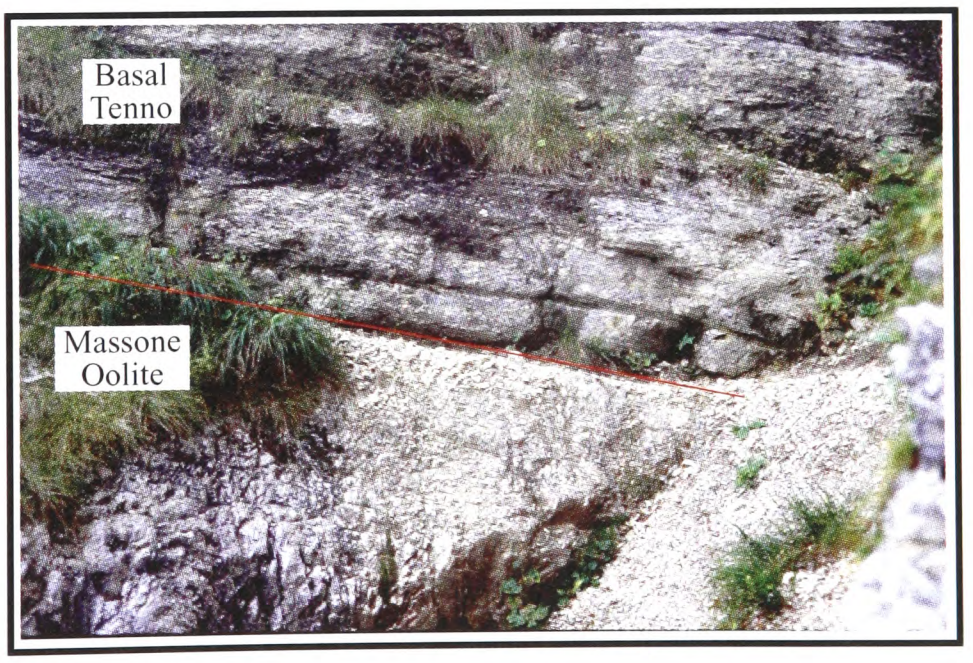

Plate A4.2.iv. The conatct between the Massone Oolite and overlying shales of the Basal Tenno Formation at the Colma di Malcesine.

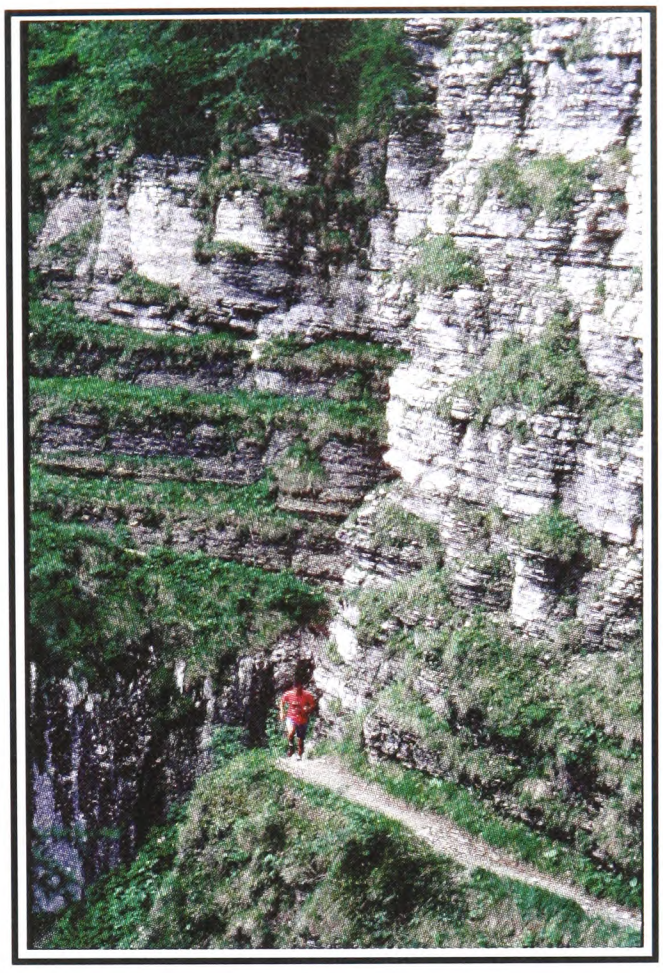

Plate A4.2.v. The cyclically-bedded Upper Tenno Formation (right fore-ground), which overlies the Basal Tenno and Massone Oolite Formations (left background) at the Colma di Malcesine.

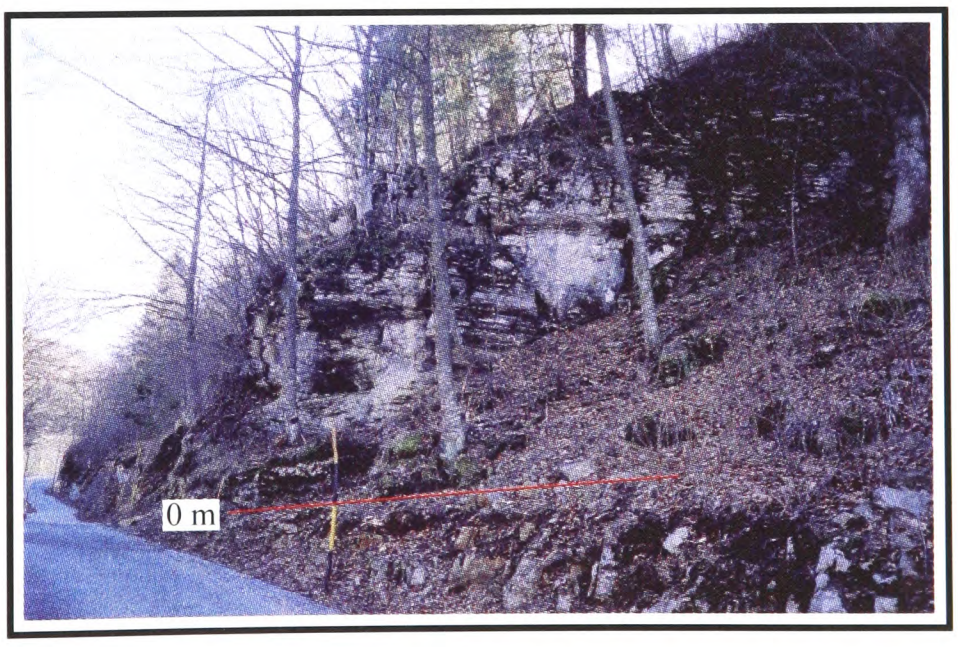

Plate A4.2.vi. The 0 m level of the Sega d'Ala section: Basal Tenno, Upper Tenno Formations and San Vigilio Oolite lie above, and the Misone and Massone Oolite Formations below.

Plate A4.2.vii. The cyclically bedded Misone Formation at the Sega d'Ala section. Scale = 1 m.

Plate A4.2.viii. Cross-bedded crinoid-rich San Vigilio Oolite at the Sega d'Ala section. Scale = 35 cm.

A4.3: Friuli outcrop photographs

Plate A4.3.i. The +357 m lime green interval and red clay interval in the Val Cellina section on the Friuli platform. Hammer for scale.

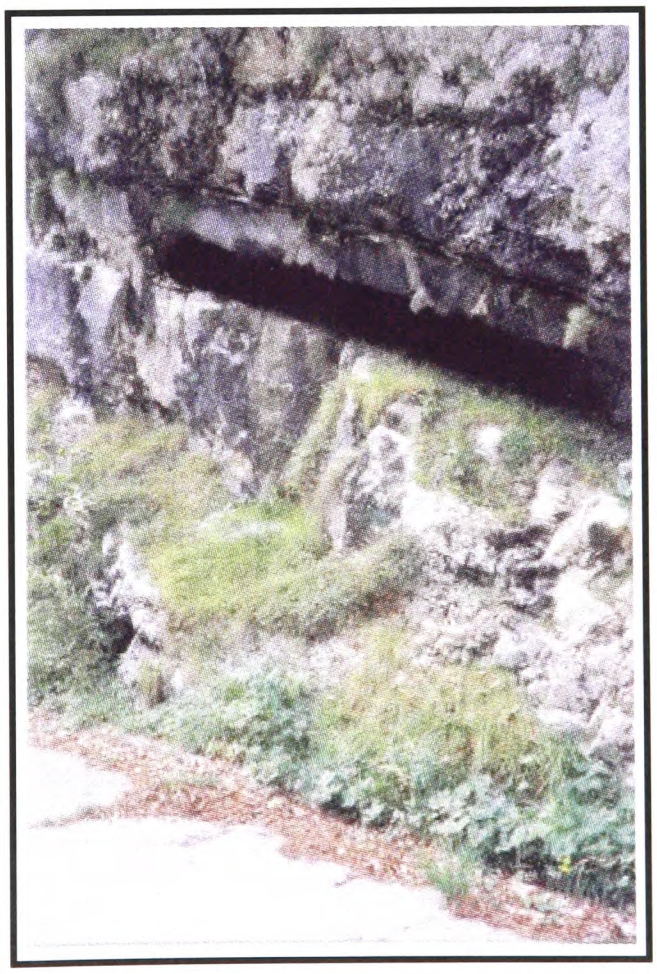

Plate A4.3.ii. The +552 m eroded clay-rich interval at the Val Cellina section. Eroded horizon = 50 cm.

Plate A4.3.iii. The Val Cellina megabreccia found between two graben-like normal faults: +720 to +760 m. Pen for scale = 14 cm.

Plate A4.3.iv. The normal fault that can be observed at +760 m in the Val Cellina section. Displacement in non-quantifiable. Ruler for scale = 2.6 m.

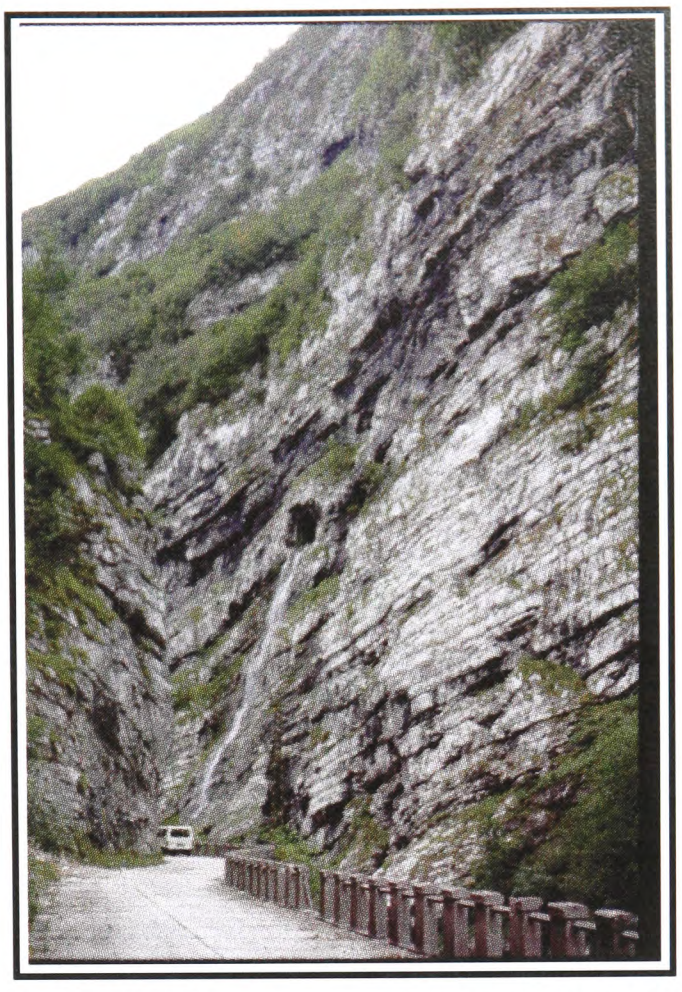

Plate A4.3.v. The cyclically-bedded limestone units of the Val Cellina section between +600 and +1000 m.

Plate A4.3.vi. An example of the typical mint-green clay horizons found between +760 and +1000 m. Hammer for scale.

A4.4: Campania–Lucania outcrop photograph

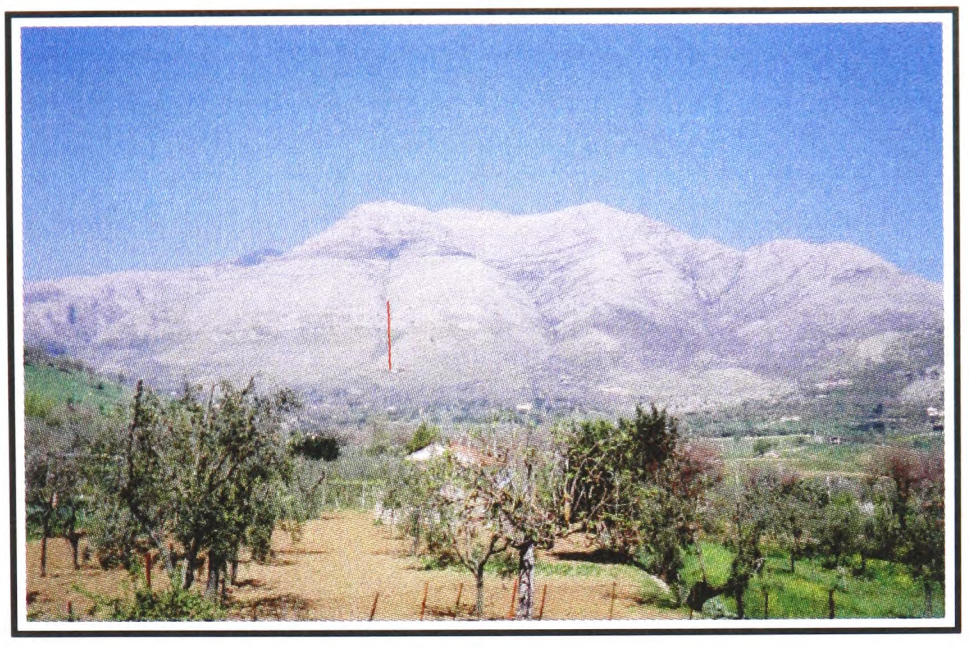

Plate A4.4.i. The view of the Monte Sorgenza, Aurunci Mountains from the approach drive described in the text. During the Mesozoic, the Monte Sorgenza was located on the western margin of the Campania–Lucania platfrom. The section studied is marked.

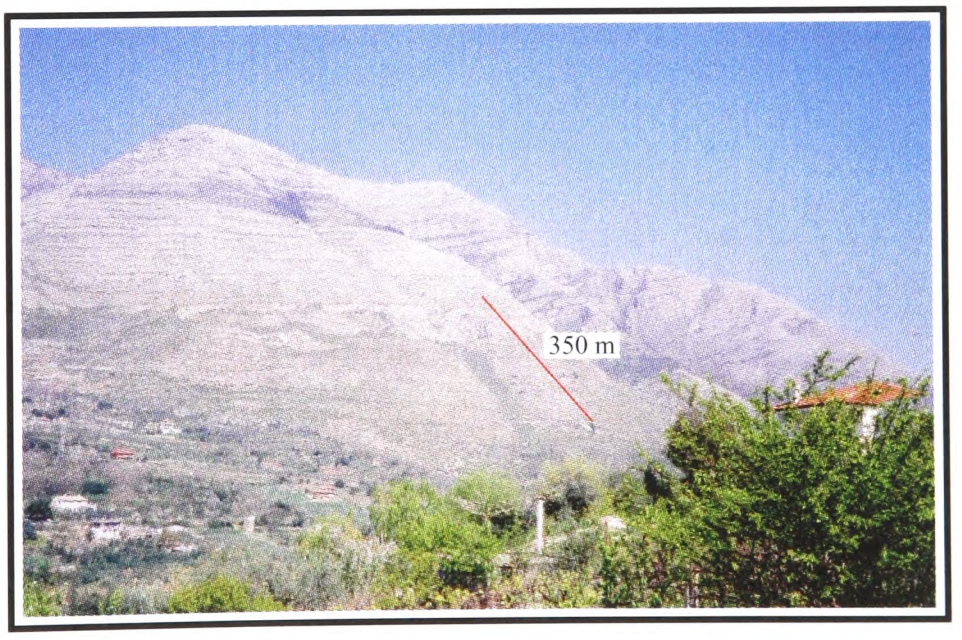

Plate A4.4.ii. The Monte Sorgenza as viewed from the town of Castellonorato. The 350 m marked is the vertical thickness of the section studied. N.B. the upsection continuation of outcrop, beyond the point studied in this project.

Plate A4.4.iii. A concentrated accumulation of *Lithiotis* observed at +83.4 m in the Monte Sorgenza section.

Plate A4.4.iv. Thin-bedded shales at +165 m in the Monte Sorgenza section. Pen for scale = 14 cm.

Plate A4.4.v. The cyclically-bedded limestone units of the Calcari Maculati at +173 m in the Monte Sorgenza section. Pen for scale = 10 cm.

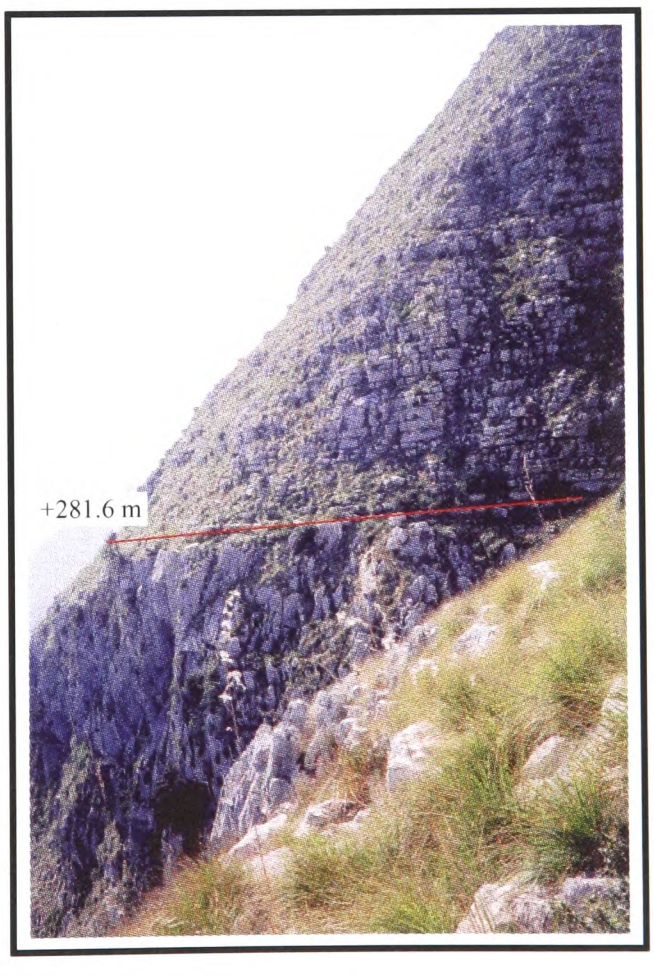

Plate A4.4.vi. The contact between the massive Calcari Oolitici and the overlying cyclically-bedded Calcari Maculati (+281.6 m).

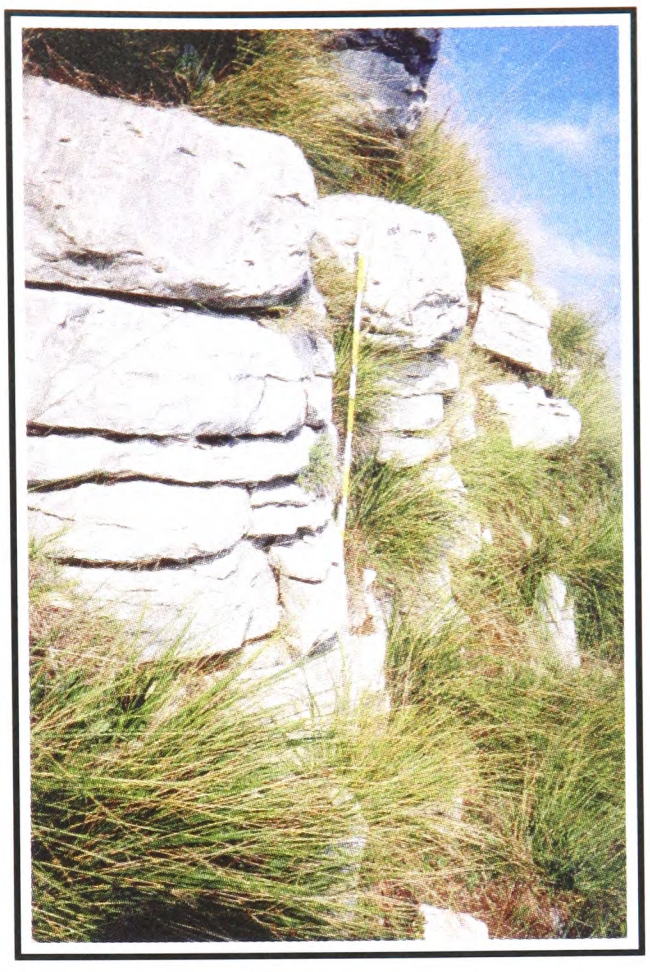

Plate A4.4.vii. The thin-bedded Calcari Maculati at +285 m in the Monte Sorgenza section. Ruler for scale = 1 m.

Plate A4.4.viii. Birdseye limestones at +337.3 (and above to the top of the studied section) in the Monte Sorgenza section. Ruler for scale = 35 cm.

Plate A4.4.ix. The Raia del Pedale road section on the Campania–Lucania platform, southern Italy.

Plate A4.4.x. The dolomitic shales at +18 m in the Raia del Pedale section. Camera for scale.

Plate A4.4.xi. The transition to massive limestone above the dolomitic shales at +25 m in the Raia del Pedale section on the Campania–Lucania platform. Ruler for scale = 2 m.

Plate A4.4.xii. Relatively thin-bedded interval of dark, 'clinky' limesone observed at +52 m in the Raia del Pedale section: the chemostratigraphically-contrained Cenomanian–Turonian boundary. Hammer for scale.

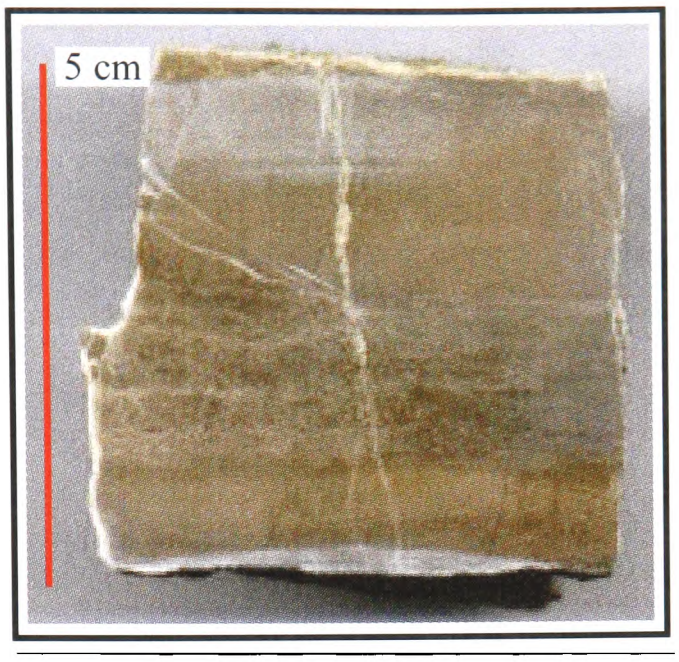

Plate A4.4.xiii. Detail of a polished hand specimen taken from +51.65 m in the Raia del Pedale section. The dark colour is due to the presence of organic matter.

Plate A4.4.xiv. Intraclastic breccia at +94 m in the Raia del Pedale section. Hammer for scale.

Plate A4.4.xv. An interval concentrated in rudist specimens and fragments at +168 m in the Raia del Pedale section. Hammer for scale.